THE UNIVERSITY
of EDINBURGH

Capacity of FRP Strengthened Steel Plate Girders against Shear Buckling Under Static and Cyclic Loading

Zaid Mohammed Kani Al-Azzawi

A thesis submitted for the degree of
Doctor of Philosophy

THE UNIVERSITY
of EDINBURGH

Rajab 1437_H May 2016

This page is intentionally left blank

Capacity of FRP Strengthened Steel Plate Girders against Shear Buckling Under Static and Cyclic Loading

by

Zaid Mohammed Kani Al-Azzawi

This thesis has been supervised by

Dr. Tim Stratford

Prof. Michael Rotter

The examining committee consisted of

Prof. Stuart Moy

Prof. Luke Bisby

This page is intentionally left blank

﴿قُلْ هَلْ يَسْتَوِي اِلَّذِينَ يَعْلَمُونَ وَالَّذِينَ لَا يَعْلَمُونَ إِنَّمَا يَتَذَكَّرُ أُوْلُواْ الأَلْبَابِ﴾

(سُورَة الزُّمَرْ: الآية 9)

Say: Are those equal, those who know and those who do not know? Only the men of understanding are mindful.

(Holly Quran- Chapter 39, Verse 9)

وقَدْ قِيلَ في العِلْم:

العِلْمُ أشْرَفُ مَا رَغِبَ فيهِ الرَّاغِبُ وأفْضَلُ ما طَلَبَ وَجَدَّ فيهِ الطَالِبُ، وأنْفَعُ مَا كَسَبَهُ واقْتَناهُ الكَاسِبُ، لِأنَّ شَرَفَهُ يُثْمِرُ عَلى صَاحِبِهِ، وَفَضْلُهُ يُنْمِي عَلى طَالِبِهِ.

الماوَرْدي، توفي سنة 450هـ (1058م)

SCIENCE is the most honourable wish for any wisher, the best thing a seeker could seek for, and the most useful earning for a gainer. This is because science honour will bear fruit on its owner and that its bounty will develop the tracker.

Al-Mawardy – *a Muslim scholar lived in Iraq, Died in 1058*

This page is intentionally left blank

To My Family...

Without YOU, I would never have done it.

This page is intentionally left blank

Declaration

This thesis and the work described within have been completed solely by Zaid Mohammed Kani Al-Azzawi at the Institute for Infrastructure and Environment in the School of Engineering at the University of Edinburgh, under the supervision of Dr Tim Stratford and Prof Michael Rotter. Where others have contributed or other sources are quoted, references are given.

Zaid Al-Azzawi
May 2016

This page is intentionally left blank

ACKNOWLEDGMENT

All praise is due to Allah, The Almighty, who helps me when I am in need and guides me for the path of truth indeed.

I start by thanking all the people of IRAQ who sponsored this work. Mesopotamians, you have made the first known civilization on earth and you taught mankind how to write; I'm sure we will overcome our calamity very soon.

My deep appreciation and gratitude for everybody who taught me right from the alphabetic till I finished my PhD. Everyone of them has a fingerprint in this work.

I would like to express my gratitude and appreciation for all the help, support, and guidance of my supervisors Dr. Tim Stratford and Prof. Michael Rotter.

Thank you Prof. Luke Bisby for being my unofficial third supervisor. Your guidance and support were always important in critical times.

Dr. Firas Assoodani; my good friend and colleague, Thank you for all your help, support, and kind review.

I would also like to express my gratitude to the unseen staff. The technicians, the administrators, and all the kind staff who works silently to help the students achieve their goals and finish their study.

Last but not least, my friends and colleagues at the University of Edinburgh who were themselves a source of inspiration and their work created a competitive atmosphere encouraging everyone to work harder and be more ambitious.

Thank you all...Your names will always be engraved in my heart.

This page is intentionally left blank

ABSTRACT

Civil engineers are presently faced with the challenge of strengthening and repairing many existing structures to assure or increase their structural safety. The reasons for this include changes in the use of structures, and increased traffic loads on bridges. In Iraq, for example, several highway bridges needed to accommodate increased axle load during the transportation of huge turbines for electricity generating stations. The requirement for structural strengthening and repair methods is, however, driven by the worldwide need to ensure the safety and sustainability of our aging infrastructure which is deteriorating at a rate faster than it can be renovated. The ever increasing damage caused by environmental effects and the corrosion of steel and deterioration of concrete, reduce structural safety and lead to disruption for the users, which can have serious economic consequences.

In a plate girder bridge, the plate girders are typically I-beams made up from separate structural steel plates (rather than rolled as a single cross-section), which are welded or, in older bridges, bolted or riveted together to form the vertical web and horizontal flanges of the beam. The two primary functions of the web plate in a plate girder are to maintain a relative distance between the top and bottom flanges and to resist the induced shear stresses. In most practical ranges of plate girder bridges' spans, the induced shear stresses are relatively low compared to the bending stresses in the flanges induced by flexure. As a result the web plate is generally chosen to be much thinner than the flanges. The web panel consequently buckles at a relatively low shear force. For steel girder structures dominated by cyclic loading, as is the case with repeated vehicle axle loads on bridges, this can lead to the so-called 'breathing' phenomenon; an out-of-plane buckling displacement that can induce high secondary bending stresses at the welded plate boundaries.

In the current work, a novel FRP strengthening technique using bonded shapes is applied to resist these out of plane deformations, and hence reduce the breathing stresses, and improve the fatigue life of the plate girder which is very different to the majority of applications of FRP strengthening that exploit the FRP for its direct tensile strength and stiffness.

The objective of the current experimental programme is to strengthen thin-walled steel girders against web shear buckling using a corrugated CFRP or GFRP panel bonded externally along the compression diagonal of the web plate. The programme was divided into three main phases, including: (1) the development of a new preformed corrugated FRP panel, and (2, 3) testing its performance in two main experimental series. The initial series involved tests on 13 steel plates strengthened with the proposed preformed corrugated FRP panel and subjected to in-plane shear loading using a specially manufactured "picture-frame" arrangement designed to induce the appropriate boundary conditions and stresses in the web plates. This initial test series investigated the performance of different forms of strengthening under static load, in preparation for another series of cyclic tests to investigate their fatigue performance. The test variables included FRP type (CFRP or GFRP), form of FRP (closed or open section), number of FRP layers, and orientation of GFRP fibres used to produce the FRP panel. In the second series, six specimens were manufactured to simulate the end panel of a plate girder. These were strengthened with the optimized FRP panel from the initial series and tested for shear buckling under repeated cyclic loading with a stress range 40-80% of the static ultimate capacity.

A considerable increase in the stiffness of the strengthened specimens is evident in the observed reductions of the maximum out-of-plane displacement. The stiffness of the strengthened specimens is assessed to be increased by a factor ranging between 3 to 9 times the stiffness of the corresponding unstrengthened specimen, depending upon the type of the FRP panel used and the aspect ratio of the tested specimens. The breathing phenomena is also significantly reduced, consequently the surface, membrane and secondary bending stresses are reduced. The 45° strengthening scheme succeeded the best both in reducing the breathing stresses and increasing the ultimate shear capacity of the specimen by 88%.

Fatigue analyses indicated that the proposed strengthening technique is able to considerably elongate the life expectancy of the strengthened plate girders by a factor ranging between 2.5 and 7 depending on the applied cyclic load amplitude. In addition, the proposed strengthening technique did not show any debonding or delamination under both static and cyclic loading which makes it a good candidate for strengthening thin-walled structural members, especially, when ductility is a

concern. In fact, the proposed strengthening technique succeeded in improving the energy absorption capacity of the strengthened specimens by a factor ranging between 1.5 and 2.5 times the corresponding control specimen which means that the ductile failure type associated with shear buckling of steel plate girders is not only maintained, but it was improved as well. This type of ductile failure is not common in other types of FRP strengthening techniques.

Finally, a geometrical and material non-linear finite element model is presented both for the steel and composite sections which showed very good correlation with test results and was capable of predicting both the strength and deformational behaviour of the tested specimens. This numerical model is used for a parametric study to support the proposed design method.

This page is intentionally left blank

Lay Summary

Civil engineers are presently faced with the challenge of strengthening and repairing many existing structures to assure or increase their structural safety. The reasons for this include changes in the use of structures, and increased traffic loads on bridges. In Iraq, for example, several highway bridges needed to accommodate increased axle load during the transportation of huge turbines for electricity generating stations. The requirement for structural strengthening and repair methods is, however, driven by the worldwide need to ensure the safety and sustainability of our aging infrastructure which is deteriorating at a rate faster than it can be renovated. The ever increasing damage caused by environmental effects and the corrosion of steel and deterioration of concrete, reduce structural safety and lead to disruption for the users, which can have serious economic consequences.

In a plate girder bridge, the plate girders are typically I-beams made up from separate structural steel plates (rather than rolled as a single cross-section), which are welded or, in older bridges, bolted or riveted together to form the vertical web and horizontal flanges of the beam. The two primary functions of the web plate in a plate girder are to maintain a relative distance between the top and bottom flanges and to resist the induced shear stresses. In most practical ranges of plate girder bridges' spans, the induced shear stresses are relatively low compared to the bending stresses in the flanges induced by flexure. As a result the web plate is generally chosen to be much thinner than the flanges. The web panel consequently buckles at a relatively low shear force. For steel girder structures dominated by cyclic loading, as is the case with repeated vehicle axle loads on bridges, this can lead to the so-called 'breathing' phenomenon; an out-of-plane buckling displacement that can induce high secondary bending stresses at the welded plate boundaries.

Imagine a sheet of paper, where two people are stretching it out and another person is trying to tear it. Imagine this sheet of paper trying to resist all these kinds of stresses and then somebody else keeps poking it with his finger repeatedly; these are the kind of stresses the web steel plate is undergoing in its daily life cycle and for decades; millions and millions of loading cycles.

In the current work, a novel FRP (fibre reinforced polymer) strengthening technique using bonded shapes is applied to resist these out of plane deformations,

and hence reduce the breathing stresses, and improve the fatigue life of the plate girder which is very different to the majority of applications of FRP strengthening that exploit the FRP for its direct tensile strength and stiffness. The objective of the current experimental programme is to strengthen thin-walled steel girders against web shear buckling using a corrugated CFRP (carbon fibre reinforced polymer) or GFRP (glass fibre reinforced polymer) panel bonded externally along the compression diagonal of the web plate.

Fatigue analyses indicated that the proposed strengthening technique is able to considerably elongate the life expectancy of the strengthened plate girders by a factor ranging between 2.5 and 7 times the corresponding unstrengthened ones. In addition, the proposed strengthening technique did not show any debonding or delamination under both static and cyclic loading which makes it a good candidate for strengthening thin-walled structural members, especially, when ductility is a concern.

TABLE OF CONTENTS

Chapter Six: Phase-3, Final cyclic Series of Tests

This page is intentionally left blank

LIST OF TABLES

LIST OF FIGURES

NOMENCLATURE AND ACRONYMS

Latin Letters	
a	Height of the isosceles triangles in section (3.71)
Acb	Area between the horizontal axis (the displacement axis) and the modified buckling curve for the control specimen
Act	Shaded area between the vertical axis (the load axis) and the modified bucking curve for the control specimen
AF	Action factor
a_{ij}	Components of the unite vector of the primed system
Asb	Area between the horizontal axis (the displacement axis) and the modified buckling curve for the strengthened specimens
Ast	Shaded area between the vertical axis (the load axis) and the modified bucking curve for the strengthened specimens, up to a load equal to 140 kN
a_w	The space between vertical stiffeners
a_w /h_w	Plate girder's panel aspect ratio
b	Base width of the isosceles triangles in section (3.71)
b_f	Flange width
b_s	Stiffener projected width
C_b	Location of the hinge in the bottom flange
C_t	Location of the hinge in the top flange
d	The lesser dimension of the stiffener spacing (a_w) and the web height (h_w)
E	Young's modulus
$e.sd.$	Error standard deviation
E_1	Tensile composite modulus of elasticity in the longitudinal direction
E_2	Tensile composite modulus of elasticity in the transverse direction
E_3	Tensile modulus of elasticity of the composite section in the third dimension (i.e normal to the plane of the FRP)
E_f	Tensile modulus of elasticity of the fibre reinforced polymer section
E_{ff}	Fibre modulus of elasticity
$E.I$	Relative energy absorption index

e'_i	Primed coordinate system unit vector
E_m	Matrix modulus of elasticity
E_s	Steel modulus of elasticity
E_x	Material modulus of elasticity in the x-direction
E_y	Material modulus of elasticity in the y-direction
E_z	Material modulus of elasticity in the z-direction
F	Fibre factor
f_u	Steel ultimate strength
f_y	Steel yield stress
G_{12}	Halphin Tsai in-plane shear modulus of the composite section in Chapter 4 and the local modulus of
G_{13}	Shear modulus of elasticity of the composite section in the 1-3 plane
G_{23}	Shear modulus of elasticity of the composite section in the 2-3 plane
G_f	Fibre shear modulus
G_m	Matrix shear modulus
G_{xy}	Material shear modulus of elasticity in the xy-plane
G_{xz}	Material shear modulus of elasticity in the xz-plane
G_{yz}	Material shear modulus of elasticity in the yz-plane
h_w	Web plate height
h_w/t_w	Plate girder's panel slenderness ratio
I_F	Flange second moment of area of an axis passing through the centroid of the flange and normal to the web plate
I_f	Second moment of area for the FRP panel
I_S	Second moment of area of the projection of the T-section formed from combining the stiffener and the web plate
k	Shear buckling coefficient determined using Equation (3.7)
k_{nn}	Normal traction separation parameter with respect to the element local *n*-coordinates
k_s	Shear buckling coefficient with simply supported boundary conditions
k_{sf}	Shear buckling coefficient according to Fujii's Equation (3.3)
k_{ss}	Tangential traction separation parameter with respect to the element local *s*-coordinates

k_{tt}	Tangential traction separation parameter with respect to the element local *t*-coordinates
l	-Direction cosine for the angle of rotation with respect to the x-direction -Inclined length of the developed tension field zone in section (7.4)
L_f	Total length of the FRP panel
m	Direction cosine for the angle of rotation with respect to the y-direction
M_{pb}	plastic moment of the bottom flange
M_{pt}	plastic moment of the top flange
n	Direction cosine for the angle of rotation with respect to the z-direction
$N_{\sigma r}$	Number of cycles determined from the normal stress criterion
$N_{\tau r}$	Number of cycles determined from the shear stress criterion
P	-Applied load -Point in the domain of the composite section in section (7.21)
P_1	Location of the point where the first major change in the slope of the curve occurs
P_{1x}	x-coordinate of P_1
P_{1x}	y-coordinate of P_1
P_2	Location of the point where the second major change in the slope of the curve occurs
P_{2x}	x-coordinate of P_2
P_{2x}	y-coordinate of P_2
P_{CM}	Ultimate load for the control unstrengthened specimens' model
P_{FM}	Ultimate load for the FRP strengthened specimens' model
P_{Fult}	Ultimate strength of the strengthened steel plate girders
P_{ult}	Ultimate shear load capacity of the plate girder panel
q_l	Dimensionless resisting shear force
R^2	R-squared
Rd	The ratio of the design equation to the numerical analysis value in chapter 3
R_F	Flange rigidity index
R_S	Stiffener rigidity index
$S.I$	Relative stiffness increase index

t	Laminate thickness
t_{ds}	Diagonal stiffener thickness
t_f	Thickness of flange
T_f	Ultimate tensile strength of the fibre reinforced polymer section
t_k	Thickness of the k^{th} layer
t_s	Thickness of stiffener
t_w	Web plate thickness
u	Translational degree of freedom in the local x-direction
Ux	In-plane displacement along the *x*-axis of the plate in section (3.72)
Uy	In-plane displacement along the *y*-axis of the plate in section (3.72)
V_{cr}	Shear force resulting from the critical buckling shear stress of a similar simply supported web plate having an aspect ratio of 1.0 and a slenderness ratio of 250
V_f	Fibre volume fraction
v	Translational degree of freedom in the local y-direction
V_m	Matrix volume fraction
V_m	Poisson's ration of the matrix
w	Dimensionless initial imperfection (h_w / w_o)
w	Translational degree of freedom in the local z-direction
w_o	Central out of flatness of the web plate (initial imperfection)
x	Factor representing the distance of the plastic hinge from the applied load
x'	Primed coordinate system
x_1	Unprimed longitudinal local coordinate axis within the plane of the composite
x_2	Unprimed transverse local coordinate axis within the plane of the composite
x_3	Unprimed local coordinate axis normal to the plane of the composite
$[a]^T$	Transpose matrix of the components of the unite vector of the primed system
[C]	Global Stiffness matrix
[C']	Local Stiffness matrix

$[C_k]$	Stiffness matrix of the k^{th} layer
[S]	Global compliance matrix
[S']	Local compliance matrix
[T]	Transformation matrix
$[T]^T$	Transpose of the transformation matrix

Greek letters

α	-Constant used in different equations in chapter 3 -Aspect ratio of web panel in section (7.4)
β	Constant used in different equations in chapter 3
γ_{max}	Maximum principal shear strain in the plane
γ_{xy}	Calculated shear strain in the x-y coordinate system
δ	Out-of-plane displacement
ε_1	Measured strain in the horizontal x-direction
ε_{12}	Calculated shear strain in the local coordinate system
ε_2	Measured strain in the vertical y-direction
ε_3	Measured strain in the tension diagonal 45°-direction
ε_{max}	Maximum principal normal strain in the plane
ε_x	Calculated membrane/secondary bending strain in the horizontal x-direction
ε_{xBott}	Measured strain in the horizontal x-direction of the compression face
ε_{xTop}	Measured strain in the horizontal x-direction of the tension face
ε_{xy}	Calculated membrane/secondary shear strain in the horizontal x-y plane
ε_{xyBott}	Calculated shear strain in the compression face
ε_{xyTop}	Calculated shear strain in the tension face
ε_y	Calculated membrane/secondary bending strain in the vertical y-direction
ε_{yBott}	Measured strain in the vertical y-direction of the compression face
ε_{yTop}	Measured strain in the vertical y-direction of the tension face
η	Factor in Calladine method (Appendix A)
θ	angle of inclination of the tension field in the web plate

θ_d	angle of inclination of the diagonal of the web plate
θ_x	Rotational degree of freedom about x-axis
θ_y	Rotational degree of freedom about y-axis
θ_z	Rotational degree of freedom about z-axis
ν	Poisson's ratio
ν_{12}	Major Poisson's ratio of the composite section
ν_{23}	Poisson's ratio of the composite section in the 2-3 plane
ν_{13}	Poisson's ratio of the composite section in the 1-3 plane
ν_f	-Poisson's ratio of the fibres in Equation (4.2). -Poisson's ratio of the fibre reinforced polymer section.
ν_{xy}	Material Poisson's ratios in the xy-plane
ν_{xz}	Material Poisson's ratios in the xz-plane
ν_{yz}	Material Poisson's ratios in the yz-plane
ξ	-Reinforcing factor, and can be assumed conservatively equal to 1. -Dimensionless flange plastic moment with the properties of the web in section (7.4) and Appendix (A).
ρ_f	Density of fibres
ρ_r	Density of the epoxy resin
σ_r	Normal stress range
σ_{yw}	Tensile yield stress of web material
τ_{cr}	Elastic buckling shear stress of web panel
τ_r	Shear stress range
τ_s	critical buckling shear stress with simply supported boundary conditions
τ_{yw}	Shear yield stress of web material
τ^R	reduced buckling shear stress due to initial imperfection
τ^P	buckling shear stress calculated according to the proposed buckling coefficients
$\emptyset$	Angle of maximum principal strain
Δ	In-plane displacement
$\Delta\varepsilon$	Measured normal strain range
$\Delta\gamma$	Measured shear strain range

ΔL	Applied load range
$\Delta\sigma_r$	Calculated shear stress range
$\Delta\tau_r$	Calculated shear stress range
$\sum e^2$	Sum of squared errors

Acronyms

3-D	Three Dimensional
AASHTO	American Association of State Highway and Transportation Officials
AISC	American Institute for Steel Construction
ASTM	American Standard Test Method
BCs	Boundary Conditions
C3D8R	General purpose three dimensional element having 8 degrees of freedom and reduced integration
CAE	Complete Analysis Environment (*Abaqus*)
CFRP	Carbon Fibre Reinforced Polymer
DIC	Digital Image Correlation
DLS	Double Lap Shear
dof	Degree of Freedom
EN	European Standards
Eq.	Equation
FEA	Finite Element Analysis
FEM	Finite Element Method
FRP	Fibre Reinforced Polymer
FVF	Fibre Volume Fraction
FWF	Fibre Weight Fraction
GFRP	Glass Fibre Reinforced Polymer
GMNA	Geometrical and Material Non-linear Analysis
GNCF	Geometrical Non-dimensional Correction Factor in Equation (3.10)
II	Initial Imperfection
LPs	Linear potentiometers displacement gauges

LYS	Lower Yield Strength
REF	Bespoke Digital Image Algorithm
S	Single Strain Gauge
S9R5	Shell element with nine nodes and five degrees of freedom
SP	Specimen
SR	Rosette strain gauge
UYS	Upper Yield Strength
YPE	Yield Point Elongation

Chapter One
Introduction

'Structurally deficient bridges "need to be really either replaced or repaired in a very dramatic way." He went on: "I don't want to say they're unsafe. But they're dangerous." '

-Ray LaHood
Former US Transportation Secretary
Interview with CBS/ 2014
(reported in the Washington Post, Feb. 2015)

1.1 BACKGROUND

Civil engineers are presently faced with strengthening and repairing many existing structures to assure or increase their structural safety. The reasons for this include changes in the use of structures, and increased traffic loads on bridges. In Iraq, for example, several highway bridges needed to accommodate increased axle load during the transportation of huge turbines for electricity generating stations (Assoodani, 2014).

The requirement for structural strengthening and repair methods is, however, driven by the worldwide need to ensure the safety and sustainability of our aging and deteriorating infrastructure. The ever increasing damage caused by environmental effects and the corrosion of steel and deterioration of concrete, reduce structural safety and lead to disruption for the users, which can have serious economic consequences. The European Community directed that all highway bridges in the United Kingdom must either be capable of carrying 40-ton vehicles by 1999 or have a weight restriction order placed on them. This directive led to a major bridge assessment programme, resulting in the need to address deficiencies in over 10,000 bridges in the UK (Kachlakev, 1998).

Similar problems are observed all over the world. In the United States for instance, the backbone of the commerce and industry consists of constructed facilities including highways, bridges, airports, and transit systems. Most of this infrastructure is deteriorating at a rate faster than it can be renovated (Kachlakev, 1998).

The National Bridge Inventory (NBI) (Wikipedia/ Federal Highway Administration) includes a structural evaluation of deck, superstructure, and

substructure, on a 0 to 9 scale. It also classifies bridges as either "structurally deficient" or "functionally obsolete". Structurally deficient means that the condition of the bridge includes a significant defect, which often means that speed or weight limits must be put on the bridge to ensure safety; a structural evaluation of 4 or lower qualifies a bridge as "structurally deficient". Functionally obsolete means that the design of a bridge is not suitable for its current use, such as a lack of safety shoulders or the inability to handle traffic volume, speed, size, or weight.

In December 2008, 72,868 bridges in the United States (12.1%) were categorized as structurally deficient, representing an estimated $48 billion in repairs, and 89,024 (12.2%) were rated functionally obsolete, representing an estimated $91 billion in replacement costs. It has been reported that to eliminate the nation's bridge deficient backlog by 2028, the US would need to invest $20.5 billion annually, while only $12.8 billion is being spent currently (Bridges, 2013 report card for America's infrastructure). Figure (1.1) shows the mapping of structurally deficient and functionally obsolete bridges in the United States (Ingraham, 2015).

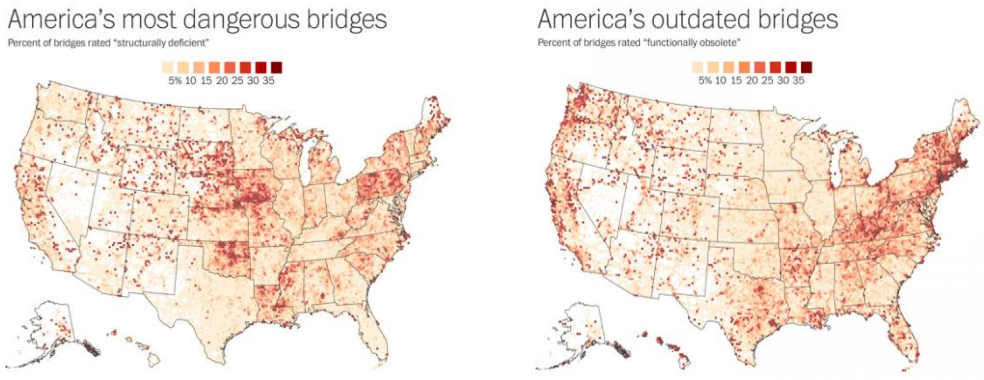

Figure (1.1): Map representing America's structurally deficient and functionally obsolete bridges, (Washington Post, 4, Feb. 2015).

1.2 STRENGTHENING TECHNOLOGIES

In spite of the fact that very serious trials were made to present reports, books, and standards to cover the practical and theoretical part of strengthening of steel structures, see for instance (Cadei et al., 2004) and (Zhao, 2014); strengthening and/or retrofitting technologies are still at a stage where most applications are based

on experience and trial and error, rather than on a sound scientific basis. In order to upgrade the bridge inventory to 21st century levels, the large volume of rehabilitation work requires the development of new technologies based on the new materials and new process with a more profound scientific approach.

Restoring the structural integrity and enhancing the strength and stiffness capabilities of aging structures is a major challenge, and the selection of the proper methods to retrofit a structure is a complex task. Different techniques exist for strengthening structures; however, most of these techniques have specific drawbacks. For instance, while traditional methods of repair, such as bolting and riveting of additional strengthening sections and welding of others, can be used, they all suffer from two primary deficiencies in that the rehabilitation itself add significant weight to the already under-capacity component or system, and that the technique is either not as reliable as needed, or takes too long (resulting in elongated periods of closure) or in itself caused further distress albeit in terms of different performance metrics (such as the addition of deleterious residual stresses initiated by welding) (Karbhari, 2014). In addition to that, on-going maintenance due to continued corrosion attack is crucial. Therefore the need for adopting durable materials and cost-effective strengthening techniques is evident.

The use of Fibre Reinforced Polymer (FRP) composites for rehabilitation and strengthening of civil engineering structures is very promising, and is becoming more widespread, particularly where applied to concrete structures, see for example (Perkins, 1986) and (Oehlers and Seracino, 2004). FRP composites consist of high strength fibres bound together with an inert plastic resin. Epoxy resins cured at room temperature are usually selected for construction applications of FRPs. However, a range of other resins, some specially formulated or requiring elevated temperature cure, are available.

FRP composites, primarily developed and used in the defense and aerospace industries, offer unique advantages in many applications where conventional materials cannot provide satisfactory service. Lightweight and natural corrosion resistance are among their main advantages over steel and metal alloys. Their high tensile strength is an excellent complement to steel properties. Their impermeability and their ability to adhere to old building materials make FRP composites systems

that outclass conventional building materials, except for the cases where drainage of water is of critical importance and when the surface of the structure is highly corroded or deteriorated. Other advantages of FRP over steel include the relative ease of surface preparation at installation, enhanced structural characteristics, and improved durability. When compared to conventional materials, the high strength-to-weight ratio, minor disruption of traffic during repair, and minimal maintenance requirements help make FRP composites an excellent candidate for rehabilitation and strengthening of infrastructures.

1.3 PLATE GIRDERS

In a plate girder bridge, the plate girders are typically I-beams made up from separate structural steel plates (rather than rolled as a single cross-section), which are welded or, in older bridges, bolted or riveted together to form the vertical web and horizontal flanges of the beam- Figure (1.2). The principal differences between the design of a rolled beam and the design of a plate girder are that the designer has greater freedom in proportioning the cross-section and the larger depth of the plate girder often results in relatively slender webs which make web buckling a significant issue.

Plate girders are used both in bridges and buildings. Depending on the design philosophy, structural function, and the required span; the designers have the choice of using either a plate girder or a truss. However, plate girders, in general, have some advantages over trusses. These advantages include the followings (Assoodani, 2014):

- Fabrication cost of plate girders is less than that of trusses.
- Erection cost and time of plate girders are usually less than that of trusses.
- Plate girders generally vibrate less than trusses under same moving loads.
- Painting and maintenance of plate girders are less costly than trusses.
- Connections are less critical for plate girders than for trusses. In a statically determinate truss, one poor connection may cause the collapse of the whole truss.
- The corresponding depth of a plate girder is usually less than the height of a comparable truss; consequently, plate girders need less clearance than trusses.

On the other hand, one disadvantage of plate girders is that they are generally heavier in weight than corresponding trusses; this is mostly true for very long spans.

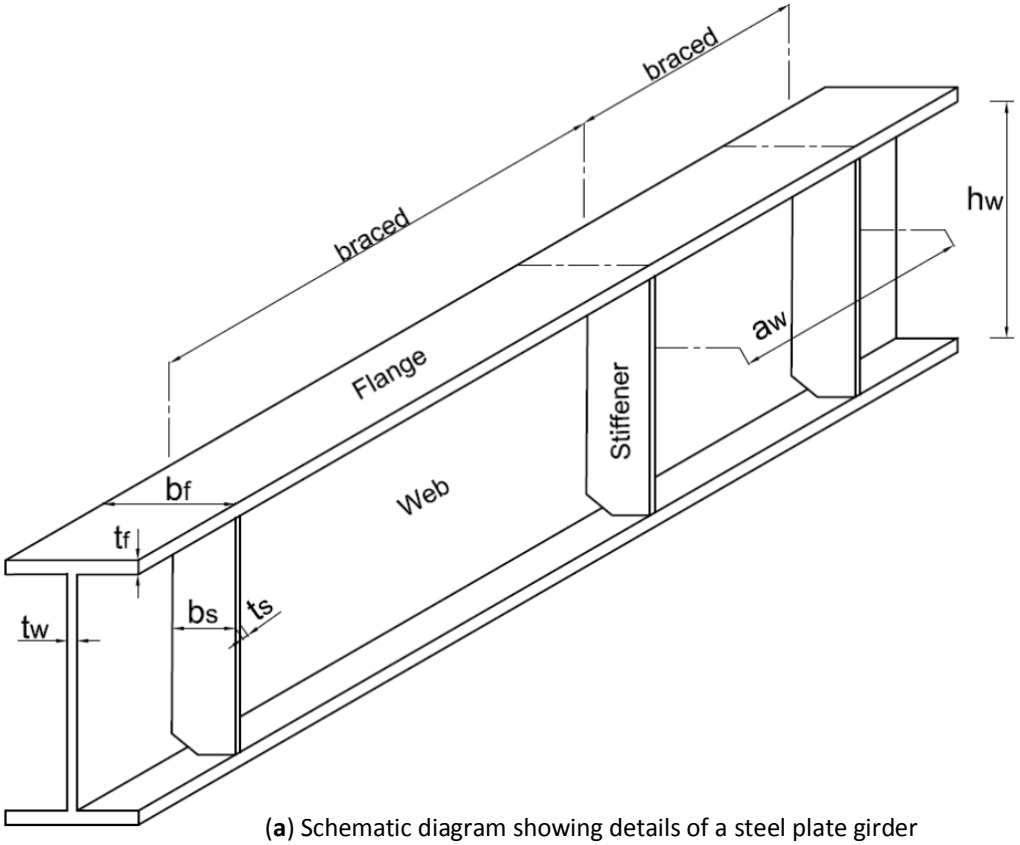

(**a**) Schematic diagram showing details of a steel plate girder

(**b**) Typical examples of steel plate girders (Washington State Dept. of Transportation)

Figure (1.2): Details and typical examples of steel plate girders.

The two primary functions of the web plate in a plate girder are to maintain a relative distance between the top and bottom flanges and to resist the induced shear stresses. In most practical ranges of plate girder bridges' spans, the induced shear stresses are relatively low compared to the bending stresses in the flanges induced by flexure. As a result the web plate is generally chosen to be much thinner than the flanges. The web panel consequently buckles at a relatively low shear force. To enhance the buckling strength, the web often reinforced with transverse intermediate stiffeners. The web design then involves a search of plate thickness and stiffener spacing to provide optimum economy in terms of the material and fabrication cost.

Tension Field Action

Tension field is a mode of shear transfer in the thin web of a stiffened plate girder which occurs after elastic local buckling takes place. In this mode, the tension diagonal of each stiffened panel behaves in the same way as the diagonal tension member of a parallel chord truss, Figure (1.3).

According to Porter et al. (1975), collapse mechanism with web subjected to pure shear can be divided into three phases as illustrated in Figure (1.4), as follows:

Stage 1. *Pre-buckled behaviour*. With a perfectly flat plate there is a uniform shear stress throughout the panel prior to buckling. There will be a principle tensile stress of magnitude τ acting at 45° to the flange and a principal compressive stress of the same magnitude acting at 135°. This stress system exists until the shear stress τ equals the critical shear stress τ_{cr}.

Stage 2. *Post-buckled behaviour*. Once the critical shear stress (τ_{cr}) is reached, the panel cannot sustain any increase in the compressive stress and it buckles. This causes a change in the load carrying system; any additional load has to be supported by a tensile membrane stress, σ_t (see Figure 1.4b).

Stage 3. *Ultimate shear capacity* V_{ult}. On further loading, the tensile membrane stress σ_t plus the buckling stress τ_{cr} produces yielding in the web. Failure occurs (see Figure 1.4c) when hinges have formed in the flanges which together with the yield zone forms a plastic mechanism and the panel fails.

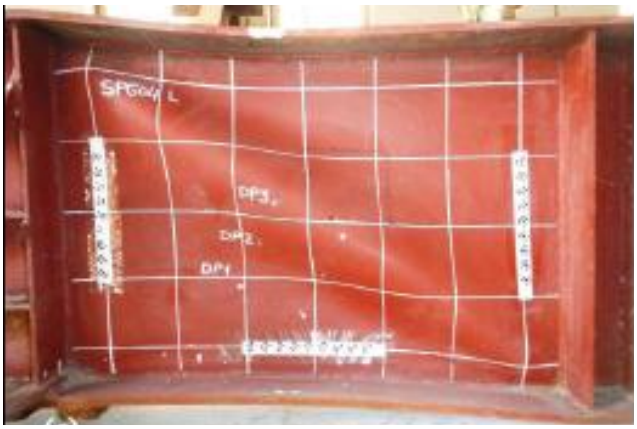

(**a**) Photo of post-buckling of end web plate

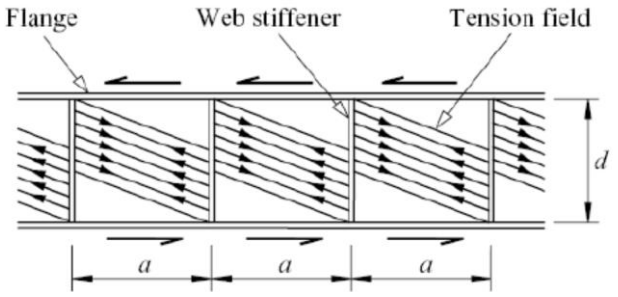

(**b**) Schematic of tension field action

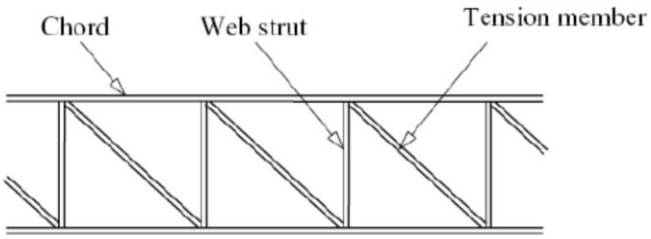

(**c**) Truss analogy of tension field

Figure (1.3): Tension field in a stiffened web of a plate girder, (Assoodani, 2014).

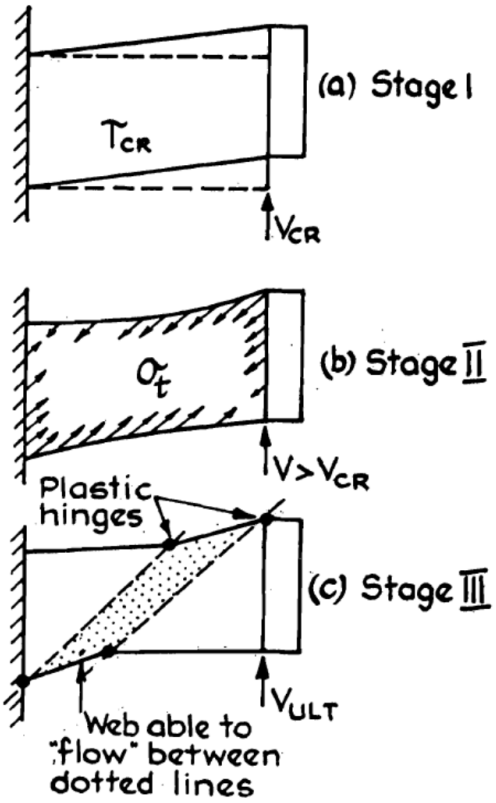

Figure (1.4): Collapse mechanism considered by Porter et al. (1975).

1.4 MOTIVATION

The quote at the start of this chapter (LaHood, 2015), states how bridge area "Not unsafe, but dangerous". This paradox in defining structural deficiency reveals how serious the problem is and extensive work from lab research to field application is urgently required.

In the last two decades, the use of FRP has emerged as a promising technology in structural engineering. However, most of the work has been focused on reinforced concrete structures (Kachlakev, 1998). The main reason that FRP composites have not been more widely applied to strengthen steel structures until recently is their low tensile modulus of elasticity. The low tensile stiffness compared to steel means that the FRP does not carry sufficiently large stresses to make it effective when acting compositely with the steel. Modern Carbon Fibre Reinforced Polymers (CFRP), however, has a typical tensile strength and modulus of elasticity of more than 1,200MPa and 165GPa, respectively, making it a promising material to strengthen

steel structures, unlike (for example), Glass Fibre Reinforced Polymers (GFRP). Unlike concrete structures, however, thin-walled steel members are susceptible to buckling instability. Consequently, the FRP strengthening is not always required to provide flexural strength. Lower modulus of elasticity GFRP material can effectively be used to prevent out-of-plane displacement of thin-walled structures by careful choice of strengthening geometry, a concept that is explored and exploited in the current work.

For steel girder structures dominated by cyclic loading, as is the case with repeated vehicle axle loads on bridges, web panels buckle at relatively low shear forces because of their slender geometrical properties, usually chosen by designers to reduce the self weight of the structure, especially in long span bridges. This can lead to the so-called 'breathing' phenomenon; an out-of plane buckling displacement that can induce high secondary bending stresses at the welded plate boundaries. Figure (1.5) shows an example of out-of-plane web buckling for the Fresh Kills Bridge in Staten Island (New York City Department of Transportation, 2012).

Based on the researcher observation as a structural engineer and the above review, it is found worthy to explore the field of strengthening steel plate girders, especially thin-walled ones, against web shear buckling both under static and cyclic load.

Figure (1.5): Fresh Kills Bridge in Staten Island (New York City Dept. of Transportation, 2012).

1.5 RESEARCH OBJECTIVES

The main idea in the current work is proposing an easy to install, easy to inspect and cost effective FRP strengthening technique to resist the web out-of-plane deformations due to breathing phenomenon and/or strengthening the steel structure to endure higher ultimate loads at the same time; while maintaining the typical ductile failure of steel plate girders. In addition to that, observing the fatigue performance of the FRP strengthening system which will play a major role in the design recommendations and life prediction of the retrofitted steel plate girders.

The research in this thesis has the following main objectives:

- better understand the available knowledge of traditional strengthening techniques for steel plate girders, giving special attention to strengthening thin-walled steel plate girders against shear buckling;
- evaluate the deformation behaviour and failure modes of bare and FRP strengthened steel plate girders under both static and cyclic loading;
- determine the increase in stiffness and ultimate capacity of the strengthened plate girders in comparison to the bare steel ones;
- study the effectiveness of FRP strengthening schemes of steel plate girders under long-life cyclic shear loading and its efficiency in prolonging the fatigue life of the plate girder;
- develop analytical/numerical models to simulate the behaviour and strength of both bare and FRP strengthened steel plate girders under long-life cyclic shear loading.

1.6 SCOPE OF PROJECT

Slender plates such as the webs of plate girders are used in a variety of structural engineering applications for material efficiency and due to their postbuckling reserve of stiffness and strength. In-plane loading of thin steel web plates close to (or even exceeding) their buckling load results in out-of-plane displacements, which in turn induce high secondary bending stresses at the welded plate boundaries. Previous researches have found that the magnitude of these stresses can be as high as the yield stress of the web in some cases (Yen and Muller, 1966). Repeated out-of-plane

displacement due to cyclic loading in bridges can result from, for instance, moving vehicle axle loads causing a breathing phenomenon as previously mentioned. Fatigue performance of plate girders due to secondary bending stresses resulting from breathing of the web plate is of particular concern.

In the current work, an FRP strengthening technique using bonded shapes is applied to resist these out of plane deformations, and hence reduce the breathing stresses, and improve the fatigue life of the plate girder (Figure 1.6). Note that this is very different to the majority of applications of FRP strengthening that exploit the FRP for its direct tensile strength and stiffness.

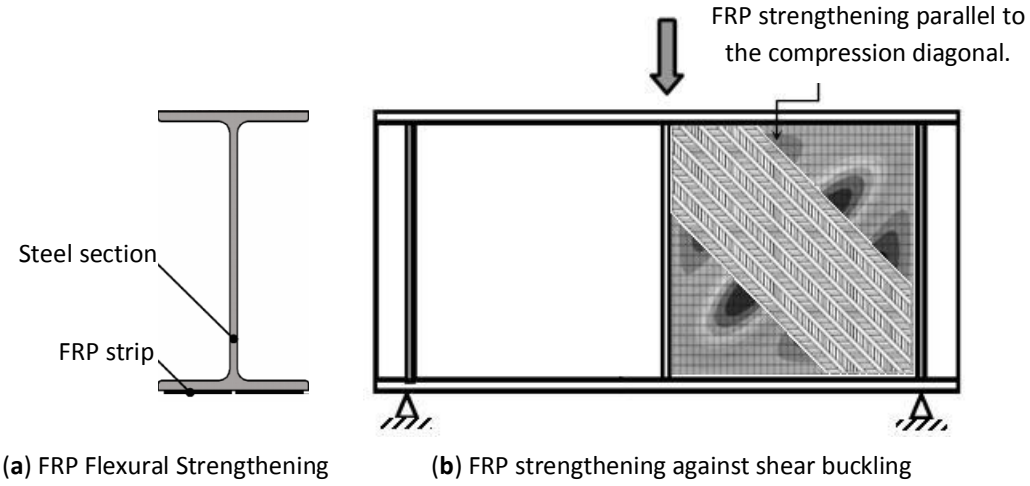

Figure (1.6): Schematic showing the proposed strengthening technique compared to a typical flexural FRP strengthening.

Limited work is available on strengthening the web plate of a steel plate girder against shear buckling; this is the basis of the central problem treated herein. The research presented in this thesis explores three central themes:

(1) phase-I: Designing a new preformed FRP corrugated section for strengthening slender web plates against shear buckling by bonding it along the compression diagonal of the plate. This FRP section is meant to be stiff enough to reduce the out-of-plane displacement and consequently reducing the high secondary bending stresses on the plate welded boundaries and at the same time the FRP-strengthened section can be ductile enough to preserve the typical ductile failure of the steel plate girder in shear.

(2) phase-II: Testing the efficiency of this new composite section under static loading taking into consideration as many variables as possible; such as, FRP material, number of layers of the FRP laminate, geometry of the FRP section, position and shape of the end cut of the FRP panel, and orientation of the glass fibres.
(3) phase-III: Validating the efficiency of the optimized FRP composite section under cyclic loading, simulating the case of moving axle load in bridges.

To address the first theme, linear finite element modelling along with some simplified analytical calculations for the second moment of area of the proposed composite section was performed, leading to the selection of the shape and dimensions of the proposed FRP section. In addition to that, an extensive material wise series using numerous double-lap shear and tension specimens was performed. This led to the selection of the resin and epoxy and the determination of the mechanical properties of the FRP used throughout this work.

For the second and third themes, two main experimental series were performed. The initial series involved testing steel plates strengthened with the proposed preformed corrugated FRP panel and subjected to in-plane shear loading using a specially manufactured "picture-frame" arrangement designed to induce appropriate boundary conditions and stresses to simulate web plates in realistic plate girders under in-plane shear stresses. The initial test series investigated the performance of different forms of strengthening under static load, in preparation for a subsequent series of cyclic tests to investigate their fatigue performance. In the second series six specimens were manufactured to simulate the end panel of a plate girder. These were strengthened with the optimized FRP panel from the first series and tested for shear buckling under cyclic loads.

1.7 THESIS OUTLINE

The following is a brief outline of each chapter.

Chapter 2: Background and literature review discusses the main fields of the study, namely: performance of bare steel plate girders under static loading mainly in shear, fatigue performance of bare steel plate girders under cyclic loading, general FRP strengthening of steel plate girders, and the available literature of FRP

strengthening of steel plate girders against shear buckling. The review tracks experimental, analytical, design issues, and field applications related to the study. In addition to that, the chapter provides some review of buckling of orthotropic composite plates under various loading and boundary conditions.

Chapter 3: A finite element study of the boundary conditions and initial imperfection effect on the behaviour of steel plate girders focuses on shedding more light on the effect of the rigidity of flanges and stiffeners at their junction with the web steel plate on the boundary conditions and consequentially the critical buckling shear stress of a plate girder, this was done through linear buckling analysis using commercially available software Abaqus. The effect of initial imperfection was also investigated through non-linear finite element simulation of one panel of a plate girder under pure shear. In addition, analytical and numerical models were proposed for diagonally stiffened steel plate girders.

Chapter 4: Phase-1, FRP panel geometric design and material experimental programme develops a procedure for designing and manufacturing the new preformed corrugated FRP section to be adhesively bonded to the web steel plate compression diagonal, and to determine the mechanical properties of the FRP laminate used in producing this new panel which will be used throughout this work. An experimental programme to select the best resin and epoxy is also illustrated. In addition, linear buckling analysis of the proposed composite section was also performed.

Chapter 5: Phase-2, initial static series of tests presents the experimental research programme of the initial static series of 13 tests performed on FRP strengthened steel plates using the proposed preformed corrugated FRP panel, utilizing several variables that affect the performance of the FRP composite section. Test setup, configuration, instrumentations, and illustration of the specially designed testing rig “picture-frame” which has been used for the static in-plane shear tests in this series is, also, presented. The chapter presents, analyses, and discusses the test results in form of experimental parametric study taking the effect of the tested variable on the strength and behaviour of FRP strengthened steel plates against shear buckling. Effect of the type of the FRP material, section of the FRP panel, number of

layers of FRP laminate, shape and location of the end cut of the FRP panel, and the orientation of the glass fibres; are all taken into consideration. Curves representing the out-of-plane and in-plane displacements, stiffness and toughness, and strain are presented

Chapter 6: Phase-3, final cyclic series of tests illustrates test results of the final cyclic series of tests of the experimental work. The chapter analyse and discuss the test results of the first three specimens which have been tested statically to serve as precursor for the last three specimens tested under cyclic loading with a stress range between 40% and 80% from their ultimate capacity. The optimized section was taken from the data of the initial series and the variables explored were only the type of the FRP material and the configurations of the FRP panels. Curves representing the out-of-plane and in-plane displacements, stiffness and toughness, and strain are presented. The chapter presents, analyse, and discuss the test results in form of experimental parametric study taking the effect of the tested variable on the strength and behaviour of FRP strengthened steel plates against shear buckling. Geometrical and material non-linear finite element modelling is also performed in this chapter for the unstrengthened steel plate girders.

Chapter 7: Design method for FRP-steel composite section presents a parametric study for the effect of different variables on the behaviour of FRP strengthened steel plate girders against shear buckling. The parametric study uses a new proposed non-linear numerical composite model to address the effect of the aspect ratio and the slenderness ratio of the web on the behaviour of both unstrengthened and strengthened steel plate girders. The chapter ends with several concluding remarks. In addition, the chapter investigates several design issues regarding the present work taking into consideration the experimental results and numerical models. New design equations and limitations are also proposed.

Chapter 8: Conclusions and recommendations highlights the main conclusions, novelty, and practical significance arising from the research work presented in the thesis, gives recommendations for use by designers, and summarizes areas for future research which is required as the structural community moves

towards solving the problem of deteriorating, structurally deficient, and functionally obsolete steel plate girders.

In addition to that, several appendices were provided for ease of access to information and design equations.

CHAPTER REFERENCES

ASSOODANI F.A. (2014). "Shear behaviour and strength of CFRP retrofitted steel plate girders and steel-concrete composite plate girders," PhD thesis, University of Technology, Iraq, 746 pp.

BRIDGES, ASCE (2013) REPORT CARD FOR AMERICA'S INFRASTRUCTURE, http://infrastructurereportcard.org/a/#p/home.

BUREAU OF TRANSPORTATION STATISTICS (2008). "Transportation statistics annual report 2008," United States Department of Transportation, Research and Innovative Technology Administration, USA.

CADEI J.M.C., STRATFORD T.J.L., HOLLAWAY C., DUCKETT W.G. (2004). "Strengthening metallic structures using externally bonded fibre-reinforced polymers," CIRIA, London, 235 pp.

CHRISTOPHER I. (4 Feb. 2015). "Mapping America's most dangerous bridges," Washington Post.

DAMIAN K. (1998). "Strengthening bridges using composite materials," FHWA-OR-RD-98-08, Oregon State University, 160 pp.

KARBHARI V.M. (2014). "Rehabilitation of metallic civil infrastructure using fiber-reinforced polymer (FRP) composites," Woodhead publishing series in Civil and Structural Engineering, 440pp.

NATIONAL BRIDGE INVENTORY DATABASE (NBI), Federal Highway Administration, Wikipedia, https://en.wikipedia.org/wiki/National_Bridge_Inventory.

NEW YORK CITY DEPARTMENT OF TRANSPORTATION (2012). "New York City Bridge Traffic Volumes 2010," New York, 256 pp.

OEHLERS D.J. and SERACINO R. (2004) "Design of FRP and steel plated RC structures," ELSEVIER, 222 pp.

PERKINS P.H. (1986). "Repair, Protection and Waterproofing of Concrete Structures," updated edition, Elsevier Applied Science Publishers, London and New York, 302 pp.

PORTER D.M., ROCKEY K.C., and EVANS H.R. (1975). "The collapse behaviour of plate girders in shear," Journal of The Structural Engineer, Vol. 53, No. 8, pp. 313-325.

YEN B.T. and MUELLER J.A. (1966). "Fatigue tests of large-size welded plate girders," Welding Research Council, Bulletin No. 118, pp 1-25.

ZHAO X.L. (2014). " FRP strengthened metallic structures," Taylor & Francis Group, 263 pp.

This page is intentionally left blank

Chapter Two
Background and Literature Review

2.1 OVERVIEW

Increased traffic loads, in conjunction with many bridges coming to the end of their design life, are the causes for load restrictions on many bridges. For steel structures, deficiencies may also be due to corrosion that results in cross-section losses. It is estimated that 40 percent of the bridges in North America are deficient to such a degree that they require some form of rehabilitation or replacement (McKenna and Erki, 1994). In 2008, it was reported that 72,520 bridges in the United States were structurally deficient (about 13.3% of the total number of bridges) (Bureau of Transportation Statistics, USA, 2008). Steel bridges (which are mainly composite) comprise about 50% of the structurally deficient bridges and almost 40% of the functionally obsolete ones.

Corrosion damage can cause progressive weakening of structural elements, but it may also be localized in the form of pits and holes causing stress concentrations that can result in crack initation (Karbhari and Shulley, 1995). Corrosion may also reduce the flexural and shear strength in a region subjected to high bending and/or shearing forces, respectively, cause web buckling or crippling and result in reduction of the fatigue resistance of the member.

Apart from the need for strutural rehabilitaion, strengthening may also be required as a result of increasing the dead load, due to widening of the roadway, resurfacing or increasing the alignment to overcome differential setlement (Tavakkolizadeh and Saadatmanesh, 2001). In Iraq, several cases of increasing the capacity of highway bridges were required to accommodate increased axle load during transportation of huge turbines for electricity generating stations (Assoodani, 2014). Strengthening steel structures with CFRP materials is a viable solution for rehabilitation and strengthening. In addition to strengthening a structure, CFRP reinforcement may be necessary to reduce the possibility of buckling, reduce cyclic strains to improve fatigue performance, or to repair cracks.

A literature review has been conducted to evaluate the state-of-the-art in steel plate girders and their strengthening with FRP materials. The literature review is

presented in three main sections. The first section presents a general review of the analysis for shear buckling of isotropic plates, orthotropic plates, and plate girders; then briefly describes the history of theoretical analysis of steel plate girders, several key methods are demonstrated and discussed. Then a brief review of fatigue analysis of steel plate girders due to the breathing phenomenon is presented. The second section provides an overview of the development of strengthening metallic structures using FRP materials, intially with their application in the aircaraft industry to the most recent demonstration projects for strengthening bridges with CFRP materials. The behaviour of the bonded joints, especially metal to composite joints, is then examined. This is followed by an examination of the durability of bonded joints as well as proposed prevention methods. In the third section, the limited experimental investigations, analytical solutions, and numerical modelling of shear strengthening and rehabilation of steel plate girders using FRP materials are reviewed.

2.2 THE STABILITY, LOAD CARRYING CAPACITY, AND FATIGUE OF OF PLATE GIRDERS LOADED MAINLY IN SHEAR

In this section, the stability of steel plates is considered. Mainly, buckling and post-buckling resistance of steel plates due to in-plane shear stresses will be discussed. The shear buckling can be defined as the out-of-plane displacement relative to the un-deformed plane of the steel plate prior to applying shear loads. The section starts by describing the buckling of isotropic steel plates which is a simplification of a plate girder model where the web plate can be isolated from the flanges and stiffeners by applying appropriate boundary conditions on its perimeter and be analyzed accordingly. Then, a brief description of buckling of orthotropic plates is presented which covers the basics of buckling of the new composite section resulting from strengthening the original steel plate with an FRP section. The section then moves towards buckling of steel plate girders accompanied by a detailed review of the ultimate load carrying capacity of steel plate girders, which is usually a sum of the elastic buckling strength and postbuckling reserve of strength of the plate girders. Finally, the fatigue of steel plate girders loaded mainly in shear is discussed.

2.2.1 Stability of Plates

2.2.1.1 *Stability of Isotropic Flat Plates*

According to Gaylord and Gaylord (1972), the solutions of problems of buckling of flat plates with various in-plane force systems acting on the edges are all derived from a single equation of equilibrium relating the edge forces to the displacement w normal to the plate. Figure (2.1) shows a rectangular flat plate with stresses f_x and f_y (tension positive) and shear stresses f_v distributed along the middle line at the edges. The equation of equilibrium is

$$\frac{EI}{1-\mu^2}\left(\frac{\partial^4 w}{\partial x^4}+2\frac{\partial^4 w}{\partial x^2\,\partial y^2}+\frac{\partial^4 w}{\partial y^4}\right)=t\left(f_x\frac{\partial^2 w}{\partial x^2}+2f_v\frac{\partial^2 w}{\partial x\,\partial y}+f_y\frac{\partial^2 w}{\partial y^2}\right) \tag{2.1}$$

where:

$I=t^3/12$: moment of inertia of cross-sectional area of a unit strip of plate ,

t: plate thickness,

μ: Poisson's ratio,

w: transverse (out-of-plane) deflection at a point in the middle plane of the plate.

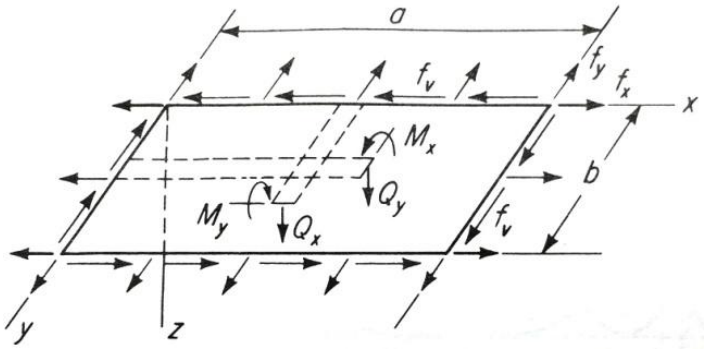

Figure (2.1): Rectangular plate edge stresses, (Gaylord and Gaylord, 1972).

The bending moments are given by

$$M_x=-\frac{EI}{1-\mu^2}\left(\frac{\partial^2 w}{\partial x^2}+\mu\frac{\partial^2 w}{\partial y^2}\right) \tag{2.2a}$$

$$M_y=-\frac{EI}{1-\mu^2}\left(\frac{\partial^2 w}{\partial y^2}+\mu\frac{\partial^2 w}{\partial x^2}\right) \tag{2.2b}$$

where M_x and M_y are the moment per unit width of sections parallel to the y and x axes, respectively- Figure (2.1). The shearing resultants Q_x and Q_y shown in Figure (2.1) are

$$Q_x = -\frac{EI}{1-\mu^2}\frac{\partial}{\partial_x}\left(\frac{\partial^2 w}{\partial x^2}+\frac{\partial^2 w}{\partial y^2}\right) \tag{2.3a}$$

$$Q_y = -\frac{EI}{1-\mu^2}\frac{\partial}{\partial_y}\left(\frac{\partial^2 w}{\partial y^2}+\frac{\partial^2 w}{\partial x^2}\right) \tag{2.3b}$$

Details of the derivation can be found in Timoshenko (1989).

If f_x is compressive (negative) and w is independent of y, Equation (2.1) reduces to

$$\frac{EI}{1-\mu^2}\frac{\partial^4 w}{\partial x^4}+f_x t\frac{\partial^2 w}{\partial x^2}=0 \tag{2.4}$$

This is the differential equation for bending of a bar of unit width and thickness t acted upon by a compressive force $f_x t$. The solution for hinged ends is

$$f_x t=\frac{\pi^2 EI}{(1-\mu^2)a^2} \tag{2.5}$$

where a is the length of the strip in the direction of x- Figure (2.1). Similarly, with w independent of x, the third and sixth terms of Equation (2.1) gives the critical load for a strip of length b in the direction of y. The second term of Equation (2.1) results from distortion of an element of the plate by twisting moments acting on the element.

Figure (2.2) shows a flat plate, hinged on all four edges, which as buckled under the uniform edge compression f_x. For this case, Equation (2.1) reduces to

$$\frac{EI}{1-\mu^2}\left(\frac{\partial^4 w}{\partial x^4}+2\frac{\partial^4 w}{\partial x^2\,\partial y^2}+\frac{\partial^4 w}{\partial y^4}\right)+f_x t\frac{\partial^2 w}{\partial x^2}=0 \tag{2.6}$$

Equation (2.6) can be satisfied for certain values of f_x by

$$w = w_{mn} sin\frac{m\pi x}{a} sin\frac{n\pi y}{b} \qquad \begin{matrix} m=1,2,3,\ldots \\ n=1,2,3,\ldots \end{matrix} \tag{2.7}$$

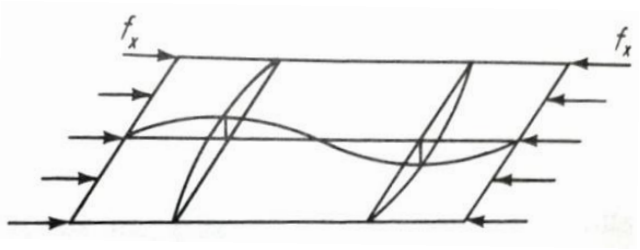

Figure (2.2): Rectangular plate under axial compression, (Gaylord and Gaylord, 1972).

It is clear that the solution also satisfies the boundary conditions since $w = 0$ at the four edges and, from Equations. (2.2) bending moments are zero at the four edges. Substituting w from Equation (2.7) into Equation (2.6) gives

$$\frac{EI}{1-\mu^2}\left(\frac{m^4\pi^4}{a^4} + 2\frac{m^2n^2\pi^2}{a^2b^2} + \frac{n^4\pi^4}{b^4}\right) - f_x t\frac{m^2\pi^2}{a^2} = 0 \tag{2.8}$$

from which

$$f_x t = \frac{\pi^2 EI}{(1-\mu^2)}\frac{\left({}^{m^2}/_{a^2} + {}^{n^2}/_{b^2}\right)^2}{{}^{m^2}/_{a^2}} = \frac{\pi^2 EI}{1-\mu^2}\left(\frac{m}{a} + \frac{n^2}{m}\frac{a}{b^2}\right)^2 \tag{2.9}$$

This equation gives an infinite number of values of the compressive force $f_x\ t$. However, we are interested in the smallest value at which a buckled configuration can exist. It is clear that $f_x\ t$ is smallest when $n = 1$, which means that the plate buckles in one half wave transverse to the direction of loading. Therefore,

$$f_x t = \frac{\pi^2 EI}{(1-\mu^2)a^2}\left(m + \frac{1}{m}\frac{a^2}{b^2}\right)^2 \tag{2.10}$$

where m is the number of half waves in the direction of f_x. If $m = 1$,

$$f_x t = \frac{\pi^2 EI}{(1-\mu^2)a^2}\left(1 + \frac{a^2}{b^2}\right)^2 \tag{2.11}$$

This equation is identical to Equation (2.5) except for the factor in parentheses. Furthermore, $f_x\ t$ in Equation (2.11) approaches the value given by Equation (2.5) as a/b decreases. Thus, the second term in parentheses measures the stiffening of the plate which results from support of the unloaded edges.

It would appear from Equation (2.11) that $f_x\ t$ increases without limit as the width b of the plate decreases. This would be true if the plate buckled in only one

longitudinal half wave. However, the possibility of multiple-wave buckling modes must be investigated. For this purpose, it is convenient to rewrite Equation (2.10) in the form

$$f_x t = \frac{\pi^2 EI}{(1-\mu^2)b^2}\left(m\frac{b}{a}+\frac{1}{m}\frac{a}{b}\right)^2 \tag{2.12}$$

Substituting $I=t^3/12$ into this equation and using the notation

$$k = \left(m\frac{b}{a}+\frac{1}{m}\frac{a}{b}\right)^2 \tag{2.13}$$

and denoting the critical value of f_x by F_{cr}, we get

$$F_{cr} = \frac{k\,\pi^2\,E}{12(1-\mu^2)\left(\frac{b}{t}\right)^2} \tag{2.14}$$

The ratio of the length *a* to width *b* of a plate is called its *aspect ratio*. Values of *k* from Equation (2.13) are shown in curve *A* of Figure (2.3) along with the solutions for several other boundary conditions (Gaylord and Gaylord, 1972).

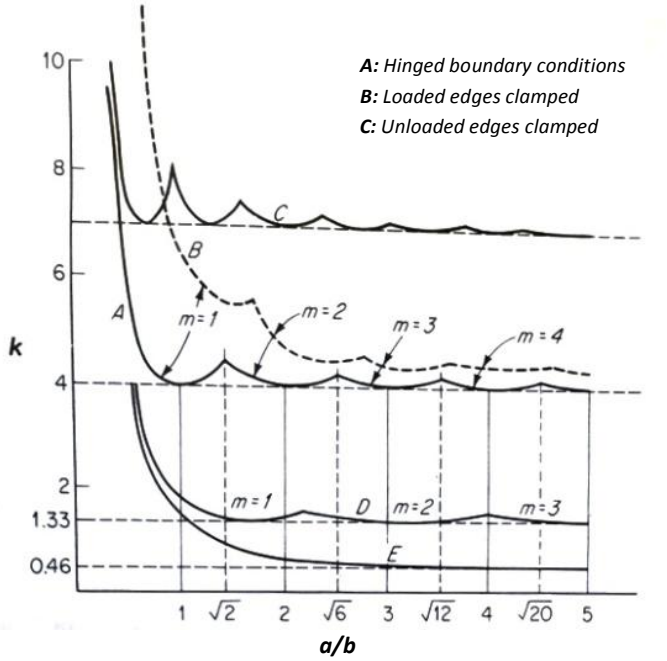

Figure (2.3): Plate buckling coefficients, (Gaylord and Gaylord, 1972).

2.2.1.2 *Stability of Orthotropic Flat Plates*

Problems related to rectangular plates with stiffeners parallel to one or both pairs of sides can be solved approximately by methods applicable to orthotropic plate theory.

The calculation of buckling strength of orthotropic plates is based on the solution of the following differential equation governing the small deflection *w(x, y)* of the buckled plate (Ziemian, 2010):

$$D_1 \frac{\partial^4 w}{\partial x^4} + 2D_3 \frac{\partial^4 w}{\partial x^2 \partial y^2} + D_2 \frac{\partial^4 w}{\partial y^4} + N_x \frac{\partial^2 w}{\partial x^2} + N_y \frac{\partial^2 w}{\partial y^2} + 2N_{xy} \frac{\partial^2 w}{\partial x \partial y} = 0 \qquad (2.15)$$

where

$$D_1 = \frac{(EI)_x}{1 - v_x v_y}$$

$$D_2 = \frac{(EI)_y}{1 - v_x v_y}$$

$$D_3 = \frac{1}{2}\left(v_y D_1 + v_x D_2\right) + 2(GI)_{xy}$$

in which N_x, N_y, and N_{xy} are in-plane forces per unit width, Figure (2.4), D is the orthotropic rigidity of the plate, $(EI)_x$ and $(EI)_y$ are flexural stiffness's, per unit width, of beam strips in the x and y directions, respectively; v_x and v_y are flexural Poisson's ratios; and $2(GI)_{xy}$ is a measure of torsional stiffness.

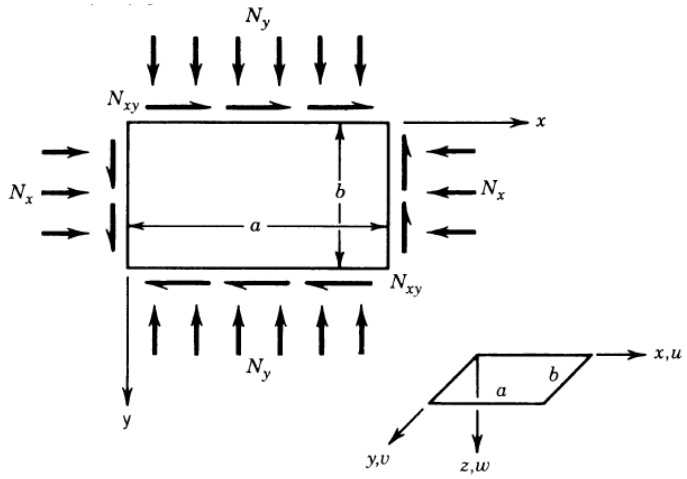

Figure (2.4): Plate subjected to axial and shear stress.

Theoretical data for the shear flow N_{xy} required to cause buckling of rectangular orthotropic plates have been collected by Johns (1971). Three of his graphs are

shown in Figure (2.5). They apply, respectively, to the boundary conditions of (*a*) all edges simply supported; (*b*) edges $y = 0$ and $y = b$ simply supported, the other two edges clamped; and (*c*) all edges clamped. In Figure (2.5), k_s stands for $N_{xy}b^2/\pi^2 D_1^{1/4} D_2^{3/4}$.

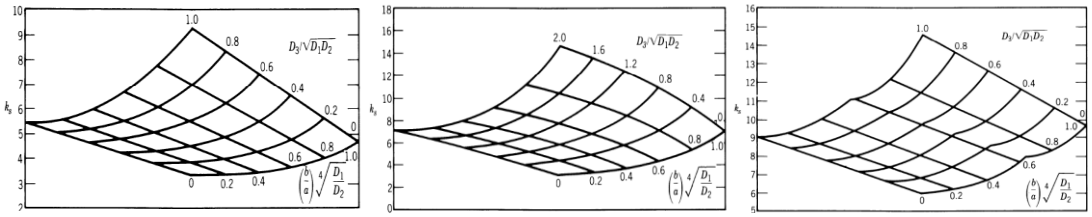

Figure (2.5): Shear buckling coefficients for orthotropic plates, (Johns, 1971).

It is common practice to treat a corrugated plate also as an orthotropic plate. However, there are indications that modelling the corrugated plate as an orthotropic plate may lead to an underestimate of its shear buckling strength (Perel and Libove, 1978). The orthotropic plate model has an additional shortcoming when applied to stiffened plates, namely its neglect of any coupling between in-plane forces and out-of-plane deflections. That is, underlying Equation (2.15) is the tacit assumption that there exists a reference plane in which the forces N_x, N_y, and N_{xy} can be applied without producing any curvatures or twist. In the case of a sheet with identical stiffening on both sides, there does of course exist such a plane (i.e. the middle surface of the sheet). If the stiffening is one-sided, however, it is usually not possible to find a reference plane that will eliminate completely the coupling between in-plane forces and out-of-plane deflections. Therefore, it is very likely that in metal plates with one-sided stiffening it can have a marked effect on the buckling loads.

Finally, orthotropic plate theory is incapable of modelling local buckling, that is, buckling in which the buckle wavelengths are of the same order as the stiffener spacing's or the widths of the plate elements of which the stiffeners are composed (Ziemian, 2010).

2.2.1.3 *Stability of Orthotropic Composite Plates*

An orthotropic plate is one whose material properties are orthogonally anisotropic; a uniformly stiffened plate is reduced to this case by effectively "smearing" the

stiffness characteristics of its stiffeners over the domain of the plate. Clearly, the theory is best applicable when the spacing of the stiffeners is small.

The governing differential equation for buckling of a symmetric anisotropic (i.e. no extensional-bending coupling, B_{ij} = 0.0) plate under in-plane axial loading can be expressed as

$$D_{11}\frac{\partial^4 w}{\partial x^4} + 4D_{16}\frac{\partial^4 w}{\partial x^3\,\partial y} + 2(D_{12} + 2D_{66})\frac{\partial^4 w}{\partial x^2\,\partial y^2} + 4D_{26}\frac{\partial^4 w}{\partial x\,\partial y^3} + D_{22}\frac{\partial^4 w}{\partial y^4} - N_x\frac{\partial^2 w}{\partial x^2} - 2N_{xy}\frac{\partial^2 w}{\partial x \partial y} - N_y\frac{\partial^2 w}{\partial y^2} = 0 \quad (2.16)$$

where D_{ij} (i, j = 1, 2, 6) is the orthotropic plate bending stiffness coefficients; N_x is the in-plane uniformly distributed compressive stress in the x-direction, N_y is the in-plane uniformly distributed compressive stress in the y-direction and N_{xy} is the in-plane uniformly distributed shear stress; w(x, y) is the buckled shape function of the plate (Elena-Felicia Beznea and Ionel Chirica, 2011). For symmetrically laminated cross-ply plates (specially orthotropic plates) there is no coupling between bending and twisting. So, (D_{16} = D_{26} = 0), and their panel properties are obtained from a combined micromechanics/ macromechanics approach. Then the simplified form of Equation (2.16) after accounting for the in-plane shear stress only becomes

$$D_{11}\frac{\partial^4 w}{\partial x^4} + 2(D_{12} + 2D_{66})\frac{\partial^4 w}{\partial x^2\,\partial y^2} + D_{22}\frac{\partial^4 w}{\partial y^4} - 2N_{xy}\frac{\partial^2 w}{\partial x \partial y} = 0 \quad (2.17)$$

$$D_{ij} = \frac{1}{3}\sum_{k=1}^{N}\bar{Q}_{ij}^{k}\,(\bar{Z}_k^3 - \bar{Z}_k^3) \quad (2.18a)$$

where $\bar{Q}_{ij}$ is the stiffness matrix of the individual lamina. The thickness and position of every ply can be calculated from the following equation

$$t_k = z_k - z_{k-1} \quad (2.18b)$$

and

$$\bar{z}_k = z_{k-1} + \frac{t_k}{2} \quad (2.18c)$$

2.2.2 Stability and Capacity of Steel Plate Girders

2.2.2.1 *Introduction to Buckling of Plate Girders*

Buckling is an instability phenomenon that can occur if a slender (thin-walled) plate is subjected to axial pressure (i.e. compression). At a certain given critical load the plate will buckle suddenly in the out-of-plane transverse direction. The compressive force could be coming from pure axial compression or generated by bending moment, shear or local concentrated loads; or by any combination among them. If the structural member is compact, the load-carrying capacity is governed by the yield stress of the material, rather than buckling strength capacity.

Eurocode defines four cross-section classes with reference to the local buckling risk. The level of the slenderness ratio of the individual plates of the cross-section governs the ability (or inability) for plastic rotational capacity. These four classes in the Eurocode are for girders subjected to a bending moment are defined as follows:

1. Class I, the cross-section is so compact (i.e. with sufficient low slenderness ratio and high plastic rotational capacity) that it is possible to form a mechanism with plastic hinges in a statically indeterminate system. Girders in class 1 are normally standard hot-rolled profiles.
2. Class II, the cross-section is also here compact, but not enough to be able to form a mechanism in a statically indeterminate system.
3. Class III, the cross-section can be characterized as semi-compact, having a reduced capacity for full plastification, due to the local buckling risk on the compression side. These girders are normally welded profiles.
4. Class IV, the cross section is thin-walled, i.e. having such high slenderness ratio that buckling will occur before yielding is reached in the outermost fibre. Post-critical reserve effects enable though for yielding to be reached in the extreme fibre in the ultimate limit state design. An effective net cross-section, where the buckled zone is removed from the gross cross-section (due to the loss of stiffness in that area) is used. Examples of profiles in class 4 are welded bridge girders.

In bridge construction, as well as in aircraft and hull structures, it is necessary to save material, and therefore the structural members are made of thin-walled sections because too much part of the load carrying capacity should not be eaten by the self-

weight alone. A heavy and compact section bridge is also costly with respect to the extra need of foundation and substructure dimensions. Slender girders are usually higher with respect to their cross-sectional dimensions, with higher stiffness relative to a compact cross-section, leading to reduced deflection under the same loading.

One way of further increasing the load-carrying capacity of a slender plate is by the aid of intermediate stiffeners, which minimize the free spacing of the parts subjected to compression. A plated bridge girder is normally stiffened in both the longitudinal and transverse directions; provided that the stiffeners are sufficiently strong to, the risk of buckling is restricted to the plate areas in between the stiffeners. The maximum load carrying capacity of these plate panels is then governed by the plate local buckling risk, however, taking the post-critical reserve of strength into consideration.

The general expression for the critical buckling stress (irrespective of the type of stress distribution) is given by Equation (2.14):

$$\sigma_{cr} = k \cdot \frac{\pi^2 E}{12(1-\nu^2).\left(\frac{b}{t}\right)^2} = k \cdot D \frac{\pi^2}{tb^2}$$

where:

σ_{cr}: elastic buckling stress,

D: flexural rigidity of the plate = $\frac{Et^3}{12(1-\nu^2)}$

t: plate thickness,

b: plate height/width,

E: Young's modulus,

ν: Poisson's ratio,

k: buckling coefficient.

The so-called buckling coefficient k varies depending on the type of stress distribution, and on the quotient between the length (denoted a) and the width (denoted b) of the plate. The quotient b/t is the slenderness ratio of the plate. Plate buckling has (in contrast to global buckling of a column or a strut, or the lateral-torsional buckling of a beam) a post-critical load carrying capacity that enables additional load to be carried after local buckling has occurred. A plate is in that sense internally statically indeterminate, which postpones the collapse of the plate when

buckling occurs and takes it to a higher ultimate load level. The post-buckling reserve of strength is taken into consideration in the ultimate limit state design of plates. The maximum capacity consists of two parts: the buckling load plus the additional postbuckling load.

2.2.2.2 *Elastic Shear Buckling of Plate Girders*

A simply supported girder is a statically determinate structure; however, with respect to the internal mode of action, and the way load is transferred by shear, the system is statically indeterminate. The ability to redistribute load and find alternative load-paths is connected to an intuitive understanding of the behaviour of structures in general. For a plate girder, there is a post-critical reserve of strength that enables for additional loading; beyond shear buckling; this will be discussed in the next section, comparing several key analytical methods available in the literature. Equation (2.14) can be used to calculate the critical buckling shear stress for any plate girder panel provided that the boundary conditions are known or assumed (usually conservatively) in order to calculate the shear buckling coefficient *k*. For simply supported boundary conditions applied to the four edges of the plate and a pure in-plane shear stress, *k* can be found from the following equations (Gaylord and Gaylord, 1972)

$$k_{ss} = 4.00 + \frac{5.34}{(a_w/h_w)^2} \qquad a_w/h_w < 1 \tag{2.19a}$$

$$k_{ss} = 5.34 + \frac{4.00}{(a_w/h_w)^2} \qquad a_w/h_w \geq 1 \tag{2.19b}$$

where k_{ss} is the critical shear buckling coefficient for simply supported boundary conditions. Other boundary conditions will be discussed in Chapter 3 in detail.

2.2.2.3 *Ultimate Load Carrying Capacity- A Historical Background*

In 1885, Wilson (an Engineer of Bridges and Buildings employed by the Pennsylvania Railroad Co.) presented a set of specifications (Wilson, 1886) before the American Society of Civil Engineers which was very similar to the specifications of 1884 (McKeel and Miller, 2006). Wilson is consequently always credited with the first study of the postbuckling strength of plate girder web panels.

Wagner (1931) on the other hand, was the first to present a diagonal tension theory for aircraft structures with very thin web panels. He used a uniform tension

field to determine the post-buckling strength of a panel in pure shear, see Figure (2.6). He assumed the flanges to be rigid and the web to very thin. This method is suitable for aircraft structures where extremely thin plates attached to very rigid boundary elements are encountered. Hence it is of little practical use in civil engineering structures.

However, according to Basler (1960), in 1916, the Norwegian H. H. Rode wrote dissertation (Rode, 1916) in which one chapter deals with the webs of plate girders. It appears that he may have been the first to mathematically formulate the effect of a tension field or truss action which develops after the web loses its rigidity due to buckling. Rode proposed evaluating its influence by considering a tension diagonal of a width equal to 80 times the web thickness.

Basler (1960), is credited with the first ultimate load method for predicting the failure load of plate girders. A web plate which is subjected to shear will, prior to buckling, develop equal tensile and compressive direct stresses inclined at 45° and 135° to the flanges. However, once the web plate buckles and it loses its capacity to carry any additional compressive loading, a new load carrying mechanism is developed, the web carrying the additional shear load in the manner of a conventional truss, and the diagonal compressive stress remains constant.

In the late 1950s, extensive studies were undertaken on the post-buckling behaviour of web panels by Basler and his team. As a result of these and subsequent studies (Basler, 1961a, 1961b and 1963), AISC added the post-buckling strength into its specifications in 1963, and AASHTO followed suit in 1973. Thereafter, with the move towards limit state design concepts in steel structures, the studies initiated by Basler and his team were followed by several modified failure theories to achieve a better correlation between theory and tests.

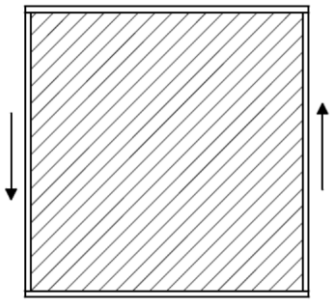

Figure (2.6): Plate tension field by Wagner, (1931).

Post-Buckling Shear Strength of Plate Girders

Basler's method is a result of a fruitful team work for a big project launched at the Fritz Engineering Laboratory, Lehigh University, in 1960 and jointly sponsored by the American Institute of Steel Construction, the Pennsylvania Department of Highways, the U.S. Department of Commerce Bureau of Public Roads, and the Welding Research Council. Four reports were submitted in May 1960 reporting tests of plate girders in bending, shear, and combined shear and bending under static load (Basler et al., 1960b,c,d and e) followed by two reports dealing with cyclic fatigue tests (Yen and Cooper, 1962) and (Yen and Muller, 1965). The last two reports will be dealt with separately in section (2.2.3). Nevertheless, Basler (1960a) submitted (solely) the last report in December 1960, which was published in the Journal of the Structural Division one year later (Basler, 1961a).

There exist several methods that deal with the postbuckling strength of the so called "diagonal tension beam" used in the aircraft industry before Basler. Among them and the most interesting is the method of incomplete diagonal-tension proposed by Kuhn et al. (1952a and b) which is a compromise between "shear resistant" webs, in which no buckling takes place before failure, and diagonal-tension webs obeying the laws of "pure" diagonal tension. According to Kuhn et al., the state of pure diagonal tension is an ideal one that is only approached asymptotically. Truly shear-resistant webs are possible but rare in "aeronautical" practice. In practice, all webs fall into the intermediate region of "incomplete diagonal tension". They presented a full engineering theory of incomplete diagonal tension which may be regarded as a method for interpolating between the two limiting cases of pure-diagonal-tension and "shear-resistant" webs, the limiting case being included. Plane webs as well as curved webs are considered. Kuhn et al. actually modified Wagner's method, simplified some the complicated terms, and added empirical formulation for more conservative estimation of shear capacity. In the author's opinion, Kuhn et al. were ahead of their time when they proposed adding the effect of diagonal tension forces on the flange and taking its capacity into consideration using what they called the "portal frame effect" (even if they did not recommend accounting for it as a conclusion); they even added a flange flexibility index to account for the rigidity of the flanges modifying the first one proposed by Wagner. In addition to that, they

proposed equation to calculate the critical buckling shear stress taking into consideration different plate boundary conditions:

$$\tau_{cr,elastic} = k_{ss}E\left(\frac{t}{b}\right)^2\left[R_a + \frac{1}{2}(R_b - R_a)\left(\frac{b}{a}\right)^3\right] \quad (2.20)$$

where k_{ss} is the theoretical buckling coefficient for a plate with simply supported edges having a width b and a length a (where $a > b$). The coefficients R_a and R_b are coefficients of edge restraint, taken as $R = 1$ for simply supported edges and $R = 1.62$ for clamped edges; the subscripts denote the edge to which the coefficient applies.

It is worth mentioning that Kuhn et al.'s work was revisited seventeen years later by Tsongas and Ratay (1969) to validate their proposed method. They tested full-scale diagonal-tension beams, representative of spacecraft construction (at their time). Unfortunately, their work was limited to very thin chem-milled aluminium alloy web sheet. Fourteen specimens were static-tested, four were fatigue tested. However, they concluded that the NACA method (as they refer to Kuhn et al. work in their report) correctly predicted the mode of failure (stiffener and sheet) and that the measured ultimate loads of all fourteen static test panels exceeded the lowest allowable loads computed by the NACA method, regardless of whether or not the actual failure mode was the same as the mode corresponding to the lowest predicted allowable load. When the test ultimate loads were compared with the NACA allowable loads for the actual modes of failure, an average conservatism of 16% was obtained for sheet failures and 13% for stiffener failures.

Basler's Method for Predicting the Ultimate Capacity of Plate Girders Loaded Mainly in Shear

Basler (1961a) assumed that the flanges of most girders were so flexible that they could not withstand the lateral loading imposed by the inclined tensile field, and established that in such a case the girder fails when the web panel develops an off-diagonal yield band, (Figure 2.7). The ultimate shear load for a web panel as calculated by Basler is given by

$$V_{ult} = \tau_{cr}ht + \frac{\sigma_t^y ht}{2\sqrt{1+\alpha^2}} \quad (2.21)$$

$$\text{where} \quad \sigma_t^y = \sigma_{yw}\left(1 - \frac{\tau_{cr}}{\tau_{yw}}\right) \quad (2.22)$$

and

τ_{cr}: the critical shear stress,

τ_{yw}: the shear yield stress of web material,

h: the clear depth of web plate between flanges,

t: the thickness of the web plate,

σ_t^y: the web membrane stress in tension field,

σ_{yw}: the tensile yield stress of web material,

α: the aspect ratio of web panel = a/h, and

a: the clear width of web panel between stiffeners.

By making the assumption that σ_t^y could be represented by Equation (2.22) which does not allow for the effect of the inclination of the tensile field, Basler was able to show that the "off-diagonal band" would develop at an inclination equal to half the inclination of the web diagonal (i.e. $\theta_d/2$).

According to Porter et al. (1975), it was pointed first by Gaylord and later by Fujii and Sleberg that Equation (2.21) does not actually represent the true resistance of Basler model which is correctly given by:

$$V_{ult} = \tau_{cr} ht + \frac{\sigma_t^y ht}{2\sqrt{1+\alpha^2}+\alpha}\left(1 - \frac{\tau_{cr}}{\tau_{yw}}\right) \tag{2.23}$$

However, the modified Basler equation gives very conservative results for the ultimate shear load while the original Basler's equation gives much more reliable results. Figure (2.8) shows that the difference between the original and modified Basler's equations is very significant for plate girders with slender webs and that the accuracy of the equation increases with reducing the slenderness of the web panel (i.e. increasing its critical buckling shear stress).

Many variations of the post-buckling tension field have been developed since Basler's work. Only the key methods will be mentioned in the following.

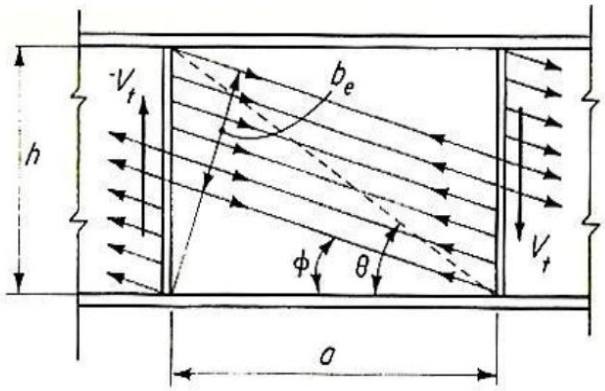

Figure (2.7): Inclined yield band according to Basler, (Gaylord and Gaylord, 1972).

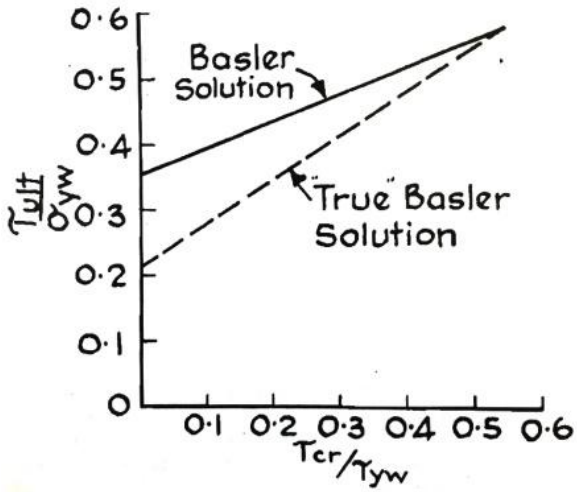

Figure (2.8): Variation of Basler original and modified solution, (Porter et al., 1975).

Other Methods for Predicting the Ultimate Capacity of Plate Girders Loaded Mainly in Shear

Fujii et al. (1971) derived a method with beam mechanisms in each flange with interior yield hinge at the central, mid-panel, see Figure (2.9).

In the same year, Ostapenko and Chern (1971) proposed a new version of the Basler collapse mechanism. The model assumed was similar to that assumed by Basler except that they allowed for a variation of the membrane stress across the section, as shown in Figure (2.10). In addition, they stated that the flange would contribute to the strength of the girder and they allowed for the development of a

picture frame type of mechanism in which hinges formed at the flanges over the transverse stiffeners.

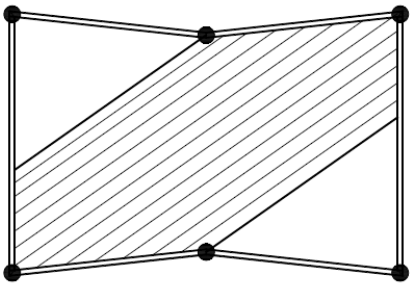

Figure (2.9): Tension field with yield hinges in the flange mid-points by Fujii et al., (1971).

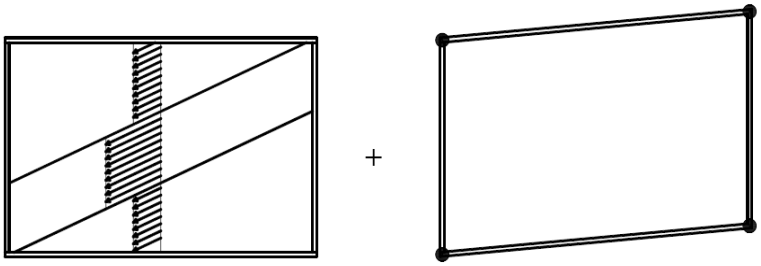

Figure (2.10): Tension field action and frame mechanism by Ostapenko and Chern (1971).

Rockey and Skaloud (1972) presented a plastic method of design for plate girder webs which allows for the influence of flange rigidity upon the post buckled behaviour of webs. The design procedure (which is based on an extensive study of the behaviour of 40 plate girders tested by them) has been checked against other experimental data available in the literature. In their study, they showed that the collapse mode of the plate girders involved the development of plastic hinges in the tension and compression flanges. Based on this they considered that the collapse of plate girders could be represented by the two phase action shown in Figure (2.11). However, they restricted their analysis to the beam action, Figure (2.11a).

Based on the above discussion, Rockey and Skaloud (1972) proposed their method for plate girder webs allowing for the influence of flange rigidity for the first time, and V_{ult} is seen to have the value given by

$$V_{ult} = 2C.t\ sin^2\theta_d \sigma_t^y + \tau_{cr} dt \qquad (2.24)$$

C is the position of plastic hinges in tension and compression flanges for symmetrical girder in pure shear, (Figure 2.11a), and θ_d is the inclination of web panel diagonal.

Porter et al. (1975) pointed out that one weakness in the Rockey-Skaloud model is the assumption that the angle of inclination of the tensile band coincides with the inclination of the panel diagonal.

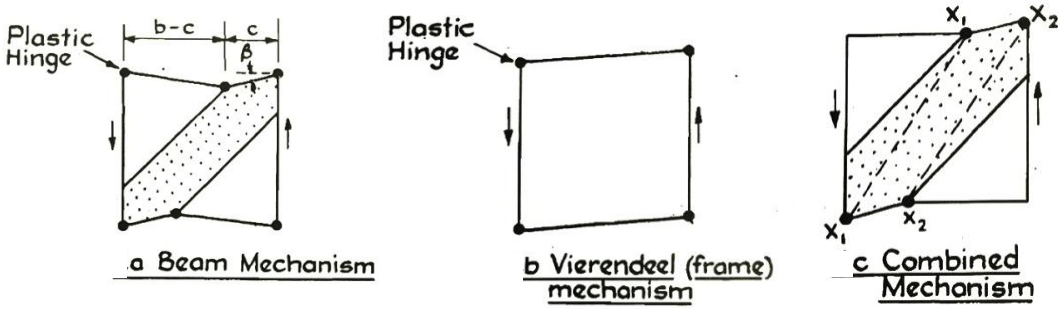

Figure (2.11): Mechanism involved in collapse of shear panel (Porter et al., 1975).

In 1973, Calladine presented a study of plastic collapse of the end panel of a plate girder under high shearing load by the means of the upper bound theorem. In his paper, Calladine stated that at the time the most comprehensive theory was Rockey and Skaloud (1972) but that it does, nevertheless, contain unsatisfactory features. The aim of Calladine (1973) paper was

(i) to establish a more rational version of Rockey and Skaloud's theory;
(ii) to extended to cover panels subjected to both shear force and bending moment; and
(iii) to investigate the special case of failure of the end vertical member of a plate girder.

According to Porter et al. (1975), Calladine's method was established for the specific case of a web with negligible buckling resistance allowing him to assume that the action of the web could be represented by a series of parallel tendons, that the webs would fail when the shear panels develop a mechanism of the form shown in Figure (2.11c). In addition, he showed that both the position of the hinges and the inclination of the membrane field varied with the rigidity of the flanges.

Unfortunately, Calladine did not account for the case encountered in practical engineering where the web has a significant load carrying capacity before it buckles.

He did, however, consider the case of a very thick web which will yield before it buckles and showed that in this case failure would occur by the web yielding together with the development of hinges at the corners of the panel.

As a result, he submitted a design method for suppression of collapse by a mechanism which involves plastic bending in the vertical end post. This design method enables the designers to proportion the overhang at the end of a girder so as to maintain the required anchorage for sustaining the assumed stress field at postbuckling stage. Calladine's method is presented in detail in Appendix (A).

In 1975, Porter et al. presented a new ultimate load carrying capacity method of design, known later as the "Cardiff Method", which can be used for predicting the failure load of conventional plate girders having webs reinforced by both longitudinal and transverse stiffeners, hybrid girders and unsymmetrical girders, loaded primarily in shear. The method provides identical upper and lower bound solutions. Furthermore, many of the existing solutions are special cases of this more general solution.

The Cardiff method is applicable (in the form presented in Porter et al., 1975) to internal web panels where the panel under consideration is supported along its transverse boundaries by adjacent web panels. Porter et al. (1975) suggested that collapse mechanisms for end bay panels require special attention because of the flexibility of the end posts, but Calladine (1973) solved this problem for the case of very thin web. Alternatively, a rigid end post consisting of two double-sided load-bearing transverse stiffeners may be used to anchor the tension field at the end of a plate girder (BS 5950-1) and was discussed further by Hansen (2006).

Porter et al. assumed that the web panels are simply supported along their boundaries. This is a lower limit assumption. The upper limit of the boundary conditions of web panels is that the flanges provide a fully clamped condition, while the vertical stiffeners providing a simple edge support. The correct buckling solution lies somewhere between these two extreme bounds.

Furthermore, and since the method is confined to study web panels loaded primarily in shear, the effect of bending stresses on the shear buckling stress of the web and the variation of the membrane stress in tension field ($\sigma_t{}^y$) over the web panel can be ignored.

The Cardiff Method is based on a thorough literature review and experimental observations and measurements via other research workers (such as: Basler and Rockey-Skaloud), as well as the research work conducted by the authors in Cardiff University. As a final concluding remark, the Cardiff method is a general method for predicting the failure load of webs loaded in shear. The method has been shown to be capable of accurately predicting the overall collapse behaviour of transversely and longitudinally stiffened panels loaded in shear (Assoodani, 2014).

Finally, Appendix (B) presents a step by step algorithm of Cardiff Method for predicting the ultimate load capacity of steel plate girders.

Many other researchers have dealt with the problem of post-buckling reserve of strength for plate girders mainly loaded in shear, e.g. Sakai et al. (1966), Bergfelt (1973), Höglund (1973), Nishino & Hasegawa (1977), Narayanan and Adorisio (1983), and Kuranishi et al. (1988). However, the solution by Porter et al. (1975) is the one adopted in the 1993-edition of Eurocode 3 (EC3 1993), with some further modification not discussed here.

In the newest edition of Eurocode 3 (EC3 2006), the method by Porter et al. (1975) has been removed and substituted by a method based on the rotated stress field developed by Höglund (1973). Höglund has modified his own theory several times. The newest version of the rotated stress field theory is found in (Höglund, 1995), which is adopted in EC3 (2006) with few empirical modifications. A description of the method in EC3 (2006) is given in (Johansson et al. 2001).

In 1988, Kuranishi et al. (1988) investigated the tension field action and collapse mechanism of shear panels isolated from plate girders by the technique of finite element method. They paid special attention to the influence of the rigidity of flanges and the boundary conditions of one panel. Figure (2.12) illustrates their model. They concluded several remarks which agree with the previous illustrated work, except for one very important conclusion, which is that the tension field can form without any anchor action by flanges or side members. In these cases, the tension field is anchored by the gusset plate action, which is the development of the high biaxial stress state in the corner end zone of the tension field. However, these

high tensile and compressive stresses do not have the direct effect on the formation of the collapse mechanism.

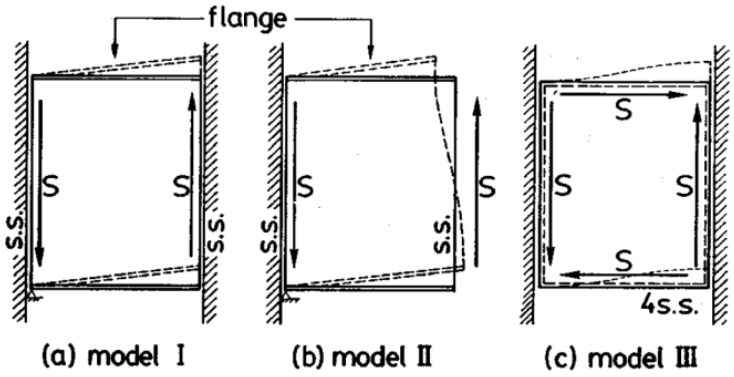

Figure (2.12): Models with various boundary conditions, (Kuranishi et al., 1988).

In 1991, al-Sarraf and Hamoodi presented an equilibrium method of assessing the ultimate shear capacity of plate girders having vertical and inclined web stiffeners. The method presents an extension of the Cardiff solution for predicting the ultimate shear of plate girders. They stated that earlier studies at Cardiff have demonstrated the validity of small-scale model testing for plated structures. Hence the experiments reported have been carried on scaled down models using 1.5mm webs. The results of eight tests on model girders having different orientations of web stiffeners were reported and the validity of their proposed method was tested accordingly. Figure (2.13) illustrate the stiffener configuration of their test specimens. They obtained the elastic critical shear stress in the non-rectangular web by solving the basic differential equation using the method of finite differences. A rapid method of assessing the upper and lower bound of the ultimate shear capacity was also presented to avoid the complications involved in the prediction of elastic critical shear stress of such webs. The ratio of predicted ultimate load to observed ultimate load was between 0.87 and 1.13 for lower and upper bound, respectively, leaving a margin of error of 13%; which may be considered relatively high.

In 2003, Real et al. studied the shear strength and behaviour of slender stainless steel plate girders. Their research work has been divided into two experimental programmes. Data generated in the first programme enabled the observation of non-linear behaviour of stainless steel and drawn some useful conclusions for designing

stainless steel structures. Tests were performed on nine girders covering a wide range of web slenderness values and several aspect ratios of the web panel, these being the two determining factors of the element response under shear load. The second experimental programme focused on the response of stainless steel plated girders, mainly loaded in shear, to identify the differences between the behaviour of the slender webs in girders with rigid and non-rigid end posts, (Figure 2.14). They conclude that the behaviour of stainless steel plates under shear load is analogous to that of carbon steel plates. In the beams tested, a tension field band developed as a new resistant mechanism after reaching the shear buckling load level but this behaviour is clearly influenced by the material non-linearity. In addition, they re-affirmed the generally accepted idea that the rigid end posts provide an increase in the plate girder capacity.

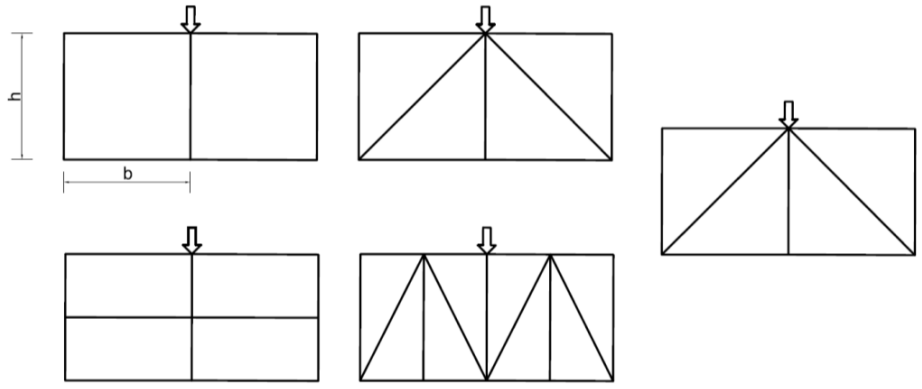

Figure (2.13): Details of test specimens, (al-Sarraf and Hamoodi, 2015)- Reproduced.

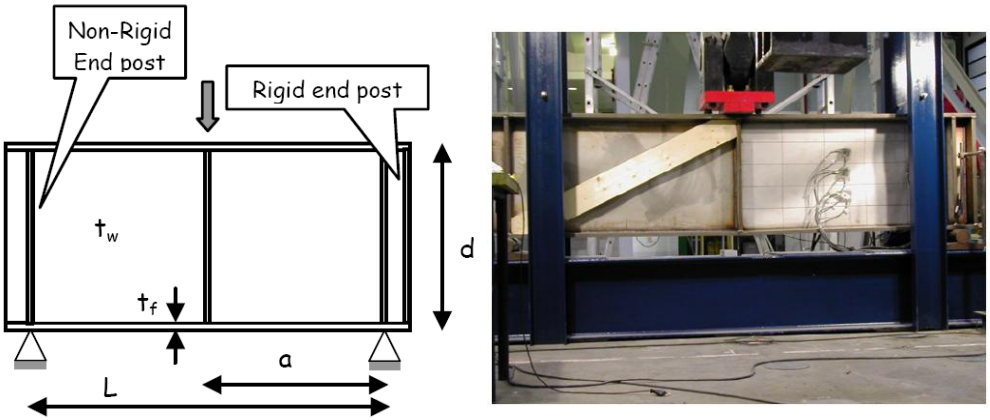

Figure (2.14): Test specimen geometry and loading scheme of Series II, (Real et al., 2003).

In 2006, a new revolutionary method proposed by Yoo and Lee revisited the fundamental assumptions used in most of classical failure theories for post-buckled web plates under shear. Based on their previous work experience for more than a decade (Lee et al., 1996, 1998, 1999, 2002, and 2003), they carried out nonlinear finite-element analysis on web panels having different aspect and slenderness ratios. The results of the nonlinear analysis revealed that the diagonal compression continuously increases in close proximity to the edges after buckling; thereby producing in the web panel a self-equilibrating force system that does not depend on the flanges and stiffeners, see Figure (2.15). This concluding remark is contrary to the assumption that the compressive stresses remain more or less constant almost the same as that at the instant of elastic buckling of the web similar to the conclusion of Kuranishi et al. (1988).

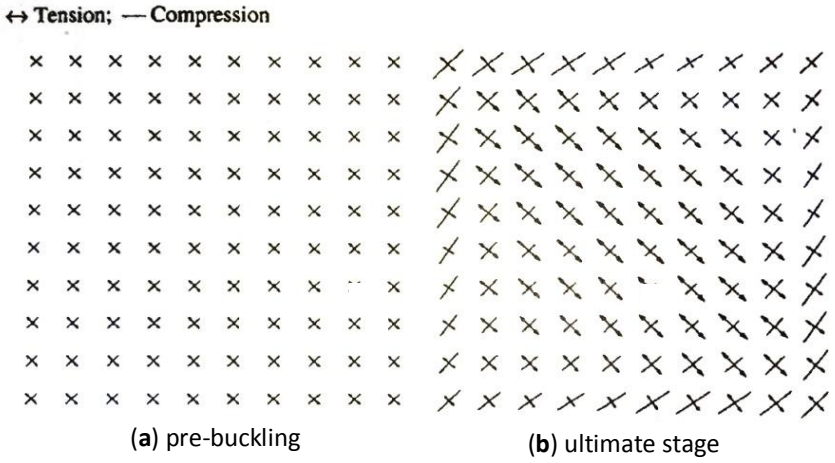

Figure (2.15): Distribution of principal stresses under pure shear in the web, (Yoo and Lee, 2006).

Yoo and Lee (2006) stated that despite their adoption of incorrect assumptions, most of the existing theories predict the shear strength well enough for design purposes as the suggested equations were derived through extensive calibration with experimental data. The consequences resulting from their examination are summarized as follows:

- As the intermediate transverse stiffeners are not subjected to the large axial compressive force predicted by the Basler model (although they are subjected to some compression by virtue of their continuity with the web), the

requirement for the area of the transverse stiffener developed by Basler is irrelevant.

- All forces developed during post-buckling are self-equilibrated within the web panel. This means that even end panels can develop post-buckling strengths.

Eventually, they suggested that the restriction of ignoring any tension field in the end panels needs to be revisited. Following on from this, in 2009, Lee et al. presented two papers (Lee et al. 2009a and b) dealing with theory behind the anchoring mechanism and the source of plastic hinge-like failure mode, respectively. The main conclusions in their two papers were:

- Even with flanges that are heavy enough to function as rigid anchors, the anchoring mechanism cannot completely develop unless the flanges are supported by incompressible transverse stiffeners.
- When the transverse stiffeners are incompressible, even ordinary flanges are capable of substantially contributing to the post-buckling strength through the anchoring mechanism.
- The primary reason why the anchoring mechanism by the flanges contributes little to the post-buckling strength in ordinary plate girders is that the transverse stiffeners used are axially too flexible to be treated as incompressible.
- Axially forces developed in the transverse stiffeners attached to ordinary plate girders due to the anchoring mechanism are negligibly small; and utilisation of the flange anchoring mechanism in practical designs is beyond the realm of possibility because it requires an unimaginably high axial stiffness of the transverse stiffeners.
- The anchoring mechanism is virtually nonexistent in ordinary plate girders. The tension field developed in the web panel is mostly attributable to the post-buckling mechanism developed by the function of the lateral supports presented by Yoo and Lee (2006).

Finally, they recommended the reflection of the more valid design equation of Lee and Yoo (1998) in the new design codes for a more rational design as all specifications are updated periodically, reflecting what has been learned.

According to Assoodani (2014), Alinia et al. (2004) modelled and analysed a number of full-scale plate girders to determine their shear failure mechanism characteristics. The objective of this numerical nonlinear large deflection elasto-plastic finite element study was to clarify how, when, and why plastic hinges that emerge in experimental tests actually form. The analysis, also, concluded that:

- Detached plates simulation does not represent the true behaviour of plate girder web panels.
- Shear-induced plastic hinges occur only in the flanges of end panels after the formation of partial-inclined yield zones in webs. They do not occur in mid-panels.
- The formation of plastic hinges is due to the shear deformation of girders, directly pertained to the stiffness of end-posts and flange dimensions. The location of plastic hinges is not directly related to the stresses imposed by the inclined tension fields.
- When the flange thickness is more than three times the web thickness, the failure mode is always in shear, and if this ratio is less than two, the flexure failure mode governs. In the intermediate ranges, the failure mode depends on the web slenderness ratio.
- The addition of end-posts provides more fixity to flange plates and increases the ultimate resistance of plate girders.
- Eurocode 3 gives the most conservative ultimate capacity for plate girders, while the Cardiff model over estimates them. The AISC results for medium to stocky flanges produce closest results to the FEM. The AASHTO and Basler results are very similar and they always overestimate the capacity. Höglund's theory is always safe and reasonably close to FEM.

As a concluding remark on the work of Alinia et al., and by reviewing the resulting deformed shape of plate girders with less-rigid end posts, one can recognize the formation of plastic hinges, not in the flanges only, but also in the end stiffeners. That means the formation of plastic hinges is not due to shear deformation of girders, as they stated, but also due to the action of tension field, Figure (2.16) which shows the positions of plastic hinges in two typical girders: (a) girders with less rigid end stiffeners, and (b) girders with more rigid end stiffeners.

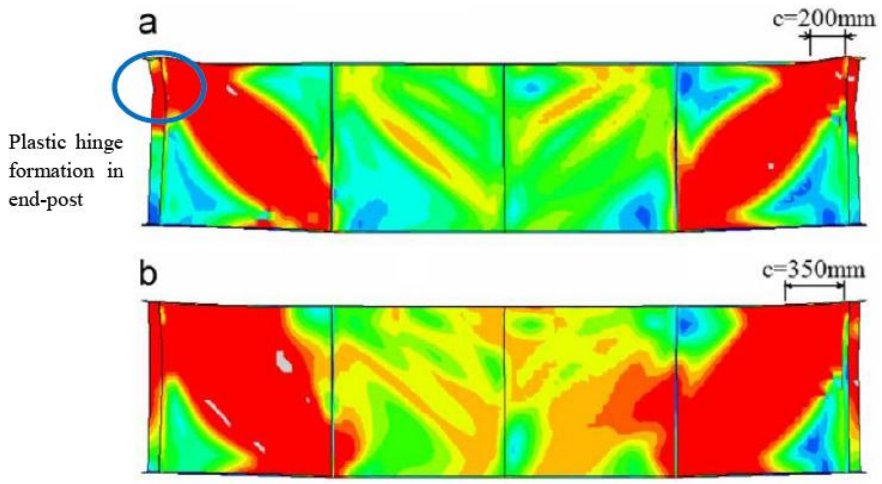

Figure (2.16): The position of plastic hinges. (**a**) Girders with less rigid end stiffeners, and (**b**) girders with more rigid end stiffeners, (Assoodani, 2014).

In the same year, Takeda (2004) submitted a PhD investigating the fundamental property and characteristics on various points of girder structures toward their rational design by means of experimental methods in combination with several approximate analyses. Emphasis was made of the deformability of plate girders as an important factor from the standpoint of absorption of earthquake energy, taking the damaged states of the Great Hanshin-Awaji Earthquake as an illustrative example.

Takeda (2004) studied both constant and variable depth plate girders in different load states and combinations. Figure (2.17) shows typical models for the tapered girders experimental series in his work. Takeda's theoretical work agrees with most of the previously mentioned theories. Most importantly, he concluded that the shear panel of the tested plate girders showed an excellent stability and energy absorbing capacity when attacked by repetitive elastic (high-cycle) and inelastic (low-cycle) in-plane shear load. In addition, he proposed a modified equation for predicting the load carrying capacity of tapered plate girders. The equation follows the traditional assumption of dividing the ultimate shear load carrying capacity of the panel into two parts; the critical buckling shear stress arising from the frame (beam) action, which was found using finite element analysis- Figure (2.18a and b), were $\bar{\alpha}$ is the average panel aspect ratio (length divided by the average depth of the tapered panel); and the diagonal tension field action which was modified from Ostapenko and Chern model (1969) neglecting the effect of the upper web triangle, see Figure

(2.18c). From this figure also, the equilibrium condition for deriving the force applied on the intermediate stiffener can be seen as well.

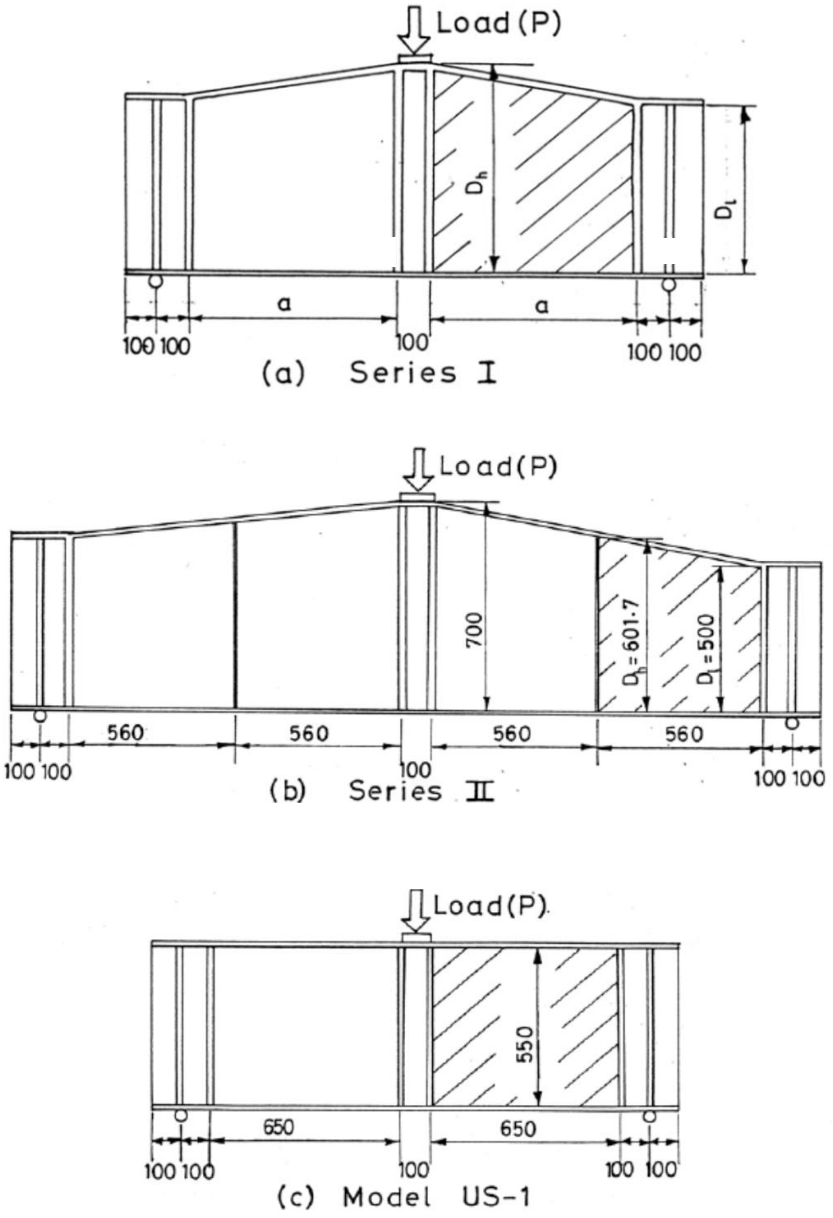

Figure (2.17): Tapered girders experimental models, Takeda (2004).

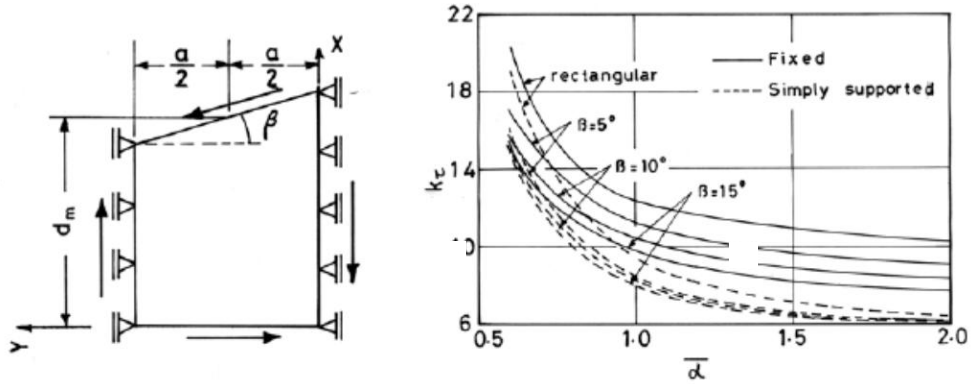

(**a**) Trapezoidal panel analytical model. (**b**) Shear buckling coefficient curves.

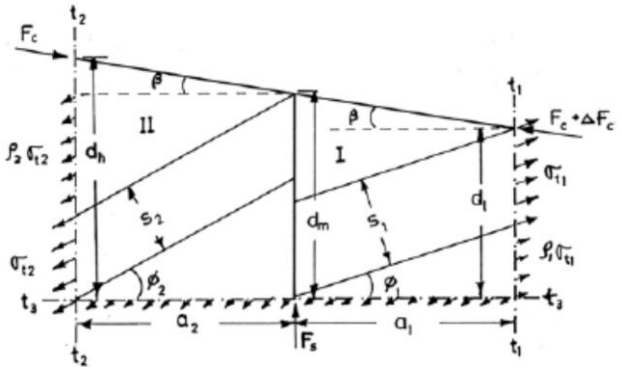

(**c**) Equilibrium conditions applied to adjacent web panels and its effect on the intermediate stiffener.

Figure (2.18): Tapered girders analytical models, (Takeda, 2004).

Hansen (2006) adopted both an upper and lower bound plasticity model to determine the post-buckling strength of steel plate girders. The model was a horizontal, simply supported steel plate girder with double symmetrical I-section and transverse web stiffeners is considered. In order to simplify the calculations, the web compressive strength was neglected as an additional safety margin and a perfectly plastic material was assumed. The assumed yield criterion was identical to Tresca's yield criterion without the compressive parts. Furthermore, the web plate is assumed simply supported at all the boundaries, i.e. at the flanges and external stiffeners.

The interesting part in this method is that it incorporates the strength of the transverse stiffeners and assumes that the tensile bands may pass the transverse stiffeners, which is often observed in tests but neglected by other methods according to Hansen (2006).

The load-carrying capacity according to the solution of the lower bound theorem, see Figure (2.19), can be expressed by the following non-dimensional value, τ/f_{yw} as

$$\frac{\tau}{f_{yw}} = \begin{cases} \sqrt{\psi(1-\psi)} & for\ \psi < \frac{1}{2} \\ \frac{1}{2} & for\ \psi \geq \frac{1}{2} \end{cases} \tag{2.25}$$

where:

τ: is the ultimate shear stress,

ψ: is the mechanical degree of stiffening $= \emptyset \frac{f_{ys}}{f_{yw}} = \frac{A_s n}{L t_w} \frac{f_{ys}}{f_{yw}}$,

A_s: is the total cross-sectional area of a single stiffener,

L: is the shear zone length,

n: the number of internal stiffeners,

φ: the stiffener ratio,

f_{yw}: the yield stress of the web,

f_{ys}: the ultimate stress of the stiffeners (either the buckling stress or the yield stress, the lower being decisive).

It is worth mentioning that the lower-bound solution does not take the rigidity of the flanges into considerations, following Basler's criteria.

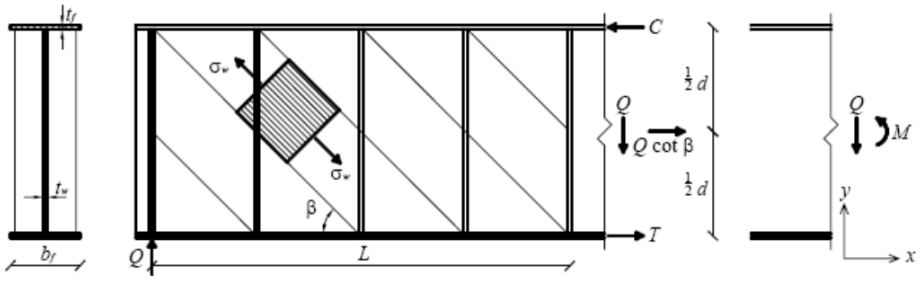

(**a**) Diagonal tension stress field for the lower-bound solution.

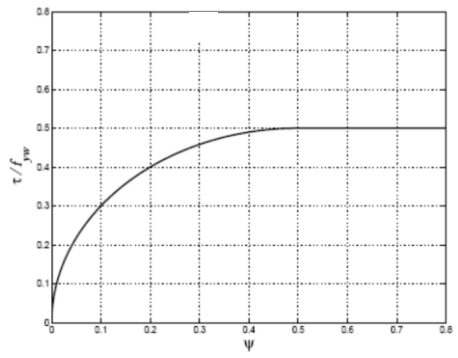

(**b**) Lower-bound solution.

Figure (2.19): Lower-bound model and solution, (Hansen, 2006).

On the other hand it is easy to take the rigidity of flanges into considerations with the upper bound solution. Consequently, the internal work, i.e. dissipation, consists of three contributions; namely, the bending of flanges, the deformation of the web in the parallelogram-shaped area, and compression of the internal stiffeners, see Figure (2.20). As a conclusion the load carrying capacity was expressed in the following

$$\frac{\tau}{f_{yw}} = \frac{1}{2}\left(\sqrt{1+tan^2\theta} - tan\,\theta\right) + \frac{\eta}{{}^{L}/_{d}-tan\theta} + \psi\, tan\,\theta \qquad (2.26)$$

subjected to minimizing the equation with the free parameter, here θ, which yields

$$\frac{d}{d\tan\theta}\left(\frac{\tau}{f_{yw}}\right) = 0 \quad \Rightarrow \quad \frac{1}{2}\frac{\tan\theta}{\sqrt{1+tan^2\theta}} - \frac{1}{2} + \frac{\eta}{\left({}^{L}/_{d}-tan\theta\right)^2} + \psi = 0 \qquad (2.27)$$

where η is a nondimensional parameter representing the flanges bending stiffness

$$\eta = 4\frac{M_{pf}}{d^2 t_w f_{yw}} = 2\frac{b_f t_f^2}{d^2 t_w}\frac{f_{yf}}{f_{yw}}$$

and

M_{pf}: is the flange plastic moment,
f_{yf}: is the flange yield stress,
b_f: is the flange width,
t_w: is the web thickness,
d: is the web depth,
θ: is the yield band inclination angle with the transverse stiffener axis.

Unfortunately, no analytical expression was proposed and a numerical solution is required to solve Equations (2.26) and (2.27). However, the upper-bound solution for a plate girder with an aspect ratio (L/d) equals 1.0 and 2.0 is provided in Figure (2.21) and it is compared with the lower-bound one. Hansen proceeded by modifying the circular fan method used for reinforced concrete beams and implemented it as a design method for steel plate girders for several load cases.

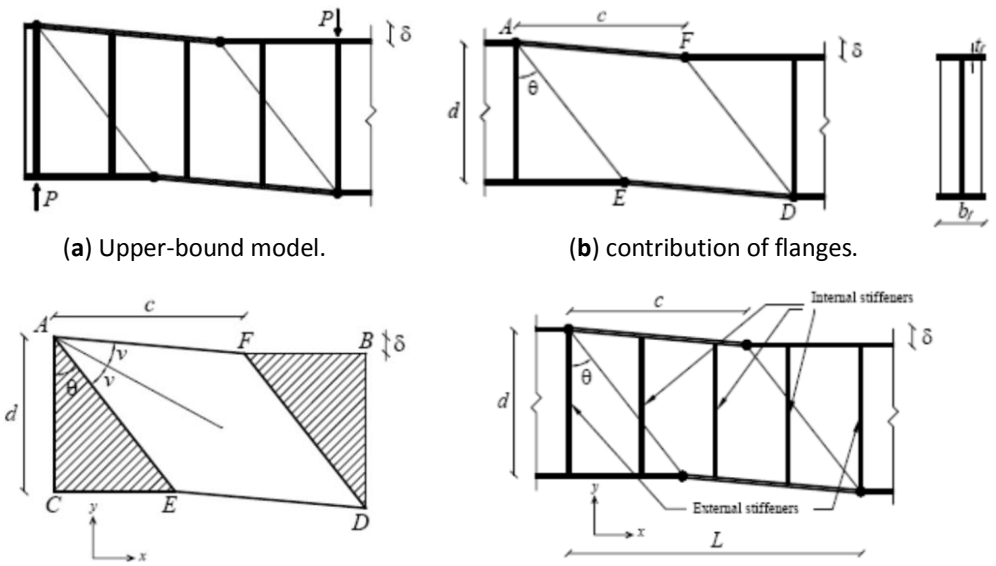

(**a**) Upper-bound model. (**b**) contribution of flanges.

(**c**) contribution of the web. (**d**) contribution of the intermediate stiffeners.

Figure (2.20): upper-bound model, (Hansen, 2006).

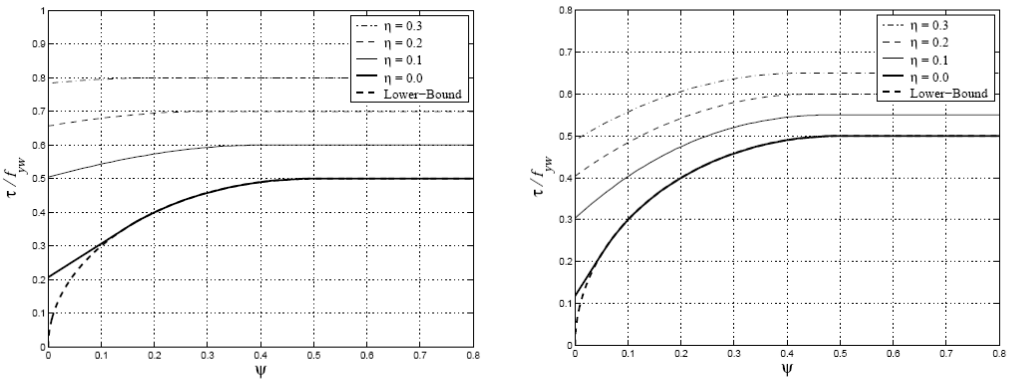

(**a**) L/d = 1.0. (**b**) L/d = 2.0.

Figure (2.21): upper-bound solution, (Hansen, 2006).

Recently, in 2014, Ajeesh and Sreekumar studied the influence of initial imperfection of plates on the shear resistance of hybrid plate girders fabricated using slender plate elements. Nonlinear FEA was performed to compute the ultimate shear strength of a hybrid girder. Imperfection analysis was performed by varying the magnitude of imperfection on web panel of the hybrid plate girder to compare the variation in ultimate shear strength. The study was also done by varying the yield strength and slenderness ratio of web panel. The result of the study indicates that

- The ultimate shear strength of hybrid plate girders decreases with increasing the magnitude of initial imperfection.
- The effect of imperfection on shear strength was significantly high for plate girder with low web slenderness ratio and high yield strength of web panel. The percentage reduction in shear strength was 21% for low values of web slenderness ratio (h_w / t_w = 88).
- The maximum lateral deflection, as well as the vertical deflection of plate girder model increase with increasing imperfection magnitude from h_w /100000 to h_w /10, see Figure (2.22) where the load is plotted versus maximum lateral deflection.

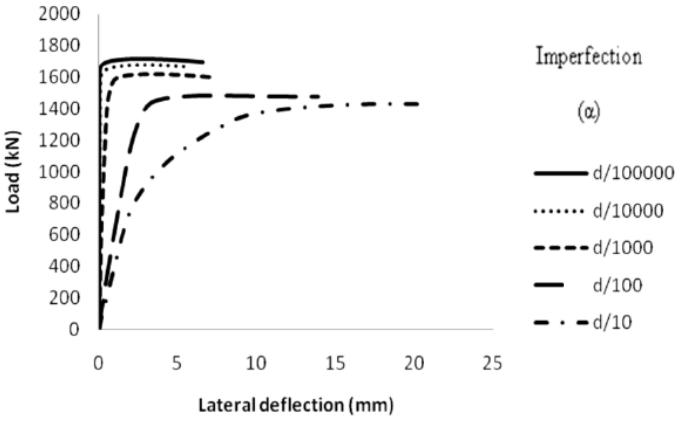

Figure (2.22): Plot of load versus maximum lateral deflection, (Ajeesh and Sreekumar, 2014).

To sum up the information narrated in this section; in spite of the fact that the ultimate shear capacity of steel plate girders loaded mainly in shear (Which is the sum of the elastic buckling and post-buckling resistance of plate girders), was thoroughly studied since the beginning of the last century; there still no global consensus of the mechanism associated with the failure of steel plate girders and that different standards provide different design methods based on empirically modified plastic failure theories. Recent finite element based analysis (Lee et al., 1998, for instance) is not in full agreement with the findings of the major adopted methods like Basler's and the Cardiff method. The problem gets rather complicated and challenging when trying to propose a general solution covering the whole range of ordinary and thin-walled steel plate girders. Another difficulty is the question of

generality of the solution in taking into consideration the problem associated with the web panel being an intermediate or end panel and its relation to the rigid or semi-rigid end posts.

Generally, there are three options in choosing a method to analyse or design a steel palate girders loaded mainly in shear; Basler's method adopted in the American standards; the Cardiff and Höglund methods adopted in the Eurocode; or going to the more recent un-standardized methods like the shear cell method (Lee et al., 1998) or the circular fan method (Hansen, 2006). In addition, it has been shown that finite element analysis could be an acceptable alternative for more complicated cases.

2.2.3 Fatigue of Steel Plate Girders

During the industrial evolution, sudden and inexplicable brittle failures often occurred. These brittle failures often occurred with cyclic loading; therefore they were often denoted as *fatigue failures*. Empirical investigations began, but with a lack of understanding of the complex nature of the fatigue failure, more and more brittle failures occurred when welded connections became common. The many brittle failures in the welds of the *Liberty* Ships during the Second World War are well-known, as are the crashes of de *Havillands* Comet jet airplanes, where the window openings were unfavourably designed, causing large stress concentration to occur (Hansen, 2006).

An understanding of brittle fracture began with the work of Griffith (1921, 1924) in England. He examined failures in glass, and showed that existing initial cracks induced large stress concentrations, which led to crack growth with consumption of the existing elastic energy without further supply of energy. In the USA, Irwin (1948) and Orowan (1948) modified Griffith's theory to a form useful for metallic materials. They showed that the plastic work in the vicinity of the crack tip has to be taken into account, which is by far the most important contribution for metallic materials. Furthermore, Irwin introduced the notation stress intensity factors.

Finally, Paris et al. (1961) showed that crack growth due to cyclic loading may be described by the variation of the stress intensity factors at the crack tip.

It was first pointed out by Yen and Muller (1965) and followed by several researchers such as (Goodpasture and Stallmeyer, 1967), (Paterson et al., 1970), and (Maeda, 1971); when a thin-walled plate girder is subjected to repeated loading, there are possibilities of the initiation and propagation of fatigue cracks along the fillet welds around the web panel boundaries.

In girders under shear, Type 4 cracks are initiated at the toe, on the web side of the fillet welds, near the corners where the diagonal tension field is expected to be anchored. The cause of cracking, as shown in Figure (2.23), is the plate bending stresses at the weld toe. Theses bending stresses are caused by the out-of-plane deformation of the web under in-plane shear (Narayanan and Roberts, 1991).

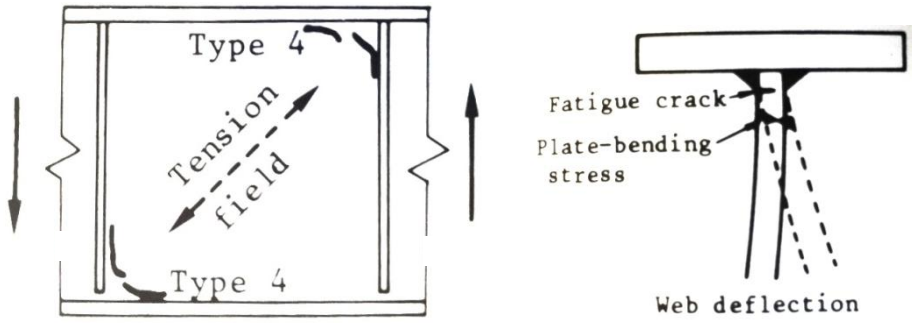

(**a**) Shear fatigue cracks in thin-walled plate girder (**b**) Plate secondary bending stresses

Figure (2.23): Plate girders fatigue cracks and secondary stresses, (Narayanan and Roberts, 1991).

In the early 1960's Yen and Muller performed fatigue tests on nine large-size thin-web girders in the Fritz Engineering Laboratories at the University of Lehigh; investigating the fatigue behaviour of thin-walled girders including the effect of lateral web deflections for the formulations of design recommendations. The repeated cyclic load was applied at a rate of 250 cycle/minute. Full details of the specimens, instrumentation, displacement and strain measurements can be found in (Yen and Muller, 1965 and 1966). They concluded that the membrane stresses measured near panel boundaries were in reasonable agreement with beam theory predictions at practical loads, and comparing these stresses with numbers of cycles at crack initiation no clear correlation was observed. It was also found that secondary bending stresses were caused by lateral web deflections under cyclic loading. The

magnitude of theses stresses was as high as the yield stress of the web in some cases. The initial locations of cracks along the flanges were shown to be in the regions of the highest secondary bending stresses, and comparing these stresses with the number of cycles at crack initiation a clear correlation was observed (Yen and Mueller, 1966).

Okura and Maeda (1985) presented a numerical model based on finite element analysis to estimate the fatigue strength at 2×10^6 cycles of loads. Using the relation between load and secondary bending stresses due to out-of-plane deformation of the web, they expressed the relation in terms of the in-plane shear stress as a function of the web slenderness ratio.

$$\frac{\tau_o}{\sigma_e} = k_{cr}\eta_o + \frac{3}{4}(1-v^2)\theta\xi_o \tag{2.28a}$$

$$\frac{\sigma_b}{\sigma_e} = S\eta_b + \sqrt{A^2\xi_o^2 + B^2} - B \tag{2.28b}$$

where

τ_o is the average shear stress of the section,

$\sigma_e = \frac{\pi^2 E}{12(1-v^2).\left(\frac{b}{t}\right)^2}$, is the fundamental stress.

and

$\eta_o = \sqrt{\frac{e}{e+re_o}}$,

$\xi_o = \left[0.61\left\{\left(\frac{e}{t_w}\right)^2 + 2\frac{e_o}{t_w}\frac{e}{t_w}\right\}^{0.5} + 0.39\frac{e_o+e}{t_w}\right]\left\{\left(\frac{e}{t_w}\right)^2 + 2\frac{e_o}{t_w}\frac{e}{t_w}\right\}^{0.25}\sqrt{\frac{e_o+e}{t_w}}$,

$\eta_b = \frac{1}{2}\left\{\frac{e}{t_w} + \sqrt{\frac{e}{t_w}\left(\frac{e}{t_w} + r\frac{e_o}{t_w}\right)}\right\}$,

e_o: is the initial deflection at the centre of the plate,
e: is the additional out-of-plane deflection at the centre of the plate,
k_{cr}: is the buckling coefficient,
σ_b: is the secondary bending stress,
S: is the increase in secondary bending stress per an out-of-plane deflection unit of the buckled shape,
r: is a coefficient depending on the boundary conditions in the out-of-plane direction,
θ, A, B: coefficients determined from the results of the finite element analysis.

The values of r, k_{cr}, S, θ, A, and B are listed in Table 2.1 for combinations of boundary conditions and in-plane shear loading.

Table 2.1: values of the coefficients, extracted from Okura and Maeda (1985)

	Simply supported BC's				**Two edges simply supported and two edges clamped BC's**				**Clamped BC's**			
a/b	**0.5**	**0.75**	**1.0**	**1.5**	**0.5**	**0.75**	**1.0**	**1.5**	**0.5**	**0.75**	**1.0**	**1.5**
r	1.0	1.0	1.0	1.0	0.74	0.74	0.74	0.74	0.54	0.54	0.54	0.54
k_{cr}	26.03	13.29	9.33	7.07	26.88	15.47	12.58	11.13	42.46	21.31	14.67	11.49
S					17.51	25.60	25.27	23.79	98.46	42.90	24.32	23.82
θ	5.12	4.35	3.46	2.03	5.59	4.61	3.66	2.40	8.07	5.08	3.97	2.47
A					15.18	15.93	14.51	10.96	19.99	25.82	17.93	12.81
B					40.46	36.01	33.61	36.44	0.0	111.81	71.07	62.20

According to Okura and Maeda (1985), 2×10^6 cycles fatigue strength of fillet welds subjected to secondary bending stress is about 166.7 MPa in stress range. Using this number and letting σ_{bmin} and σ_{bmax} denote the secondary bending stresses corresponding to the minimum and maximum in-plane shear stresses, τ_{omin} and τ_{omax} , respectively, and solving Equation (2.28) under the condition of

$$\sigma_{bmax} - \sigma_{bmin} = 166.7 \tag{2.29}$$

The relation between the maximum in-plane shear stress for $2x10^6$ cycles fatigue strength and the web slenderness ratio can be obtained for the values of the parameter R defined as

$$R = \tau_{omin}/\tau_{omax} \tag{2.30}$$

Figure (2.24) shows the effect of slenderness ratio, the stress ratio, and the aspect ratio, respectively. From this figure it can be concluded that

- in the region of the web slenderness ratio less than about 200, the fatigue strength decreases with an increase in the initial out-of-plane deflection. When the web slenderness ratio exceeds about 200, however, the fatigue strength becomes not influenced by the magnitude of the initial imperfection,
- the fatigue strength becomes larger as the aspect ratio decreases,

- the influence of the stress ratio on the fatigue strength is small.

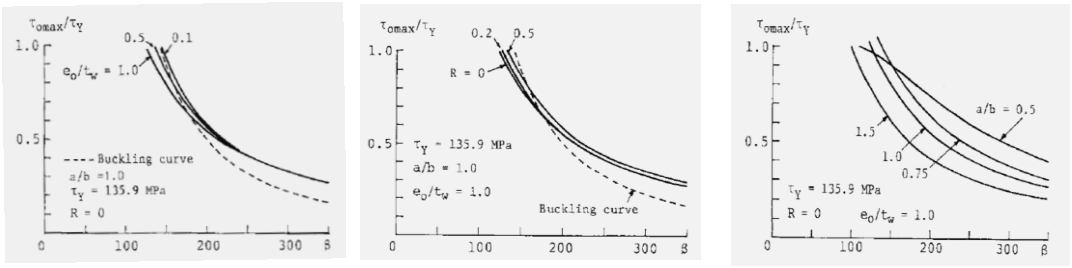

(**a**) Influence of slenderness ratio (**b**) Influence of stress ratio (**c**) Influence of aspect ratio

Figure (2.24): Effect of different parameters on the strength of plate girder, (Okura and Maeda, 1985).

Roberts et al. are pioneers in studying the fatigue of plate girders loaded mainly in shear. Roberts et al. (1995) noticed that during fatigue tests the girders exhibited considerable web plate breathing, with pronounced shear buckles forming and reforming along the tension diagonals of the web panels during cyclic loading. Fatigue cracks formed along the toes of the welds between the web and boundary members, in regions of high secondary bending stresses caused by out-of-plane (buckling) deformations. The number of load cycles to fatigue crack initiation varied considerably; for higher load ranges the rate of propagation of fatigue cracks was reasonably uniform, while for lower load ranges it was variable.

On the basis of their work, Roberts et al. (1996) stated that stress ranges at potential fatigue crack locations could be predicted using nonlinear finite element analysis (FEA) or approximate analytical solutions. They also presented a modified tension field theory for slender plate girders with web cut-outs. In their analysis, they assumed that the shear strength varies linearly with the effective depth of the cut-out. Hence, the residual shear strength V_{res} is given as a ratio from the ultimate shear strength V_u

$$V_{res} = V_u \left\{1 - \frac{d_c \cos\theta + h_c \sin\theta}{d_w \sec\theta}\right\} \tag{2.31}$$

where d_c and h_c are the vertical and horizontal crack projection length in the web, respectively; and θ is the angle of inclination of the diagonal tension field with the horizontal flange.

Škaloud and Zörnerová continued to study fatigue of slender plates. They presented several papers dealing with all possible variables. In 2010, Škaloud and Zörnerová, based on all of their previous work, studied the limit state for the webs of steel plate girders subjected to repeated loading, and stated that the response is affected by the cumulative damage process generated in the web under repeated loading. Several variables were studied, including the effect of shear loading range, shear force ratio, flange size, initial imperfections, quality of fillet welds, and size effect. Based on the results obtained they examined several approaches for defining the fatigue limit state of thin-walled steel girders under repeated loading and proposed two equations that can be used in the design of thin-walled plate girders accounting for the breathing phenomenon (a repeated out-of plane buckling displacement that can induce high secondary bending stresses at the welded plate boundaries). Škaloud and Zörnerová (2010) stated that the influence of the slenderness ratio and the aspect ratio is reflected in the S-N (Stress to Number of loading cycles) curves by the role of the quantity τ_{cr}, the (linear-buckling-theory) critical load of the web. In fact, according to Škaloud and Zörnerová, τ_{cr} can also take account for the boundary conditions of the web.

The fatigue limit state S-N curve proposed by Škaloud and Zörnerová (2010) can be expressed mathematically as follows

$$\log\left(\Delta\tau/\tau_{cr} + 1\right) = -0.1027 \log N + 0.7537 \qquad (2.32)$$

$\Delta\tau$ is the shear stress range, τ_{cr} is the critical stress given by the linear buckling theory, and N is the number of the loading cycle to which the web is subjected.
For serviceability limit state (initiation of first crack) can be given as

$$\log\left(\Delta\tau/\tau_{cr} + 1\right) = -0.0756 \log N + 0.5265 \qquad (2.33)$$

2.2.3.1 *Fatigue Resistant Design*

For unclassified details, Eurocode-3 (1993) recommends that the fatigue assessment be based on the geometric stress range. This is defined as the maximum principal stress range in the vicinity of a weld. The S-N curves under consideration here are the 125-N/mm^2 normal stress range curve and the 80-N/mm^2 shear stress range

curve, at 2×10^6 cycles which are the highest classification curves for welded joints, see Figure (2.25). The normal stress range curve is defined by:

$$\log N_{cr} = 12.601 - 3\log\sigma_{nr} \quad (N_{cr} \le 5\times10^6) \tag{2.34a}$$

$$\log N_{cr} = 16.536 - 5\log\sigma_{nr} \quad (N_{cr} > 5\times10^6) \tag{2.34b}$$

with a cut-off limit of 51 N/mm^2 at 10^8 cycles. The shear stress range is defined by:

$$\log N_{\tau} = 15.801 - 5\log\tau_{nr} \tag{2.34c}$$

with a cut-off limit of 36 N/mm^2 at 10^8 cycles.

The results are similar to those determined using AASHTO standards, due to the fact that the effect of the welds and other stress concentrations is reflected in the ordinate of the S-N curves for the various detail categories. The slope of the regression line fit to the test data for the welded details is typically in the range 2.9 to 3.1. Therefore, in the Eurocode-3, as well as in the AASHTO and AISC codes, the slopes have been standardized at 3.0 (Dexter and Fisher, 1999).

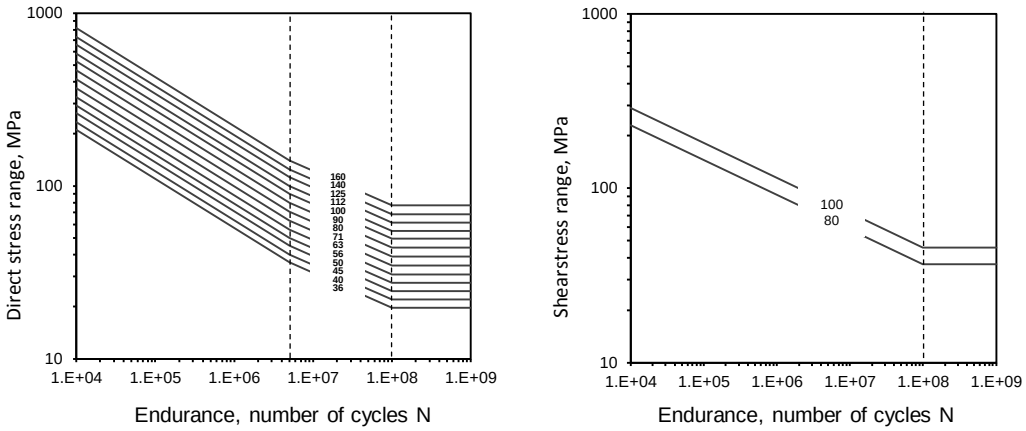

Figure (2.25): Eurocode 3 (1993) S-N curves for normal and shear stress ranges, reproduced.

To sum up the main points in this section, it is important to understand the consequence of the breathing phenomenon on the fatigue life expectation of slender plate girders, where repeated out-of-plane displacement can cause very high secondary bending stresses on the web plate welded boundaries. These repeated bending stresses (due to the repeated nature of vehicle axle load in bridges), could be

as high as the steel plate yielding stress causing premature cracking and consequently failure of the plate girder in shear. There exists standard method to estimate the fatigue life expectancy of a plate girder depending on its condition, but yet we still far from finding a reliable cost effective solution for this problem which comprises a major part of the core of this study.

2.3 STRENGTHENING OF METALLIC STRUCTURES WITH FRP

2.3.1 General

Fibre reinforced polymer (FRP) composites consist of fibres made from materials such as carbon, glass, or aramid embedded in a resin matrix. The fibres of the composite can be positioned into different orientations to most efficiently follow the stress distribution of the structure. An FRP sheet is flexible enough to strengthen curved surfaces. FRP materials are also resistant to corrosion, and hence maintenance and painting can be kept to a minimum. The weakest link in a properly applied FRP-metal system is the adhesive. The bond behaviour between FRP and metal depends on the material properties of the adhesives and the surface preparation.

2.3.1.1 *Problems Associated with Strengthening of Steel Structures*

Strengthening of steel structures and bridges may be required due to the need to increase the load carrying capacity and/or due to damage that has occurred over time that resulted in a lower structural capacity than the designer intended. Typically, these problems are associated either with cross-section losses resulting from prolonged corrosion or fatigue damage that leads to cracking in the vicinity of fatigue sensitive details.

Rehabilitation is typically more economical than replacement of the structure, but conventional methods of repair are often less effective and could increase the maintenance costs (Karbhari and Shulley, 1995). Current methods of repairing steel beams with fatigue damage include drilling holes at the tips of cracks to reduce the crack tip radius. Welding used to repair cracks in steel structures by adding new material to the crack area will typically lead to poor fatigue performance, in addition to the fact that field-welding is likely to be poor (Allan et al., 1988). Furthermore,

welding can also cause metallurgical changes to the parent material, resulting in premature failure (Price and Moulds, 1991).

To reduce the induced stresses, or to repair corrosion damage of steel members, splices may be bolted over damaged areas, or steel cover plates may be welded along the tension flange of the beam. An alternative rehabilitation method is the application of external post-tensioning. Both of these methods result in the potential for further corrosion damage and the addition of significant dead weight. Furthermore, welding of additional steel plates induces significant residual stresses which could cause poor fatigue performance. If bolting is used instead of welding, the drilling of holes results in loss of cross-section as well as the introduction of local stress raisers, that requires additional strengthening material to be used. Strengthening by bonding FRP materials has been shown to be more suitable for strengthening steel structures than previous techniques; however, the most appropriate method depends upon the type of the structure and its function, in addition to the current condition of the structure.

2.3.1.2 *Cost-wise Analysis of using FRP Materials for Strengthening Steel Structures*

There are many advantages in favour of the use of FRP materials for repair and rehabilitation of bridges and structures. Cost savings may be realized through labour saving and reduced requirements for staging and lifting material. The dead weight added to a structure is minimal due to the high strength to weight ratio of FRP materials and there is typically little visual impact on the structure, such that good aesthetics can be maintained with little loss of bridge clearance. Due to the ease of application, disruption of traffic during construction may be reduced or eliminated. Some FRP application processes allow the FRP to be formed into complex shapes, exactly matching the surface configuration of the existing structure. Application of bonded FRP material results in reduced stress-concentrations as compared to mechanical fastening and does not generate thermal induced residual stresses and heat-affected areas in the metal as welding (Grabovac et al., 1991).

FRP materials have become widely established for strengthening of concrete structures in flexure and shear, as well as to provide ductility increases for concrete columns. CFRP sheets may be applied by a wet lay-up process, building up the number of layers or plys necessary according to the strengthening requirements.

Alternately, unidirectional FRP strips can be manufactured to a desired width and thickness using a pultrusion process. For concrete structures, these strips can be directly bonded to the surface, or a groove may be cut into the concrete and the strips bonded within the groove, using a near surface mounted technique. For strengthening steel structures, near-surface mounting would be difficult to achieve and is anyway not necessary since bond failures will not occur within the substrate, as is often the case for FRP materials bonded to concrete surfaces.

Despite the high material costs associated with FRP materials, when overall costs for a strengthening project are determined, overall project costs are typically reduced. The advantages of the use of carbon fibre to repair metallic structures have been shown in the strengthening of tunnel supports for the London underground railway system (Moy et al., 2001). In this project, the difficult access and the impossibility of a lengthy service shut down led to short-term cost competitive use for CFRP materials. Long-term cost benefits were even more favourable due to the expected durability of the CFRP materials used. Gillespie et al. (1996) conducted a cost analysis comparing the cost of rehabilitation with the cost of replacement of a bridge with corroded steel girders. The actual costs were determined from the awarded repair bid for a bridge that had suffered severe corrosion loss. The costs of the rehabilitation were scaled from the costs incurred from the rehabilitation of a girder for testing. The total cost of the rehabilitation was 28 percent of the cost of replacement, with most of the cost savings associated with the fact that there is no need to replace the concrete deck in the case of rehabilitation. Thus, although material costs of the CFRP may be significant, these material costs do not significantly affect the cost benefit since the material costs are often a small portion of the overall project costs.

In order to reduce the amount of CFRP needed to achieve a given stiffness enhancement, or to more efficiently use standard modulus CFRP materials, prestressed CFRP strips may be used. These strips are stressed before bonding the strip to the steel. With epoxy applied to the prestressed strip, the stress is maintained in the strip until the epoxy is fully cured. Once the epoxy is cured, the stress may be released. While bonding of unstressed CFRP strips reduces the extra stresses due to

live loads placed on a structure, bonding of prestressed strips relieves existing dead-load stresses (Schnerch, 2005).

Despite the fact that GFRP has much lower price than CFRP, it is not popular in strengthening of steel structures due to its low tensile modulus of elasticity. This is partly also due to that most previous applications used FRP in tension needing a large modulus of elasticity compared to the substructure. However, this problem can be overcome by using pultruded GFRP or specially designed section profiles to be used for strengthening thin-walled steel sections against local buckling.

2.3.1.3 *Applications of Strengthening Metallic Structures Using FRP*

There are numerous applications where bonded FRP materials have been successfully used for repair and strengthening of metallic structures, typically those of aluminium or steel, and a lot of cast iron in UK. Bonding of FRP materials to metallic structures was first used in mechanical engineering drawback. Both the aerospace and naval industries have made use of CFRP materials for repair of fatigue damage to these structures. The offshore oil and gas industry has also made use of CFRP materials for increases in blast protection. Particularly noteworthy the extreme environmental conditions these structures may be subjected to large changes in temperature for aircraft skins and salt-water spray for marine structures. However, it is worth mentioning at this stage that most of the strengthening applications targeted enhancing the flexural strength of the structure both under static and dynamic loading, rather than shear strengthening which is the main concern of the current study.

Bonded CFRP repairs were first shown to be successful for stopping crack growth occurring on the aluminium skin of subsonic and supersonic aircraft (Armstrong, 1983). CFRP strengthening of metallic aircraft structures that were defective, cracked or corroded have been shown to be a highly cost effective method for extending the service life and maintaining high structural efficiency. This has been shown by over 10,000 fatigue cracking or corrosion repairs being performed on Australian and US military aircraft, illustrating the acceptance of the technique in an application where safety and durability are critical (Aglan et al., 2001).

Use of adhesive in the repair of metallic structures is also established in the repair of ships (Allan et al., 1988). For naval applications, FRP strengthening is cost

effective since the repair or strengthening can be carried out from the most accessible side, and no stripping out of compartments in the immediate area of the repair is necessary. Welding also results in inferior fatigue performance compared to bonding. These types of naval structures are subjected to cyclic stresses due the wave loads, operational loading and mechanically induced loads from the propeller and engine forces that are transmitted to the structure (Grabovac et al., 1991). A reinforcement system by wet lay-up of CFRP material was developed to reduce the effect of cyclic stresses and to prevent cracking of the structure.

Blast walls have also been strengthened for an oil production platform that required strengthening through a previous accident (Galbraith and Barnes, 1995). The strength of the walls was limited by the flexural strength of vertical beams that supported the steel wall plates. In order to maintain production during the repair, in conjunction with clearance restrictions, CFRP strengthening was determined to be the most suitable option for strengthening the deficient beams. Another strengthening project made use of high modulus CFRP materials for strengthening the primary steel members of offshore oil production platform in the North Sea (Barnes, 1996).

According to Schnerch (2005), the first metallic structure in the world strengthened with prestressed CFRP laminates was the cast iron Hythe Bridge. CFRP strengthening was chosen for this structure since it did not require closure of the bridge during the rehabilitation, which was central to the transportation network in Oxford, England. The bridge was originally constructed in 1874, and consists of eight, inverted tee-section cast iron beams. These beams span 7.8m, with brick jack arches and infill material between the beam flanges and the deck. Assessment of the structure showed that it was capable of supporting 7.5 tonnes, but required strengthening to 40.0 tonnes. Strengthening was successfully completed using prestressed CFRP strips, permitting the cast iron to be free from tensile stresses during normal traffic loading.

Hollaway and Cadei (2002) report the work of several other cast iron bridges in the UK that have been strengthened with CFRP materials, including the Tickford Bridge in Newport Pagnell. This bridge was strengthened using a wet lay-up process of CFRP prepreg sheets, which was particularly suited to strengthening the curved surface of the historic beams. The king Street Railway Bridge in Mold required the

strengthening of six cast iron girders to allow 40 tonne vehicles to use the bridge. In this case, temporary struts relieved a portion of the load of the bridge during the strengthening process. The strengthening material was then applied, followed by removal of the struts, resulting in partially prestressing the CFRP strips. In this case the CFRP strips carry a portion of the dead load, unlike in standard applications where the CFRP strips only carry the live load applied to the beam after strengthening.

Various steel bridges have also been strengthened in UK with CFRP strips. The Slattocks Canal Bridge was strengthened using unstressed CFRP strips (Luke 2001b). This bridge consists of rolled steel joists, spanning 7.62m, and supporting a reinforced concrete deck slab. Strengthening consisted of 8mm thick strips that were 100mm wide, bonded to the tension flange of each beam. A steel bridge on the London Underground at Acton in West London was also strengthened with CFRP to reduce the live load stresses by 25 percent (Moy and Nikoukar, 2002). As the bridge carried insignificant dead load and cyclic loading was due to train traffic, the reduction in live load stresses was expected to have a significant beneficial effect on the fatigue life of the bridge.

In the United States, at least three bridges have been strengthened with bonded CFRP strips. Bridge 1-704 over Christina Creek in Delaware was selected for strengthening with CFRP strips (Miller et al., 2001). It has high traffic loads, with 6000 trucks crossing the bridge daily. Strengthening was completed using 5.25mm thick strips, resulting in a stiffness increase of 12 percent, based on vehicle load tests before and after the strengthening. Using the method of transformed sections, a strain decrease of 10 percent was predicted. It was noted that no particular amount of strengthening was required and the project requirements were directed towards providing long-term performance and durability data. The Sauvie Island Bridge in Washington has also been strengthened using two different types of CFRP systems (Mosallam, 2004).

Three spans of a bridge in Iowa were strengthened by bonding CFRP strips in the positive moment regions (Phares et al., 2003). Surface preparation of the girder by sandblasting was followed by cleaning the steel and the sanded CFRP strips with acetone before application of a primer to the steel. The primer prevented direct

contact between the FRP material and the steel, reducing the potential for galvanic corrosion, and could be quickly applied following the sandblasting, thereby bonding to the high-energy surface of the steel. Analysis showed that the stiffness of the bridge girder could be modestly increased by 1.2 percent per ply of CFRP strips (Lee et al., 2005). Different strengthening configurations were applied with the intent of examining the long-term durability including the effect of strengthening on the top side of the tension flange on an edge girder that is exposed directly to environmental exposure.

There is at least one bridge in the United States being strengthened by post-tensioning with CFRP materials (Phares et al., 2003). This bridge was post-tensioned with CFRP tendons that were mechanically anchored and connected to the web of the bridge after strengthening showed that the bridge stiffness was essentially unchanged, but the load capacity of the bridge was increased.

2.3.2 Bond and Surface Preparation

Bonded joints are often the most effective way to join two different adherents, as the resulting stress concentrations at the joints are lower than for bolted connections. Furthermore, the anisotropic nature of most CFRP materials would preclude bolting as a connection method since the strength of these materials perpendicular to the fibre direction is relatively low, resulting in a tendency to split. To ensure full utilization of the applied CFRP material, a high degree of performance is necessary from the bond. Two basic requirements for good bond are, direct contact between the adhesive and the steel and CFRP substrates, as well as the removal of weak layers or contamination at the interface (Hutchinson, 1987). A careful, meticulous approach is necessary when dealing with bonding since it may be difficult to verify the quality of the bond and due to the local effect of bond stresses, any local defect of the bond may result in complete debonding of the applied strengthening material.

2.3.2.1 *Mechanism of Adhesion*

Four mechanisms have been proposed to explain adhesion: adsorption, mechanical interlocking, diffusion and electrostatic attraction (Mays and Hutchinson, 1992). The adsorption mechanism is claimed to be favoured, with mechanical keying also playing an important role. If the adhesive and substrate are in direct contact, the

molecules of the adhesive can be physically adsorbed onto the surface of the substrate through van der Waal's forces. Also these secondary bonds are able to explain the necessary forces to be generated for typical adhesive bond; primary bonding provides more environmentally stable interfaces since water molecules cannot easily break theses primary bonds. Furthermore, based on thermodynamic principles if only secondary forces are acting between a metal to adhesive interface, water at the interface will nearly always result in desorption of the adhesive from the metal substrate (Gettings and Kinloch, 1997). This means that water must be prevented from getting to the interface in sufficient quantities for adhesive bonds that rely on secondary bonds. Alternatively, primary bonds may be developed to resist desorption of the adhesive. This may be achieved by the use of silane primers in adhering steel interfaces, where the silane primary bonds with the steel substrate, resulting in a much more environmentally stable bond.

Mechanical interlocking takes place as a liquid adhesive fills into the pores of an irregular surface. Once hardened, the adhesive and substrate become mechanically interlocked as one. A rough surface also improves energy dissipation, since any cracks formed near the adhesive-substrate interface will be required to change direction as a result of the irregular surface, diverting any cracks into the bulk polymer. Too much roughness may be detrimental, as large surface irregularities create interfacial stress concentrations and proper wetting of deep voids in the surface is difficult due to air entrapment. Optimum surface roughness or profile will vary from one adhesive to another (Sykes, 1982). Additionally, a rough surface will have a larger surface area than a normal one, allowing more area for adsorption to occur. One means of achieving a roughened steel surface is by grit blasting. In this case, the surface roughness is affected by the grit size and the angle of impingement of the grit.

Adhesive joint failure may be categorized in one of two different ways. Failure within the adhesive is called cohesive failure, while a failure between the interface between the adhesive and one of the substrates is an adhesive failure. Improvement to the adhesive strength will typically improve the joint strength if the failure mechanism is cohesive. However, there will be little or no effect if the failure is adhesive. Alternately, improvement in the surface preparation or in the compatibility

between the adhesive and substrate materials will improve the joint strength if the failure is adhesive.

2.3.2.2 *Adhesive Selection*

Previous work has illustrated the importance of surface preparation, adhesive working time, curing methods and prevention of the formation of galvanic couples in selecting and appropriate resin/adhesive system (Rajagopalan et al., 1996). Good adhesion in general requires that there is direct contact between the adhesive and the substrate, without any weak layers or contamination at the interface. Different types of adhesives have been used to bond CFRP to steel, but generally room-temperature cured epoxies have been chosen due to their superior performance and ease of use. Epoxies contain several components including, the resin, flexibilizers, tougheners, fillers and hardeners (Mays and Hutchinson, 1992). The role of the flexibilizers is to improve the impact resistance and peel strength of the adhesive. Tougheners absorb fracture energy and are especially important in considering the fatigue behaviour of the joint. Fillers may be used to reduce the cost of an adhesive or to improve the gap filling capability of an adhesive. The most important component of the adhesive may be the hardener.

The effect of the hardener is to control the pot-life or the length of time that the adhesive may be applied before it loses its workability. Working an adhesive beyond its pot life may also affect the bond strength, since more and more of the adhesive has completed the reaction process beyond the pot life. The pot life and rate of cure development are also important factors in determining the amount of material that can be applied at one time. Generally it is desired that all stages of the bonding process from the start of mixing the adhesive components to clamping of the joint be completed within the pot life. Allen et al. (1982) notes that cure time is halved for each 8°C rise in temperature or doubled for each 8°C reduction in temperature. The cure time determines when clamps may be removed from the joint and when it may be subjected to its full design loading. Below a certain temperature the epoxy may never set. For most epoxies this temperature is just above freezing (0°C).

The local ambient temperature of steel must be considered, especially when considering the long-term loading of the adhesive. These temperatures may reach 65°C inside a steel box girder (Frieze and Barnes, 1996). If an adhesive is used

beyond the glass transition temperature of the adhesive, creep effects may become significant. Rajagopalan et al. (1996) recommends a glass transition temperature of at least 60°C for infrastructure applications. Adhesives may also have different glass transition temperatures depending on the temperature that the adhesive is subjected to during curing. While these effects need to be considered, Frieze and Barnes (1996) noted that if the peak stress is less than 30 percent of the ultimate stress, and the service temperature is within the operating range, creep effects may be ignored.

2.3.2.3 *Surface Preparations*

Surface preparation of the steel must be undertaken to enhance the formation of chemical bonds between the adherend and the adhesive. This requires a chemically active surface that is free from contaminants. In general, higher energy surfaces are more likely to produce suitable bond strengths. Grit blasting is one method of producing a high-energy surface. Steel surfaces contaminated with oils, corrosion products or mill scale, are low energy surfaces.

Most surface treatment involves cleaning, followed by removal of weak layers and then re-cleaning (Mays and Hutchinson, 1992). Hashim (1999) expands the definition of surface preparation to include seven steps: roughening, degreasing, marking, application of the adhesive, positioning of clamps, curing and removal of clamps. Degreasing is a necessary first step in preparing most metals to remove, oils and other potential contaminates. Brushing, ultrasonic or vapour degreasing systems claimed to be most efficient in removing this surface contamination, especially when sufficient amounts of solvent are used. Contamination may then be removed with the excess solvent, rather than simply redeposited on the surface as the solvent evaporates.

For iron and plain carbon steel, very little surface treatment is necessary provided their surfaces are free from rust and mill scale (Mays and Hutchinson, 1992). Under normal conditions, the oxide layer (Fe_2O_3) is only about 3 nanometres thick and the outermost oxygen molecules hydrate to form a high density of hydroxy1 groups. This surface then adsorbs several molecules layers of bound water. It is these hydrated polar groups that forms bonds with polar organic resins. However, most steel structures that are in need of rehabilitation some degree of

surface preparation is required to achieve a high-energy surface. Corrosion products are weakly bonded and mill scale, which is formed when carbon steels are formed by hot working of the steel and its reaction with the air, form a thick oxide scale that is also not suitable for bonding.

The most effective means of achieving a high-energy steel surface is by grit blasting (Sykes, 1982, Hutchinson, 1987, and Hollaway and Cadei, 2002). Parker (1994) found that for composite joints, those that were grit blasted had higher peel strengths than those that were hand abraded. Grits are found to have a clean cutting action, unlike wire brushing, which can cut into the metal exposing a clean surface (Sykes, 1982). Grit blasting procedures, using angular grit, remove the inactive oxide and hydroxide layer by cutting and deformation of the base material. Similar to the findings for preparation of steel when using acrylic adhesives, Dodiuk and Kenig (1988) found that grit blasting followed by a solvent wipe was superior to solvent wiping alone.

The composition of the grit used for the grit blasting procedure must also be compatible with the adhesive being used. Gettings and Kinloch (1997) found by X-ray photoelectron spectroscopy that the surface of grit-blasted adherends, that some of the grit particles remain embedded in the metal surface. For the typical types of grit studied, this contamination did not have any effect on the bond strength. If the grit is recycled, all surfaces to be grit blasted should be degreased with a suitable solvent to prevent contamination of the grit.

The size of the grit will also affect the surface profile of the steel. Harris and Beevers (1999) confirmed that finer grit particles produced smoother surfaces than coarser particles in an investigation using three-dimensional profilometry measurements. For two of the three grits studied, smoother surfaces exhibited higher surface energy readings as determined from static contact angle measurements. However, the initial joint strengths were independent of the coarseness of the grit. Furthermore, the long-term durability was not affected by the surface profile. Steel lap joints, immersed in de-ionized water at 60°C for up to 12 weeks, showed no difference in strength for two different surface textures.

Following grit blasting, the surface may be contaminated with fine abrasive dust. It has generally been agreed that abrasive dust should be removed prior to

bonding. Hollaway and Cadei (2002) state that the dust should be removed by dry wipe or by a vacuum head with brushes and that solvent cleaning should be avoided. This is due to the assumption that solvent wiping only partially removes the dust, and redistributes the remaining dust evenly on the entire surface. However, several different studies have shown that solvents may be used to clean the surface after grit blasting without resulting in poor bond performance (El-Damatty and Abushagur, 2003, Photiou et al., 2004). If solvents are used, it may be beneficial that they be applied in excess so that any debris removed by the solvent is removed from the surface and is not redeposited after the solvent evaporates.

It is also of importance to consider that as short a time as possible be taken between the grit blasting and the initial adhesive or primer application (Allan et al., 1988). Too long of a time between the surface preparation can result in adhesive failure between the steel substrate and the adhesive. Matta et al. (2004), in performing fatigue tests on cracked and uncracked steel specimens repaired with CFRP materials, found that in all cases failure was by debonding. This was likely due to the extended period of time between grit blasting and strengthening of three days, compared with other studies that have typically performed the strengthening immediately following the surface preparation.

Adhesion promoters, such as silanes, have been shown to increase the durability of steel-epoxy bonds without affecting the initial bond strength (McKnight et al., 1994). Silanes are hybrids of silica and organic materials related to resins that have been shown to increase the environmental failure resistance of aluminium and steel to epoxy joints (Hutchinson, 1987). Hashim (1999) notes that silane primers can be used to inhibit corrosion and promote adhesion. Allan et al. (1988) reports that silane can be used on grit blasted aluminium surfaces to considerably increase the durability of the interface. As such, they have been used in field applications such as the strengthening of bridge 1-704, which carries southbound traffic on Interstate 95 in Delaware (Miller et al., 2001).

Silanes adhesion promoters are noted to also greatly reduce the variability of bond performance, while protecting the freshly prepared surface from damage, exposure to environmental conditions and contamination (Hutchinson, 1987). Application of a 5 percent solution of silane primer applied to a grit blasted surface

results in a water-stable interface. Some adhesives incorporated silane in their formulation, but naval application experience has shown this to be less effective than a separate silane layer (Allan et al., 1988). Gettings and Kinloch (1997) found that durability was improved only when there was evidence of primary bonding between the polysiloxane primer and the steel surface.

Other types of chemical surface treatment are also available. Sykes (1982) reports that phosphate treatments that are widely use in preparing steel for painting may increase bond strength, while preventing debonding and corrosion at breaks in the coating. However, these techniques may involve the use of strong chemicals and may only be practical under factory conditions as opposed to site conditions typically encountered in rehabilitation and structural applications (Hollaway and Cadei, 2002).

CFRP can take several forms including dry fibre sheets that are applied by wet lay-up in situ on the structure. Surface preparation for these sheets is minimal, since the individual fibres typically have a sizing agent applied to them. It is important that these sheets be kept clean until the time of application, since the contaminants may affect the bond performance. Pultruded CFRP strips may also be bonded directly to the surface of the structure. For preparation of the CFRP strips, Hollaway and Cadei (2002) recommend that the CFRP be manufactured with a peel-ply on one or both side of the CFRP strip. The peel-ply is a sacrificial layer of glass fibre and polymer material that may be removed immediately prior to bonding to reveal a clean and textured surface that is suitable for bonding. If a peel-ply is not available, then the CFRP strips must be lightly abraded and carefully cleaned to remove and sanding residue. The procedure recommended by Hollaway and Cadei (2002) was to abrade the strips on the side to be bonded with sandpaper and then clean the surface with a solvent.

Fernando et al. (2013) presented a systematic experimental study to identify a surface-adhesive combination that will avoid adhesion failure at the steel adhesive interface. They used different steel surface preparation methods, including solvent cleaning, hand grinding, and grit blasting, and different commonly used adhesives were examined. Fernando et al. (2013) investigated surface characterization using three key parameters (namely surface energy, surface chemical composition, and surface roughness and topography). Their test results showed that adhesion failure at

the steel/adhesive interface can be avoided if the steel surface is properly grit blasted before bonding and a suitable adhesive is used.

2.3.2.4 *Behaviour of FRP to Metal Joints*

The primary function of an adhesive joint is to transfer loads by shear. Its strength depends on the cohesive strength of the adhesive, and the degree of adhesion to the bonding surfaces (Hutchinson, 1987). For infinitely stiff adherends, the shear stress and strain are constant throughout the bonded surface. However, if the adherends have some degree of elasticity, then the stress and strain in the bond line change, with the interfacial shear stress maximized at the joint ends and minimized at the middle of the joint (Price and Moulds, 1991). Considering lap joints with a small overlap length, since the stresses are highest at the ends of the joint, increasing the length of a bonded joint, in the direction of the applied load, does not generally significantly increase the joint strength. However, increasing the joint width usually does increase the strength. Failure may then be governed by the peak interfacial shear stress exceeding the shear strength of the adhesive. However, peel stresses generally also develop due to eccentricities in the joint. While the bond is typically most critical at the ends of the CFRP plate, material discontinuities associated with the crack may also result in critical bond stresses. As noted by Buyukozturk et al. (2004), once the critical stress in the adhesive is reached, debonding may result from the most energetically favourable crack propagating through the steel/adhesive interface, the CFRP/adhesive interface, the adhesive or within the CFRP material. As with the strengthening of concrete structures, by extending the length of the CFRP material as close to the support as possible, the potential of debonding failures can be decreased.

Regardless of the type of joint, the stress concentrations are generally highest at the ends and are very low in the middle of the joint. Methods of optimizing joint strength are usually ways of reducing the stress concentration occurring at the ends so that the bond stresses are distributed more evenly along the adhesive interface. Techniques to reduce the stress concentration include, providing a spew fillet of excess adhesive at the ends of the joint, to taper the edge of the adherends, to increase the thickness of the adhesive, or to reduce the elastic mismatch between two different adherends with perforations.

Spew fillets, result from excess epoxy being squeezed out of the joint when pressing or clamping one adherend to another. Adams and Wake (1984) have shown that a 45-degree spew fillet that has the same thickness as the adherend can reduce the shear stress by 29 percent compared to the case if no fillet was present. Apart from the immediate benefit in reducing the shear stress, it has also been noted that the spew fillet should be left in place, since they improve the durability of the joint (Hollaway and Cadei, 2002) by providing greater resistance to water penetration into the joint. This indicates that the long-term benefit of a spew fillet may be even greater than its short-term benefit.

Tapering of adherends at their edge avoids imposing a local stress concentration at the patch boundary. For lapped joints it was recommended that the peel stresses should be designed out of the joint by tapering the ends of the overlap (Hart-Smith, 1980). In the case of joints made to FRP adherends, it was also noted that this would also reduce the possibility of an interlaminar failure within the FRP. Allan et al. (1988) recommended finishing steel to CFRP joints with a 10:1 taper (5.7 degrees) at their ends to reduce stress concentrations. This technique has also been successfully used in the field by Miller et al. (2001) used a 45 degree angle at all the CFRP ends for the strengthening of a bridge in Delaware. Where tapering of the material is difficult to achieve, stepping may be used as an alternative method. Aglan et al. (2001) found that by producing a stepped multi-layer bonded joint; the stress concentration at the end of a joint could also be reduced.

An alternative method of reducing the stress concentration at the end of the joint, the adhesive thickness may also be increased. Wright et al. (2000) found that increasing the thickness of the bond line resulted in a reduction in the stiffness of the adhesive layer, reducing the stress concentration at the ends of the joint and thereby increasing its overall strength. Slight edge preparation of the steel work was shown to further reduce the stress concentration. Earlier work had shown that increasing the adhesive thickness was more effective than tapering the adhesive (Price and Moulds, 1991).

It may be possible to combine the effects previously discussed to further reduce the stress concentration by producing a reverse-tapered joint. For this type of joint the adherend is tapered, while the adhesive thickness is also increased as a result of

taper. This means that what is thought of as an upside down taper, is actually better than the standard taper. Price and Moulds (1991) found this type of joint to be superior for loads that are applied statically or cyclically. For steel plates bonded to aluminium the use of a reverse-taper improved the fatigue life by about a factor of four (Allan et al., 1988). For repairs consisting of multiple plys of thinner CFRP material, like sheets, the interlaminar shear and peel stresses can be reduced by reverse tapering of subsequent plys of material. This was accomplished by reducing the length of each ply so that the longest layer is on the outside and progressively thinner layers are towards the inside (Ong and Shen, 1992). Analytical modelling of single lap joints has also showed that reversed tapering is a highly efficient technique in reducing the stress peaks in both the adherend and in the adhesive, thereby improving joint strength (Hildebrand, 1994).

One alternate technique that has been demonstrated is the perforation of adherends to reduce the mismatch in their elastic modulus (Melograna and Grenestedt, 2002). Circular and triangular holes were cut by water jet into the steel at the bond area at variable spacing, to reduce the stress concentration at the ends while providing mechanical keying for the adhesive. This technique was shown to significantly increase the joint compared to joints without perforations. There was no difference found in the use of triangular or circular holes.

Research has also been conducted to determine the development length of CFRP sheets and strips bonded to steel. Miller et al. (2001) performed tension tests on steel plates that were reinforced on each side with CFRP laminate. Eleven strain gauges were positioned along the length of the sample on one side, and five gauges on the other to compare with an analytical model. Both the experimental data and the analytical model indicated that the force transfer occurs within 100mm of the end of the CFRP strip.

The bond length of CFRP sheet bonded to very high strength (VHS) steel tubes was determined by Jiao and Zhao (2004). This type of steel has very high yield (1350 MPa) and ultimate strengths (1500 MPa), but the useable strength was greatly reduced at the concentration of tow tubes when welded. An experimental study was conducted to minimize the loss in strength when joining the tubes. Two of the steel tubes were either joined by use of CFRP material alone or a combination of CFRP

material and welding. It was found that CFRP material could strengthen the butt-welded tubes to restore the full yield capacity. Furthermore, for four plys of the CFRP material, it was found that a development length of 75mm was sufficient to achieve the full strength increase.

Nozaka et al. (2005) published study on the bond length of CFRP strips applied to a flexural member. In this case the development length was defined as the shortest length that maximizes the load transferred to the CFRP strip. In this study the focus was on cracked steel girders. For the strips and adhesives studied, the failure was always by debonding. It was noted that the shear ductility seemed to be the most important parameter in ensuring a high CFRP strain at failure, since the adhesive would rapidly yield as the CFRP was loaded. Cyclic loading and heat curing of the adhesive were found to have insignificant effect on the bond. The development length found for the adhesives studied was found to be less than 203mm.

In 2005, Al-Emrani et al. studied the behaviour and strength of steel elements strengthened with bonded carbon-fibre laminates. A new type of test specimen has been developed for this purpose based on extensive FE analysis. Five specimens, a control specimen and four with various types of adhesively-bonded carbon-fibre-laminates were tested. Figure (2.26a) shows the test specimen developed to achieve the objectives of the tests. The shape and dimensions of the specimen were chosen so that successive yielding of the steel adherent can be obtained (starting from the middle of the specimen) and the fracture modes expected to be obtained in steel beams with bonded CFRL can be resembled.

Figure (2.26b) shows the load-displacement curves obtained for the four composite elements. The results obtained from the reference specimen are also shown for comparison. They concluded that the delay in the on-set of yielding in the composite specimens in comparison to the reference specimen is highest for the laminates with high elastic modulus and that the highest degree of strengthening (i.e. increase in the ultimate load) was obtained from the specimen that contained the laminates with the lowest stiffness and the lowest thickness, they also reported that even the ductility was highest for this specimen. Specimen with stiffer laminate produced slightly lower strengthening effect, but by far lower ductility.

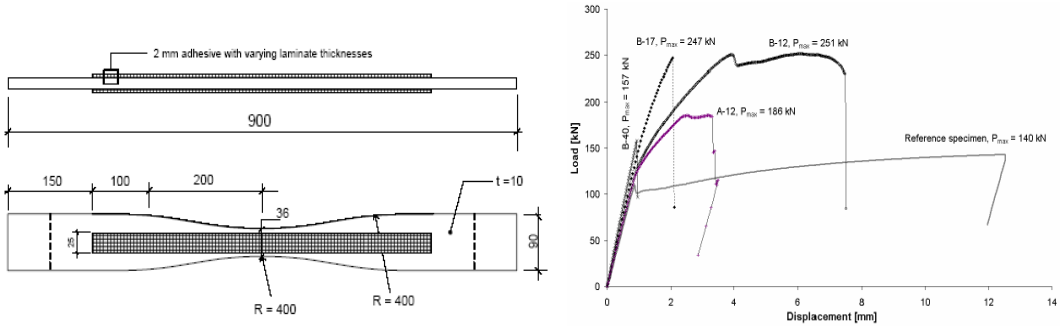

(**a**) shape and dimensions of the test specimen (**b**) Load-deformation curves

Figure (2.26): Test specimen and load deflection curves, (Al-Emrani et al., 2005).

In 2006, Dawood & Rizkalla, conducted an experimental program to investigate the bond and splice behavior of CFRP laminates. Three different configurations of double-lap shear coupons, shown schematically in Figure (2.27a-c), were tested. The objective of the first phase was to determine the effectiveness of implementing a reverse taper detail at various critical locations throughout the spliced joint. For all three joint configurations, strains were measured at various locations along the splice joint using electrical resistance strain gauges.

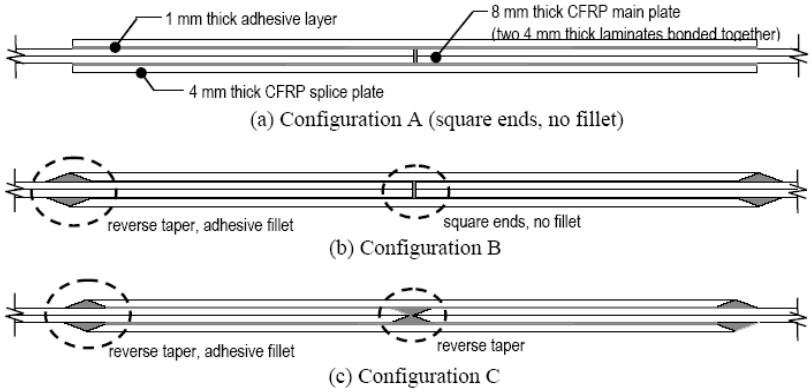

Figure (2.27): Double shear lap specimen test configurations, (Dawood and Rizkalla, 2006).

The measured load-strain behavior for all three of the joint configurations at the centre of the splice joint for the double-lap shear coupons is shown in Figure (2.28a). The initial stiffness of all three joints was similar, and then a sudden increase of the measured strain was observed for joint configurations A and B. This was likely due to cracking of the adhesive within the joint due to a stress concentration near the

square plate end at the centre of the joint. The load strain behavior of Joint configuration C did not exhibit a similar increase which suggests the reverse taper was effective in reducing the stress concentration near the plate end.

In addition, a two-dimensional finite element model was also developed to predict the bond stress distributions along the length of an adhesively bonded joint. The model was used to predict the stress distributions for the square ended double-lap shear coupon which was tested as joint configuration A in the experimental program. The coupon was modelled using standard 8-node quadratic elements with an average side length of approximately 1 mm. A quarter of the coupon was modelled using the symmetry boundary conditions and a tensile load of 80 kN was applied along the longitudinal axis of the coupon. The adhesive was modelled as an isotropic material and the CFRP was modelled as an orthotropic material. The deformed shape of the finite element mesh near the end of the CFRP splice plate is shown in Figure (2.28b). The effect of peeling at the plate end due to the localized bending effect is evident in the figure. This effect is due to the eccentricity of the CFRP splice plate relative to the applied load. From the finite element analysis, the longitudinal stress distribution along the length of the splice plate was determined at three different levels through the thickness of the CFRP splice plate. The distribution of the longitudinal stresses at each of these three levels is shown in Figure (2.28c).

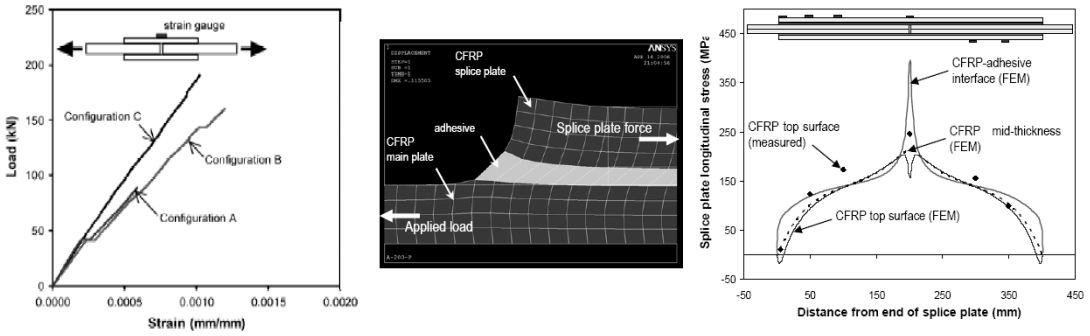

(**a**) Load-strain behaviour (**b**) Localized deformed shape (**c**) Longitudinal stress distribution

Figure (2.28): Test results and FEM , (Dawood and Rizkalla, 2006).

In 2006 also, Fawzia et al., (2006a), conducted an experimental program to obtain the shear stress versus slippage relationship, a series of double strap tension type bond were tested. The strain and stress distributions measured in the specimens for

two different bond lengths. The results show a preliminary bi-linear bond-slip model may be adopted for CFRP sheet bonded with steel plate. Figure (2.29a) shows the schematic specimen configuration.

The measured strain distribution along the bond length was used by integration to calculate local slips. Actually this local slip is the relative displacement between the CFRP sheet and the steel plate. Calculated bond stresses and slips were combined to obtain the local bond-slip curves. Bond-slip curves obtained from experimental data are approximated as a bi-linear shape modifying the original Hart-Smith model. A schematic view is presented in Figure (2.29b) which can be defined by three parameters δ_1, τ_f and δ_f . The initial stiffness of the bond-slip curve is high, representing linear elastic state. Fawzia et al. concluded that the strain distribution profiles show that strain level is significant over a limited bond length and that when de-bonding occurs at most highly stressed end, less or almost zero stress is transferred at that end; and the maximum shear stress location shifts towards the unloaded end of the specimen.

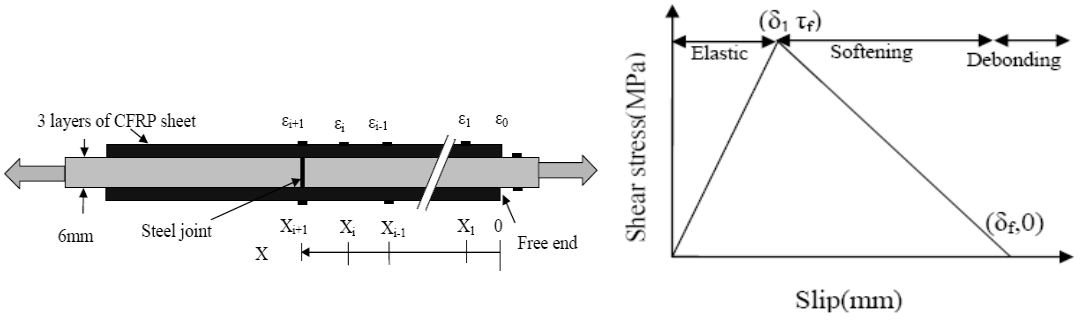

(**a**) Test specimen and instrumentation (**b**) Bond-slip model approximation

Figure (2.29): Test specimen and bond-slip model, (Fawzia et al., 2006).

In 2007, several researchers reviewed the up to date development in the field of bond behaviour of metal/FRP. Zhao and Zhang (2007) provided a state of the art review of the bond between steel and FRP, the strengthening of steel hollow section members, and fatigue crack propagation in the FRP-Steel system. In addition, they mentioned the areas were the need for more work is required.

Duong and Wang (2007) also published a book "Composite Repair: Theory and Design" and presented the theory of bonded doublers and bonded joints providing various analytical models for determining stresses in bonded joints and

doublers that are relevant to the repair geometries. The presented analytical models account for various important effects, such as: elastic-plastic adhesive, geometrically nonlinear deformation, triaxial stresses on plastic yielding, adherend stress concentration, and corner singularity at the termini of the adhesive layer. Several criteria for failure assessment of bonded joints and doublers are also discussed.

Pasternak et al. (2010) published a paper presenting a detailed analysis of using adhesives in reinforcement of steel structures. Two types of structures were experimentally investigated (box girders and knee joints). Test results were compared with finite element models performed with Abaqus. In addition, they provided a brilliant summary of the analytical model originally derived by Kim and Kedward (2001) which is capable of predicting the 2-dimensional shear stress distribution of the adhesive layer for any infinite/finite FRP doubler adhesively bonded to a metal plate. The model is illustrated herein as follows after correcting some editorial mistakes

The stress state caused by the bending moment

$$\tau_{yz}^{a} = t_o \lambda \left[\frac{\sinh(\lambda y)}{\cosh(\lambda c)} \left(\frac{N_y(x)}{2t_o} - \frac{D_o}{\lambda^2} \right) + \frac{\cosh(\lambda y)}{\sinh(\lambda c)} \frac{N_y(x)}{2t_o} \right] \tag{2.35a}$$

$$\lambda = \sqrt{\frac{G_a}{t_a} \left(\frac{1}{E_o t_o} + \frac{1}{E_i t_i} \right)} \tag{2.35b}$$

$$D_o(x) = \frac{G_a}{t_a} \frac{N_y(x)}{E_i t_i t_o} \tag{2.35c}$$

$$N_y(x) = \sigma_y^o(x) t_o \tag{2.35d}$$

The stress state caused by shear force

$$\tau_{xz}^{a}(x,y) = t_o \frac{\partial \tau_{xy}^{o}(x,y)}{\partial y} \tag{2.36a}$$

$$\tau_{xy}^{o}(x,y) = \sum_{m=1}^{\infty} \sum_{n=1}^{\infty} \left[\begin{array}{c} \frac{4}{ab} \int_0^a \int_0^b C_o \sin\left(\frac{m\pi x}{a}\right) \sin\left(\frac{n\pi y}{b}\right) dy dx \\ \hline \left(\frac{\pi m}{a}\right)^2 + \left(\frac{\pi n}{b}\right)^2 + \lambda^2 \\ \sin\left(\frac{m\pi x}{a}\right) \sin\left(\frac{n\pi y}{b}\right) \end{array} \times \right] \tag{2.36b}$$

$$\lambda = \sqrt{\frac{G_a}{t_a} \left(\frac{1}{G_o t_o} + \frac{1}{G_i t_i} \right)} \tag{2.36c}$$

$$C_o(x,y) = \frac{G_a}{G_i}\frac{N_{xy}(x,y)}{t_a t_i t_o} \tag{2.36d}$$

$$N_{xy}(x) = \tau_{xy}^{i}(x)t_i \tag{2.36e}$$

The interaction formula for bending moment and shear force is described as follows

$$\tau^a = \sqrt{(\tau_{xz}^a)^2 + \left(\tau_{yz}^a\right)^2} \leq \tau^y \tag{2.37}$$

where E_o , E_i , G_o , G_i , t_o , and t_i are Young's modulii, shear modulii and thickness of additional plate and web respectively, G_a and t_a are the shear module and thickness of adhesive, $c = b/2$, a and b are the web length and width of the doubler (adhesive joint), $N_y(x)$ is the shear force in web, σ_y^o is the normal stress in the web caused by external load, $\tau_{xy}^{\ i}$ is the shear stress in web caused by external load, $\tau_{yz}^{\ a}$ is the shear stress in adhesive layer caused by bending moment, $\tau_{xz}^{\ a}$ is the shear stress in adhesive layer caused by shear force, τ^a is the resultant shear stress in adhesive layer, and τ^y is the shear carrying capacity in the adhesive layer.

Figure (2.30) provides further details from Kim and Kedward (2001) and an example of the adhesive shear stress distribution for a reinforced web panel from Pasternak et al. (2010). It is worth mentioning that reinforcement in this study was done by bonding metal plates to the original metal section and not FRP composites.

In 2012, Uriayer introduced new specimen of steel-CFRP composite developed in accordance with standard test method and definition for mechanical testing of steel (ASTM–A370). Fifteen specimens were prepared and divided into five groups depending upon the number of layers of CFRP (SikaWrap-300C) with modulus of elasticity of 230GPa and adhesive (Sikadure-330) with modulus 3800MPa. All steel strips had dimensions of 200mm in length and 20mm in width and 1.5mm thickness. Single-layered to five-layered strips three each were prepared by applying CFRP laminates on one side of a steel strip that configures the specimen. The final stage of preparing the specimens was to put the second steel strip.

Uniaxial tensile tests were conducted to determine yield strength and ultimate strength of specimens. Test results showed that the stress-strain curves of the composite specimens were bilinear prior to the fracture of laminate and that the yield

and ultimate loads increased with the increase of the number of layers of CFRP; see Figure (2.31a).

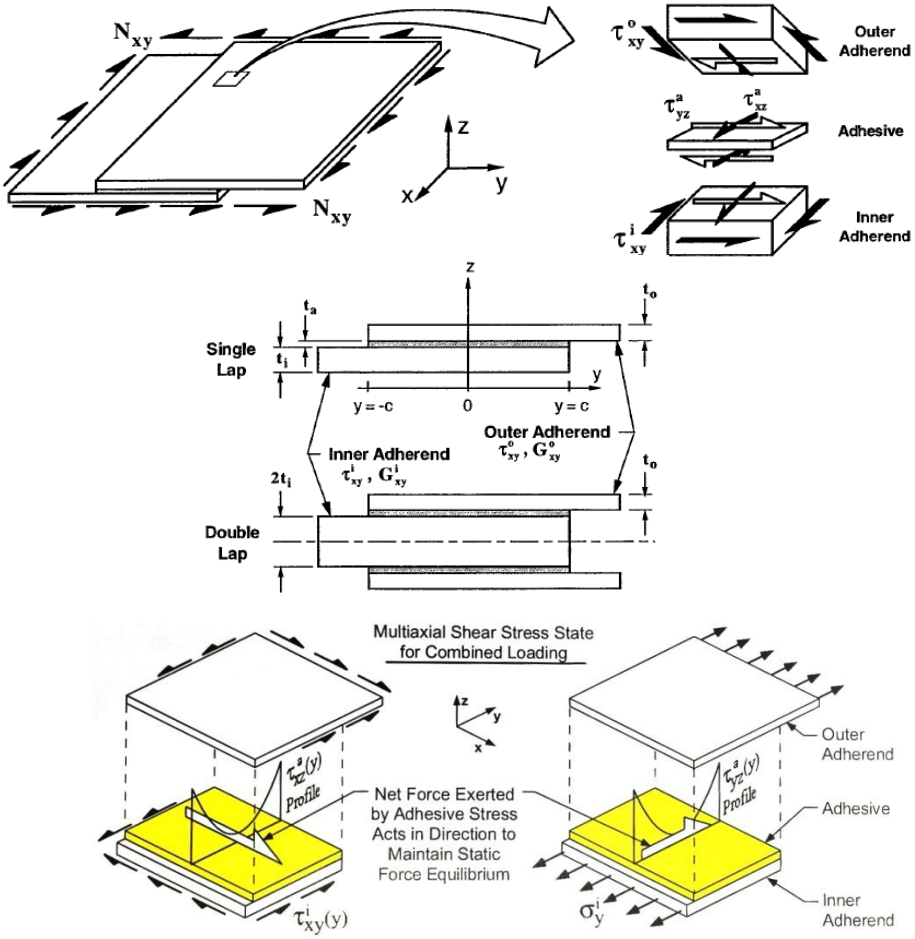

(**a**) Illustration of the stress distribution in adhesive joint, (Kim and Kedward, 2001)

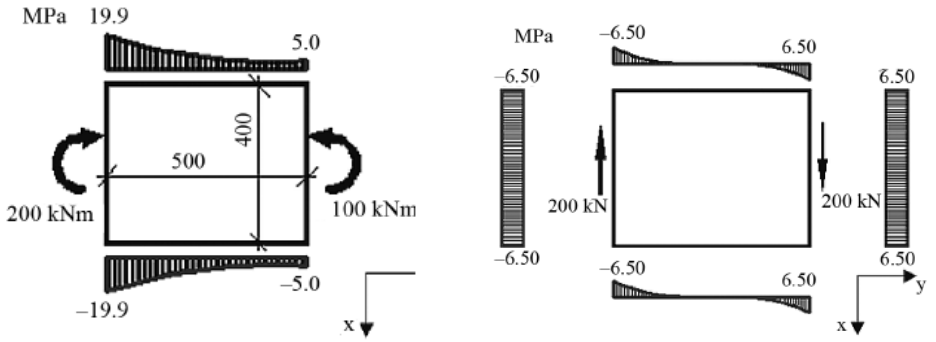

(**b**) Adhesive shear distribution of a doubler in bending and shear, (Pasternak et al. 2010).

Figure (2.30): Illustration of the stress distribution of a strengthened web panel.

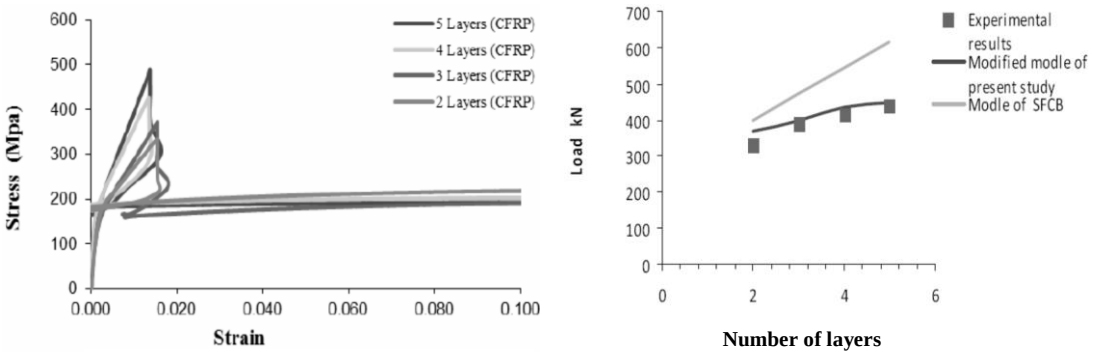

(**a**) stress-strain curves (**b**) stress vs. CFRP number

Figure (2.31): Test results and theoretical model, (Uriayer, 2010).

Finally, a modified formula of strength carrying capacity based on strain distribution across layers is proposed and validated by experimental results. The predicted values agreed well with experimental ones, see Figure (2.31b). The formula is a combination between Wu et al. (2010) model for predicting the stress-strain relationship of CFRP strengthened steel bar in uniaxial tension, where they assumed constant strain distribution across the layers; and an empirical model by Fawzia et al. (2006b) for predicting the distribution of strain across the layers of CFRP originally derived for circular hollow steel tubular section under tensile load. The model can be described in the following equation

$$\sigma_{ult} = \left(f_y . A_s + \sum_{i=1}^{n} A_{CFRP,i} . E_{CFRP} \frac{\varepsilon_{u.CFRP}}{\sqrt{i}}\right) / A \qquad (2.38)$$

where i represent the layer number (1 being the first layer), $\varepsilon_{u.CFRP}$ is the ultimate strain in the corresponding CFRP layer, f_y and A_s are the steel yield strength and cross-sectional area, respectively. E_{CFRP} and $A_{CFRP,i}$ are the elastic modulus and cross-sectional area of the CFRP layer, respectively.

2.3.2.5 Behaviour of FRP to Metal Bonded Joints Subjected to Cyclic Loading

Several researchers have illustrated the improved fatigue performance of steel and aluminium members bonded using FRP strips. Bonding of CFRP and metallic materials was seen as the best way to join the lightweight materials used by the aviation industry. Smith and Hardy (1977) studied aluminium to CFRP scarf joints.

Scarf joints were used due to the reduced stress concentration at the ends of the joint, compared to a typical lap joint. Load was applied at 5Hz to 40 percent of the static strength of the joint. Failure was by debonding, followed by delamination, whereby the adhesive failed in fatigue at one end of the joint, leading to progressive debonding. Grabovac et al. (1991) conducted tests of metallic plates with non-uniform thickness, which represented the aluminium deck structure of a navy frigate at the welded junction of two different thickness plates. This detail leads to cracking for frigates in service. A reinforcement scheme was developed that was capable of reducing the critical stresses by 50 percent.

Mays (1990) conducted an extensive set of fatigue and creep tests using steel-to-steel double-lap specimens using one of four types of adhesives. Specimens were subjected to different temperatures ranging from -25 to 75°C and some specimens were also subjected to aging effect. The fatigue performance of an adhesive was found to be affected by the glass transition temperature relative to the ambient temperature of the joint in service. The joint strength decreased dramatically when the adhesive was subjected to temperature beyond its glass transition temperature. There was less correlation between the endurance limit and the static ultimate strength of a joint than between the endurance limit and the stress range the joint was subjected to. The endurance limit of an adhesive was thought to exist, though its exact value was not calculated. Instead, a lower bound to the fatigue performance of joints between temperatures of -23°C and 45°C, accounting for aging, was extrapolated to 7×10^8 cycles, representing a 120 year design life for a bridge. A limiting stress range of 4.0 MPa was proposed. For creep, the sustained stress was recommended to exceed 25 percent of the short-term strength.

Similarly, Cadei et al. (2004) noted that the peak adhesive shear stress in a fatigue cycle should not exceed 20-30 percent of its ultimate static failure stress. Reedy and Guess (1993) noted that for extended fatigue life of a joint, adhesive yielding must be avoided since material damage and crack initiation could occur under cyclic plastic straining. He estimated that it would limit the applied loads such that the average shear stress for a tubular lap joint be less than 5 MPa.

Miller et al. (2001) conducted fatigue tests on two full-scale bridge girders rehabilitated with CFRP plates for 10 million cycles at a stress range that might be

expected in the field. Throughout the 10 million cycles, the CFRP plates were periodically monitored and inspected for debonding. Visual inspection and tapping tests were unable to detect any evidence of debonding. Furthermore, static testing revealed no change in global stiffness. This confirms the findings of Frieze and Barnes (1996) who found that the fatigue behaviour of the CFRP material itself to be superior to steel. Furthermore, it was also noted that the retained strength of adhesive joints between CFRP and steel varies between 45-55 percent at room temperature, indicating that the fatigue performance of the steel is the limiting factor.

Liu et al. (2010) conducted tests to understand the influence of fatigue loading on the bond between steel and CFRP. They used both normal-modulus (240 GPa) and high-modulus (640 GPa) CFRP sheets. The specimens were tensioned to failure after enduring a preset number of fatigue cycles that ranged from 0.5 to 10 million at different load ratios ranging from 0.15 to 0.55, the residual ultimate static strength were referred to as (F_2). The load ratio is defined as the ratio of the maximum value of the applied load (P_{max}) to its static ultimate strength (F_1).

The relationship between the load ratio (P_{max}/ F_1), bond strength ratio (F_2/ F_1), and preset number of fatigue cycles (N) are shown in Figure (2.32a) while Figure (2.32b) shows the slippage between the FRP and steel after 1 million cycles of loads. They concluded that for normal-modulus CFRP, the reduction in bond strength is around 20-30% even when the load ratio is 0.3 with the preset fatigue cycles of 8 millions. For joints with high-modulus CFRP sheets, it was found that the fatigue loading does not affect the bond strength even when the load ratio is as high as 0.55 and the number of fatigue cycles is up to 10 millions. Another conclusion was that the fatigue loading does not change the failure modes in comparison to the static tests.

Wu et al. (2013) had the same conclusion when they studied the influence of fatigue cycles on the bond between high-modulus CFRP and steel. It was revealed that the influence on the bond strength is minimal (less than 4.5%) and the effect of fatigue loading on stiffness of the tested specimens was about 10%.

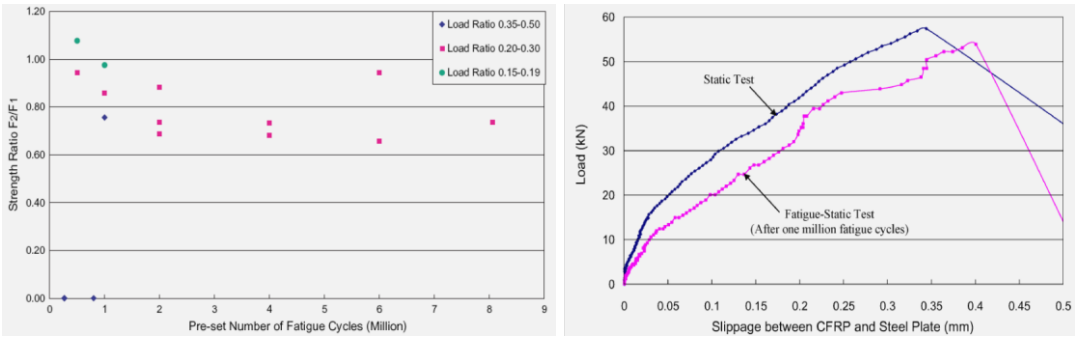

(**a**) Strength ratio for normal-modulus CFRP (**b**) Load-displacement curves

Figure (2.32): Test results, (Liu et al., 2010).

2.3.3 Durability

Short-term strength is not as important as durability, as the long-term durability of the bond is critical to the service life of the rehabilitation scheme. The effects of moisture or temperature that is acting in conjunction with an applied stress may influence the behaviour of the joint due to stiffness change of the resin resulting from the exposure (Karbhari an Shulley, 1995). In general, adhesive joints subjected to high humidity, saturation with water or extreme temperatures, will result in a reduction in joint strength.

Considerable work has been conducted on the durability of FRP materials themselves subjected to moisture, hydrothermal effects, temperature cycling, exposure to ultraviolet radiation, creep and fatigue (Hollaway and Cadei, 2002). In particular for CFRP materials, moisture does not have any degrading effect on the fibres themselves, but absorption of water by the resin may change the mechanical properties of the CFRP that are dominated by the resin. The same is true for creep and fatigue, whereby the carbon fibres themselves do not creep or fatigue appreciably, but the resin dominated properties may be affected. Freeze-thaw effects on FRP materials would be expected to be negligible provided that the FRP was of good quality, manufactured without a significant percentage of interconnected voids that could fill with water. To protect against ultraviolet damage, it is typical to apply an ultraviolet resistant coating over any FRP material to shade it for any exposure.

The polar molecules which given an adhesive its adhesive properties also make the adhesive inherently hydrophilic (Hutchinson, 1987). Adhesives become plasticized by water absorption, greatly affecting their mechanical properties. This is

also true for the FRP itself, where water absorption results in the reduction in the matrix dominated properties (Parker, 1994).

Thermal effects may degrade the bond performance of steel to FRP joints either alone or in combination with water (Hollaway and Cadei, 2002). Freezing temperatures may cause either the adhesive or the CFRP to crack or harden. Combined with freeze-thaw cycling, the stresses induced by this type of thermal loading can result in debonding. Conversely, high temperatures may result in softening of the adhesive to an extent that viscoelastic effects become significant. Hollaway and Cadei (2002) recommended that the composite material and the adhesive have a glass transition temperature of at least 30°C above the maximum design temperature.

The book *Durability of Composite for Civil Structural Applications*, edited by Karbhari (2003), provides details of the durability of FRP composites under all environmental and mechanical conditions. These areas include FRP under aqueous solution, thermal effects, fatigue loading, creep, and fire. The book also discusses material properties, resin, and adhesive types for civil applications.

However, most of the work related to durability of FRP composite was associated with concrete (wan et al., 2006 and Dai et al., 2010). Büyüköztürk (2001) found that degradation of bond strength could be up to 70% after only 8 weeks of moisture exposure.

Dawood and Rizkalla (2010) tested 44 CFRP plate-steel double shear joints after it was exposed to severe environmental conditions for different durations, up to six months. Specimens that were bonded using thin adhesive layer exhibited 60% degradation of the measured bond strength after 6 months of exposure. Specimens that were pre-treated with silane coupling agent prior to bonding exhibited essentially no degradation of the bond strength over the six months exposure duration. However, in this study, the CFRP-steel system applied using the wet lay-up method was not examined, where the environmental effect may be more severe without a clear adhesive layer as an insulator between the CFRP and steel (Zhao, 2014)

More recently, Nguyen et al. (2012) performed a series of double-shear pull tests on CFRP sheet-steel joints at different load levels (20, 50 and 80% of their

ultimate load measured at room temperature) with constant temperatures from 35 to 50°C (i.e. temperatures below and above the glass transition (T_g , 42°C) of the adhesive) or with cyclic thermal loading between 20 and 50°C. It was found that adhesively bonded steel-CFRP double-shear pull tests joints exhibits an obvious time-dependant behaviour, meaning, higher target temperature or larger applied load results in shorter time to failure. It was recommended that in practice the adhesive layer should be kept at least 7 to 10°C below T_g of the adhesive to avoid strength degradation of the structure due to temperature effect.

To the author's knowledge, the only durability data available on strengthening of steel bridges is the one reported by Hutchinson (1996), where he cited observations of the first major steel plate bonding project in the UK, which occurred in 1975, when four pairs of concrete bridges were also strengthened. Cores were taken through the bonded interface that was twenty years old at the time of testing. These bridges used two types of epoxy adhesives, and used grit blasting for the surface preparation for the steel as is currently recommended for strengthening of steel structures. Silane primers were not used on steel surface, so the test of durability of this interface was even more severe. Cores were taken through the steel plate, cutting through the bonded interface and into the concrete surface. Lap shear specimens were fabricated from some of the material taken from the cores. In spite of the fact that the surface preparation was claimed to be not very good, with smooth areas and dust particles apparent on the steel surface, the bond strengths were satisfactory based on the limited data available. Some specimens were soaked in a solvent to remove the adhesive, to observe the steel surface directly. It was found that no steel surface corrosion was evident, but that the completed grit blasting was not very uniform.

2.4 STRENGTHENING OF PLATE GIRDERS WITH FRP COMPOSITES

There has been relatively little work investigating the use of bonded FRP materials for shear strengthening of steel members. Most available research focuses on the use of FRP for flexural strengthening of corroded bridge girders and addressed the use of bonded FRP materials on only the tension flange of simple girders (Mertz et al.,

1996, Mertz et al., 2002, Miller et al., 2002, Chacon et al., 2004, Shield et al., 2004, and Schnerch, 2005). Most investigations of the use of CFRP strips attached to the tension flange of I-girders have demonstrated modestly improved flexural capacity-proportional to the CFRP applied, but little improvement to girder stiffness (Harries, 2009).

FRP composite materials have recently been used to enhance the stability of steel members. In this application, the high stiffness and linear behavior of FRP materials are utilized to provide ‘‘bracing’’ that improves the buckling and post-buckling behavior of steel components. Recent research has demonstrated that the application of FRP reinforcement can lead to improvements in the flange local buckling (FLB), web local buckling (WLB) and flexural torsional buckling (FTB) behaviours of steel members. This application is not aimed at increasing the load-carrying capacity of the steel section, although this may certainly be accomplished if desired. The application is instead aimed at providing stability (in the sense of bracing) to the steel member through the addition of supplemental stiffness at strategic locations.

FRP strengthening of beams and plate girders is a subject of wide research and implications starting from simply strengthening the tension flange to the more complicated applications of strengthening the compression flange, webs, and bearing posts. However, the current study is focused on shear buckling of thin-walled steel plate girders; therefore, only shear strengthening of steel plate girders is going to be reviewed in this section, relevant to the current study.

In 2004, Patnaik and Bauer presented experimental work consisted of two types of strengthening of steel beams with CFRP laminates, namely, one to increase the flexural strength, and the other to increase shear strength of beams. Three beams, among six, were designed to fail in shear. Two of these beams were strengthened with CFRP strips attached to the webs, Figure (2.33); the third beam was used as a control specimen for comparison. The failure mode of the control beam indicated elastic web buckling, while the web of shear strengthened beam appeared to have failed by yielding followed by inelastic web buckling.

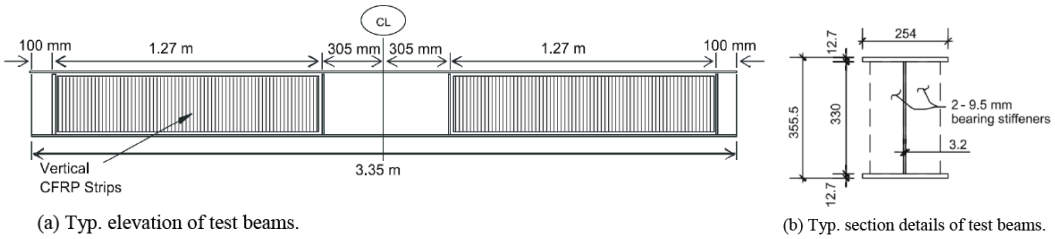

(a) Typ. elevation of test beams.

(b) Typ. section details of test beams.

Figure (2.33): Typical details of test beams, (Patnaik and Bauer, 2004).

A typical failure mode of shear series beams is shown in Figure (2.34), where the FRP strip was peeled out after test. All the three beams failed in a ductile manner and it was possible to sustain the load for a short time even after the initiation of web shear buckling. From the test results, it was concluded that the AISC LRFD specifications conservatively underestimate shear strength of such built-up steel beams. However, apparently the strengthening scheme proposed by Patnaik and Bauer (2004) is not cost effective, as the technique proposes attaching CFRP laminates to the entire area of the web compared with only 26% increase in shear strength.

Figure (2.34): Typical failure of beam in shear, (Patnaik and Bauer, 2004).

Another research in 2004 by Sayed-Ahmed presented a numerical analysis based on the finite element modelling to investigate the web buckling and failure loads of steel I-section beams with bonded CFRP strips. The CFRP strips were 100mm wide by 1.4mm thick, and they were bonded to the steel web via a 1mm thick epoxy resin. He stated that despite the fact that this may not be the best configuration; the CFRP strips were bonded at the mid-height of the web to match the configuration of the mid-height steel stiffeners of plate girders.

The beams spanned over 12.0m and they are subjected to 2 point loads dividing the span into 3 parts, these loading points were used as lateral supports as well to prevent lateral torsion-flexure buckling. Layered shell elements were adopted to model the web parts with the bonded CFRP strips, see Figure (2.35). The finite element results reveal that bonding the CFRP strips to web of Class 4 sections (refer to section 2.2.2.1 for details on section classifications), significantly delayed web buckling and increased the critical load by about 30% to 60% depending on the web slenderness ratio. For Class 3 section, the enhancement in the critical load was in the order of 22%. However, the increase in the ultimate load-carrying capacity in this study was negligible (0% for class 1 section and from 2 to 9% for the rest three classes).

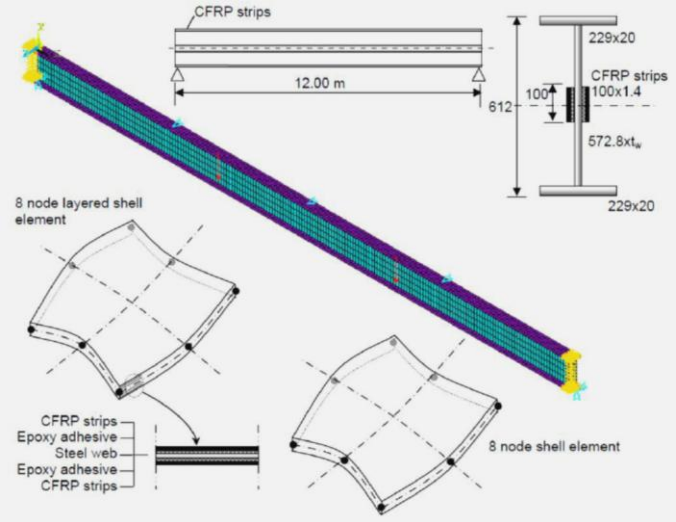

Figure (2.35): Typical beam section and FEM, (Sayed-Ahmed, 2004).

Okeil et al. presented a more efficient strengthening technique in 2009 by introducing additional stiffness to buckling prone regions in thin-walled steel sections. They studied improving the out-of-plane stiffness of web panels by bonding pultruded GFRP sections; see Figures (2.36a and b). Details of the shear strengthened plate girder are given in Figure (2.36c), while Figures (2.36d and e) show the finite element out-of-plane displacement contour lines and the normalized load-deflection curve, respectively.

The tested girder was designed to fail in shear buckling mode and test results show that the failure load for the strengthened girder was 56% higher than the

unstrengthened one. However, by close examining the failed specimen photo, Figure (2.36b); it is true that the web did buckle and the GFRP pultruded section started debonding, but, it is also obvious that the failure was because of the end support stiffener crippling due to the un-expected load increase or poor design detailing and more load-carrying capacity could have been expected. Nevertheless, according to Okeil et al. the enhancement in the load carrying capacity was accompanied by significant reduction in the deformation ductility from 4.44 to 2.04 (the deformation ductility is the ratio of the ultimate deflection to the critical deflection at first buckling), see Figure (2.36e). This indicates that the proposed strengthening technique reduced the ductility more than 100%.

(**a**) strengthened specimen

(**b**) failed specimen

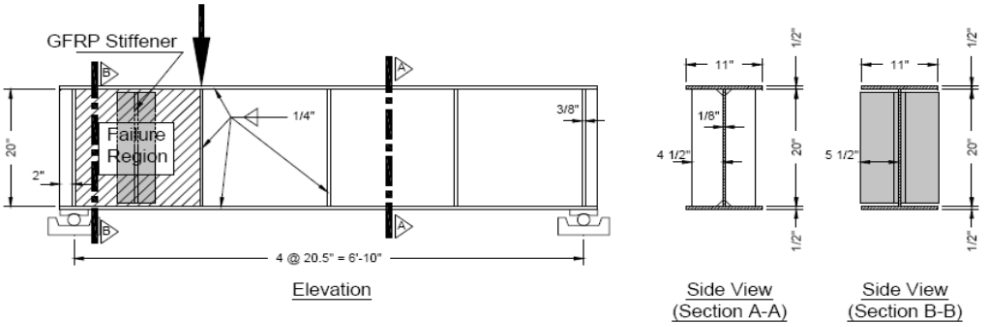

(**c**) details of the GFRP stiffened beam

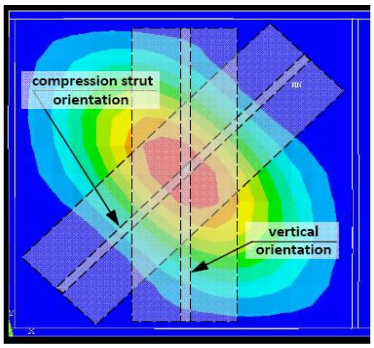

(**d**) FEA contour lines

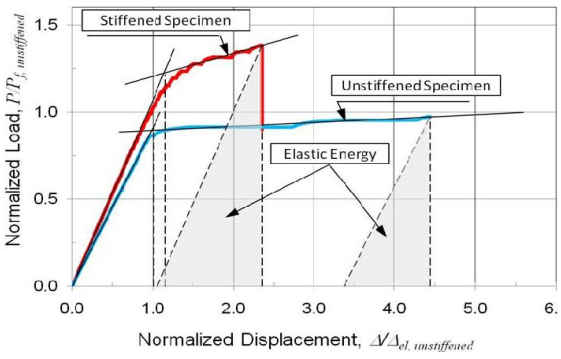

(**e**) FEA contour lines

Figure (2.36): Typical beam section and FEM, (Okeil et al., 2009).

In 2012, Okuyama et al. investigated the reinforcement effect and debonding behaviours of CFRP strengthened steel plate girders. They performed shear buckling tests on seven plate girders having two different aspect ratios of web, namely, 1.0 and 1.5. The former and latter girders were called G1 and G2, respectively. The details and dimensions of the girders are shown in Figures (2.37a and b). Table 2.2 shows the experimental cases.

Table 2.2: Experimental cases, (Okuyama et al., 2012)

Specimen No.		Reinforcing type	Aspect ratio
1	G1-1	Without reinforcing	1.0
	G1-2	Bi-axial sheet (±45°)	
	G1-3	Uni-axial sheet	
2	G2-1	Without reinforcing	1.5
	G2-2	Bi-axial sheet (±45°)	
	G2-3	Bi-axial sheet (±33.7°)	
	G2-4	Uni-axial sheet	

Figures (2.37c through f) show the bonding configuration of CFRP sheets. All CFRP sheets had the same modulus of elasticity (640GPa), but two different thicknesses. The sheets used in retrofitting Specimen G1-2 were 0.0715mm in thickness, while the sheets of all other specimens were 0.143mm in thickness. CFRP sheets were bonded on both sides of web. In all cases, two CFRP layers are laminated on each side of the web.

Low elastic putty layers were inserted between steel and CFRP sheets in order to improve the performance of out-of-plane deformation in all cases. The material properties of fibre sheets, Epoxy resin and CFRP sheets are shown in Table 2.3. In addition, Young's modulus, E_p, Poisson's ratio v_p, and the thickness of putty were, respectively, 66MPa, 0.3 and 0.8mm. Young's modulus, E_s , Poisson's ratio, v_s , and the thickness of web were, respectively, 200GPa, 0.3 and 6mm. Unfortunately, they did not specify the steel yield strength, f_y , at all.

Table 2.3: Material properties of CFRP sheets, (Okuyama et al., 2012)

		Sign	Unit	G1-2	G1-3	G2-2	G2-3	G2-4
Fiber sheet	Young's modulus	E_{cfL}	GPa	751	743	662	697	687
		E_{cfT}	GPa	20.6	20.6	20.6	20.6	20.6
	Poisson's ratio	n_{cfL}	-	0.31	0.31	0.31	0.31	0.31
		n_{cfT}	-	0.33	0.33	0.33	0.33	0.33
	Tensile strength	s_{cfB}	GPa	2.424	2.697	2.186	2.123	2.476
	Mass per unit area	M_{cf}	g/m^2	150	300	300	300	300
	Density	r_{cf}	g/cm^3	2.10	2.10	2.10	2.10	2.10
	Thickness	t_{cf}	mm	0.0715	0.1430	0.1430	0.1430	0.1430
Epoxy resin	Young's modulus	E_m	GPa	3.242	3.242	3.242	3.242	3.242
	Poisson's ratio	n_m	-	0.38	0.38	0.38	0.38	0.38
	Mass per unit area	M_m	g/m^2	300	600	600	600	600
	Density	r_m	g/cm^3	1.17	1.17	1.17	1.17	1.17
	Thickness	t_m	mm	0.2564	0.5128	0.5128	0.5128	0.5128
CFRP	Thickness	t_c	mm	0.3279	0.6558	0.6558	0.6558	0.6558
	Carbon fiber content	V_f	-	0.218	0.218	0.218	0.218	0.218
	Young's modulus	E_L	GPa	166	165	147	155	152
		E_T	GPa	3.972	3.972	3.972	3.972	3.972
	Poisson's ratio	n_L	-	0.365	0.365	0.365	0.365	0.365
		n_T	-	0.009	0.009	0.010	0.009	0.010

Test results of the experimental work are presented in Figures (2.37g and h) and Table 2.4. For all specimens, displacements progressed linearly until the maximum load. After reaching the maximum load, load decreased gradually due to the breaking of CFRP sheets for the reinforced specimens. The tension field action was observed in test panels for each specimen regardless of the reinforcement. Breaking of CFRP sheets progressed along the fibre orientation angles; see Figure (2.37i). Test results confirmed that the CFRP sheet improves shear strength by about 6-29%.

Table 2.4: Result of experiment, (Okuyama et al., 2012)

Specimen No.		Reinforcing type	Maximum load (kN)		Effect of reinforcing (%)
			Experiment P_{max}	Basler P_u	
1	G1-1	Without reinforcing	1182	1216	-
	G1-2	Bi-axial sheet (±45°)	1255		6.18
	G1-3	Uni-axial sheet	1328		12.35
2	G2-1	Without reinforcing	918	980	-
	G2-2	Bi-axial sheet (±45°)	1173		27.78
	G2-3	Bi-axial sheet (±33.7°)	1186		29.19
	G2-4	Uni-axial sheet	1162		26.58

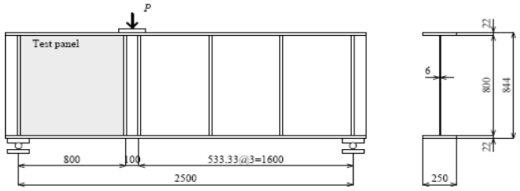

(**a**) case G1 (aspect ratio of web=1.0)

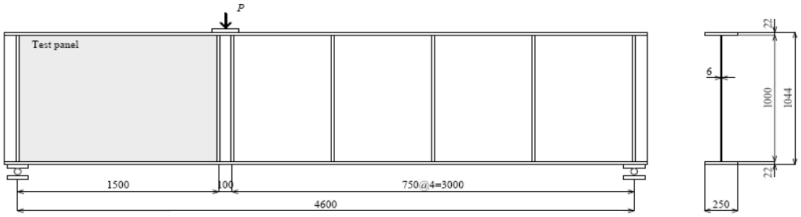

(**b**) case G2 (aspect ratio of web=1.5)

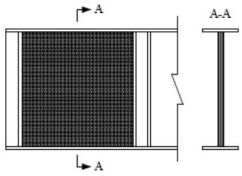

(**c**) specimen G1-2

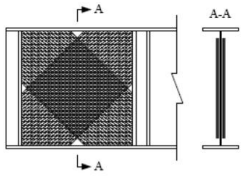

(**d**) specimen G1-3

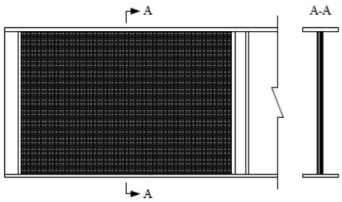

(**e**) specimens G2-2 and G2-3

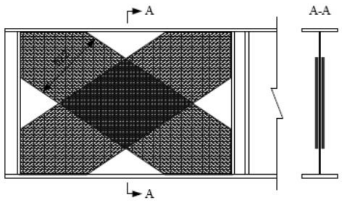

(**f**) specimen G2-4

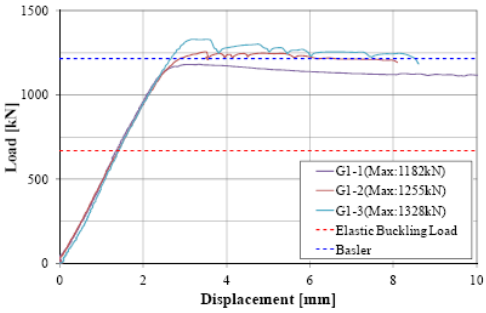

(**g**) case G1

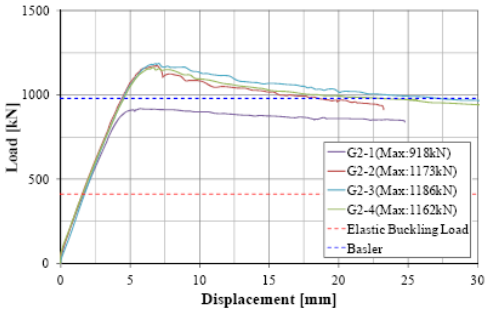

(**h**) case G2

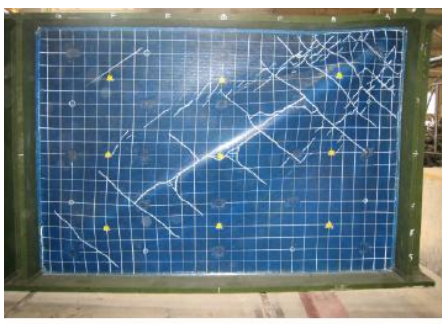

(**i**) specimen G2-3

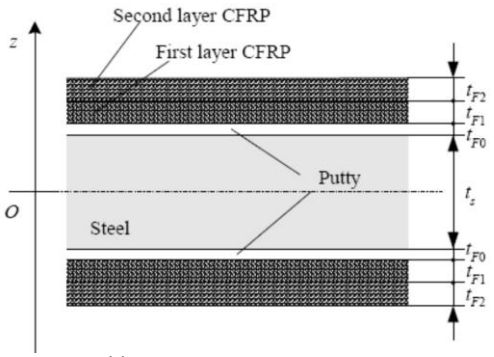

(**j**) composite cross-section

Figure (2.37): Details of the experimental work, (Okuyama et al., 2012).

On the other hand, Okuyama et al. (2012) presented an evaluation method for predicting the ultimate shear load-carrying capacity of steel plate girders strengthened with CFRP sheets. They focused on deriving a new elastic shear buckling stress, τ_{crv}, by integrating the flexural rigidity, D_v, with respect to web thickness as follows; see Figure (2.37j).

$$\tau_{crv} = k_s D_V \frac{\pi^2}{h^2(t_s + 2t_{F0} + 2t_{F1} + 2t_{F2})} \tag{2.39a}$$

Where k_s is the shear buckling coefficient, t_{F0} is thickness of putty layer, and t_{Fi} is the thickness in layer i of CFRP (i =1, 2). D_V is flexural rigidity of steel plate bonded CFRP sheets, which is given as (after correcting the editorial mistakes in the original paper)

$$\begin{aligned} D_v &= \int_{\frac{-t_s}{2}}^{\frac{t_s}{2}} \frac{E_s}{1-v_s^2} z^2 dz + 2\int_{\frac{t_s}{2}}^{\frac{t_s}{2}+t_{F0}} \frac{E_{F0}}{1-v_{F0}^2} z^2 dz + 2\int_{\frac{t_s}{2}+t_{F0}}^{\frac{t_s}{2}+t_{F0}+t_{F1}} \frac{E_{F1}}{1-v_{F1}^2} z^2 dz \\ &\quad + 2\int_{\frac{t_s}{2}+t_{F0}+t_{F1}}^{\frac{t_w}{2}+t_{F0}+t_{F1}+t_{F2}} \frac{E_{F2}}{1-v_{F2}^2} z^2 dz \\ &= \frac{E_s t_s^3}{12(1-v_s^2)} + \frac{2E_{F0}}{3(1-v_{F0}^2)}\left\{\left(\frac{t_w}{2}+t_{F0}\right)^3 - \left(\frac{t_s}{2}\right)^3\right\} + \frac{2E_{F1}}{3(1-v_{F1}^2)}\left\{\left(\frac{t_w}{2}+t_{F0}+t_{F1}\right)^3 - \left(\frac{t_s}{2}+t_{F0}\right)^3\right\} + \\ &\quad \frac{2E_{F2}}{3(1-v_{F2}^2)}\left\{\left(\frac{t_w}{2}+t_{F0}+t_{F1}+t_{F2}\right)^3 - \left(\frac{t_s}{2}+t_{F0}+t_{F1}\right)^3\right\} \end{aligned} \tag{2.39b}$$

where, E_{F0} is young's modulus of putty, v_{F0} is Poisson's ratio of putty, t_{F0} is the thickness of the putty. E_{Fi} and v_{Fi} are Young's modulus and Poisson's ratio of CFRP in layer i (i =1, 2), respectively.

In order to evaluate shear strength of steel girder bonded CFRP on its web, an evaluation method is proposed based on the Basler's equation. Three equations are derived according to how post-buckling strength is incorporated in composite section, Equations (2.40 through 2.42), where, Q_u , Q_y , τ_{cr} , τ_y , σ_y , and α represent, respectively, ultimate shear strength, yield shear strength, elastic shear buckling stress, yield shear stress (= $\sigma_y/\sqrt{3}$), yield stress and aspect ratio of test panel web (= width b / height h).

$$\frac{{}_A Q_u}{Q_y} = \frac{\tau_{crv}}{\tau_y} / + \frac{\sqrt{3}}{2} \frac{1-\tau_{crv}/\tau_y}{\sqrt{1+\alpha^2}} \tag{2.40}$$

$$\frac{{}_B Q_u}{Q_y} = \frac{\tau_{crv}}{\tau_y} / + \frac{\sqrt{3}}{2} \frac{1 - \tau_{crv} / \tau_y}{\sqrt{1+\alpha^2}} \left(1 + \frac{E_L \bar{t}_c}{E_s t_s} \right) \tag{2.41}$$

where, E_L is young's modulus of main direction of CFRP and $\bar{t}_c$ is total thickness of CFRP of tensile direction (= $2t_{cf}$).

$$\frac{{}_C Q_u}{Q_y} = \frac{\tau_{crv}}{\tau_y} / + \frac{\sqrt{3}}{2} \frac{1 - \tau_{crv} / \tau_y}{\sqrt{1+\alpha^2}} \left(1 + \frac{1}{1 - \tau_{crv} / \tau_y} \frac{\sigma_{cfB}}{\sigma_y} \frac{\bar{t}_{cf}}{t_s} \right) \tag{2.42}$$

where, σ_{cfB} is tensile strength of the fibre sheets and $\bar{t}_{cf}$ is total thickness of CFRP sheets in tensile direction (= $2t_{cf}$).

Table 2.5 shows the comparison between the maximum loads obtained from the test and shear strength calculated by the proposed three methods. For all of specimens, it can be seen that evaluation *method B* has a reasonable accuracy, in which the contribution of CFRP sheets are considered until the steel plate became yielded. CFRP sheets bonded on the both sides of web can increase the flexural rigidity of web, and have the contribution to elastic shear buckling stress. The CFRP sheets bonded on the area where steel yielded did not debond because of the lower elastic putty layers, while deformation proceeded. After exceeding the maximum loads, the CFRP sheets cannot take charge of load.

Table 2.5: Results of calculations, (Okuyama et al., 2012)

Case	α	Maximum load (kN)				A/ Experiment	B/ Experiment	C/ Experiment
		Experiment	A	B	C			
G1-1	1.0	1,182	1,216	1,216	1,216	1.029	1.029	1.029
G1-2		1,255	1,235	1,282	1,379	0.984	1.021	1.099
G1-3		1,328	1,277	1,358	1,598	0.961	1.022	1.203
G2-1	1.5	918	980	980	980	1.068	1.068	1.068
G2-2		1,173	1,016	1,102	1,273	0.866	0.939	1.085
G2-3		1,186	1,022	1,111	1,272	0.862	0.937	1.072
G2-4		1,162	1,020	1,109	1,312	0.878	0.954	1.129

In another study in the same year and by the same team, Wakabayashi et al. (2012) made an attempt to simulate the web corrosion attack of steel plate girders by reducing the thickness of the web mechanically at the junction with the bottom

tension flange. Four plate girders were tested for shear buckling, two of which had 50% web material loss and the other two were simulating a through-hole (severe corrosion condition). From each group one was strengthened with CFRP sheet and the other kept as a control specimen. Figure (2.38) show the test specimens and results represented in load displacement curves.

Wakabayashi et al. (2012) concluded that load-carrying capacity in shear is recovered by CFRP sheets appropriately bonded on the corroded webs, even when severe corrosion (i.e. through-hole) occurs. The necessary number of CFRP sheets is determined from the thickness of CFRP sheet converted to steel, which is calculated from both Young's modulii. The converted thickness of CFRP sheet should be larger than the reduced thickness of corroded part, and then CFRP sheets should be bonded to the corroded parts in the direction of ±45 degrees.

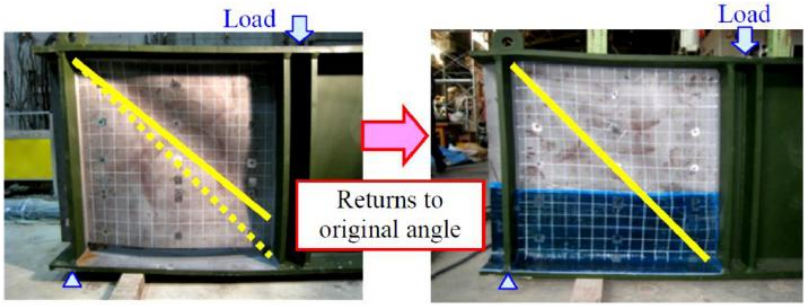

(a) specimens after test

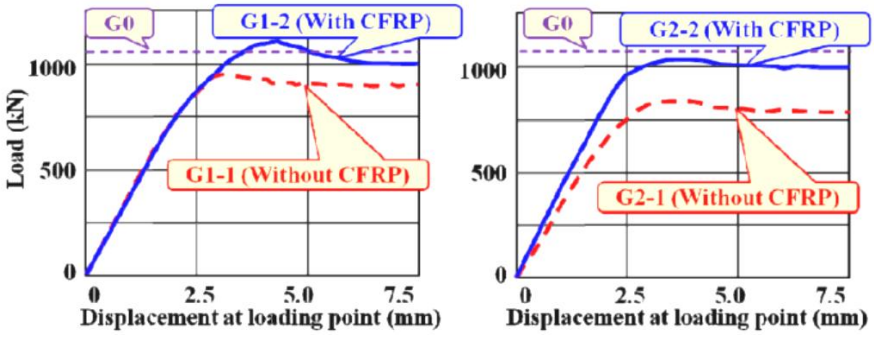

(b) load vs. displacement under point load

Figure (2.38): Details of the experimental work, (Wakabayashi et al., 2012).

Bhutto (2014) investigated the use of pultruded FRP composites and fabrics to strengthen webs of steel plate girders. His PhD work can be considered as an extended version of Okeil et al. work (2009). Eight specimens were tested in the study; Table 2.6 illustrates the specimens' designation and their corresponding

ultimate load and compares it to the finite element model predictions. Figure (2.39) shows some of the specimens and the load deflection curves both for the experimental results and finite element models.

Table 2.6: Test and FEA results, (Bhutto, 2014)

Specimen	Strengthening scheme	Ultimate load (kN)		% increase due to strengthening	Ratio of FEA to test load
		FEA	Test		
Group 1: *Unstrengthened control specimens*					
B1	Unstrengthened	235	230	---	1.02
B9	Unstrengthened	295	---	---	---
Group 2: *GFRP pultruded section strengthened specimens*					
B2	2 vertical GFRP pultruded sections	287	277	1.20	1.03
B5	1 vertical GFRP pultruded sections	368	380	1.29	0.97
B6	1 diagonal GFRP pultruded sections	456	437	1.48	1.04
B8	2 vertical GFRP pultruded sections beneath the load	271	285	0.97	0.95
Group 3: *FRP fabric strengthened specimens*					
B3	4 layers of CFRP	627	287	1.25	2.18
B4	8 layers of GFRP	653	354	1.54	1.84
B7	4 layers of GFRP	489	428	1.49	1.14

With respect to the GFRP pultruded section strengthening, the maximum increase in the ultimate load carrying capacity was 48%, this is for specimen B6 with the diagonal strengthening alignment. On the other hand, the maximum increase of the load carrying capacity for the specimens strengthened with fabric sheets was 54% for specimen B4 with 8 layers of GFRP fabric.

However, once again by close examining the failure mode of the control specimen in Figure (2.39a), it can be seen that the failure was due to the end support stiffener crippling (same problem we had before with Okeil et al. (2009) work). This unfortunately leads to reduction in the control specimen tested capacity; consequently leading to overestimation of the increase in the ultimate load carrying capacity estimated in Table 2.6. Another drawback in Bhutto's work is that specimen B9 is not a tested specimen but only a finite element simulation for the control

specimen of the second series of tests (S2) where there was an increase in the yielding strength of steel of 30% over the first series because different steel was used.

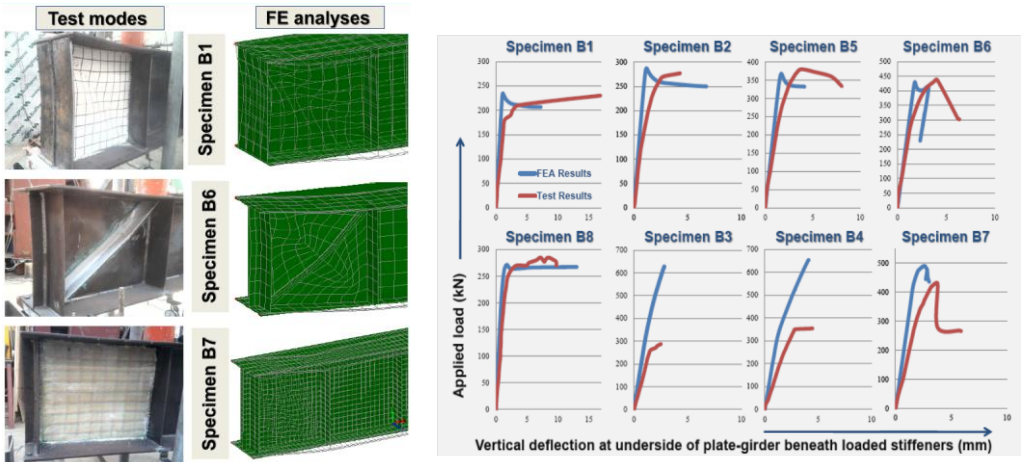

(**a**) specimens modes of failure (**b**) load vertical displacement responses

Figure (2.39): Details of the experimental work and FEA, (Bhutto, 2014).

More recently, Assoodani (2014) presented a large experimental programme studying the shear behaviour and strength of steel plate girders and steel-concrete composite plate girders retrofitted with CFRP composites bonded adhesively to the web plate and loaded primarily in shear. The programme included two main series, the first one was a small scale plate girders used to optimize the best strengthening technique; and the second series was a full-scale steel and steel-concrete composite plate girders used to quantify the effectiveness of strengthening the web with the optimized technique. Table 2.7 shows the details for the two main series. A combination between pultruded CFRP plates (Carbodur M914) and fabric CFRP sheets (Wrap 230 C45) was used to strengthen the plate girders, see Figure (2.40).

Table 2.7: Details of the tested specimens, (Assoodani, 2014)

No.	Specimen	h_w [mm]	t_w [mm]	$\lambda = h_w / t_w$	b_w [mm]	L_0 [mm]	$\alpha = b_w / h_w$	Retro'd	Type of CFRP	Deck Slab
1	RG0	250	1.00	250	371	850	1.48	No	NA	No deck
2	RG1		1.25	200				No	NA	No deck
3	RG2							Yes	Carbodur M914	No deck
4	RG3							Yes	Wrap 230 C45	No deck
5	RG4							Yes	Carbodur M914	No deck
6	RG5							Yes	Carbodur M914	No deck
7	RG6							Yes	Carbodur M914	No deck
8	SPG01	490	2.00	245	724.5	1,868		No	NA	No deck
9	SPG02							Yes	Carbodur M914 + Wrap 230 C45	No deck
10	SPG03							Yes	Carbodur M914	No deck
11	CPG01							No	NA	RC deck
12	CPG02							Yes	Carbodur M914 + Wrap 230 C45	RC deck
13	CPG03							Yes	Carbodur M914	RC deck
14	SPG04		3.00	163		2,100		No	NA	No deck
15	SPG05							Yes	Carbodur M914 + Wrap 230 C45	No deck
16	SPG06							Yes	Carbodur M914	No deck
17	CPG04							No	NA	RC deck
18	CPG05							Yes	Carbodur M914 + Wrap 230 C45	RC deck
19	CPG06							Yes	Carbodur M914	RC deck

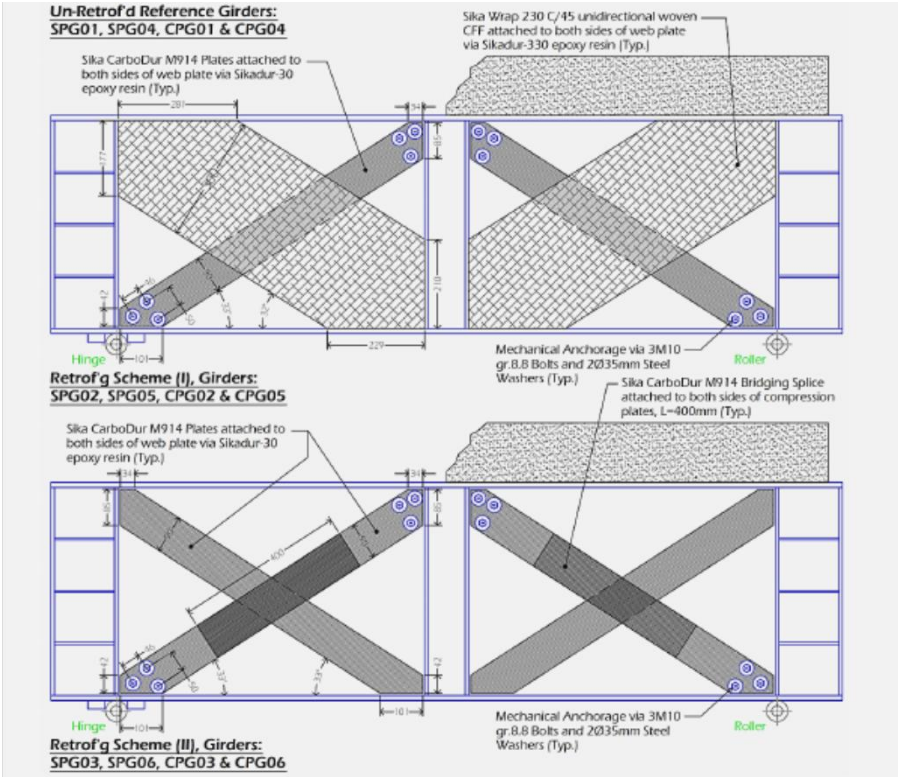

Figure (2.40): Details of retrofitting schemes, (Assoodani, 2014).

Table 2.8 shows the experimental results for the full-scale steel plate girders tests and Figure (2.41) shows photos for the tested specimens and the load-deflection curves. It is worth mentioning that each series is divided into two groups, namely, web slenderness ratios of 245 and 163 corresponding to steel plate's thicknesses of 2 and 3mm, respectively. The maximum increase in the capacity of the strengthened specimens was 132% which was for the specimen strengthened with mechanically anchored pultruded CFRP plates in both tension and compression diagonals of the web.

Table 2.8: Experimental test results, (Assoodani, 2014)

No.	Girder No.	Panel Tested	P_u [kN]	$P_{1st\ DB}$ [kN]	$P_{major\ DB}$ [kN]	Δ_u [mm]	Δ_{max} [mm]
1	SPG01	Both	181.43	-	-	12.56	81.00
2	SPG02	LHS	370.70	313.81	343.23	6.99	11.66
3		RHS	392.27	353.04	392.27	16.75	17.68
4	SPG03	LHS	366.78	333.44	366.78	6.47	16.66
5		RHS	421.69	411.88	421.69	30.50	33.83
6	SPG04	Both	357.94	-	-	5.56	37.46
7	SPG05	LHS	594.28	490.33	594.28	9.23	12.83
9		RHS (1st trial)	549.17	-	-	NA	21.50
10		RHS (2nd trial)	470.72	372.65	470.72	28.12	34.53
11	SPG06	LHS	657.05	657.05	657.05	25.91	33.71
12		RHS	539.37	470.72	539.37	8.91	16.56

(**a**) unstrengthened specimen

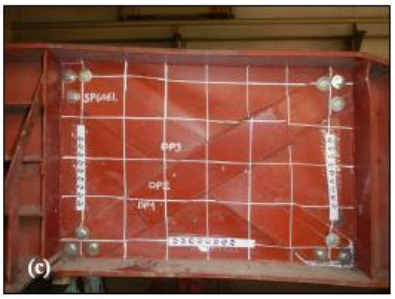

(**b**) strengthened specimen

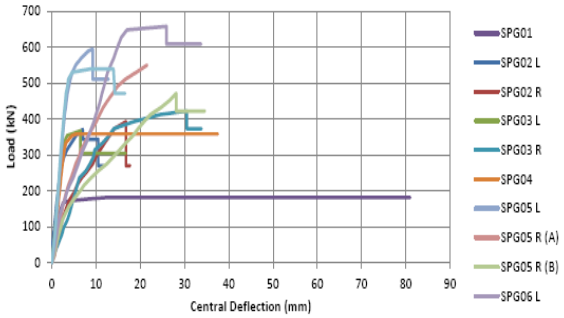

(**c**) Load-deflection curves

Figure (2.41): Specimen failure mode and results of steel plate girders tests, (Assoodani , 2014).

Table 2.9 shows the experimental results for the full-scale steel-concrete composite plate girders tests and Figure (2.42) shows photos for the tested specimens and the load-deflection curves. The maximum increase in the capacity of the strengthened specimens was 63%, but this time it was for the specimen strengthened with both pultruded CFRP plates and fabric CFRP sheets in both compression and tension diagonals of the web, respectively.

Table 2.9: Experimental test results, (Assoodani, 2014)

No.	Girder No.	P_u [kN]	$P_{1st\ DB}$ [kN]	$P_{Major\ DB}$ [kN]	$P_{1st\ conc.\ crack}$ [kN]	Δ_u [mm]	Δ_{max} [mm]
1	CPG01	394.23	-	-	333.34	12.25	14.97
2	CPG02	641.35	490.33	641.35	470.72	10.33	11.06
3	CPG03	615.86	529.56	615.86	470.72	6.45	10.93
4	CPG04	578.59	-	-	294.24	8.57	9.19
5	CPG05	802.18	627.63	784.53	529.62	8.36	11.65
6	CPG06	826.70	804.15	826.70	411.93	8.87	11.29

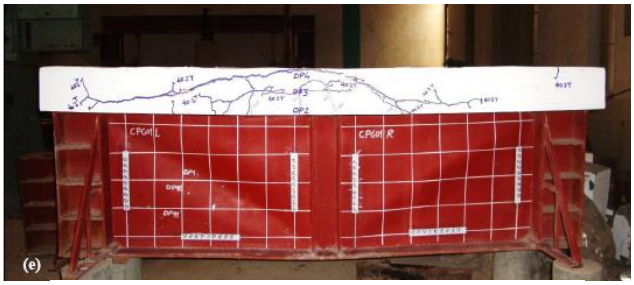

(**a**) unstrengthened specimen

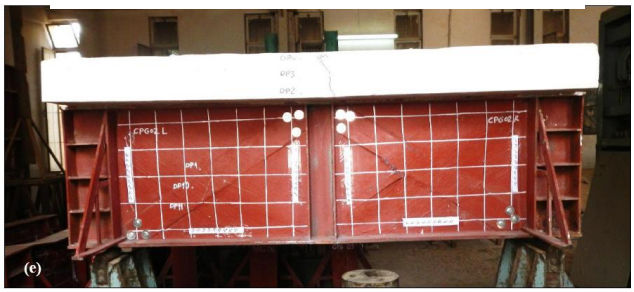

(**b**) strengthened specimen

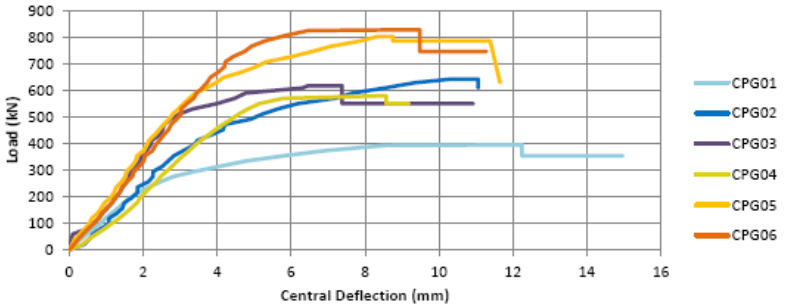

(**c**) load-deflection curves

Figure (2.42): Specimen failure mode and results of steel-concrete composite plate girders tests, Assoodani (2014).

In addition to that, several design equations were reviewed and a modified design equation was proposed based on the work previously illustrated by Okuyama et al. (2012); the equation showed very good correlation with available data. Extensive parametric study was performed taking into considerations all possible parameters, such as, web aspect ratio, slenderness ratio, effect of type of CFRP, effect of amount of CFRP, effect of retrofitting scheme, and effect of composite action between concrete deck slab and steel plate girder. Eventually, design procedures and guidelines were provided.

To sum up, limited attempts to strengthen the web of beams and plate girders against shear buckling were carried out by different researchers. Although these attempts succeeded in increasing the buckling strength and the ultimate capacity of the plate girders moderately, but it failed in developing a rigorous, cost effective, and easy to install strengthening technique that takes into account the importance of the ductile failure mode of the steel plate girders. In addition to that, none of these researches addressed the breathing phenomenon and how their proposed strengthening technique will help in reducing it.

CHAPTER REFERENCES

AASHTO, LRFD-SI Units (2007). "Standard Specifications for Highway Bridges," 4th Ed., Washington, D.C, USA.

ADAMS R.D. and WAKE W.C. (1984) "Structural adhesive joints in engineering," Elsevier Applied Science Publications, London and New York.

AGLAN H., WANG Q.Y., and KEHOE M. (2001) "Fatigue behaviour of bonded composite repairs," Journal of Adhesion Science and Technology, V. 15, No. 13 pp. 1621-1634.

AISC, LRFD (1994). "Manual of Steel Construction, Load and Resistance Factor Design," 2nd Ed., Vol. I and II, Chicago, Illinois, USA.

AJEESH S.S. and SREEKUMAR S. (2014) "Effect of Imperfection on Shear Behaviour of Hybrid Plate Girder," Inter. Jrnl. of Modern Eng. Research (IJMER), Vol. 4, Issue 5, pp. 43-48.

AL-EMRANI M., LINGHOFF D. and KLIGER R. (2005). "Bonding Strength and Fracture Mechanisms in Composite Steel-CFRP Elements," Proceedings of the Inter. Symposium on Bond Behaviour of FRP in Structures (BBFS 2005), Chen and Teng (editors), Inter. Institute for FRP in Construction, pp. 425-433.

ALINIA M.M., SHAKIBA M. and HABASHI H.R. (2009) "Shear Failure Characteristics of Steel Plate Girders," Thin-Walled Structures, No. 47, pp. 1498-1506.

ALLAN R.C., BIRD J., and CLARKE J.D. (1988) "Use of adhesives in repair of cracks in ship structures," Materials Science and Technology, V. 4, pp. 853-859.

ALLEN K.W., CHAN S.Y.T. and ARMSTRONG K.B. (1982) "Cold-setting adhesives for repair purposes using various surface preparation methods," International Journal of Adhesion and Adhesives, Vol. 2, No. 4, pp. 239-247.

AL-SARRAF S.Z. and HAMOODI M.J. (1991). "The prediction of the collapse load of plate girders having slender webs, vertical and inclined stiffeners," Eng. and Technology, a scientific Journal. Published by the University of Technology, Baghdad, Vol. 10, No. 1, pp. 8-25.

AL-SARRAF S.Z. and HAMOODI M.J. (1991). "The Prediction of the Collapse Load of Plate Girders Having Slender Webs, Vertical and Inclined Stiffeners," Eng. and Technology, a scientific Jrnl. published by the University of Technology, Baghdad, Vol. 10, No. 1, pp. 8-25.

ARMSTRONG K.B. (1983) "Carbon fibre fabric repairs to metal aircraft structures," Engineering with Composites, Proceedings of the Third Technology Conference SAMPE European Chapter, London, England, pp. 8.1-8.12.

ASSOODANI F. A. (2014). "Shear behaviour and strength of CFRP retrofitted steel plate girders and steel-concrete composite plate girders," PhD thesis, University of Technology, Iraq, 746 pp.

BAKER A.A., ROSE LR.E., and JONES R. (2002). "Advances in bonded composite repair of metallic aircraft structure," Amsterdam: Elsevier.

BARNES F.J. (1996) "Composite materials in the UK offshore oil and gas industry," SAMPE Journal, Vol. 32, No. 2, PP. 12-17.

BARNES, F.J. (1996) "Composite materials in the UK offshore oil and gas industry," SAMPE Journal, V. 32, No. 2, PP. 12-17.

BASLER K. (1960a). "Strength of plate girders in shear," Fritz Engineering Laboratory Report No. 251-20, Lehigh University, 61 pp.

BASLER K. (1961a). “Strength of Plate girders in shear,” Journal of the Structural Division, American Society of Civil Engineers, Proc. No.2967, ST7- Part I, pp. 151-180.

BASLER K. (1961b) . “New provisions for plate girder design,” In: Proc. AISC National Engineering Conf., New York, pp. 65-74

BASLER K. (1961c). “Strength of Plate girders under combined bending and shear,” J. Struc. Div. ASCE 87, pp. 181-190.

BASLER K. (1963). “Strength of plate girders in shear,” Trans. ASCE 128, pp. 683-719.

BASLER K. and THURLIMANN B. (1959). “Plate girder research,” In: Proc. AISC National Engineering Conf., New York.

BASLER K., YEN B.T., MULLER J., and THÜRLIMANN B. (1960b). “Web buckling tests on welded plate girders- Part 1: Overall introduction and the test girders,” Fritz Engineering Laboratory Report No. 251-11, Lehigh University, 42 pp.

BASLER K., YEN B.T., MULLER J., and THÜRLIMANN B. (1960c). “Web buckling tests on welded plate girders- Part 2: Tests on plate girders subjected to bending,” Fritz Engineering Laboratory Report No. 251-12, Lehigh University, 48 pp.

BASLER K., YEN B.T., MULLER J., and THÜRLIMANN B. (1960d). “Web buckling tests on welded plate girders- Part 3: Tests on plate girders subjected to shear,” Fritz Engineering Laboratory Report No. 251-13, Lehigh University, 25 pp.

BASLER K., YEN B.T., MULLER J., and THÜRLIMANN B. (1960e). “Web buckling tests on welded plate girders- Part 4: Tests on plate girders subjected to bending and shear,” Fritz Engineering Laboratory Report No. 251-14, Lehigh University, 20 pp.

BERGFELT A. (1973). “Plate Girders with Slender Web-Survey and a Modified Calculation Method,” Report No. 11 2.2. Oslo: Nordiske forskningsdagar for stålkonstruksjoner.

BHUTTO M.A. (2014). “FRP-STRENGTHENING OF WEBS OF STEEL PLATE-GIRDERS,” PhD thesis, School of Built Environment, Heriot-Watt University, 280 pp.

BRITISH STANDARDS INSTITUTION, Technical Committee B/521 (BS 5950-1: 2000). “Structural Use of Steelwork in Building, Part 1: Code of Practice for Design – Rolled and Welded Sections,” London, UK, 222 pp.

BRITISH STANDARDS INSTITUTION, Technical Committee B/525 (BS 5400-3: 2000). “Steel, Concrete, and Composite Bridges, Part 3: Code of Practice for Design of Steel Bridges,” London, UK, 198 pp.

BUREAU OF TRANSPORTATION STATISTICS (2008). “Transportation statistics annual report 2008,” United States Department of Transportation, Research and Innovative Technology Administration, USA. National Bridge Inventory Database (NBI), Federal Highway Administration, Wikipedia, https://en.wikipedia.org/wiki/National_Bridge_Inventory.

BÜYÜKÖZTÜRK O., OGUZ G., and ERDEM K. (2004) “Progress on understanding debonding problems in reinforced concrete and steel members strengthened using FRP composites,” Construction and Building Materials, Vol. 18, No. 1, pp. 9-19.

CADEI, J.M.C., STRATFORD T.J., HOLLAWAY L.C., and DUCKETT W.G. (2004). ”Strengthening Metallic Structures Using Externally Bonded Fibre-Reinforced Polymers. CIRIA, Publication C595, London, UK, 234 pp.

CALLADINE C.R. (1973). “ A plastic theory for collapse of plate girders under combined shearing and bending moment,” Journal of the Structural Engineer, Vol. 51, No. 4, pp. 147-154.

CHACON A., CHAJES M., SWINEHART M., RICHARDSON D., and WENCZEL G. (2004). "Applications of advanced composites to steel bridges: a case study on the Ashland bridge," Proceedings of the fourth conference on advanced composites for bridges and structures, Calgary.

DAWOOD M., and RIZKALLA S. (2006). "Bond and Splice Behavior of High Modulus CFRP Materials Bonded to Steel Structures", 3rd International Conference on FRP Composites in Civil Engineering (CICE 2006), Miami, Florida, USA.

DAWOOD M., and RIZKALLA S. (2006). "Environmental durability of a CFRP system for strengthening steel structures," Construction and Building Materials, 24(9), pp. 1682-1689.

DEXTER R.J. and FISHER J.W. (1999) "Fatigue and Fracture," Structural Engineering Handbook, Ed. Chen Wai-Fah, Boca Raton: CRC Press LLC.

DODIUK H. and KENIG S. (1988) "The effect of surface preparation on the performance of acrylic adhesive joints," International Journal of Adhesion and Adhesives, Vol. 8, No. 3, pp. 159-166.

DUONG C.N. and WANG C.H. (2007). "Composite Repair: Theory and Design," Elsevier, U.K., 1st ed., 479 pp.

EL-DAMTTAY A.A. and ABUSHAGUR M. (2003). "Testing and modelling of shear and peel behaviour for bonded steel/FRP connections," Thin-Walled Structures, 41(11), pp. 987-1003.

Elena-Felicia Beznea and Ionel Chirica (2011). "Buckling and Post-buckling Analysis of Composite Plates, Advances in Composite Materials - Ecodesign and Analysis," Dr. Brahim Attaf (Ed.), 27 pp.

ESTRADA I., REAL E., and MIRAMBELL, E. (2008). "Shear Resistance of Stainless Steel Plated Girders with Transverse and Longitudinal Stiffening", Journal of Constructional Steel Research, Elsevier, Vol. XX No. XX, 16 pp.

EUROPEAN COMMITTEE FOR STANDARDISATION (ENV 1997). Eurocode 3: Design of steel structures- Part 1-5: Supplementary rules for planer plated structures without transverse loading, ENV 1993-1-5.

EUROPEAN COMMITTEE FOR STANDARDISATION (EC3 1993). Eurocode 3: Design of Steel Structures- Part 1-1: General Rules and Rules for Buildings. EN 1993-1-1: 1993. Brussels: CEN.

EUROPEAN COMMITTEE FOR STANDARDISATION (EC3 2005). Eurocode 3: Design of Steel Structures- Part 1-1: General Rules and Rules for Buildings. EN 1993-1-1: 2005. Brussels: CEN.

EUROPEAN COMMITTEE FOR STANDARDISATION (EC3 2006). Eurocode 3: Design of Steel Structures- Part 1-5: Plated Structural Elements. EN 1993-1-5: 2006. Brussels: CEN.

FAWZIA S., ZHAO X.L., AL-MAHAIDI R. and RIZKALLA S.H. (2006a) "Preliminary Bond-Slip Model for CFRP Sheets Bonded to Steel Plates," 3rd International Conference on FRP Composites in Civil Engineering (CICE2006), Dec. 13-15, Miami, Florida, USA.

FAWZIA S.R., AL-MAHAIDI R., ZHAO X.L., and RIZKALLA S. (2006b) "Strengthening of circular hollow steel tubular sections using high modulus CFRP sheet," Construction and building Materials, 21, 839-845.

FERNANDO D., TENG J.G., YU T., and ZHAO X.L. (2013) "Preparation and characterization of steel surfaces for adhesive bonding," Journal of Composite Construction, ASCE, Vol. 17, No. 6, pp. 1-10.

FRIEZE P.A. and BARNES F.J. (1996) "Composite materials for offshore application- New data and practice," Proceedings of the 28th Annual Offshore Technology Conference, Vol. 3, Construction and Installation, Houston, Texas, May 6-9, pp. 247-253.

FUJII, T., FUKOMOTO, Y., NISHINO, F. and OKUMURA, T. (1971). "Research works on ultimate strength of plate girders and Japanese provisions on plate girder design,". IABSE Colloquium, 21-48.

GALBRAITH D.N. and Barnes F. (1995) "Beryl Bravo- blast walls conversion: Development and testing of steel/carbon fibre composite," Proceedings of the 5th International Offshore and Polar Engineering Conference, The Hague, The Netherlands, pp. 229-236.

GAYLORD E.H. and GAYLORD C.N. (1972). "Design of steel structures," McGraw-Hill Book Company, New York, 663 pp.

GETTINGS M. and KINLOCH A.J. (1997) "Surface analysis of polysiloxane/metal oxide interfaces," Journal of Materials Science, Vol. 12, No. 12, pp. 2511-2518.

GILLESPIE J.W. Jr., MERTZ D.R., KASAI K., EDBERG W.M., DEMITZ J.R., and HODGSON I. (1996) "Rehabilitation of steel bridge girders: Large scale testing," Proceedings of the 1996 11th Technical Conference of the American Society for Composites, Atlanta, Georgia, pp. 231-240.

GOODPASTURE D.W. and STALLMEYER J.E. (1967). "Fatigue behavior of welded thin web girders as influenced by web distortion and boundary rigidity," C.E. Studies SRS No. 328, University of Illinois.

GRABOVAC I., BARTHOLOMEUSZ R.A., and BAKER A.A. (1991) "Fibre composite reinforcement of metallic plates of varying thickness and contour," International Conference of Aircraft Damage Assessment and Repair, Melbourne, Australia, pp. 231-238.

GRIFFITH A.A. (1921). "The phenomena of rupture and flow in solids," Phil. Trans. Roy. Soc. London, Vol. A 221, pp. 163-197.

GRIFFITH A.A. (1924). "The Theory of Rupture," Proc. 1st Conf. Appl. Mech. Delft.

HANSEN T. (2006). "Theory of Plasticity for Steel Structures- Solutions for Fillet Welds, Plate Girders and Thin Plates," PhD thesis, Technical University of Denmark, 239 pp.

HARRIES K.A., PECK A.J., and ABRAHAM E.J. (2009). "Enhancing stability of structural steel sections using FRP," Thin-Walled Structures 47 (2009), pp. 1092–1101.

HARRIS A.F. and BEEVERS A. (1999) "The effect of grit blasting on surface properties for adhesion," International Journal of Adhesion and Adhesives, Vol. 19, No. 6, pp. 445-452.

HART-SMITH L.J. (1980) "Further developments in the design and analysis of adhesive-bonded structural joints," ASTM Special Technical Publication 749, Joining of Composite Materials: A Symposium, K.T. Kedward, ed., pp. 3-31.

HASHIM S.A. (1999) "Adhesive bonding of thick steel adherends for marine structures," Marine Structures, Vol. 12, No. 6, pp. 405-423.

HENDY C.R. and PRESTA F. (2008). "Transverse web stiffeners and shear moment interaction for steel plate girder bridges," The Structural Engineer, Nov., pp. 13-26.

HILDEBRAND M. (1994) "Non-linear analysis and optimization of adhesively bonded single lap joints between fibre-reinforced plastics and metals," International Journal of Adhesion and Adhesives, Vol. 14, No. 4, pp. 261-267.

HÖGLUND T. (1973). “Design of Thin Plate I-Girders in Shear and Bending with Special Reference to Buckling,” No. 94. Stockholm: Kungl. Tekniska Högskolan, Inst. for bygnadsstatik.

HÖGLUND T. (1995). “Strength of Steel and Aluminium Plate Girders: Shear Buckling and Overall Web Buckling of Plane and Trapezoidal Webs – Comparison with Tests,”. Tech. Report No. 4. Stockholm: Royal Institute of Technology, Department of Structural Engineering.

HÖGLUND T. (1999). “TALAT Lecture 2301: Design of Members - Advanced Level,” EAA-European Aluminium Association, TALAT: Training in Aluminium Application Technologies, Stockholm, 1999, 125 pp.

HOLLAWAY L.C. and CADEI J. (2002) “Progress in the technique of upgrading metallic structures with advanced polymer composites,” Progress in Structural Engineering Materials, V. 4, No. 2, pp. 131-148.

HUTCHINSON A.R. (1987) “Surface pretreatment- the key to durability,” Proceedings of the International Conference on Structural Faults & Repair, University of London, pp. 235-244.

HUTCHINSON A.R. (1996). “Strengthening of the Quinton Bridges with externally bonded steel plate reinforcement,” Bridge Management 3: Inspection, Maintenance and Repair, The 3rd International Conference on Bridge Management, University of Surrey, Guilford, UK, April 14-17, pp. 743-750.

IRWIN G. R. (1948). “Fracture Dynamics,” Fracturing of Metals, American Soc. for Metals, Cleveland, pp. 147-166.

JIAO H., and ZHAO X.L. (2004) “CFRP strengthened butt-welded very high strength (VHS) circular steel tubes,” Thin-Walled Structures, Vol. 42, Nu. 7, pp. 963-978.

JOHANSSON B., MAQUOI R. and SEDLACEK G. (2001). “New Design Rules for Plated Structures in Eurocode 3,” Journal of Constructional Steel Research, 57, 279-311.

JOHNS D.J. (1971). “Shear Buckling of Isotropic and Orthotropic Plates: A Review,” Tech. Rep. R&M No. 3677, British Aeronautical Research Council, London, 34 pp.

KARBHARI V.M. (2003). “Durability of composites for civil structural applications,” Oxford, Woodhead Publishing Limited.

KARBHARI V.M. and SHULLEY S.B. (1995) “Use of composites for rehabilitation of steel structures determination of bond durability,” Journal of Materials in Civil Engineering, V. 7, No. 4, pp. 239-245.

KARBHARI V.M. and SHULLEY S.B. (1995). “Use of composites for rehabilitation of steel structures determination of bond durability,” Journal of Materials in Civil Engineering, v. 7, n. 4, pp. 239-245.

Kim H. and Kedward K. (2001). “Stress analysis of in-plane, shear loaded, adhesively bonded, composite joints and assemblies,” Office of Aviation Research, Washington, D.C. 20591, Final Report, 28 pp.

KUHN P., PETERSON P., and LEVIN L. (1952a). “A summary of diagonal tension, Part I- Methods of analysis,” Technical note 2661, Langley Aeronautical Laboratory, Langley Field, Va., 131 pp.

KUHN P., PETERSON P., and LEVIN L. (1952b). “A summary of diagonal tension, Part II- Experimental evidence,” Technical note 2662, Langley Aeronautical Laboratory, Langley Field, Va., 81 pp.

KURANISHI S., NAKAZAWA M. and IWAKUMA T. (1988). "On the Tension Field Action and Collapse Mechanism of a Panel under Shear," Japan Society of Civil Engineering, Structural Eng./ Earthquake Eng., Volume 5, No. 1, Tokyo, pp. 161s-171s.

LEE S.C. and YOO C.H. (1998). "Strength of Plate Girder Web Panels under Pure Shear," ASCE, Journal. of Structural Eng., Vol. 124, No. 2, pp. 184-194.

LEE S.C. and YOO C.H. (1999). "Experimental study on ultimate shear strength of web panels," Journal of Structural Eng., 125(8), pp. 838-846.

LEE S.C. and YOO C.H., and YOON Y. (2002). "Behavior of intermediate transverse stiffeners attached on web panels," Journal of Structural Engineering, 128(3), pp.337-345.

LEE S.C. and YOO C.H., and YOON Y. (2003). "New design rules for intermediate transverse stiffeners attached on web panels," Journal of Structural Engineering, 129(12), pp.1607-1614.

LEE S.C., DAVIDSON J.S., and YOO C. H. (1996). "Shear buckling coefficients of plate girder web panels," Computers & Structures, Vol. 59, No 5, pp. 789-795.

LEE S.C., LEE D.S PARK C.S., and YOO, C.H. (2009b) "Further Insights into Post-buckling of Web Panels. II: Experiments and Verification of New Theory," ASCE, Journal of Structural Eng., Vol. 135, No. 1, pp. 11-18.

LEE S.C., LEE D.S., and YOO, C.H. (2009a) "Further Insights into Post-buckling of Web Panels. I: Review of Flange Anchoring Mechanism," ASCE Journal of Structural Eng., Vol. 135, No. 1, pp. 3-10.

LEE Y.S., WIPF T.J., BRENT M.P., and KLAIBER F.W. (2005) "Evaluation of a steel bridge girder strengthened with CFRP post-tension bars," Transportation Research Board 84th Annual Meeting, Washington, D.C.

LIU H.B., ZHAO X.L., and AL-MAHAIDI R. (2010). "Effect of fatigue loading on bond strength between CFRP sheets and steel plates," International Journal of Structural Stability and Dynamics, 10(1), pp. 1-20.

LUKE, S. (2001a) "Strengthening of structures with carbon plates- case histories for Hythe Bridge, Oxford and Qafco Prill Tower, Qatar," Network Group for Composites in Construction, First Annual Conference, BRE, Watford, England.

LUKE, S. (2001b) "The use of carbon fibre plates for the strengthening of two metallic bridges of an historic nature in the UK," International Conference on FRP Composites in Civil Engineering, Hong Kong, China, V. 2, J.G. Teng, Ed., pp. 975-983.

MAEDA Y. (1971). "Ultimate static strength and fatigue behavior of longitudinally stiffened plate girders in bending," IABSE, London Colloquium, pp. 269-282.

MATTA F. (2003). "Bond between steel and CFRP laminates for rehabilitation of metallic bridges," MSc, Faculty of Engineering, University of Padua, Padua.

MATTA F., KARBHARI V.M., TINAZZE D., and VITALIANI R. (2004) "Static and Fatigue behaviour of steel/CFRP adhesive bonds for the rehabilitation of metallic bridges," Mechanics of Masonry Structures Strengthened with FRP-materials: Modelling, Testing, Design, Control, December 6-7, Venezia, Italy.

MAYS G.C. and HUTCHINSON A.R. (1992) "Adhesives in civil Engineering," Cambridge University Press, New York, 333 pp.

MAYS G.S. (1990). "Fatigue and creep performance of epoxy resin adhesive joints," Transport and Road Research Laboratory, 58 pp.

MCKEEL W.T. and MILLER A.B. (2006). “History of early bridge specifications: A reprint of a paper by J.N. Clary,” final report VTRC 07-R10, Virginia Transportation Research Council, 132 pp.

MCKENNA J.K. and ERKI M.A. (1994). “Strengthening of reinforced concrete flexural members using externally applied steel plates and fibre composite sheets- a survey,” Canadian Journal of Civil Engineering, v. 21, no. 1, pp. 16-24.

MCKNIGHT S.H., BOURBAN P.E., GILLESPIE J.W. Jr., and KARBHARI V.M.(1994) “Surface preparation of steel for surface bonding applications,” Infrastructure: New Materials and Methods of repair, Proceedings of the 3rd Materials Engineering Conference, ASCE, Kim D. Basham, Ed., Nov 13-16, San Diego, California, pp. 1148-1155.

MELOGRANA J.D., and GRENESTEDT J.L. (2002) “Improving Joints Between Composites and Steel Using Perforations,” Composites: Part A, Vol. 33, pp. 1253-1261.

MERTZ D.R. and GILLESPIE J.W. (1996). “Rehabilitation of steel bridge girders through the application of advanced composite materials,” NCHRP-IDEA Project 11, 30 pp.

MERTZ D.R., GILLESPIE J.W., CHAJES M.J., and SABOL S.A. (2002). “The rehabilitation of steel bridge girders using advanced composite materials,” NCHRP-IDEA Project 51, 25 pp.

MILLER T.C., CHAJES M.J., MERTZ. D.R., and HASTINGS J.N. (2002) “Strengthening of a steel bridge girder using CFRP plates,” ASCE Journal of Bridge Engineering, 6(6), 514–522.

MILLER T.C., MICHAEL J.C, DENNIS R.M., and JASON N.H. (2001) “Strengthening of a steel bridge using CFRP plates,” ASCE Journal of Bridge Engineering, Vol. 6, No. 6, pp. 514-522.

MOSALLAM A.S. (2004) “Evaluation and construction of composite strengthening systems for the Sauvie Island Bridge,” Proceedings of the Second International Conference on FRP Composites in Civil Engineering- CICE 2004, Adelaide, Australia, December 8-10, pp. 715-723.

MOY S.S.J. and NIKOUKAR F. (2002) “Flexural behaviour of steel beams reinforced with carbon fibre reinforced polymer composite,” Proceedings of the First International Conference on Advanced Polymer Composites for Structural Applications in Construction, Southampton University, UK, April 15-17, pp. 195-202.

MOY S.S.J., HILL P., MORIARTY J., DIER A.F., KENCHINGTON A., and IVERSON B. (2001) “Strengthening of tunnel supports using carbon fibre composites,” Proceedings of the Institution of Mechanical Engineering, Part L, Journal of Materials: Design and Applications, V. 215, pp. 235-243.

NARAYANAN R. and ROBERTS T.M. (1991). “Structures subjected to repeated loading- stability and strength,” Elsevier Applied Science, London and New York, 281 pp.

NARAYANAN, R. and ADORISIO D. (1983). “Model Studies on Plate Girders,” Journal of Strain Analysis, Volume 18 , No. 2, London.

NARMASHIRI K., JUMAAT M.Z., and RAMLI SULONG N. H. (2010). “Shear Strengthening of Steel I-Beams by using CFRP Strips,” Scientific Research and Essays, Vol. 5, No.16, pp. 2155-2168.

NGUYEN T.C., YU B., AL-MHAIDI R., and ZHAO X.L. (2012). “Time dependent behaviour of steel/CFRP double strap joints subjected to combined thermal and mechanical loading,” Composite Structures, 94(5), pp. 1826-1833.

NISHINO F. and HASEGAWA A. (1977). “Consideration on Basler's Shear Strength Theory,” Stability of Steel Structure, Report No. 7816 (Preliminary Report), Liege, pp. 243-248.

NOZAKA K., SHIELD C.K., and HAJJAR J.F. (2005) “Effective bond length of carbon-fibre-reinforced polymer strips bonded to fatigued steel bridge I-girders,” Journal of Bridge Engineering, ASCE, Vol. 10, No. 2, pp. 195-205.

OKEIL A.M., BINGOL Y., and FERDOUS M.R. (2009). “A Novel Technique for Stiffening Steel Structures,” Final Report No. FHWA/LA.08/441, State Project No. 736-99-1447, Dept. of Civil and Environmental Eng., Louisiana State University, Baton Rouge, LA, USA, 78 pp.

OKURA I. and MAEDA Y. (1985). “Analysis of deformation-induced fatigue of thin-walled plate girders in shear,” Proc. Of JSCE Structural Eng./ Earthquake Eng., Vol. 2, No. 2, pp. 377s-384s.

OKUYAMA Y., MIYASHITA T., WAKABAYASHI D., KOIDE N., HIDEKUMA Y., KOBAYASHI A., HORIMOTO W., and NAGAI, M. (2012) “Shear Buckling Test for Steel Girder Bonded CFRP on its Web,” Proceedings of Conference of Inter. Institute for FRP in Construction (IIFC), Rome, Italy, 13-15 June, 8 pp.

OLARU V.D., NICOLAU M., DIMACHE A. and MODIGO M. (2004). “Ultimate shear of plated girders in shear,” the Annals of "Dunarea De Jos", University of Galati, Fascicle X Applied Mechanics, ISSN 1221-4612, Romania, pp. 59-64.

ONG C.L. and SHEN S.B. (1992) “The reinforcing effect of composite patch repairs on metallic aircraft structures,” International Journal of Adhesion and Adhesives, Vol. 12, No. 1, pp. 19-26.

OROWAN E. (1948). “Fracture and Strength of Solids,” Reports on Progress in Physics, Vol. XII, 185 pp.

OSTAPENKO, A. and CHERN, C. (1969). “Ultimate strength of plated girders under shear,” Fritz Engineering Laboratory Report No. 328.7, Lehigh University.

OSTAPENKO, A. and CHERN, C. (1971). “Ultimate strength of longitudinal stiffened plate girders under combined loads,”. IABSE Colloquium, pp. 301-313.

PARIS P.C., GOMEZ R.E., and ANDERSON W.E. (1961). “A Rational Analytic Theory of Fracture,” The Trends in Engineering, 13(1), pp. 9-14.

PARKER B.M. (1994) “Adhesive bonding of fibre-reinforced composites,” International Journal of Adhesion and Adhesives, Vol. 14, No.. 2, pp. 137-143.

PASTERNAK H., KUBIENIEC G., and PIEKARCZYK M. (2010). “Adhesives in strengthening of steel structures,” Engineering Structures and Technologies, Vol. 2, No. 2, pp. 45-50.

PATERSON P.J, CORRADO J.A., HUANG J.S., and YEN B.T. (1970). “Fatigue and static tests of two welded plate girders,” Welding research Council, Bull. No. 155.

PATNAIK A.K. and BAUER C.L. (2004). “Strengthening of Steel Beams with CFRP Laminates,” Proceedings of 4th Inter. Conference on Advanced Composite Materials in Bridges and Structures, Calgary, Alberta, Canada, July 20-23, 8 pp.

PEREL D. and LIBOVE C. (1978). “Elastic Buckling of Infinitely Long Trapezoidally Corrugated Plates in Shear,” Trans. ASME J. Appl. Mech., Vol. 45, pp. 579–582.

PHARES B.M., TERRY J.W., KLAIBER F.W., ABU-HAWASH A., and Lee Y.S. (2003) “Strengthening of steel girder bridges using FRP,” Proceedings of the 2003 Mid-Continent Transportation Research Symposium, Ames, Iowa.

PHOTIOU N.K., HOLLAWAY L.C., and CHRYSSANTHOPOULOS M.K. (2004) “An ultra-high modulus carbon/glass fibre composite system for structural upgrading of steel members,”

Proceedings of the 2nd International Conference on FRP Composites in Civil Engineering-CICE2004 , Seracino, R., ed., December 8-10, pp. 741-748.

PORTER D.M., ROCKEY K.C., and EVANS H.R. (1975). "The collapse behaviour of plate girders in shear," Journal of The Structural Engineer, Vol. 53, No. 8, pp. 313-325.

PRICE A. and MOULDS R.J. (1991) "Repair and strengthening of structures using plate bonding," Construction and Building Materials (UK), V. 5, No. 4, pp. 189-192.

RAJAGOPALAN G., IMMORDINO K.M., and Gillespie J.W. Jr. (1996) "Adhesive selection methodology for rehabilitation of steel bridges with composite materials." Proceedings of the 11th Technical Conference of the American Society for Composites, October 7-9, Atlanta, Georgia, pp. 222-230.

REAL E., ESTRADA I., and MIRAMBELL E. (2003) "Experimental and Numerical Investigation on Shear Response of Stainless Steel Plated Girders," the Steel Construction Institute, Polytechnique University of Catalonia, Spain, 2003.

REDDY J.N. (2004). "Mechanics of Laminated Composite Plates - Theory and Analysis," CRC Press, USA, 2nd Edition, 831 pp.

REEDY E.D. and Guess T.R. (1993). "Composite-to-metal tubular lap joints: strength and fatigue resistance," International Journal of Fracture, Vol. 63, No. 4, pp. 351-367.

ROBERTS T.M., DAVIES A.W., and BENNETT R.J.H. (1995). "Fatigue shear strength of slender web plates," Journal of Structural Engineering, pp. 1369-1401.

ROBERTS T.M., OSMAN M.H., ŠKALOUD M., and ZÖRNEROVÁ M. (1996). "Fatigue crack propagation and residual strength of slender web panels," International Colloquium on Stability of Steel Structures, Budapest, Vol.1, pp. 291-298.

ROCKEY K.C. and SKALOUD M. (1972). "The ultimate load behaviour of plate girders loaded in shear," The Structural Engineer, No. 1, Vol. 50, pp. 29-47.

RODE H.H. (1916). "BEITRAG ZUR THEORIE DER KNICKERS CHEINUNGEN," Wilhelm Engelmann Verlag, Leipzig, (Dissertation), and Eisenbau, Vol. 7, pp. 121, 157, 210, 239, 296.

SAKAI F., DOI K., NISHINO F. and OKUMURA T. (1966). "Failure Tests of Plate Girders using Large Sized Models," Tokyo: Dept. of Civ. Eng., University of Tokyo.

SAYED-AHMED E.Y. (2004). "Strengthening of Thin-Walled Steel I-Section Beams using CFRP Strips," Proceedings of 4th Inter. Conference on Advanced Composite Materials in Bridges and Structures, Calgary, Alberta, Canada, July 20-23, 8 pp.

SCHNERCH D.A. (2005) "Strengthening of steel structures with high modulus carbon fibre reinforced polymer (CFRP) materials," PhD Thesis, North Carolina State University, 265 pp.

SHAAT A., SCHNERCH D., FAM A., and RIZKALLA S. (2004). "Retrofit of steel structures using Fibre-Reinforced Polymers (FRP): State-of-the-art," Transportation Research Board (TRB) Annual Meeting, Washington, USA, 18 pp.

SHIELD C., HAJJAR J., and NOZAKA K. (2004). "Repair of fatigued steel bridge girders with carbon fiber strips," Technical Report No. MN/RC 2004-02, Department of Civil Engineering, University of Minnesota.

ŠKALOUD M. and ZÖRNEROVÁ M. (2010). "The fatigue and serviceability limit states of the webs of steel girders subjected to repeated loading," SDSS'Rio 2010 Stability and Ductility of Steel Structures, Rio de Janeiro, Brazil.

SMITH M.A. and Hardy R. (1977) “Fatigue research on bonded carbon fibre composite/metal joints,” Composites, Vol. 8, No. 4, pp. 25-261.

SYKES J.M. (1982) “Surface treatments for steel,” Surface analysis and pretreatment of plastics and Metals, D.M. Brewis, Ed., Applied Science Publishers, Ltd., Essex, England, pp. 153-174.

TAKEDA H. (2004). “A fundamental study on simplified analysis of buckling, load-carrying capacity and deformability of girders,” PhD thesis, Kyoto University, 197 pp.

TAVAKKOLIZADEH M. and SAADATMANESH H. (2001). “Repair of cracked steel girder using CFRP sheet,” Creative System in Structural and Construction Engineering, Proceedings of the 1st International Structural Engineering and Construction Conference, Amarjit Singh, ed., Honolulu, Hawaii, pp. 461-466.

TIMOSHENKO S. and GERE J.M. (1989). “Theory of elastic stability,” Second renewed edition, Dover Publications Inc., Mineola, New York, originally published: New York, McGraw-Hill Book, 1961, 541 pp.

TOSNGAS A.G., and RATAY R.T. (1969). “Investigation of diagonal-tension beams with very thin stiffened webs,” Structural Mechanics Section, Grumman Aerospace Corporation, Bethpage, New York 11714, Prepared for The National Aeronautics and Space Administration (NASA), Manned Spacecraft Center, 98 pp.

WAGNER H. (1931). “Flat sheet metal girder with very thin metal web- Sheet metal girders with spars resistant to bending- The stress in uprights- Diagonal tension fields,” Technical Memorandum No. 606, Part III, National Advisory Committee for Aeronautics (NACA), Hampton, 48 pp.

WAKABAYASHI D., MIYASHITA T., OKUYAMA Y., KOIDE N., KOBAYASHI A., HIDEKUMA Y., HORIMOTO W., and NAGAI M. (2012) “Study on Repair Method using CFRP for Corroded Steel Girder Ends”, 28th US-Japan Bridge Eng. Workshop, Portland, Oregon, USA, Oct. 8-10, 12 pp.

WILSON J.M. (1886). “On Specifications for Strength of Iron Bridges,” Transactions of the American Society of Civil Engineers, Vol. XV, p. 405-414.

WRIGHT P.N.H., WU Y., and GIBSON A.G. (2000) “Fibre reinforced composite-steel connections for transverse ship bulkheads,” Plastics, Rubber and Composites, Vol. 29, No. 10, pp. 549-557.

WU C., ZHAO XL., CHIU WK., and AL-MHAIDI R. (2013). “Effect of the fatigue loading on the bond behaviour between UHM CFRP plates and steel plates,” Composites Part B: Engineering, 50(2013), pp. 34-353.

WU G., LUO Z., SUN Z., and HU X. (2010). “Mechanical properties of steel-FRP composite bar under Uniaxial and cyclic tensile loads, Journal of materials in civil engineering,” ASCE, 22(10), 1056-1066.

YEN B.T. and COPPER P.B. (1962). “Fatigue tests of welded plate girders,” Fritz Engineering Laboratory Report No. 251-26, Lehigh University, pp. 31.

YEN B.T. and MULLER J.M. (1965). “Fatigue tests of welded plate girders in shear,” Fritz Engineering Laboratory Report No. 303.6, Lehigh University, pp. 38.

YOO C.H. and LEE S.C. (2006) “Mechanics of Web Panel Post-buckling Behaviour in Shear,” ASCE, Journal of Structural Eng., Vol. 132, No. 10, pp. 1580-1589.

ZHAO X.L. (2014). “FRP-Strengthened metallic structures,” CRC Press, 263 pp.

ZHAO X.L. and ZHANG L. (2007). “State-of-the-Art Review on FRP Strengthened Steel Structures,” Journal. of Eng. Structures, Elsevier, U.K., No. 29 pp. 1808–1823.

ZIEMIAN R.D. (2010). “Guide to stability design criteria for metal structures,” 6th edition, Wiley, New York, 1024 pp.

Chapter Three

A Finite Element Study of the Boundary Conditions and Initial Imperfection Effect on the Behaviour of Steel Plate Girders

3.1 INTRODUCTION

The two essential functions of the web plate in a plate girder are to maintain a relative distance between the top and bottom flanges and to resist shear stresses. In most practical ranges of plate girder bridge spans, the shear stresses are relatively low compared to bending stresses in the flanges induced by flexure. As a result, the web plate is typically much thinner than the flanges. The web panel is therefore prone to buckling at comparatively low shear forces. To enhance the web's buckling strength, it is often reinforced with transverse stiffeners. The web design then involves a selection of plate thickness and stiffener spacing to provide optimum economy in terms of the material and fabrication costs.

In the design of plate girder web panels, according to AISC (1963 and 1994), AASHTO (1973 and 2007), and EN 1993-1-5 (2004) specifications, the post-buckling strength is added to the elastic buckling strength. To calculate the elastic buckling strength, the boundary conditions of the web panel that is stiffened by transverse intermediate stiffeners must be determined.

In current practice, the elastic shear buckling stress of a web panel with transverse stiffeners is estimated using the conservative assumption that the web panel has simply supported boundary conditions at the junctions with the flange and the stiffener. The study presented in this chapter explores this assumption using a more realistic approach, both numerically, through approximately 5000 numerical analysis runs, and experimentally.

This chapter starts with a brief background of the design aspects that led to this study then moves to demonstrate the available methods to determine the shear buckling coefficients of steel plate girders. Further ahead, the analytical model, finite element model, convergence study, and parametric study of the shear buckling coefficients and their relation to the boundary conditions are presented with a proposed general equation based on nonlinear multivariate regression analysis. Then,

the initial imperfection effect is considered in three different modes and a simple equation taking its effect on the critical buckling shear stress is presented. Finally, a new approach based on analytical and finite element analysis is presented to determine the shear buckling coefficients of diagonally stiffened steel plate girders.

This chapter serves as a benchmark (determining the buckling shear stresses for bare steel plate girders) for the more complicated case of the orthotropic composite section resulting from strengthening the steel plate girders with FRP sections as will be seen in Chapters 5, 6 and 7.

3.1.1 Background

Despite early work on web shear post-buckling behaviour (Wilson, 1886), and diagonal tension field theory developed later by Wagner (1931), elastic buckling was used as the basis for design of plate girder webs until the 1960s. This was largely because formulas to predict the elastic bifurcation buckling strength of a web plate are relatively simple, and have been known for many years, whereas a comprehensive and simple procedure for ultimate strength design was not available.

In the late 1950s, extensive studies were undertaken on the post-buckling behaviour of web panels by Basler and Thurlimann (1959). As a result of these and subsequent studies (Basler, 1961a, 1961b and 1963), AISC added the post-buckling strength into its specifications in 1963, and AASHTO followed suit in 1973. Thereafter, with the move towards limit state design concepts in steel structures, the studies initiated by Basler and Thurlimann were followed by several modified failure theories to achieve a better correlation between theory and tests (Lee et al., 1996).

To calculate the elastic buckling strength, the boundary conditions of the web panel that is stiffened by transverse intermediate stiffeners must be determined. It is generally assumed that transverse stiffeners are sufficiently stiff to form nodal lines of the sinusoidal buckling waves on the web. This assumption is well justified, since the transverse stiffeners are designed to meet this condition. On the other hand, the web panel is elastically restrained at the junction between the web and flanges. The degree of the elastic restraint depends on many geometric parameters, such as a_w/h_w , h_w/t_w , b_f/h_w , t_f/t_w , and t_s/t_w , where a_w is the transverse stiffener spacing, h_w is the girder depth, b_f is the flange width, t_f is the flange thickness, t_s is the stiffener

thickness, and t_w is the web thickness (see Figure 1.2a in Chapter 1 for more details). Although the notion of the real boundary condition at the juncture of the web and flanges to be somewhere between simple and fixed has been recognized for some time, it has always been idealised, mainly due to lack of means to evaluate it in a rational manner. For example, Basler (Basler, 1963) and Porter et al. (Porter et al., 1975) assumed that the web panel was simply supported at the junction, while Chern and Ostapenko (Chern and Ostapenko, 1969) obtained the ultimate strength by assuming that the junction was a fixed support.

Another controversial aspect of this problem is that the Cardiff method (Porter et al., 1975) places a much greater demand on stiffener strength than does Hoglund's rotated stress field theory (Hoglund, 1973). The Cardiff method requires the stiffeners to play the role of compression members in a truss, with the web plate acting as a tension diagonal. Hoglund's theory requires the stiffeners only to carry the small part of the tension field anchored by the flanges at collapse; no force is induced in the stiffeners in mobilising the post-critical resistance of the web. In the absence of a stiff flange to contribute to the shear resistance, the stiffeners only elevate the elastic critical shear stress of the web. Adequate stiffness is simply required to ensure that the theoretical elastic critical shear resistance of the panel is achieved, or at least very nearly achieved since no stiffener can be completely rigid.
Earlier drafts of EN 1993-1-5 required web stiffeners to be designed for a force loosely (but not exactly) based on Hoglund's theory, together with a check for adequate stiffness. These early drafts raised concern in the UK because the rules indicated that much smaller forces are induced in the stiffeners than would be derived from the tension field theory approach traditionally used in BS 5400: Part 3. As a result, late in its drafting EN 1993-1-5 was modified to include a stiffener force criterion more closely aligned to that in BS 5400: Part 3. The rules for stiffener design in EN 1993-1-5 are thus no longer consistent with the rotated stress field theory and indicate that a significantly greater axial force acts in the stiffener, with a consequent loss of economy. However, the rules for design of the web panel remain based on Hoglund's rotated stress field theory, creating an inconsistency (Hendy and Presta, 2008).

This inconsistency leads back to the subject of the current chapter in this study: what boundary conditions are realistic for both the stiffener and flange junctions with the web, because underestimating them will lead to uneconomic and conservative design while on the other hand overestimating the boundary conditions could reduce safety, especially when fatigue is taken into considerations, as this could lead to even more breathing of the web, as discussed previously in Chapter 2. Therefore, an extensive parametric study of approximately 5000 specimens were tested numerically using finite element analysis, to find the effect of flange and stiffener rigidities in addition to the effect of initial imperfection on the critical buckling shear stress of plate girders.

3.2 ELASTIC BUCKLING STRENGTH IN PURE SHEAR STRESS

The elastic buckling strength in Basler's approach as well as in the Cardiff method is calculated considering the web panel simply supported on all sides. According to Timoshenko (1961):

$$\tau_{cr} = \frac{k_s \pi^2 E}{12(1-\nu^2)} \left(\frac{t_w}{h_w}\right)^2 \qquad (3.1)$$

where

τ_{cr} : elastic buckling shear stress of web panel

t_w : web plate thickness

h_w : web plate height

E : Young's modulus

ν : Poisson's ratio

k_s : shear buckling coefficient

$$k_s = 5.34 + \frac{4.0}{(a_w/h_w)^2} \qquad a_w/h_w \geq 1 \qquad (3.2.a)$$

$$k_s = 4.0 + \frac{5.34}{(a_w/h_w)^2} \qquad a_w/h_w < 1 \qquad (3.2.b)$$

where

a_w : is the space between vertical stiffeners.

Fujii (1971), on the other hand, recommends fixed condition for the web sides along the flanges. The shear buckling coefficient for this condition is given in graphical form by Fujii and as regression formula derived by Bulson (1970).

$$k_{sf} = 8.98 + \frac{5.61}{(a_w/h_w)^2} - \frac{1.99}{(a_w/h_w)^3} \qquad a_w/h_w \geq 1 \qquad (3.3.a)$$

$$k_{sf} = \frac{5.34}{(a_w/h_w)^2} - \frac{2.31}{(a_w/h_w)} + 8.39(a_w/h_w) - 3.44 \qquad a_w/h_w < 1 \qquad (3.3.b)$$

Based on over 300 numerical results, Lee et al. (1996) proposed the following two simple equations:

$$k = k_s + \frac{4}{5}\left(k_{sf} - k_s\right)\left[1 - \frac{2}{3}\left(2 - \frac{t_f}{t_w}\right)\right] \qquad \frac{1}{2} < \frac{t_f}{t_w} < 2 \qquad (3.4.a)$$

$$k = k_s + \frac{4}{5}\left(k_{sf} - k_s\right) \qquad \frac{t_f}{t_w} > 2 \qquad (3.4.b)$$

where k_s is the simply supported buckling coefficient and k_{sf} is given in Equation (3.3).

Equation (3.3) will be adopted in this study to determine the shear buckling coefficients for hybrid boundary conditions of the web plate where it is considered simply supported at its junction with the stiffener and clamped at the junction with the flange; while Equation (3.4) will be used for the sake of comparison with the proposed equation later in section (3.4)

3.3 FINITE ELEMENT ANALYSIS

3.3.1 Analytical Model

Figure (3.1a) shows the plate girder model adopted in this study. A two panel's plate girder is modelled to take the stiffener effect on the buckling shear stress into account, in addition to the usual flange effect. The stiffener effect is usually neglected in calculations and simply supported boundary conditions in the junction between the web plate and the stiffener are assumed. In this study, a single one sided whole height stiffener was used with three different projected widths (b_s) of 70, 110, and 150mm. This was done to take the effect of rigidity of the stiffener and its second moment of area on the geometrical boundary conditions at the junction with the web plate. The figure also shows the load pattern which was necessary to

simulate the case of pure shear so it can be compared with the theory. The width of the flange (b_f) was chosen to be 340mm which satisfies most of the available standards for plate girder design, but with minimum requirements, this is to ensure that worst case scenario is taken into account in this study, and hence it is safely applicable for other range of flange widths. It is worth mentioning that all other model dimensions were taken similar to a previous study by Lee et al. (2002) for the sake of comparison. In their study, they were trying to find out the effect of stiffener on the postbuckling strength of plate girders, while in this study it is used to find the effect of stiffener on the critical buckling shear stress but with much wider range of variables. The yield strength (f_y), Poisson's ratio (v), and the modulus of elasticity (E) were taken as 355MPa, 0.3, and 200 GPa, respectively, and were kept constant in this study.

3.3.2 Finite Element Model

The finite element model used in this study is shown in Figure (3.1b). The height of the model (h_w) was kept constant at 2000mm while the span was variable to account for different aspect ratios (a_w/h_w). Based on an extensive convergence study (section 3.3.3), the model was built using S9R5 element type, which is not available in Abaqus standard CAE[1] and can be used only through Abaqus input files. Matlab code was written to create the parts' nodes and element incidences and then the input file was created. S9R5 is a shell element which deals mostly with slender plates and was derived originally according to Kirchhoff thin plate bending theory. The size of the web elements was chosen to be $h_w/20$ based on the abovementioned convergence study, while the size of the flange and stiffener elements were taken equal to 100×20mm and 50×20mm, respectively and it was validated through another minor convergence study. The web, flange, and stiffener mesh can be seen in Figure (3.1b) and the applied boundary conditions are illustrated in Table 3.1.

[1] A general purpose finite element analyzer that employs implicit (i.e. traditional) scheme. CAE refers to Complete Abaqus Environment.

Table 3.1: Boundary conditions used for the model

		u	v	w	θ_x	θ_y	θ_z
Flange	**Left**	Fix	Fix	Fix	Fix	Fix	Free
	right	Free	Free	Fix	Fix	Fix	Free
Web	**Left**	Fix	Fix	Fix	Fix	Free	Fix
	right	Free	Free	Fix	Fix	Free	Fix

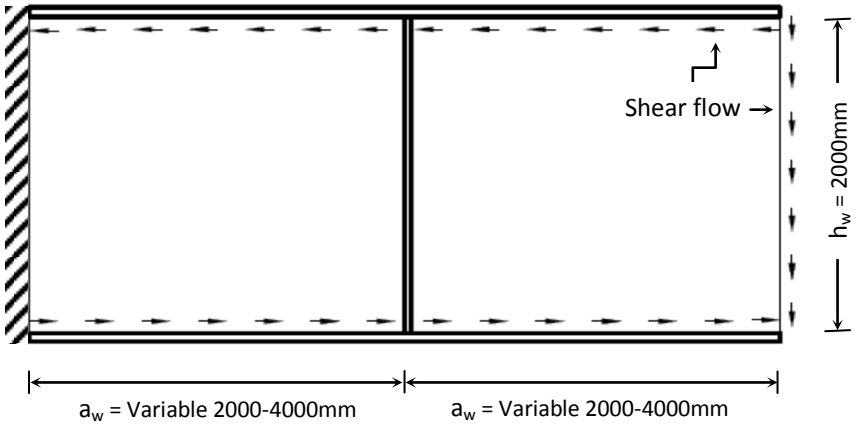

(**a**) Plate girder analytical model

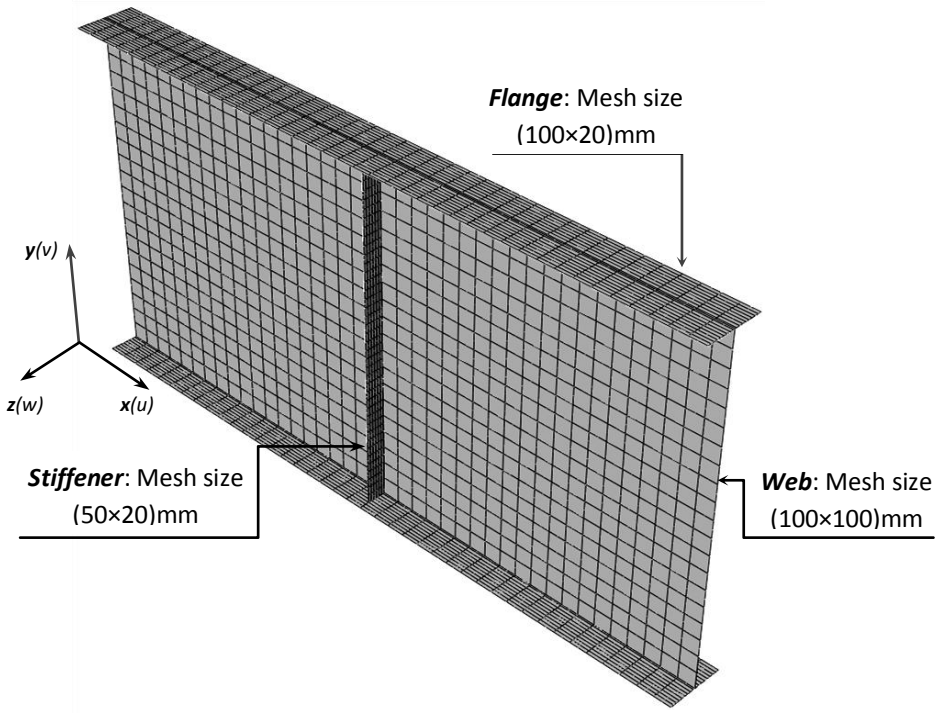

(**b**) Finite element mesh, loading scheme is shown in (a) and boundary conditions are detailed in Table 3.1

Figure (3.1): Analytical and finite element model adopted in the parametric study.

3.3.3 Convergence Study

The model adopted in the convergence study was chosen to be a typical web plate with practical dimensions of 2000×2000mm. The plate aspect ratio was taken as a_w/h_w=1.0 and kept constant throughout the convergence study. The variables were the type of the element (S4R, S8R, and S9R5) and the slenderness ratio (h_w/t_w) which were taken as 1000, 500, 250, 200, 166.667, 142.857 and 125 corresponding to a plate thicknesses of 2, 4, 8, 10, 12, 14, and 16, respectively. Both simply supported and clamped boundary conditions were investigated and shear stress was applied to the plate boundaries as shown in Figure (3.1a).

Figure (3.2) shows the convergence of the critical buckling shear stress versus the inverse of the degrees of freedom (dof) for specimens with clamped and simply supported boundary conditions. The dof was calculated each time according to the number of element used and the corresponding degrees of freedom of each node in the element according to the compatibility requirement. Using the inverse of dof gives the opportunity to predict the element size that will result in exactly the same theoretical value or as close as possible. The theoretical values in the figure are calculated using Equation (3.1) with a buckling coefficient (k_s) typically equal to 9.34 for plates with simply supported boundary conditions and an aspect ratio (a_w/h_w=1.0), however, for the same plate but with clamped boundary conditions the value of k_s is taken equal to 14.71 according to Budiansky and Connor (1948). S9R5 showed superior behaviour with much less number of elements and the size of $h_w/20$ (100mm) was chosen. This size helped in reducing the time required for the huge number of simulation runs without compromising convergence. It is worth mentioning that this mesh size corresponds to an inverse dof of 0.00038, 0.00013, and 0.00012, for elements S4R, S8R, and S9R5, respectively. These mesh sizes are a compromise between those required for the clamped and simply supported boundary conditions, for all the range of slenderness ratios, as can be seen from Figure (3.2). However, for the web plate, S9R5 element type was chosen for its superior behaviour with a square element size of ($h_w/20$ =100mm).

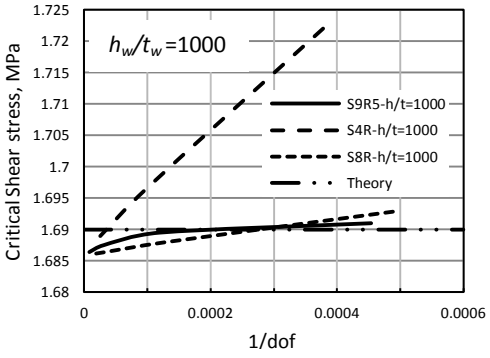

(a) Simply supported BCs.

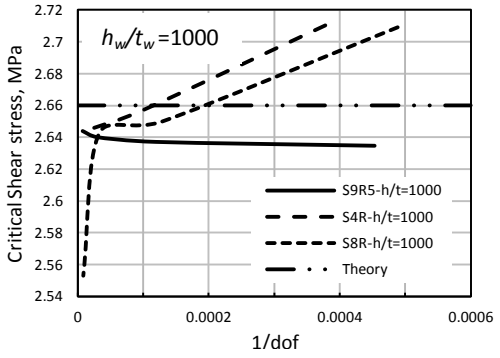

(b) Clamped BCs.

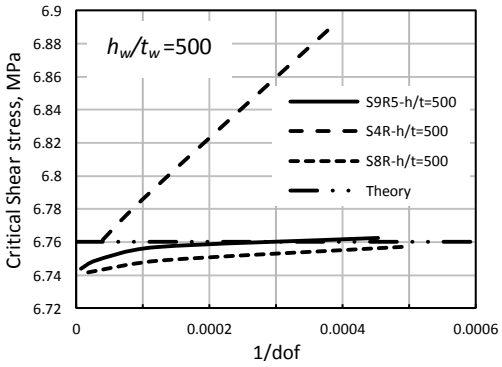

(c) Simply supported BCs.

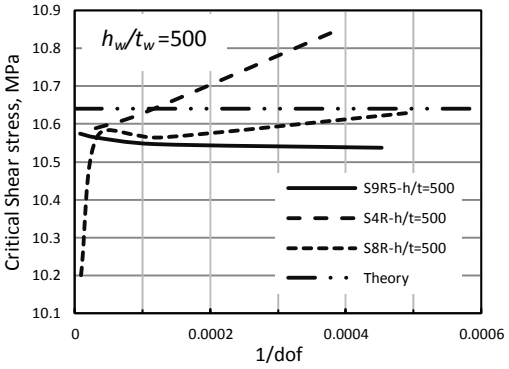

(d) Clamped BCs.

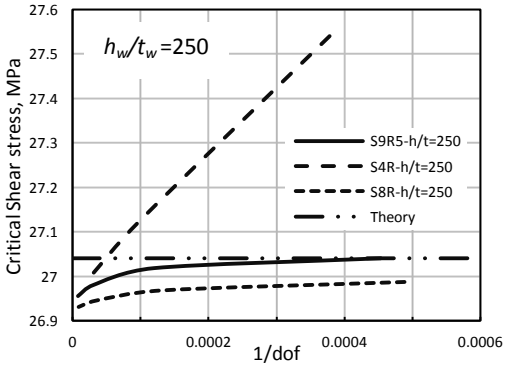

(e) Simply supported BCs.

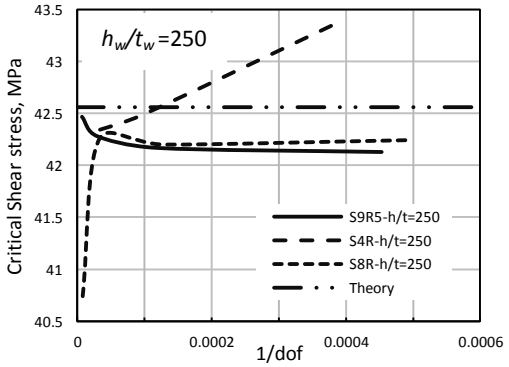

(f) Clamped BCs.

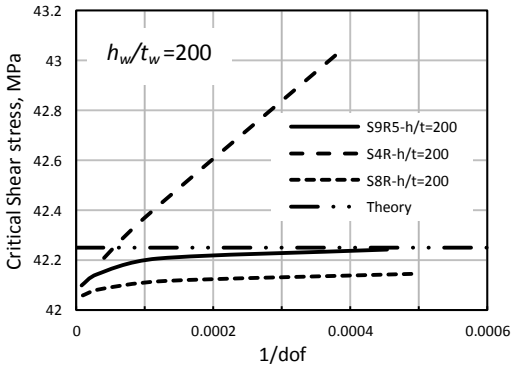

(g) Simply supported BCs.

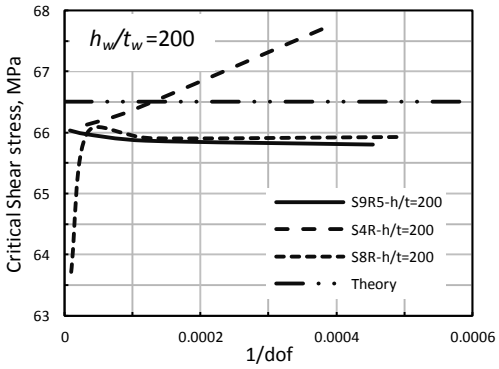

(h) Clamped BCs.

Figure (3.2): Critical buckling shear stress versus the inverse of the degrees of freedom for different slenderness (h_w/t_w) ratios (the *y*-axis scale differs from one graph to another for illustration purposes).

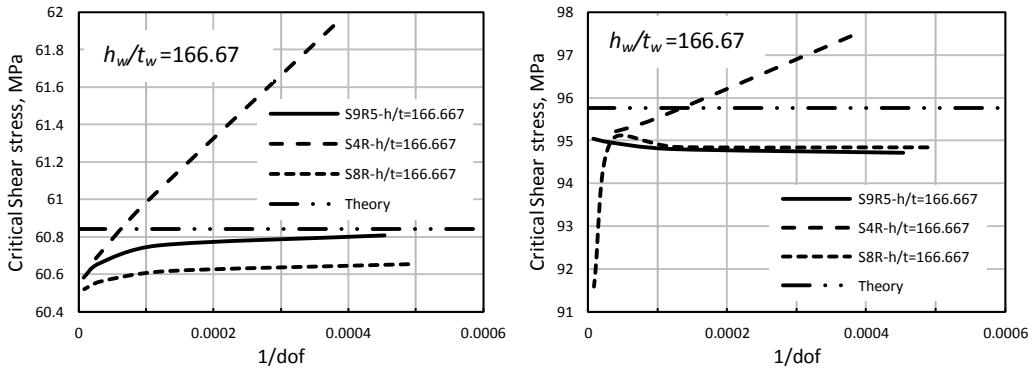

(i) Simply supported BCs.

(j) Clamped BCs.

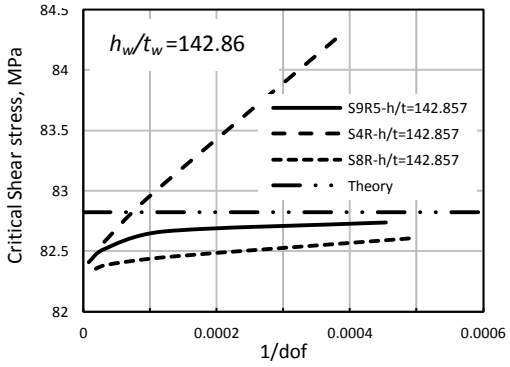

(k) Simply supported BCs.

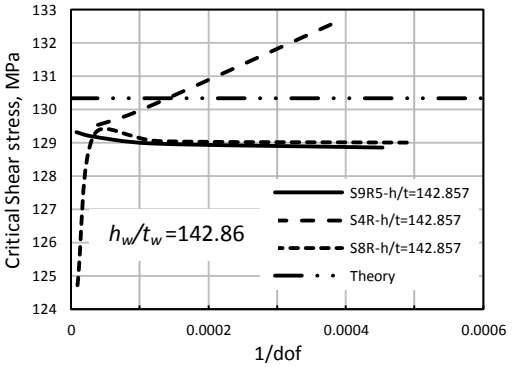

(l) Clamped BCs.

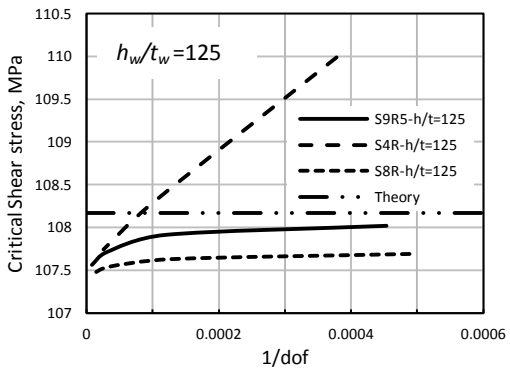

(m) Simply supported BCs.

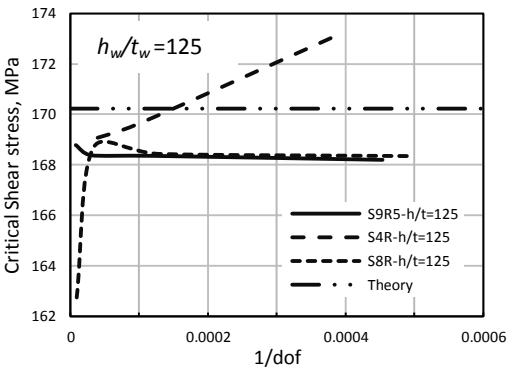

(n) Clamped BCs.

Figure (3.2 Cont.): Critical buckling shear stress versus the inverse of the degrees of freedom for different slenderness (h_w/t_w) ratios (the *y*-axis scale differs from one graph to another for illustration purposes).

3.3.4 Parametric Study

An extensive parametric study with approximately 5000 numerical analyses has been performed. The key variables were the aspect ratio (a_w/h_w), the slenderness ratio (h_w/t_w), the stiffener projected width (b_s), the flange thickness (t_f), the stiffener thickness (t_s), and the effect of initial imperfection (II). The range of variables is chosen within the practical limits as follows:

a_w/h_w = 1.0 to 2.0 with a_w = 2000 to 4000 mm,

h_w/t_w = 125 to 250 with t_w = 8 to 16 mm,

b_s = 70 to 150 mm,

t_f = 2 to 50 mm,

t_s = 2 to 50 mm,

II = $h_w/125000$ to $h_w/100$; with a_w/h_w = 1.0.

Dimensionless parameters are used to characterise the flange rigidity (R_F , as proposed by Rockey and Skaloud, 1972) and the stiffener rigidity (R_S):

$$R_F = \frac{I_F}{a_w^3\, t_w} \tag{3.5.a}$$

$$R_s = \frac{I_S}{h_w^3\, t_w} \tag{3.5.b}$$

where:

R_F: is the flange rigidity index.

R_S: is the stiffener rigidity index.

I_F: is the flange second moment of area of an axis passing through the centroid of the flange and normal to the web plate.

I_S: is the second moment of area of the projection of the T-section formed from combining the stiffener and the web plate.

Figures (3.3a) to (3.3c) show the relation between critical buckling shear stresses coefficients and the flange rigidity index. There is a dominant pattern where the effect of the flange starts increasing sharply at lower flange thicknesses (where $R_F \longrightarrow 0$), and then reaches a plateau where increasing the flange thickness (R_F) does not increase the buckling coefficients any more. This behaviour is more apparent with higher slenderness ratio. However, the same behaviour does not apply for the stiffener effect where increasing its second moment of area (reflected in R_S) has an average linear pattern as can be seen from Figures (3.4a) to (3.4c), however, it is still possible to detect a typical three discontinuities in each curve. These hunches represent the three stiffener projection widths (70, 110, and 150mm) adopted in this parametric study, from which it can be noted that increasing the stiffener thickness is less effective, in increasing the shear buckling coefficients values, for stiffeners with higher projected width (b_s). Nevertheless, this increase in the buckling coefficient

due to stiffener rigidity is reduced with increasing the aspect ratio of the specimens to be insignificant and almost flat with an aspect ratio of 2, see Figure (3.4c).

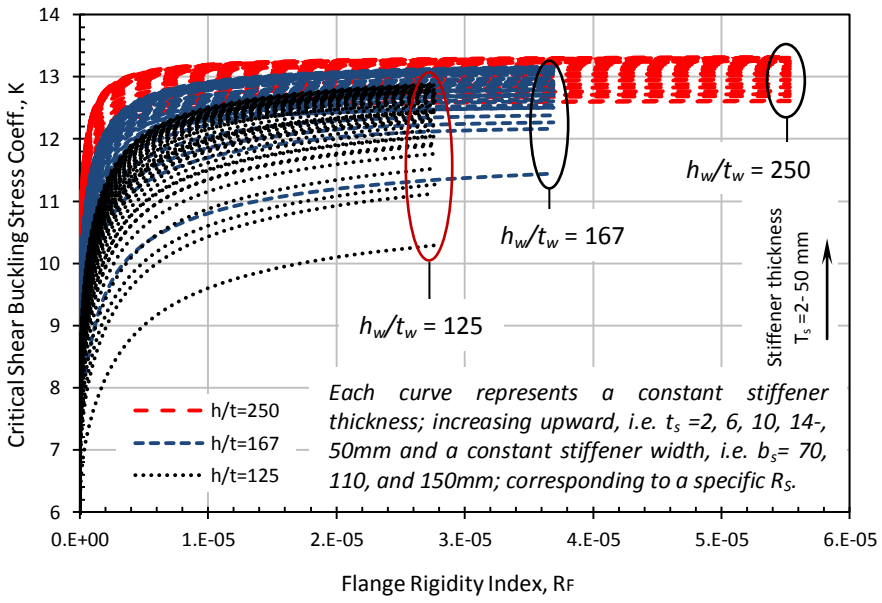

(**a**) a_w/h_w = 1.0

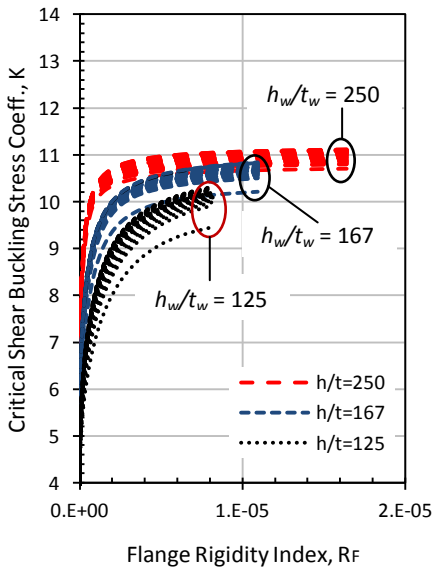

(**b**) a_w/h_w = 1.5

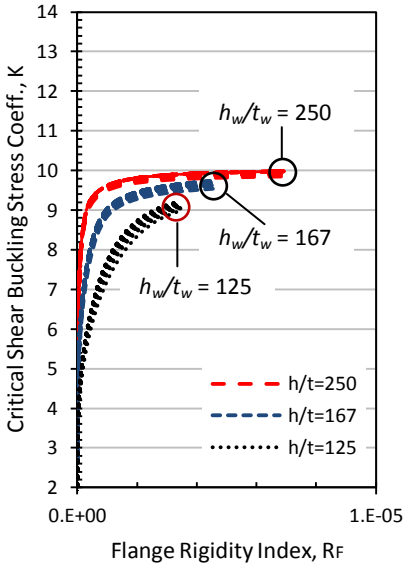

(**c**) a_w/h_w = 2.0

Figure (3.3): Shear buckling coefficient versus flange rigidity index.

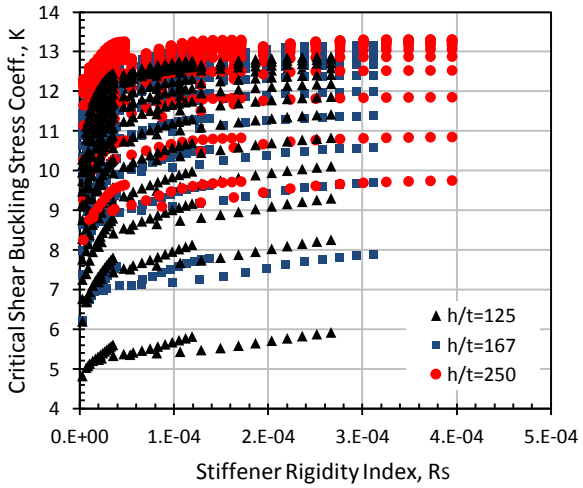

(**a**) a_w/h_w = 1.0

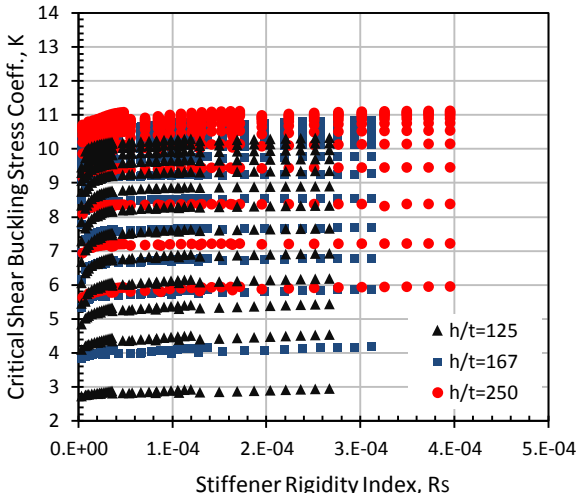

(**b**) a_w/h_w = 1.5

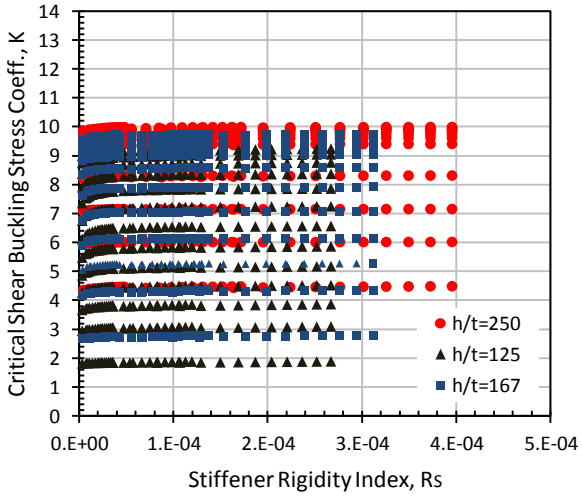

(**c**) a_w/h_w = 2.0

Figure (3.4): Critical buckling shear stress coefficient versus stiffener rigidity index; each curve represents a constant flange thickness; increasing upward, i.e. t_f =2, 6, 10, 14-, 50mm; corresponding to a specific R_F.

Figures (3.5a) to (3.5c) demonstrate the buckling modes for three models with heavy (t_f =50mm), medium (t_f =26mm), and light (t_f =2mm) flanges corresponding to a flange rigidity index (R_F) of 1.1×10^{-5}, 1.5×10^{-6}, and 7.0×10^{-10}, respectively. All the models have the same aspect ratio (a_w/h_w =1.5), slenderness ratio (h_w/t_w =167), and stiffener sectional dimensions of (110×26mm), these are the middle range of variables adopted in this study. It is obvious that the behaviour gets stiffer with increasing flange thickness. On the other hand Figures (3.5d) to (3.5f) show the buckling modes for three models with heavy (t_s =50mm), medium (t_s =26mm), and light (t_s =2mm) stiffeners corresponding to a stiffener rigidity index (R_S) of 1.4×10^{-4}, 8.7×10^{-5}, and 1.1×10^{-5}, respectively. The models have the same abovementioned parameters, except that the flange is kept constant with a thickness of (t_f =26mm). Again it can be seen that the behaviour is getting stiffer with increasing the stiffener thickness and hence the assumption that the boundary condition in the junction between the stiffener and the web plate is merely simply supported is not valid all the time and more investigation is needed.

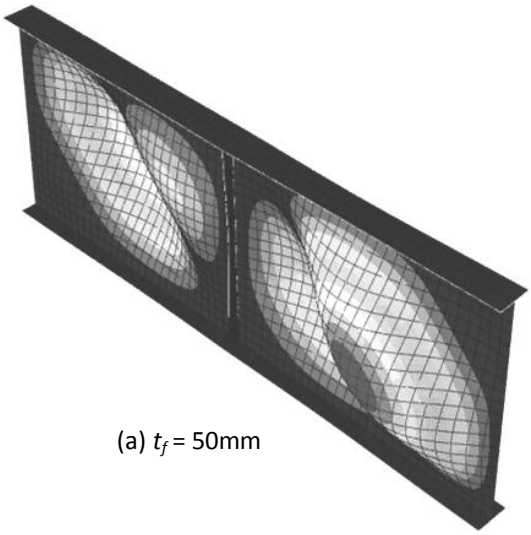

(a) t_f = 50mm

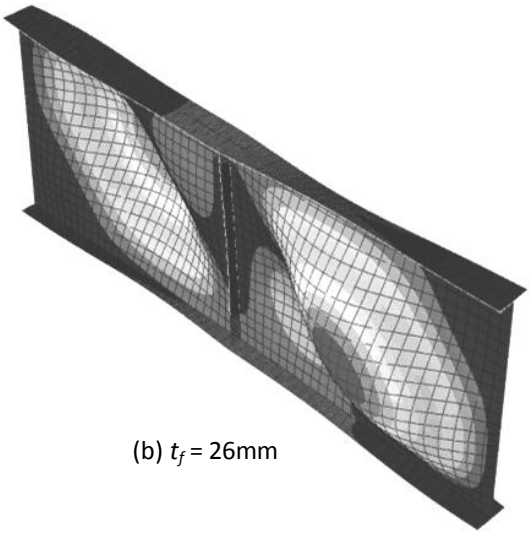

(b) t_f = 26mm

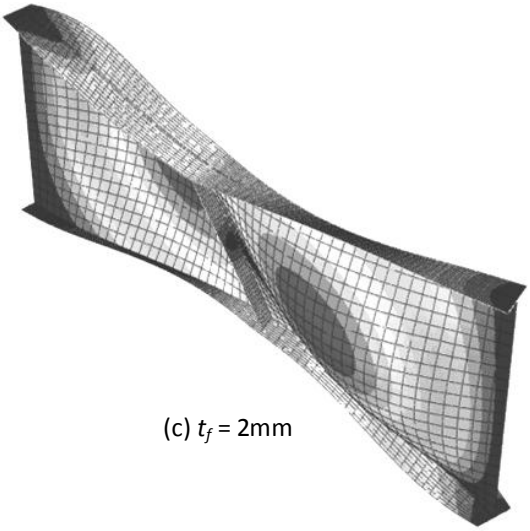

(c) t_f = 2mm

Figure (3.5): Buckling modes of the plate girder model for different parameters.

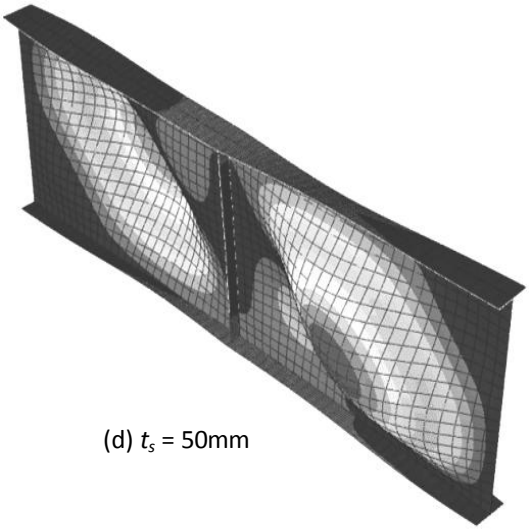

(d) t_s = 50mm

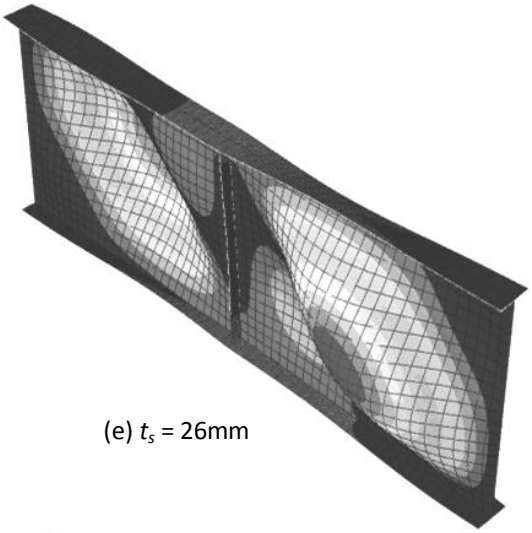

(e) t_s = 26mm

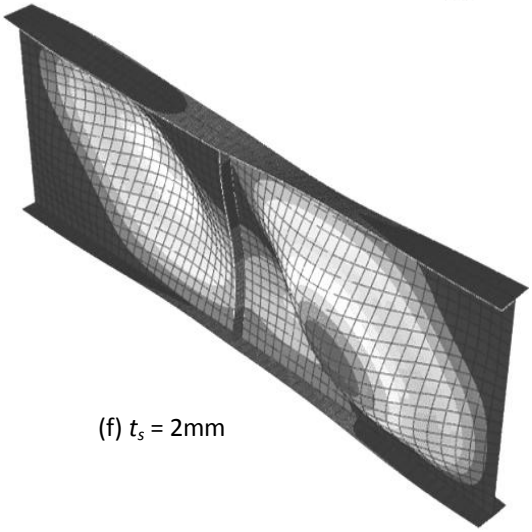

(f) t_s = 2mm

Figure (3.5 Cont.): Buckling modes of the plate girder model for different parameters.

3.4 ANALYSIS OF RESULTS AND DESIGN APPROACH

Figures (3.6a) to (3.6c) show how the calculated critical buckling shear stress coefficient varies with the non-dimensional parameter (t_f/t_w) for aspect ratios (a_w/h_w) of 1.0, 1.5, and 2.0, respectively. Only data with practical design ranges of t_f/t_w and $t_s/t_w \geq 1.0$ were considered in the analysis. From Figure (3.6a), it can be seen that, for specimens with ($a_w/h_w = 1.0$), the curves are rather scattered, leading to the conclusion that the stiffener effect is significant in determining the shear buckling coefficients. However, by observing both Figures (3.6b) and (3.6c) for specimens with aspect ratios of 1.5 and 2.0, respectively, it can be noted that the curves are starting to gather and consolidate in groups depending on their slenderness ratios (h_w/t_w). This behaviour is more apparent in Figure (3.6c) for specimens with an aspect ratio of 2.0. Consequently, it can be assumed that the effect of stiffener rigidity on the value of shear bucking coefficients is significant for specimens with an aspect ratio (a_w/h_w=1.0), moderate with specimens having an aspect ratio (a_w/h_w=1.5), and insignificant for longer specimens having an aspect ratio (a_w/h_w=2.0). This new conclusion in this work will lead to a more economic design because it will lead to higher critical buckling shear stress estimations, especially for plate girders with low aspect ratios.

In this work, the previous conclusion made by Lee et al. (1996) is verified. The buckling coefficients are rather higher than the simply supported boundary condition case and the effect of flange rigidity in the junction between the flange and the web panel should be taken into consideration. However, according to the current parametric study, the work by Lee et al. (1996) overestimates the shear buckling coefficients for specimens with small values of ($t_f/t_w \leq 3.0$), especially the ones having small flange width.

Applying Lee et al. equation (Equation 3.4) as illustrated in Figures (3.6a) to (3.6c) shows that some of the data points in this study are out of its bounds and it is not safe to use the equation for all the data ranges. However, Al-Azzawi et al. (2015) modified Equation (3.4), by shifting it, to be more conservative and to achieve better correlation with their data as follows:

$$k = k_s + \frac{4}{5}\left(k_{sf} - k_s\right) \times \left[1 - \frac{1}{1.5}\left(3 - \frac{t_f}{t_w}\right)\right] \qquad 1.5 < \frac{t_f}{t_w} < 3 \qquad (3.6.a)$$

$$k = k_s + \frac{4}{5}\left(k_{sf} - k_s\right) \qquad \frac{t_f}{t_w} > 3 \qquad (3.6.b)$$

where k_s and k_{sf} are the same as in Equations (3.2) and (3.3).

A more sophisticated, conservative and continuous equation covering the whole range of data with better correlations (see section 3.6) as shown in Figure (3.6) can be stated as follows:

$$k = k_s + \frac{0.9\left(k_{sf} - k_s\right)}{1 + e^{-\alpha\left(\frac{t_f}{t_w} - \beta\right)}} \qquad (3.7.a)$$

where:

$\alpha = 2.5$ and $\beta = \frac{a_w}{h_w} + 0.5$

In addition, the following constraints should be taken into consideration:

- The effect of stiffener rigidity on the critical buckling shear stress coefficient for specimens with an aspect ratio $a_w/h_w \leq 1.0$ may be taken as follows:

$$k_{Stiffener\ Effect} = k + 0.5\ ln\left(\frac{t_s}{t_w}\right) \qquad (3.7.b)$$

- k must be reduced for specimens with slenderness ratio $h_w/t_w \leq 125$ and $t_f/t_w \leq 1.5$ by the following factor:

$$k_{Slenderness\ Effect} = k - \left(\frac{a_w}{h_w} - 1\right) \qquad (3.7.c)$$

To the best of the author's knowledge, this reduction factor due to the slenderness ratio effect of the web plate is not mentioned elsewhere. This could lead to unconservative design in cases where shear buckling is significant.

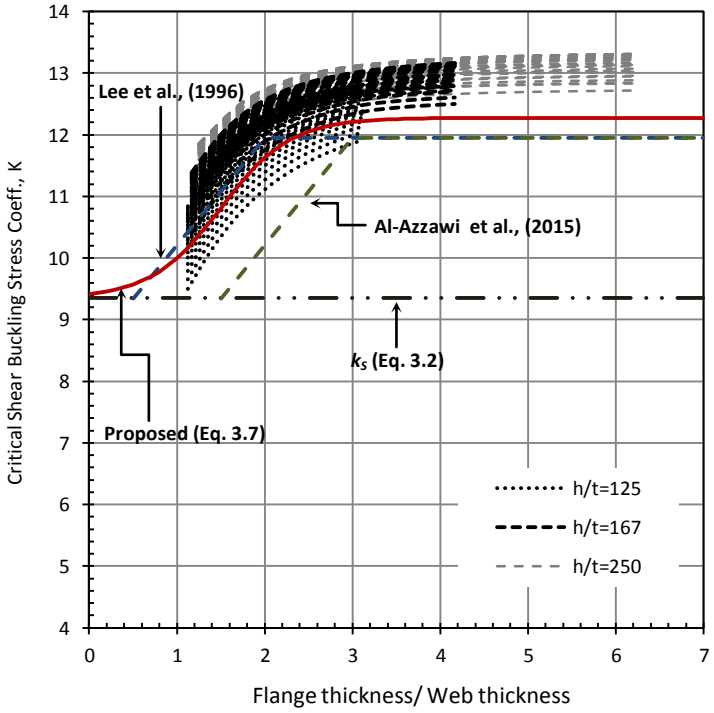

(**a**) a_w/h_w = 1.0

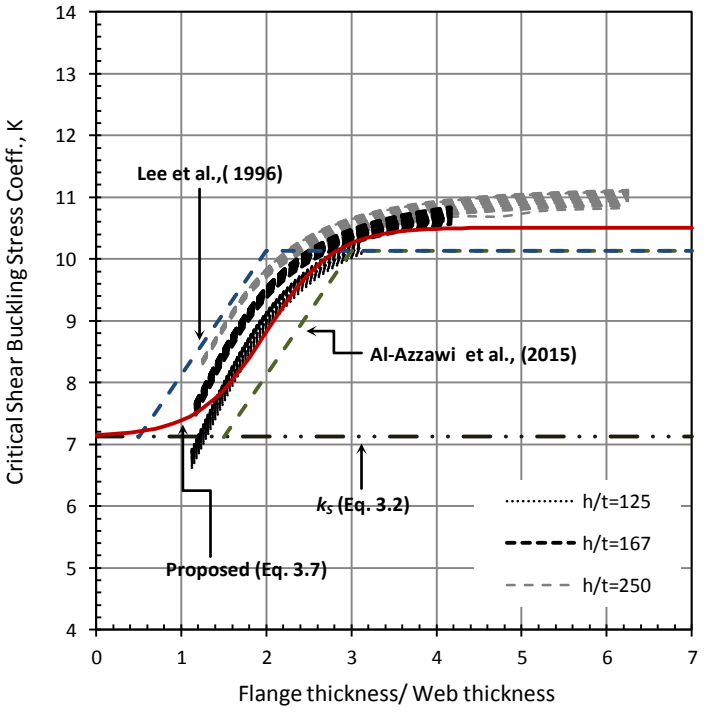

(**b**) a_w/h_w = 1.5

Figure (3.6): Design envelopes for the critical buckling shear stress coefficient.

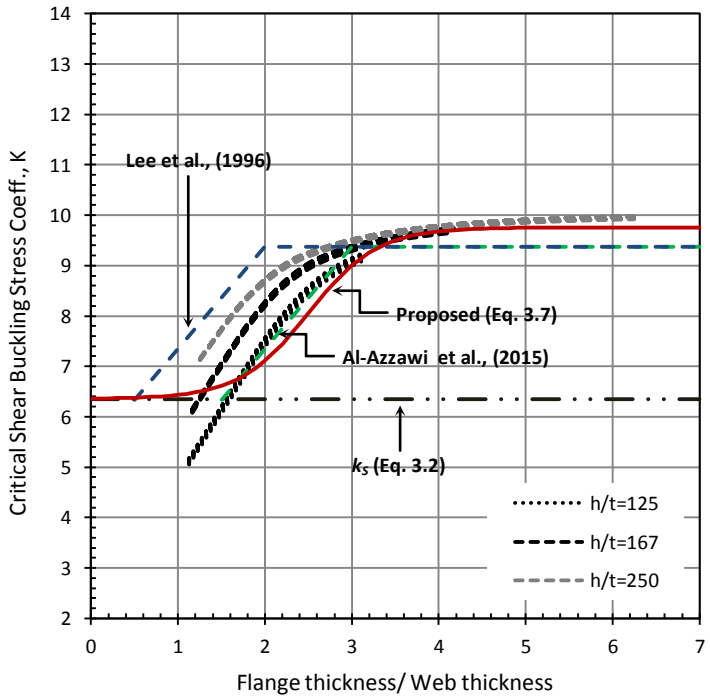

(**c**) a_w/h_w = 2.0

Figure (3.6 Cont.): Design envelopes for the critical buckling shear stress coefficient.

To sum up, an extensive parametric study was performed using finite element analysis to revisit the assumption of using simply supported boundary conditions in determining the shear buckling coefficients for plate girders loaded mainly in shear. This assumption is adopted in most current standards of practice like AISC (1994), AASHTO (2007), and EN 1993-1-5 (2004) specifications. It was shown that flange rigidity affects the degree of elastic restraining at the junction between the flange and the web. The value of the shear buckling coefficients depends on the degree of this elastic restraint. Consequently a new equation was proposed to determine the shear buckling coefficients as a function of (t_f/t_w). It was shown that the proposed equation correlates better to the extensive range of data studied in this work. In addition, it was shown that stiffeners' rigidity plays an important role in restraining the web boundaries and increasing its shear buckling resistance, this is especially true for plate girders with low aspect ratios.

3.5 VALIDATION OF THE PROPOSED DESIGN EQUATION

Table 3.2 illustrate the predictions of the proposed Equation (3.7) along with its constraints in comparison to Lee et al. (1998) and Al-Azzawi et al. (2015) equations where, $\sum e^2$, *e.sd.*, R^2, and *Rd* refer to the sum of the squared errors, the error standard deviation, the R-squared, and ratio of the design equation to the numerical analysis value, respectively. *Rd* values <1 and >1 refer to safe and unsafe estimation of the shear buckling coefficients, respectively. It is worth mentioning that the relative error was used in Table 3.2. This error is calculated by dividing the difference in the shear buckling coefficient values, determined numerically and from the respective equation (i.e. proposed Equation 3.7), Lee et al. Equation (3.4), and Al-Azzawi et al. Equation (3.6), by the numerical value obtained from the finite element analysis, which is assumed to be the reference value in this study.

From Table 3.2 it can be seen that the proposed Equation (3.7) shows a better correlation with the data and much more accurate and conservative estimation for the critical buckling shear stress coefficients. The data in Table 3.2 is based on 2718 point out of a total of 4563 numerical analysis after excluding the unpractical range of data where the thickness of the flange and stiffener is less than the thickness of the web. Figure (3.7) compares the data in Table 3.2 in a more illustrative way.

Table 3.2: Comparison of the proposed Equation (3.7), Lee et al. (1998), and Al-Azzawi et al (2015)

Method	a_w/h_w	$\sum e^2$	*e.sd.*	R^2	*Rd*
Proposed Eq. (3.7)	1.0	0.7	2.34	0.87	0.98
	1.5	1.98	3.16	0.93	0.97
	2.0	4.75	5.75	0.89	0.96
Lee et al.	1.0	4.21	3.39	0.69	0.94
	1.5	5.76	7.89	0.79	1.01
	2.0	22.33	13.76	0.76	1.06
Al-Azzawi et al.	1.0	8.99	5.3	0.83	0.92
	1.5	9.32	4.89	0.91	0.91
	2.0	4.93	5.77	0.89	0.95

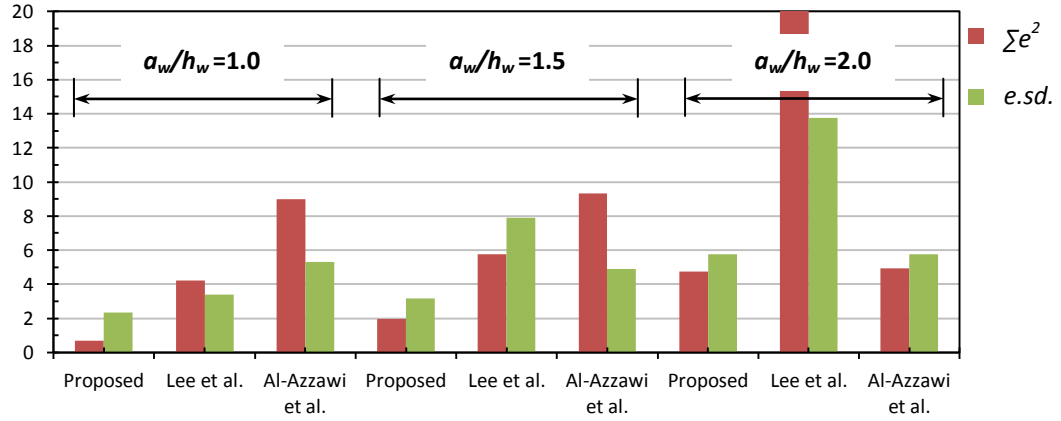

(**a**) Comparison of $\sum e^2$ and error standard deviations

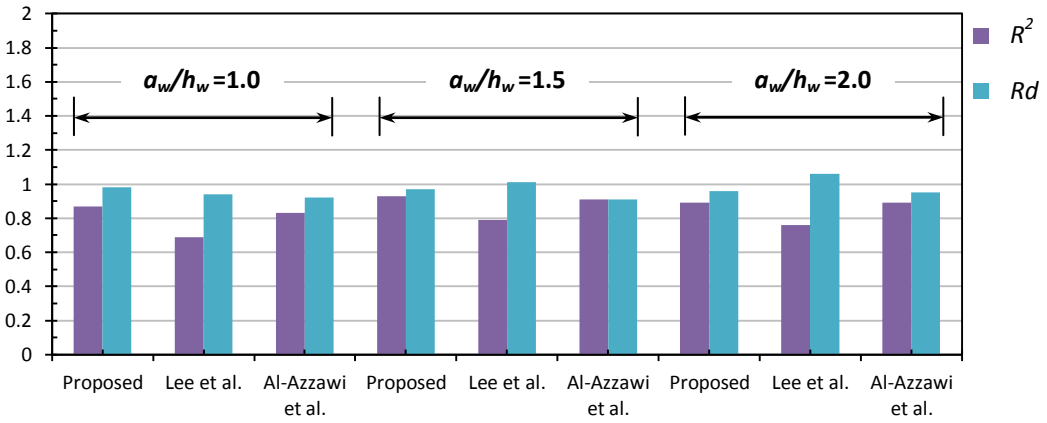

(**b**) Comparison of R-squared and Rd.

Figure (3.7): Bar chart comparing the values in Table 3.2.

3.6 INITIAL IMPERFECTION EFFECT

Irrespective of the degree of sophistication of the numerical method used, the main drawback of any procedure attempting to use numerical results as a basis for deriving design data remains the uncertainty related to the magnitudes and distributions of the initial deformations and residual stresses (Grondin et al., 1999). Initial imperfections in structures that have not been subjected to damage loads usually result from the fabrication process.

According to all the international standards the author is aware of (e.g. AISC (1994), AASHTO (2007), and EN 1993-1-5 (2004)), initial distortion (or variation from flatness) for web panels with intermediate transverse stiffener is allowed and

the maximum varies from $d/80$ to $d/130$ depending upon panel dimensions and stiffener configurations, where d is the lesser dimension of the stiffener spacing (a_w) and the web height (h_w). Previous studies have shown that, as the initial out-of-flatness increases, the bending stresses are significantly magnified, resulting in reduced ultimate shear strength especially for web panels with low slenderness ratios (h_w/t_w) where the membrane action is not dominant (Lee et al., 1998). However, in this part of the study an attempt was made to predict the effect of initial imperfection on the critical buckling shear stress in both aspects of its magnitude in comparison to the theory and its behaviour demonstrated in the buckling curves.

Among several imperfection types, only web initial out-of-flatness is considered; the effect of stiffener imperfection is not considered. Three types of initial out-of-flatness are considered as shown in Figure (3.8), namely, initial imperfection similar to the expected buckling modes (II-1), initial imperfection against the expected buckling modes (II-2), and a neutral buckling mode which lies in the middle between the first two types (II-3). Figures (3.8a) to (3.8c) show the shapes of the three initial imperfection types considered in this study. The first two types of the initial imperfection (II-1 and II-2) were found using the elastic Eigen buckling modes. These modes were initiated using the buckling analysis available in Abaqus CAE, and then imposed as an initial imperfection using Abaqus script commands in the input file. The third type of the initial imperfection (II-3) was created via Matlab where the web was created with the required initial imperfection using a double trigonometric series as follows:

$$u(x,y) = w_o \, sin\left(\frac{n\pi x}{a_w}\right) sin\left(\frac{m\pi y}{h_w}\right) \tag{3.8}$$

where w_o is the central initial imperfection and n & m were taken equal to 1.0 for simplicity. Afterward, a full geometrical and material nonlinear analysis (GMNA) was performed to find the overall behaviour of the specimen up to the ultimate failure. The same boundary conditions and material properties were used except that a constant strain hardening of (E/100) was added to the steel stress strain curve to account for material nonlinearity.

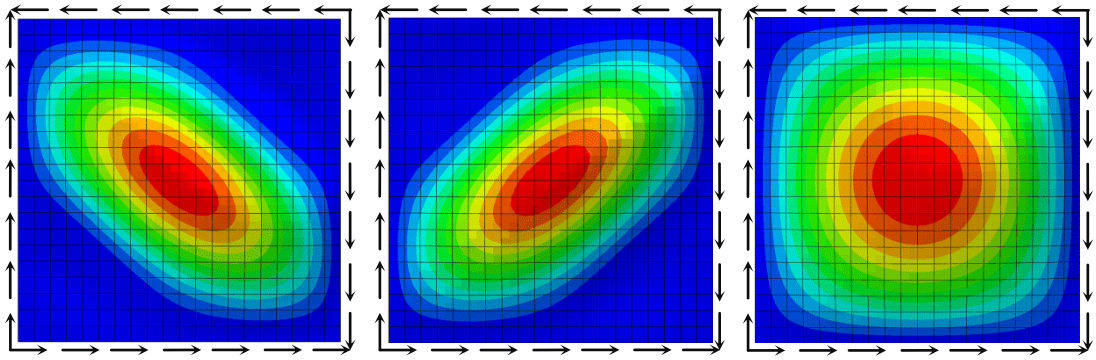

(**a**) II-1 pattern (**b**) II-2 pattern (**c**) II-3 pattern

Figure (3.8): Illustration of the three initial imperfection types adopted in this study.

Figure (3.9) compares the applied shear stress versus the web central out-of-plane displacement (to be called buckling curves from now on) for specimens with initial imperfection range from $h_w/125000$ to $h_w/100$ for the three imperfection categories shown in Figure (3.8), (II-1, II-2, and II-3). An absolutely plane elastic plate remains plane for applied loads smaller than the critical buckling load. If the load is increased beyond the critical value, the plate starts to buckle. However, the behaviour of real plates differs from the one for elastic plates due to inelastic material behaviour and initial imperfections. From Figure (3.9), it can be seen that, typically, there are three loading stages. Stage-1 (pre-buckling) is an elastic stage where the applied shear stress is less than the elastic critical buckling stress, stage-2 (post-buckling) starts after buckling occurs where the tension field forms providing a considerable post-buckling strength, since the increase in tension is limited only by the yield stress, and stage-3 (yielding plateau and failure) where the tension diagonal starts to yield causing high buckling deformations leading to failure of the specimen. The ultimate strength may be determined by appropriate buckling curves that provide, like buckling struts, a reduction factor (as a function of a non-dimensional plate slenderness factor) to be applied to the yield stress (Vayas and Iliopoulos, 2014) or using nonlinear finite element analysis.

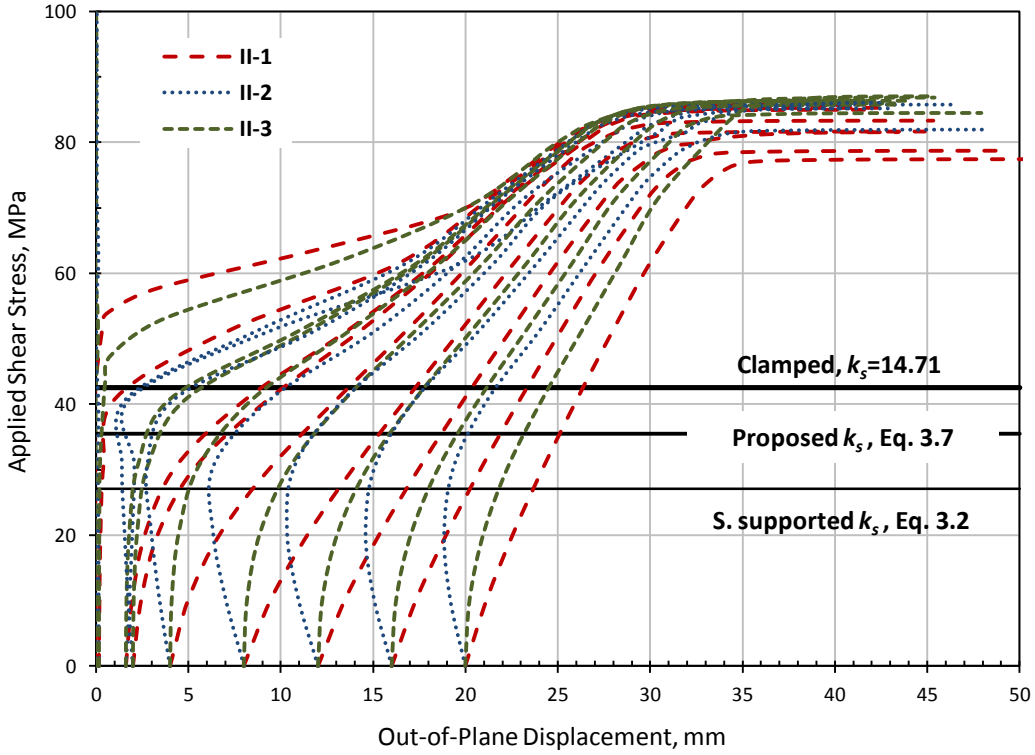

(**a**) h_w/t_w= 250, Initial imperfections (II = h_w/125000 to h_w/125)

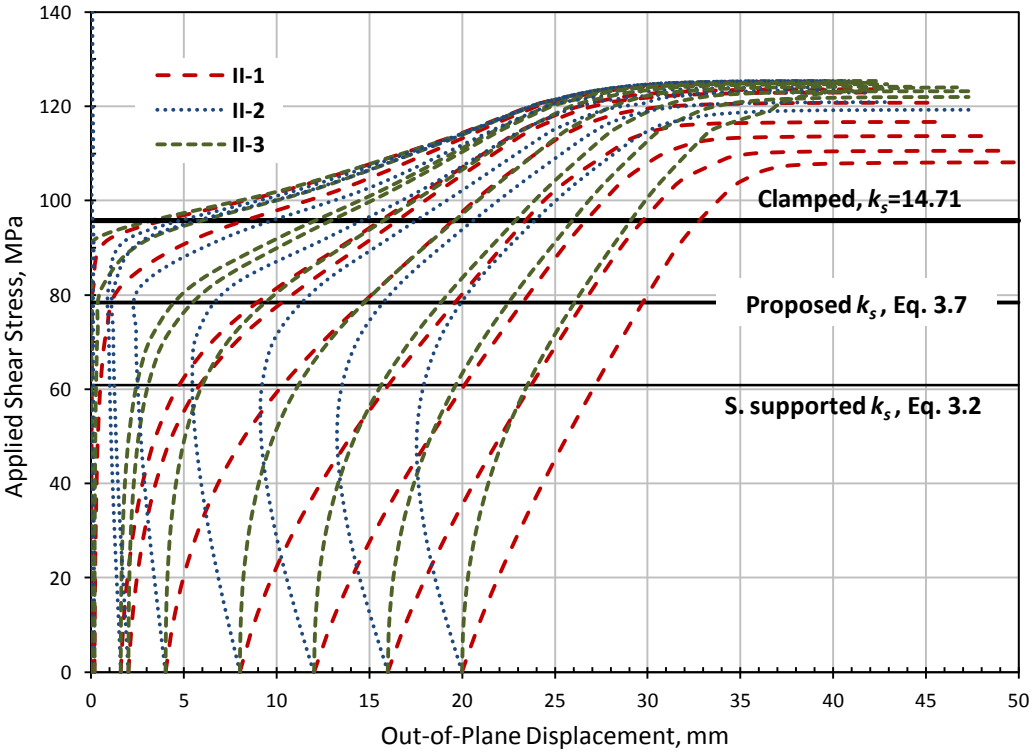

(**b**) h_w/t_w= 167.667, Initial imperfections (II = h_w/125000 to h_w/125)

Figure (3.9): Web central out-of-plane displacement for specimens with initial imperfection.

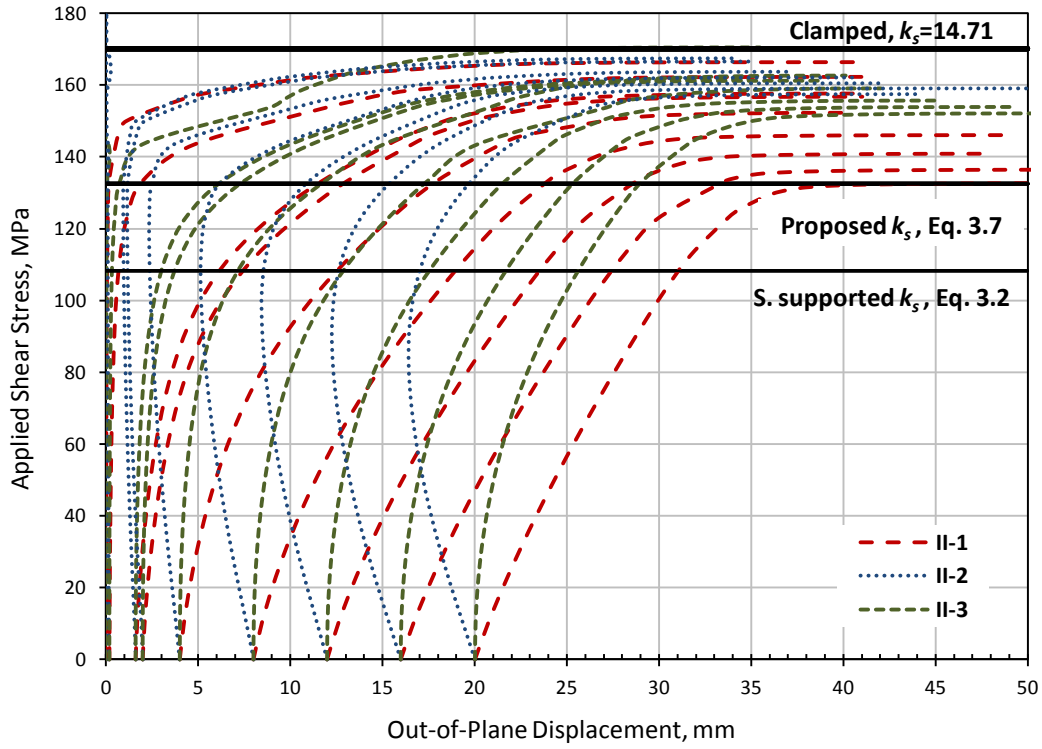

(**c**) h_w/t_w= 125, Initial imperfections (II = h_w/125000 to h_w/125)

Figure (3.9 Cont.): Web central out-of-plane displacement for specimens with initial imperfection.

Apart from Southwell method (Southwell, 1932) and the 'change of slope' method (Cox, 1951), there is no standard method to determine the critical buckling stress from a buckling curve. However, Donnell (1938) showed that Southwell's method was strictly valid only if the differential equation governing the deformation were linear, so that the buckling of plates, in which 'part at least of the extensional strains are proportional to the square of the normal displacement' should be properly excluded. On the other hand, the change of slope method is not very conclusive as well, because of its high sensitivity to the initial slope of the buckling curve and the initial imperfection as can be seen in Figure (3.10a), which provides typical buckling curves with different initial imperfections. Nevertheless, as can be seen from Figure (3.9), specimens with II-1 mode initial imperfection have always the lowest buckling stress and specimens with II-2 mode initial imperfection have always the highest buckling stress, while the specimens with neutral type of initial imperfection (II-3)

always lie between the two of them. This increase in the buckling stress of II-2 type specimens may be related to the additional energy required to reform and alter the buckling mode from an II-2 mode to an II-1 mode. The II-2 imperfection mode acts as prestressing to the web plate and increases its buckling stress while the II-1 imperfection mode does not require the same amount of energy as it has already taken the shape required for the buckling to initiate. From Figures (3.9) and (3.10), the effect of the type of initial imperfection is well obvious and it affects both the critical buckling stress as well as the ultimate shear capacity of the specimen. However, in this chapter we are more concerned with buckling stresses and the ultimate strength will be dealt with separately in Chapter 6.

In the absence of a rigorous method to determine the buckling stress from the obtained buckling curves, the neutral initial imperfection mode (II-3) was plotted alone against the out-of-plane displacement again in Figures (3.10b) to (3.10d) for specimens having slenderness ratios of 250, 167, and 125, respectively. From these figures it can be seen (visually) that the proposed buckling stress equation (Equation 3.7) succeeded in predicting the buckling stresses for specimens with small initial imperfection (e.g. h_w /1250). However, it is noted that there is a tendency for the buckling stress values to decrease with increasing the initial imperfection. Since both Southwell and the change of slope methods did not work properly for the model adopted in this study, it was decided to adopt the simply supported buckling stress as the minimum reference value with an initial imperfection of (h_w /125), since this an accepted assumption in most standards, as previously mentioned. This way, a simple linear equation can be proposed taking into account the initial imperfection effect on the critical buckling shear stress value by letting the maximum buckling shear stress be calculated using the proposed buckling coefficients Equation (3.7) with an almost flat plate having an initial imperfection of (h_w /1250) and the minimum buckling shear stress calculated from the standard simply supported Eqs. (3.1) and (3.2) for a plate with relatively high initial imperfection of (h_w/125). This equation is annotated on Figures (3.10b) to (3.10c) and can be stated as follows:

$$\tau^R = \tau_s + \left[\left(\frac{\tau^P - \tau_s}{\frac{h_w}{125} - \frac{h_w}{1250}}\right)\left(\frac{h_w}{125} - \frac{h_w}{w}\right)\right] \qquad (3.9\text{-a})$$

$$w = \frac{h_w}{w_o} \qquad 100 \leq \frac{h_w}{w_o} \leq 12500 \qquad \text{(3.9-b)}$$

where

τ^R : is the reduced buckling shear stress due to initial imperfection, MPa,

τ^P : is the buckling shear stress calculated according to the proposed buckling coefficients, MPa,

τ_s : is the critical buckling shear stress with simply supported boundary conditions, MPa,

w_o : is the central out of flatness of the web plate, mm.

Equation (9-a) can be approximated and further simplified with a maximum error of 2.55% and a standard deviation of 1% as follows:

$$\tau^R = \tau_s + \left[(\tau^P - \tau_s)\left(1 - \frac{125}{w}\right)\right] \qquad \text{(3.9-c)}$$

Figure (3.11) shows a comparison between the proposed Equation (3.9a) and simplified Equation (3.9c).

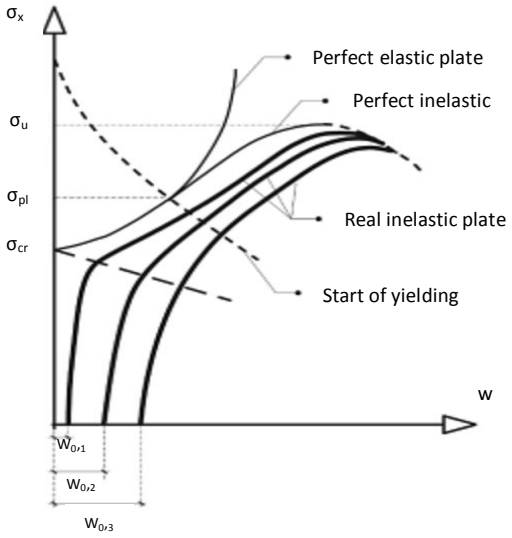

(**a**) Typical buckling curves for plates with initial imperfection, (Vayas and Iliopoulos, 2013)

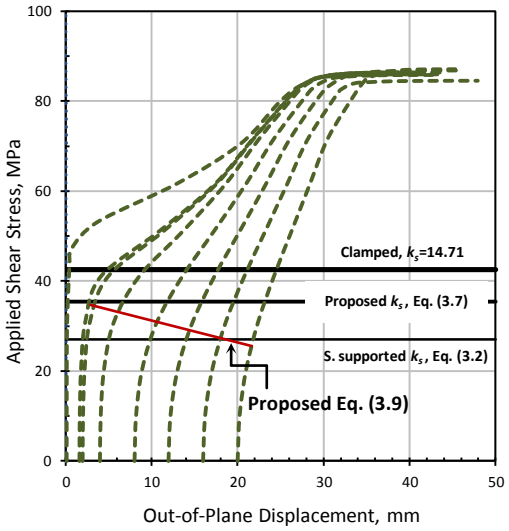

(**b**) h_w/t_w= 250, Initial imperfections (II = h_w/125000 to h_w/125)

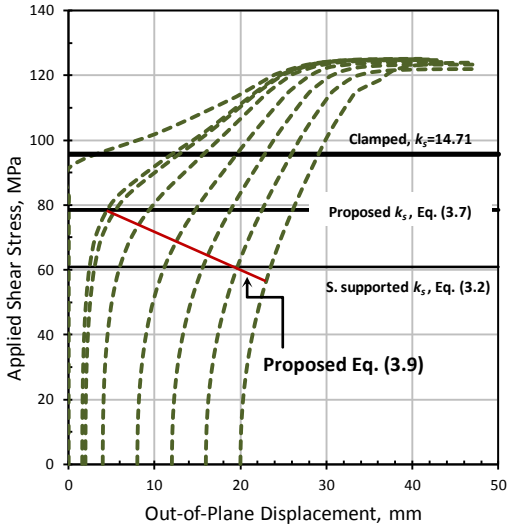

(**c**) h_w/t_w= 167, Initial imperfections (II = h_w/125000 to h_w/125)

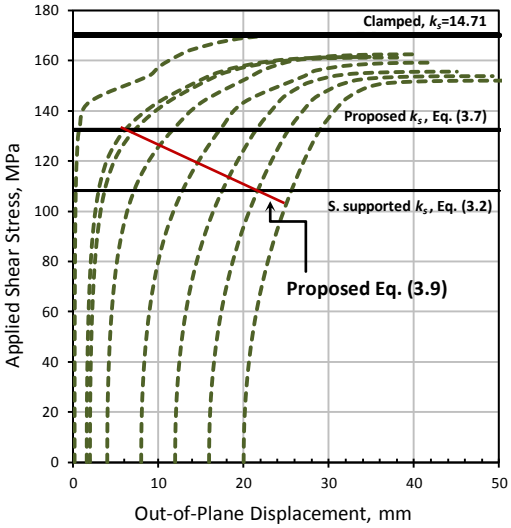

(**d**) h_w/t_w= 125, Initial imperfections (II = h_w/125000 to h_w/125)

Figure (3.10): Proposed reduction in the critical buckling shear stresses due to web initial imperfection.

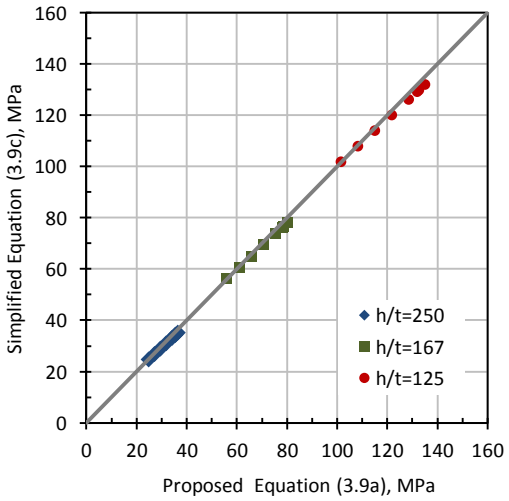

Figure (3.11): Comparison between the bucking stresses determined using the proposed Equation (3.9a) and the simplified version Equation (3.9c).

3.7 PLATE GIRDERS WITH DIAGONAL STIFFENERS

In the current study, the quest for finding a theoretical background for determining the critical buckling shear stress of diagonally stiffened plate girders, loaded mainly in shear, was not very successful. The shear buckling stress of diagonally stiffened bare steel plates may be considered as a benchmark for the more complicated composite section of FRP strengthened plate girders which depend on bonding profiled FRP sections along the compression diagonal of the web plate as will be seen in Chapters 5 and 6.

In this section the critical shear buckling stress of diagonally stiffened plates will be introduced, Figure (3.12) shows the proposed analytical model. The model depends on the diagonally symmetric properties of plates subjected to pure shear stress. The assumption made was to divide the plate into two equal triangles by applying the appropriate boundary conditions on the plate perimeter and solving it numerically using finite element analysis. This model requires providing a diagonal stiffener sufficiently strong to provide a minimum of simply supported boundary conditions along the compression diagonal of the plate, which implies that the stiffener will not deform during buckling. Both simply supported and clamped boundary conditions are investigated.

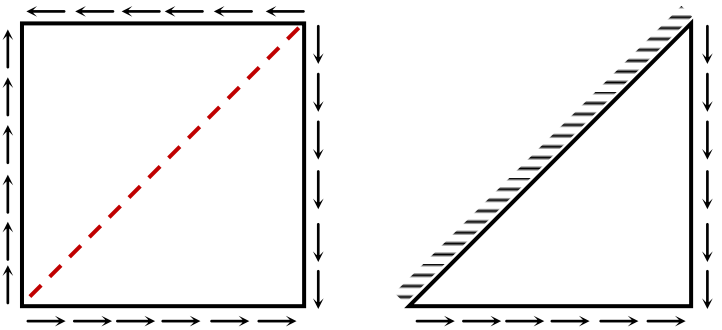

(**a**): Original model (**b**): Triangular model

Figure (3.12): Analytical model adopted for diagonally stiffened plates.

3.7.1 Cox and Klein Isosceles Triangular Plate Model

Cox and Klein (1955) solved the problem of buckling of isosceles triangular plates under uniform compression and shear for both simply supported and clamped boundary conditions. Their solution used Equation (3.1), with the condition of replacing the usual height of the plate (h_w) by the base width (b), see Figure (3.13). From this figure, the shear buckling coefficient for a triangular plate with an aspect ratio (a/b=0.5 which is analytical to a square plate with an aspect ratio a_w/h_w=1.0) having both simply supported and clamped boundary conditions are 25 and 55, respectively.

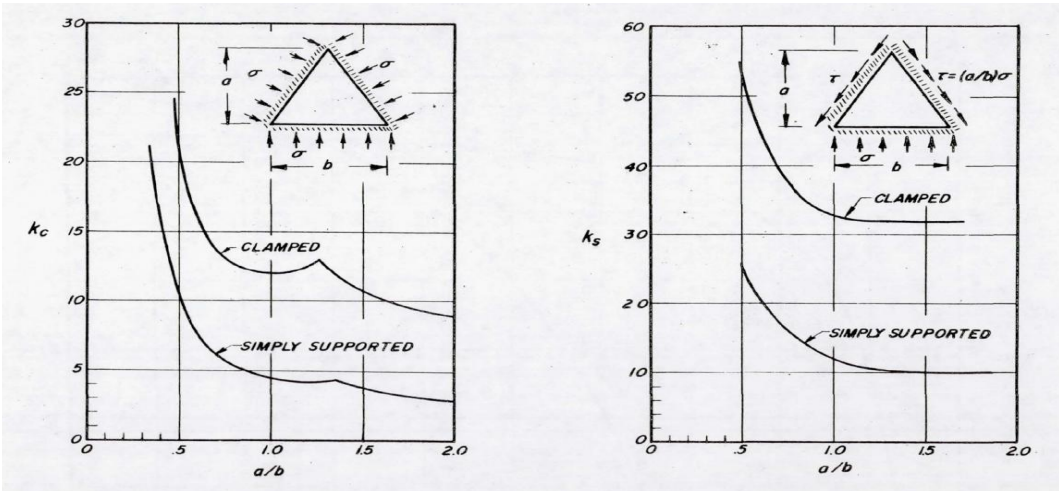

(**a**) Compression stress (**b**) Shear stress

Figure (3.13): Cox and Klein model for isosceles plates, (Cox and Klein, 1955).

An attempt was made to numerically recreate Cox and Klein model investigating the applicability of modelling triangular plates using finite element analysis. A square

plate having a slenderness ratio of 250 was cut into two halves (2 isosceles triangles) and modelled via Abaqus (3.10), using S9R5 element type, to recreate Cox and Klein model with the same loading and boundary conditions, see Figure (3.14). For the sake of comparison, the loading in this model was a compression shear loading which is in the reverse direction of the usual tension shear loading of diagonally stiffened shear panels. This was done for the sake of comparison between the finite element and the analytical model which provides the solution for this case only. Table 3.3 compares the results of the finite element model with Cox and Klein model. From this table it can be seen that the numerical model underestimates the buckling stress by 5% for the simply supported boundary condition case while it overestimates the buckling stress for the clamped boundary condition case by 6%. An average error of 5.5% does not suggest a very good agreement between the analytical and numerical solutions but can be accepted as a good indication that the model is working. Nevertheless, the true boundary conditions are practically somewhere between the simply supported and clamped boundary conditions which could lead to some reduction in the resulting numerical error, but this cannot be proved without further investigation which was not performed in the current study.

Table 3.3: Comparison of the numerical results with Cox & Klein model

	Analytical	**Numerical**	**Error**
S. supported B.C's	36.1	34.3	+5%
Clamped B.C's	79.5	84.8	-6%

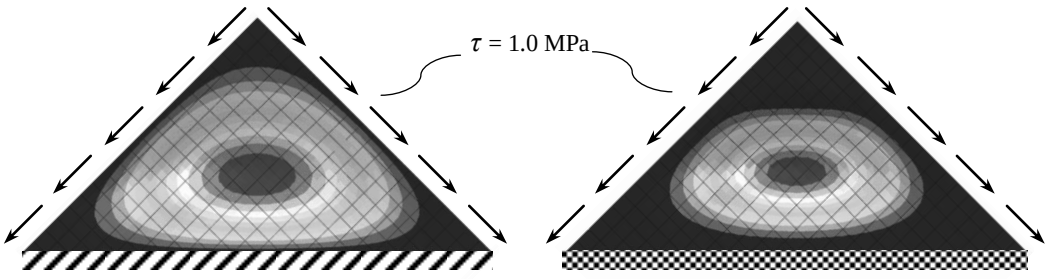

(**a**) Simply supported B.C's (**b**) Clamped B.C's

Figure (3.14): Cox and Klein model using finite element analysis.

3.7.2 Comparison of Rectangular and Triangular Models

The plate in Figure (3.12) was modelled numerically using Abaqus. In the first case the whole plate was modelled with the boundary conditions applied to the plate perimeter and the compression diagonal (model-I). In the second case, the rule of symmetry was exploited and only one half (triangle) of the plate was modelled with twice the applied load (model-II). In both cases, simply supported and clamped boundary conditions were investigated. In addition to that, three aspect ratios, namely, 1.0, 1.5, and 2.0, were taken into considerations.

For illustration purpose, Figure (3.15) shows one model for a specimen having an aspect ratio of 1.0 with clamped boundary conditions on the plate perimeter and compression diagonal. Table 3.4 illustrates the results of the 12 numerical models.

Table 3.4: Critical buckling shear stresses, MPa

S.S. B.Cs		Aspect ratio (a_w/h_w)	Clamped B.Cs	
Model-I	**Model-II**		**Model-I**	**Model-II**
89.9	89.0	**1.0**	124.9	124.6
63.4	58.6	**1.5**	86.6	82.5
52.4	44.0	**2.0**	70.0	62.4

From Table 3.4 it can be seen that the hypothesis of using a triangular plate with twice the applied shear stress instead of the diagonally stiffened square plate works almost perfectly for plates having an aspect ratio of 1.0. However, the accuracy of this assumption declines with increasing the aspect ratio from 1.0, with an average accuracy of 99%, to 1.5 and 2.0, with an average accuracy of 94% and 87%, respectively. This lack of accuracy can be justified by the fact that triangle is not an isosceles anymore (halving a rectangle with an aspect ratio 1.5 or 2.0 will lead to symmetric but not isosceles triangles). This means that Cox and Klein model is not valid anymore and the applied shear stress must be corrected accordingly. Non-dimensional geometrical correction factors can be suggested to be multiplied by the critical buckling shear stress for the non-isosceles triangular plates. This non-dimensional factor can be expressed as follows:

$$GNCF = \sqrt[4]{\frac{a_w}{h_w}} \tag{3.10}$$

where *GNCF* is the geometrical non-dimensional correction factor calculated by taking the ratio of the root of the area of a non-isosceles to the root of the area of a similar isosceles triangle. Re-analyzing Model-II (the triangular plate model) with the proposed correction factors increased the accuracy of the model to an acceptable level with an average of 96.5% and 97% for plates with aspect ratios of 1.5 and 2.0, respectively.

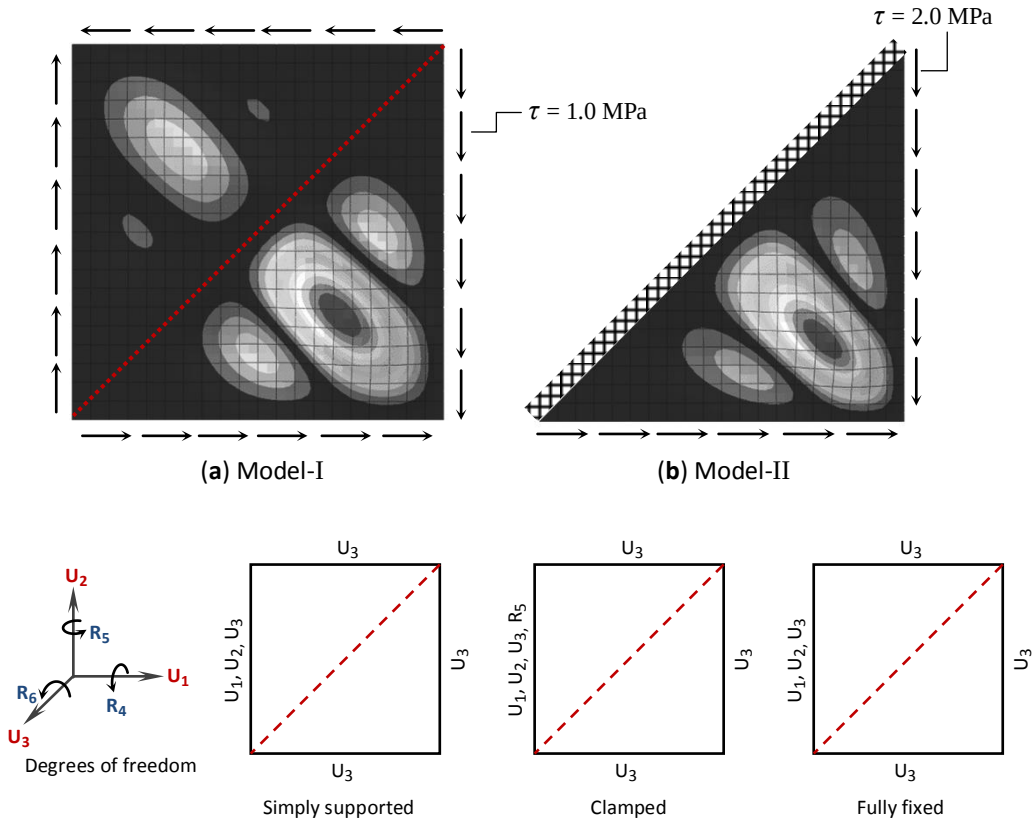

(**a**) Model-I (**b**) Model-II

(**c**) Restrained degrees of freedom in the finite element model

Figure (3.15): Buckling modes of square and triangular plates.

The critical buckling shear stress coefficient for diagonally stiffened plates can be calculated using a reverse form of Equation (3.1) and the critical buckling shear stress determined using model-I, these values are shown in Table 3.5. The simply supported boundary conditions were imposed by restraining only the out of plane

displacement of the plate perimeter and compression diagonal while the clamped boundary conditions refer to fixing all degrees of freedom in the plate perimeter and compression diagonal except for the in-plane displacement (*Ux*,*Uy*) of the plate simulating a diagonal stiffener strong in the major axis and weak in the minor one. The fully fixed boundary conditions refer to the same as above except that in-plane displacement of the plate was restrained in the compression diagonal to simulate an infinitely stiff diagonal stiffener. In all cases, the *x*,*y* displacement was restrained in the left hand side perimeter of the plate for stability requirements. Figure (3.15c) illustrates the above explained boundary conditions in detail.

Table 3.5: Critical buckling shear stresses coefficients

a_w / h_w	S.S. BCs	Clamped BCs	Fully Fixed BCs
1.0	31.09	43.18	62.18
1.5	21.92	29.93	46.66
2.0	18.13	24.20	32.56

The numerically determined value of the shear buckling coefficient for a diagonally stiffened simply supported plate with an aspect ratio of 1.0 was 31.09 which is in agreement with the value of 30 reported by Åkesson (2007). For the same plate and same boundary conditions if we divide the plate into two triangles and multiply the shear load by a factor of 2 we will get a buckling shear coefficient of 62.18 which is in good agreement with the value of 62.0 reported by Wittrick (1953a and b) for positive shear buckling of an isosceles triangular plate with simply supported boundary conditions. This corresponds as well to the same value predicted from the fully fixed boundary conditions of the rectangular plate (Model-I), which further confirms the findings. The author did not have access to more case studies that can be compared with the predicted ones in this study.

The above buckling coefficient values form the minimum and maximum envelopes for shear buckling analysis of diagonally stiffened plates. However, these theoretical conditions are unlikely to be fulfilled and further investigation is needed for the practical cases where the diagonal stiffener provides neither simply supported nor fixed boundary conditions in the junction with the plate compression diagonal.

This analysis will be provided as a parametric study in the following sections using finite element method.

3.7.3 Finite Element Modelling of Diagonally Stiffened Plate Girders

3.7.3.1 *Analytical Model*

Figure (3.16) shows the analytical model adopted in this section for diagonally stiffened plate girders. A typical two-span plate girder having an aspect ratio ranging from 1.0 to 2.0 was considered for simplicity. The dimensions, sectional and material prosperities were kept the same as in the previous section (3.3.1) for the sake of comparison. However, to reduce the variables in this parametric study, the flange thickness (t_f) and the transverse stiffener thickness (t_s) were kept constant at triple the thickness of the web plate ($3\times t_w$) to ensure the consistency of the outcomes and to independently estimate the effect of the diagonal stiffener. In addition, the projected width b_s of all stiffeners was kept constant at 110mm, which is the average stiffener width in the previous parametric study, refer to section 3.3.1.

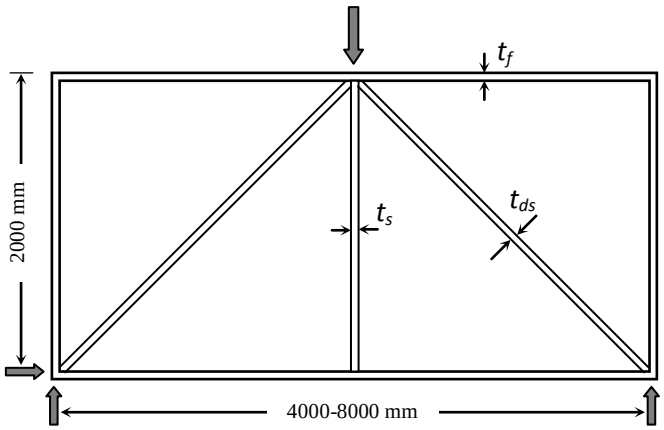

Figure (3.16): Analytical model adopted in the diagonal stiffener study.

3.7.3.2 *Finite Element Model*

The finite element model adopted for studying the effect of diagonal stiffeners on the critical buckling shear stress of plate girders was built using the same procedures as adopted in the previous parametric study (section 3.3.2), except for adding two external stiffeners to relieve the stress concentration at the diagonal stiffeners' external junctions. The load was applied at the middle of the plate girder and simply supported boundary conditions were imposed at the two supports (Figure 3.16). The

buckled shape of a specimen with an aspect ratio of 1.0, slenderness ratio of 167, and a diagonal stiffener thickness of 12mm is shown in Figure (3.17)

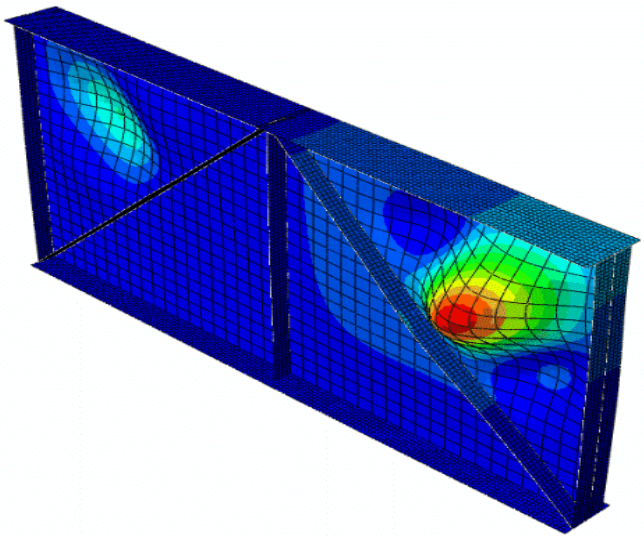

Figure (3.17): Finite element model buckling mode.

3.7.3.3 *Convergence Study*

The same convergence study as in section (3.3.3) was adopted in this section. However, some minor convergence analysis was performed to make sure that the new model does converge towards the theoretical values predicted in section (3.7.2).

3.7.3.4 *Parametric Study*

As mentioned above the flange thickness (t_f) and the transverse stiffener thickness (t_s) were kept constant at three times the thickness of the web plate ($3\times t_w$). The projected width b_s of all the stiffeners was kept constant at 110mm, leaving us with the following range of variables:

a_w/h_w = 1.0 to 2.0 with a_w = 2000 to 4000 mm,

h_w/t_w = 125 to 250 with t_w = 8 to 16 mm,

t_{ds} = t_w to 50 mm, (i.e. the minimum thickness equals the web thickness).

where t_{ds} is the diagonal stiffener thickness, see Figure (3.16).

Figure (3.18) shows the critical buckling shear coefficients for the whole data range of this parametric study. It can be seen that the critical buckling shear stress is mostly dependent on the aspect ratio of the web (a_w/h_w) and it goes up as the plate aspect

ratio become closer to 1.0 (square plate). For the same aspect ratio the buckling stress increases with increasing the ratio of (t_{ds}/t_w), however, the rate of increase is again dependent on the aspect ratio and gets higher with decreasing the aspect ratio from 2.0 to 1.0. Finally, it can be seen that the slenderness ratio has a minor effect on the buckling stress and this effect descends with increasing the aspect ratio. This could be related to the assumption that longer diagonally stiffened plate girders (with high aspect ratios) tends to behave in a way more similar to trusses and hence the plate thickness play a minor role in the overall structural response.

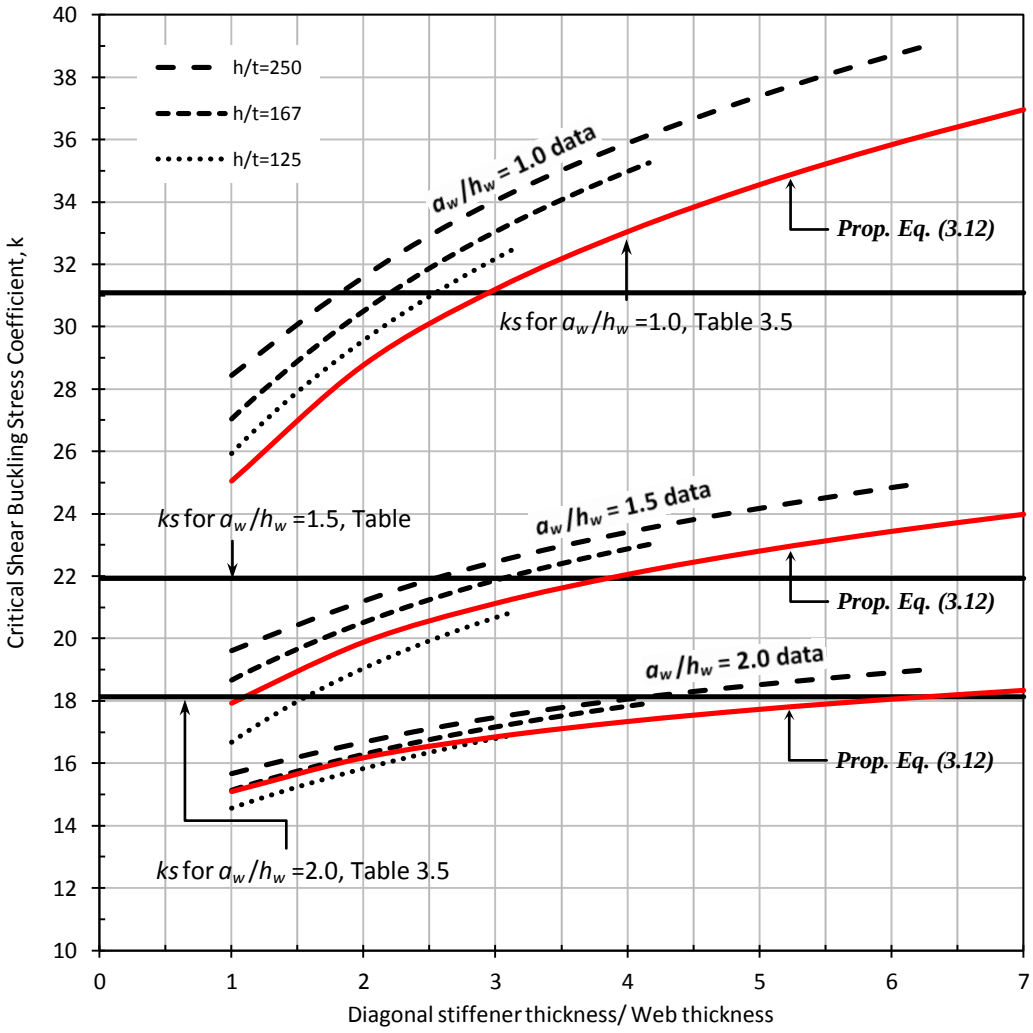

Figure (3.18): Buckling shear stress coefficients for diagonally stiffened plate girders.

3.7.4 Analysis of Results

From Figure (3.18), it can easily be shown that there is a limiting factor which allows reaching the simply supported boundary condition buckling coefficient for diagonally stiffened steel plate girders, this factor can be expressed as follows:

$$\frac{t_{ds}}{t_w} \geq \frac{a_w}{h_w} + 2.0 \tag{3.11}$$

Beyond this limit the buckling coefficients may be increased even more to a specific value, however, reducing this limit will reduce the buckling coefficient as well.

For the whole range of data, the following general equation can be proposed:

$$k = \alpha \left(\frac{t_{ds}}{t_w}\right)^{\beta} \qquad 1.0 \leq \frac{t_{ds}}{t_w} \leq 6.25 \tag{3.12}$$

where:

$$\alpha = 1.5k_s - 0.5k_{sf}$$

$$\beta = 0.1\left(3 - \frac{a_w}{h_w}\right)$$

k_s and k_{sf} represent the simply supported and clamped boundary condition buckling coefficients predicted in Table 3.5.

Many sub-equations can be derived from non-linear regression analysis with more correlation to a specific range of data. However, it is thought that a general formula would be more beneficial on the expense of some accuracy. Equation (3.12) has R-squared values of 0.95, 0.82, and 0.92 for diagonally stiffened plate girders with an aspect ratio of 1.0, 1.5, and 2.0, respectively.

3.8 SUMMARY AND CONCLUSIONS

A numerical approach using finite element analysis was adopted in this chapter to determine the critical buckling shear stress coefficients of steel plate girders with transverse and diagonal stiffeners. The conservative assumption, adopted in most international standards like AISC (1963 and 1994), AASHTO (1973 and 2007), and EN 1993-1-5 (2004), where simply supported boundary conditions are applied at the junction between the web plate, flange, and stiffeners, is revisited and care was made to address the effect of the elastic restraining degree at the junction due to flange and

stiffener rigidities. An extensive parametric study to estimate the effect of several important variables on the shear bucking coefficients was performed using linear buckling finite element analysis. It has been found that the traditional assumption of simply supported boundary conditions at the junction between the web plate and the flange is rather conservative and that the effect of elastic restraining in increasing the buckling strength of the web plate due to the rigidity of the flange should be taken into considerations for the studied range of aspect ratios between 1.0 and 2.0.

Increasing the thickness of the flange between one and three times the thickness of the web (t_f/t_w =1.0 to 3.0) resulted in significant increase in the critical buckling shear stress depending on the aspect ratio of the web plate, while there was no increase in the buckling strength beyond this limit (t_f/t_w =3.0). The same argument holds for the effect of rigidity of the transverse stiffeners but to a lower extent and limited to an aspect ratio of 1.0 because the effect of the stiffener rigidity was found to be insignificant and may be neglected for higher aspect ratios. A general design equation is proposed (Equation 3.7) taking all these factors into consideration and will be used in determining the critical buckling shear stress as a part of the design method proposed later in Chapter 7.

The effect of web initial imperfection was also studied using nonlinear finite element analysis. Three modes of initial imperfection were considered and a simplified linear equation (Equation 3.9) was proposed to reduce the estimated critical buckling stress due to web initial imperfection.

Finally, the shear buckling coefficients for diagonally stiffened plate girders were determined using finite element analysis based on theoretical models solving the shear buckling problem for isosceles triangle plates and a new design equation is proposed (Equation 3.12).

CHAPTER REFERENCES

AASHTO, LRFD-SI Units (2007). "Standard Specifications for Highway Bridges," 4th Ed., Washington, D.C, USA.

AASHTO, Standard Specifications for Highway Bridges (1973). 11th Ed. American Association of State Highway Officials, Washington, DC.

AISC, LRFD (1994). "Manual of Steel Construction, Load and Resistance Factor Design," 2nd Ed., Vol. I and II, Chicago, Illinois, USA.

AISC, Specification for the design, Fabrication and Erection of Structural Steel for Building (1963). 6th Edn. American Institute of Steel Construction, New York.

ÅKESSON B. (2007). "Plate buckling in bridges and other structures," CRC Press, 163 pp.

AL-AZZAWI Z., STRATFORD T., ROTTER M., and BISBY L. (2015). "Effect of flange and stiffener rigidity on the boundary conditions and shear buckling stress of plate girders," 16th European Bridge Conference, 23-25th June, Edinburgh, 12 pp.

BASLER K. (1961a) . "New provisions for plate girder design," In: Proc. AISC National Engineering Conf., New York, pp. 65-74

BASLER K. (1961b). "Strength of Plate girders under combined bending and shear," J. Struc. Div. ASCE 87, pp. 181-19.

BASLER K. (1963). "Strength of plate girders in shear," Trans. ASCE 128, pp. 683-719.

BASLER K. and THURLIMANN B. (1959). "Plate girder research," In: Proc. AISC National Engineering Conf., New York.

BRITISH STANDARDS INSTITUTION, Code of Practice for Design of Steel Bridges (1982). Milton Keynes, BSI 1982, BS 5400: Part 3.

BUDIANSKY B. and CONNOR R.W. (1948). "Buckling stresses of clamped rectangular flat plates in shear," Technical Report No. 1559, NACA, Washington, 11 pp.

BULSON P. S. (1970). "Stability of Flat Plates," Elsevier, New York.

CEN, Eurcode 3: Design of Steel Structures , Part 1.5 (2004). "Plated structural elements," Milton Keynes, BSI, ENV 1993-1-5.

CHERN C. and OSTAPENKO A. (1969). "Ultimate strength of plate girder under shear," Fritz Engineering Laboratory. Report No. 328.7, Lehigh University.

COX H. L (1951). "Note on the Southwell method for estimating critical load," Reports and Memoranda No. 2696, Aeronautical Research Council, London. 10 pp.

COX H. L. and KLEIN B. (1955). "The buckling of isosceles triangular plates," J. Aero. Sci., Vol. 22, No. 5, pp. 321 -325.

DONNELL (1938). "On the application of Southwell's method for the analysis of buckling tests," Stephen Timoshenko- 60th Anniversary Volume, Macmaillan, 27 pp.

FUJII, T., FUKOMOTO, Y., NISHINO, F. and OKUMURA, T. (1971). "Research works on ultimate strength of plate girders and Japanese provisions on plate girder design,". IABSE Colloquium, 21-48.

GRONDIN G.Y., ELWI A.E., and CHENG J.J.R. (1999). "Buckling of stiffened steel plates- a parametric study," Journal of Constructional Steel Research 50 (1999), pp. 151-175.

HENDY C.R. and PRESTA F. (2008). “Transverse web stiffeners and shear moment interaction for steel plate girder bridges,” The Structural Engineer, Nov., pp. 13-26.

HÖGLUND T. (1973). “Design of Thin Plate I-Girders in Shear and Bending with Special Reference to Buckling,” No. 94. Stockholm: Kungl. Tekniska Högskolan, Inst. for bygnadsstatik.

LEE S.C. and YOO C.H. (1998). “Strength of Plate Girder Web Panels under Pure Shear,” ASCE, Journal. of Structural Eng., Vol. 124, No. 2, pp. 184-194.

LEE S.C. and YOO C.H., and YOON Y. (2002). “Behavior of intermediate transverse stiffeners attached on web panels,” Journal of Structural Engineering, 128(3), pp.337-345.

LEE S.C., DAVIDSON J.S., and YOO C. H. (1996). “Shear buckling coefficients of plate girder web panels,” Computers & Structures, Vol. 59, No 5, pp. 789-795.

PORTER D.M., ROCKEY K.C., and EVANS H.R. (1975). “The collapse behaviour of plate girders in shear,” Journal of The Structural Engineer, Vol. 53, No. 8, pp. 313-325.

ROCKEY K.C. and SKALOUD M. (1972). “The ultimate load behaviour of plate girders loaded in shear,” The Structural Engineer, No. 1, Vol. 50, pp. 29-47.

SOUTHWELL (1932). “On the analysis of experimental observations in problems of elastic stability,” Proc. Roy. Soc., A, Vol. 135, 601 pp.

TIMOSHENKO S. and GERE J.M. (1989). “Theory of elastic stability,” Second renewed edition, Dover Publications Inc., Mineola, New York, originally published: New York, McGraw-Hill Book, 1961, 541 pp.

VAYAS I. and ILIOPOULOS A. (2014). ”Design of Steel-Concrete Composite Bridges to Eurocodes,” CRC Press, 584 pp.

WAGNER H. (1931). “Flat sheet metal girder with very thin metal web- Sheet metal girders with spars resistant to bending- The stress in uprights- Diagonal tension fields,” Technical Memorandum No. 606, Part III, National Advisory Committee for Aeronautics (NACA), Hampton, 48 pp.

WILSON J. M. (1886). “On Specifications for strength of iron bridges,” Trans. ASCE, 15, 401-403 and 489-490.

WITTRICK W.H. (1953a). “Buckling of a Right-Angled Isosceles Triangular Plate in Combined Compression and Shear (Perpendicular Edges Simply Supported, Hypotenuse Clamped),” Rep . SM . 220, Aero. Res. Labs., Dept. Supply, Melbourne.

WITTRICK W.H. (1953b). “Buckling of a Right-Angled Isosceles Triangular Plate in Combined Compression and Shear (Perpendicular Edges Clamped, Hypotenuse Simply Supported),” Rep. SM. 211, Aero. Res. Labs., Dept. Supply, Melbourne.

Chapter Four

PHASE-1

FRP Panel Geometric Design and Material Experimental Programme

4.1 INTRODUCTION

The objective of the experimental programme is to develop a system having the ability to increase the out-of-plane stiffness and strengthen the web plates. The system in the current work is meant to be applied to the web of an end panel in a steel bridge, where high shearing forces are typically exerted. While limited previous work has shown that strength increases are possible for steel structures reinforced with FRPs, relatively little stiffness increase has been observed to date. To provide out-of-plane stiffness increase to thin steel web plates while minimizing material cost, a novel preformed corrugated FRP panel will be introduced in this chapter (Phase-1).

To investigate any structural problem, the mechanical properties of the materials used in building the structure should be determined according to the available standard test methods. The conducted test results in this study will be compared with standard ones in the relevant sections. This chapter describes the optimization method for the proposed strengthening technique along with determining the mechanical properties of the FRP and steel used throughout this study.

The optimized FRP profiled section in this phase will be used in phase-2 (chapter 5) for an initial series of tests made to prove the validity of the proposed strengthening technique in stiffening steel plates against buckling under in-plane static shear loading. The initial series of tests will be used to choose among different variables associated with the optimization process as well; such as, type of FRP (CFRP or GFRP), the number of layers of fabric for the same fibre volume fraction, the bonded length along the compression diagonal, the FRP panel section (open vs. closed section), the orientation of the glass fibres, and the shape of the preformed panels' end cut. Finally, the optimized FRP panel from Phase 1 and 2 will be further investigated in Phase-3 (Chapter 6) for its efficiency in increasing the out-of-plane

stiffness of the webs of steel plate girders against shear buckling and reducing the breathing phenomenon under cyclic loads, a typical loading scheme for structures like bridges.

Figure (4.1) shows a schematic diagram illustrating the planned experimental programme in the present work.

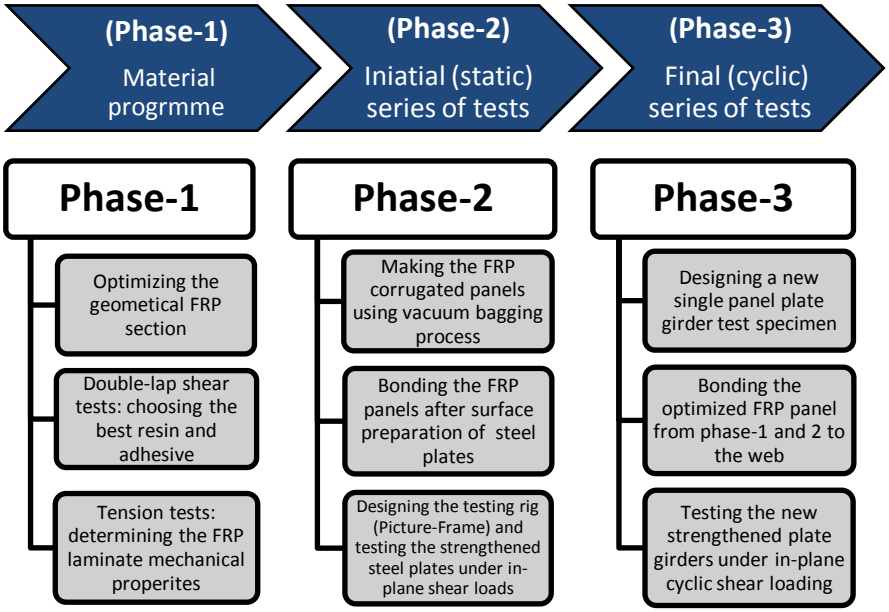

Figure (4.1): Schematic diagram of the present experimental programme.

4.2 OPTIMIZATION OF THE STRENGTHENING TECHNIQUE

4.2.1 Analytical Modelling

Figure (4.2) provides details of the analytical model adopted in the current study. The initial plate shown in Figure (4.2a) is a square steel plate of 500×500mm having a slenderness ratio (h_w/t_w) of 250, where h_w and t_w represent the height and thickness of the steel plate, respectively. Figure (4.2b) and (4.2c) show the classical (i.e. flat sheet) and proposed (i.e. profiled) FRP strengthening techniques, respectively. In the classical technique, several layers (plies) of FRP are bonded using wet-layup process usually over the entire area of the steel plate, to produce a composite section with greater stiffness. The strengthening technique used here is based on a preformed corrugated FRP panel bonded to the compression diagonal of the web plate, which is a more efficient use of FRP material due to the higher flexural rigidity of the profiled

shape. Preliminary FEA confirmed that the specimens strengthened with the proposed diagonal corrugated profiled FRP panel had higher stiffness and critical buckling shear stress.

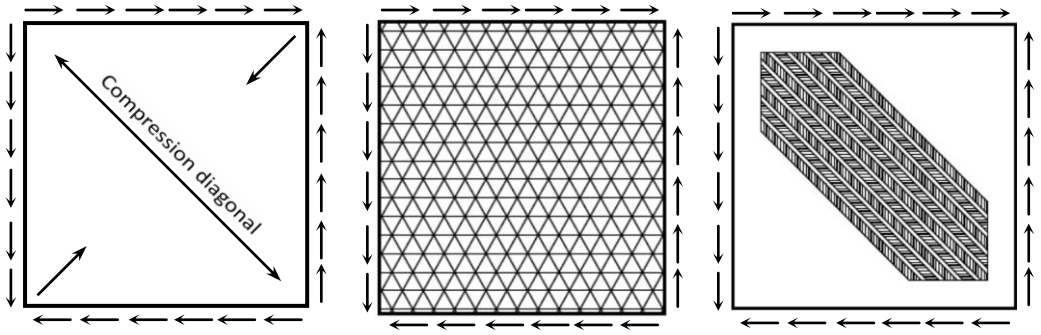

Figure (4.2): Analytical model adopted in this study.

4.2.2 Cross-Section of FRP Profiled Plate

Figure (4.3) shows three selected types of corrugated profiled FRP plates; with rectangular, semi-circular, and half-hexagonal profiles, respectively. Several preliminary trials have been made before these ones using hand calculation techniques to optimize the corrugation section with different shapes, heights, widths, and number of corrugations per section. These calculations were based on Euler strut model in axial compression and plates under pure shear conditions. The sectional dimensions of the panel were chosen to consume the least possible FRP material and bonding epoxy quantities, whilst not providing excessive geometrical stiffness, which might lead to brittle failure like most other FRP strengthening techniques. The chosen preformed corrugated FRP panels had typical widths of 195mm, with variable lengths and end cut shapes. Perfect bond was assumed between the FRP and the steel plate in all modelling cases for optimizing the corrugation geometry.

Each of the three profiled shapes was tested numerically using elastic bucking analysis available in the FEA code *Abaqus*. The FRP panels were assumed to be made of GFRP laminate with a thickness of 1.4mm and a modulus of elasticity of 14.4GPa. The FRP section was bonded (tie constrained) to an S275 steel plate having dimensions of 615×245×2mm. Fixed boundary conditions were imposed at both ends of the steel plate, except for the in-plane axial displacement at the loaded edge. This plate was used to represent a compression diagonal strip from the steel plate as

shown in Figure (4.4). A reduced integration linear 4-noded shell element (S4R) was used for both the steel and the FRP.

The results of this preliminary FEA showed that Euler critical buckling loads were 10.3kN, 7.3kN, and 8.4kN for the steel plates strengthened with the rectangular, semi-circular, and half-hexagonal corrugated sections, respectively. In spite of the fact that the rectangular section had the highest buckling load, it was excluded from the results because it is thought that the sharp edges of this section will act like stress concentrators for both FRP composite and the bonding strips. The semi-circular and half-hexagonal profiled sections were chosen for further numerical investigation.

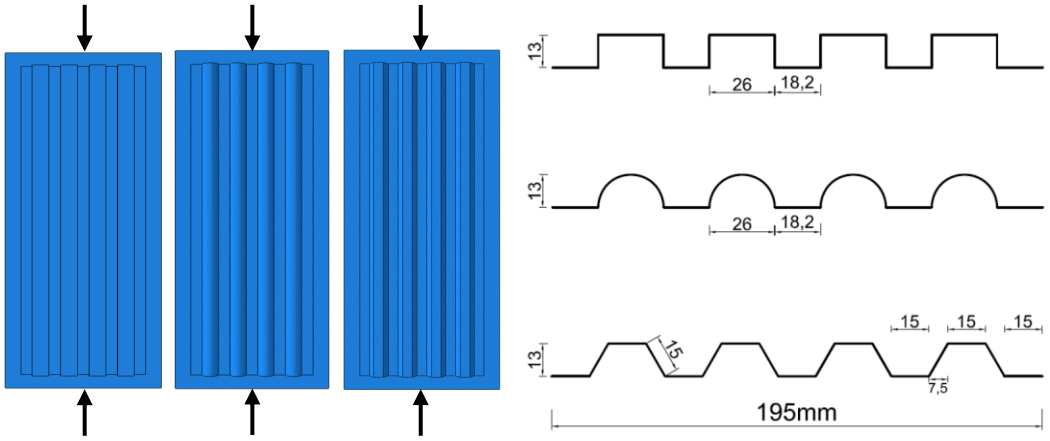

(**a**) Composite section profile (**b**) FRP panel corrugation sections

Figure (4.3): Composite section profile and sectional dimensions.

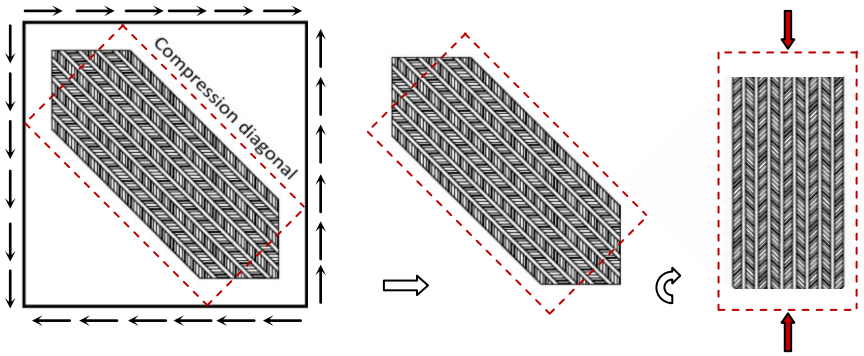

Figure (4.4): Strengthened steel plate under pure shear stress and the compression diagonal strip used for Euler buckling analysis.

At this stage it is worthwhile emphasizing that choosing the right geometrical properties for the FRP strengthening panel is not an easy and straightforward process. Different variables need to be taken into considerations for a successful

optimization criterion including, but not limited to, type of the FRP used, bonding requirement, size of the specimen, required stiffening level, and some practical considerations with respect to applicability in the field. Based on the observations in this study, it is recommended to limit the second moment of area of the stiffening FRP section so that the ultimate shear capacity of the strengthened composite steel-FRP section does not exceed the shear field capacity of a similar perfectly flat steel plate (the shear field capacity can be found by multiplying Mises shear stress ($\sqrt{f_y}/3$) by the height (h_w) and thickness (t_w) of the steel plate).

4.2.3 Finite Element Analysis

Figure (4.5) shows the predicted buckling modes of the FEA model for a (500 × 500 × 2mm) steel plate strengthened with flat wet-layup GFRP covering the full surface area of the plate, along with buckling modes for the same plate strengthened with either the proposed semi-circular or half-hexagonal corrugated GFRP panels; both having the same thickness and material properties. The critical buckling shear stresses (τ_{cr}) were 43.5MPa, 114.0MPa, and 122.6MPa, for the flat, semi-circular, and half-hexagonal sections, respectively, in comparison to τ_{cr} = 42.5MPa for the initial steel plate without strengthening with clamped boundary conditions.

From the above results, it appears that the new proposed half-hexagonal corrugated FRP panel has the highest buckling stress and therefore it was chosen as the corrugated section to be used throughout this study; the hexagonal section increased the buckling strength by a ratio of approximately three to one in comparison to the control one. A fast parametric study showed that for the classical strengthening technique to achieve the same buckling stress as the proposed one, a 5.9mm thickness GFRP laminate would be required, covering the full surface of the plate. The proposed preformed corrugated FRP panel reduced the required FRP by approximately 8 times (volumetrically) and the required bonding epoxy surface area by 7 times. This did not only reduce the cost of the strengthening process, but it also did not affect the bond strength of the specimen and helped in maintaining the ductile failure associated with un-reinforced steel plate girders, as will be seen later in Chapters 5 and 6.

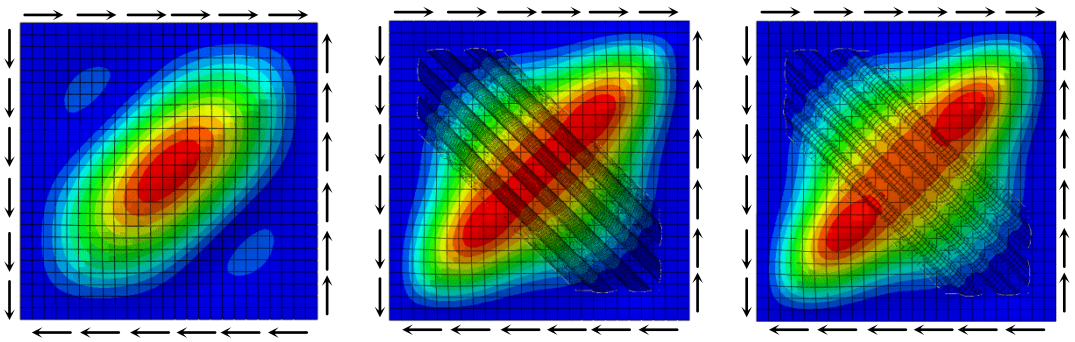

(**a**) Classical technique (**b**) Semi-circular section (**c**) Half-hexagonal section

Figure (4.5): Finite element model of classical and proposed strengthening techniques.

4.3 MATERIAL PROGRAMME

4.3.1 FRP Laminate Material and Geometrical Properties

Four types of woven FRP cloth were used: Carbon fibre 2/2 twill 12k 450g, carbon fibre 2/2 twill 12k 650g, biaxial glass cloth 440g, and biaxial glass cloth 600g. Table 4.1 gives the manufacturer specified properties of the carbon and glass fibres.

Two types of carbon and glass fibre sheets were used in order to maintain the same fibre volume fraction (FVF) for the 2 and 3 layer preformed corrugated FRP panels. Although the longitudinal properties of a composite are dominated by the fibre properties, important parameters such as its ultimate elongation will depend also on the saturating resin used, especially when biaxial fabric sheets are used; this will lower the fibre volume fraction in the longitudinal dimension causing the tensile strength and modulus to be reduced. Despite the reduced tensile strength and modulus of elasticity, this distribution is still preferable in the more complex stress states such as for shear in thin steel plates.

Table 4.1: Manufacturer's fibre properties

	PYROFIL TR50S 12K carbon fibre	**Glass fibre**
Tensile strength (MPa)	2950	2200
Tensile modulus (GPa)	142	80
Ultimate elongation (millistrain)	-	3.5
Typical density g/cm^3	1.82	2.6
Fibre mass per unit length (mg/m)	800	-

4.3.2 Double Lap Shear Tests

Double lap shear (DLS) tests were used for the epoxy selection programme. Test specimens consisted of two plates fabricated from Grade s275 steel, with dimensions as shown in Figure (4.6). These two plates were joined together with preformed GFRP or CFRP sheet panels. Surface preparation for the steel consisted of sanding with 120 grit emery paper to achieve a uniform surface that was free from surface contamination and mill scale. Schnerch (2005) suggested that for the preparation of small areas this provides good mechanical keying suitable for adhesive bonding to steel. Immediately prior to application of the resin, the surface was cleaned with acetone. The plates were clamped using a jig to maintain their alignment during curing.

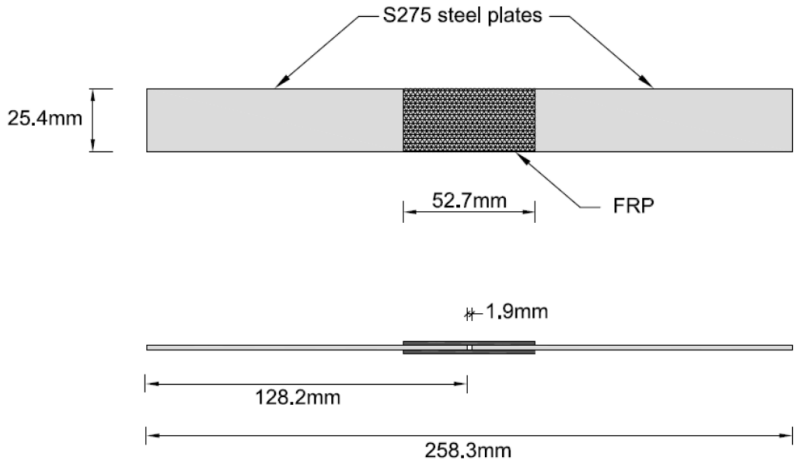

Figure (4.6): Front and side views of typical double lap shear specimen.

During bonding, a uniform coating of epoxy was applied to one side of the steel plate in the bonded region, and the FRP panel was placed onto the steel plates, with 25.4mm of overlap on each of the steel plates. The sheets were then pressed into the resin on the steel plates. A 1.9mm gap was left between the steel plates to minimize the effect of end-to-end bonding. Once the resin had cured sufficiently, the same procedure was repeated on the reverse side. Specimens were cured for at least seven days prior to testing. Figure (4.7) shows the test setup and specimens before and after testing. The CFRP specimens typically failed in debonding due to their high tensile strength while GFRP ones failed typically in shear forming a butterfly shear effect as can be seen in Figure (4.7d).

Three different epoxies were trialled to find the best one for the wet lay-up process and the bonding process. Epoxy resins tested were EL2 resin, Tyfo-s saturant, and Sikadur-330; all of them are two components epoxy matrix material for general bonding applications. Table 4.2 shows their mechanical properties as reported by the manufacturers. Table 4.3 summarizes the average shear strength for the trialled tests. Each value in the table is the average of three tests. In spite the fact that Tyfo-s had the highest bonding average shear stress, EL2 resin was chosen for saturation process due to its easier mixing-curing requirements. Sikadur-330 was chosen as the bonding adhesive for its superior bonding characteristics and its consistency.

Table 4.2: Manufacturer's epoxy-resin properties

	EL2 Cure regime Not Reported	**Tyfo-s** 3-days Curing at 60°C	**Sikadur-330** 7-days Curing at 23°C
Tensile strength (MPa)	67.0-75.0	50.0	30.0
Tensile modulus (GPa)	-	3.18	4.5
Elongation at break (%)	6.0-8.0	5.0	0.9
Flexural strength (MPa)	120.0-130.0	123.4	-
Flexural modulus (GPa)	3.6-4.0	3.12	3.8
Typical mixed 2-component density (g/cm^3)	1.05-1.15	1.11	1.3

Table 4.3: Double shear lap test series results

Specimen	**Load, kN**	**Stress, MPa**
GFRP-600-ES	6.47	5.38
CFRP-650-ES	11.82	9.83
GFRP-600-TS	8.25	6.86
CFRP-650-TS	12.39	10.3
GFRP-600-EE	4.47	3.94
CFRP-650-EE	9.15	7.61
GFRP-600-TE	5.46	4.54
CFRP-650-TE	8.77	7.29
GFRP-600-ET	3.03	2.52
CFRP-650-ET	6.8	5.66

- The first 4 letters stands for glass or carbon fibre reinforced polymer.
- The numbers stand for the weight of the fabric g/m^2.
- The last 2 letters stand for the resin used, E for EL2, T for Tyfo, and S for Sikadur-330. While the order of them specifies which one of them is the saturating resin and which one is the bonding epoxy, as the first stands for the saturating resin and the second for the bonding epoxy.

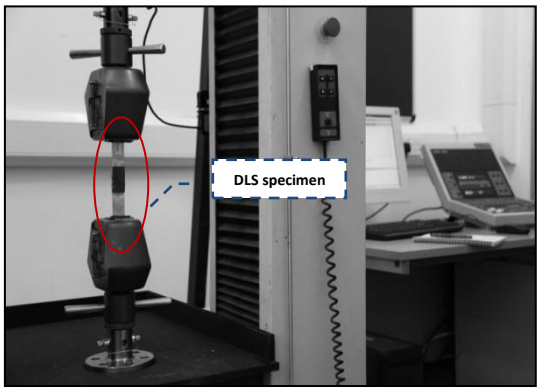

(**a**) DLS test specimen and setup

(**b**) DLS before testing

(**c**) CFRP DLS after testing

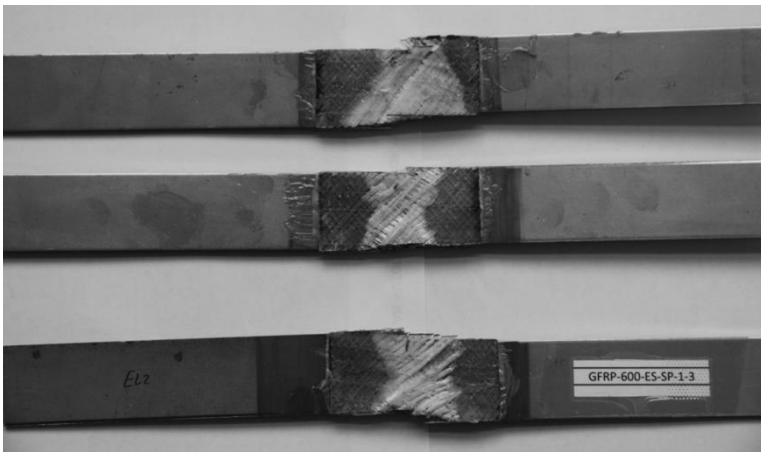

(**d**) GFRP DLS after testing

Figure (4.7): DLS test setup and specimens before and after testing.

4.3.3 Tension Tests

Tension tests were performed to determine the mechanical properties of the CFRP and GFRP sheets using the chosen epoxy from the DLS tests. Test panels were fabricated by wet lay-up whereby the dry fibre sheets were saturated with resin bonded onto a flat release board. The fabric sheets then were covered with a peel ply and a breather layer cloth to absorb the extra resin and then vacuum bagged using a 1.0 bar vacuum pump. Using the vacuum bagging process allowed consistent control of the thickness of the panels and the highest possible fibre volume fraction (FVF) within the section. Figure (4.8) shows the vacuum bagging process for one of the panels.

After sufficient curing at room temperature, the panels were cut into coupons 50mm in width using a tile saw. Pre-manufactured tapered GFRP tabs were bonded to each coupon to prevent premature failure in the wedge action grips of the testing machine. All tabs were bonded using EL2 resin. After bonding, the tabs and adhesive were allowed to cure at room temperature for at least 48 hours before testing.

Figure (4.8): Vacuum bagging process.

The FVF of the specimens was calculated based on the weights of the dry fibre fabric before saturation. Prior to saturation, each length of fabric was carefully weighed. After the FRP panels had achieved sufficient working strength, the entire panel was again weighed to find the weight of the added epoxy resin. The fibre weight fraction (FWF) was calculated in this manner and the fibre volume fraction could then be determined from:

$$FVF = \frac{1}{\left\{1+\frac{\rho_f}{\rho_r}\left(\frac{1}{FWF}-1\right)\right\}} \tag{4.1}$$

where:

FVF = Fibre Volume Fraction.

FWF = Fibre Weight Fraction.

ρ_f = Density of fibres.

ρ_r = Density of the epoxy resin.

The thickness of each coupon was measured at six locations; the width was measured at three locations. Averages of these were used to determine the cross-sectional area of the coupons. All coupons were tested using an electro-mechanical Instron testing frame, under crosshead stroke control at a rate 1.0mm/minute with data recorded at 1.0 Hz. Strains were measured using digital image correlation (DIC). Specimens were painted with a high-contrast pattern and a series of images were captured at 0.2 Hz using a digital camera. A bespoke DIC algorithm (REF) was used to track the movement of pixel patches in the images. Figure (4.9) shows the test setup along with specimens before and after testing.

Table 4.4 gives the mechanical properties of the GFRP and CFRP used in this study along with some other practical aspects, where $\boldsymbol{T_f}$ is the ultimate tensile strength**,** $\boldsymbol{\nu_f}$ is Poisson's ratio, and $\boldsymbol{E_f}$ is the tensile modulus of elasticity of the FRP section. Each value typically represents the average of three unless otherwise mentioned in Table 4 where the superscript stands for the number of averaged tested points. Very high fluctuation was detected in determining Poisson's ratios for the composite materials using DIC technique and the minimum determined values were adopted for convenience.

Table 4.4: Mechanical and geometrical properties of FRP used in this study

Specimen	FVF	T_f, MPa	ν_f	E_f, GPa	Note
CFRP-650	0.58	527.66[3]	0.28[1]	32.23[3]	2-Layers
CFRP-450	0.59	704.51[3]	0.22[1]	48.12[3]	3-Layers
GFRP-600-45°-45°	0.49	34.45[2]	0.50[1]	7.35[2]	2-Layers
GFRP-440-45°-45°	0.48	61.57[2]	-	18.02[2]	3-Layers
GFRP-600-0°-90°	0.49	238.56[2]	0.52[1]	18.71[2]	2-Layers
GFRP-440-0°-90°	0.48	294.14[2]	0.72[1]	14.34[2]	3-Layers

Note: The superscripts in brackets represent the number of performed tests.

Figure (4.10) shows the stress-strain curves for all of the tension specimens tested in this work. The failure was highly dependent on the material type (GFRP vs. CFRP) and the number of layers of FRP fabric sheets in the specimen. The CFRP specimens typically failed in rupture of the specimen somewhere in the middle. However this rupture was very brittle for 2-layered specimens with signs of interlaminar delamination in comparison with 3-layered ones which showed more ductile failure type as can be seen in Figure (4.9c and d). With respect to the GFRP, the failure was more dependent on the glass fibre orientation where the 45° fibre orientations showed more integrity and ductility as can be shown in Figure (4.9f) where even necking took place for the GFRP-440-45° (3-Layers) specimens; whereas the 0-90° showed more severe fracture, but this could be justified by its significantly higher tensile strength. It is worth mentioning here that this significantly high tensile strength of the 0-90° glass fibre orientations wasn't accompanied by any increase in the modulus of elasticity as can be noted from Figure (4.10c and d).

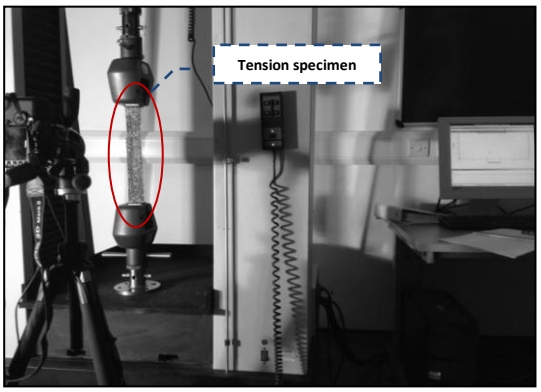

(**a**) Tension specimens with DIC test setup

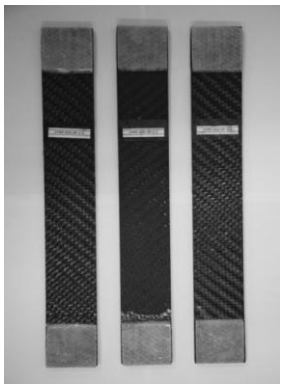

(**b**) Specimens before test

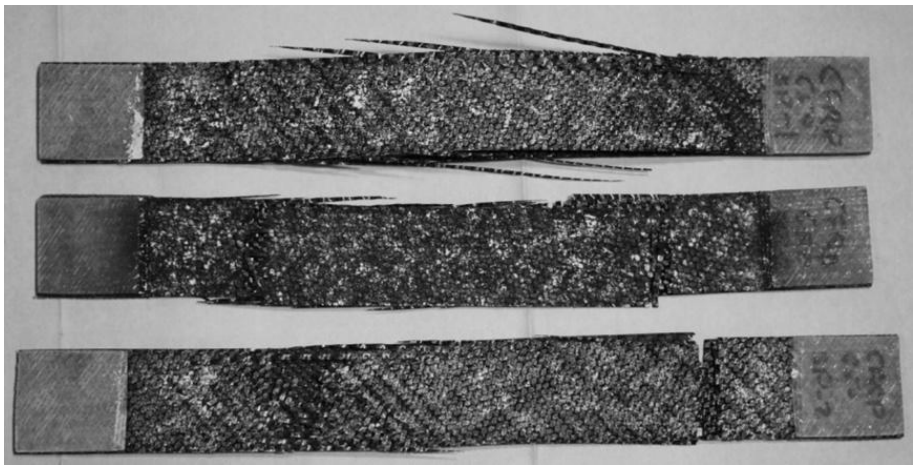

(**c**) CFRP-650 (2-Layers)

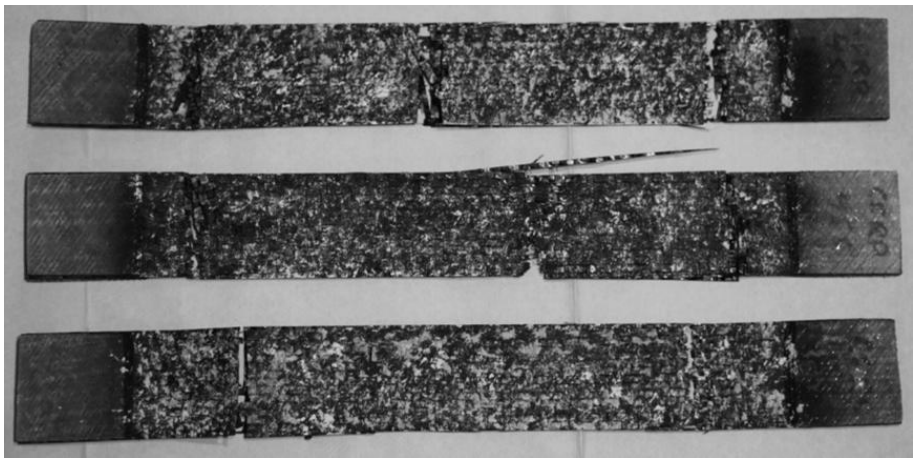

(**d**) CFRP-450 (3-Layers)

Figure (4.9): Tension specimens with DIC test setup and specimens after failure.

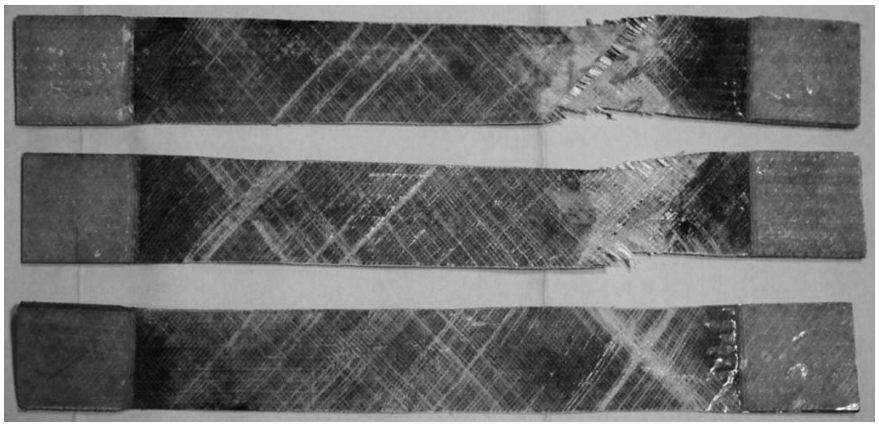

(**e**) GFRP-600-45° (2-Layers)

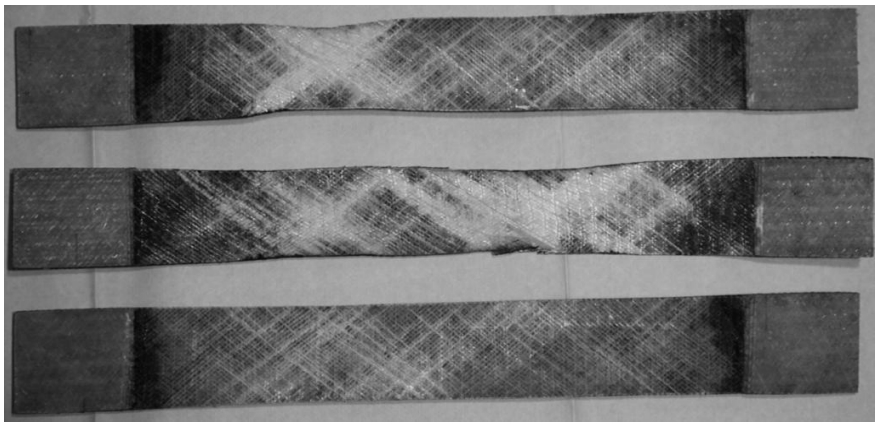

(**f**) GFRP-440-45° (3-Layers)

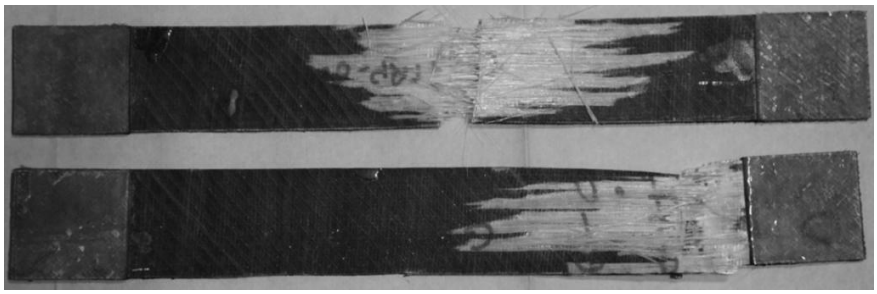

(**g**): GFRP-600-0°-90° (2-Layers)

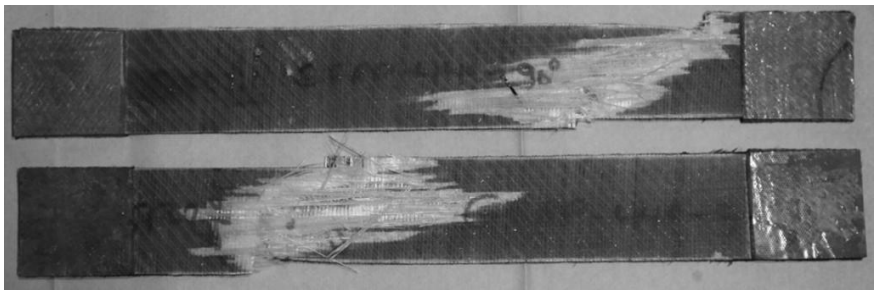

(**h**): GFRP-440-0°-90° (3-Layers)

Figure (4.9 Contd.): Tension specimens with DIC test setup and specimens after failure.

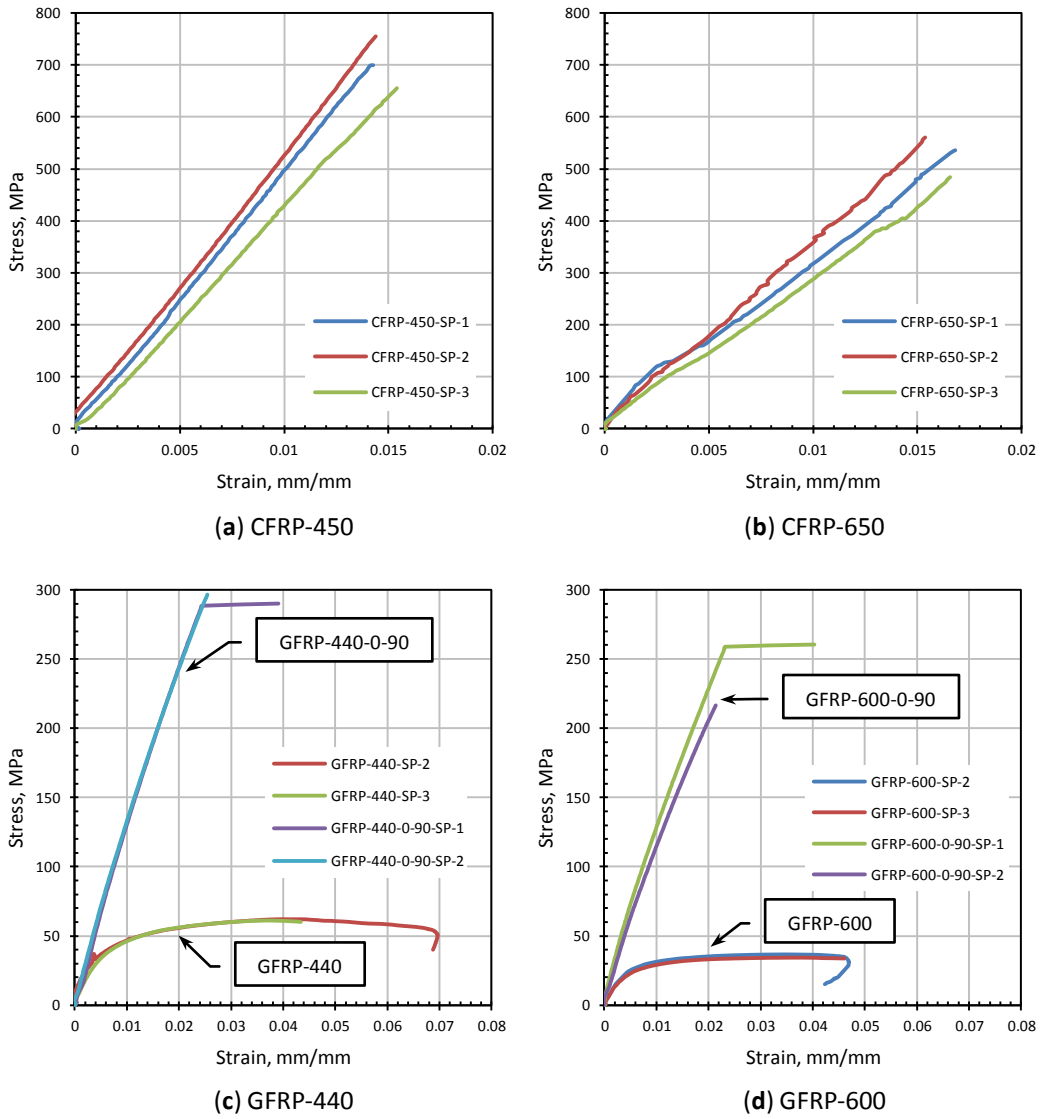

Figure (4.10): FRP tension specimens' stress-strain curves.

4.3.4 Theoretical Calculation of the Composite Mechanical Properties

The following calculations use the simplified theoretical equations available in composite material text books such as (Autar, 2006 and Reddy, 2004) and the available basic mechanical properties sent by the manufacturer. The missing part of data was assumed according to the available values in the literature.

$$E_1 = E_2 = E_{ff}V_f + E_mV_m \tag{4.2.a}$$

$$v_{12} = v_fV_f + v_mV_m \tag{4.2.b}$$

$$\frac{G_{12}}{G_m} = \frac{1+\xi\eta V_f}{1-\eta V_f} \quad (4.2.c)$$

$$\eta = \frac{(G_f/G_m)-1}{(G_f/G_m)+\xi} \quad (4.2.d)$$

where:

E_1 , E_2 : are the tensile composite modulus of elasticity in the longitudinal and transverse directions, respectively.
E_{ff} , E_m : are the fibre and the matrix modulus of elasticity, respectively.
V_f , V_m : are the fibre and matrix volume fractions, respectively.
v_{12} : is the major Poisson's ratio of the composite.
v_f, v_m : are Poisson's ratios of the fibre and the matrix, respectively.
G_{12} : is the Halphin Tsai in-plane shear modulus of the composite.
G_f, G_m : are the fibre and matrix shear modulus, respectively.
ξ : is the reinforcing factor, and can be assumed conservatively equal to 1.

Table 4.5 shows the theoretical calculated values in comparison to the experimentally determined ones for CFRP-450 (3-Layered) and the GFRP-440-45° (3-Layered) composite laminate. These two laminates are the ones that will give the best strengthening for the steel plate as will be seen in Phase-2 (Chapter 5) of the experimental work.

Table 4.5: Composite mechanical properties

	GFRP-440-45°		**CFRP-450**	
Property	**Theoretical**	**Experimental**	**Theoretical**	**Experimental**
E_1 & E_2 , GPa	22.09	18.02	43.88	48.12
v_{12}	0.28	-	0.30	0.22
G_{12} , GPa	3.41	n/a	4.03	n/a

4.4 MANUFACTURING THE CORRUGATED FRP PANELS

As mentioned earlier, in order to provide stiffness increase to the thin steel plates while minimizing the cost of the applied material, a new preformed corrugated FRP panel is used in this study.

The Hex preformed corrugated sections were made by wet layup process using the two types of CFRP and GFRP fabric sheets with two and three layers in an

attempt to maintain the same FVF for all specimens. Vacuum bagging was adopted because of the difficulty of moulding the hexagonal section with traditional techniques.

Firstly, the mould was polished with a releasing agent and left to dry for 24 hours then it was gently greased with wax. Afterward, peel-ply cloth was laid to prevent the FRP from sticking to the mould, and then sufficient quantity of resin was applied to the peel-ply cloth before placing the first FRP fabric sheet layer. This helped ensure a proper amount of resin covered the surface of the FRP from the inner face and a good surface texture was achieved to help bond it to the steel later on. The peel-ply helped keeping the bonding surface of the FRP uncontaminated until the time of bonding it to the steel. Next, each FRP sheet layer was generously covered with resin and shaped to fit the mould profile until the last layer which was covered again with a peel ply and a breathing cloth to help in collecting the extra resin and distribute it within FRP lamina and inter-lamina homogenously. Everything including the mould was then bagged and voids were firmly secured using special gum to prepare it for vacuum bagging. A one bar vacuum pump was used to compress the system together to make sure that the FRP does take the mould's shape, reducing the resin to the minimum sufficient amount, and distribute it homogeneously.

Figure (4.11) shows the vacuum bagging consumable materials along with the first FRP corrugated panel manufacturing attempt. The system was left for at least 24 hours to cure in room ambient temperature and then the FRP panel was de-moulded and shaped by cutting the extra fringes using a band saw.

(**a**) The preformed FRP panel

(**b**) Vacuum bagging consumable materials

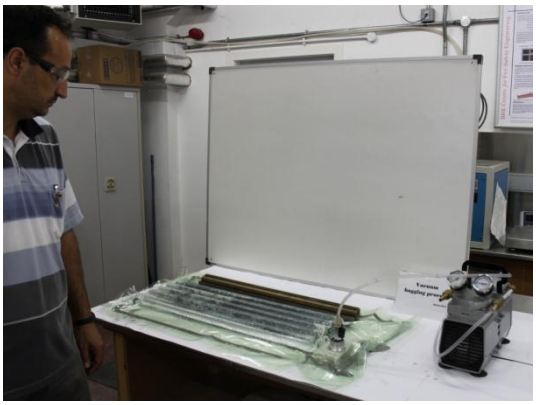

(**c**) Vacuum bagging process

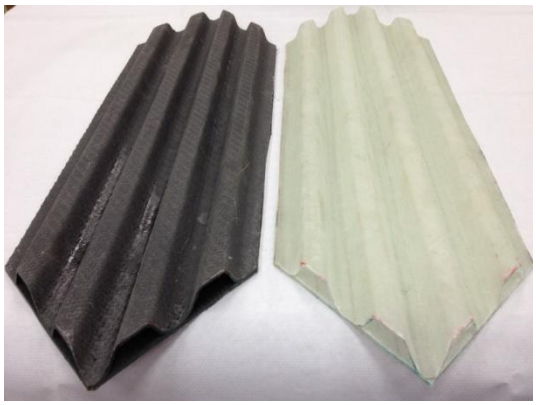

(**d**) Produced Hex closed section panels

Figure (4.11): Preformed FRP corrugated panel and vacuum bagging materials.

4.5 STEEL PLATE MECHANICAL PROPERTIES

First of all, it is worth mentioning that ASTM E8 permits both standard, sub-size, flat, and rounded test specimens. The selected sizes of test specimens in the present study are standard flat specimens. Sheet-type (12.7 x 203.2mm) is used for testing metallic materials in the form of sheet, plate, flat wire, strip, band, hoop, rectangles, and shapes ranging in nominal thickness from 0.127 to 19mm. Plate-type (38.1 x 457.2) specimen is used for testing metallic materials in the form of plate, shapes, and flat material having a nominal thickness of 4.75mm or over.

In the current study, the suitable type of test specimens is the sheet-type because it covers all used gauges of steel plates in the experiments which range from thickness 2.0mm to 12.0mm.

4.5.1 Steel Specimens Details

The experimental programme consists of two main series, the initial series of static tests (phase-2) and the final series of cyclic tests (phase-3). In the initial series only 2mm gauge steel plates are used while the final series involved using 2, 8, 10, and 12mm thick steel plates for the web, transverse stiffeners, secondary longitudinal stiffeners, and flanges; respectively. These were welded together to build up the plate girders. The dog-bone coupon tests will be referred to accordingly as S2 for the initial series and S3 for the final series to be compatible with their designation phase-2 and phase-3, respectively. The series identifiers are in the form SI-T(mm)-X, where I refers to the initial or final series of tests (2 or 3), T is the plate thickness, and X is the specimen number corresponding to the thickness T. Figure (4.12) explains the steel dog-bone coupon identifiers.

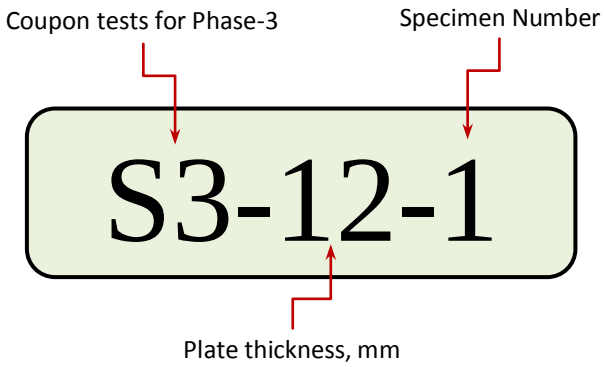

Figure (4.12): Explanation of the designation identifiers for the steel coupons.

Figure (4.13) illustrates the schematic of test specimens for dog-bone steel coupons according to ASTM E8-04. Table 4.6 shows the dimensions and tolerances of all steel plate coupons of Series S2 and S3 in comparison to the standard ones. The actual measurements listed in the tables are the same for all test specimens of each series, as the coupons are cut in groups. Table 4.7 illustrate the thicknesses and the allowable tolerances of the plates used in the present study according to the EN 10051 specifications which are very close to the ASTM standards A568M.

Table 4.6: Dimensions and tolerances of steel plate coupons

Measure	Nominal, mm	Actual, mm	Difference, mm	Tolerance, mm
G	50.8	50.80	0.00	± 0.127
W	12.7	12.75	+ 0.05	± 0.254
R, min.	12.7	12.75	+ 0.05	-
L	203.2	203.2	0.00	-
A, min.	57.15	101.2	+ 44.05	-
B	50.8	50.5	+ 0.30	-
C	19.05	19.01	- 0.04	-

Table 4.7: Thicknesses and tolerances of steel plates, S2 and S3

Source	Nominal, mm	Actual, mm	Difference, mm	Tolerance, mm
Web	2.0	1.92	- 0.08	± 0.17
Flanges	12.0	11.80	-0.20	± 0.40
Stiffeners	8.0 10.0	7.94 9.92	-0.06 -0.08	± 0.33 ± 0.37

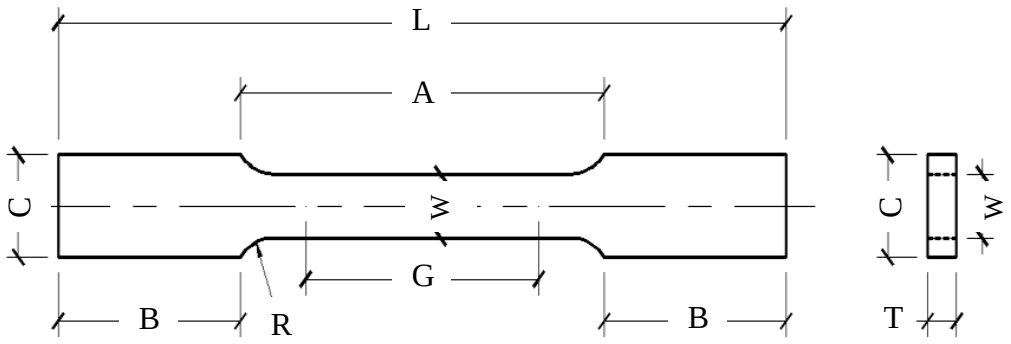

Figure (4.13): Schematic of test specimens of dog-bone steel coupon.

4.5.2 Steel Specimens Tests

To determine the engineering properties of steel plates, uniaxial tension tests were performed on dog-bone coupons cut from the same plate used in building up the girder using a 600kN serve-hydraulic universal testing machine with computer control (Instron 600LX). Strains were measured using digital image correlation

(DIC). Specimens were painted with a high-contrast pattern and a series of images were captured at 0.2 Hz using a digital camera. A bespoke DIC algorithm (REF) was used to track the movement of pixel patches in the images. Figure (4.14) shows the test setup along with specimens before and after testing.

(**a**) Instron 600LX universal testing machine

(**b**) Test set-up.

(**c**) Dog-bone steel coupon before test

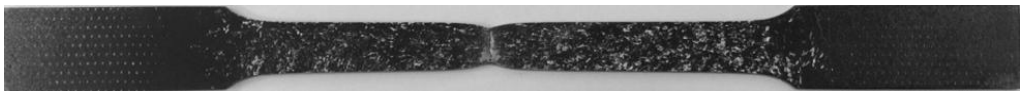

(**d**) Dog-bone steel coupon after test

Figure (4.14): Dog-bone steel coupons and testing machine.

Table 4.8 tabulate the tested steel yield strength (f_y), ultimate strength (f_u), and modulus of elasticity (E_s) for the tested specimens of series S2 and S3. Figure (4.15) shows the stress strain curves for all tested dog-bone steel plate specimens in this work. Figure (4.15a) is dedicated for the 2mm thickness steel plates which were tested in Phase-2 of this experimental programme. From this figure, it can be seen that there is a delay in reaching the ultimate load accompanied with high ductility represented by the high tensile elongation gained. This might be attributed to the fact

that very low loading rate was used (0.2mm/min). This was done in order for the DIC to be able to capture the elastic strain part. However, this led to significant reduction in the expected steel yield strength and modulus of elasticity as can be seen in Table 4.8.

Table 4.8: Steel mechanical properties, S2 and S3

Source	**Thickness mm**	f_y, **MPa**	f_u, **MPa**	E_s, **GPa**
Series-2:				
Steel Plate	2.0	257.99	373.07	173.74
Series-3:				
Web	2.0	280.38	347.05	-
Stiffeners	8.0 10.0	426.96 387.35	527.98 533.16	-
Flanges	12.0	277.962	450.41	-

Figure (4.15b,c,d, and e) show the stress strain curves for specimen tested in Phase-3, namely, 2, 8, 10, and 12mm taken from the web, stiffeners, and flange of the plate girders; respectively. A higher loading rate of 1.0mm/min was used in testing these samples to avoid the technical creep associated problem faced in Phase-2, however, this caused another problem which is that the DIC is not capable of capturing the elastic strain anymore. This was due to the very limited images captured at the initial elastic stage of loading caused by the relatively high speed of the applied stress. For this reason, the strain recorded by the DIC for Phase-3 specimens was ignored and the data from the Instron 600LX extensometer was adopted after multiplying it by a constant correction factor to account for the strain of the machine grips themselves. The factor was predicted so the steel modulus of elasticity would be as close to the globally accepted value of 200GPa as possible. The yield and ultimate stresses are still correctly determined according to the ASTM E8-04 specification which permits the determinations of yield strength by any of the following methods: Offset Method, Extension-Under-Load Method, Autographic Diagram Method and Halt-of-the-Force Method. Figure (4.16) shows typical stress-strain diagrams for steel where in Figure

(4.16a) the steel exhibits yield point elongation (YPE) and upper and lower yield strengths, while Figure (4.16b) shows only a hint of YPE.

Generally speaking, the tests were capable of determining the yielding and ultimate tensile strength of the steel specimens but, unfortunately, were not capable of determining the steel modulus of elasticity within an acceptable margin of tolerance. Hence, the globally accepted value of 200GPa for steel modulus of elasticity is adopted in this work. Another important note here is that the yield strength of steel specimens tested in phase-2 was much less than the expected ones reported by the manufacturer due to the abovementioned reasons. Thus, the standard value of f_y = 275MPa for s275 steel will be adopted in this work for Phase-2, and this was verified by tension tests of Phase-3 which used the same source of 2mm plates and had an average yield strength of 280.38 MPa.

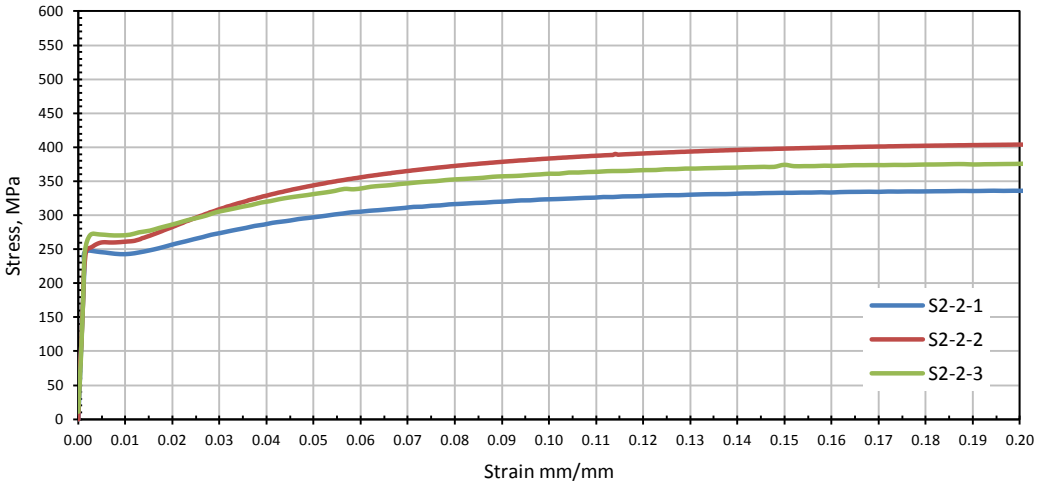

(**a**) Stress-strain curves for steel specimens of series-2

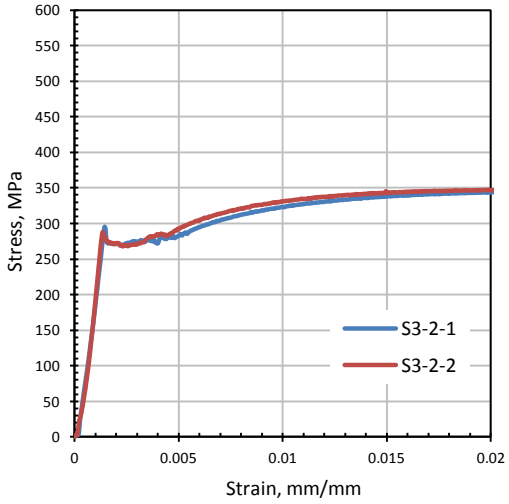

(**b**) S3-2mm specimens

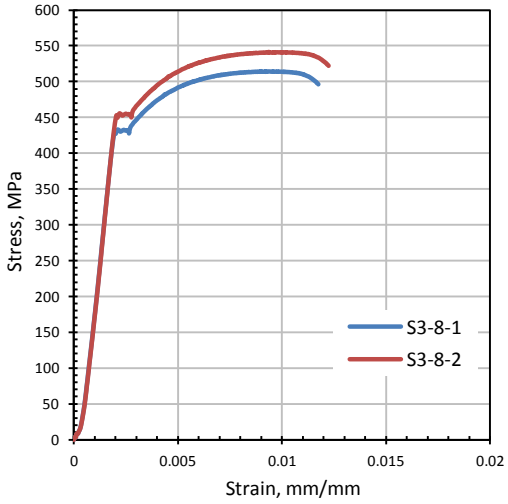

(**c**) S3-8mm specimens

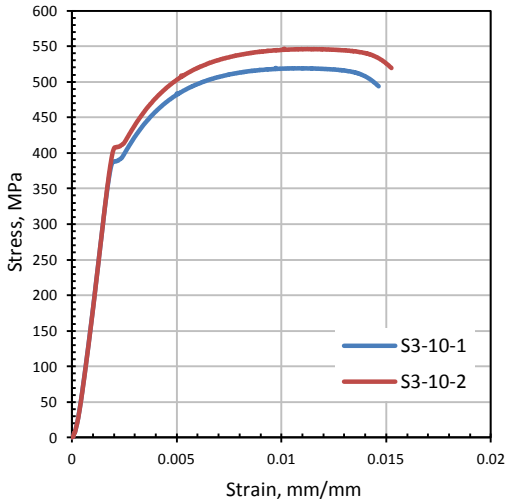

(**d**) S3-10mm specimens

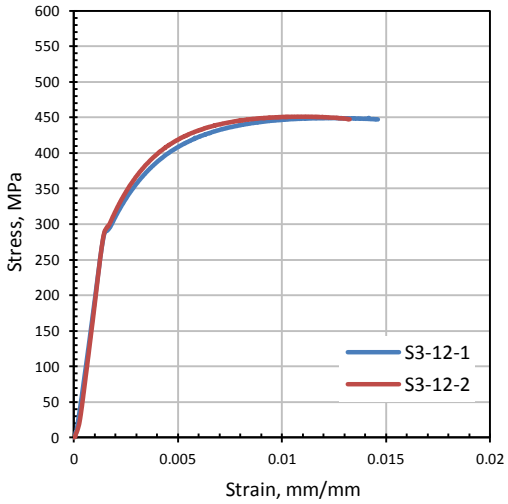

(**e**) S3-12mm specimens

Figure (4.15): Stress-strain curves for steel specimens (for series-2 in (**a**) the strain was measured using DIC, while for series-3 in (**b** to **e**) it was measured using the cross-head travel after multiplying it by a correction factor).

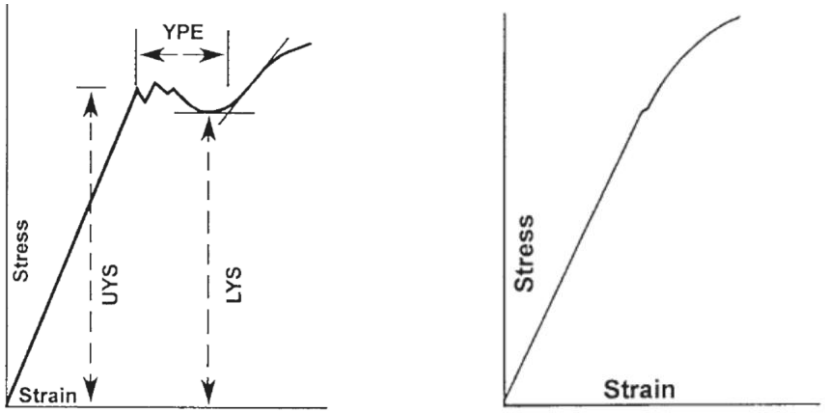

(**a**) Stress-strain diagram showing yield point elongation and upper and lower yield

(**b**) Stress-strain diagram with an inflection but no YPE.

Figure (4.16): Typical Stress-strain curves for steel specimens.

4.6 SUMMARY AND CONCLUSIONS

In this chapter, the geometrical properties of the proposed FRP corrugated strengthening panel were optimized and the material properties were determined.

Both manual calculations and linear buckling finite element analysis was performed to choose the best section among the three proposed ones. The hexagonal FRP corrugated section showed the best performance and managed to reduce the required FRP material by approximately 8 times (volumetrically) and the required bonding epoxy by 7 times.

Based on the observations in this study, it is recommended to limit the second moment of area of the stiffening FRP section so that the ultimate shear capacity of the strengthened composite steel-FRP section does not exceed the shear field capacity of a similar perfectly flat steel plate (the shear field capacity can be found by multiplying Mises shear stress ($\sqrt{f_y}/3$) by the height (h_w) and thickness (t_w) of the steel plate).

The material properties for different FRP laminates which will be used in making the proposed corrugated FRP panels were determined using an extensive experimental programme both for the GFRP and CFRP. The resin and the bonding epoxy were chosen using double-lap shear tests and the material mechanical properties for the FRP were measured experimentally using tension tests. These were also compared with the theoretically calculated ones.

The yield strengths of the steel plates were determined using tension tests performed on steel dog-bone specimens and the modulus of elasticity was assumed to be the typical 200GPa for the steel throughout this work.

CHAPTER REFERENCES

ASTM, Committee ASTM (2014): "Designation A568M, Standard Specifications for General Requirements for Steel, Sheet, Carbon, Structural, and High-Strength, Low-Alloy, Hot-Rolled and Cold-Rolled," Annual Book of ASTM Standards, ASTM Inter., West Conshohocken, USA, 31 pp.

ASTM, Committee ASTM E28 (2004): "Designation E8-04, Standard Test Methods for Tension Testing of Metallic Materials," Annual Book of ASTM Standards, ASTM Inter., West Conshohocken, USA, 17 pp.

AUTAR K.K. (2006) " Mechanics of Composite Materials," 2nd edition, Taylor & Francis, 457 pp.

EUROPEAN COMMITTEE FOR STANDARDISATION (EN-10002-1-2001): "Metallic Structures Tensile Testing- Part 1: Method of test at ambient temperature," 56 pp.

EUROPEAN COMMITTEE FOR STANDARDISATION (EN-10051-1-2001): "Continuously hot-rolled strip and plate/sheet cut form wide strip of non-alloy and alloy steel – Tolerances on dimensions and shape," 16 pp.

REDDY J.N. (2004). "Mechanics of Laminated Composite Plates - Theory and Analysis," CRC Press, USA, 2nd Edition, 831 pp.

SCHNERCH D.A. (2005) "Strengthening of steel structures with high modulus carbon fibre reinforced polymer (CFRP) materials," PhD Thesis, North Carolina State University, 265 pp.

Chapter Five

PHASE-2

Initial Static Series of Tests

5.1 INTRODUCTION

To provide stiffness increases to thin steel web plates while minimizing material cost and preserving the ductile failure type associated with steel plate girders, a new preformed corrugated FRP panel was introduced in Chapter 4 (Phase-1).

The proposed FRP profiled section will be checked in this chapter through an initial series of tests (Phase-2) to prove its validity in stiffening steel plates against buckling under in-plane static shear loading. The main objective of this initial series of tests is to determine the most effective arrangement for strengthening (stiffening) thin-walled steel plates against out-of-plane displacement under the action of in-plane static shear loading. The tested variables can be listed in the followings:

- The type of FRP used (CFRP or GFRP).
- The number of layers of fabric for the same nominal fibre volume fraction.
- The bonded length along the compression diagonal.
- The FRP panel section (open vs. closed section).
- The orientation of the glass fibres with respect to the axis of corrugation for GFRP profiled panels.
- The shape of the FRP panels' end cut.

Figure (5.1) shows the geometry, section, end cut shape and position, and fibre orientation for the preformed corrugated FRP panels. The geometry and section were already discussed in Chapter 4; while the end cut shape and position were chosen for practical convenience to explore different scenarios and their effect on the behaviour of the strengthened specimens. The dimensions of the steel plate and the FRP corrugated panels are kept constant during this initial series of tests (phase-2).

Finally, the optimized FRP panel from this series will be further investigated in Phase-3 (Chapter 6) for its efficiency in increasing the stiffness of the webs of steel plate girder against shear buckling and reducing the breathing phenomenon under cyclic loads, a typical loading scheme for structures like bridges.

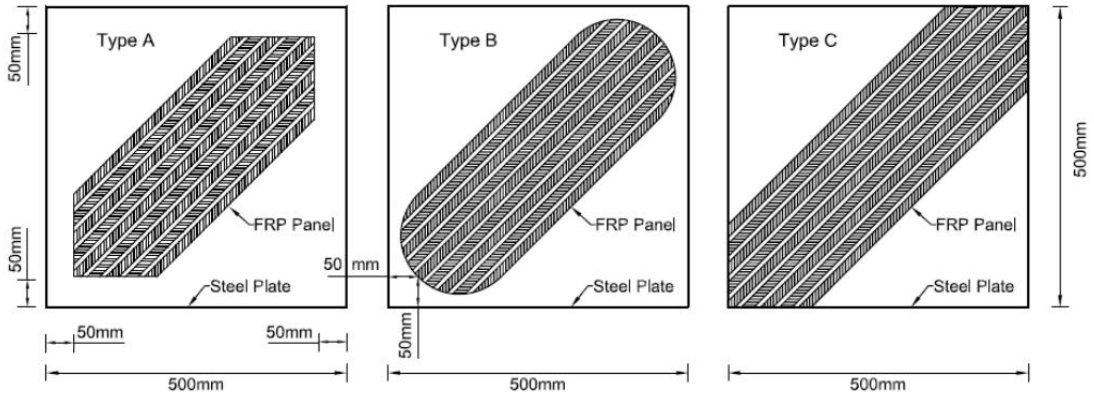

(**a**) FRP strengthening configurations

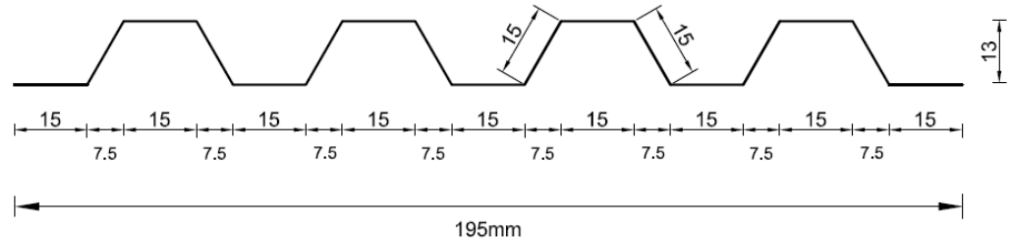

Open FRP section

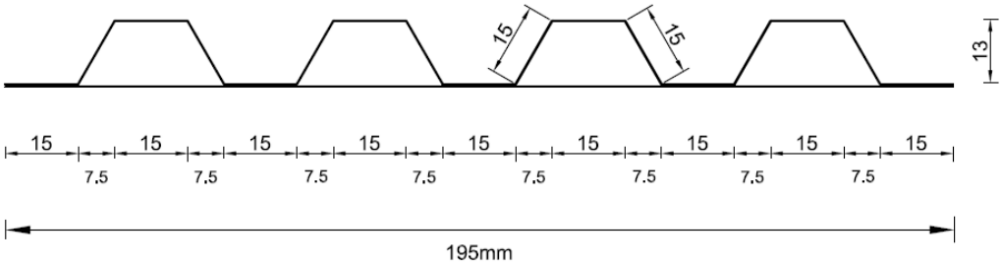

Closed FRP section

(**b**) Open versus closed FRP corrugated sections

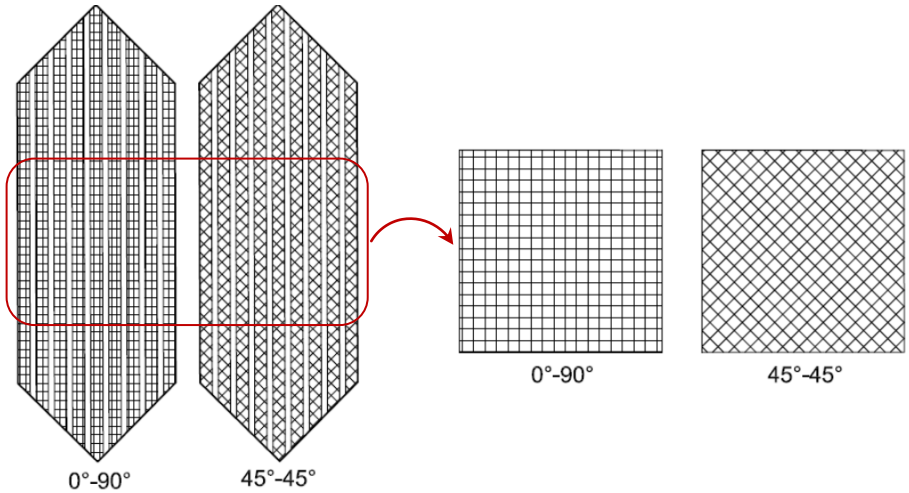

(**c**) Fibre orientations with respect to the axis of corrugation

Figure (5.1): Position, section, and end cut shape of FRP panels used in Phase-2.

5.2 SPECIMEN DESCRIPTION AND DESIGNATION

The specimen that will be used throughout this initial series of tests is a typical square S275 steel plate having the dimensions of 600×600 mm and a thickness of 2mm. It is important to note that these are the total dimensions of the steel plate including a 50mm edge strip that will be clamped in the testing rig (section 5.3), therefore the net dimensions that will be tested are 500×500mm. These dimensions result in an aspect ratio (a_w/h_w =1.0) and a slenderness ratio (h_w/t_w =250).

The dimensions of the steel plate were chosen to simplify the process of designing and building the testing rig, as discussed in detail in section (5.3). The relatively high slenderness ratio of 250 was chosen for two reasons; the first one is that this slenderness ratio is at the end of the allowed practical margin and hence it is worthwhile exploring, and the second reason is that the more slender the plate is, the more the effect of the strengthening technique will be revealed. An additional reason for using these relatively light plates is to keep the test loads within the limits that do not affect the big testing frame in the structures lab. The plates have a typical yielding strength of 275MPa and a modulus of elasticity of 200GPa as was shown in detail in Chapter 4.

As mentioned in the above introduction, there are several variables varied in the design of the bonded FRP panel which led to 13 tests in this series. To identify the specimens in this series of tests, each specimen was given a unique designation to distinguish them effectively. The designation is

G/CFRP-2/3L- (0°-90°/45°-45°)- A/B/C

where:

C/G:	Refers to Glass or Carbon Fibre Reinforced Polymers,
2/3:	Refers to 2 or 3 Layers of the FRP composite,
0°-90°:	Refers to the perpendicular glass or carbon filaments distribution,
45°-45°:	Refers to the angled filament distribution in the case of glass fibres only,
A/B/C:	Refers to the three types of the end cut shape of the FRP panel as can be seen in Figure (5.1a).

For example, CFRP-2L-(0°-90°)-A, refers to a carbon fibre panel having 2 layers of fabrics with perpendicular filament arrangement and a type A end cut shape.

5.2.1 Test Variables

The parameters varied in the current study were the type of FRP (CFRP or GFRP), the number of layers of fabric for the same fibre volume fraction, the bonded length along the compression diagonal, the FRP panel section (open vs. closed section), the orientation of the glass fibres with respect to the axis of corrugation, and the shape of the preformed panels' end cut. These are shown in Table 5.1; refer to Figure (5.1) for additional details.

Table 5.1: Test variables

Ref.	Specimen	FRP type	Panel type	No. of layers	Fibre orientation
SP-1-4	Control Specimen	-	-	-	-
SP-2	GFRP-2L-(45°-45°)-A	Glass	Type A	2-Layers	+45°/-45°
SP-3	CFRP-2L-(0°-90°)-A	Carbon	Type A	2-Layers	0°/90°
SP-4	GFRP-2L-(45°-45°)-A-Closed*	Glass	Type A	2-Layers	+45°/-45°
SP-5	CFRP-2L-(0°-90°) - A-Closed*	Carbon	Type A	2-Layers	0°/90°
SP-6	GFRP-3L-(45°-45°)-A	Glass	Type A	3-Layers	+45°/-45°
SP-7	CFRP-3L-(0°-90°)-A	Carbon	Type A	3-Layers	0°/90°
SP-8	GFRP-2L-(0°-90°)-A	Glass	Type A	2-Layers	0°/90°
SP-9	GFRP-3L-(0°-90°)-A	Glass	Type A	3-Layers	0°/90°
SP-10	GFRP-2L-(45°-45°)-B	Glass	Type B	2-Layers	+45°/-45°
SP-11	CFRP-2L-(0°-90°)-B	Carbon	Type B	2-Layers	0°/90°
SP-12	GFRP-2L-(45°-45°)-C	Glass	Type C	2-Layers	+45°/-45°
SP-13	CFRP-2L-(0°-90°)-C	Carbon	Type C	2-Layers	0/90

* Closed refers to the closed section FRP panel (see Figure 5.1)

5.3 DEVELOPMENT OF THE TEST METHOD

The classical method for testing the shear panel of plate girders is to test small or large scale plate girders, combining the two end panels into one plate girder because the end panels represent the most critical shear loading along a plate girder's span, see Figure (5.2a). However, this is a costly method because every time a variable is changed in the experimental programme a new specimen has to be built for the new test.

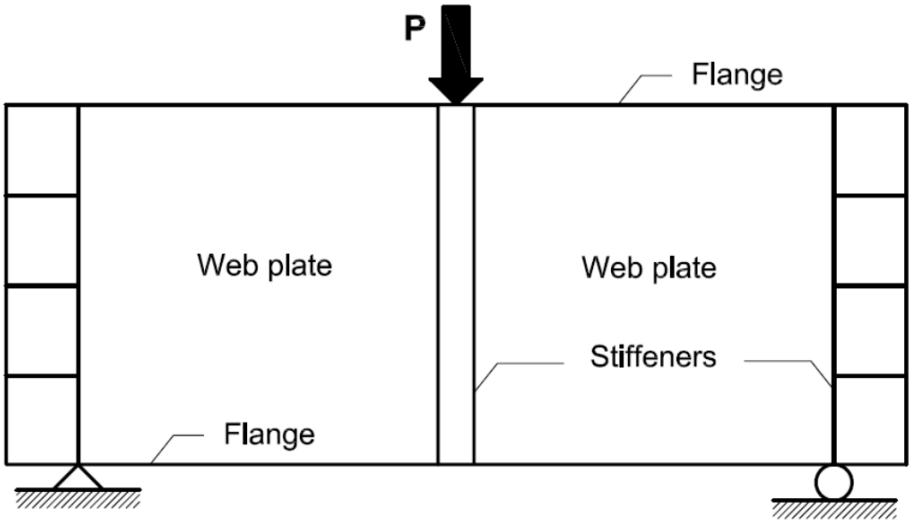

(**a**) Typical steel plate girder specimen

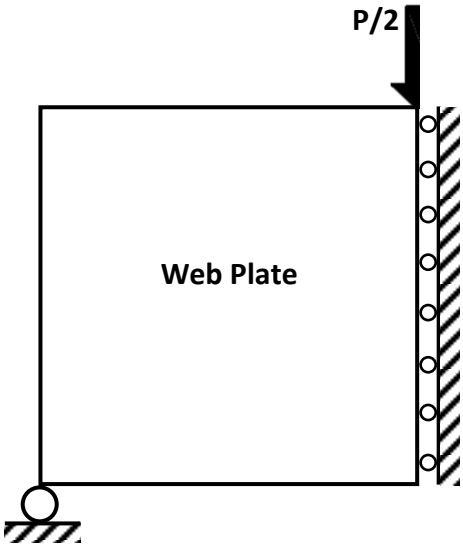

(**b**) Symmetric boundary conditions

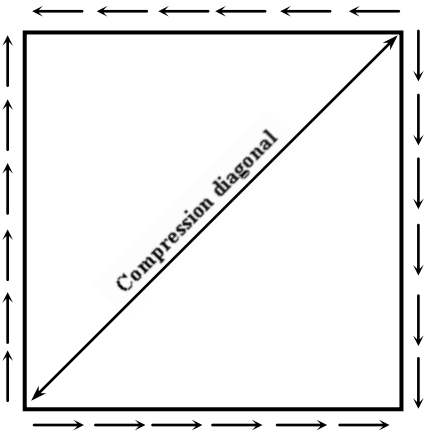

(**c**) Analytical model under pure shear

Figure (5.2): Exploiting symmetry in the shear test of a steel plate girder specimen.

In theory, both for analytical and numerical analysis, usually the rule of symmetry is exploited to the optimum by modelling only half of the symmetric member or structure to reduce the cost of calculations. However, this is considered very difficult from a practical point of view because of the arising problems associated with applying the correct boundary conditions on only one half of the member. Figure (5.2b) illustrates the symmetric boundary conditions for the steel plate girder shown, while Figure (5.2c) shows the analytical case where a web plate is under pure shear condition. In both cases the plate shear resistance is greatly dependent on the applied boundary conditions at the web plate four edges (Lee et al., 1996).

In the current work a new testing rig is introduced (called "Picture-Frame" from now on). The picture-frame is capable of holding a flat steel plate, applying clamped boundary conditions and in-plane shear loading, simulating the web of a steel plate girder with heavy flanges and stiffeners, see Figure (5.3). The new testing rig clamps the steel plate boundaries into a stiff steel frame using bolts that do not penetrate the steel plate itself to avoid stress concentrations. They rely on the friction between the frame grip and the steel plate, which was extended 50mm from its four sides inside the picture-frame. The picture-frame is capable of moving only in-plane using 4-hinged beam-chain mechanism and thus applies in-plane shear force on the steel plate. The in-plane movement is achieved using 8 mirrored hinges (instead of 4) to avoid cutting the steel plate corners which will affect the stress distribution and to make sure that the loads are applied throughout these corners for a better simulation of buckling of steel plates under shear loading.

The boundary conditions at the junction between the web, flanges and stiffeners, was discussed in Chapter 3. It was shown that it is almost impossible to reach the fixed boundary conditions at the web plate boundaries for plate girders with practical flanges and stiffeners' sections; however, simply supported boundary conditions are not realistic either (especially for thin-walled web plates). With the picture-frame testing mechanism, it is practically very difficult to apply realistic boundary conditions to the plate boundaries with different elastic restraining degrees at the junction depending on the rigidity of the flanges and stiffeners. Therefore, fixed boundary condition was chosen because it is easier to implement and it is more realistic for plates with high slenderness ratios.

It is worth mentioning that a minor cost study was performed and the cost of manufacturing each steel plate girder specimen like the one in Figure (5.2a) exceeded £2000. Building the picture-frame itself cost a similar amount but it is built for unlimited number of tests, each test then costs only the price of the tested steel plate.

The validity of the design of the picture-frame testing rig was established using finite element simulations which included modelling different scenarios with respect to the boundary conditions applied to the steel plate, the location of the hinges, and the distribution of the stresses developed in each component of the frame and the tested steel plate, Figure (5.4) shows the final finite element model which is built and used in the current series. More details of the finite element model are discussed in section (5.7).

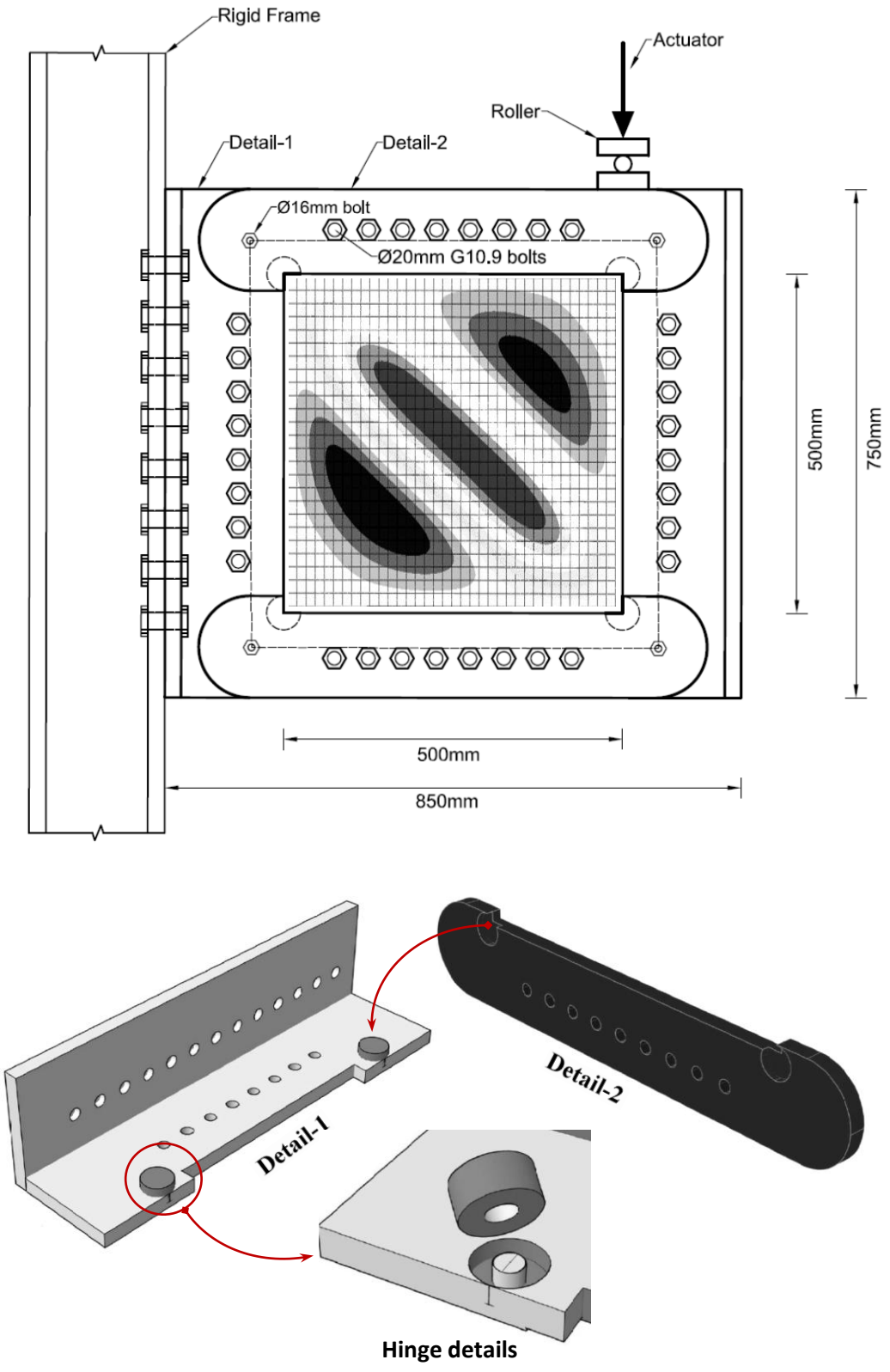

(**a**) Picture-frame diagram and details

Figure (5.3): Picture-frame analogy.

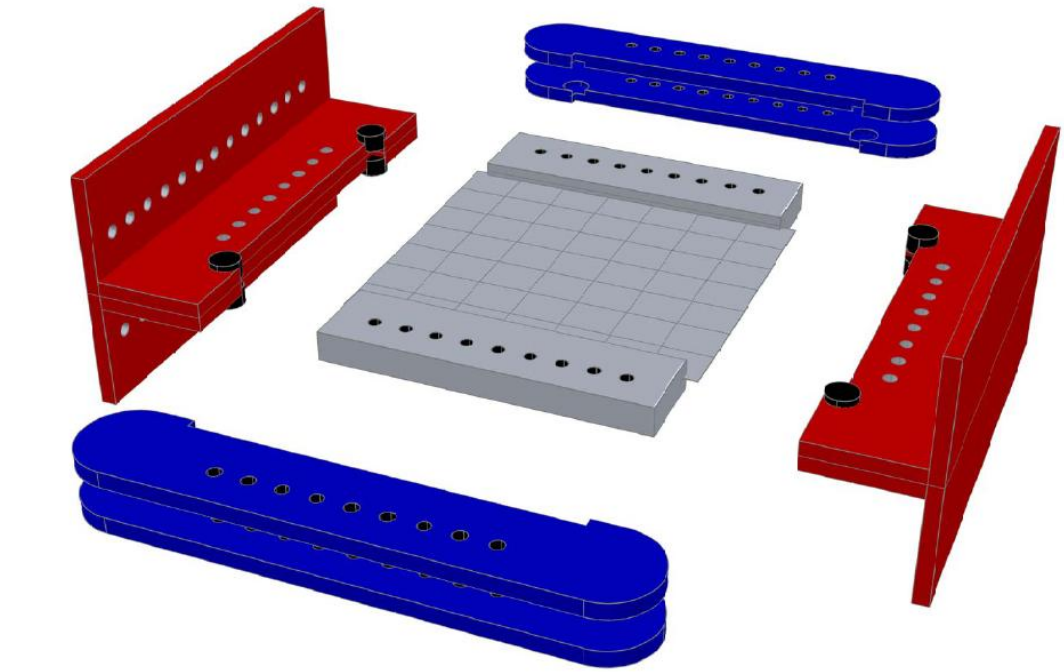

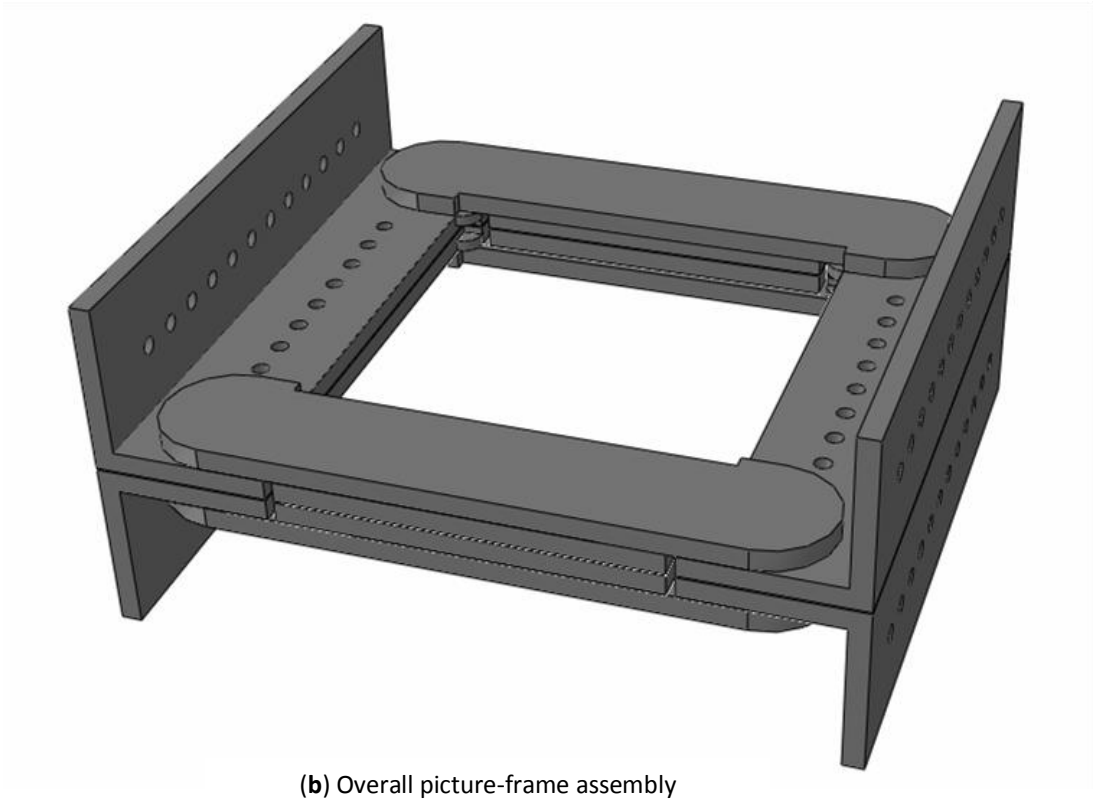

(**b**) Overall picture-frame assembly

Figure (5.3 Cont.): Picture-frame analogy.

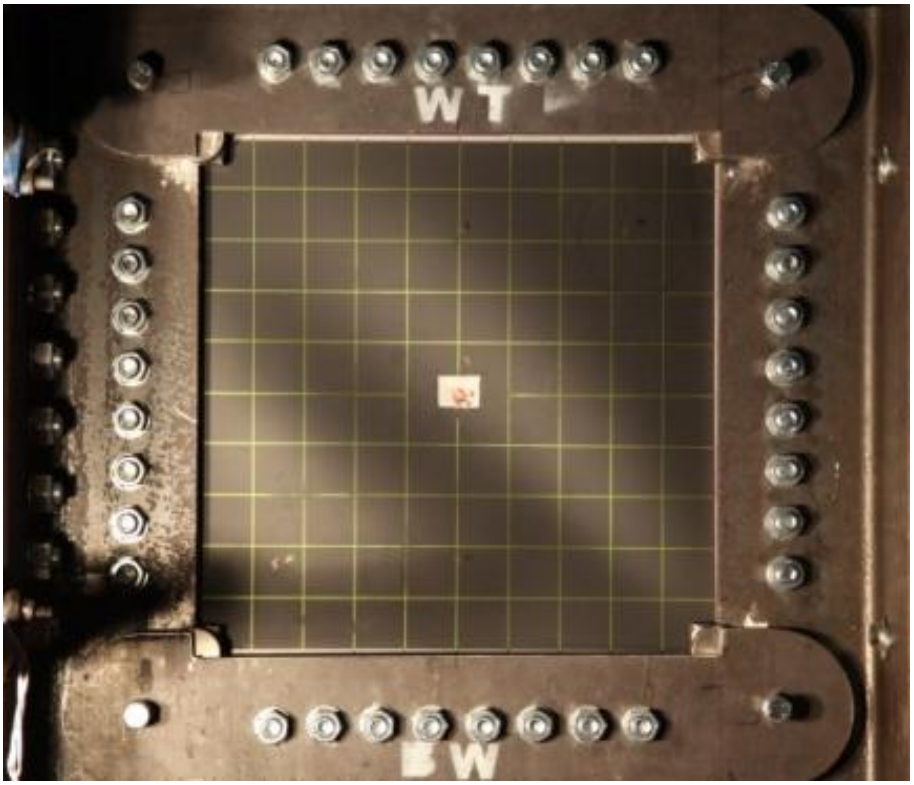

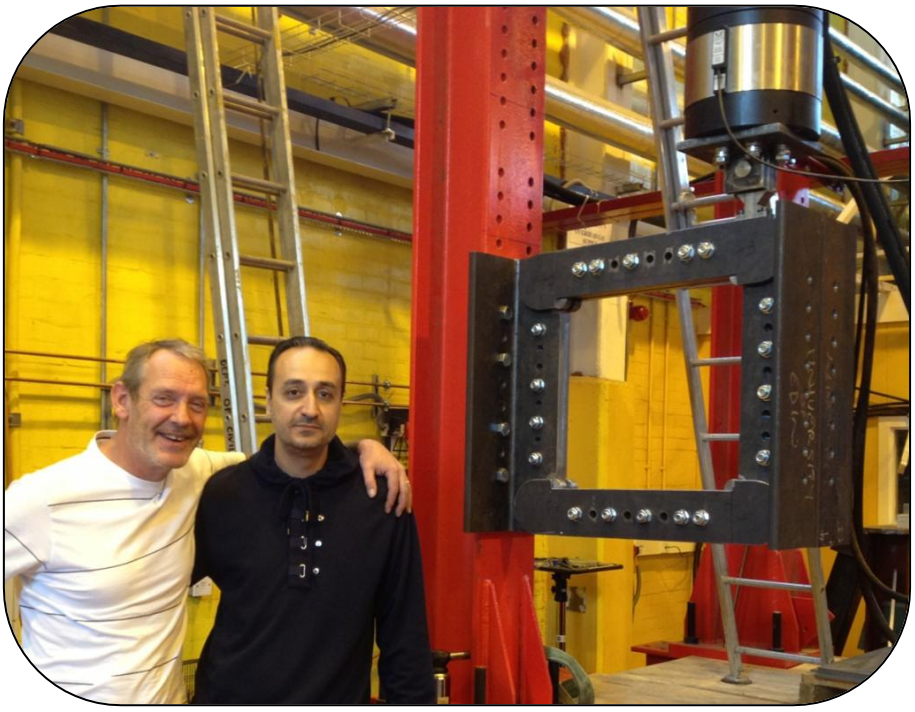

(**c**) Final assembly of the picture-frame in the lab

Figure (5.3 Cont.): Picture-frame analogy.

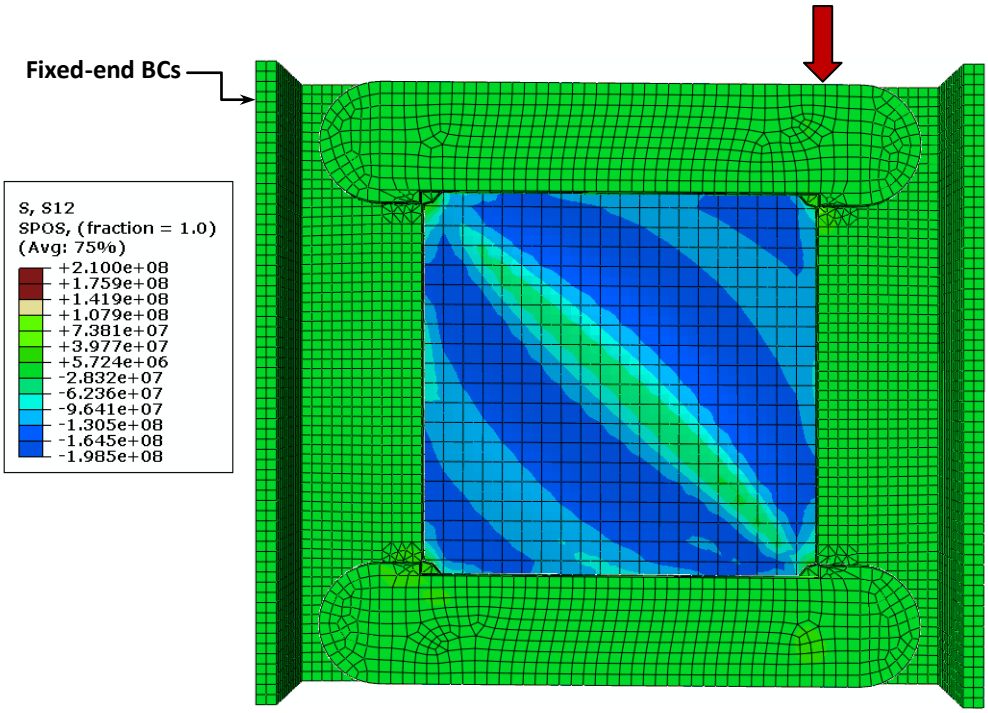

(**a**) Shear stress distribution (N/m^2)

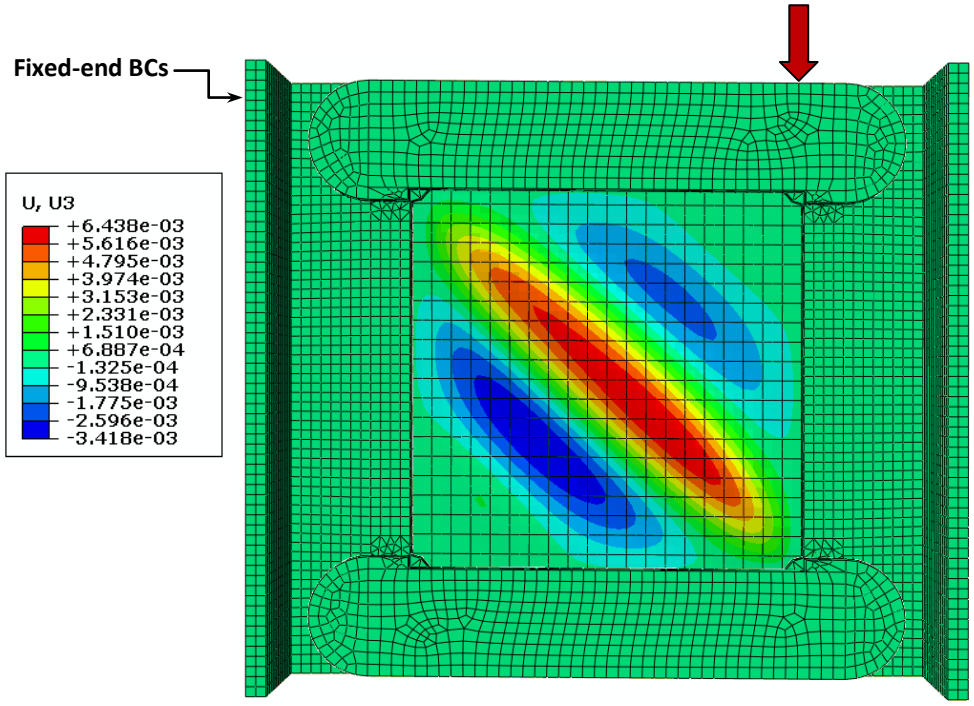

(**b**) Out-of-plane displacement (m)

Figure (5.4): Finite element modelling of the picture-frame.

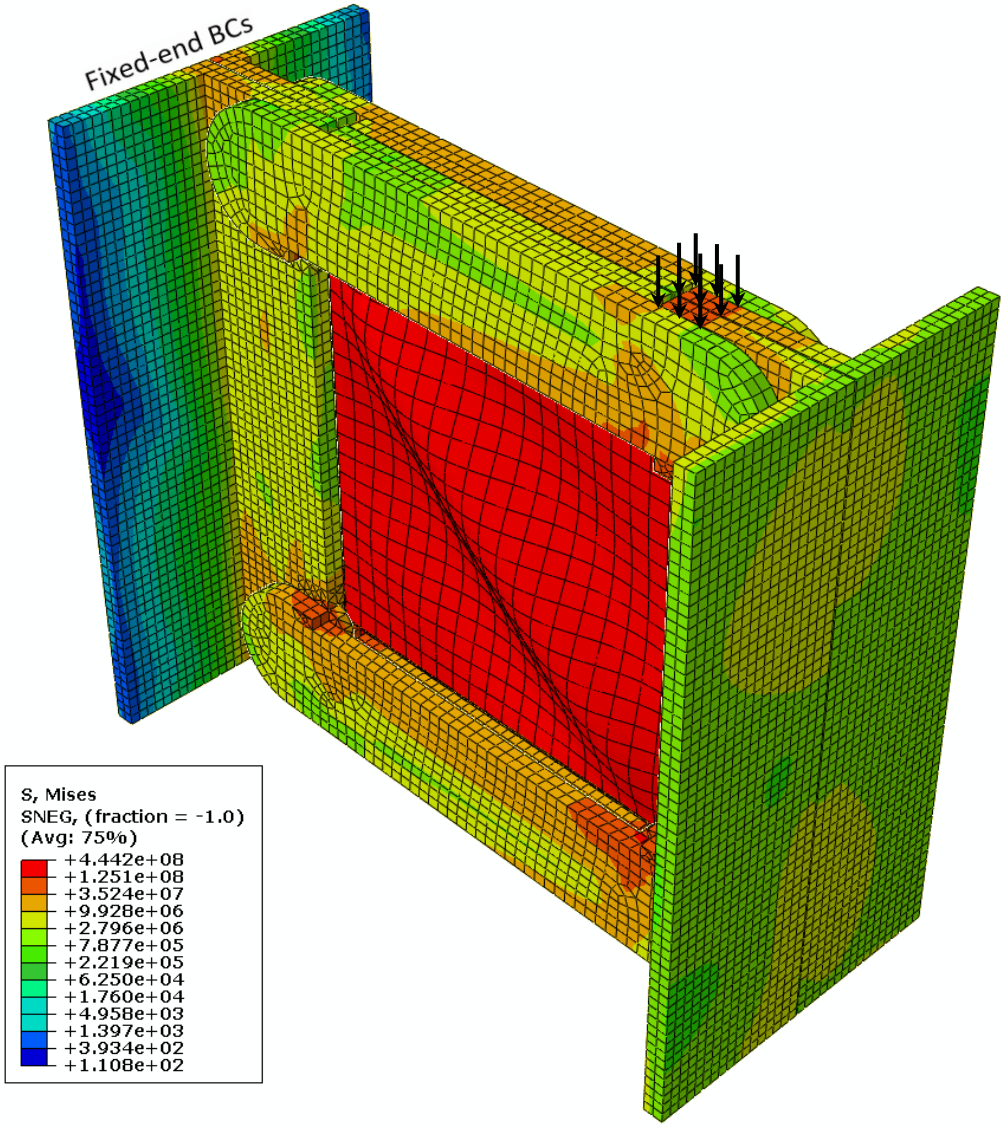

(**c**) Three dimensional visualization of logarithmic scale Von Mises stress distribution in the plate and picture-frame components (N/m^2)

Figure (5.4 Cont.): Finite element modelling of the picture-frame.

5.3.1 Testing Rig Setup

In spite of the fact that the picture-frame is a testing rig itself, it needs a bigger frame to be attached to. This bigger frame needs to be stiff enough to hold the picture-frame in position and hold the actuator during the application of the load without showing any significant deformations during the test. Figure (5.5) shows a schematic drawing for the overall configuration in addition to some photos for the assembly process.

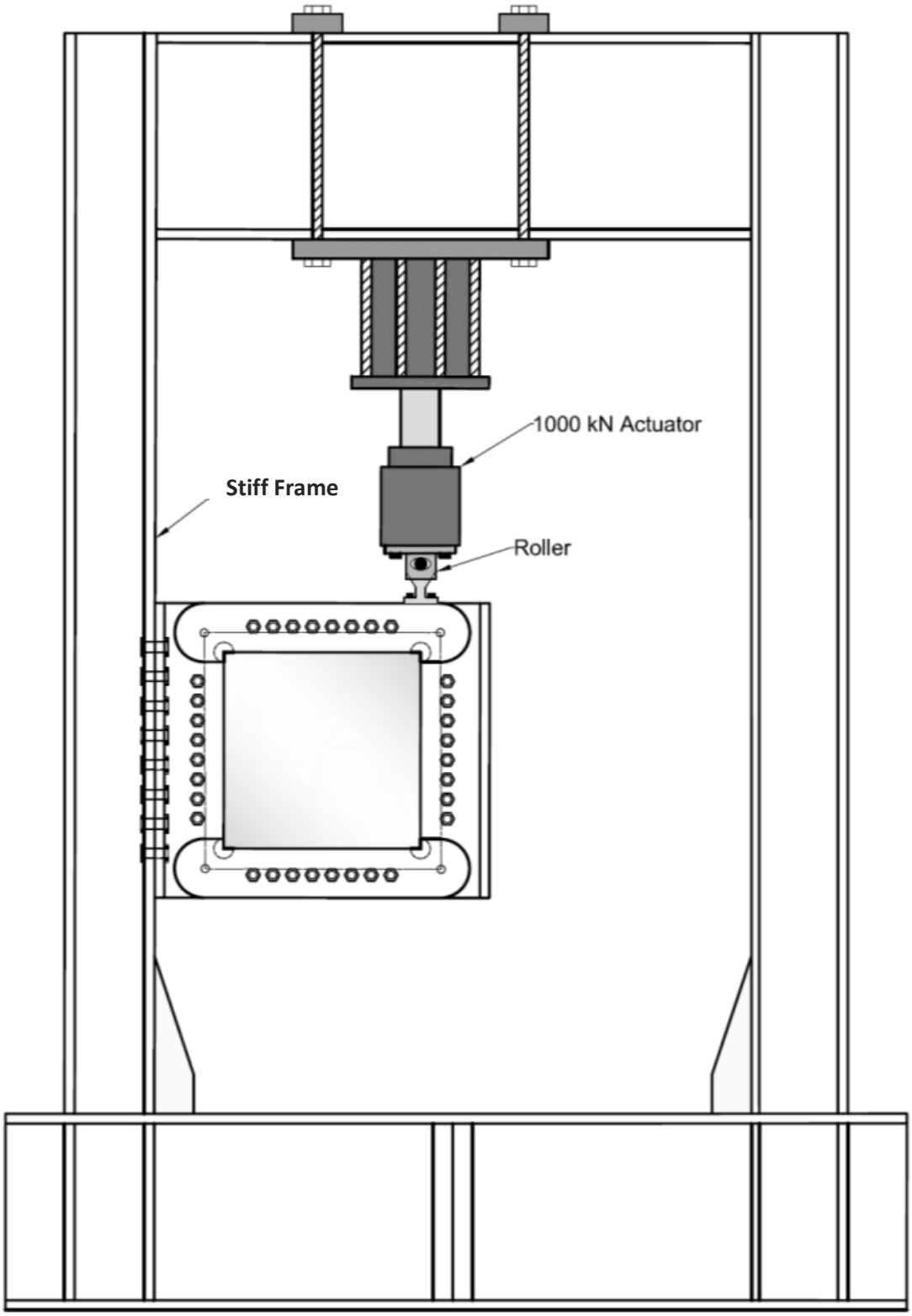

(**a**) Diagram showing the big frame in the structures lab holding the actuator and the picture-frame

Figure (5.5): The overall configuration of the test setup for the picture-frame.

(**b**) Re-assembling the big red frame in the structures lab with the technician staff

(**c**) Final Configuration

Figure (5.5 Cont.): The overall configuration of the test setup for the picture frame.

5.4 SPECIMEN PREPARATION

Except for the control specimen, which was an intact steel plate and was not strengthened with FRP, the following procedure applies for all the other 12 specimens. First the specimen was grit blasted to the required texture according to ASTM D2651 which allows using grit blast for preparing the surface of the metal for bonding. The grit blasting was performed in a blast cabinet with an average air pressure of 7.0 bars. The grits used were grade 60 aluminium oxide abrasive powder. Figure (5.6) shows the texture of a grit blasted steel plate in addition to a photo showing the used blast cabinet. During grit blasting, an effort was made to keep the angle of application of the grits constant to obtain almost the same texture for all the specimens, this was verified later with pull-off adhesion tests which gave a close average of bond strength for all the specimens; refer to section (5.4.1).

The specimen was then cleaned with a brush and a vacuum cleaner until a surface clean from dust was reached. It was then washed with acetone generously to make sure that the steel surface is free from all contamination which could cause premature debonding failure. The epoxy was then mixed, according to the manufacturer's specifications, then applied to the steel plate and the FRP panel after removing the peel-ply cloth. The peel-ply helped in keeping the FRP panel uncontaminated and with a good bonding texture. Then the FRP panel was attached to the specimen using a special fixture to hold it in position, see Figure (5.7). The same procedure was applied for the pull-off test dollies (refer to section 5.4.1) which were bonded at the same time using the same epoxy. Finally, a uniformly distributed load was applied to press the panel toward the steel plate to reduce air bubbles. The load was maintained for 24 hours and then removed. Figure (5.7) shows photos for the bonding process.

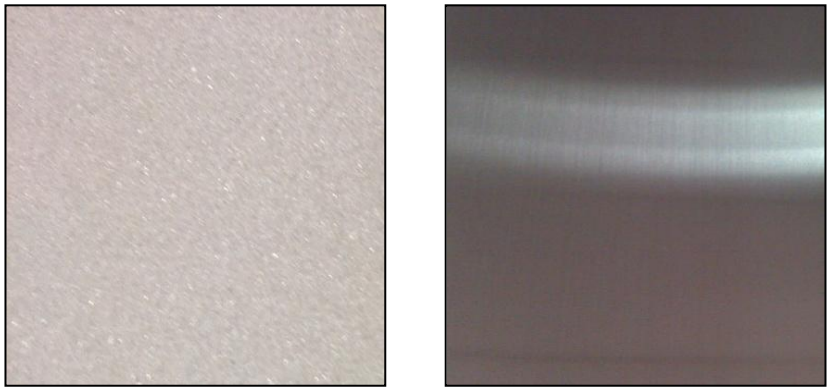

After grit blasting Before grit blasting

(**a**) Part of a steel plate before and after gritting

(**b**) Grit blasting cabinet and grit abrasive powder

Figure (5.6): Grit blasting technique.

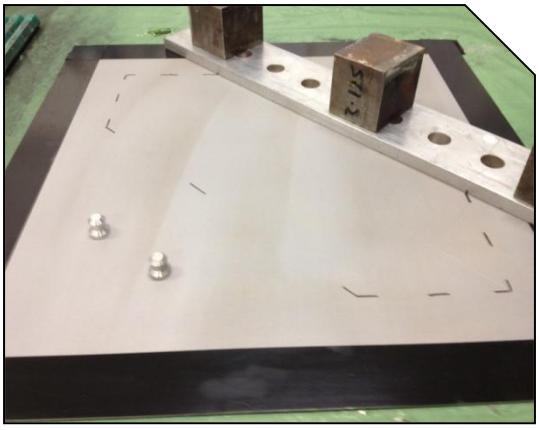

(**a**) Marking the specimen layout

(**b**) Peeling the peel ply of the FRP

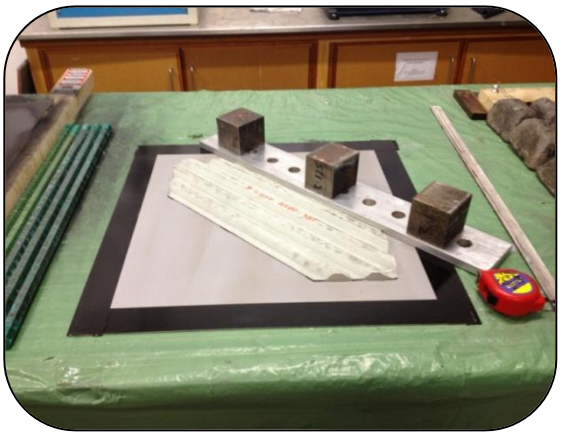

(**c**) Preparing the specimen for bonding

(**d**) Mixing the 2-component epoxy

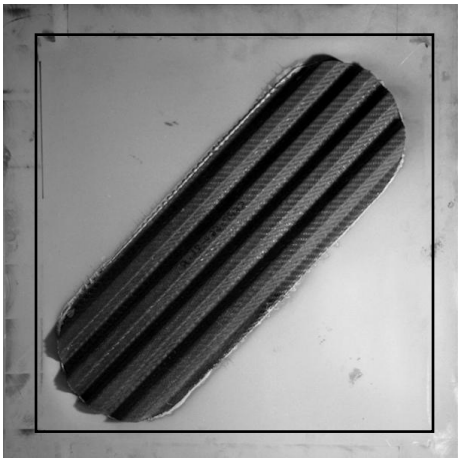

(**e**) Specimen after bonding the FRP panel

Figure (5.7): The bonding process.

5.4.1 Adhesion Test

The adhesion energy of the surface was determined using a 20mm pull-off dolly with digital adhesion tester according to ASTM D4541-09. Adhesion tests were performed after 24 hours and 7 days of curing at room temperature. The adhesion strength varied between an average of 7.65 MPa and 8.21 MPa for the 24 hour and 7 day tests, respectively. Figure (5.8) shows the adhesion test.

(**a**) Digital adhesion tester

(**b**) Adhesion test

(**c**) A dolly after test

Figure (5.8): The Adhesion test.

5.4.2 Assembling the Picture-Frame for the Test

After the plate was strain gauged (refer to the instrumentation section 5.5), it was painted and taken to the structures lab to be inserted in the picture-frame. First the picture-frame was dis-assembled, and then the steel plate was carefully inserted in

the right position using a specially made jig. Afterward, the picture-frame was re-assembled and the required grip was fulfilled by tightening thirty-two 20mm G10.9 high-strength bolts to the required torque. The bolts were tightened from inward to outward in three cycles to make sure no gaps are left between the steel plate and the picture-frame. The first cycle was done with a torque of 200 N.m, the second cycle was with a torque of 400 N.m and the final cycle was performed with a torque of 600 N.m with the aid of a torque multiplier. Figure (5.9) shows a picture of the tightening process.

The picture-frame was then lifted using a 5-ton girder crane and fixed in position within the big red frame using sixteen 24mm G8.8 bolts. Again the bolts were tightened in two cycles, to a minimum torque of 200 N.m, to make sure that the picture-frame is fully fixed to the big frame, see Figure (5.5)

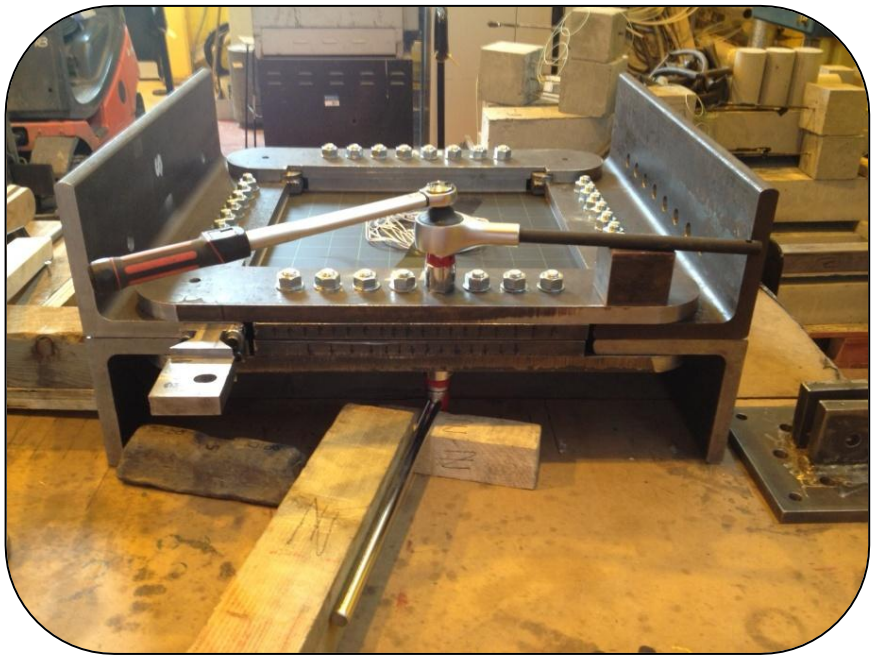

Figure (5.9): The tightening process.

5.5 TEST INSTRUMENTATION

Figure (5.10) shows the test instrumentation for the initial series of tests (phase-2). A single strain gauge rosette was used in the centre of the plate to record the vertical, horizontal, and diagonal tension strain. The strain gauge readings along with the ten displacement gauges (LPs) were recorded at a rate of 1.0 Hz using a data acquisition system. The location of the LPs and strain gauges are shown in the figure, where S refers to strain gauge and LP refers to linear potentiometer. For the control specimen (SP-1.4) only, the rosette strain gauge was attached from both sides in the centre of the steel plate in order to be able to capture the secondary bending and membrane strain. This was not possible with the other 12 strengthened specimens, because the FRP panel covered the central area of the steel plates.

Five of the LPs (LP1-LP5) which had a capacity of 30mm were used to determine the plates' out-of-plane displacements, two 30mm LPs (LP6-LP7) ensured that there was no rigid body rotation for the picture-frame (out-of-plane movement), one 100mm LP (LP-8) was used to determine the deflection at the bottom end of the plate under the applied load, and another two 25mm LPs (LP9-LP10) measured the in-plane rotation in the big frame column.

Tests were performed using a 1000kN servo-hydraulic Instron actuator at a stroke rate of 1.0 mm/minute. Before each test, the central out-of-flatness (initial imperfection) of the steel plate was measured using a calibre with the aid of a specially made jig. The initial imperfections for the thirteen test specimens ranged between 0.4 and 0.5mm. Figure (5.11) shows photos for the instrumentation and the picture-frame after testing.

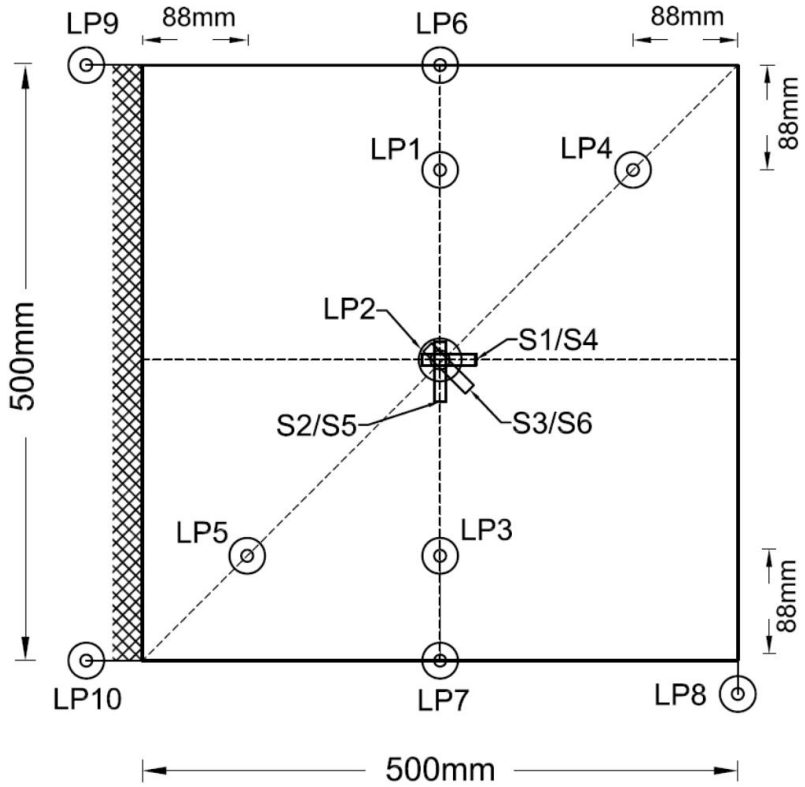

Figure (5.10): Test instrumentations.

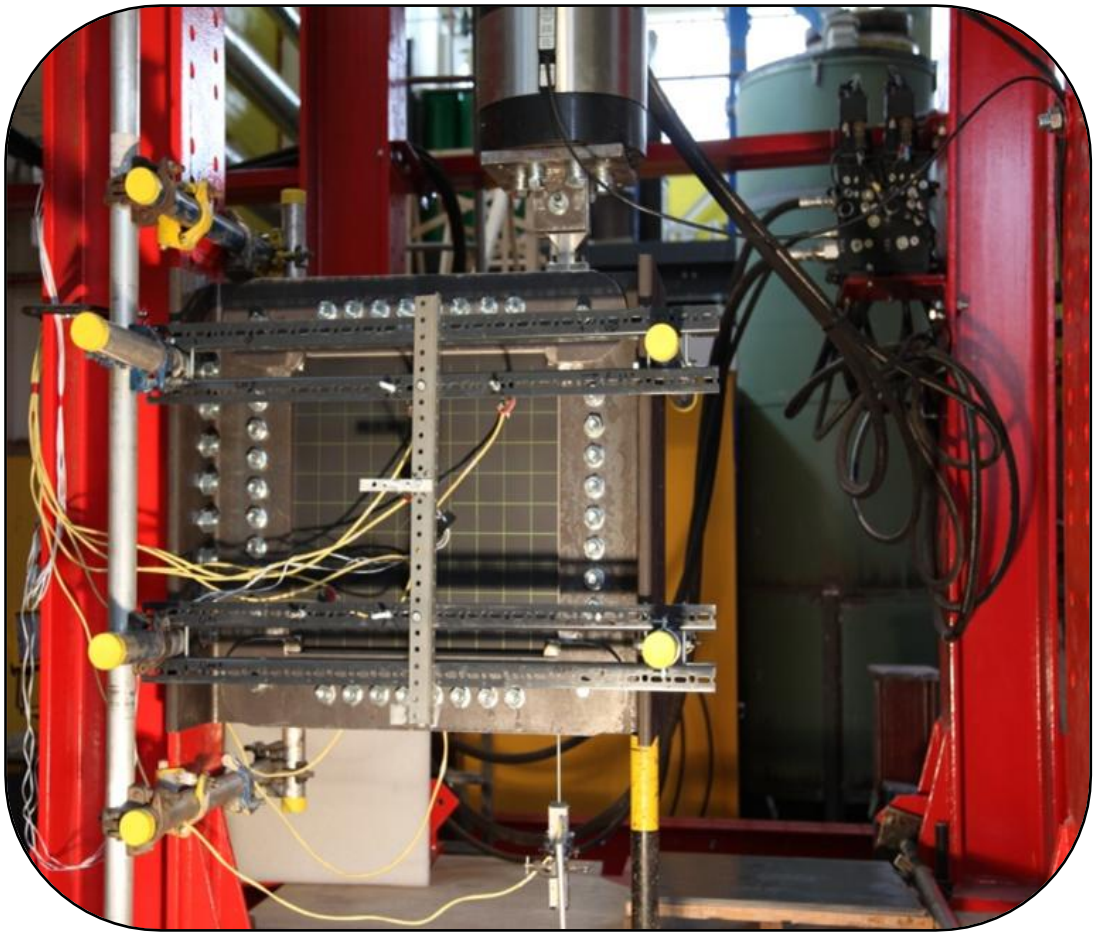

(**a**) Test instrumentation

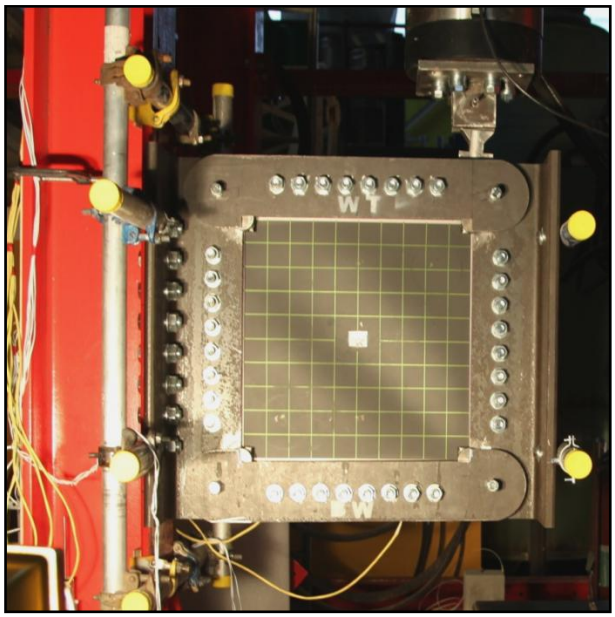

(**b**) Front view after control specimen test

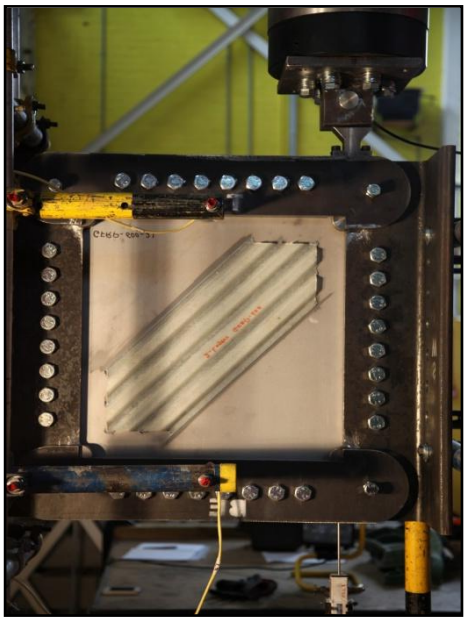

(**c**) Rear view after a GFRP strengthened test

Figure (5.11): Test instrumentation and picture-frame after test.

5.6 EXPERIMENTAL RESULTS, ANALYSIS, AND DISCUSSION

In this section, the experimental results are reported in four main sections; namely, the central out-of-plane displacement (section 5.6.1), the in-plane deflection (section 5.6.2), the non-central out-of-plane displacement (section 5.6.3), and strain (section 5.6.4). In each section, the results were analyzed and the effect of different variables is discussed and compared.

Table 5.2 shows the test results for the thirteen plates tested in this initial series of tests. From this table, it can be seen that for the strengthened specimens, the ultimate capacity is slightly increased between 5.6% and 24.1% depending on the type of the FRP panel used in strengthening them. The lowest strength increment (5.6%) resulted from strengthening the steel plate with GFRP-2L-(45°-45°)-A (SP-2) while the highest increase in strength is achieved using CFRP-2L-(0°-90°)-C (SP-13); details of these specimen can be found in Table 5.2. This relatively low increment in the ultimate capacity of the FRP strengthened steel plates might be attributed to the fact that the proposed strengthening technique in the current work is originally designed to increase the stiffness and buckling strength rather than increasing the ultimate capacity of the strengthened specimen as will be discussed in detail later in this section.

The ultimate load is defined as the load where the specimen starts to undergo high deformations without the need to increase the applied shear load significantly. In most cases, the loading curve managed to reach a horizontal plateau representing yielding of the steel plate and in some other cases the loading curve reached to something similar to a yielding plateau but with some minor load increment due to strain hardening of the steel plate and the stiffening effect of the FRP panel. In a few cases the test was stopped for technical and safety reasons when the deformations were very high or when the load reached a level that could affect the testing rig. This latter case took place only once with testing SP-13. However, the buckling load is not very straightforward to determine like the ultimate load and needs more investigation.

For the control specimen, the buckling load is estimated to be around 40.0 kN using the change in slope method. However, the buckling load for the strengthened specimens could not be detected because the out-of-plane displacement behaviour

was significantly altered and neither the change in slope nor Southwell method is applicable for determining the bucking load. This will be discussed and more investigated in the following section (5.6.1).

Table 5.2: Initial series of test results

Ref.	Specimen	Buckling load, kN	Ultimate load, kN
SP-1-4	Control Specimen	≈ 40.0	140.0
SP-2	GFRP-2L-(45°-45°)-A	-	147.8
SP-3	CFRP-2L-(0°-90°)-A	-	160.5
SP-4	GFRP-2L-(45°-45°)-A-Closed	-	149.3
SP-5	CFRP-2L-(0°-90°)-A-Closed	-	165.0
SP-6	GFRP-3L-(45°-45°)-A	-	157.0
SP-7	CFRP-3L-(0°-90°)-A	-	153.3
SP-8	GFRP-2L-(0°-90°)-A	-	155.1
SP-9	GFRP-3L-(0°-90°)-A	-	155.3
SP-10	GFRP-2L-(45°-45°)-B	-	161.3
SP-11	CFRP-2L-(0°-90°)-B	-	166.2
SP-12	GFRP-2L-(45°-45°)-C	-	153.0
SP-13	CFRP-2L-(0°-90°)-C	-	173.8

5.6.1 Central Out-of-Plane Buckling

Figure (5.12) plots the load versus out-of-plane displacement for each of the 13 specimen. From this figure, typical patterns of behaviour can be detected. For the control specimen the behaviour is tri-linear where the curve starts linearly at the initial stage of loading then it suddenly changes slope indicating the critical buckling shear stress. After first buckling, the web buckles sideways and only the diagonal in tension is working. This results in the formation of wrinkles, and instead of the pure shear state before buckling occurs; simple tension exists in the wrinkle direction (i.e. diagonal tension). The development of the tension field results in a post-buckling reserve of strength, as illustrated by the non-linear part of the curve for the control specimen in Figure (5.12). Since the limit for the steel in tension is its yield strength,

the specimen continues to resist shear loading until the diagonal tension yields; this is demonstrated by the upper flat portion of the curve in the figure.

The behaviour of the strengthened specimens is different and from Figure (5.12), it can be divided into three categories depending on the type of the FRP panel used. The first category followed the tri-linear behaviour of the control specimen but with a stiffer response, a good example of this type of behaviour is the CFRP strengthened specimens in Figure (5.12a). The second category showed a bilinear response where the linear initial stage of loading continued without showing any sign of buckling until it reached close to the ultimate capacity where it curved dramatically towards the failure plateau. This bilinear type of behaviour can be seen in the GFRP strengthened specimens in Figure (5.12c). Finally, the third category is associated with specimens which altered their predesigned failure mode to a reversed buckling mode in the opposite direction. This reversed buckling mode can be seen in the GFRP strengthened specimens in Figure (5.12c and d). More details will be given in the next subsequent sections.

Generally, due to the proposed unsymmetrical way of strengthening the plate from one face only, there is an induced pre-buckling mode which succeeded (most of the tests) in forcing the buckling mode to the FRP face farthest away from the steel plate where the maximum tension stresses exists, and this increases the efficiency of the strengthening technique because FRP is superior in tension. This helped in reducing the out-of-plane displacement and reduced the secondary bending stresses, especially within working stress limits as will be farther discussed in more detail in section (5.6.1.2) and again extensively in Chapter 6.

For the control specimen, the experimental buckling stress was approximately 40.0 MPa in comparison to the theoretical 42.5 MPa (refer to Chapter 3 for the calculation of critical buckling shear stress for a steel plate with clamped boundary conditions). The value of 40 MPa is calculated by dividing the buckling load (40 kN) by the plate sectional area. However, this is just an average number estimated from the zone where the bucking curve extremely changes in slope beyond the initial linear stage, and is not based on any engineering calculations. Nevertheless, this buckling load can be detected form the diagonal tension strain curves as well where a sudden change in the curve slope can be seen around this load announcing the

development of the tension field (this will further be discussed in the strain section 5.6.4).

With respect to the strengthened specimens, no buckling loads could be determined from Figure (5.12) due to the significant alteration in the typical behaviour of shear buckling as a consequence of the proposed strengthening technique. This fact will be further supported by the finite element model in section (5.7) where no buckling load can be detected as well. In some curves within Figure (5.12), there are some indications for the development of the tension field in the tested plates. This is postulated to be caused by a minor slip in one of the tension corners of the picture-frame testing rig in some of the tests. This minor slip, its consequences, and the adopted technical measurement to prevent it are discussed in more detail in the following subsequent sections.

Typical photos for specimens after failure are given in Figure (5.13). These photos were taken after the picture-frame was dis-assembled and the steel plate is taken out. Form these photos, it can be seen that the proposed strengthening technique succeeded in reducing the out-of-plane displacement and changed the buckling mode. However, the characterized ones of these photos will be discussed in the relevant following sections.

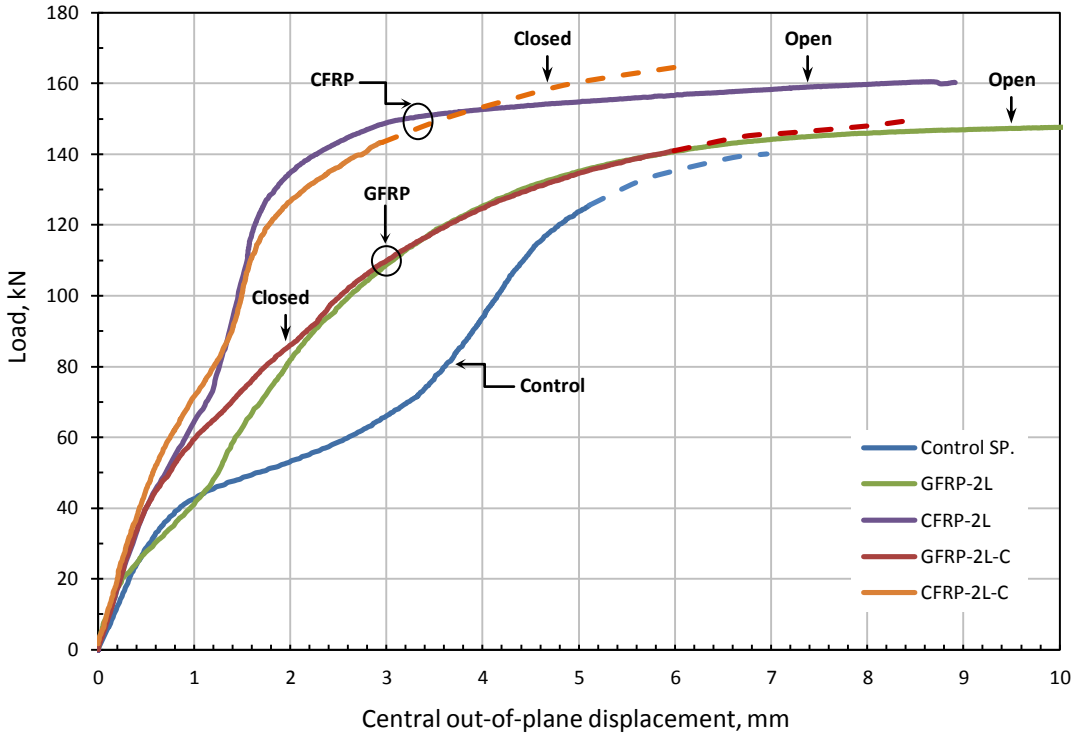

(**a)** Comparison of 2-layerd open and closed FRP sections

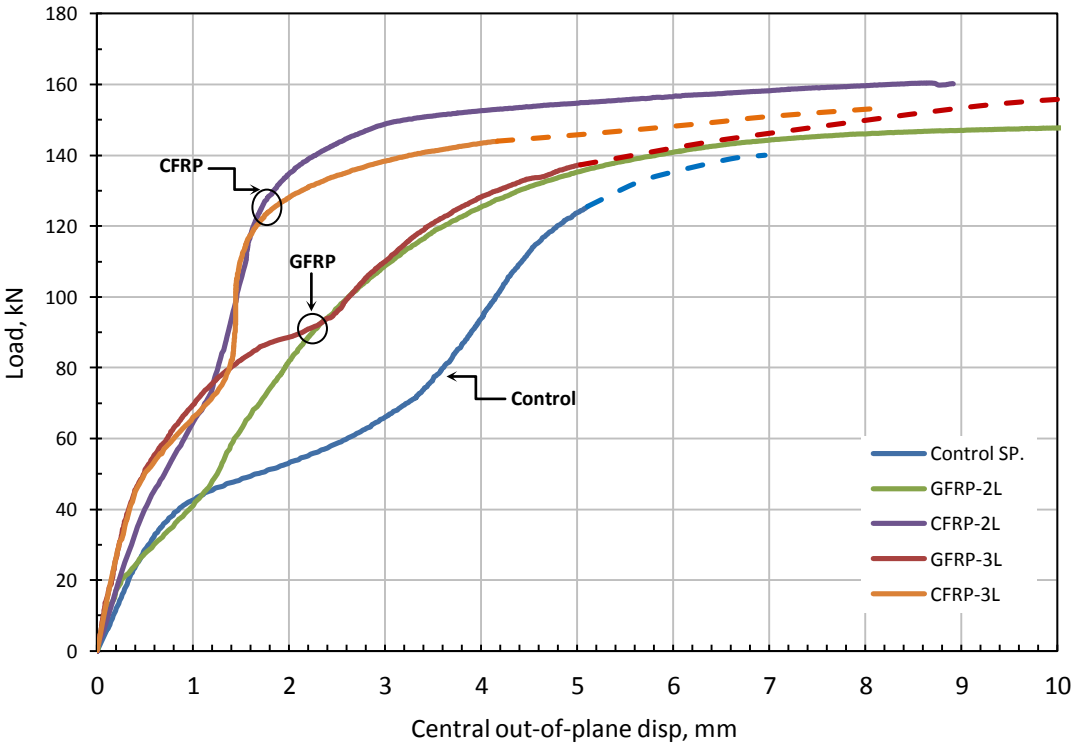

(**b**) Comparison of 2 and 3-layered FRP panels

Figure (5.12): Out-of-plane buckling curves.

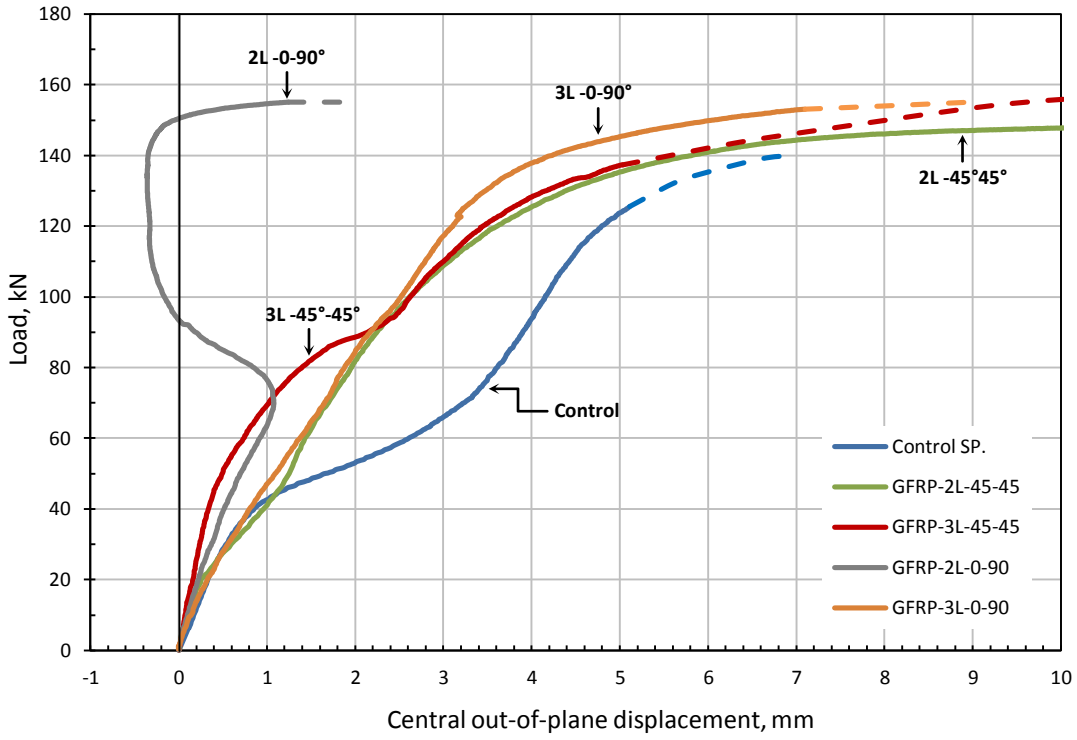

(**c**) Comparison of GFRP with different fibre orientations

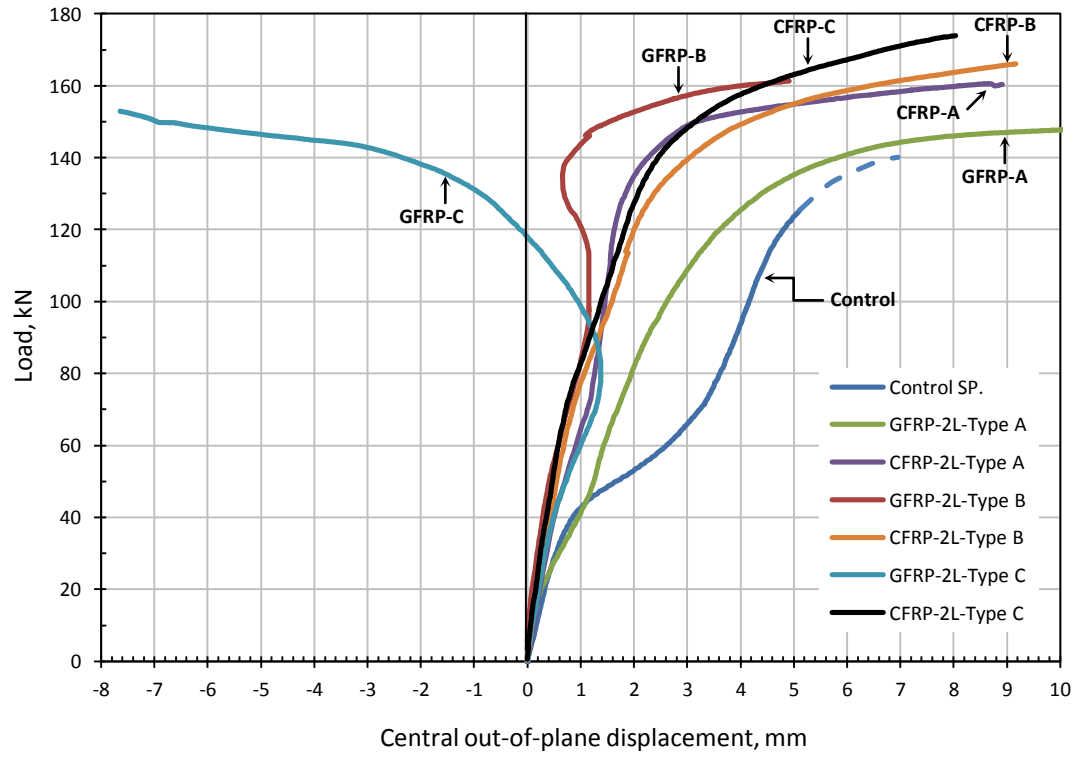

(**d**) Comparison of Type A, B, and C end cut

Figure (5.12 Cont.): Out-of-plane buckling curves.

5.6.1.1 *Variables Affecting the Central Out-of-Plane Buckling*

Figures (5.12a to 5.12d) were divided into four categories according to the tested variables: (1) the effect of FRP material (GFRP and CFRP), (2) the effect of section (open versus closed), (3) the number of FRP layers, (4) the orientation of the GFRP used with respect to the axis of corrugation, and (5) the effect of the end cut of the FRP panel.

Effect of the Strengthening Section and FRP Material Type

Figure (5.12a) is a comparison between the open and closed FRP panel sections. It is clear that the closed section FRP panels were not significantly stiffer than the open section ones, even though these had higher second moment of area and much larger bonding area.

The initial response is slightly different and it is postulated that it is due to a minor gripping slip in the tension diagonal, mainly with testing specimens SP-2 (GFRP-2L-(45°-45°)-A) and SP-3 (CFRP-2L-(0°-90°)-A). This may have caused a small slack in the specimen, causing the curves to turn concave down during their initial stages until the slack was taken up. The slip took place because there was no mechanical anchorage between the plate and the picture-frame and the grip was solely dependent on the friction according to the original design. For the remaining tests, eight 16mm diameter bolts were added to the picture-frame (refer to Figure 5.3 for the location of the 16mm bolts) to ensure that the steel plate was effectively clamped and the slip prevented in the initial stages. However, this precaution caused the load to fluctuate at the final stages for some of the tests (referred to with dashed lines in the figures).

Figure (5.12a) also shows that the CFRP and GFRP strengthened specimens had similar stiffness in the initial loading stages, while the CFRP ones had higher stiffness during later loading stages. This is expected because in the initial loading stages the plate is not yet buckled and the stiffness of the strengthening material plays a limited role; however for higher loading stages (after the specimen has already buckled), the stiffness of the strengthening material plays a major role as it reduces the out-of-plane displacement.

Effect of the FRP Number of Layers

Figure (5.12b) illustrates the effect of increasing the number of FRP layers for the same fibre volume fraction. From this figure it can be seen that the three-layer GFRP panels were more effective in the initial stages but had the same stiffness in the later stages. However, the three-layer GFRP panel showed more integrity and did not crack at the ultimate load the way the two-layer GFRP one did; this can be seen by comparing the failed specimens' photos in Figure (5.13b) and (5.13f). In contrast, the three-layer CFRP panel behaved almost the same as the two-layer one and had even lower ultimate capacity.

Effect of Glass Fibre Orientation with respect to the Axis of Corrugation

Figure (5.12c) shows the effect of the fibre orientation for the GFRP panels. It can be seen that changing the glass fibre orientation from the default of this work, (i.e. 45˚-45˚) to 0˚-90˚ had no clear effect on the results of the 3-layered GFRP specimen (SP-9) but affected the two-layered 0˚-90˚ GFRP specimen (SP-8) which had a very stiff but brittle behaviour and led to an alternative mode of failure in the opposite direction to that expected. This could be justified by examining the failed specimen photo in Figure (5.13h) where it can be shown that the FRP panel cracked near the bottom compression corner causing the specimen to alter its buckling mode because this corner usually suffers from severe deformation due to the thrust effect of the sharp triangular end cut associated with type-A FRP panels.

Effect of the End-Cut Shape and Position

Figure (5.12d) shows the effect of the end-cut shape and position for the FRP panels. It can be seen that in the case of GFRP the round cut (Type-B) succeeded in increasing the stiffness of the specimen in both the initial and final stages of loading, in addition to increasing the ultimate load capacity. In the case of CFRP, the round end-cut (Type-B) did not obviously improve the behaviour. The same observation does not hold for the longer FRP panels with triangular end-cuts (Type-C). This type of panel only improved the stiffness of the specimen in the initial loading stages, while the direction of the buckling was reversed in the higher loading stages (i.e. beyond 80 kN). Nevertheless, the CFRP long panel with triangular end-cuts (Type-

C) improved both the stiffness and ultimate capacity; however the test was halted when the applied load exceeded 173 kN (for technical/safety reasons).

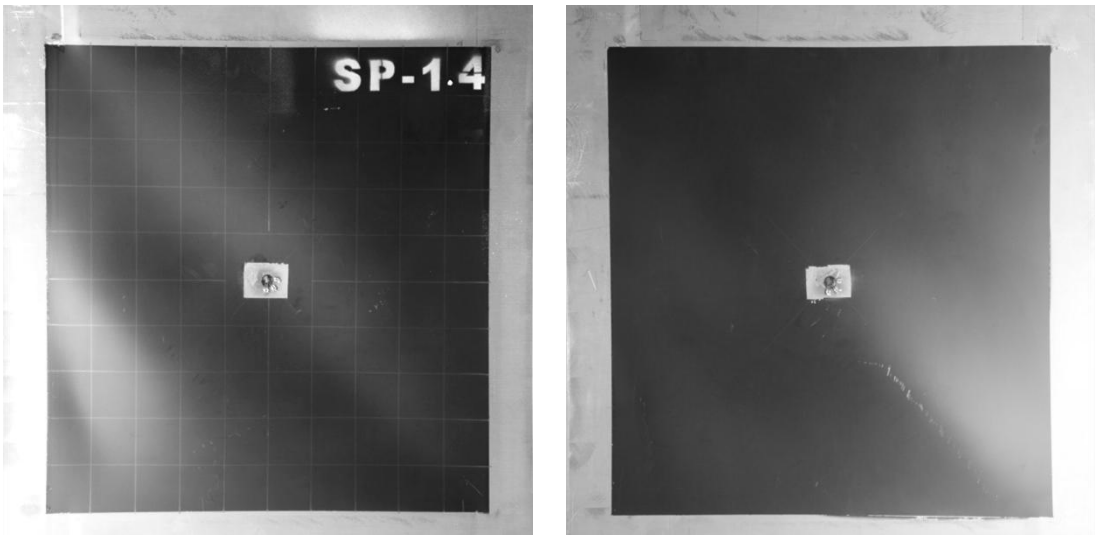

Front face Back face

(**a**) SP-1, Control Specimen

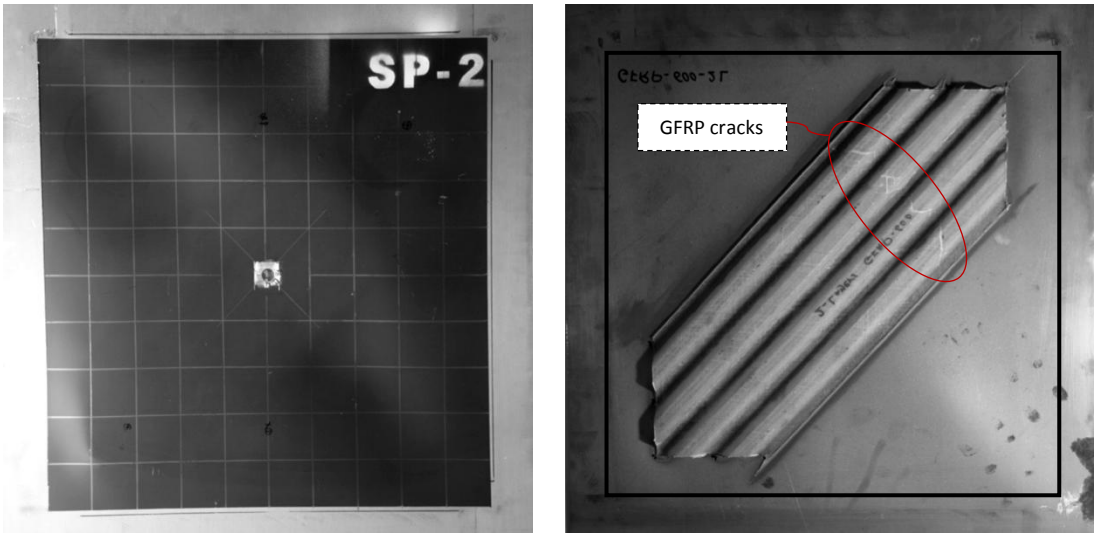

Front face Back face

(**b**) SP-2, GFRP-2L-45°-45°-A

Figure (5.13): Specimens' photos after failure.

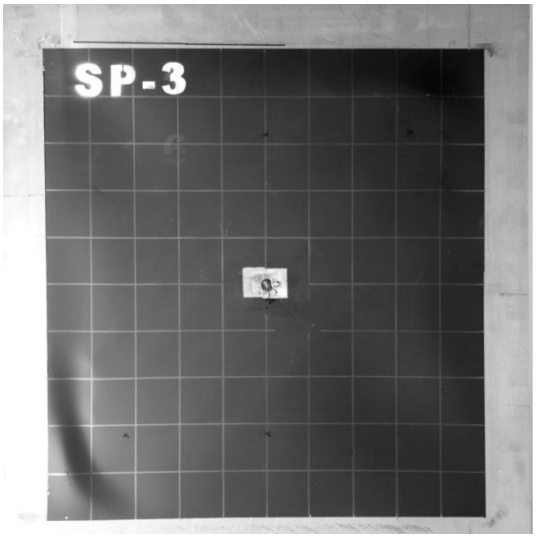

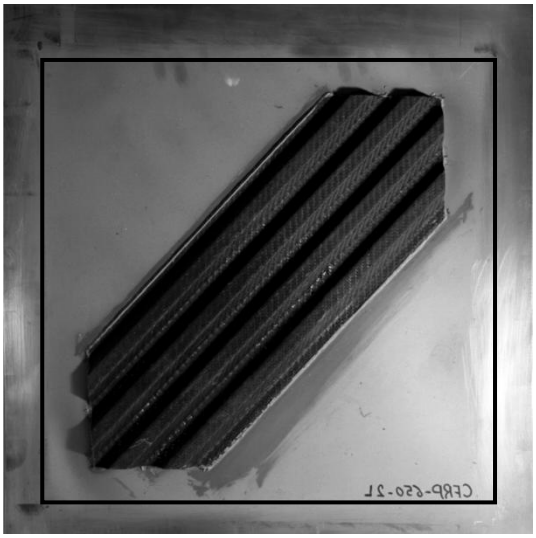

Front face Back face

(**c**) SP-3, CFRP-2L-0°-90°-A

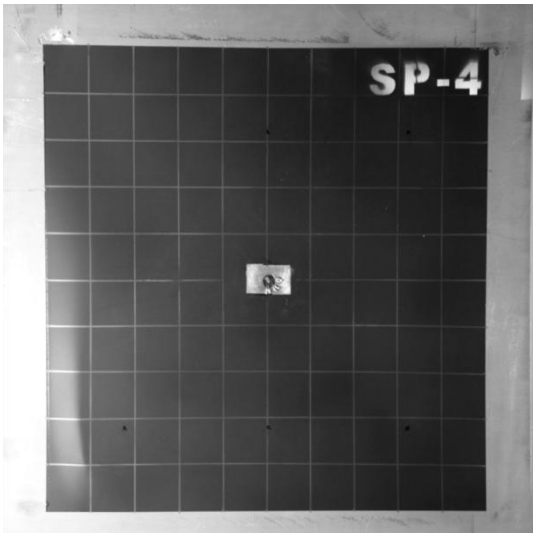

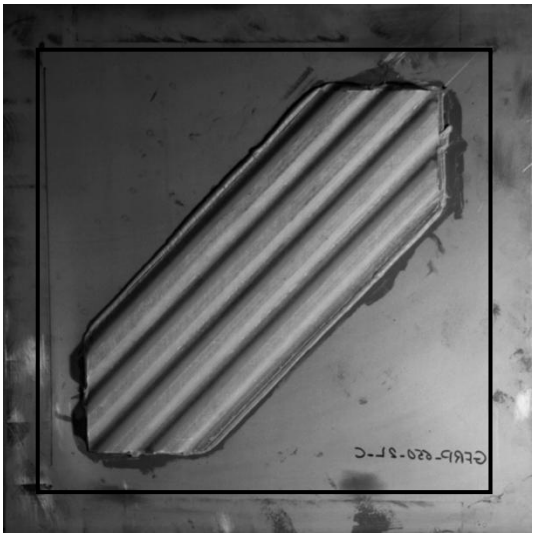

Front face Back face

(**d**) SP-4, GFRP-2L-45°-45°-A-Closed section

Figure (5.13 Cont.): Specimens' photos after failure.

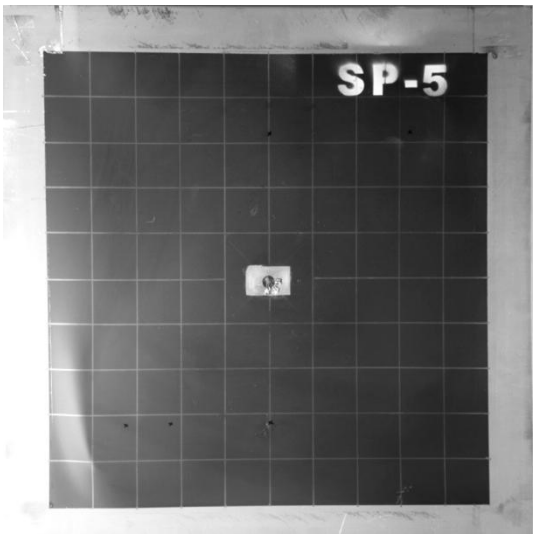

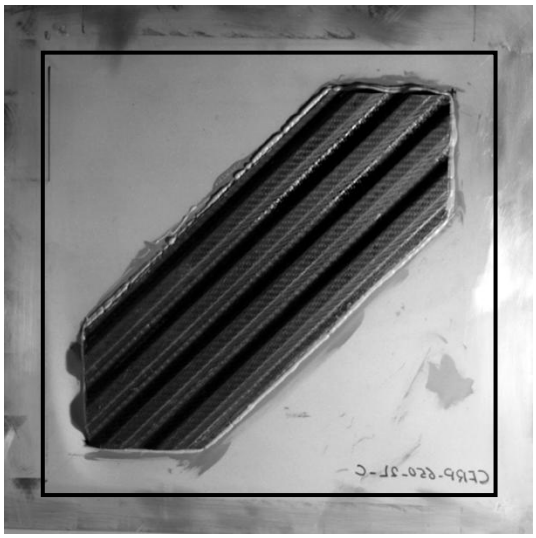

Front face Back face

(**e**) SP-5, CFRP-2L-0°-90°-Closed section

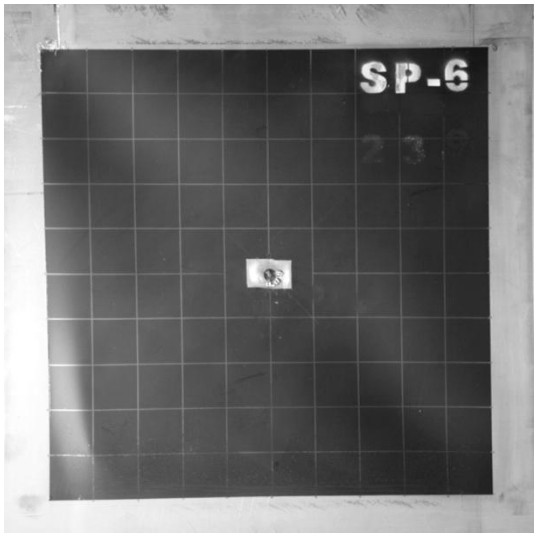

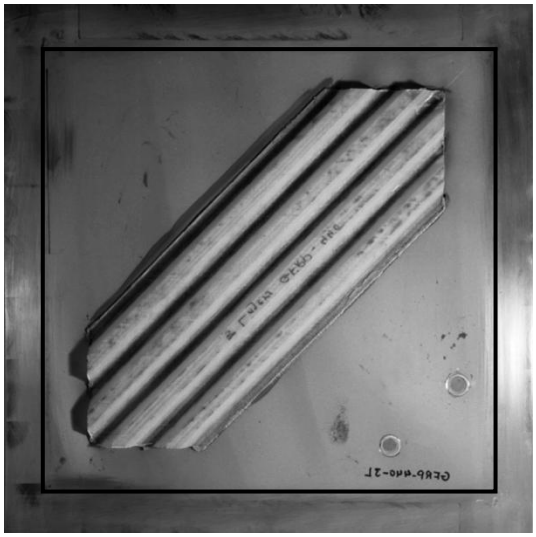

Front face Back face

(**f**) SP-6, GFRP-3L-45°-45°-A

Figure (5.13 Cont.): Specimens' photos after failure.

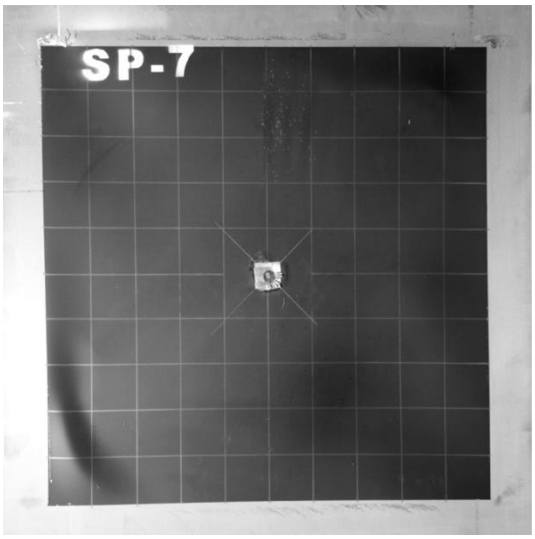

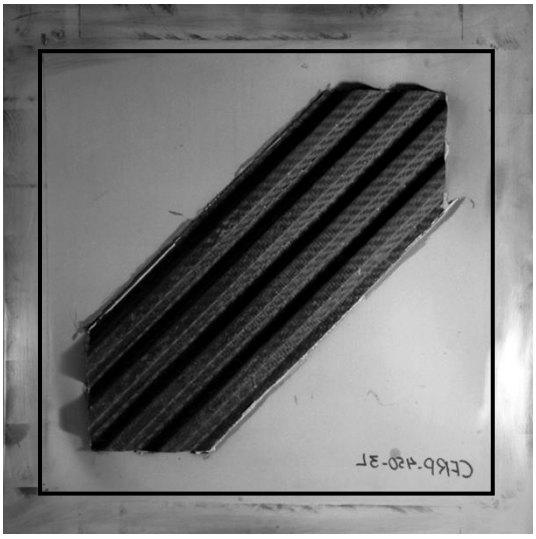

Front face Back face

(**g**) SP-7, CFRP-3L-0°-90°-A

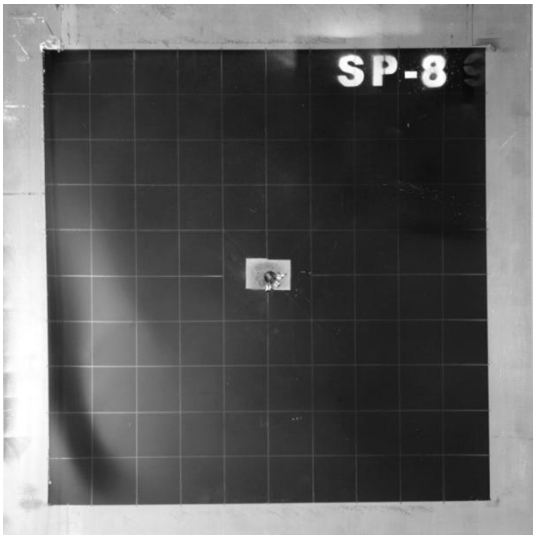

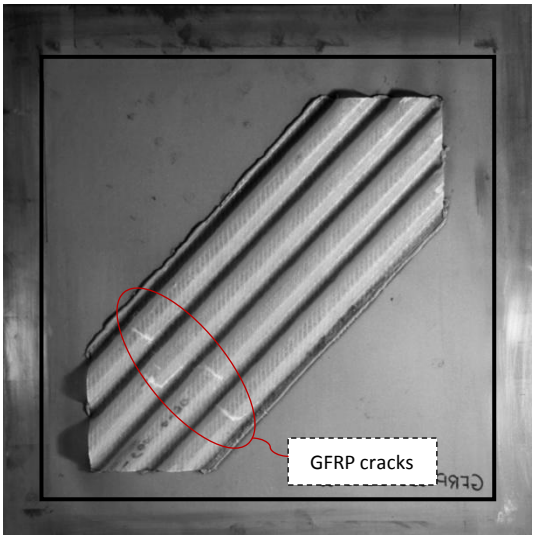

Front face Back face

(**h**) SP-8, GFRP-2L-0°-90°-A

Figure (5.13 Cont.): Specimens' photos after failure.

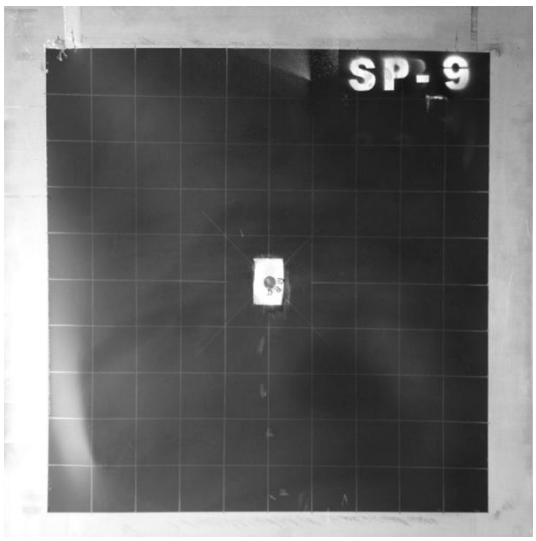

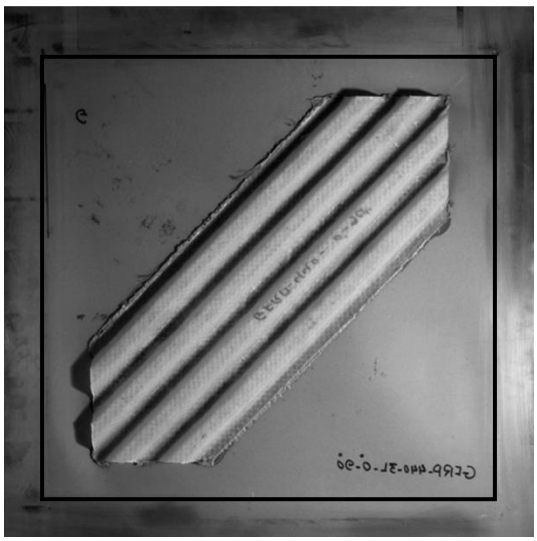

Front face Back face

(**i**) SP-9, GFRP-3L-0°-90°-A

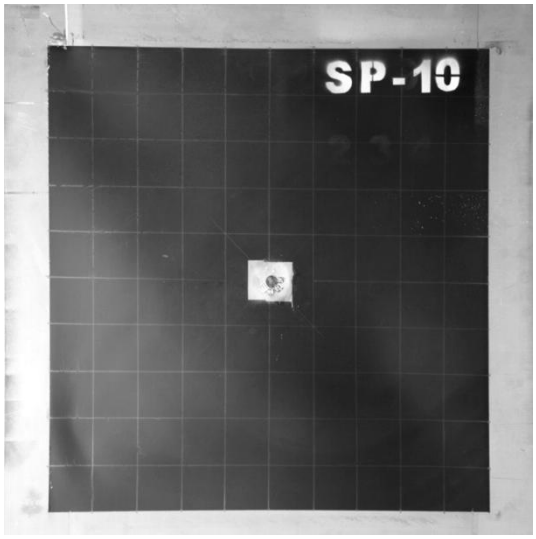

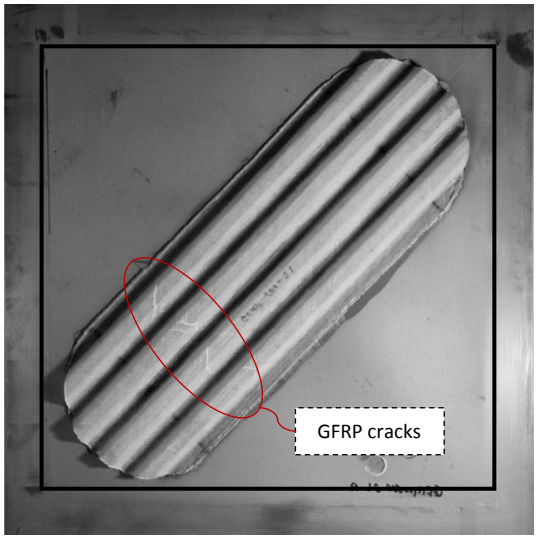

Front face Back face

(**j**) SP-10, GFRP-2L-45°-45°-B

Figure (5.13 Cont.): Specimens' photos after failure.

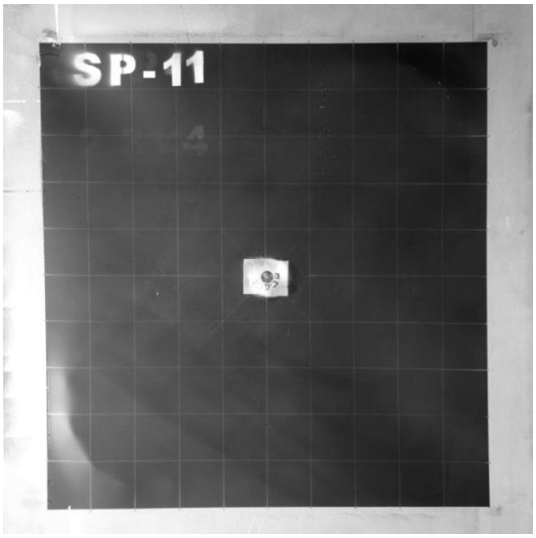

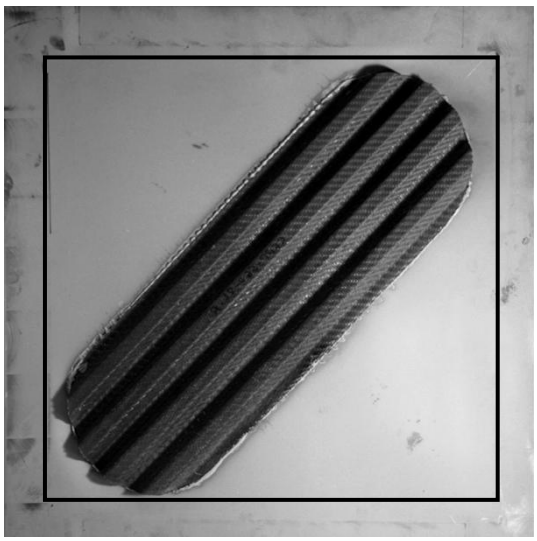

Front face Back face

(**k**) SP-11, CFRP-2L-0°-90°-B

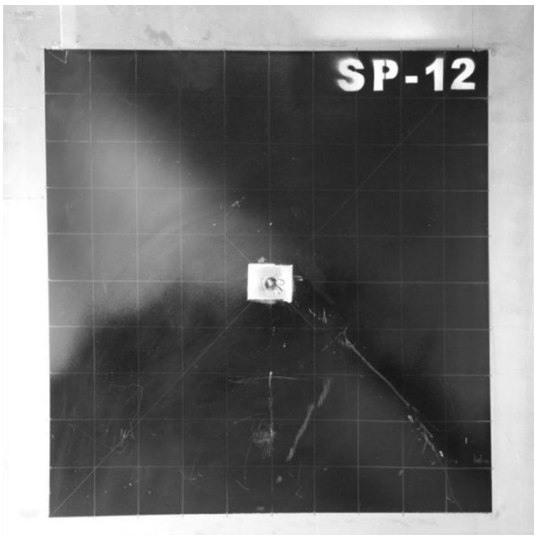

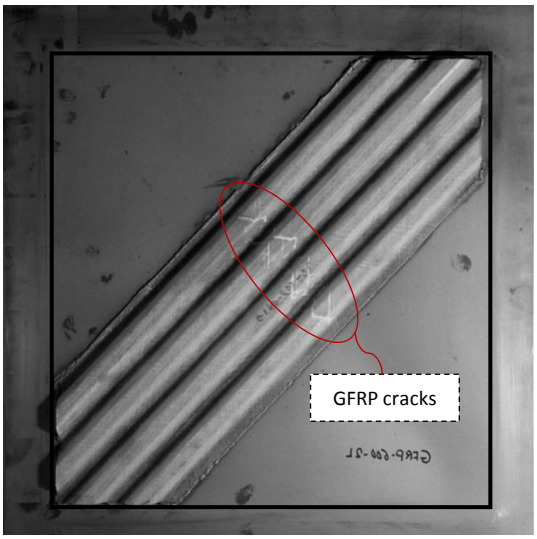

Front face Back face

(**l**) SP-12, GFRP-2L-45°-45°-C

Figure (5.13 Cont.): Specimens' photos after failure.

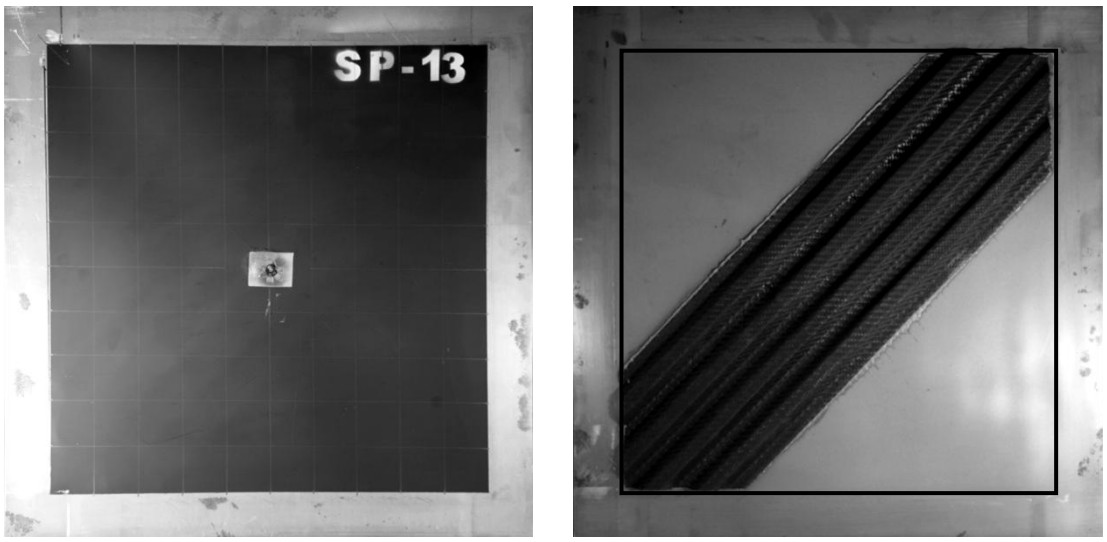

Front face Back face

(**m**) SP-13, CFRP-2L-0°-90°-C

Figure (5.13 Cont.): Specimens' photos after failure.

5.6.1.2 *Assessing the Stiffening Effect of the FRP Panel*

Despite the fact that there is an obvious buckling behaviour for the control specimen as can be seen from its buckling curve, see Figure (5.12); no obvious buckling load could have been estimated from the buckling curves for the other 12 strengthened specimens. This is why there are no values stated for the buckling load in Table 5.2. However, observing the non-central buckling curves, as will be seen later in section (5.6.3), revealed more sharp alterations in their behaviour once buckling occurred and this could be considered a sign for estimating the buckling load, but from another perspective, it is hard to tell whether these signs of buckling in the abovementioned curves are induced by the buckling itself or by the slack due to the slippage discussed earlier. Nevertheless, the slack itself is believed to start when buckling is initiated, but this is still not enough to estimate the buckling load on a scientific base.

For further investigation of the buckling load and to address the problem of the initial slack in the curves due to the minor slippage at the initial loading stage as mentioned above, the buckling curves were reproduced; see Figures (5.14a) through (5.14m). These are the same as Figure (5.12) except that the buckling curve for each of the thirteen tested specimens is shown alone compared to the modified buckling curve for the control specimen. The two axes in Figure (5.14) where transferred into

dimensionless ones. For the load axis, this was done by dividing the applied load by the corresponding shear yielding load using Mises criteria where the yielding shear stress can be taken equal to ($f_y/\sqrt{3}$). For the displacement axis, this was performed by dividing the out-of-plane displacement by a limiting displacement (which is believed to be the limit where the behaviour of the curves turns into non-linear). The value of 1.0 mm is chosen as this limit because it represents the average limit between linear and non-linear parts in all the tests.

In Figure (5.14), the slack caused by the abovementioned minor slippage was treated by drawing a hypothetical parallel curve removing this problem, as can be seen from the dashed line in the figures.

Looking at Figures (5.14b) to (5.14m) for the 12 strengthened steel plates, it can be stated that the proposed strengthening technique is effective enough to alter the problem from an Eigen problem with respect to the control steel plate where bucking is a sudden phenomenon followed by the formation of the diagonal tension field, to a typical composite section plate where no sudden buckling is taking place anymore and the deformation process is progressing in a more stable manner.

The above discussion could be justified by the fact that the compression diagonal is not losing its capability in resisting the compression force induced by the applied shear load beyond buckling anymore because the bonded FRP panel is stiffening the steel plate along its compression diagonal. This is a unique case where the design is taking optimum advantage from both the steel plate and the strengthening FRP panel because of the biaxial action where the steel-FRP composite section is forming a composite strut resisting the compression force along the compression diagonal leaving the steel plate alone resisting the tension stress in the perpendicular diagonal. This is due to the fact that, usually, steel does not need strengthening in tension, see Figure (5.15).

The FRP panel is designed to be stiff with respect to its axial direction and weak from its transverse secondary axis, this will allow the FRP panel to act like an accordion where it allows the steel plate to extend with respect to its tension diagonal without having to debond and at the same time stiffening the compression diagonal of the plate. This is one of the most important reasons that justify why there is no debonding between the steel plate and the FRP panel (even with high deformation at

failure stage), and how the typical ductile failure of the steel plate is not only maintained but even improved as will be seen later in this section. Another important observation is that the tension field will act as bracing force for the composite compression strut in the central area leading to more buckling resistance. This means that with the proposed strengthening technique we have both the advantage of the composite strut resisting the compression force and the biaxial action of the steel plate in resisting the shear stress at the same time, see Figure (5.15b).

However, the stiffness of the strengthened specimens is obviously much higher than the control one and this need to be quantified. To do so, an increase in stiffness index is introduced. This stiffness index can be explained by looking at Figure (5.14a), the shaded area between the vertical axis (the load axis) and the modified bucking curve was calculated for the control specimen and then compared to the same area for the other strengthened specimens. For the sake of comparison, this was done with a load equals the ultimate load of the control specimen (140.0kN). The stiffness index then can be written as

$$S.I = Act / Ast \qquad (5.1)$$

where:

S.I: is the relative stiffness increase index,

Act: is the shaded area between the vertical axis (the load axis) and the modified bucking curve for the control specimen,

Ast: is the shaded area between the vertical axis (the load axis) and the modified bucking curve for the strengthened specimens, up to a load equal to 140 kN.

Another important property that needs to be quantified as well is the change in energy absorption capacity (ductility) of the specimens. Usually the increase in the capacity of the strengthened specimen comes at a considerable reduction in the energy absorption (Okeil et al, 2009). In this study, the proposed strengthening technique is targeting the out-of-plane displacement while limited and insignificant effect is observed with the deflection curves as will be seen in more detail in section (5.6.2). This will lead to the controversial question whether we should use the deflection curves or the buckling curves to estimate the energy absorption capacity.

However, this is not the core of this study; therefore a simple energy absorption index is proposed to compare the ductility of the strengthened specimens with the control one.

The increase in energy absorption factor can be taken as the area between the horizontal axis (the displacement axis) and the modified buckling curve of the strengthened specimen divided by the same area for the control specimen, see Figure (5.14a). The limit of 10mm was chosen to be the basis of comparison because most of the tested specimens reached this value; however, the ones who were stopped before this limit for technical reasons were extended to an out-of-plane displacement equals 10mm as can be seen in all the curves in Figure (5.14). Thus, the relative energy absorption index can be stated as:

$$E.I = Asb / Acb \qquad (5.2)$$

where:

- E.I: is the relative energy absorption index,
- Asb: is the area between the horizontal axis (the displacement axis) and the modified buckling curve for the strengthened specimens,
- Acb: is the area between the horizontal axis (the displacement axis) and the modified buckling curve for the control specimen.

Table 5.3 illustrate the values both for the relative stiffness and energy absorption indices. It can be seen that the proposed strengthening technique succeeded in increasing the stiffness 3 times and that was not on the expense of energy absorption as it is improved up to 50%. It is worth mentioning that these two factors were not calculated for specimens with irregular buckling curves where the mode of buckling is altered (i.e. SP-8, SP-10, and SP-12).

Table 5.3: Increase in stiffness and energy absorption indices for the initial series

Ref.	Specimen	Stiffness index	Energy absorption index
SP-1-4	Control Specimen	1.0	1.0
SP-2	GFRP-2L-(45°-45°)-A	1.4	1.1
SP-3	CFRP-2L-(0°-90°)-A	2.9	1.4
SP-4	GFRP-2L-(45°-45°)-A-Closed	1.6	1.2
SP-5	CFRP-2L-(0°-90°)-A-Closed	2.6	1.4
SP-6	GFRP-3L-(45°-45°)-A	1.8	1.2
SP-7	CFRP-3L-(0°-90°)-A	3.0	1.3
SP-8	GFRP-2L-(0°-90°)-A	-	-
SP-9	GFRP-3L-(0°-90°)-A	1.6	1.2
SP-10	GFRP-2L-(45°-45°)-B	-	-
SP-11	CFRP-2L-(0°-90°)-B	2.7	1.4
SP-12	GFRP-2L-(45°-45°)-C	-	-
SP-13	CFRP-2L-(0°-90°)-C	3.2	1.5

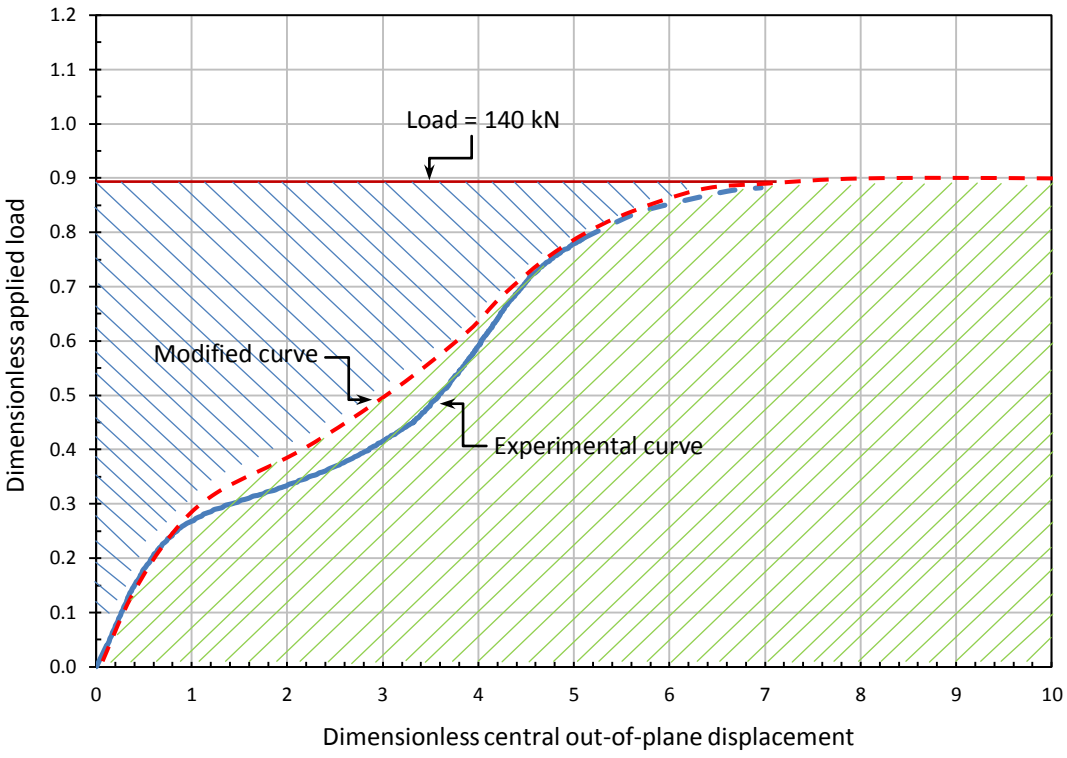

(**a**) Control specimen, SP-1.4

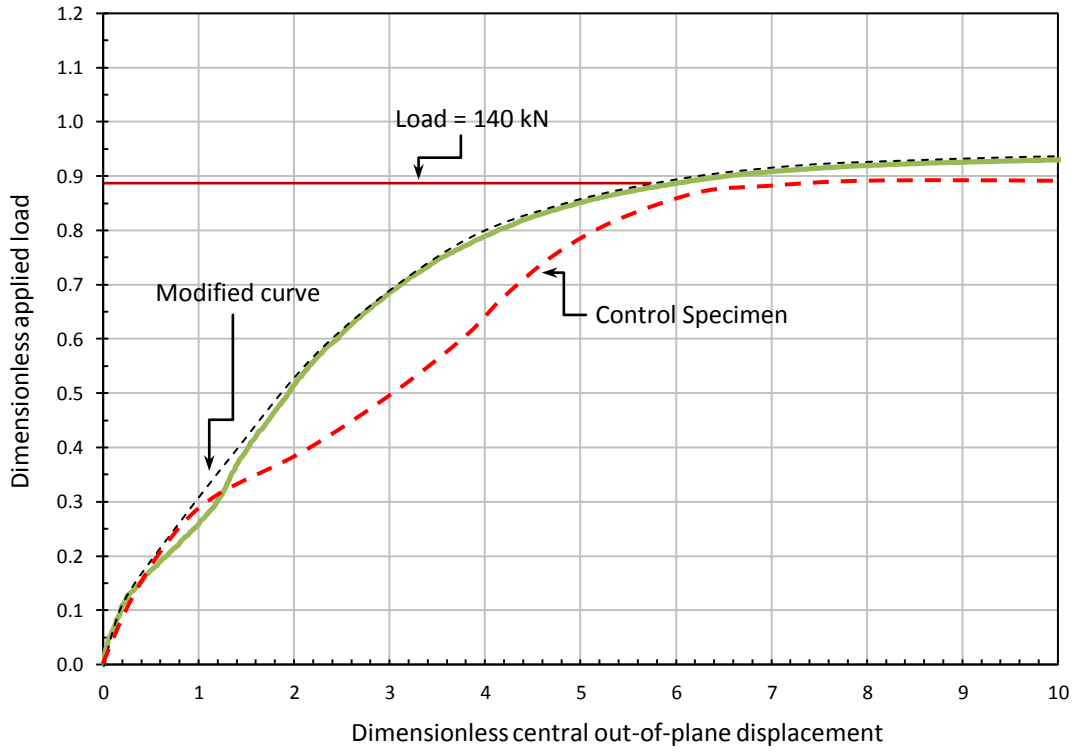

(**b**) SP-2, GFRP-2L-45°-45°-A

Figure (5.14): Buckling curves.

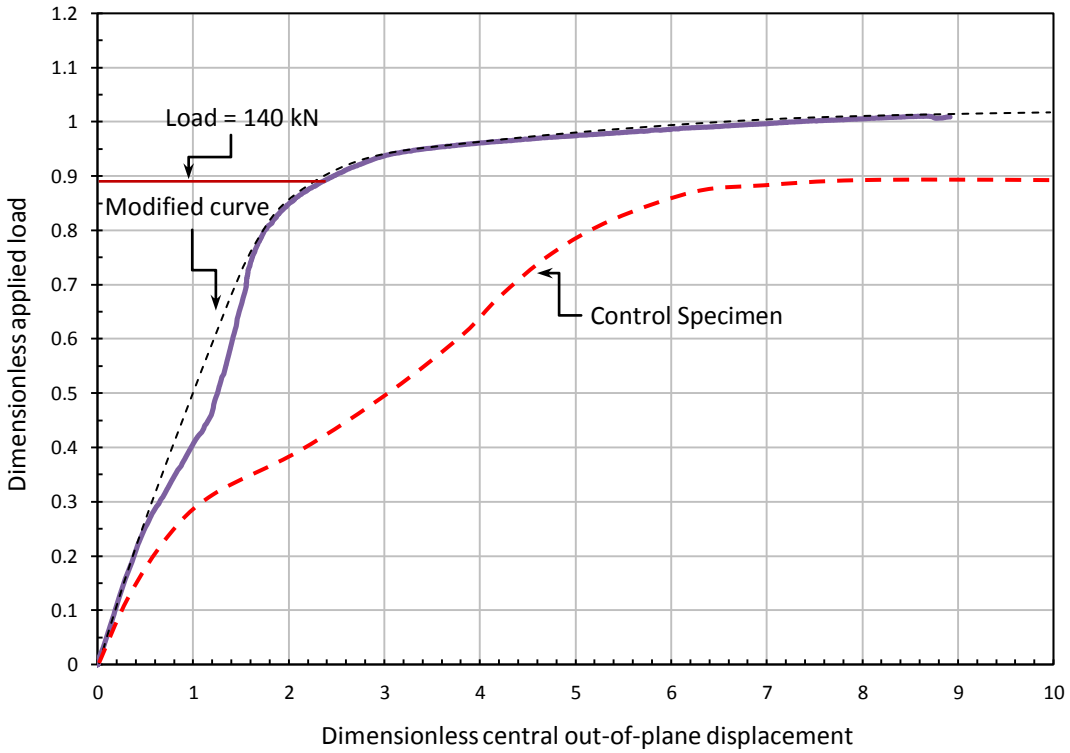

(**c**) SP-3, CFRP-2L-0°-90°-A

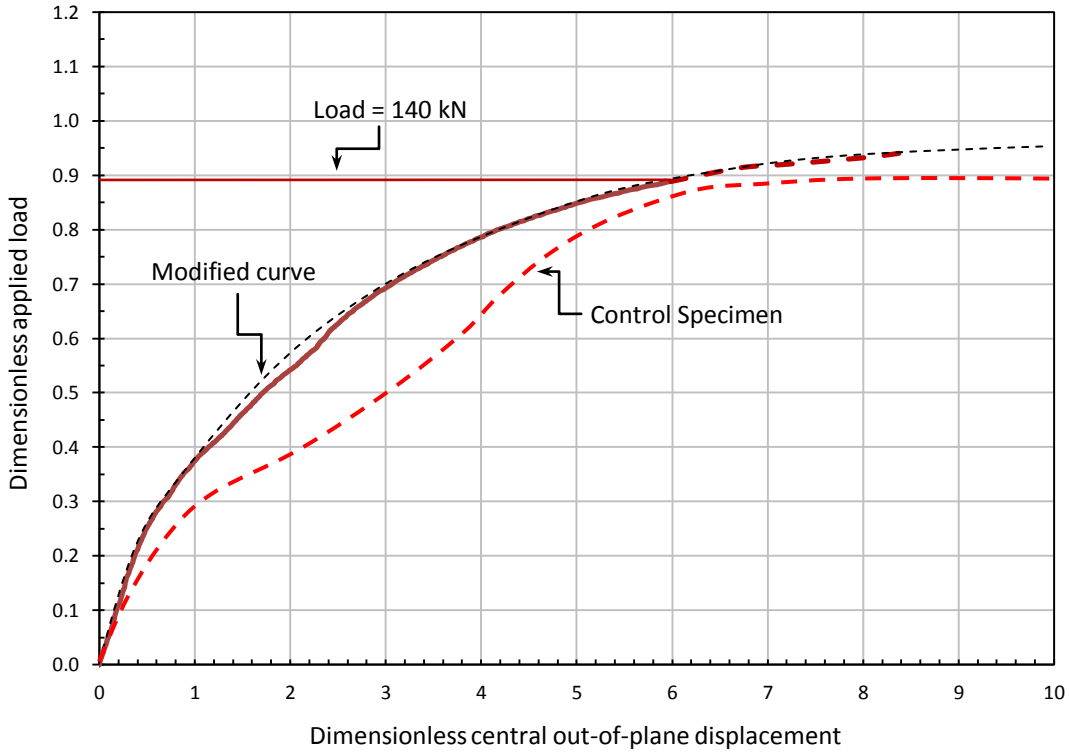

(**d**) SP-4, GFRP-2L-45°-45°-A-Closed section

Figure (5.14 Cont.): Buckling curves.

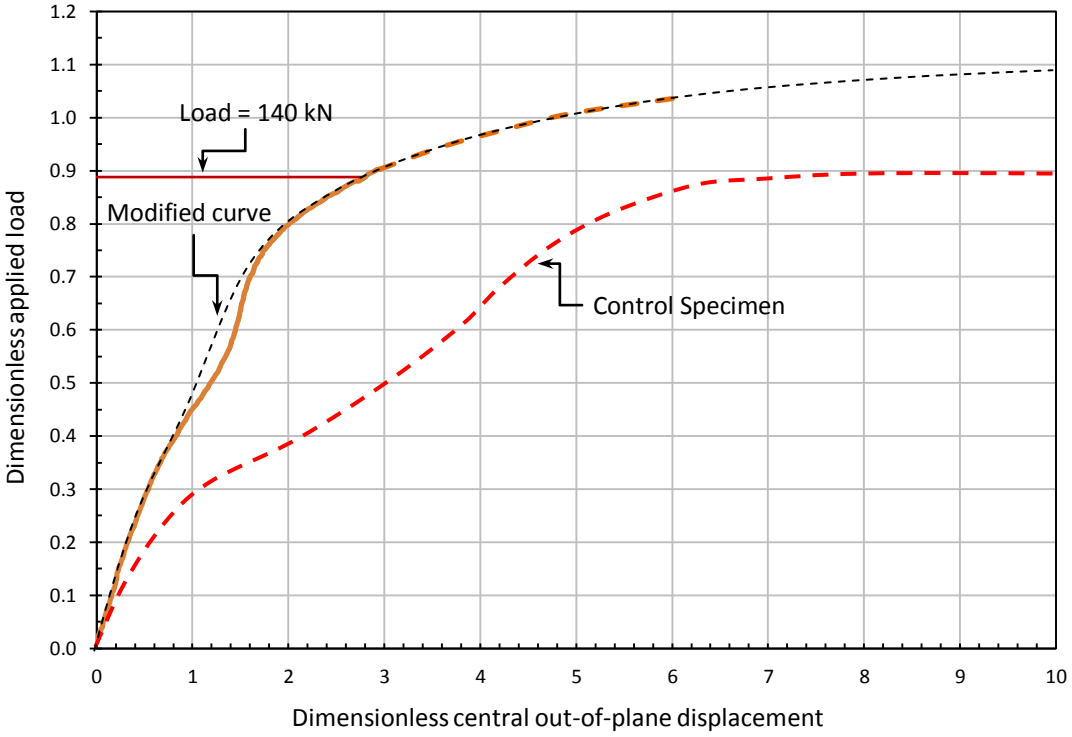

(**e**) SP-5, CFRP-2L-0°-90°-Closed section

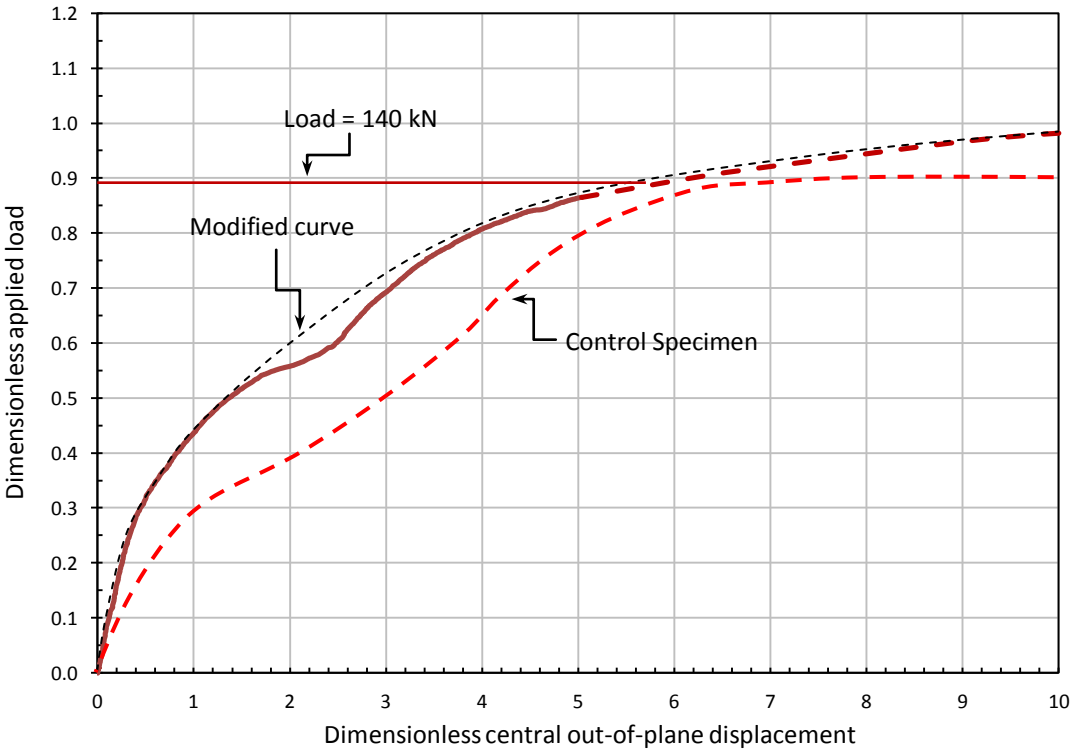

(**f**) SP-6, GFRP-3L-45°-45°-A

Figure (5.14 Cont.): Buckling curves.

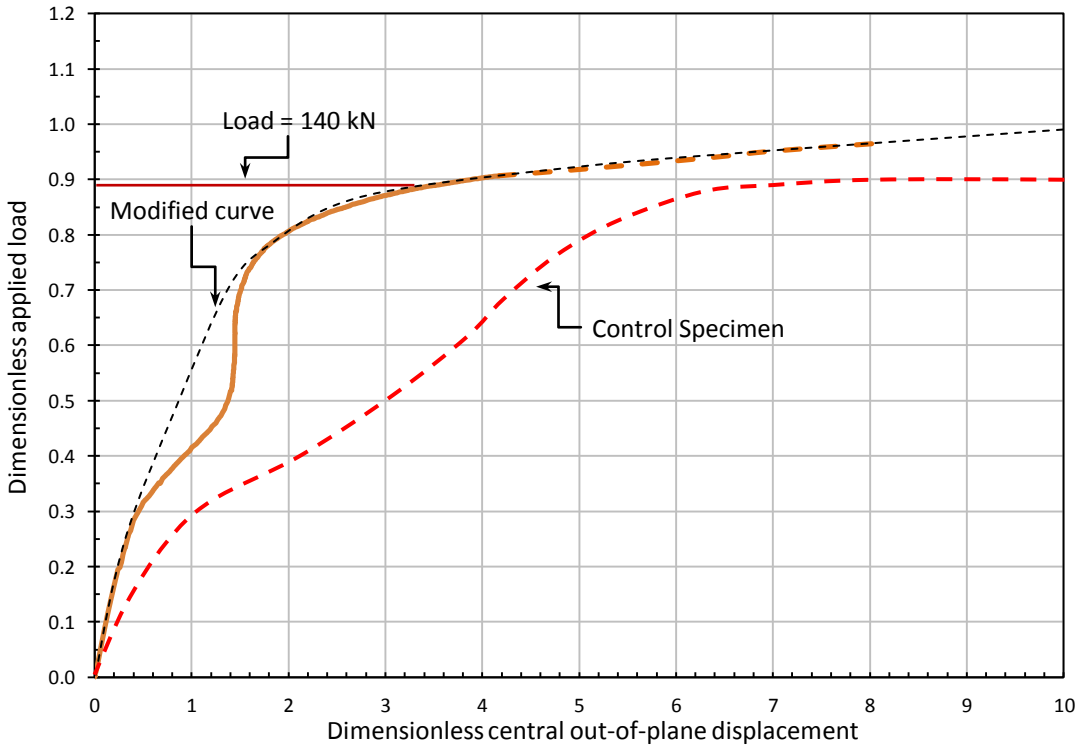

(**g**) SP-7, CFRP-3L-0°-90°-A

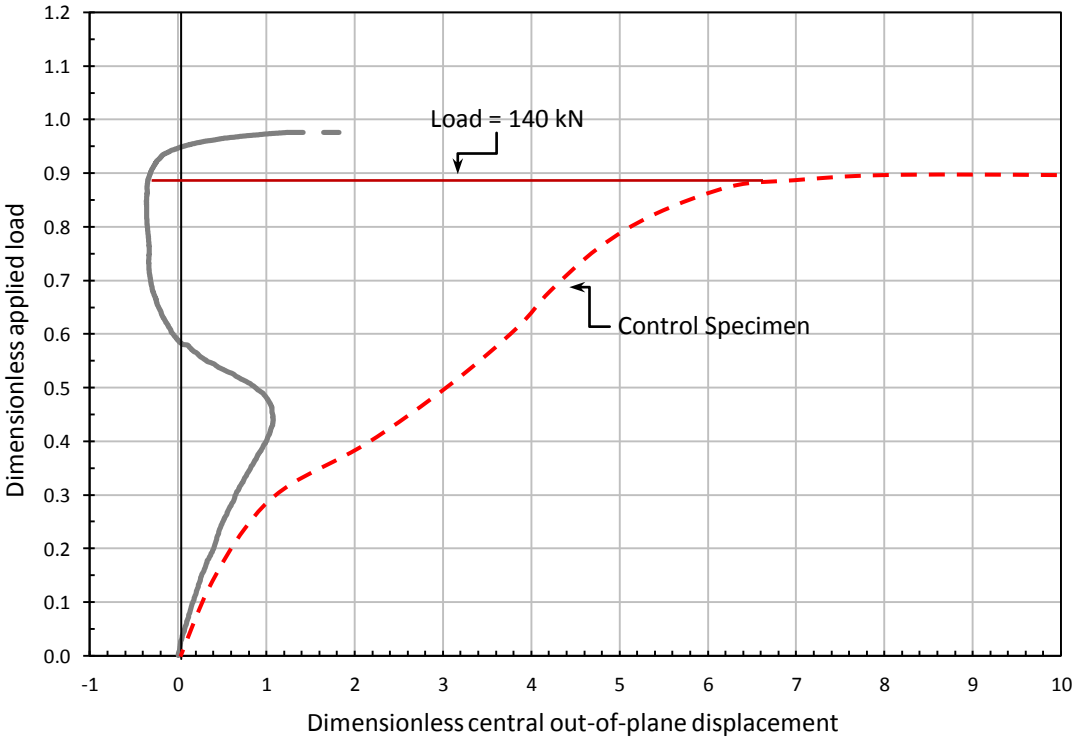

(**h**) SP-8, GFRP-2L-0°-90°-A

Figure (5.14 Cont.): Buckling curves.

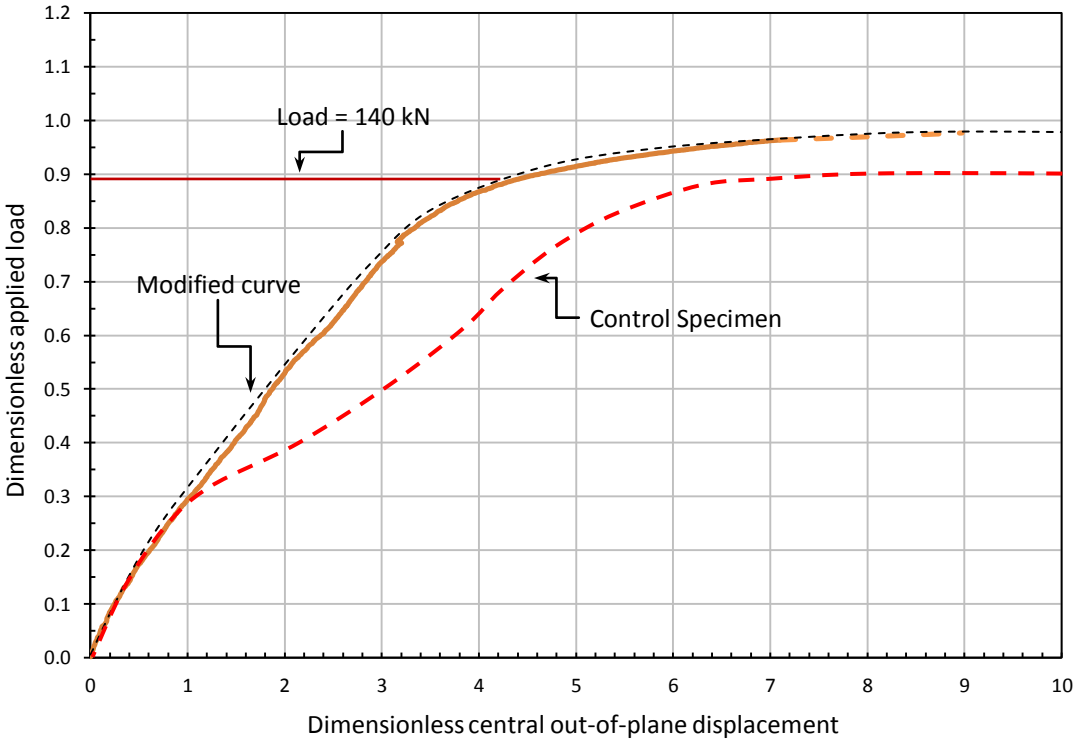

(**i**) SP-9, GFRP-3L-0°-90°-A

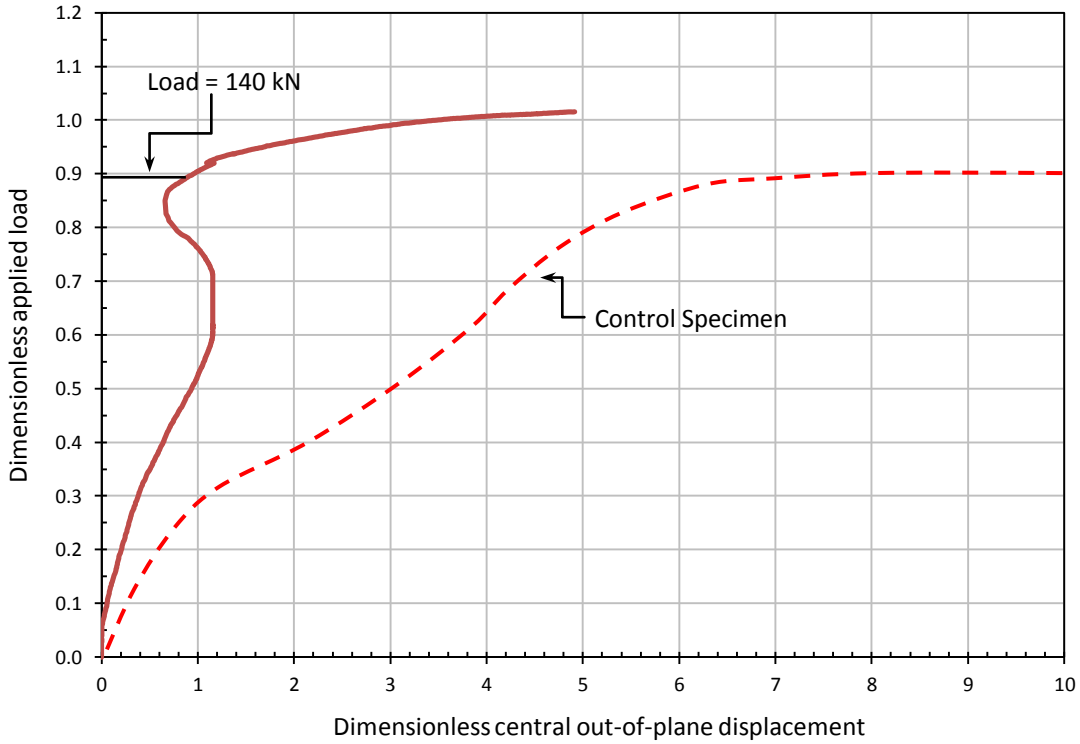

(**j**) SP-10, GFRP-2L-45°-45°-B

Figure (5.14 Cont.): Buckling curves.

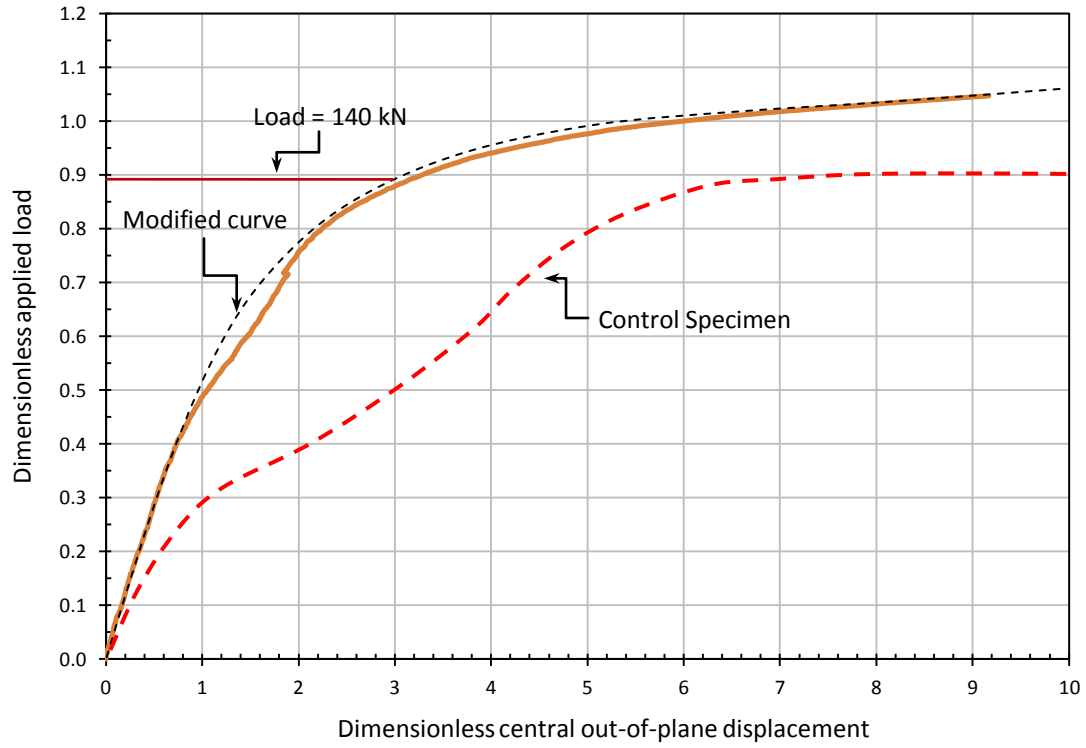

(**k**) SP-11, CFRP-2L-0°-90°-B

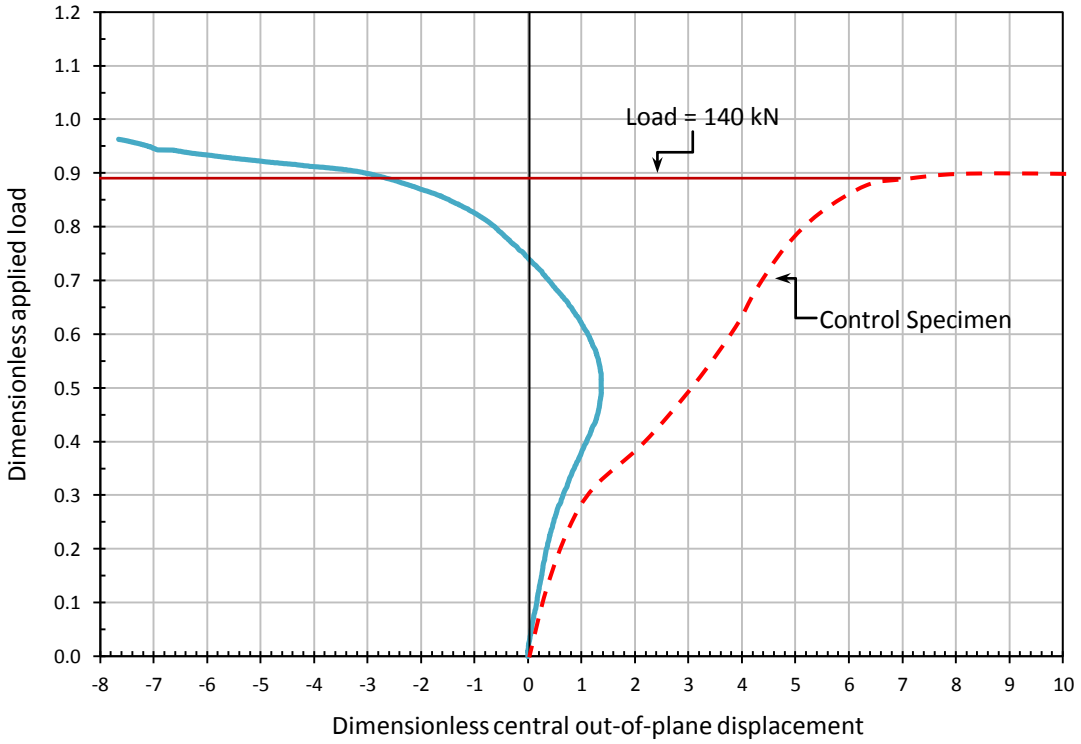

(**l**) SP-12, GFRP-2L-45°-45°-C

Figure (5.14 Cont.): Buckling curves.

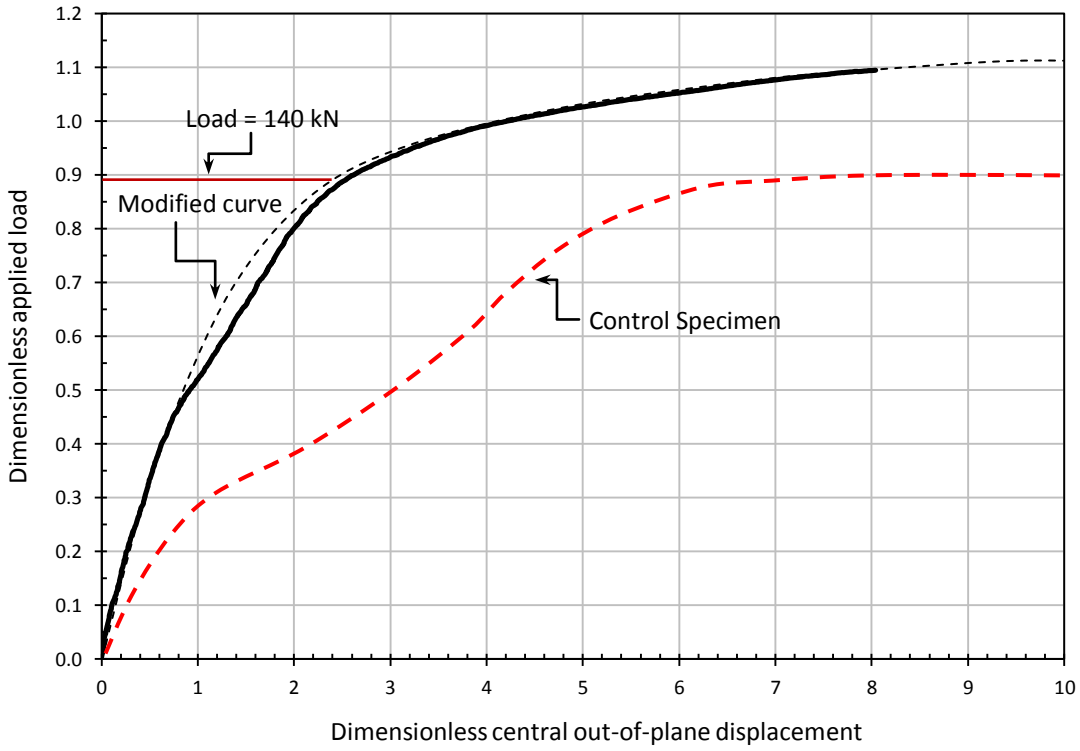

(**m**) SP-13, CFRP-2L-0°-90°-C

Figure (5.14 Cont.): Buckling curves.

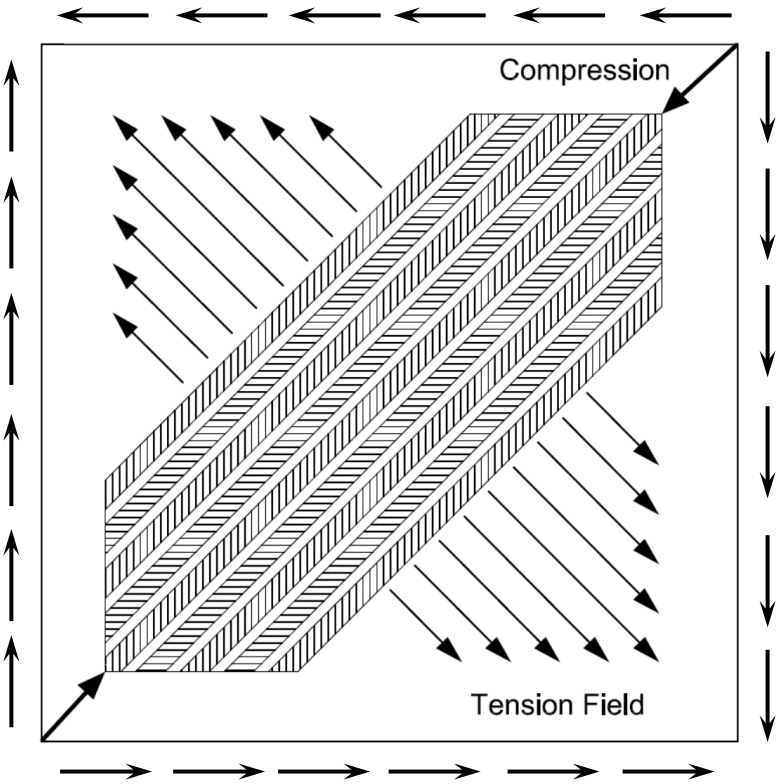

(**a**) Biaxial action of the strengthened composite plate

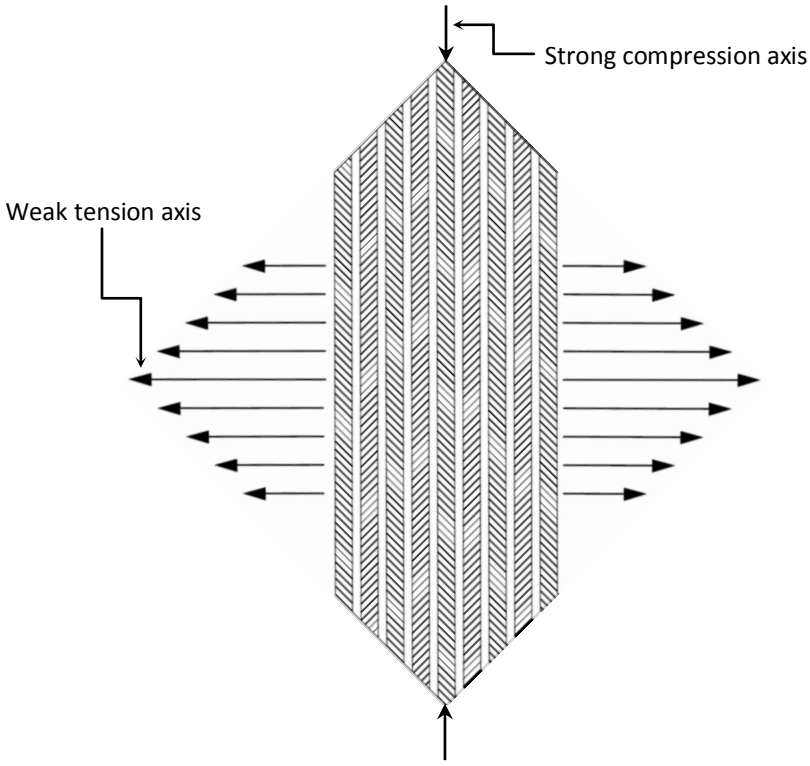

(**b**) Strong versus weak axis of the FRP panel

Figure (5.15): The bracing action of the tension field for the composite compression strut.

5.6.2 In-Plane Deflection

Figures (5.16a) to (5.16d) show the load versus in-plane deflection curves in four categories, as was the case for out-of-plane buckling in the previous section. Figure (5.16a) shows the effect of using closed sections versus open sections, in addition to the bonded area available for bonding the FRP panel to the steel plate. Figure (5.16b) shows the effect of using two-layer FRP panels versus three-layer panels. Figure (5.16c) shows the effect of fibre orientation for GFRP panels, and Figure (5.16d) shows the effect of end cut on the deflection response. These deflection curves are adjusted to remove the rigid body rotation of the column in the big frame testing rig where the picture-frame was attached. This in-plane rigid body rotation was measured using LP-9 and LP-10; refer to the instrumentation section (5.5).

From these figures it appears that no obvious trends can be indicated, except that generally, the strengthening technique insignificantly increases the stiffness, ductility, and ultimate capacity. It can be seen from the figures that the curves are consolidated together forming semi-bundles which further proves the argument mentioned above that they dose not form a good indication for the proposed strengthening technique which is originally does not target the in-plane deflection.

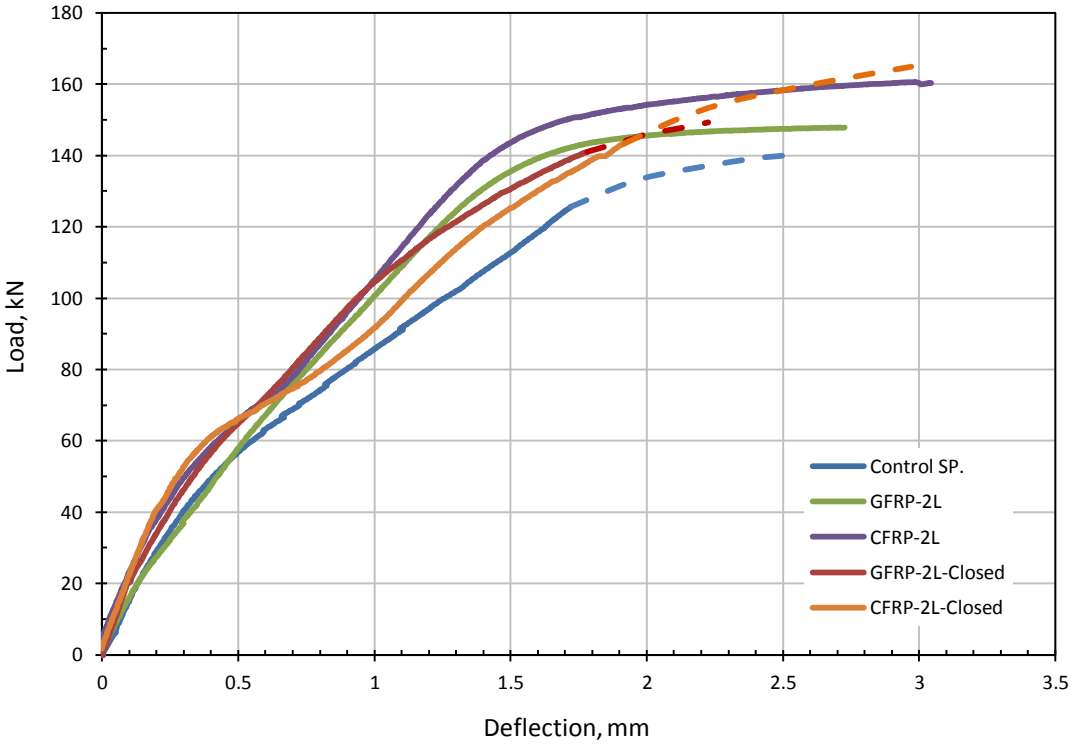

(**a**) Comparison of 2-layerd open and closed FRP sections

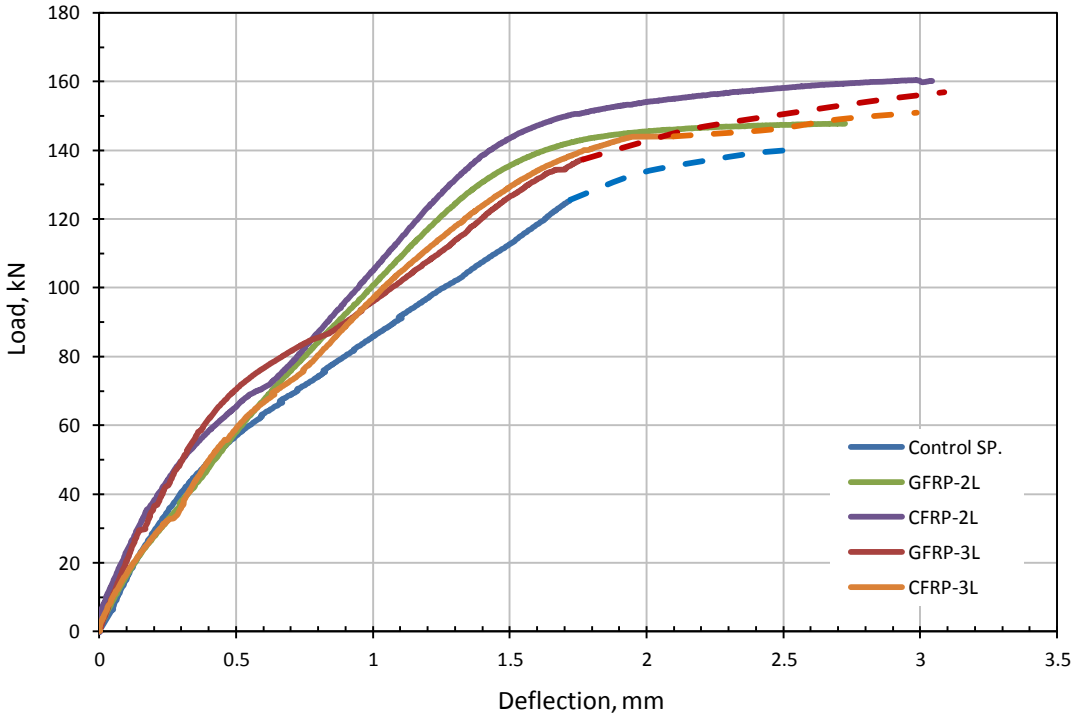

(**b**) Comparison of 2 and 3-layered FRP panels

Figure (5.16): In- plane deflection curves.

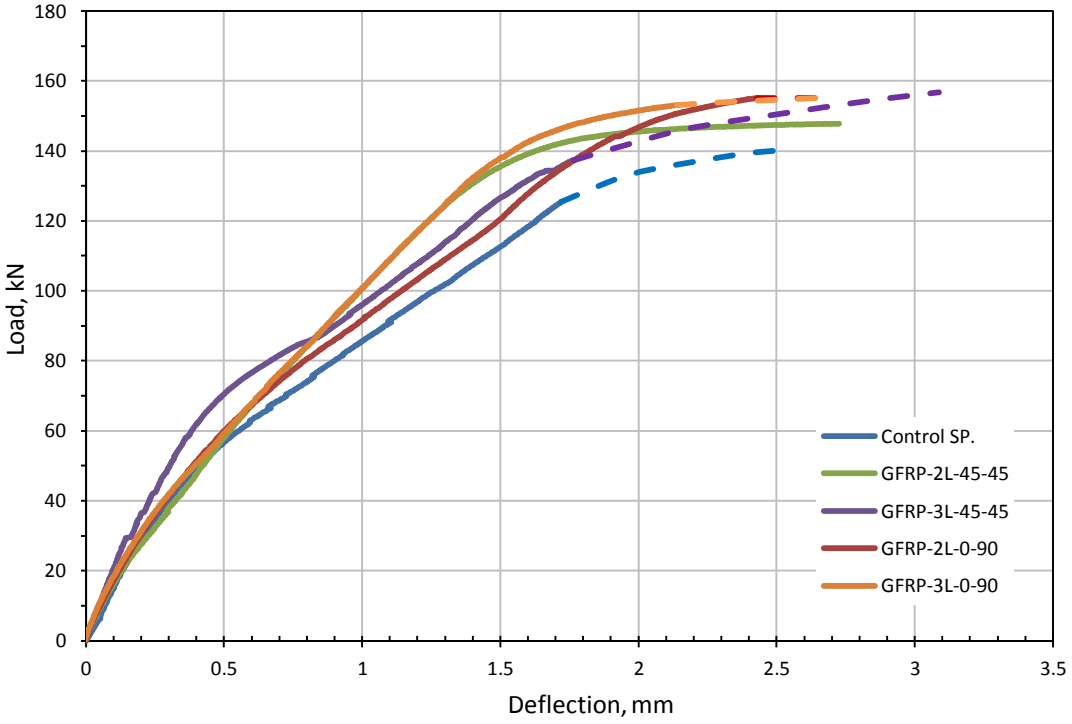

(**c**) Comparison of GFRP with different fibre orientations

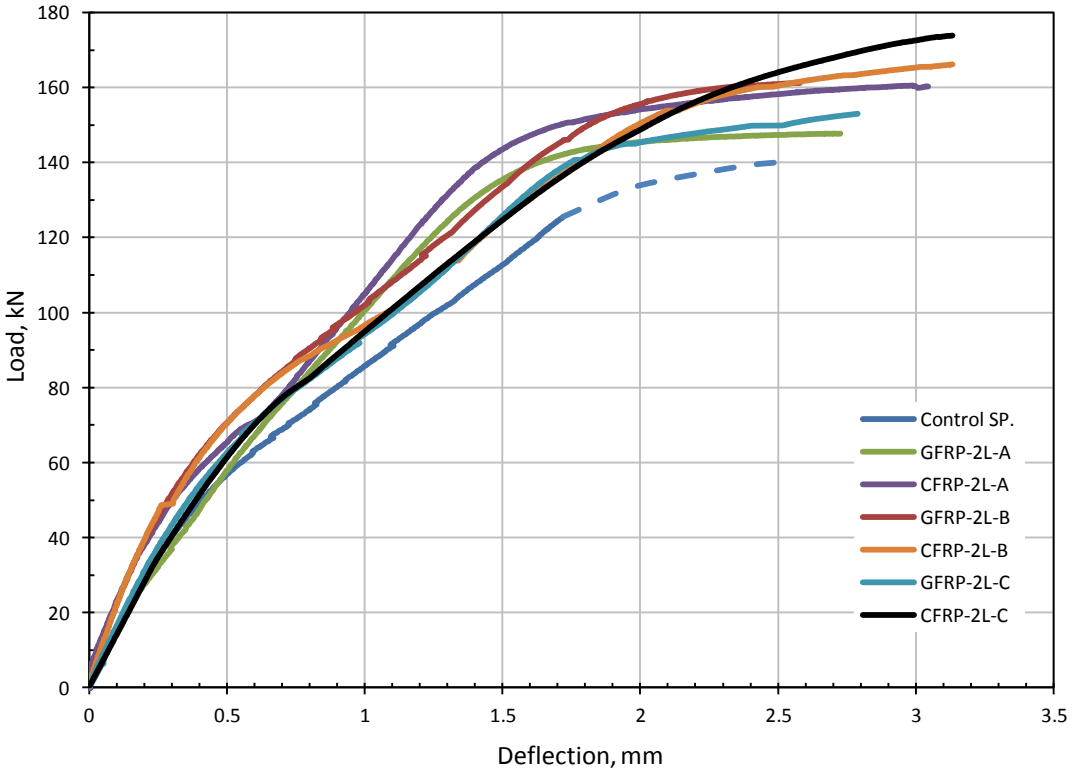

(**d**) Comparison of Type A, B, and C end cut

Figure (5.16 Cont.): In- plane deflection curves.

5.6.3 Non-Central Out-Of-Plane Displacement

In addition to LP-2 (the central out-of-plane displacement gauge which has been studied in detail in section 5.6.1), LP-1 and LP-3 helped in determining the vertical middle section buckling profile of the plate, while LP-4 and LP-5 provided an idea about the compression diagonal buckling mode, refer to Figure (5.10) for more details.

Figure (5.17a) illustrates the out-of-plane displacements of the control specimen for the non-central four displacement gauges. From this figure, it can be seen that the curves for LP-1, LP-3 and LP-4, LP-5 are matching as expected (symmetric buckling wave) until buckling takes place around 40.0 kN. Beyond buckling, there is an obvious diversion in the curves followed by an intersection point near the ultimate loading stage. This behaviour is altered for the FRP strengthened specimens. For all type A specimens (SP-2 to SP-9), Figures (5.17b) to (5.17i), respectively, we can see that there is an obvious diversion right over from the beginning of the test, especially with respect to LP-4 and LP-5 which represents the compression diagonal buckling profile. This might be caused by the thrust effect of the triangular sharp edge at the end of the FRP panel. This phenomenon is reduced by using the round edge (Type B) and the long panels (Type C), see Figures (5.17j) to (5.17L).

The shape of the out-of-plane contour lines is greatly affected by the stiffness of the FRP panel and the shape and position of the end cut. In addition, the orientation of the fibres, in the case of GFRP panels, affected the buckling shape of the plate and altered the direction of the out-of-plane displacement in more than one case; this was discussed in more detail earlier in section 5.6.1 as well.

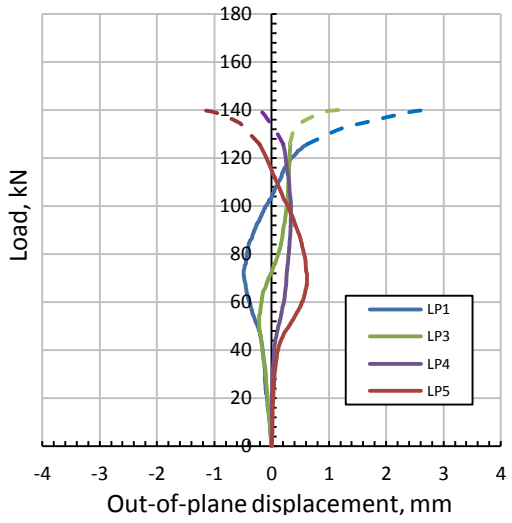

(**a**): SP-1, Control Specimen

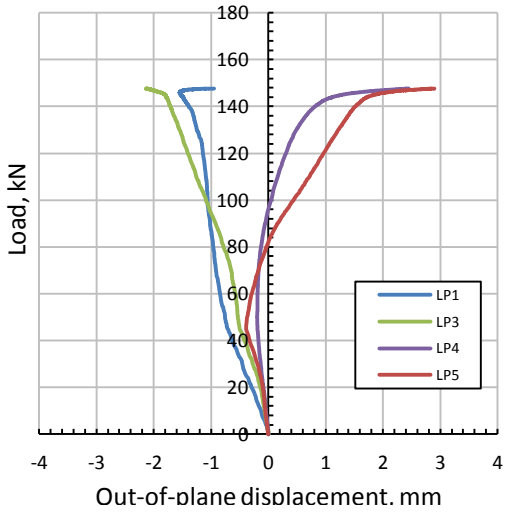

(**b**) SP-2, GFRP-2L-45°-45°-A

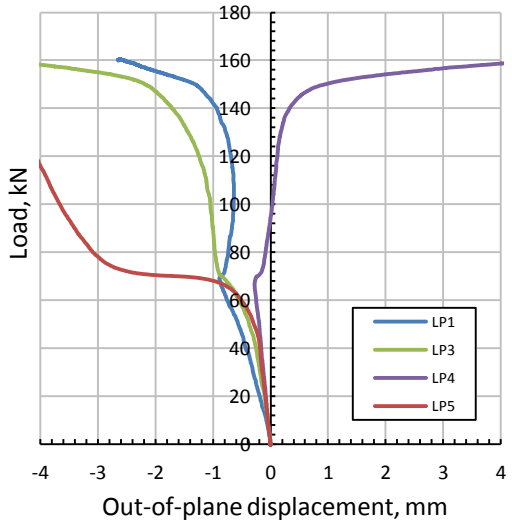

(**c**): SP-3, CFRP-2L-0°-90°-A

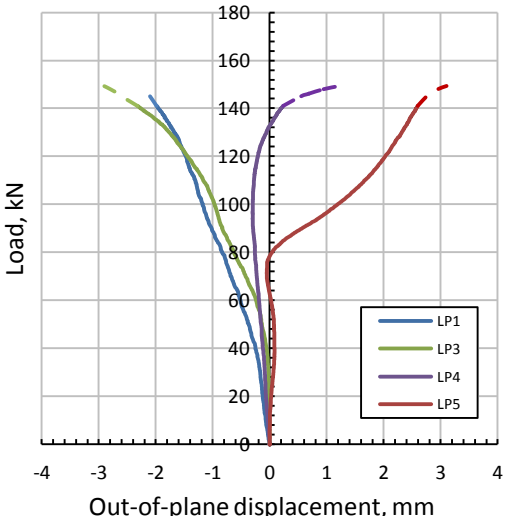

(**d**) SP-4, GFRP-2L-45°-45°-A-Closed section

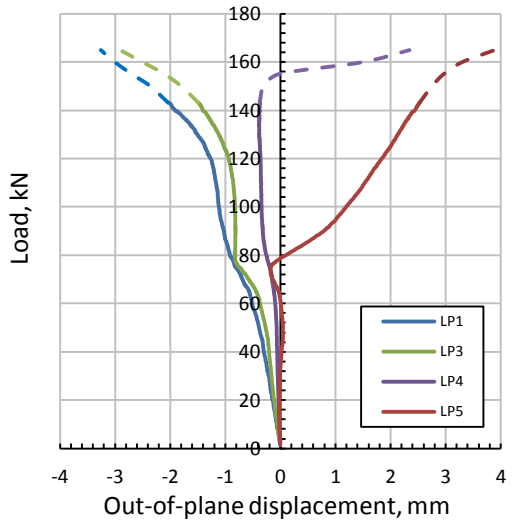

(**e**): SP-5, CFRP-2L-0°-90°-Closed section

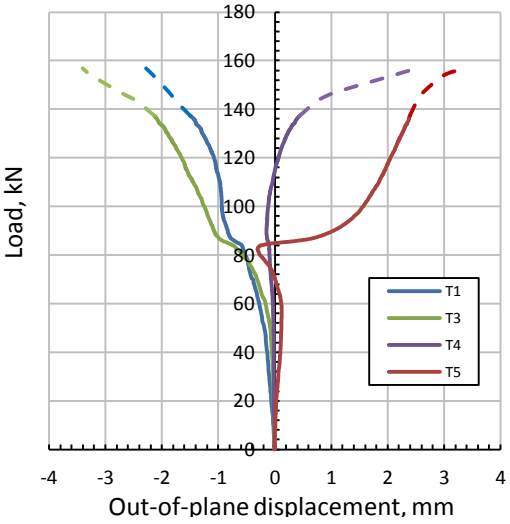

(**f**) SP-6, GFRP-3L-45°-45°-A

Figure (5.17): Non-central out-of-plane displacement.

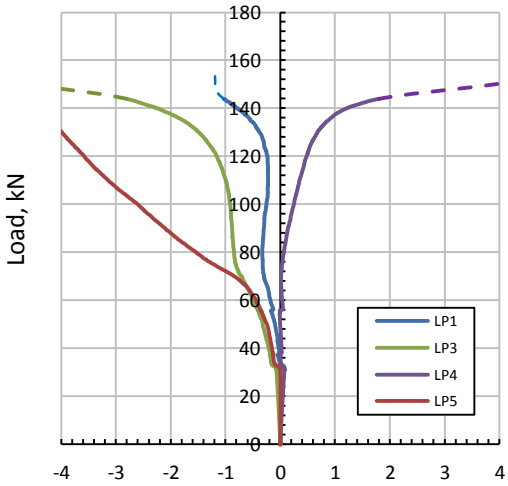

(**g**): SP-7, CFRP-3L-0°-90°-A

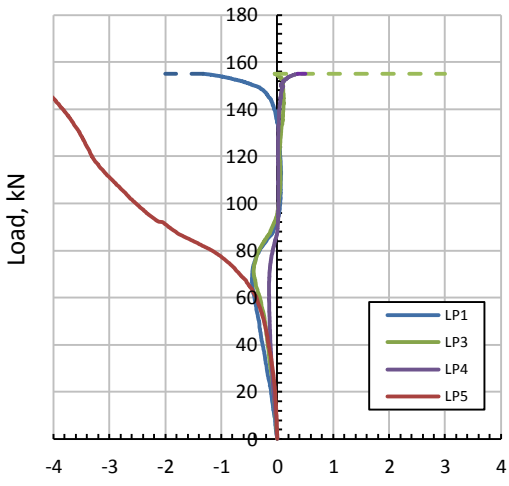

(**h**) SP-8, GFRP-2L-0°-90°-A

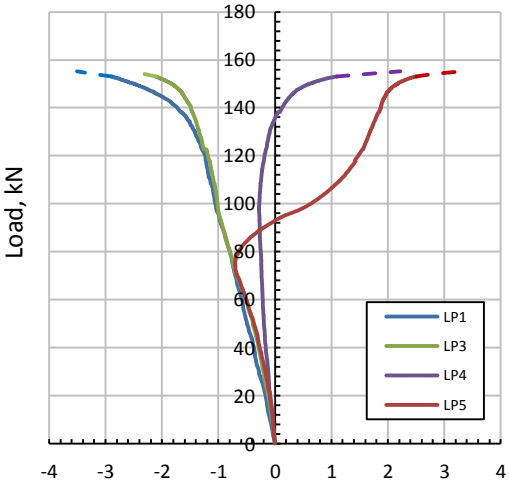

(**i**): SP-9, GFRP-3L-0°-90°-A

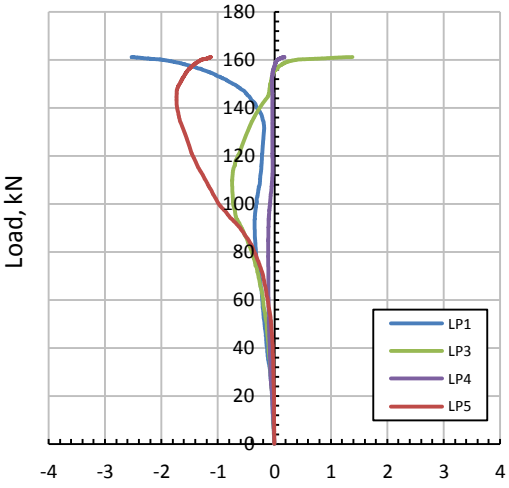

(**j**) SP-10, GFRP-2L-45°-45°-B

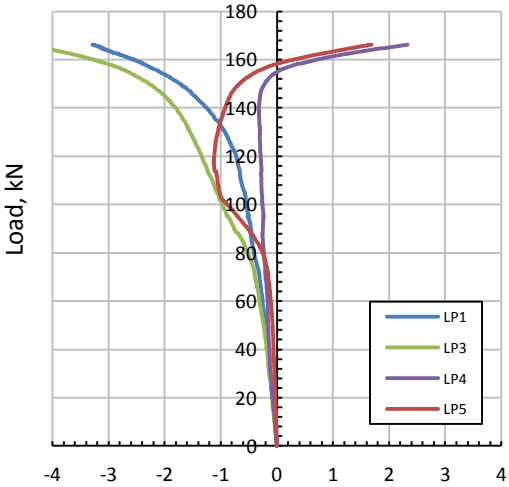

(**k**): SP-11, CFRP-2L-0°-90°-B

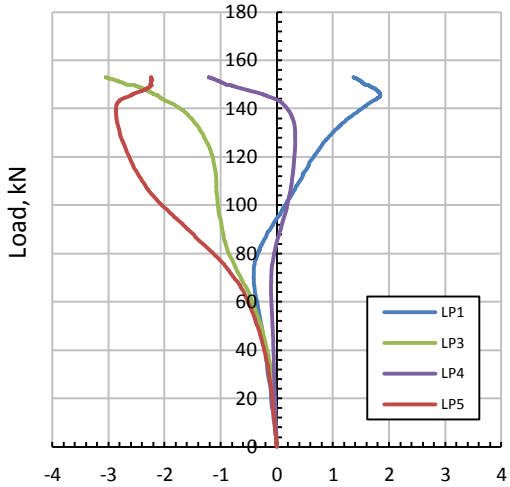

(**L**) SP-12, GFRP-2L-45°-45°-C

Figure (5.17 Cont.): Non-central out-of-plane displacement.

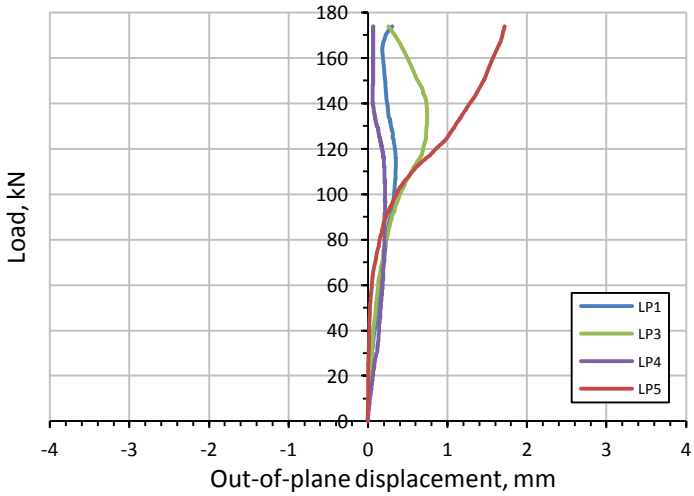

(**m**): SP-13, CFRP-2L-0°-90°-C

Figure (5.17 Cont.): Non-central out-of-plane displacement.

5.6.4 Strain

The steel plate strain was measured only at the centre of the plate. Two 45°/90° 3-element Rosette type FRA-6-11 were used to measure the strain in the horizontal (1-x), vertical (2-y), and tension diagonal (45°) directions for both the plate faces in the case of control specimen without FRP strengthening. However, the strain was measured only for one face in the case of FRP strengthened plates due to the difficulty associated with attaching a strain gauge with the FRP panel bonded at the same position, this measured strain was usually at the compression face due to the pre-buckling modes initiated by the strengthening technique as mentioned earlier, refer to Figure (5.10) for more details about the distribution of the strain gauges.

The strain readings were used to determine the shear strain and to calculate the secondary bending strain in the case of control specimen (SP-1). Figure (5.18a) illustrates the strain readings and the calculated shear strain for both faces of the control specimen (SP-1) while Figures (5.18b) to (5.18m) shows the one face strain readings and their calculated shear strain for all FRP strengthened specimens.

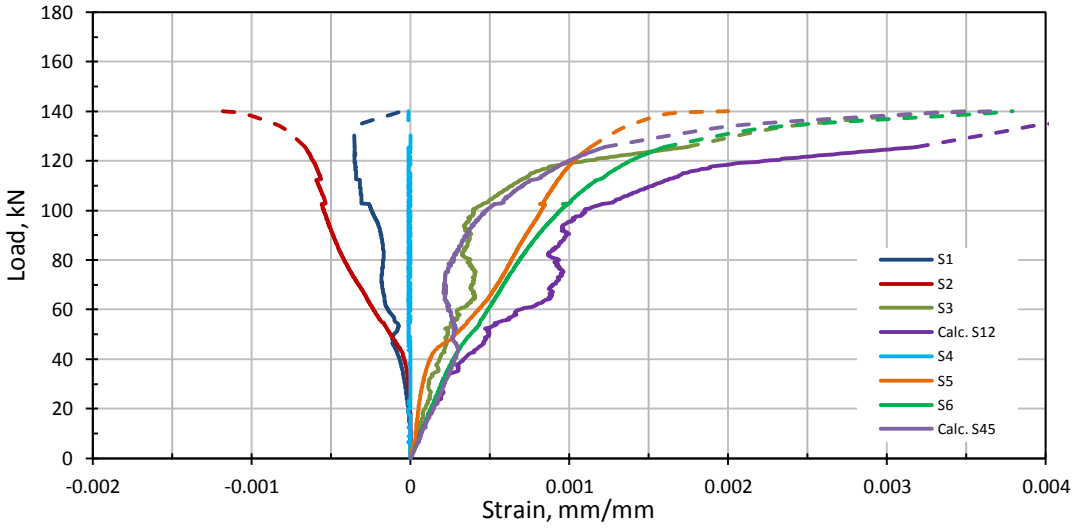

(**a**): Control specimen, SP-1.4

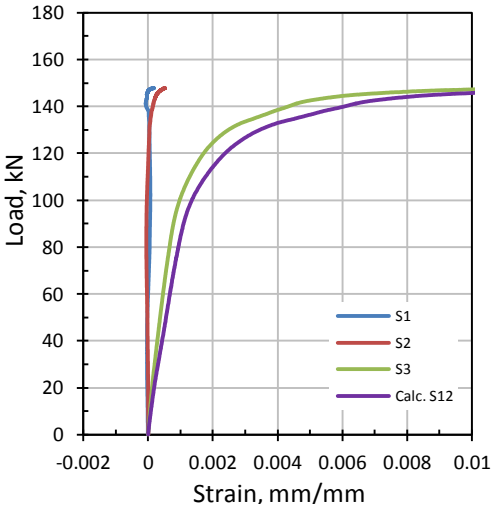

(**b**): SP-2, GFRP-2L-45°-45°-A

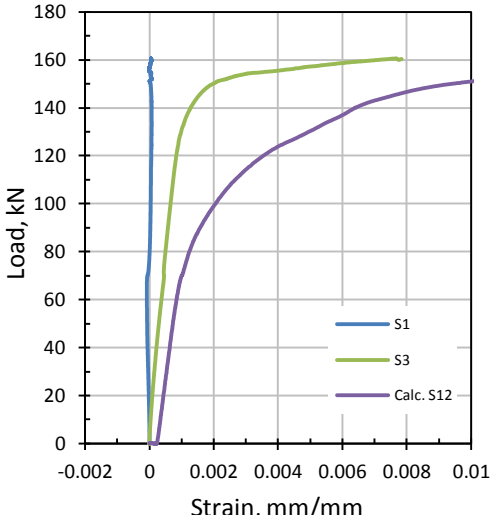

(**c**) SP-3, CFRP-2L-0°-90°-A

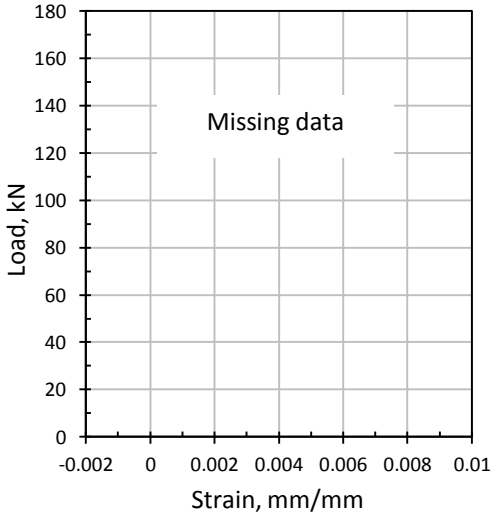

(**d**): SP-4, GFRP-2L-45°-45°-A-Closed

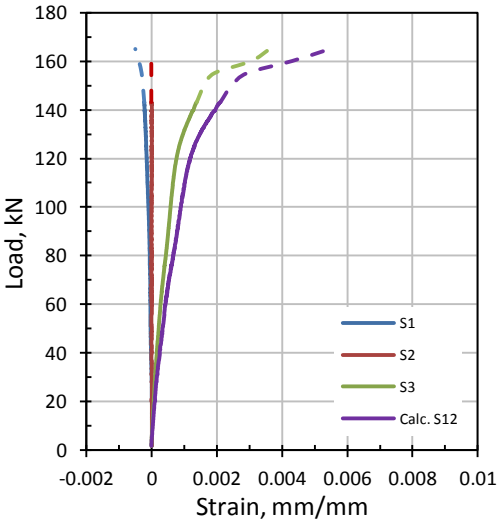

(**e**) SP-5, CFRP-2L-0°-90°-Closed

Figure (5.18): Central strain of the specimens.

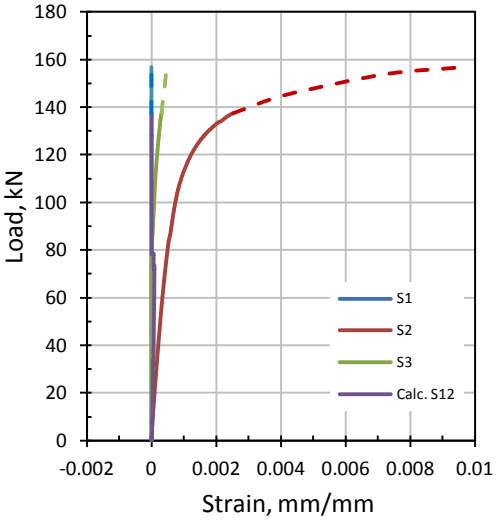

(**f**): SP-6, GFRP-3L-45°-45°-A

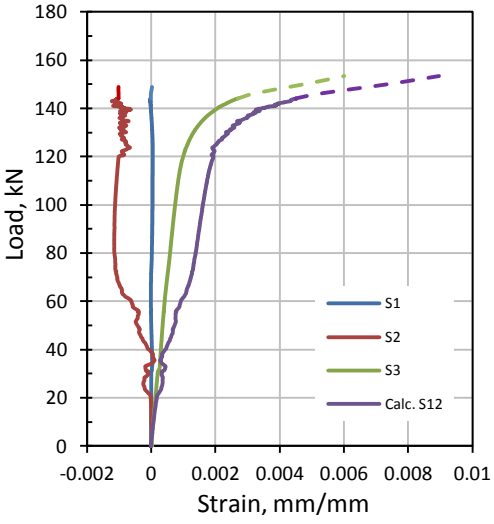

(**g**) SP-7, CFRP-3L-0°-90°-A

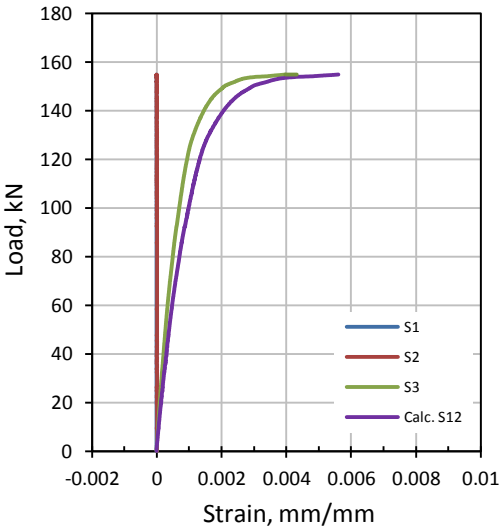

(**h**): SP-8, GFRP-2L-0°-90°-A

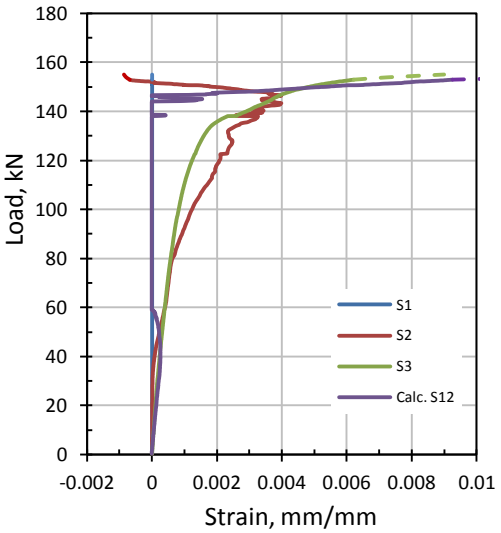

(**i**) SP-9, GFRP-3L-0°-90°-A

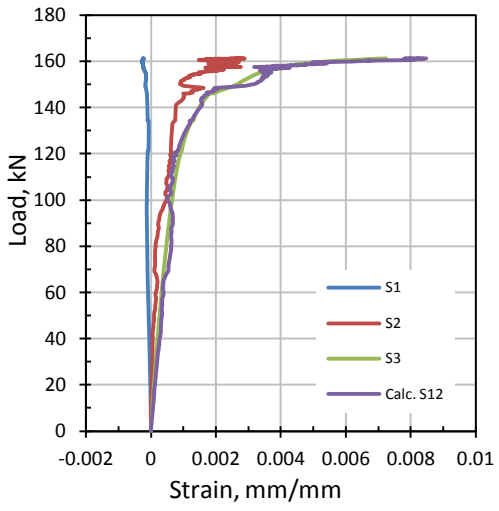

(**j**): SP-10, GFRP-2L-45°-45°-B

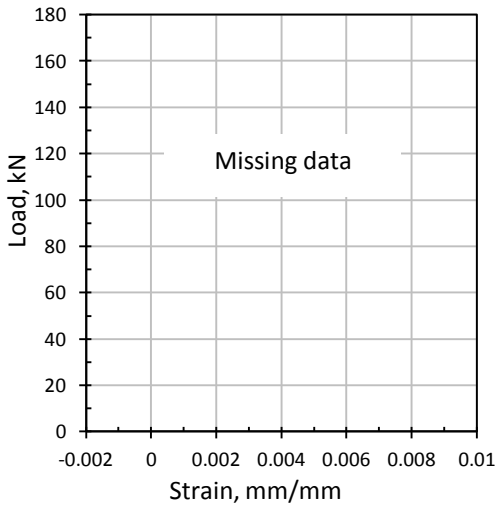

(**k**) SP-11, CFRP-2L-0°-90°-B

Figure (5.18 Cont.): Central strain of the specimens.

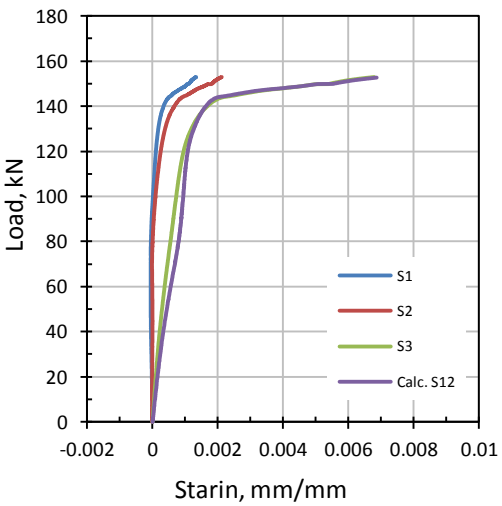

(**L**) SP-12, GFRP-2L-45°-45°-C

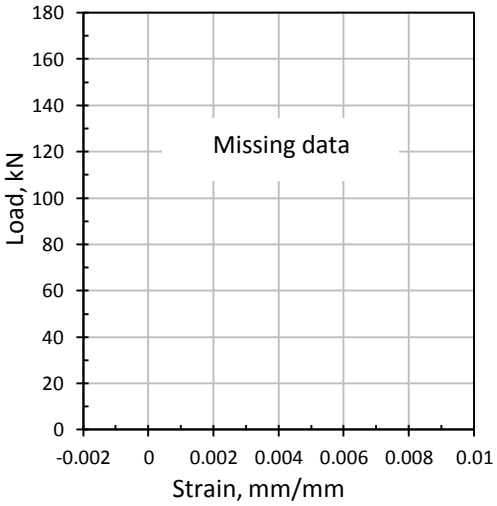

(**m**) SP-13, CFRP-2L-0°-90°-C

Figure (5.18 Cont.): Central strain of the specimens.

The shear strain (γ_{xy}) or (ε_{12}) is calculated according to the following reversed rosette analysis equation:

$$\varepsilon_{12} = \sqrt{2(\varepsilon_1 - \varepsilon_3)^2 + 2(\varepsilon_2 - \varepsilon_3)^2 - (\varepsilon_1 - \varepsilon_2)^2} \quad (5.3)$$

where:

ε_1 = measured strain in the horizontal x-direction.

ε_2 = measured strain in the vertical y-direction.

ε_3 = measured strain in the tension diagonal 45°- direction.

ε_{12} = the calculated shear strain.

The membrane and secondary bending strains can be found throughout the following series of equations:

Membrane strain:

$$\varepsilon_x = \frac{\varepsilon_{xTop} + \varepsilon_{xBott}}{2} \quad (5.4\text{-a})$$

$$\varepsilon_y = \frac{\varepsilon_{yTop} + \varepsilon_{yBott}}{2} \quad (5.4\text{-b})$$

$$\varepsilon_{xy} = \frac{\varepsilon_{xyTop} + \varepsilon_{xyBott}}{2} \quad (5.4\text{-c})$$

Secondary bending strain:

$$\varepsilon_x = \frac{\varepsilon_{xTop} - \varepsilon_{xBott}}{2} \quad (5.5\text{-a})$$

$$\varepsilon_y = \frac{\varepsilon_{yTop} - \varepsilon_{yBott}}{2} \quad (5.5\text{-b})$$

$$\varepsilon_{xy} = \frac{\varepsilon_{xyTop} - \varepsilon_{xyBott}}{2} \quad (5.5\text{-c})$$

where:

ε_{xTop} = measured strain in the horizontal x-direction of the tension face.

ε_{xBott} = measured strain in the horizontal x-direction of the compression face.

ε_{yTop} = measured strain in the vertical y-direction of the tension face.

ε_{yBott} = measured strain in the vertical y-direction of the compression face.

ε_{xyTop} = calculated shear strain in the tension face.

ε_{xyBott} = calculated shear strain in the compression face.

Figure (5.19) illustrates the distribution of secondary bending and membrane strains determined from the two strain gauges on the two faces of the steel plate.

Figure (5.18a) shows the strain curves for the two faces of the control steel plate (SP-1). Generally, the curves follow the logic of strain distribution in both the compression and tension faces of the specimen. All the curves tend to start linearly at the initial loading stage and then divert according to their position and direction. However, all of them show a dip around the estimated buckling load of 40.0 kN. Beyond buckling, the curves tend to behave non-linearly until failure takes place. The most important ones among them are S3 and S6 which represent the diagonal tension strain for both faces. The calculated shear strain follows the same pattern of the diagonal strain reflecting its major effect in addition to the minor effect of the other two strains represented by Equation (5.3). Except for the diagonal and calculated shear strains which exceeded the value of yielding strain (0.001375) several times at the final loading stage, the highest strain measured was S5 for the control specimen tension face with a value of 0.002.

The strain readings for SP-4, SP-11, and SP-13 were lost due to malfunction in the strain gauges while SP-3 had individual missing strain readings (S2) as can be seen in Figure (5.18c). In some other cases, readings were recorded, but they are

obviously disturbed. All this may be attributed to either physical damage during the bolt tightening process or due to an electronic short from the data acquisition used in the tests.

Looking at Figure (5.18) generally, there is no change in the behaviour of the strain distribution that can be detected. The general behaviour shows the same trend for all specimens and there are no major conclusions that can be drawn out from the strain curves at this stage. The strain at the opposite face was not measured (due to the abovementioned practical difficulty associated with bonding the FRP at the same place). This would have given the estimated reduction in the secondary bending strain. However, this problem will be discussed and treated extensively in Chapter 6 where the effect of the strengthening technique will be quantified by determining the reduced secondary bending strain in the plate welded boundaries and illustrate how this should increase the fatigue life expectancy for plate girders compared to the standards.

Finally, Figure (5.20) shows the experimental membrane and secondary bending strains for the control specimen (SP-1) calculated according to Equations (5.4) and (5.5) in addition to the maximum and minimum corresponding strains.

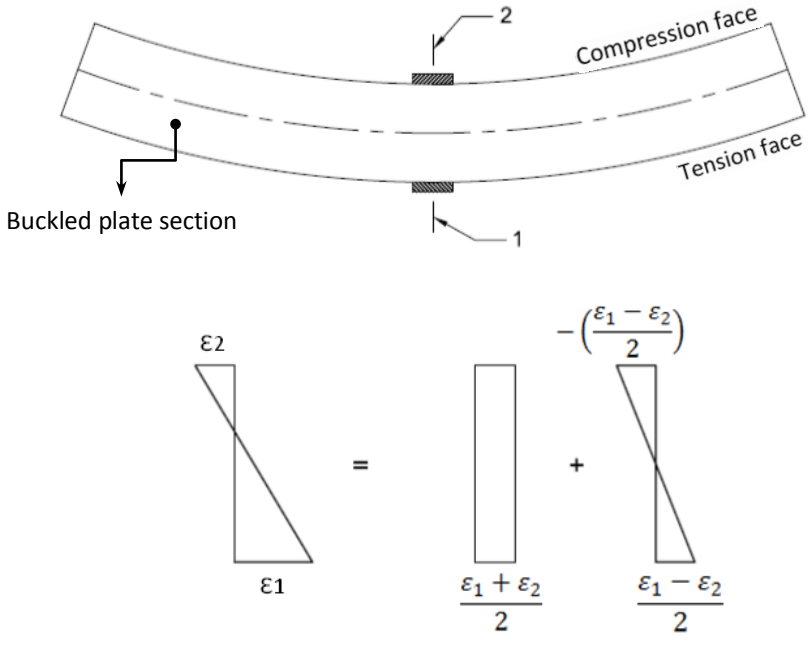

Figure (5.19): Membrane versus secondary bending strain.

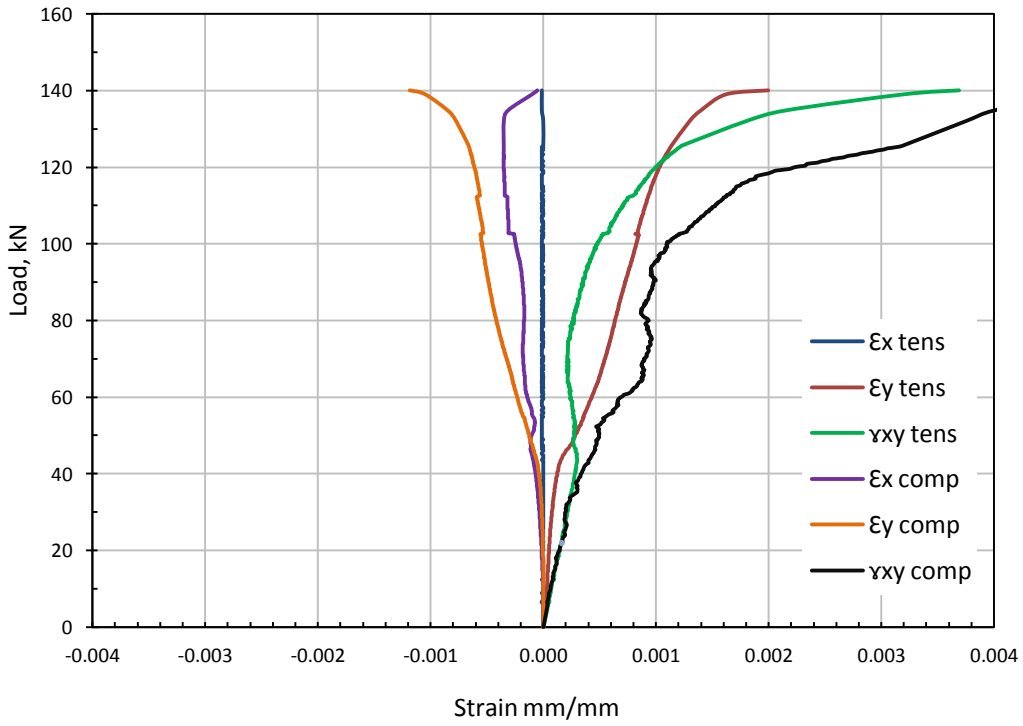

(**a**) Experimentally measured strain for both tension and compression faces of the steel plate

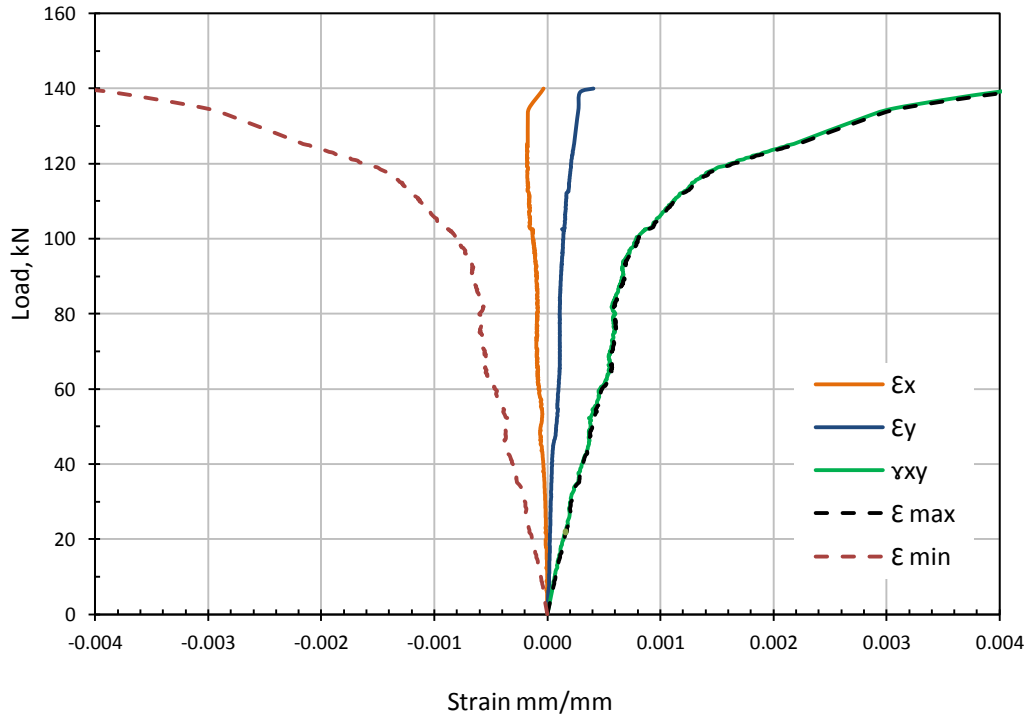

(**b**) Calculated membrane strain using Equation 5.4

Figure (5.20): Calculated membrane and secondary bending strains.

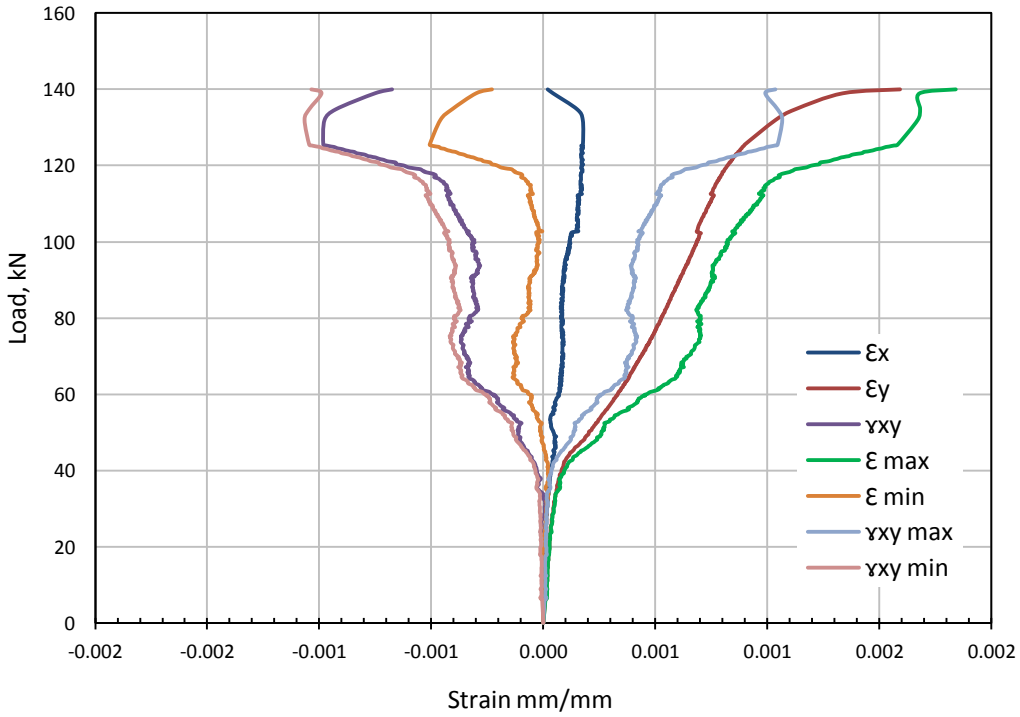

(**c**) Calculated secondary bending strain on the plate tension face using Equation (5.5)

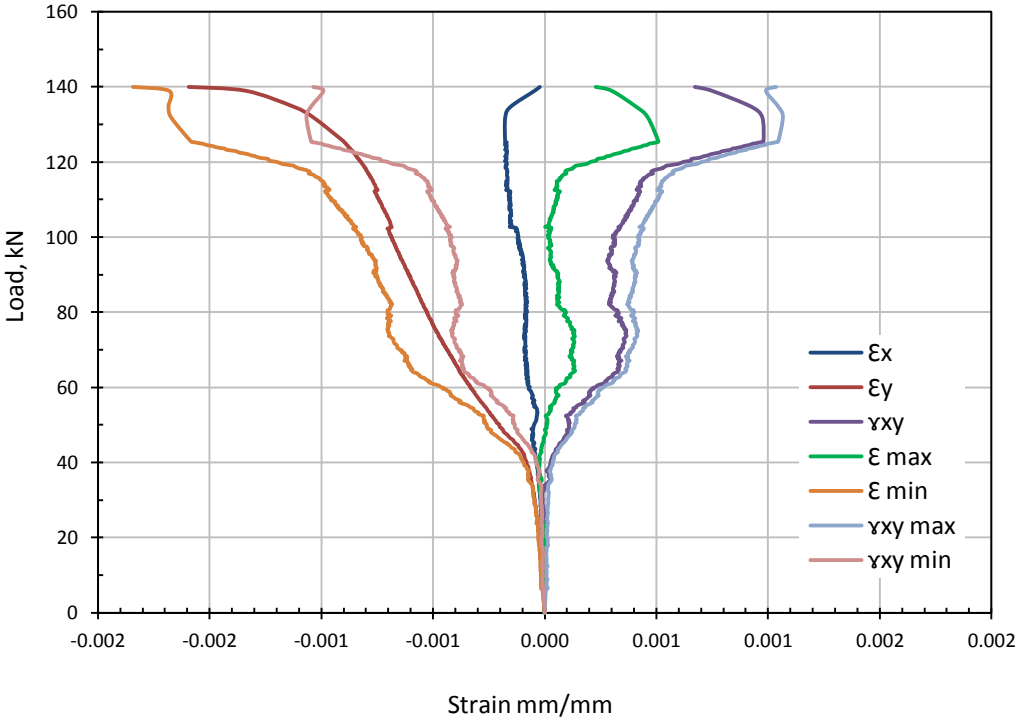

(**d**) Calculated secondary bending strain on the plate compression face using Equation (5.5)

Figure (5.20 Cont.): Calculated membrane and secondary bending strains.

5.7 NUMERICAL MODELLING

In this section, full detailed and simplified nonlinear finite element models are presented. The full 3-D finite element picture-frame model was established to make sure that the final conceptual design is working and that the induced stresses on the frame components are within working stress. However, the numerical cost for this fully detailed non-linear model was very high and the need for a simplified model was evident to be able to apply the proposed strengthening technique where even more time will be required for the composite steel-FRP section to be analyzed.

The simplified composite model presented in this section is meant for demonstrating the expected theoretical behaviour after applying the proposed strengthening technique and comparing it with the experimental behaviour to find any possible deficiencies and act upon it. This is why a simplified isotropic material constitutive model is proposed in this chapter while a fully detailed orthotropic material constitutive model is going to be presented in Chapter 7 as a part of the proposed design method.

5.7.1 Picture-Frame Model

A geometrical and material non-linear finite element analysis was used to model the picture-frame and the tested steel plate together. Commercial software (*Abaqus* 6.10) was used.

The steel plate was modelled using a nine node reduced integration shell element S9R5, which has five degrees of freedom per node. S9R5 elements are meant for slender plates and were derived originally according to Kirchhoff thin plate bending theory. This element is not available in *Abaqus* standard CAE and can be used only through an *Abaqus* input file. A Matlab code was written to create the nodes and element incidences to be incorporated in *Abaqus* input files. The size of the web elements was chosen to be 25×25mm which satisfies the condition of (h_w/20) based on the full convergence study implemented in Chapter 3. The initial imperfection was found using the elastic Eigen buckling modes; these were initiated using the buckling analysis available in *Abaqus CAE* and then the experimentally measured initial imperfection were imposed using *Abaqus* script commands in the input file, refer to Figure (5.4) to see the picture-frame finite element model stress

and out-of-plane displacement contour line distributions. The picture-frame components were initially modelled using the general purpose 3-D element (C3D8R) with dimensions ranging between 10 and 15 mm depending on their location.

Elastic-perfectly plastic steel constitutive model was adopted for the steel in this model with a modulus of elasticity (E_s) equal to 200GPa. The 2mm thickness tested steel plate had yield strength (f_y) of 275MPa while the steel frame components had a yield strength of 355MPa.

Figure (5.21a) compares the central out-of-plane displacement determined both from the test of the control specimen and its finite element simulation. It can be seen that the finite element curve matches the experimental one within the initial linear part of the curve. However, after buckling the two curves divert from each other where the finite element one shows a stiffer response. This behaviour continues until the specimen reaches the ultimate loading stage where the two curves come back together to form almost similar yielding plateau. This behaviour brings us back to the earlier mentioned slack in the curves (section 5.6.1) due to the minor grip slippage during test which starts right after buckling and ends with yielding of the steel plate.

Figure (5.21b) and (5.21c) compares the central strain obtained both from the experimental test and the finite element model, respectively. From the figures it can be seen that they both correlate well except for the (γ_{xy}) in the tension face and this is due to the malfunction in the readings of the (ε_x) strain gauge which was giving false readings very close to zero during the test.

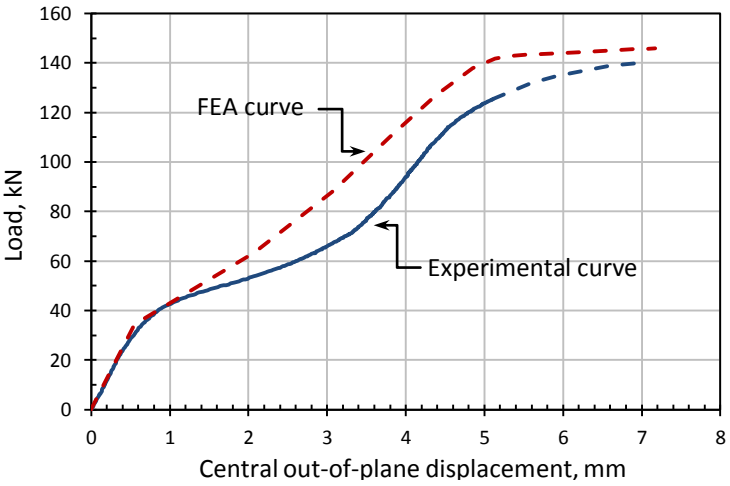

(**a**) Comparison of central out-of-plane displacement

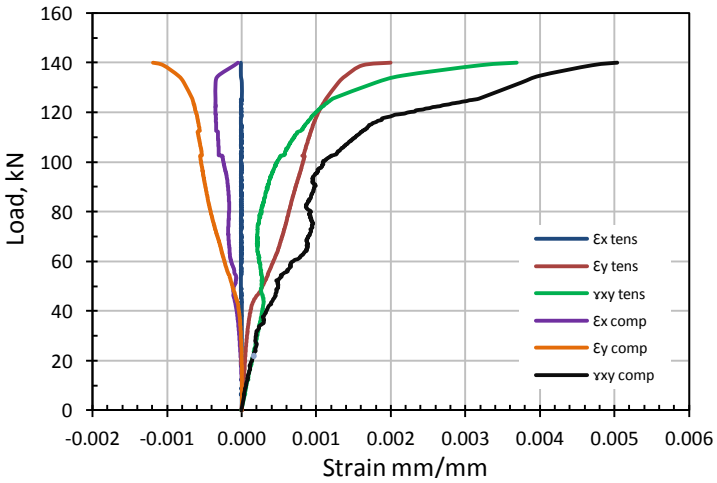

(**b**) Experimental measured central strain

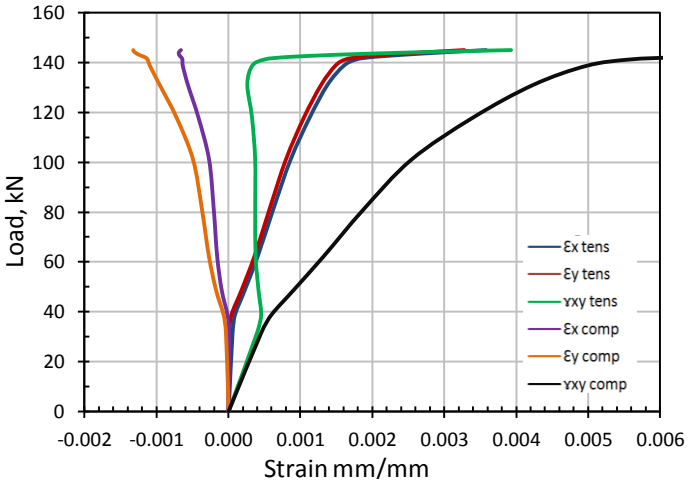

(**c**) FEA central strain

Figure (5.21): Comparison between the experimental test and finite element model results for the control specimen.

5.7.2 Simplified Picture-Frame Model

The cost of analysis for the original finite element model in the previous section is very high (36 hours). The idea behind building this initial model was to make sure that the conceptual design of the picture-frame testing rig is working and that the stresses are not exceeding the working limits in the components; and this was fulfilled. A simplified finite element picture-frame model was used to examine the composite steel-FRP section.

The simplified finite element model holds the same concept of the original picture-frame and it depends on the 4-hinge beam-chain mechanism as well. The difference is that not all the component are modelled and it was instead idealized as can be seen if Figure (5.22). The frame section was optimized by comparing the second moment of area for the original and simplified picture-frame models.

A bilinear elastic-plastic stress-strain curve was adopted for the steel constitutive model, with a modulus of elasticity (E_s) of 200GPa and yield strength (f_y) of 275MPa and 355MPa for the 2mm tested steel plate and the outer frame plates, respectively. An (E_s/100) plastic modulus slope was allowed according to the Eurocode to allow for strain hardening, see Figure (5.23). This helped in using a load control method instead of the more time consuming displacement control method used in the original finite element model.

The loading mechanism was changed as shown in Figure (5.22a) because of the divergence caused by the stress concentration in the case of using concentrated load. It is worth mentioning that the size of the element for the steel plate was reduced from 25×25mm to 20×20mm in the simplified model since the number of degrees of freedom is limited in this model. Another obvious change is the elements used for the outer frame where S4R shell elements were used instead of the 3-D element used in the original model.

The boundary conditions can be illustrated in Table 5.4 and are shown in Figure (5.22b). Each two components meeting at the four joints of the picture-frame (surface 1 and 2) were coupled in the three translational degrees of freedom (*u*, *v*, and *w*) while the in-plane rotation ($\boldsymbol{\theta_z}$) was left free to simulate the 4-hinge beam mechanism.

Table 5.4: Simplified picture-frame model boundary conditions (refer to Figure 5.22b)

Surface	u	v	w	θ_x	θ_y	θ_z
1	1	1	1	1	1	0
2	0	0	1	1	1	0
3	1	1	1	1	1	1
4	0	0	1	1	1	1

(1) stands for fixed and **(0)** stands for free.

The same element (S9R5) used for modelling the steel plate was used to model the FRP panels.

The FRP constitutive material model was an equivalent isotropic shell section and it was taken by simply multiplying the thickness of the FRP panel by the corresponding fibre volume fraction (FVF). The modulus of elasticity of the FRP panel was taken equal to 22,090MPa and 43,880MPa for the GFRP and the CFRP, respectively. These are the theoretical FRP mechanical properties calculated in Chapter 4 (refer to Table 4.5). Tie constraints are applied between the steel plate, the picture-frame, and the FRP bonding strips for simplicity, even though it is known that tie constraint will give higher capacity than the same model with cohesive surface interaction instead.

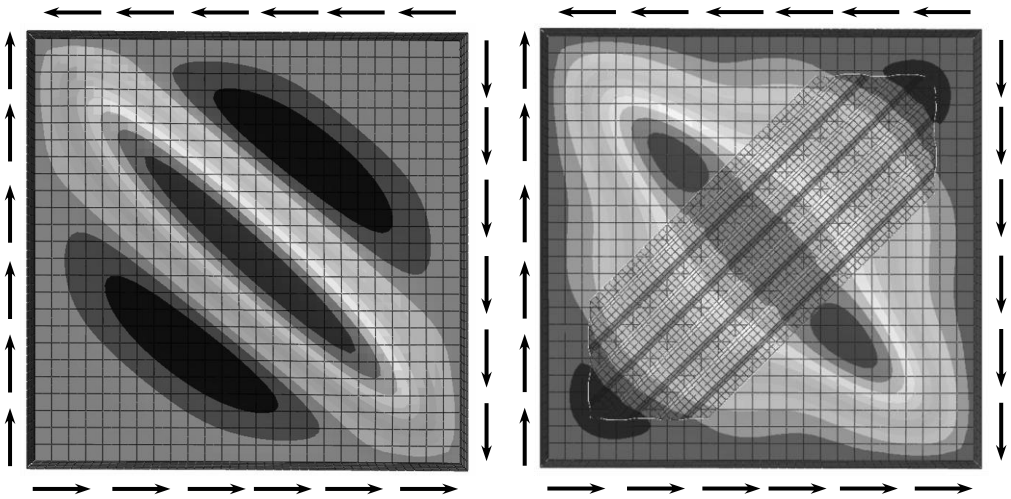

(**a**) Front view of out-of-plane displacement contours and the applied shear load for both the control specimen and an FRP strengthened one.

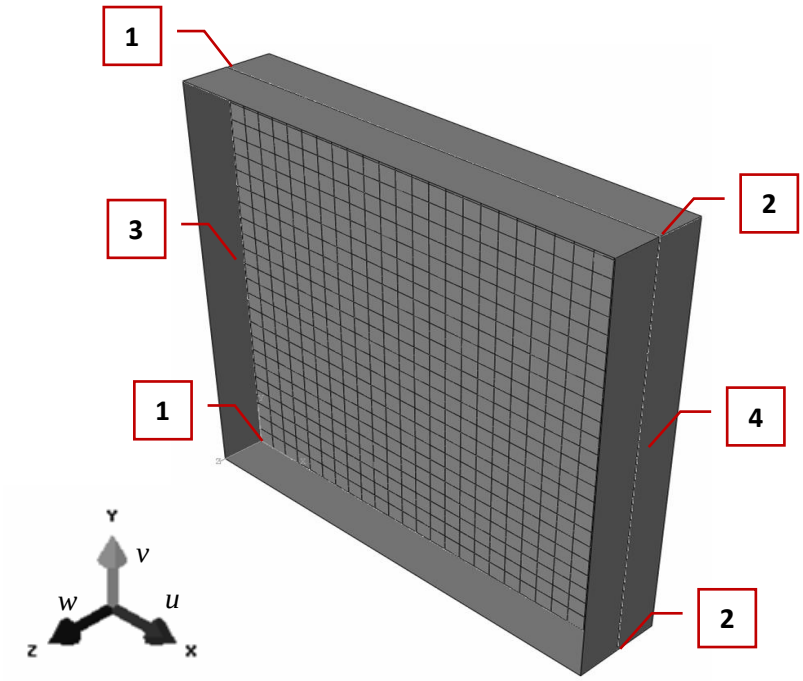

(**b**) Boundary conditions of the simplified picture frame model

Figure (5.22): Simplified picture frame finite element model.

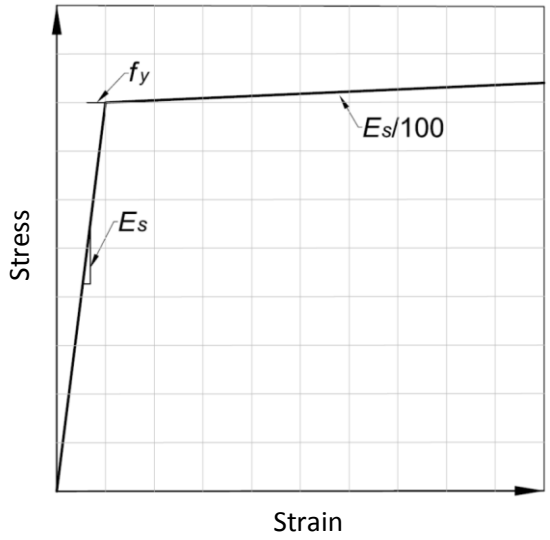

Figure (5.23): Bilinear stress-strain constitutive steel model.

Figure (5.24) compares between the experimental tests and the finite element models for the control specimen (SP-1), GFRP-3L-(45°-45°)-A (SP-6), and CFRP-3L-(0°-90°)-A (SP-7). These specimens were chosen as they represent the three-layered FRP panels which provided the best results for Type-A panels. The figure shows that the model predicts both the strength and the behaviour of the control specimen (without FRP strengthening) with reasonable accuracy, especially compared to the original picture-frame model. However, the composite model does not show the same accuracy. This may mostly be attributed to the simplifications adopted in simulating the FRP material and the above mentioned slack that took place during the test due to the minor slip at the top left corner of the picture-frame along the diagonal tension field. This problem was solved in the final series of tests by using a different testing mechanism as will be seen in Chapter 6. The finite element model curve might have approached the experimental one at the final loading stage if it did not start diverging because of the high deformation in the steel plate compression corners associated with the punching effect resulting from the sharp triangular end cut of the FRP panel (refer to Type-A in Figure 5.1a and Figure 5.22a).

With respect to the in-plane deflection, it can be seen from Figure (5.24) that the model did not succeed in obtaining a good correlation except in the initial linear part of the curve where the specimen is still in the elastic range, however, it gives the

same behaviour and trends. In general, the composite model predictions are acceptable as indicators and not as reference values. Nevertheless, as a general conclusion, it is believed that the behaviour of a real plate girder lay somewhere between the finite element model and the experiments. More finite element modelling will be shown for the final series of tests in Chapters 6 and 7.

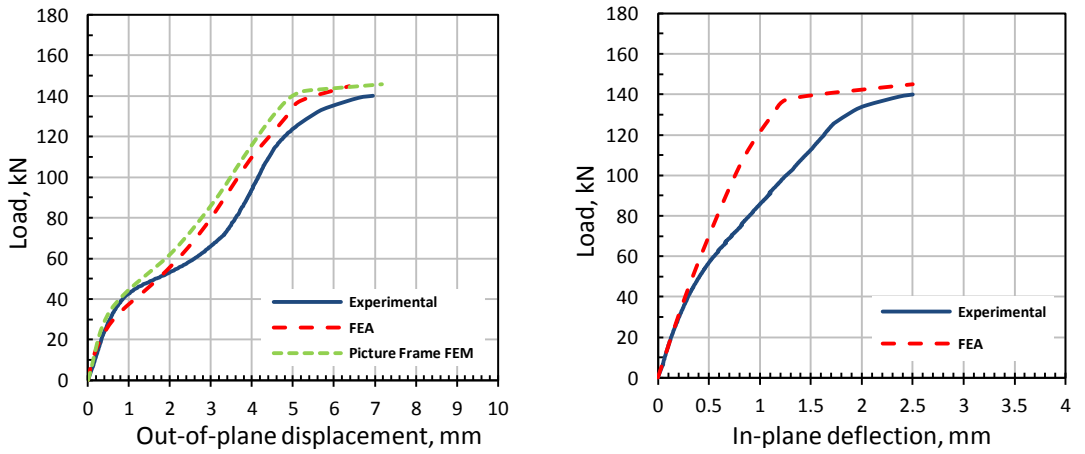

(**a**) Control specimen (SP-1)

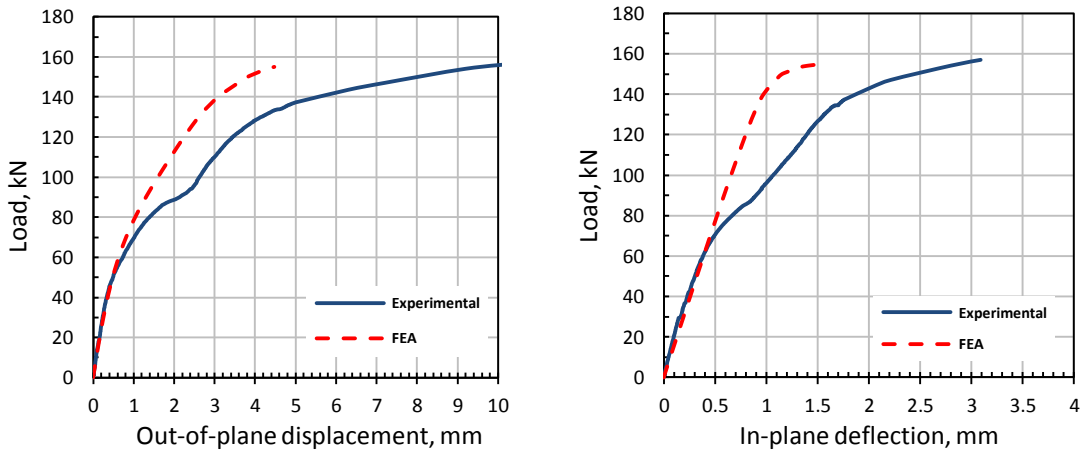

(**b**) GFRP-3L-(45°-45°)-A (SP-6)

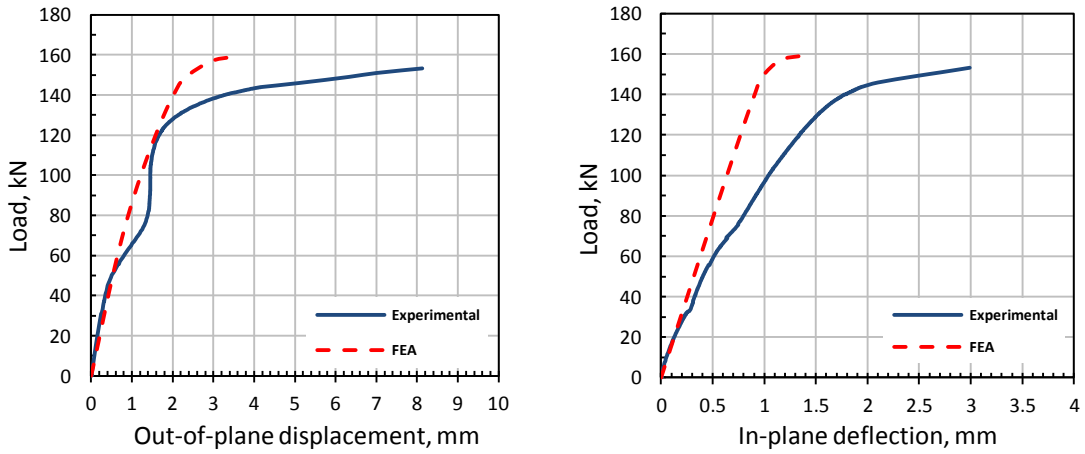

(**c**) CFRP-3L-(0°-90°)-A (SP-7)

Figure (5.24): Out-of-plane displacement from the finite element analysis.

5.8 SUMMARY AND CONCLUSIONS

A novel preformed corrugated FRP panel was introduced in Chapter 4 (Phase-1) to strengthen slender steel plates, such as the web of a plate girder, against breathing deformations of plates leading to fatigue failures.

In this chapter, the initial series of tests (Phase-2) was performed to test the efficiency of the proposed panel under static shear loading. Thirteen steel plates were strengthened with the proposed preformed corrugated FRP panel and tested using a special picture-frame rig. This was designed to hold the steel plate in position with the required boundary conditions while applying in-plane shear without the need to weld the plate into a stiff frame like the case with ordinary plate girders.

The results of the initial series of tests proved the efficiency of the proposed strengthening technique in increasing the stiffness of the steel plate section up to 3 times (with respect to the limits and data ranges adopted in this study) and consequently increasing its buckling resistance. In addition to that, the proposed strengthening technique succeeded in preserving the ductile prototype failure associated with intact (unstrengthened) steel plates, which is a very important factor in safety usually ignored by other FRP strengthening techniques. The proposed strengthening technique did not only preserve the ductile failure type but also increased the energy absorption capacity by a factor of 1.5. No bonding failure could be detected during or after the test even when the steel plate was highly deformed and fully yielded.

The variables studied in this series were:

(1) The effect of FRP material which significantly affected the stiffness and buckling resistance of the strengthened specimens. The CFRP showed more superior behaviour in increasing the stiffness and buckling resistance of the strengthened specimens due to its higher modulus of elasticity than the GFRP.

(2) The type of section (open versus closed), which showed no significant effect in increasing the stiffness and had no effect on the bonding capacity with respect to the originally proposed open section one.

(3) The number of the FRP layers used to make the corrugated panel had a significant effect on the behaviour of the strengthened specimens where the 3-layered ones showed higher capacity and much more stable and ductile behaviour especially for the GFRP ones.

(4) The orientation of the GFRP used, which was taken with respect to the corrugation axis, had a moderate effect on the capacity of the strengthened specimens. The 0°-90° succeeded in slightly increasing the ultimate strength for the 3-layered specimen while it altered the mode of failure to a more brittle one with respect to the 2-layered one.

(5) The effect of the end cut shape and position of the FRP panel was not very significant in comparing Type-A (i.e. the triangular cut) and Type-B (i.e. the circular cut) where they almost acted the same, but was significant for Type-C (i.e. the long one) even when the mode of failure was altered for the GFRP specimen. This is believed to be due to the longer dimension which provided less stiffness to the panel and consequently may have altered the mode of failure.

A geometrical and material non-linear finite element analysis was used to model the specimens in this study. A simplified picture-frame model was utilized in this study to avoid the more numerically expensive original model. The unstrengthened model was able to realistically simulate the behaviour of the specimens throughout all loading stages, while the strengthened model provided convincing results only within working stresses before reaching the failure plateau.

As a final result of this chapter with respect to the optimized FRP section, it is decided to combine the effect of using 3-layered FRP panel with the effect of having Type-C end cut both for GFRP and CFRP materials for further investigation of its efficiency under cyclic loading in Chapter 6. Then the experimental results will be used to validate a more sophisticated non-linear composite finite element model which will be used in a parametric study leading to the proposed design method in Chapter 7.

CHAPTER REFERENCES

ASTM, Committee ASTM D2651 (2008): "Standard Guide for Preparation of Metal Surfaces for Adhesive Bonding," Annual Book of ASTM Standards, ASTM Inter., West Conshohocken, USA, 6 pp.

ASTM, Committee ASTM D4541 (2009): "Standard Test Method for Pull-Off Strength of Coatings Using Portable Adhesion Testers," Annual Book of ASTM Standards, ASTM Inter., West Conshohocken, USA, 16 pp.

LEE S.C., DAVIDSON J.S., and YOO C. H. (1996). "Shear buckling coefficients of plate girder web panels," Computers & Structures, Vol. 59, No 5, pp. 789-795.

OKEIL A.M., BINGOL Y., and FERDOUS M.R. (2009). "A Novel Technique for Stiffening Steel Structures," Final Report No. FHWA/LA.08/441, State Project No. 736-99-1447, Dept. of Civil and Environmental Eng., Louisiana State University, Baton Rouge, LA, USA, 78 pp.

This page is intentionally left blank

Chapter Six

PHASE-3
Final Cyclic Series of Tests

6.1 INTRODUCTION

In the previous chapters, a new strengthening technique for stiffening thin-walled steel plates against shear buckling using bonded preformed corrugated FRP panels was proposed and optimized. In Chapter 4, the proposed FRP panel was designed, built, and its mechanical properties were determined. This new corrugated FRP panel was optimized in Chapter 5 (Phase-2, the initial series of tests) for different variables including the type of FRP used (CFRP or GFRP), the number of layers of fabric for the same fibre volume fraction, the FRP panel section (open vs. closed section), the orientation of the glass fibres with respect to the axis of corrugation for GFRP profiled panels, and the shape and position of the FRP panels' end cut. As a final conclusion from Chapter 5, the 3-layered corrugated FRP panel having Type-C end shape was chosen as the optimized FRP panel for its superior behaviour.

The optimized FRP panel will be further checked in this chapter (Phase-3, the final series of tests) for its efficiency in strengthening web plates against shear buckling under cyclic loading. The increase in stiffness and the improvement in fatigue behaviour due the reduced surface and secondary bending stresses induced by the breathing phenomenon will be investigated both for GFRP and CFRP panels.

In this chapter, the proposed strengthening system is applied to the web of a presumed end panel in a steel bridge, where high shearing forces are typically exerted. While limited previous work has shown that strength increase is possible for steel structures reinforced with FRPs, relatively little stiffness increase has been observed to date and limited care was drawn to the alteration of the collapse mechanism from a typical ductile failure of steel plate girders to the more brittle one of plate girders strengthened with the common FRP strengthening techniques known to date. However, it will be shown again in this chapter that the proposed strengthening technique did not only succeed in stiffening the web plates against shear buckling and increased their ultimate shear capacity; but it also maintained and

improved the typical ductile failure associated with intact (unstrengthened) steel plate girders.

6.2 SPECIMEN DESCRIPTION

Phase-3 comprises 3 static tests and 3 cyclic tests on single-panel specimen shown in Figure (6.1). The specimen represents an end panel of a longer plate girder made from several panels where high shearing forces exist. Instead of joining the two end panels and testing them as is common in testing plate girders under shear loading, the rule of symmetry was exploited and only one panel is tested; refer to Figure (5.2) in Chapter 5 for more details about the application of symmetric boundary conditions. The specimen was provided with rigid-end posts as can be seen in Figure (6.1) to make sure that the tension field is fully developed and that there is no significant deformation in the end stiffener which might compromise the test by leading to lower ultimate loads than the real ones.

The slenderness ratio was kept at almost the same value adopted in the initial series of tests (Phase-2) where (h_w/t_w) is equal to 245 in comparison to 250 in the initial series of tests. This value is worth investigating being at the end of the allowed practical margin and that the more slender the web is, the more the effect of the strengthening technique can be shown. However, the aspect ratio (a_w/h_w) was changed to be 1.5 in this series in comparison to 1.0 in the initial series of tests (Phase-2). The value of (a_w/h_w =1.5) is more common in the design practice both from practical and economical perspectives as long as the post-buckling shear strength of the web is taken into consideration, which is something commonly accepted by most codes of practice nowadays. Hence, it is worthwhile investigating since the aspect ratio plays a major role in the shear strength of steel plate girders.

The web plate was made from S275 grade steel while the flanges and stiffeners were made from S355 grade steel. They were welded together using a manual arc welder with continuous all-round (5mm) fillet type weld; except for the end stiffener back face which were made using Flat (flush) single-V butt weld with flat (flush) backing run, to make sure that the specimens can be attached firmly to the big testing frame without any gaps that could cause stress concentrations during the loading process.

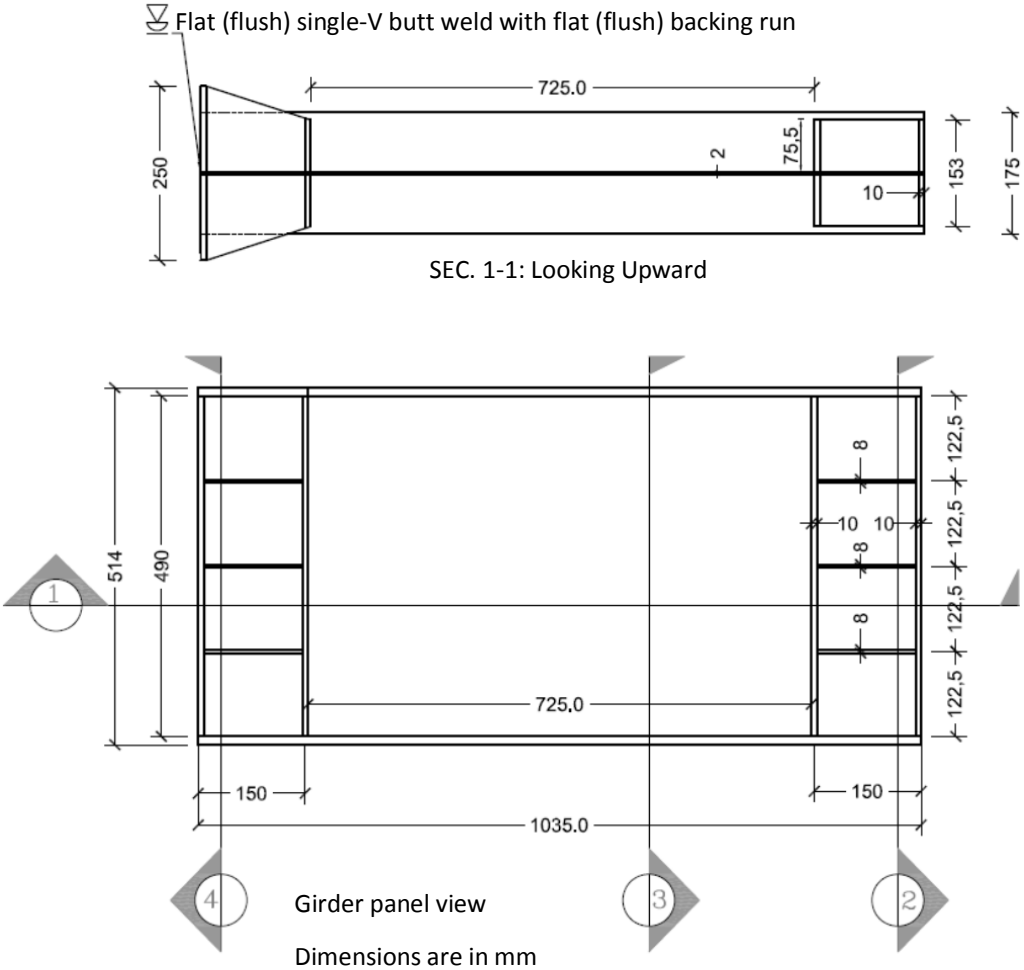

Figure (6.1): Dimensions and details of the test specimen in the final series of tests.

Table (6.1) shows the types of steel plates used in building the plate girder and their corresponding tested yield strengths; refer to Chapter 4 for more details about the steel mechanical properties.

Table 6.1: Steel mechanical properties

Source	Thickness, mm	f_y, MPa
Web	2.0	280.4
Stiffeners	8.0	427.0
	10.0	387.4
Flanges	12.0	278.0

The design of the current specimen was checked by hand calculation prior to a more detailed check using geometrical and material non-linear finite element modelling before the specimens were made and tested. It will be shown later in the numerical analysis section (6.7) that the numerical model correlated with test results and no modifications to the model were needed.

6.3 TEST VARIABLES

In this phase, the performance of the optimized FRP panel, from the initial series of tests (Phase-2), is investigated both under static and cyclic loading.

The variables investigated in this series are mainly the FRP type and alignment of the FRP panel with respect to the compression diagonal. Table 6.2 illustrates the test variables in more details while Figure (6.2) shows a schematic diagram of them. The experimental programme in this series (Phase-3) involves testing 6 plate girder sections. The first 3 specimens are the control specimen, a GFRP strengthened specimen, and a CFRP strengthened specimen. These were strengthened with a diagonal FRP panel (34°) and tested for shear buckling under static load as a precursor to the subsequent three tests on similar specimens under cyclic loading. The cyclic tests involved testing 3 specimens, 2 of them are GFRP and CFRP strengthened ones identical to the static specimens. In the third cyclic specimen (SP-

6), the alignment of the CFRP panel was changed to 45° instead of the typical diagonal alignment to check its effect on the efficiency of the proposed strengthening technique.

Table 6.2: Test variables in the final series of tests

Ref.	Specimen	FRP type	FRP Panel type	No. of layers	Fibre orientation	Loading type	FRP panel alignment
SP-1	Control	-	-	-	-	Static	-
SP-2	GFRP-3L-C	Glass	Type C	3-Layers	+45°/-45°	Static	Diagonal
SP-3	CFRP-3L-C	Carbon	Type C	3-Layers	0°/90°	Static	Diagonal
SP-4	GFRP-3L-C	Glass	Type C	3-Layers	+45°/-45°	Cyclic	Diagonal
SP-5	CFRP-3L-C	Carbon	Type C	3-Layers	0°/90°	Cyclic	Diagonal
SP-6	CFRP-3L-C	Carbon	Type C	3-Layers	0°/90°	Cyclic	45°

Note that the width of the FRP panel was increased from 195mm to 240mm in this series compared to Phase-2 for the first five specimens which were strengthened diagonally to account for the difference in the FRP panel length due to the different aspect ratios. SP-6 was an exception from this and the width of the CFRP panel was kept 195mm for this specimen because it was strengthened in a 45° alignment which holds the same length and slenderness as the initial series of tests (Phase-2); see Figure (6.2). The extension in width of the FRP section was estimated based on comparing the slenderness of the FRP panel both for the initial and final series of tests. The slenderness of the FRP panel is defined as follows:

$$Slenderness\ ratio = \frac{E_f I_f}{L_f} \tag{6.1}$$

where

E_f: is the FRP section modulus of elasticity,
I_f: is the second moment of area of the FRP panel,
L_f: is the total length of the FRP panel which equals the diagonal length of the web plate in either case.

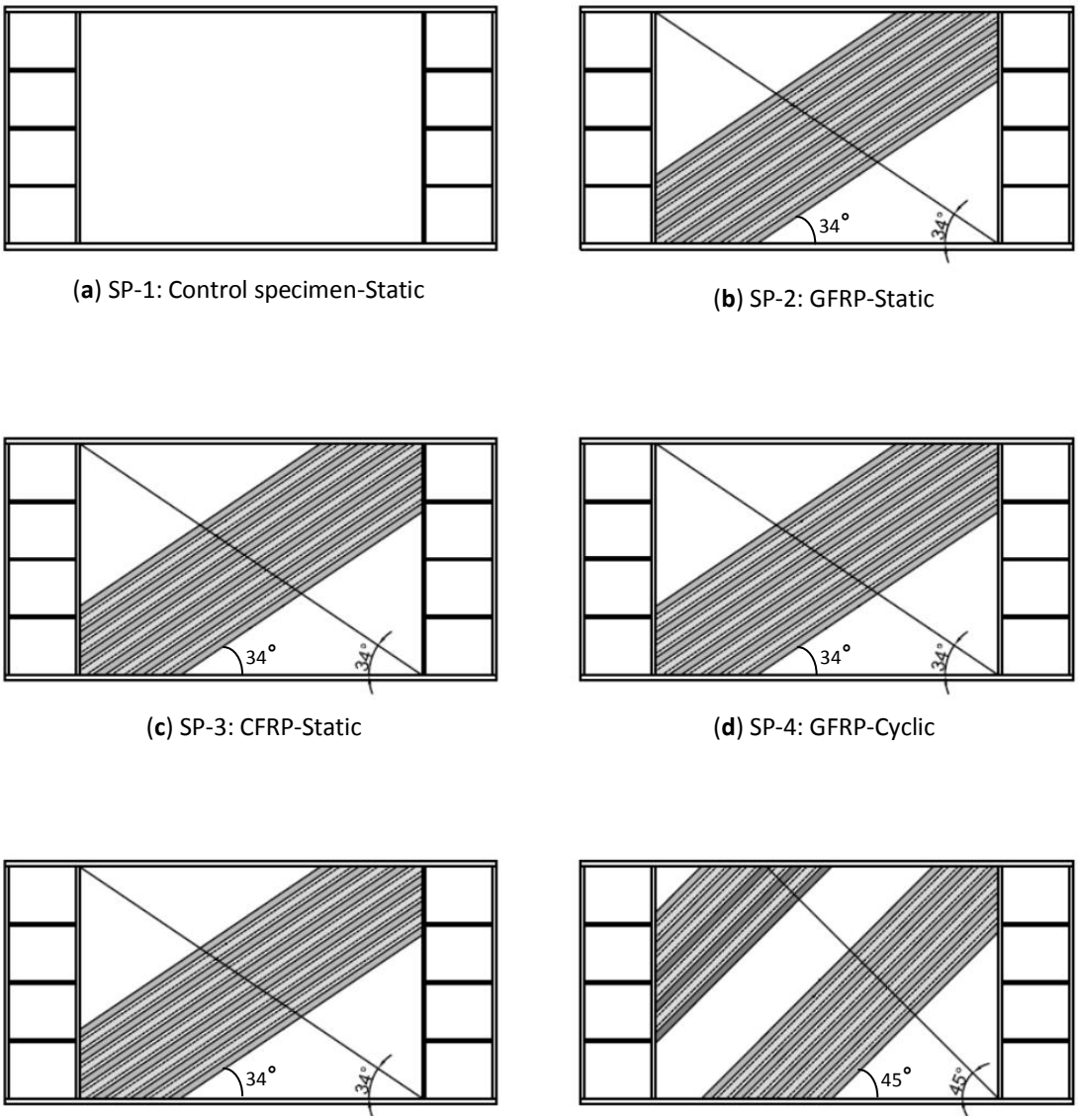

(**a**) SP-1: Control specimen-Static

(**b**) SP-2: GFRP-Static

(**c**) SP-3: CFRP-Static

(**d**) SP-4: GFRP-Cyclic

(**e**) SP-5: CFRP-Cyclic

(**f**) SP-6: CFRP-Cyclic

Figure (6.2): Specimens and variables tested in Phase-3.

Figure (6.3) compares the two sections both for the initial series (Phase-2) and the first five specimens in the final series of tests (Phase-3). From this figure, it can be seen that the corrugation section was kept the same and extended further from a width of 195mm to a width of 240mm.

The control specimen (SP-1) was tested only under static loading for several reasons; firstly, the ultimate capacity of this new specimen is needed to reflect the real increment in strength due to the proposed strengthening technique, this can only be found throughout a static test. Secondly, to be able to numerically model this

control specimen to use it as a benchmark for the composite model presented in Chapter 7 without having to incorporate the residual stresses resulting from the cyclic test which can make the model rather complicated and less likely to give high accuracy. Finally, it is more convenient to predict the fatigue strength of the control specimen using the Eurocode fatigue curves and use the limited number of available specimens to study more variables associated with the proposed strengthening technique.

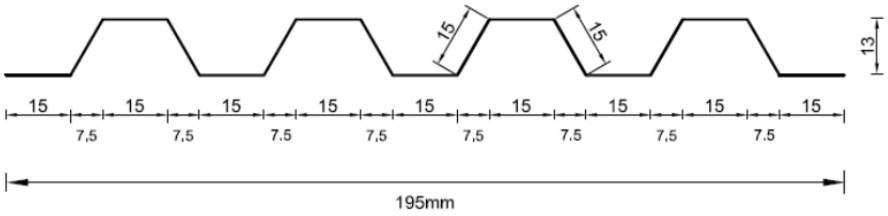

(**a**) FRP section for the initial series of tests and SP-6 in the final series of tests

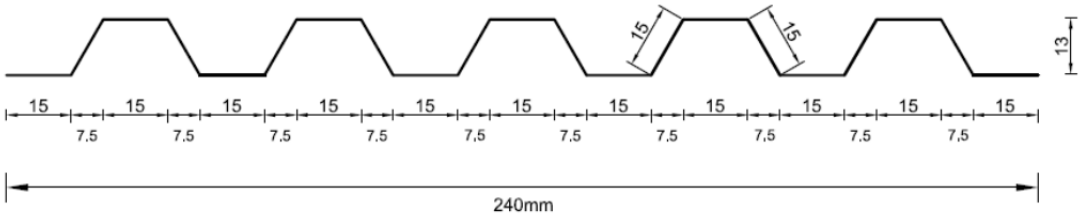

(**b**) FRP section for the first five specimens in the final series of tests

Figure (6.3): Comparison of the FRP section used both for the initial and final series of tests.

6.4 SPECIMEN PREPARATION

The same procedure used in preparing the specimen in the initial series of tests (Phase-2) was followed exactly in the final series of tests; refer to section (5.4) for more details.

Figure (6.4a) shows a photo for the specimens before bonding the FRP panel while Figure (6.4b) shows a photo for SP-3 (CFRP-diagonal) including three pull-off dollies bonded at the same time as the FRP panel.

(**a**) Specimens before bonding the FRP panels

(**b**) Specimen after bonding the FRP panel

Figure (6.4): Bonding the FRP panel in the final series of tests.

6.5 TEST INSTRUMENTATION AND SETUP

Figure (6.5) shows the details of the instrumentation used for all the specimens in the final series of tests (Phase-3).

The first three specimens, which were tested under static load to serve as a precursor for the other three cyclic tests, had exactly the same instrumentation as the initial series of tests (Phase-2); except for some variations in the locations of the LPs due to the new specimen dimensions, as can be seen in Figure (6.5a), and 4 additional single strain gauges (S7-S10) that were attached to the top and bottom flanges to measure their strain and to make sure that they are not yielding according to the initial design. A single strain gauge rosette was used in the centre of the web plate to measure the vertical, horizontal, and diagonal strain. The location of the LPs and strain gauges are shown in the Figure (6.5), where S refers to strain gauge and LP refers to linear potentiometer. For the control specimen (SP-1) only, the rosette strain gauge was attached from both sides in the centre of the steel plate in order to be able to capture the secondary bending and membrane strains, while this was not possible to achieve with the other 2 strengthened specimens because the FRP panel covered the central area of the steel plates. Five of the LPs (LP1-LP5) which had a capacity of 30mm were used to determine the web plate out-of-plane displacements, two 30mm LPs (LP6-LP7) ensured that there was no rigid-body rotation for the picture frame (out-of-plane movement), one 100mm LP (LP-8) was used to determine the deflection at the bottom end of the plate under the applied load, and another two 25mm LPs (LP9-LP10) were measuring the in-plane rotation in the big frame column. It is worth mentioning that both DEMEC buttons and DIC were trialled to measure the strain at the tension corners of the web plate as can be seen in Figure (6.5a). However, both techniques were not successful because of the out-of-plane displacement involved in the shear buckling test.

To reduce the number of channels due to the large amount of data produced by the cyclic tests, some changes were made to the instrumentation as can be seen from Figure (6.5b) and (6.5c). For the next three cyclic tests only LP-2, LP-9, and LP-10 were kept in position to measure the central out-of-plane displacement and the in-plane rotation of the tested specimen. LP-1 was moved to the new position shown in Figure (6.5b and c) because this position has shown high out-of-plane displacements

comparable or even some times exceeding the central out-of-plane displacement. This will be further discussed in the experimental results section (6.6). LP-6 and LP-7 were removed because in all previous tests the specimens showed no rigid body rotation. LP-8 was removed as well because throughout all previous tests, it has been proven that the Instron actuator readings perfectly matches the deflection measured using LP-8.

The strain gauge distribution varied depending on the FRP panel alignments and the experience gained with each test. The strain gauges were distributed within the tension field zone.

For SP-4 (GFRP) and SP-5 (CFRP), the strain gauge distribution is shown in Figure (6.5b), where an attempt was made to measure the difference in the steel plate strain in the strips where the FRP is bonded and the parallel strips were the FRP is not bonded. This was done once with an angle of 45° for SP-4 and once diagonally (with an angle of 34°) for SP-5 as can be seen in Figure (6.5b). In addition, a single rosette strain gauge was attached to both faces of the web plate at a distance of 112.5mm from the plate tension corner were the maximum strain was anticipated using the finite element model. In this way, the secondary bending stresses can be calculated and compared to the control ones.

For the final cyclic specimen SP-6 (CFRP-45°), an attempt was made to compare the secondary bending strains between the estimated location and at the corner of the tension field by using 2 rosette strain gauges at each face of the web plate. In addition, the tension field strain was measured at 45° (parallel to the expected tension field) for both the long and short CFRP panels, as can be seen from Figure (6.5c).

In all cases, the strain gauge readings along with the displacement gauges (LPs) were recorded at a rate of 10.0 Hz using a Vishay 7000 data acquisition system. Tests were performed using a 1000kN servo-hydraulic Instron actuator at a stroke rate of 1.0 mm/minute for the static tests and loading frequency of 2.0Hz for the cyclic tests. Before each test, the central out-of-flatness (initial imperfection) of the steel web plate was measured and recorded for further investigation with the numerical modelling. Figure (6.6) shows a schematic diagram of the overall testing rig.

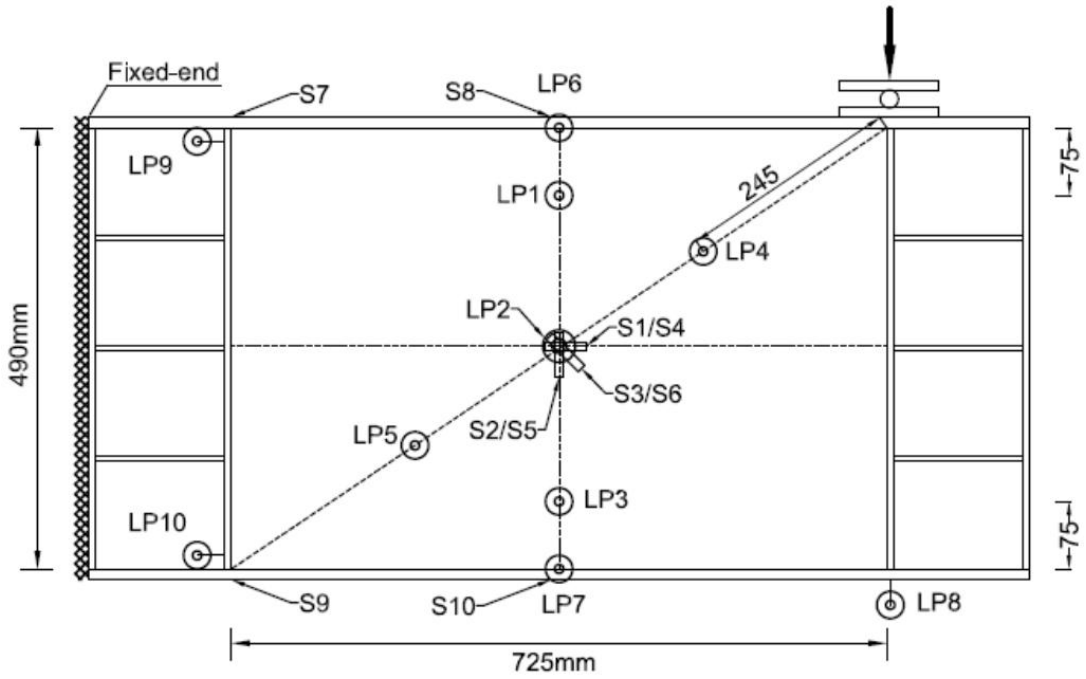

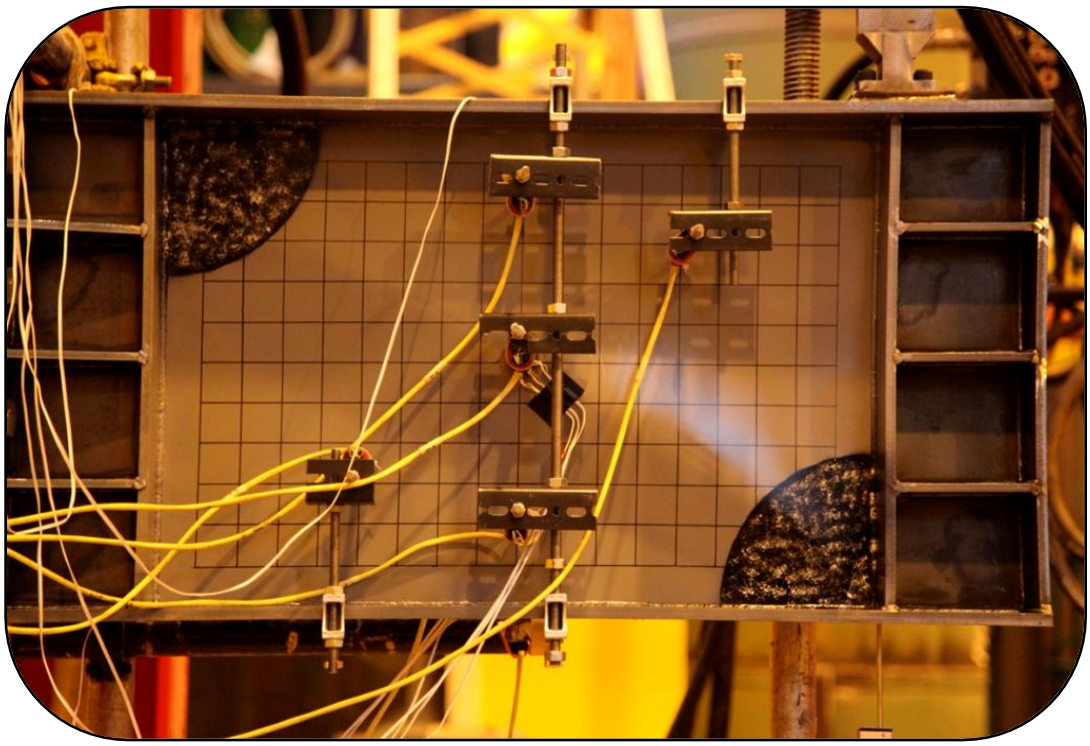

(**a**) SP-1 (Control specimen), SP-2 (GFRP), and SP-3 (CFRP) - Static tests

Figure (6.5): Test instrumentation for the final series of tests.

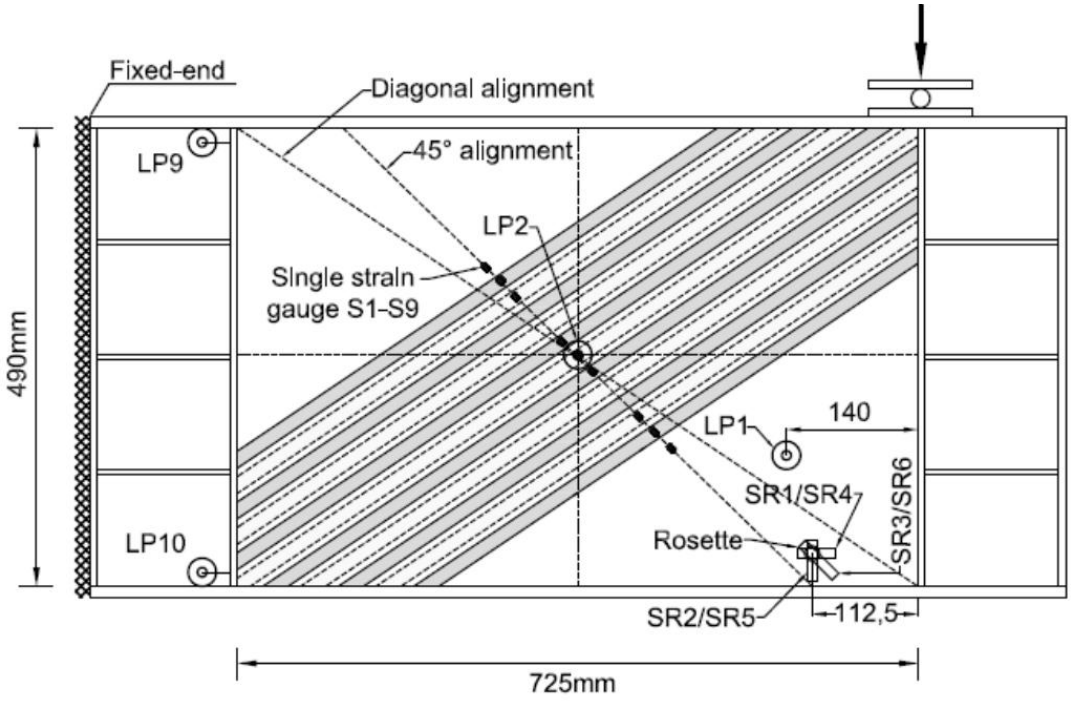

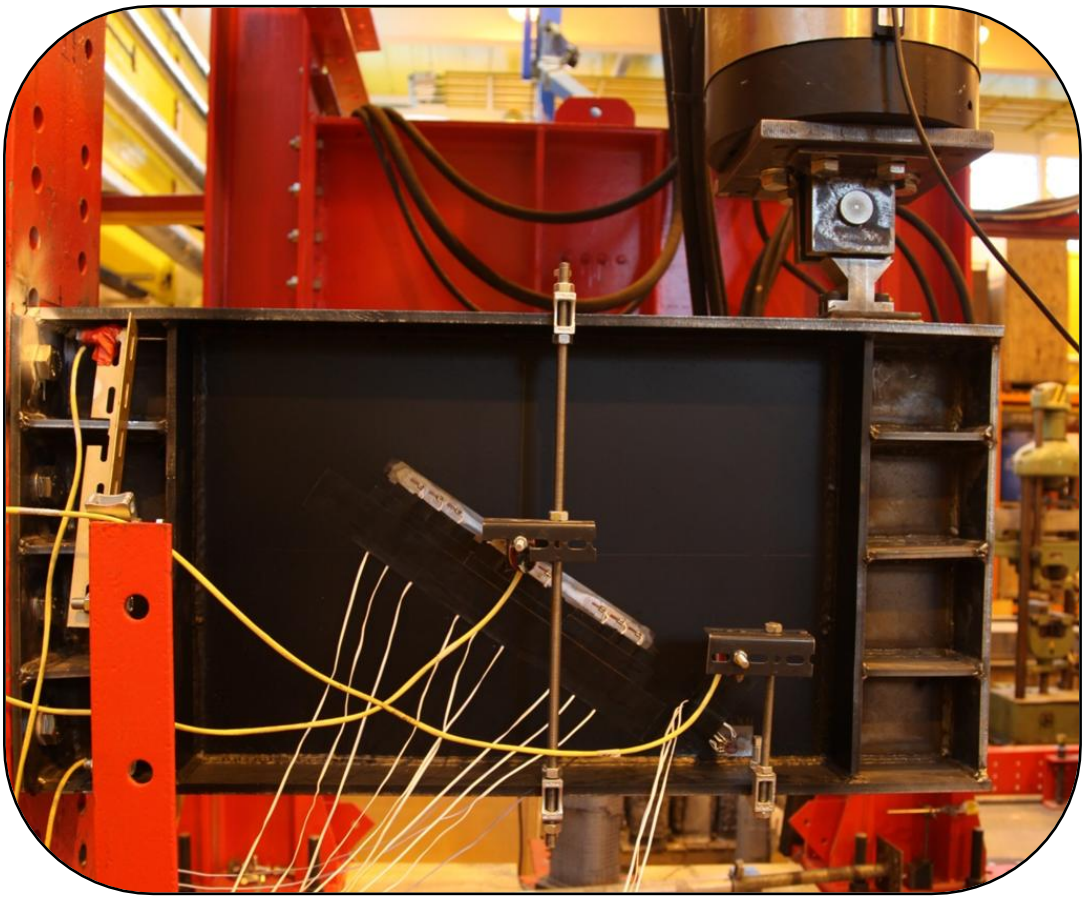

(**b**) SP-4 (GFRP) and SP-5 (CFRP) - Cyclic tests

Figure (6.5 Cont.): Test instrumentation for the final series of tests.

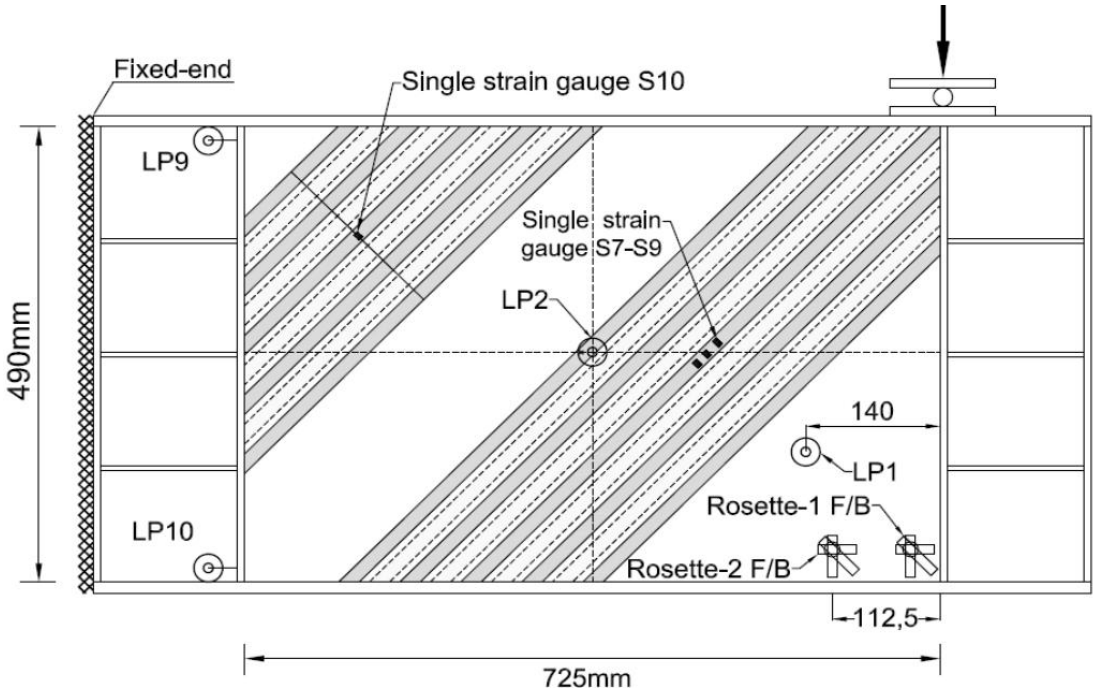

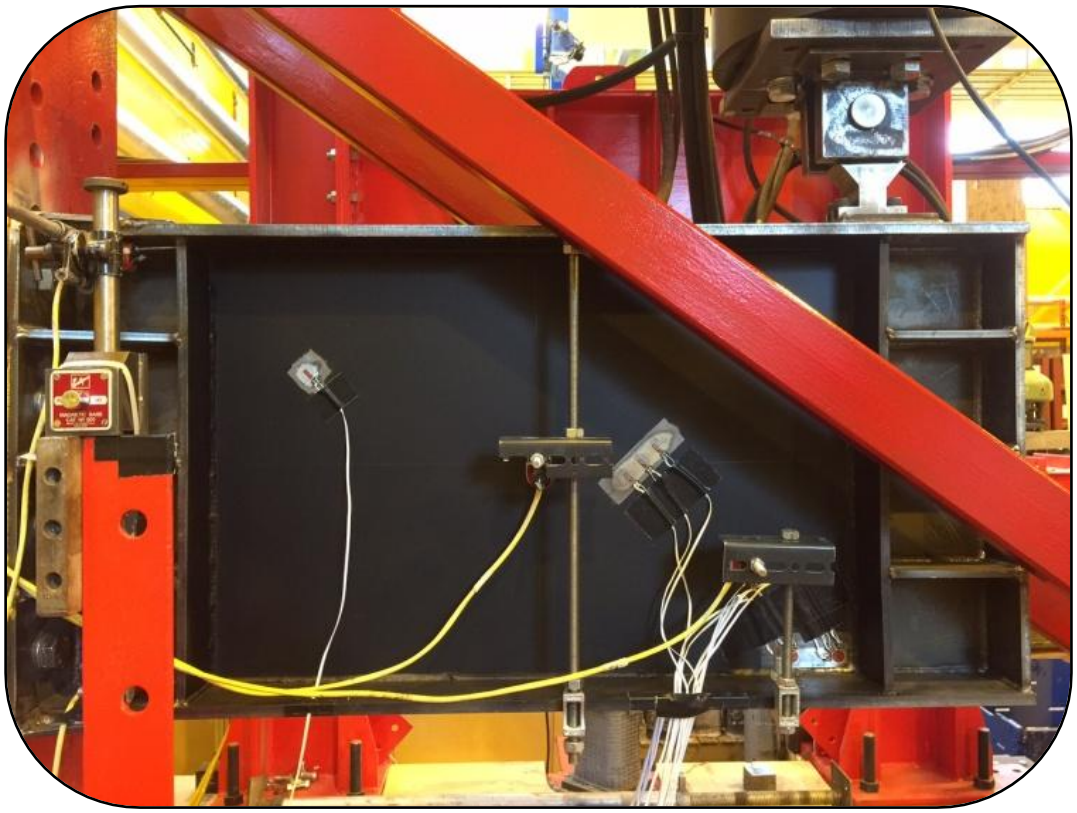

(**c**) SP-6 (CFRP) - Cyclic test

Figure (6.5 Cont.): Test instrumentation for the final series of tests.

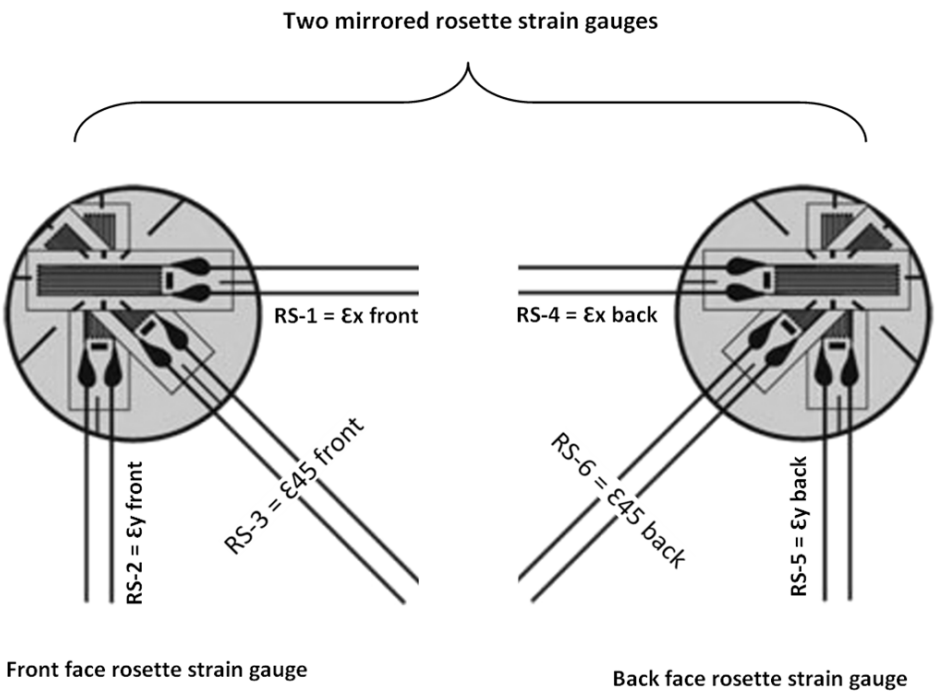

(**d**) Details of the rosette strain gauge referencing

Figure (6.5 Cont.): Test instrumentation for the final series of tests.

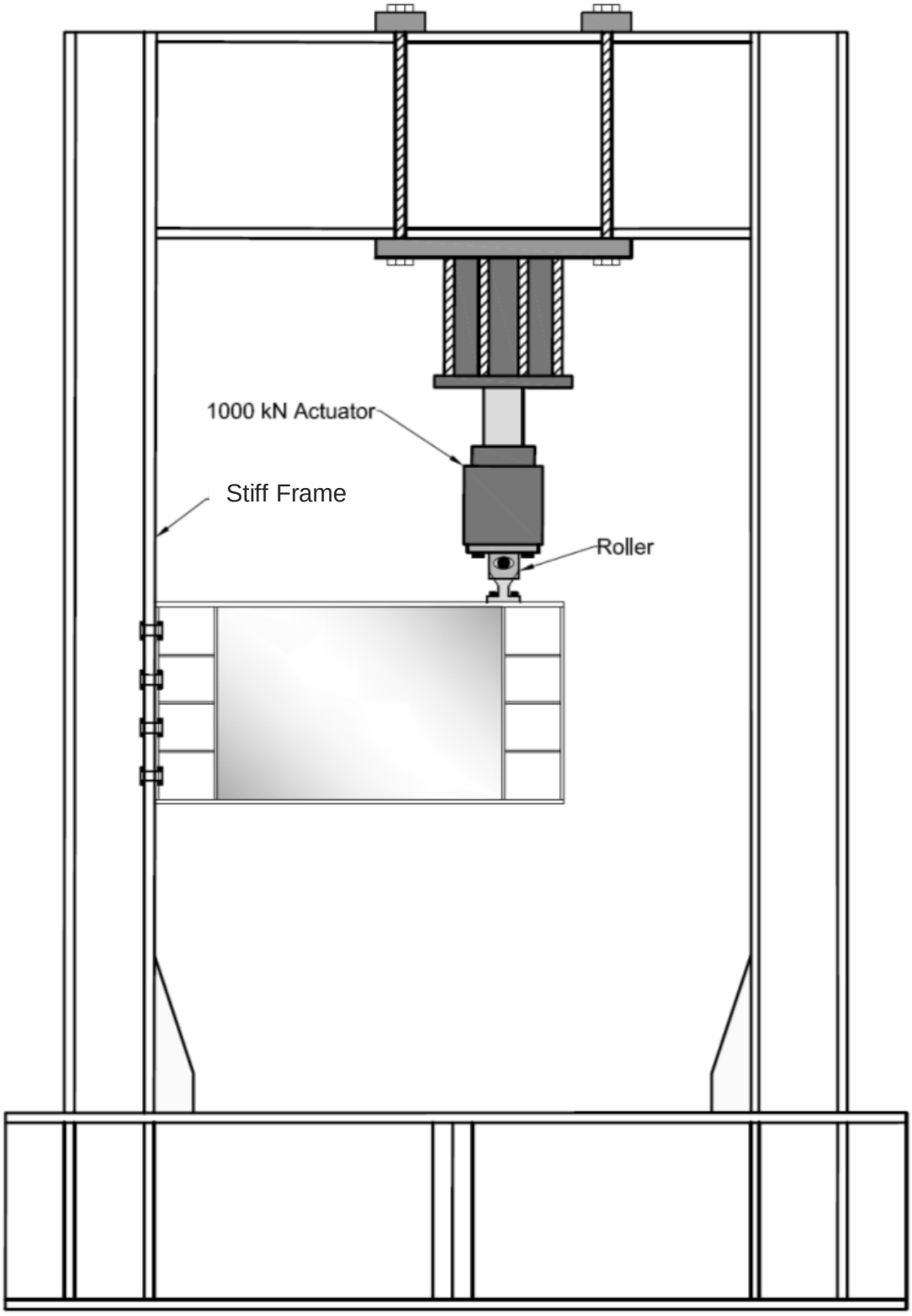

Figure (6.6): Overall test rig setup for the final series of tests.

6.6 EXPERIMENTAL RESULTS, ANALYSIS, AND DISCUSSION

The experimental programme in Phase-3 (the final series of tests) was divided into two subsequent series; a static and a cyclic series. This was an important precaution to determine the specimens' capacity experimentally in order to use it as a reference when planning for the maximum and minimum load amplitudes during the cyclic tests. Previous knowledge and experience have shown that without testing the precursor specimens under static load, significant loss of time might be faced in case the applied load ranges were not high enough to initiate fatigue propagation (i.e. within working stresses). This is something encountered in the current work even with testing the precursor control specimens. It might be attributed to the repeatability problem in structural tests where specimens made using the same materials and undergoing the same manufacturing process might show relatively different results under the same testing conditions.

6.6.1 Static (Precursor) Tests

Three specimens were fabricated and tested under in-plane static shear load. The first one was an intact steel plate girder while the second and third ones were GFRP and CFRP strengthened ones, respectively. Table 6.3 shows the test results for these three specimens.

Table 6.3: Test results for the subsequent static series in this phase

Ref.	Specimen	Loading type	Panel alignment	Initial imperfection, mm*	Ultimate load, kN	Strength increase, %
SP-1	Control	Static	-	2.76	87.9	-
SP-2	GFRP-3L-C	Static	Diagonal	+0.35	113.7	29
SP-3	CFRP-3L-C	Static	Diagonal	-1.47	105.2	20

* The minus sign means that the initial imperfection is in the reverse direction of where the FRP panel should buckle according to the designed pre-buckling mode (i.e. furthest away from the steel plate).

For the control specimen (SP-1) the load was applied in one cycle (loading-unloading), while for the other two specimens (GFRP and CFRP strengthened, respectively) the load was applied in six cycles. For each cycle the load was increased at a rate of 20% of the ultimate load of the control specimen and then un-loaded (i.e. 0.0-17.6kN, 0.0-35.2kN, 0.0-52.8kN, 0.0-70.4kN, 0.0-88.0kN, and

finally 0.0-ultimate load). This was done to find out if there is any debonding can be detected at different loading stages. However, no debonding could be detected for any specimen and under any loading stage. Nevertheless, this loading scheme succeeded in showing the accumulated out-of-plane displacement in case of buckling took place in the reversed direction to the designed one (e.g. SP-3).

The values of the ultimate load in Table 6.3 will be used as benchmarks for the subsequent cyclic series. From this table it can be seen that the ultimate load capacity increased by 29% and 20% for SP-2 (GFRP) and SP-3 (CFRP), respectively.

It was anticipated that the CFRP strengthened specimen would provide rather more increase in the ultimate shear capacity than the GFRP strengthened one would, but it did not. This could be because of the reversed buckling mode that took place during testing the CFRP strengthened specimen (SP-3). This reversed buckling mode took place because the initial imperfection was in the opposite direction to the designed prebuckling mode. Consequently, the FRP panel outer face was in compression and not in tension as would be expected. This led to a premature failure as can be seen in Figure (6.7) where the failure mode of the CFRP strengthened specimen (SP-3 in Figure 6.7c) is compared to the GFRP one in addition to the control specimen. Figure (6.7a) shows the control specimen (SP-1) after failure, where the out-of-plane deformation demonstrated by the even buckling mode wrinkles caused by the shear loading can be clearly seen compared to the low residual shear buckling deformation for the GFRP strengthened specimen (SP-2 in Figure 6.7b).

In spite the fact that there was no significant increase in the ultimate load capacity for SP-3, the stiffness is still increased, as will be seen in section (6.8). This reduces the out-of-plane deformation leading to less breathing stresses. Furthermore, in the cyclic tests it will be shown that the CFRP strengthened specimen has much higher ultimate load when it buckles towards the outer face of the FRP section.

The following sections present the experimental results in four main parts; namely, the central out-of-plane displacement (section 6.6.1.1), the in-plane deflection (section 6.6.1.2), the non-central out-of-plane displacement (section 6.6.1.3), and strain (section 6.6.1.4). In each section, the results are analyzed and the effect of different variables are discussed and compared.

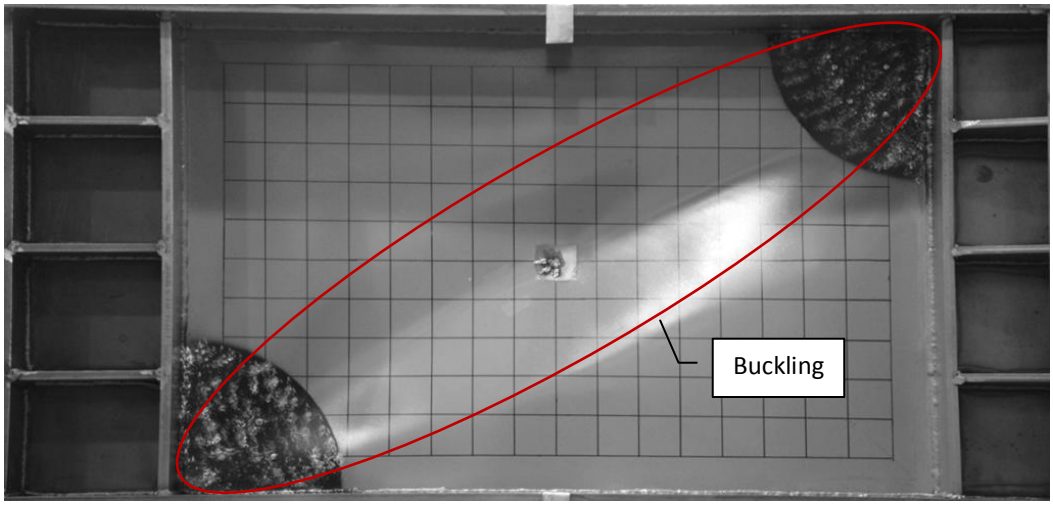

(**a**) Control specimen (SP-1)

(**b**) GFRP strengthened failed specimen (SP-2)

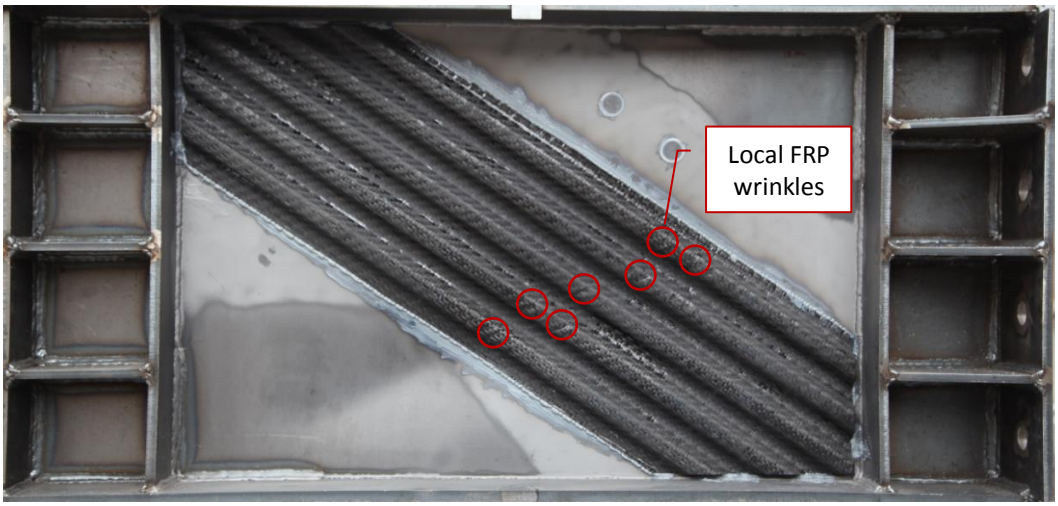

(**c**) CFRP strengthened failed specimen (SP-3)

Figure (6.7): Photos for the failed specimens in this series.

6.6.1.1 *Central Out-of-Plane Displacement*

Figure (6.8) shows the buckling curves (load versus out-of-plane displacement) for the three control specimens tested in this subsequent static series. For the sake of fair comparison, and because the experimentally tested control specimen has different initial imperfection than the strengthened specimens, another two numerical control specimens were established using finite element modelling. Figure (6.8) shows these two numerical curves using dashed lines. Each one of these two numerical control models corresponds to one of the strengthened specimens by holding the same initial imperfection (i.e. 0.35mm for SP-2 and -1.47mm for SP-3). The finite element model for the control specimen was verified against the experimental one and showed very good correlation as will be seen in the numerical analysis section (6.7).

Figure (6.8) shows that the proposed strengthening technique succeeded in stiffening the specimens against shear buckling. At a load equal to the ultimate load of the control specimen (i.e. 87.9 kN), the central out-of-plane displacement is reduced by approximately 90% both for the GFRP and the CFRP strengthened specimens. This means that the stiffness is increased significantly and that the secondary bending strains are reduced. However, this needs to be quantified numerically, as will be seen in section (6.8).

The curve for the control specimen (SP-1) in Figure (6.8) has a linear trend from the beginning of the test until it reaches close to the ultimate load where it curves towards the failure plateau where the part of plate in tension field strip is believed to start yielding. The GFRP strengthened specimen (SP-2) shows the same behaviour for the 6 cycles of loads with no evidence of delamination or debonding. However, the CFRP strengthened specimen (SP-3) showed different behaviour, where the out-of-plane displacement started accumulating with each loading cycle until failure. This took place due to the reversed buckling mode discussed above in section (6.6.1). The reversed buckling mode caused local buckling problem (forming of wrinkles) within the outer face of the corrugated FRP panel (see Figure 6.7c) leading to lower shear strength. However, this is discussed in more detail in section (6.6.1.3).

In all cases, the unloading part of the curve is roughly parallel to the loading part which indicates a ductile failure type with potential reserve of strength.

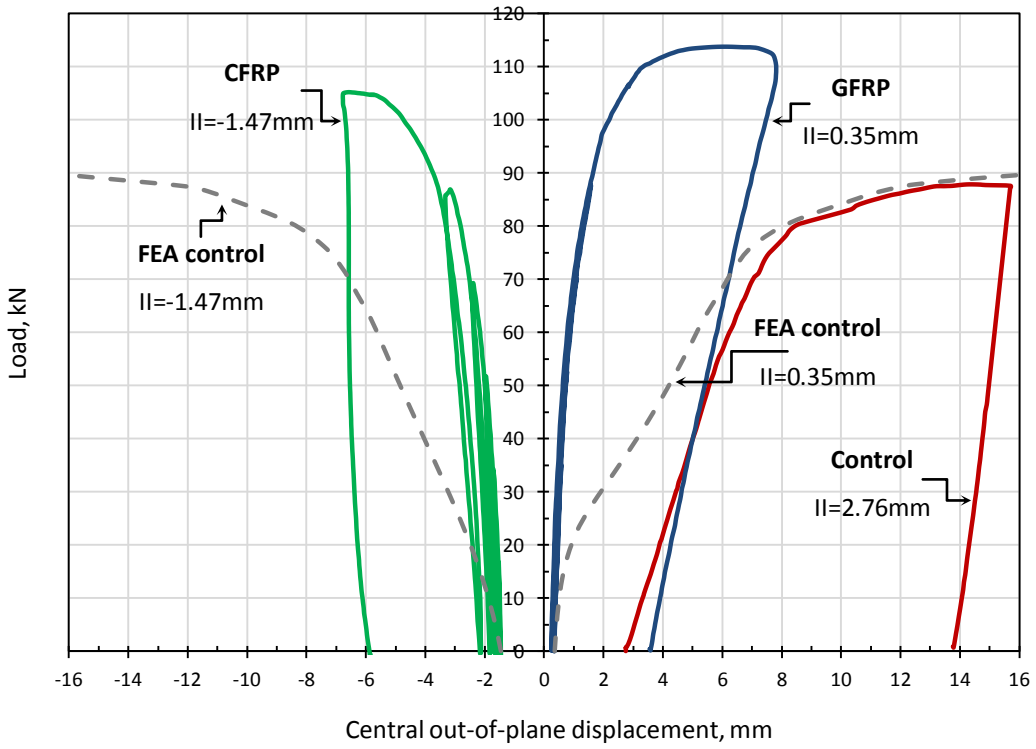

Figure (6.8): Buckling curves for the subsequent static series of tests in phase-3.

6.6.1.2 *In-Plane Deflection*

Figure (6.9) shows the in-plane load-deflection curves for the three specimens tested in this subsequent static series of tests. The figure reminds us of the same conclusion we had before in Chapter 5 for the initial series of tests (Phase-2) where the FRP strengthening technique had a moderate effect in enhancing the in-plane deflection behaviour of the strengthened specimen but with no major variations with respect the type of the FRP used. From the figure it can be seen that the GFRP and CFRP had almost the same behaviour. However, the above discussion does not mean that the strengthening technique did not improve the deflection behaviour as compared to the control specimen, on the contrary, for a load equal to the ultimate load of the control specimen (i.e. 87.9kN), the deflection is reduced approximately 50% both for the GFRP and CFRP strengthened specimens. This in-plane stiffening effect is considered good taking in consideration that the strengthening technique is targeting the out-of-plane displacement.

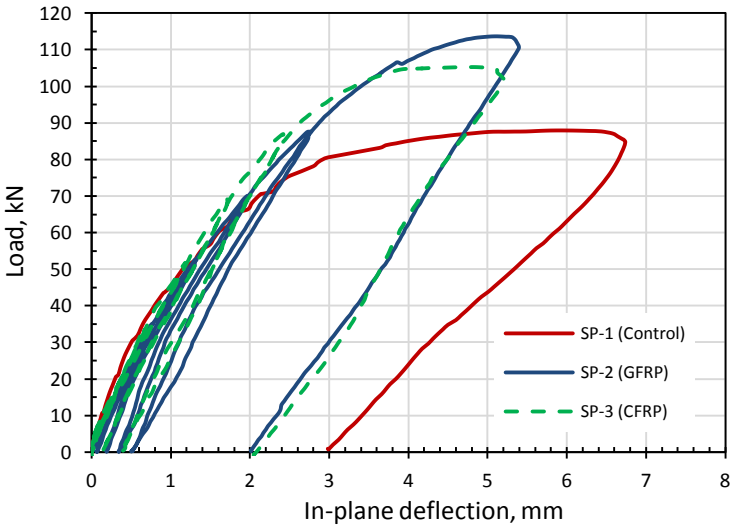

Figure (6.9): Deflection curves for the subsequent static series of tests in phase-3.

6.6.1.3 *Non-Central Out-of-Plane Displacement*

Figure (6.10) shows the non-central buckling curves for the three specimens tested in this subsequent static series of tests. It can be seen from Figure (6.10a) that the control specimen showed higher out-of-plane deformations in comparison to the GFRP strengthened one (SP-2) which can be seen in Figure (6.10b). It also can be noted that the GFRP specimen had more symmetric displacements than the control specimen, where LP-1 is close to LP-3 and LP-4 is similar to LP-5; refer to Figure (6.5a) for the location of the LPs. This was not the case with the control specimen (SP-1); however, this could be attributed to the high initial imperfection of 2.76mm associated with the control specimen in comparison to an initial imperfection of 0.35mm for SP-2.

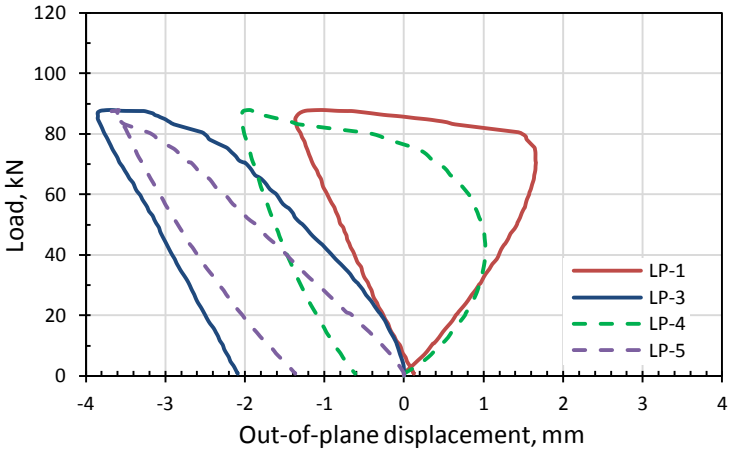

(**a**) SP-1 (Control specimen)

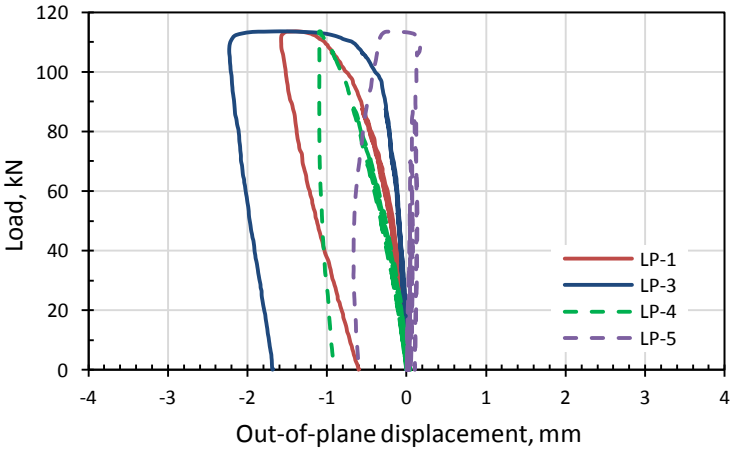

(**b**) SP-2 (GFRP)

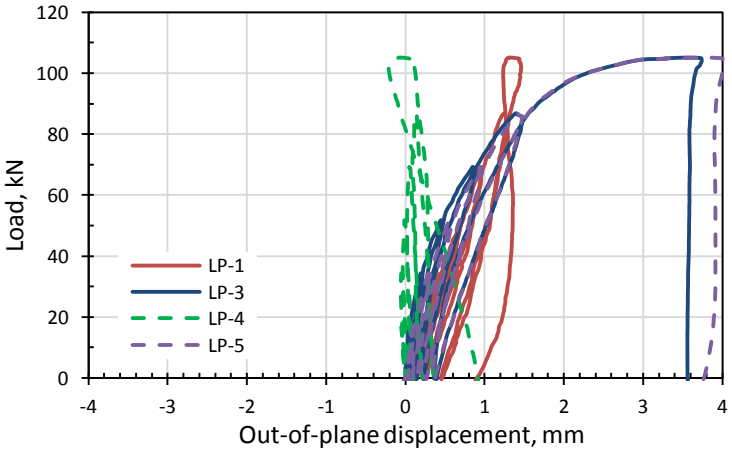

(**c**) SP-3 (CFRP)

Figure (6.10): Non-central buckling curves for the subsequent static series of tests in phase-3.

The CFRP strengthened specimen (SP-3) showed different behaviour because of the reversed mode of buckling which took place due to the reversed initial imperfection of -1.47mm. It is believed that there is another important factor that caused this problem in addition to the reversed initial imperfection. This is illustrated in Figure (6.11) where the lower unstrengthened triangular steel plate under the concentrated load is marked with the red triangle. It is believed that this area is big enough to cause the buckling collapse to initiate before the strengthening FRP panel can start resisting the buckling of the steel plate. This is because of the weakness point shown in the blue circle were the bonding strip has very low second moment of area. This caused a sequence of wrinkles to form in the weak face of the FRP panel when it is in compression as marked by the green circles in Figure (6.11).

The combination of the reversed initial imperfection and the above mentioned weakness point initiated some kind of a yield line leading to this reversed buckling mode. This problem raised the awareness of such a possibility and inspired us to change the strengthening alignment from the diagonal scheme to the more convenient 45° one in the last specimen (SP-6) as will be seen in the cyclic subsequent series. In the 45° strengthening scheme the unstrengthened triangular steel plate part is reduced in size making it less likely to alter and reverse the mode of failure unless high initial imperfections exist. In this case the initial imperfection can be detected and the FRP corrugated panel can be bonded to the side in the favour of the designed prebuckling mode. This is in case of increased ultimate strength is required; otherwise, there should be no problem because both buckling modes are showing almost the same stiffening effect within working stress limits.

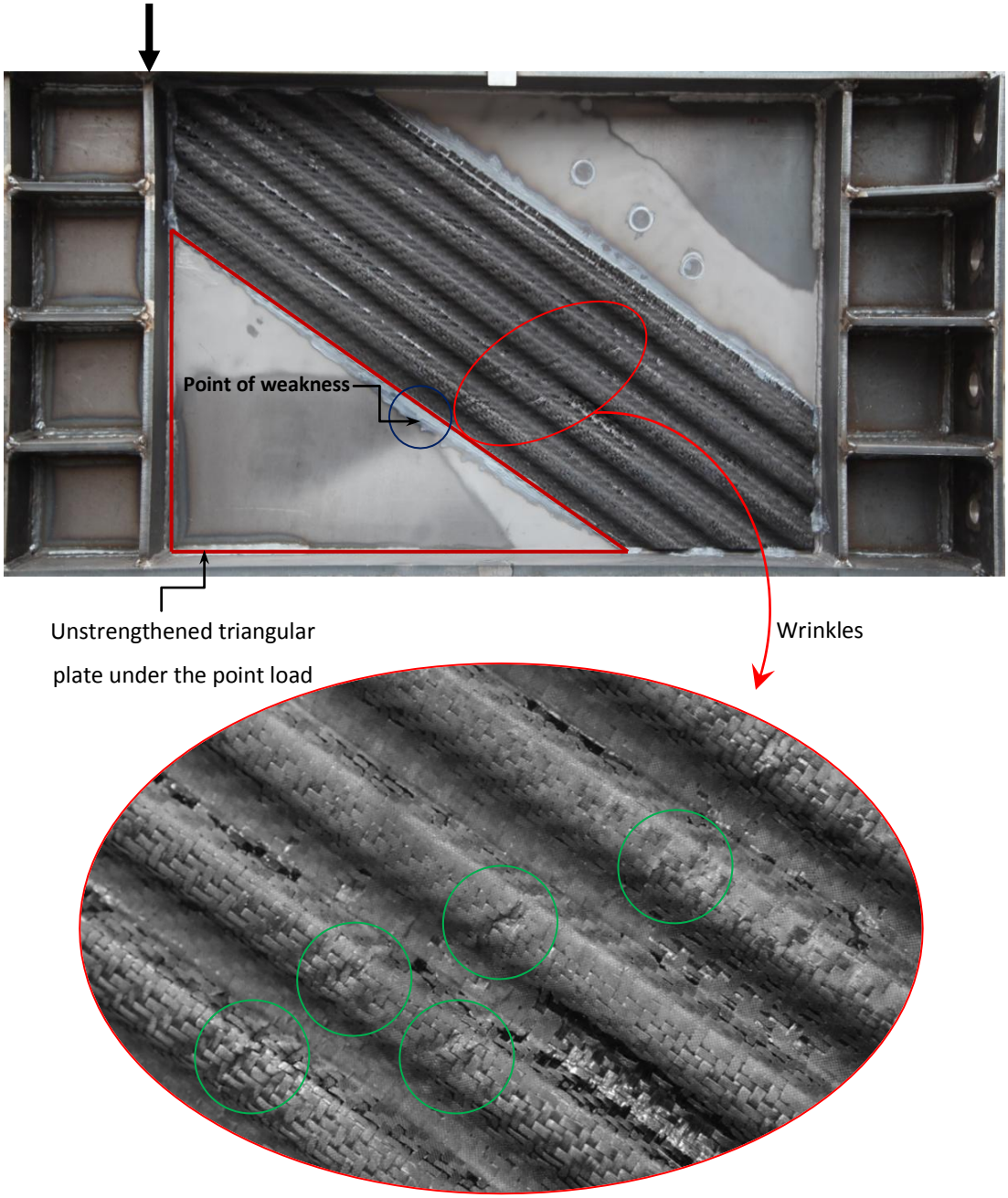

Figure (6.11): Photo showing wrinkles in the steel plate and the CFRP corrugated panel for the failed specimen (SP-3).

6.6.1.4 *Strain*

Figure (6.12) shows the strain curves for the three specimens tested in this subsequent static series of tests. Single rosette strain gauge was used in the centre of the web steel plate; refer to Figure (6.5a) for the location and orientation of its

components. Figure (6.12a) provides good illustration of the central strain distribution for both tension and compression faces of the web plate for the control specimen (SP-1). Unfortunately, it is hard to compare the control specimen strain with the corresponding strain for the GFRP and CFRP strengthened specimens (SP-2 and SP-3, respectively) because there is one missing strain in each case due to an experimental malfunction in the corresponding strain gauges. This prevented the back calculation of the shear strain (refer to section 5.6.4 in Chapter 5 to see the related equations), and hence the comparison is not valid except that, generally, the strain of the strengthened specimens is obviously less than that of the control specimen.

This problem will be addressed again in the fatigue analysis section (6.9) where the strains of the control specimen and the strengthened specimens are compared after the validation of the finite element model for the control specimen in section (6.7). More will be seen in section (6.6.2.3) as well when the strain of the cyclic test specimens is discussed.

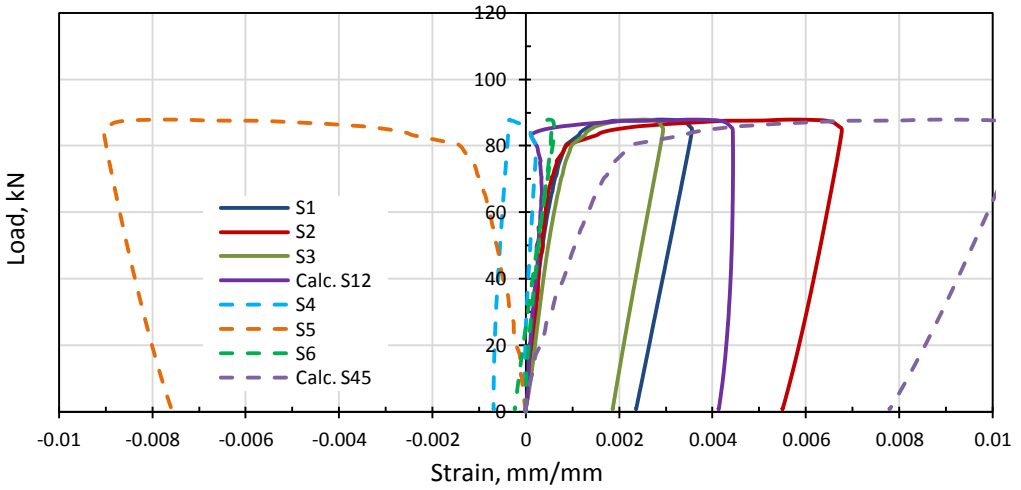

(**a**) SP-1 (Control specimen)

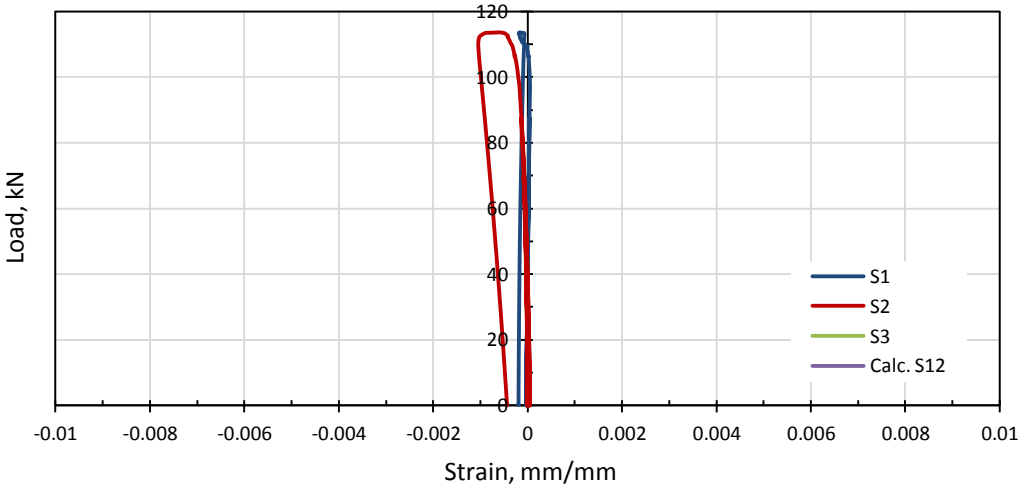

(**b**) SP-2 (GFRP)

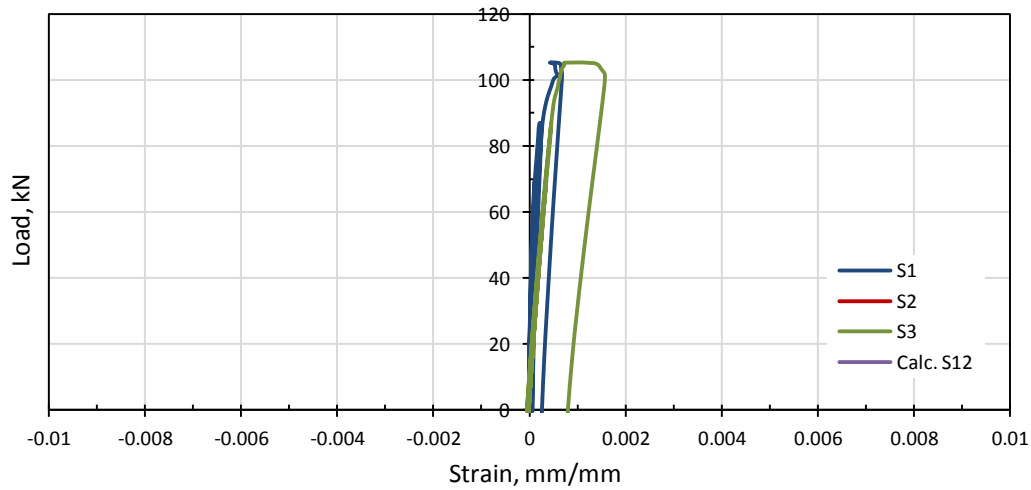

(**c**) SP-3 (CFRP)

Figure (6.12): Strain curves for the subsequent static series of tests in phase-3.

6.6.2 Cyclic Tests

In this section, the cyclic series of tests are presented and discussed. First of all, the constant cyclic loading range was decided to be 40-80% of the tested ultimate shear strength for the corresponding specimen in the previous static series of tests. Figure (6.13) illustrates the proposed loading range with the number of cycles.

The ultimate capacity of the specimen in the cyclic series was not exactly the same as the control one, but they were very good indicators to start with. This could be attributed to the repeatability problem in the structural tests discussed in the introduction of section (6.6), in addition to the accumulated residual stresses in the cyclic tests and the difference in the measured initial imperfection between the cyclic specimens and their corresponding control one. The number of the applied cycles of load was decided to be 2,000,000 cycles for each specimen with a loading frequency that ranged between 1.0 and 2.0 Hz depending on the deflection of the specimens.

The lower loading amplitude of 40% was chosen to simulate the deadweight of an average span bridge like structures while the upper loading amplitude of 80% was chosen to accelerate the fatigue propagation if any is encountered. It is known that the usual range for testing high-cycle fatigue of structural members should be within the allowable working stresses and that is between 60% and 70% of the ultimate capacity. However, in this study, it was decided to go up to 80% to make sure that the fatigue is taking place in a shorter period of time due to the time limitations of the study. The 2 million cycles were decided both for time limitations and because this number is where usually the reference fatigue strength is taken (Eurocode-3, 2005).

Three specimens (SP-4, SP-5, and SP-6) were strengthened with GFRP, CFRP-diagonal, and CFRP-45°, respectively, and tested under in-plane cyclic shear load; refer to Figure (6.2) for more information and Figure (6.5) for the instrumentation. Table 6.4 shows the details of these specimens and the corresponding test results.

Table 6.4: Test results for the subsequent cyclic series in this phase

Ref.	Specimen	Panel alignment	Loading type	Cycle range, thousands	Loading range*	Initial imperfection, mm	Ultimate residual load, kN
SP-4	GFRP-3L-C	Diagonal	Cyclic	0 - 500	35% - 70%	-0.38	128.04
				500 - 1000	40% - 80%		
SP-5	CFRP-3L-C	Diagonal	Cyclic	0 - 1000	32% - 64%	+1.14	140.07
				1000 - 2000	38% - 76%		
SP-6	CFRP-3L-C	45°	Cyclic	0 - 2000	37.5% -75%	+0.03	165.11

* This loading range is taken as the ratio between the applied load and the final residual ultimate load after 2 million cycles (1 million in the case of SP-4).

Table 6.4 describes the three specimens tested in this cyclic series showing their designations, loading type, cycle ranges, loading ranges, initial imperfections, and the ultimate residual loads. The original plan was to apply a cyclic load range of 40-80% of the ultimate capacity for each specimen. However, after the final residual test is performed, it turned out that the applied loading ranges (which is taken as the applied cyclic load divided by the final residual ultimate load) is less than the aimed ones as can be seen from the table; one success was achieved in the second 500,000 cycles applied to SP-4 where the real applied loading range was 40-80%. The ultimate residual load was determined by testing the specimen up to collapse after finishing the predesigned number of loading cycles as will be seen next section.

The cyclic test was stopped at regular frequencies between 10,000 and 50,000 cycles to check the specimens and take residual measurements. The readings were transferred and accumulated to the following cycles and so on until 2 million cycles were completed. The final residual test up to failure was performed in a similar way to the static tests in the previous series.

The specimens did not show any signs of delamination nor debonding, so it is believed that the residual ultimate loads are very close to represent the real static ultimate capacity of the specimens.

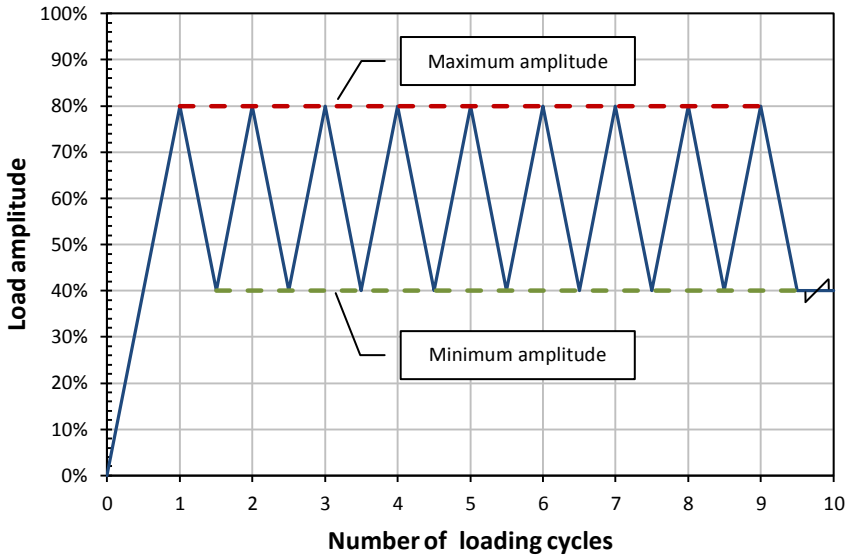

Figure (6.13): The proposed loading range for the subsequent cyclic series of tests in phase-3.

Figure (6.14) shows the failed specimens after the final residual test was performed. Figure (6.14a) shows the GFRP strengthened specimen where the failure was because the GFRP panel cracked at the ultimate load causing the steel plate to over deform in the reverse direction again. From this figure it can be seen that LP-1 failed to measure the maximum out-of-plane displacement as anticipated because the alteration in the buckling mode associated with breaking of the GFRP panel. However, it is important to note that only for this specimen; the cyclic test was stopped after 1,000,000 cycles of loads. This was done because this specimen showed very negligible breathing as will be seen in section (6.6.2.1)

Figure (6.14b) shows the CFRP strengthened specimen with diagonal alignment where the failure occurred mainly for three reasons. The first reason is the typical yield of the steel plate in the tension field, the second reason is the abovementioned weakness in the lower triangular unstrengthened part of the steel plate, and the third reason was due to the thrust effect of the CFRP panel in the compression corner of the steel web plate. This figure also shows the deformation captured with the right angle and light reflection showing the different strain distribution among the steel strips that are bonded or not bonded to the FRP panel.

This also shows how strong the bonding mechanism of the proposed FRP corrugated panels.

Figure (6.14c) shows the failed CFRP strengthened specimen with 45° alignment where it can be seen that this scheme succeeded to minimize the deformation in the web steel plate while gaining the highest strength as can be seen from the ultimate load in Table (6.4) and this will be further discussed in the next sections.

The experimental results for this subsequent cyclic series are reported in the following sections. The central out-of-plane displacement (section 6.6.1.1), the in-plane deflection (section 6.6.1.2), the non-central out-of-plane displacement (section 6.6.1.3), and strain (section 6.6.1.4). In each section, the results are analyzed and the effect of different variables are discussed and compared.

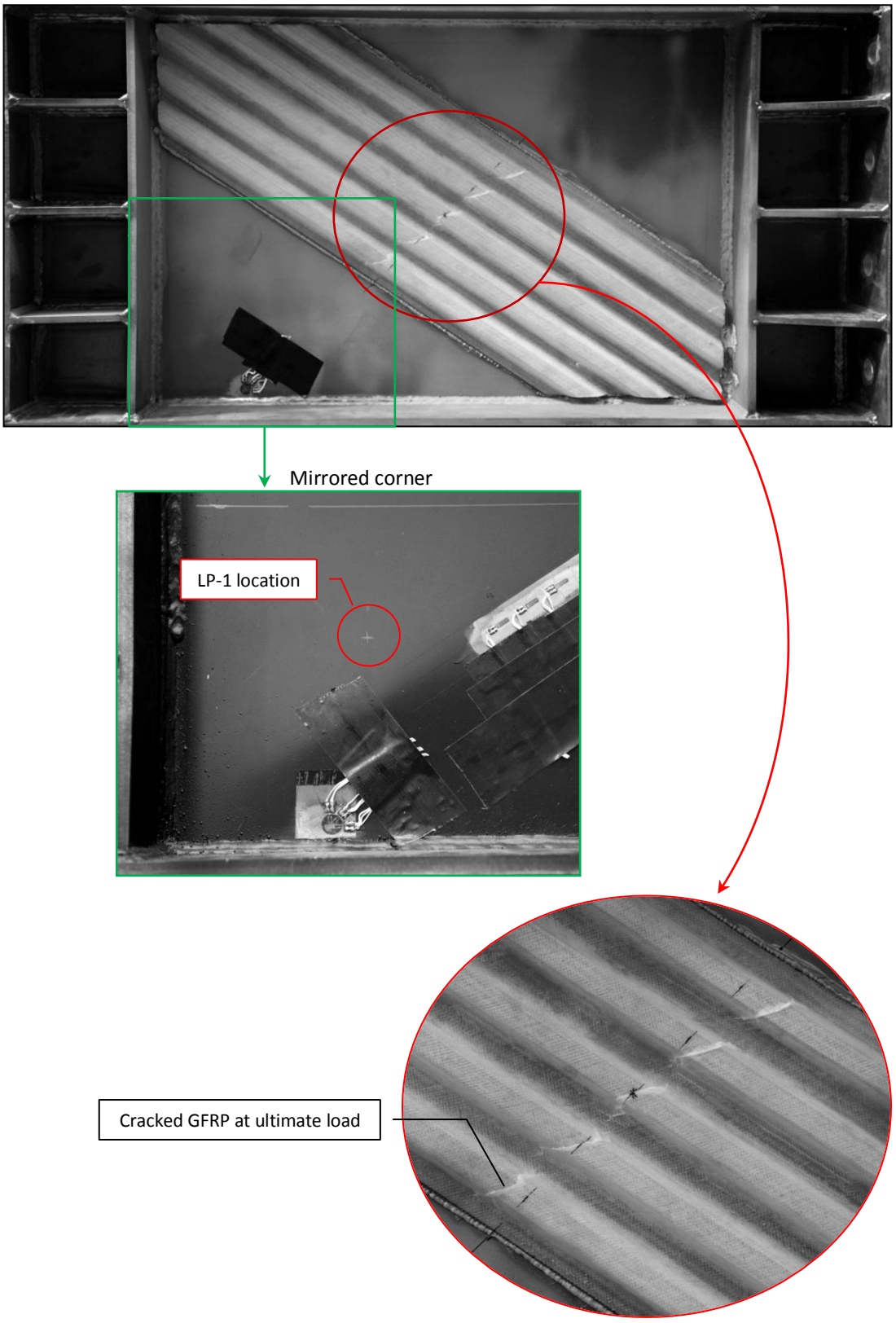

(**a**) SP-4 (GFRP)

Figure (6.14): Photos of the cyclic test specimens after final residual test.

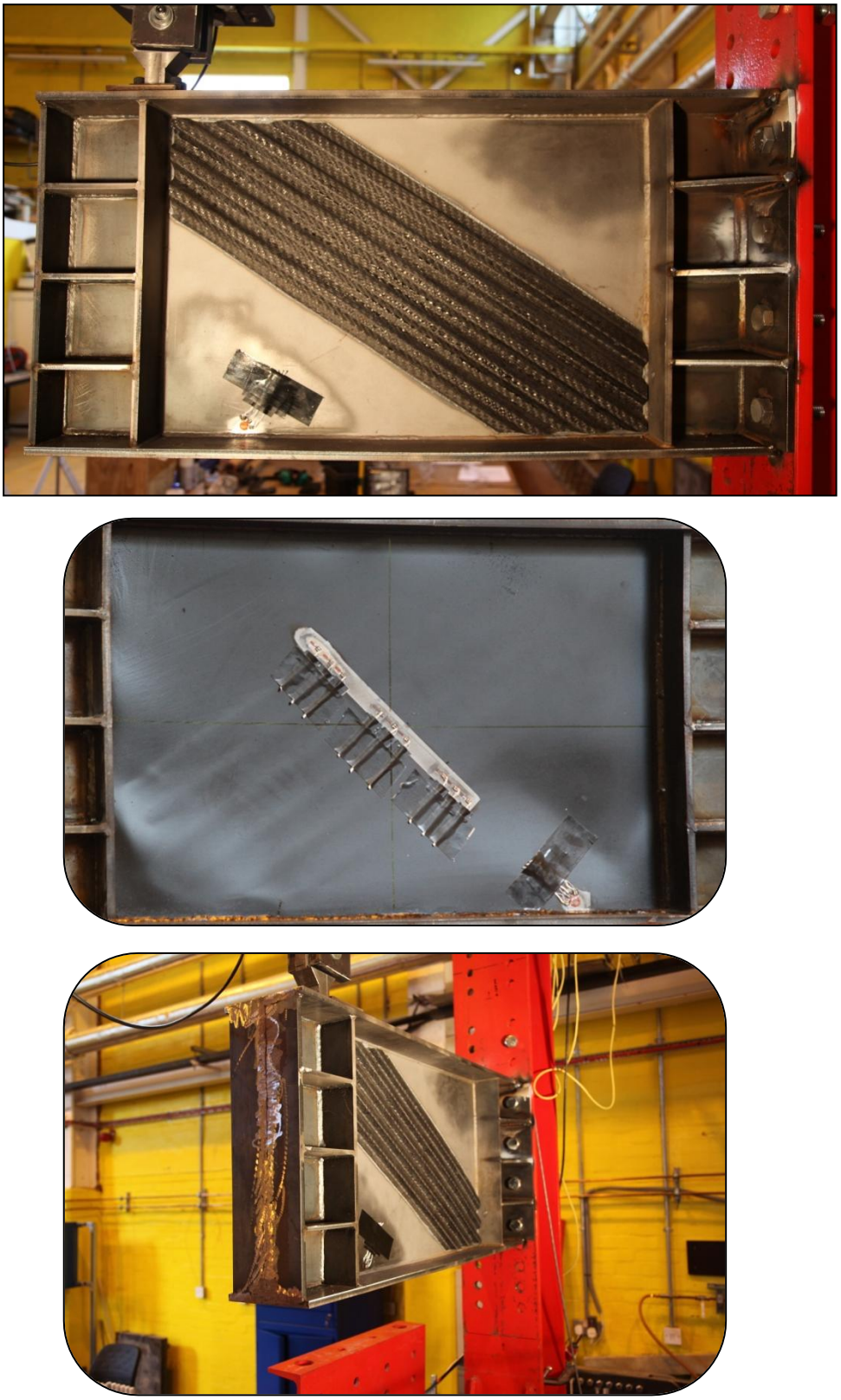

(**b**) SP-5 (CFRP-diagonal)

Figure (6.14 Cont.): Photos of the cyclic test specimens after final residual test.

(**c**) SP-6 (CFRP- 45° alignment)

Figure (6.14 Cont.): Photos of the cyclic test specimens after final residual test.

6.6.2.1 *Out-of-Plane Displacement*

Figure (6.15) shows the residual out-of-plane displacement each 100,000 cycles of load for specimens SP-4, SP-5, and SP-6. Moreover, it is important to note that the displacement values reported every 100,000 cycles are shifted so that each cycle can be distinguished, and that this does not have a physical meaning. Then the final residual test is shown, for the sake of comparison.

This plot shows that all of the residual curves for each specimen have almost exactly the same behaviour, except for the first few ones. Consequently, it can be concluded that there was no evidence of debonding or delamination during the tests within the cyclic loading range even after 2 million cycles of load. This conclusion is supported by visual observation of the specimen throughout the whole period of tests which lasted for several weeks for each specimen.

In this cyclic series, the out-of-plane displacement was measured in two different locations at the web plate; refer to Figure (6.5) in the instrumentation section. The first one is the usual central out-of-plane displacement and the second one was taken within the unstrengthened bottom triangular plate under the concentrated load where the maximum out-of-plane displacement is expected, as predicted using the finite element composite model (as will be seen later in Chapter 7). The weakness of this zone against buckling was discussed in section (6.6.1.3) for the precursor static subsequent series, especially the reversed buckling case of SP-3; refer to Figure (6.11) for more details.

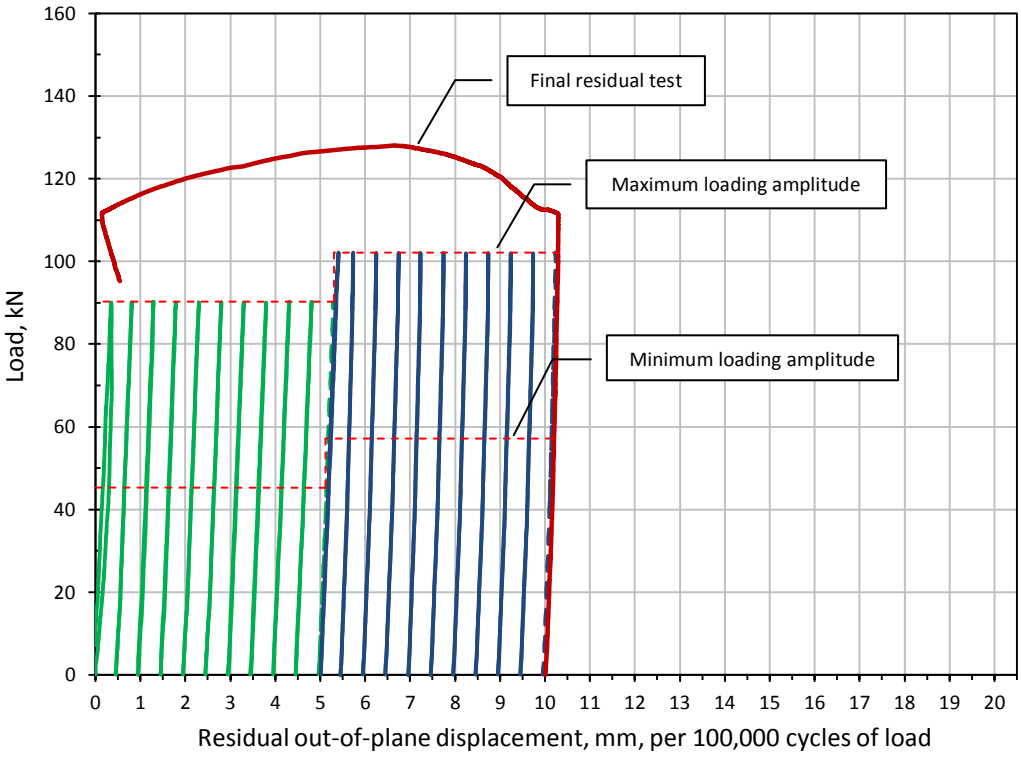

(**a**) SP-4 (GFRP- diagonal alignment)

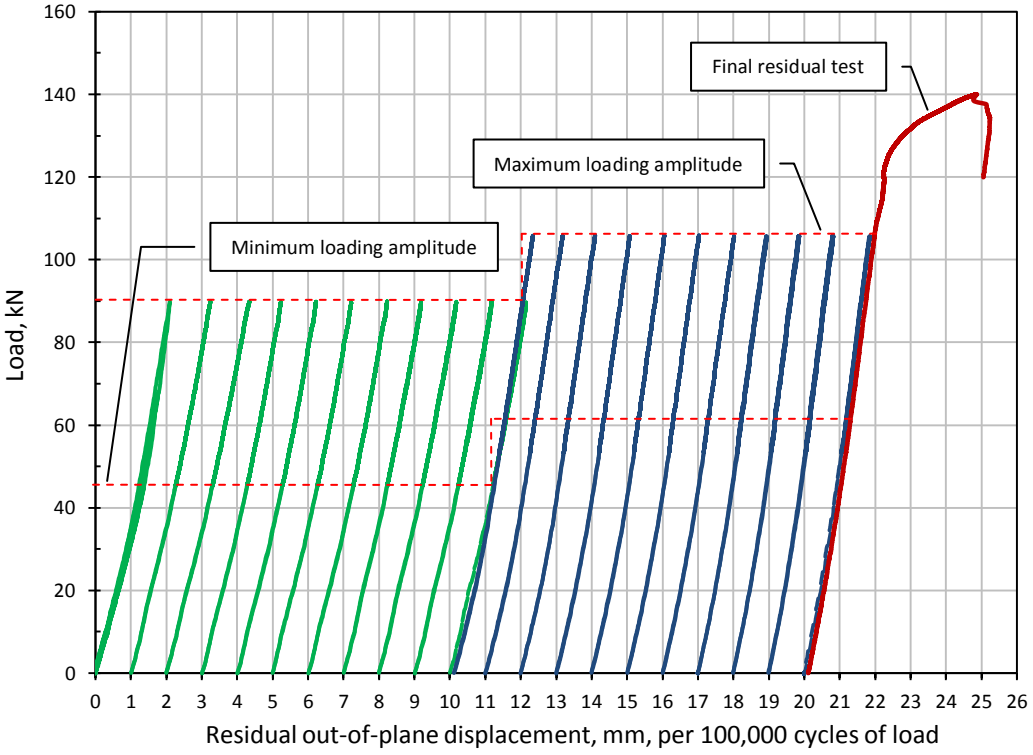

(**b**) SP-5 (CFRP- diagonal alignment)

Figure (6.15): Residual buckling behaviour of tested specimens per 100,000 cycle of load.

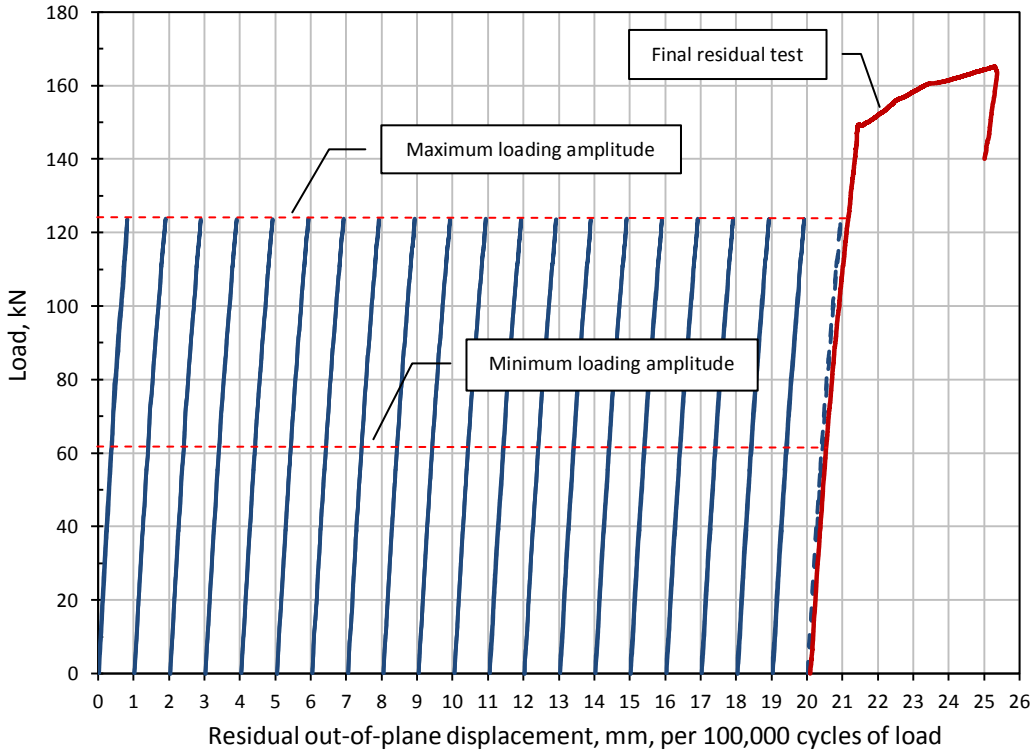

(**c**) SP-6 (CFRP- 45° alignment)

Figure (6.15 Cont.): Residual buckling behaviour of tested specimens per 100,000 cycle of load.

Maximum Out-of-Plane Displacement

Figure (6.16) compares the central displacement (LP-2) to the displacement at the maximum position (LP-1) for specimens SP-4 and SP-6 for the final residual test. Unfortunately, the idea of taking this new out-of-plane displacement measurement came late with respect to SP-5 which was the first specimen to be tested in the cyclic series. Close watching of the breathing phenomenon of SP-5 and the previous observation of the weakness of this unstrengthened triangular zone from the static series led to this extra measurement. It was very obvious during the cyclic test that the location of LP-1 breathed rather higher than the centre of the web (LP-2).

From Figure (6.16) it can be seen that both LP-1 and LP-2 had almost the same behaviour except that LP-2 went further at the very ultimate loading stage because the FRP panel was cracked and the buckling mode was altered. This figure is not very conclusive especially with missing LP-1 measurement for SP-5 and the reversed

buckling mode of SP-4. However, we are more concerned with the reduction in the secondary bending strain, and that will be discussed in the strain section (6.6.2.3).

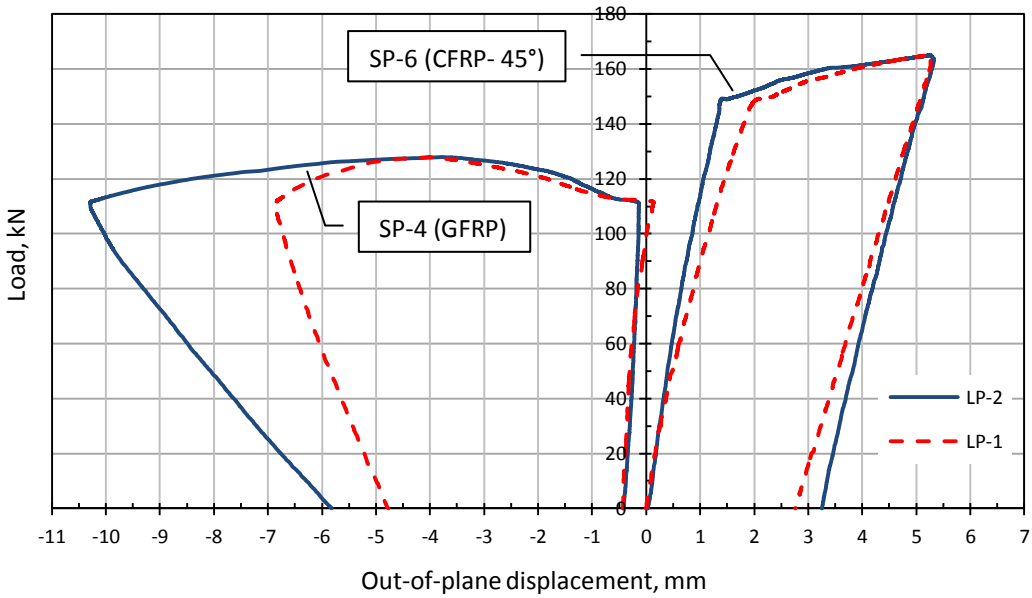

Figure (6.16): Residual buckling behaviour for tested specimens SP-4 and SP-6.

Central Out-of-Plane Displacement

Figure (6.17) compares the central out-of-plane displacements of the final residual test for the three tested specimens in this cyclic series of tests. From this figure it can be seen that the 45° alignment CFRP strengthened specimen (SP-6) succeeded the best among the three of them both in stiffening the steel plate girder web and increasing the ultimate capacity which was increased 88% with respect to the unstrengthened steel plate girder (SP-1) tested in the static series of tests and 18% over the diagonally aligned CFRP strengthened specimen (SP-5).

It is also interesting to see from Figure (6.17) that both the CFRP strengthened specimens had a typical bilinear behaviour where the load kept increasing linearly with displacement until close to the ultimate load where the slope of the curve changes dramatically to form a bilinear shape. After the slope changed, the load kept increasing but to a much smaller rate with respect to the displacement until collapse. The GFRP strengthened specimen behaved differently because of the reversed initial imperfection. The specimen tended to resist the effect of the reversed initial

imperfection by following the prebuckling mode created by the composite section but eventually the GFRP panel cracked and the mode of buckling was altered. Nevertheless, its behaviour could be approximated to a bilinear one as well.

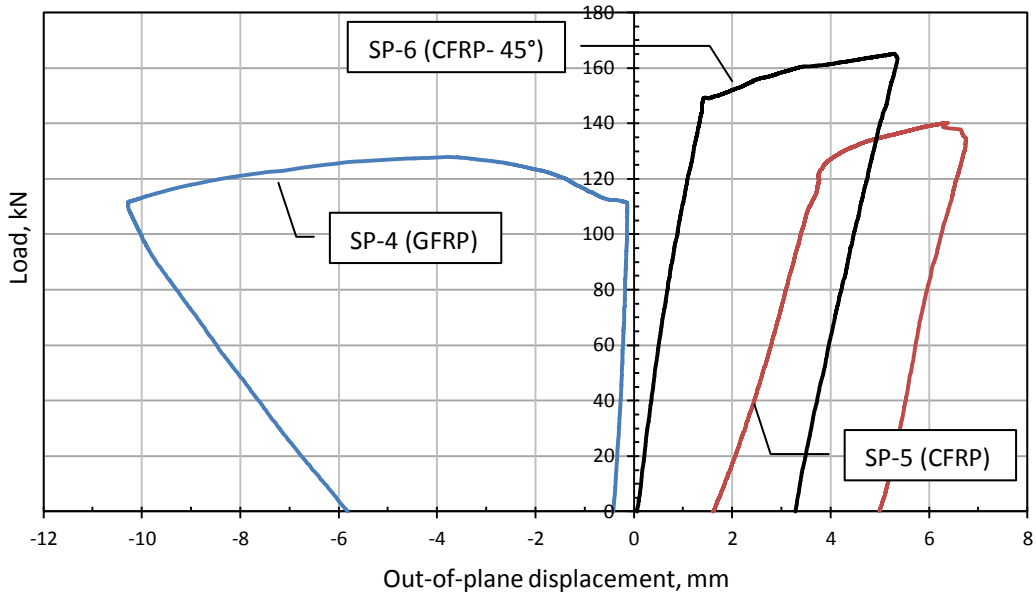

Figure (6.17): Buckling curves of the specimens tested in the cyclic series of tests.

Variation of the Maximum and Residual Out-of-Plane Displacement with Increased Number of Loading Cycles

Figure (6.18) shows the variation in the out-of-plane displacement with increasing the number of applied loading cycles. In Figure (6.18a), the maximum out-of-plane displacement is shown (the maximum refers to the measured displacement at the maximum loading amplitude after a certain number of loading cycles) while in Figure (6.18b), the residual out-of-plane displacement is presented (the residual refers to the displacements measured when the load is released after a certain number of loading cycles). From this figure, it can be seen that no significant change took place in the magnitude of the central out-of-plane displacement with increasing the number of the loading cycles for the three specimens tested in this cyclic series of tests. Even the residual out-of-plane displacements shown in Figure (6.18b) are negligible except maybe for SP-5 which had a maximum residual out-of-plane displacement of 0.48mm. This further proves the conclusion that neither debonding

nor delamination took place in the FRP panel throughout the applied 2 million cycles of load. The marked dip in the curves at loading cycle number 500,000 and 1,000,000 is due to the fact that the load range was increased from 35-70% to 40-80% and from 32-64% to 38-76% of the ultimate capacity for specimens SP-4 and SP-5, respectively. There are other minor dips that can be detected in the case of SP-5; however, these were for different reasons. The first one can be detected just beyond cycle number 200,000 where a crack took place in the welding of the outer frame near the support which was re-welded and the second one was because one of the bolts holding the specimen to the big testing rig was broken just beyond cycle number 640,000 then it was replaced by another bolt.

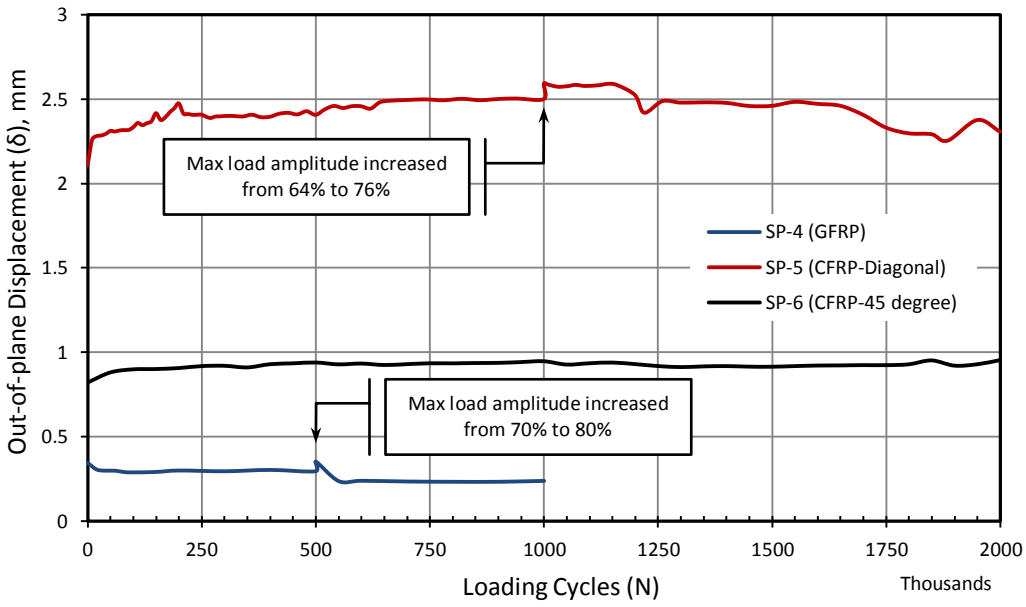

(**a**) Maximum Out-of-plane displacement

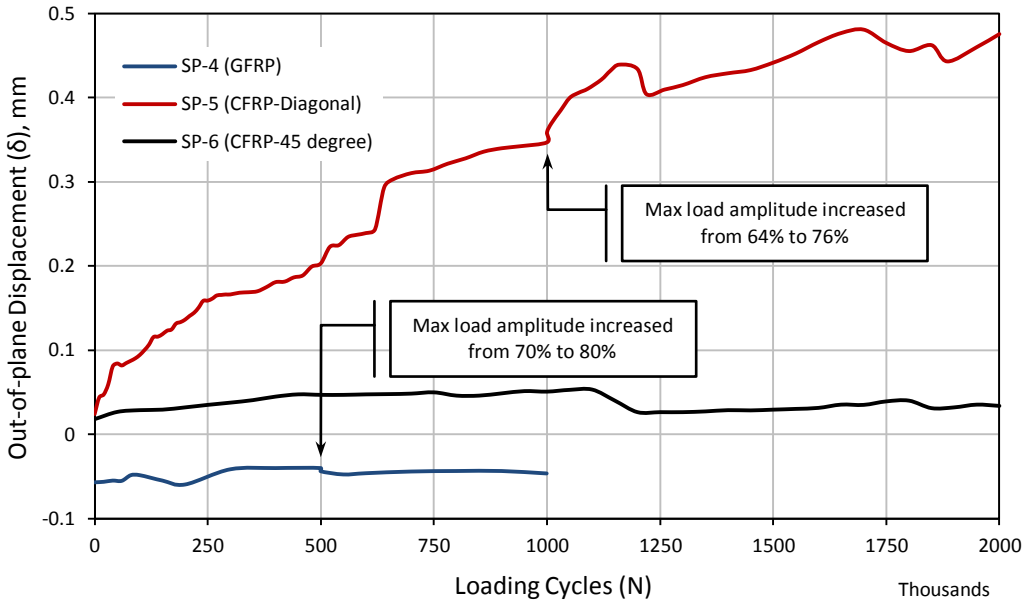

(**b**) Residual Out-of-plane displacement

Figure (6.18): Variations of central Out-of-plane displacement with increasing the number of applied loading cycles (**δ** -N).

6.6.2.2 *In-Plane Deflection*

Figure (6.19) compares the in-plane deflection for the final residual test under the point load for the three specimens tested in this cyclic series. From this figure, it can be seen that generally the specimens follow the trends of their corresponding

buckling curves with an obvious bilinear behaviour, taking into considerations the different accumulated deflection resulted from the cyclic loading of each specimen up to 2 million cycles of load. SP-5 (CFRP-diagonal strengthened specimen) showed the highest accumulated in-plane deflection among all the specimens. This behaviour looks odd in comparison to the behaviour of SP-4 (GFRP strengthened specimen) which showed much less in-plane deflection both under cyclic loading and during the final residual test. However, we should keep in mind that there are many variables affecting the performance of the specimen. These factors could be (but not limited to) that the GFRP and CFRP strengthening mostly affects the out-of-plane behaviour and not the in-plane one and this was shown previously both for the initial series of tests (Phase-2 in Chapter 5) and the precursor control specimens in this final series of tests, another important factor is the initial imperfection which affects the behaviour of the specimen significantly. The GFRP strengthened specimen had a small initial imperfection of -0.38 while the CFRP strengthened one had a considerable initial imperfection of 1.14 mm. The reversed initial imperfection plays an important role in the behaviour of the specimen as was discussed earlier.

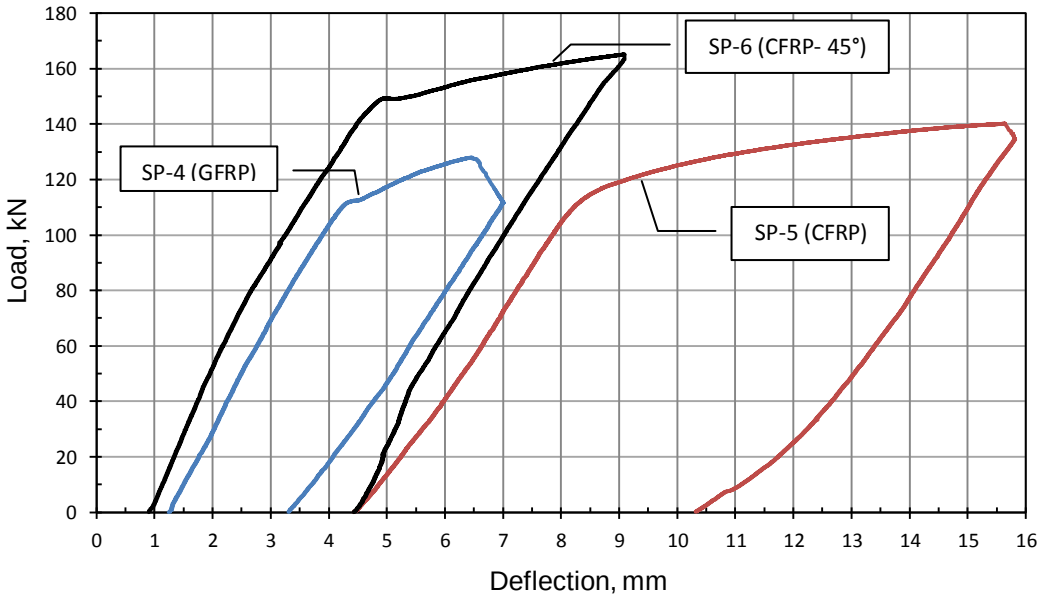

Figure (6.19): Deflection curves of the specimens tested in the cyclic series of tests.

Variation of the Maximum and Residual In-Plane Deflection with Increased Number of Loading Cycles

Figure (6.20) shows the variation of in-plane deflection with increasing the number of applied loading cycles. In Figure (6.20a) the maximum in-plane displacement is shown (the maximum refers to the measured deflection at the maximum loading amplitude after a certain number of loading cycles) while in Figure (6.20b) the residual in-plane deflection is presented (the residual refers to the deflection measured when the load is released after a certain number of loading cycles). From this figure, it can be seen that there is an obvious trend for the deflection to increase with increasing the number of loading cycles. This is true both for the maximum and residual deflection curves. For the same reasons mentioned above; SP-5 (CFRP-diagonal strengthened specimen) had the highest residual deflection of 4.4mm followed by SP-4 (GFRP strengthened specimen) with a residual deflection of 1.2mm and SP-6 (CFRP-45° strengthened specimen) with a residual deflection of 0.9mm. However, good correlation was found when comparing the ratio of the residual deflection to the initial imperfection for the three specimens (SP-4, SP-5 and SP-6). This is a good indication that the initial imperfection plays an important role in the accumulated residual deflection caused by the cyclic loading.

6.6.2.3 *Strain Measurements*

In this section, the experimentally measured strain is reported for specimens SP-4, SP-5, and SP-6 tested in this subsequent cyclic series; refer to Figure (5.6) for the location and orientation of the strain gauges. Two main strain categories were measured; namely, the strain along the tension diagonal of the steel plate in different locations (S1-S10), and the maximum strain near the welded tension corner of the web plate where the highest breathing stresses are induced (SR1-SR6). The first strain category will help in illustrating the strain distribution within the tension field, especially, the variation of the measured strain between the bonded and unbonded steel strips; while the second strain category will help in determining the reduction in the breathing stresses and consequently the improvement in the fatigue behaviour of the strengthened specimens as will be seen in section (6.9).

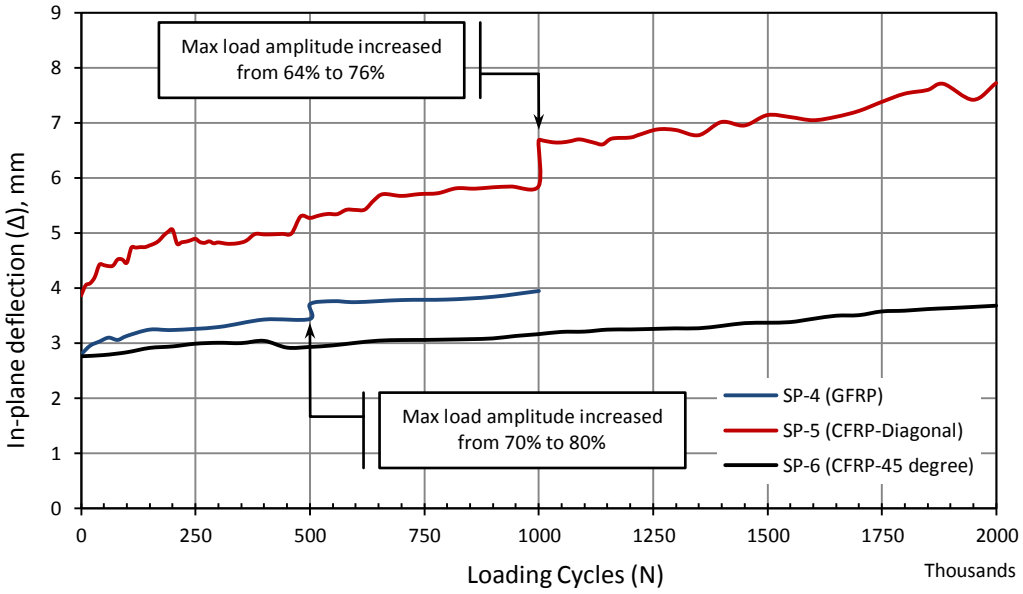

(**a**) Maximum in-plane deflection

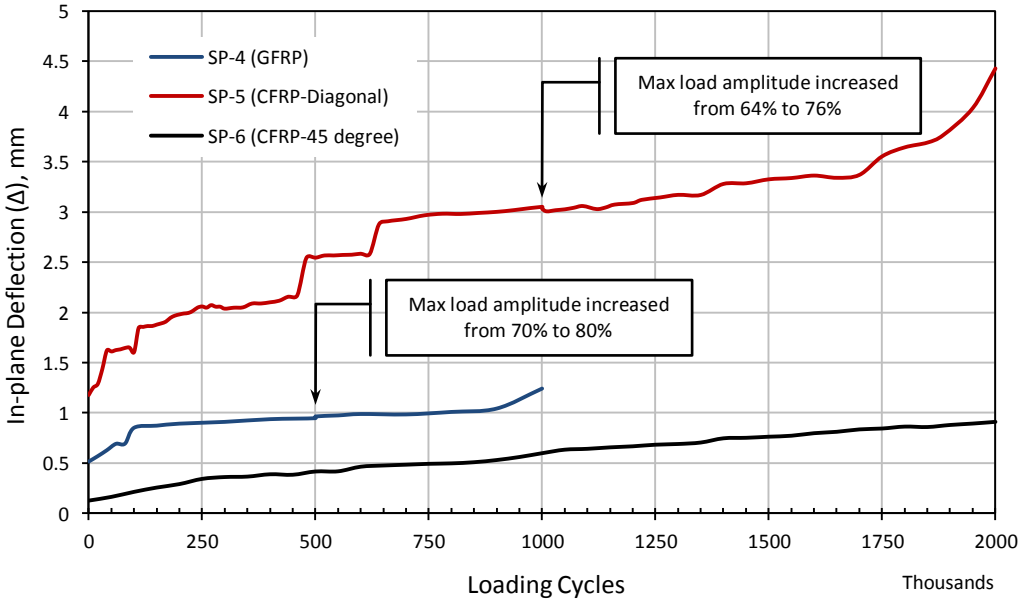

(**b**) Residual in-plane deflection

Figure (6.20): variations of in-plane deflection with increasing the number of applied loading cycles (Δ-N).

Tension Diagonal Strip

Figure (6.21) shows the strain curves in the diagonal tension strip for the final residual test of the three specimens tested in this cyclic series of tests; refer to Figure (6.5) in the instrumentation section (6.5) for the location of these strain gauges (S1 through S10). In this figure, the unloading part of the curves is not shown to produce

a clearer view. However, in all cases the unloading part of the strain curve is a straight line typically parallel to the initial linear loading part.

Figure (6.21a) shows the strain curves for SP-4 (GFRP strengthened specimen). For this specimen, the tension diagonal is adopted for aligning the strain gauges which were bonded according to a predesigned scheme planned to assure that the strain gauges are bonded to the steel plate on the basis of one under a bonded FRP strip and another one under an unbonded FRP strip, consequently, the difference in their strain rate can be detected (The difference in steel strain between the bonded and unbonded FRP strips will be further discussed separately in this section). From Figure (6.21a), it can be seen that all the curves follow the same pattern where the strain start increasing linearly with increasing the load until it reaches close to the ultimate stage then the slope of the curves changes dramatically from a linear to a non-linear behaviour until failure takes place. It can be noted that S2 and S3 have much higher yielding strain than the other strain gauges; this could be attributed to the high out-of-plane deformation in this area caused by the crack in the GFRP panel and the reversed mode of failure, this can be seen by referring to Figure (6.14a).

Figure (6.21b) shows the strain curves for SP-5 (CFRP- diagonally strengthened specimen). For this specimen, the tension diagonal was not adopted for aligning the strain gauges. Instead, a 45° tension diagonal alignment was adopted. The idea behind adopting this new alignment was to be able to compare the two different strain readings from SP-4 and SP-5 (a diagonal and a 45° alignment, respectively). This criterion was derived from the finite element model after thorough investigation of the strain distribution. From the finite element model, it was noticed that the point of maximum strain lies at a horizontal distance of 112.5mm from both the tension corners of the web plate causing the angle of maximum principal strain (∅) to be close to 45°. This concept will be revisited when discussing the strain of SP-6 later in this section because in that specimen there are two rosette strain gauges, one at the tension corner and another one at a horizontal distance of 112.5mm.

However, generally speaking the diagonal strain curves of SP-5 in Figure (6.21b) showed the same pattern as the ones described above for SP-4. The strain start increasing linearly with increasing the load until it reaches close to the ultimate

stage, then the slope of the curves changes dramatically from a linear to a non-linear behaviour until failure takes place. It is very interesting to note that both the strain curves of SP-4 and SP-5 had approximately the same initial linear slope and they both started to behave non-linearly after the applied load reached a value of 110kN. The two major differences between the curves of SP-4 and SP-5 is that the latter had much higher residual strains, as can be noted from the values of the strain at zero load level and that the ultimate yielding strains were higher than those of SP-4. This could be justified by the higher applied load associated with SP-5 and the higher initial imperfection as well.

Figure (6.21c) shows the final residual test strain curves for the strain gauges S7 through S10 of SP-6 (CFRP-45° strengthened specimen). These strain gauges can be located by referring to Figure (6.5c). They meant to show the maximum tension strain in the 45° degree tension strip for the new strengthening configuration adopted in this specimen. S7-S9 was used for the steel plate under the main CFRP panel and S10 was used for the steel plate under the secondary CFRP panel. All of them showed almost the same results as can be seen from Figure (6.21c). It is interesting to note that these strain gauges showed different behaviour than the ones for both SP-4 and SP-5. At the beginning the curves started increasing linearly with almost the same slope as in the previous two tests but to a much higher value of applied load. They succeeded to maintain their linear behaviour up to 150kN and then started to behave in a perfectly plastic manner up to a strain approximately equal to 0.002 mm/mm, then they started to strain harden. This is a good indication that the 45° strengthening configuration succeeded in improving both the strength and behaviour of the tested specimen.

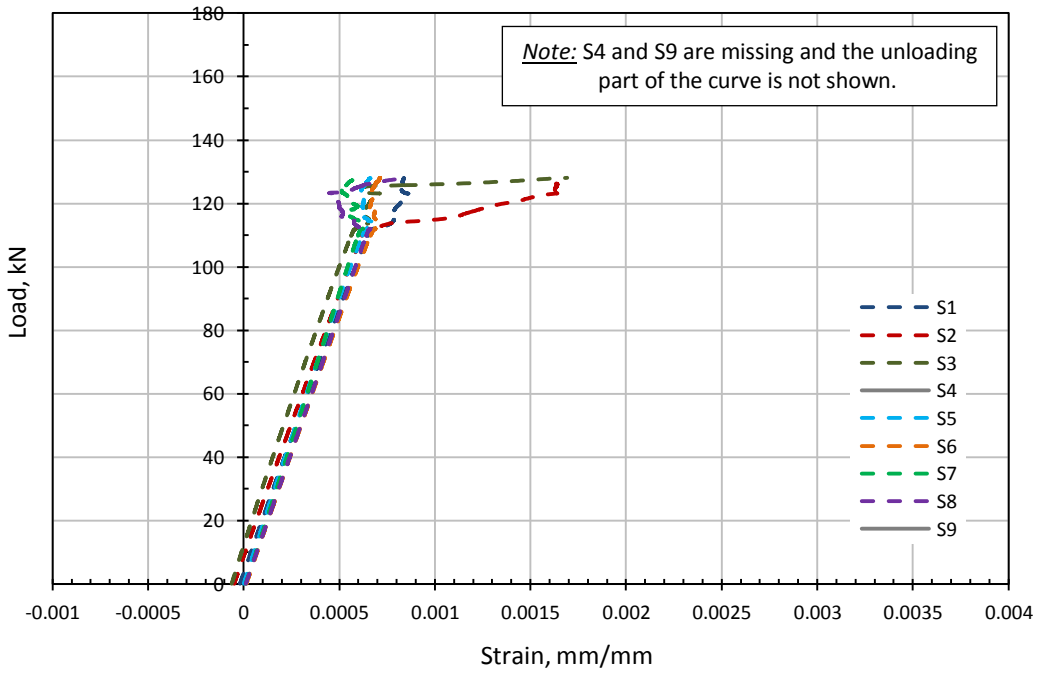

(**a**) SP-4 (GFRP strengthened specimen), the strain gauges are aligned diagonally (with an angle of 34° with respect to the horizontal axis)

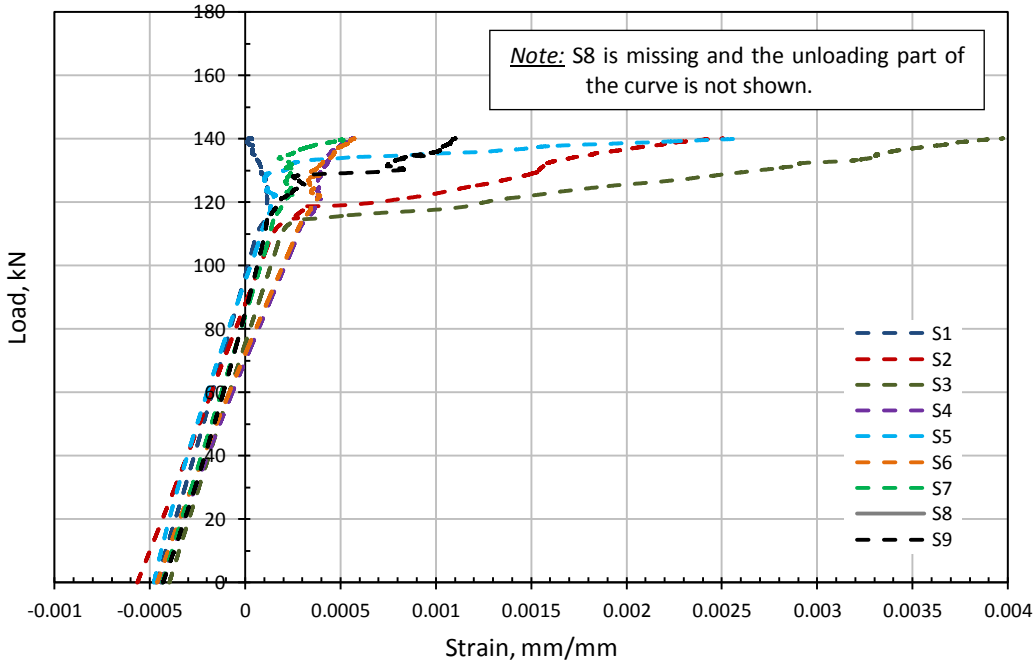

(**b**) SP-5 (CFRP-diagonal strengthened specimen), the strain gauges are aligned with an angle of 45° with respect to the horizontal axis.

Figure (6.21): Final residual test Strain curves S1 through S9 for SP-4, SP-5, and SP6.

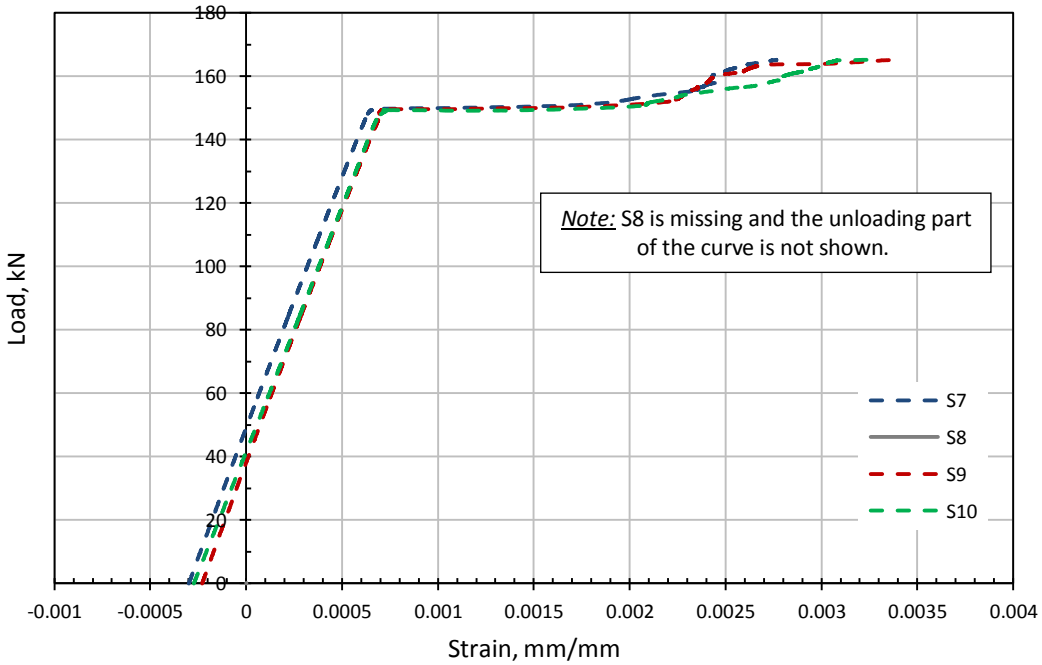

(**c**) SP-6 (CFRP-45° strengthened specimen), only four single 45° strain gauges were attached, refer to Figure (6.5c) for their locations.

Figure (6.21 Cont.): Final residual test Strain curves S1 through S9 for SP-4, SP-5, and SP6.

Tension Corner Rosette Double Face Strain Gauge Readings

Figure (6.22) shows the final residual test strain curves for the mirrored double face rosette strain gauges of the three specimens tested in this cyclic series of tests. Figure (6.22a) and (6.22b) shows the strain curves for SP-4 (GFRP strengthened specimen) and SP-5 (CFRP-diagonally strengthened specimen), respectively. For both of these specimens, one rosette strain gauge was bonded at a horizontal distance of 112.5mm from the bottom tension corner of the steel web where maximum strain is expected (one rosette strain gauge for each face of the steel plate); refer to Figure (6.5b and d) in the instrumentation section for their locations and referencing details. As for the tension strip strain gauges (S1-S9), the strain started increasing linearly with increasing shear load up to the same load value of 110kN and then the behaviour is altered significantly to a non-linear pattern up to failure. The discrepancies that can be found in comparing the strain curves for SP-4 and SP-5 can be justified by the different buckling modes and the high residual strain associated with SP-5. The

shown shear strains (γ_{xy}) were calculated using the same Equation (5.3) described in Chapter 5 for the initial series of tests (Phase-2). It can roughly be stated that the shear strains for SP-4 and SP-5 look the same taking into consideration that the ultimate load is different and the difference in the residual strains.

Figure (6.22c) and (6.22d) show the final residual test strain curves of SP-6 (CFRP-45° strengthened specimen). Two rosette strain gauge sets were bonded at the bottom tension corner of the web steel plate at a distance of 112.5mm from each other (two for each face of the steel plate); refer to Figure (6.5c and d) for their locations and referencing details. Figure (6.22c) shows the strain curves for the first (corner) rosette strain gauge set (R_1) while Figure (6.22d) shows the curves for the second set (R_2). The idea behind putting two different sets of rosette strain gauges in two different locations in the same tension corner was to experimentally validate the concept of 45° analysis illustrated by the finite element model where the tension strip tend to work in 45° angle and not diagonally (34°) as expected. The shear strain was calculated using Equation (5.3) as mentioned above. Again some aspects of similarity can be seen from these curves and the tension strip curves (S7-S10) where both of them behaved linearly up to an applied shear load of 150kN and then changed to a non-linear pattern. Comparing Figures (6.22c) and (6.22d), it is evident that the second set of rosette strain gauges (R_2- located at a distance of 112.5mm from the bottom tension corner of the steel web) had higher strain readings in all of its strain channels except ε_x which was approximately similar to the corresponding one in R_1. This further proves the 45° analysis concept mentioned above and this will be further investigated in more detail in the numerical model section (6.7).

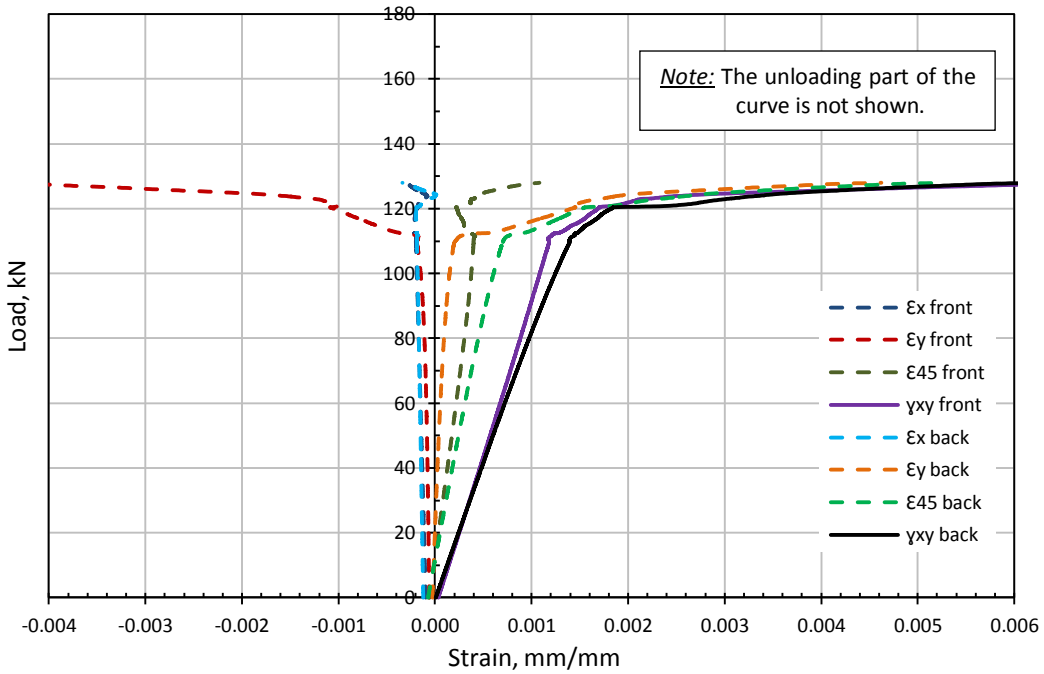

(**a**) SP-4 (GFRP strengthened specimen)

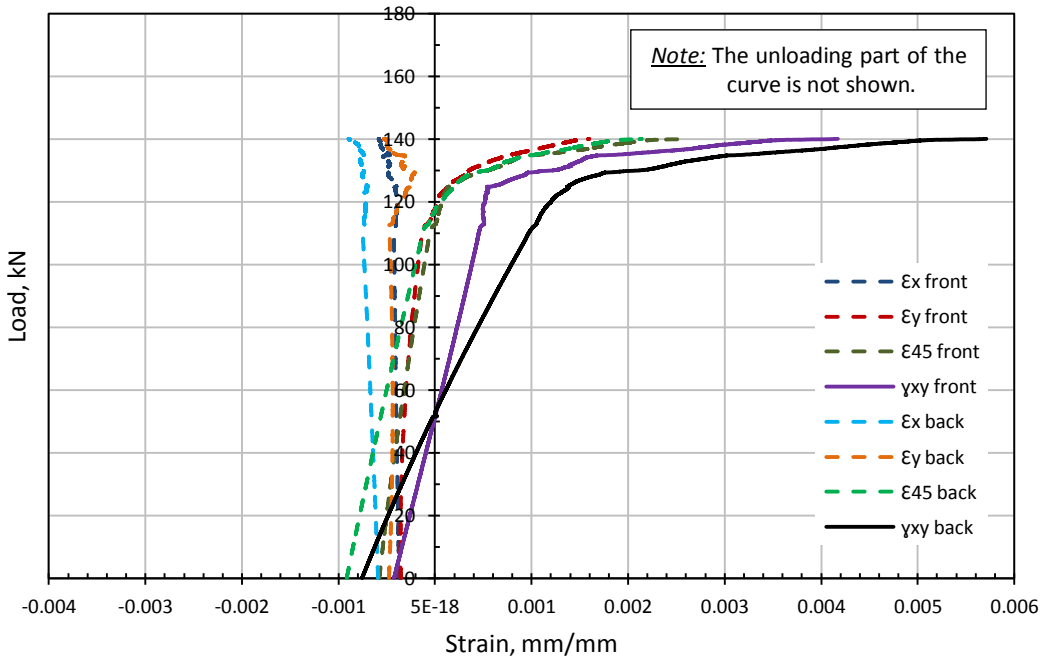

(**b**) SP-5 (CFRP-diagonally strengthened specimen)

Figure (6.22): Final residual test rosette strain curves SR-1 through SR-6 for SP-4, SP-5, and SP-6.

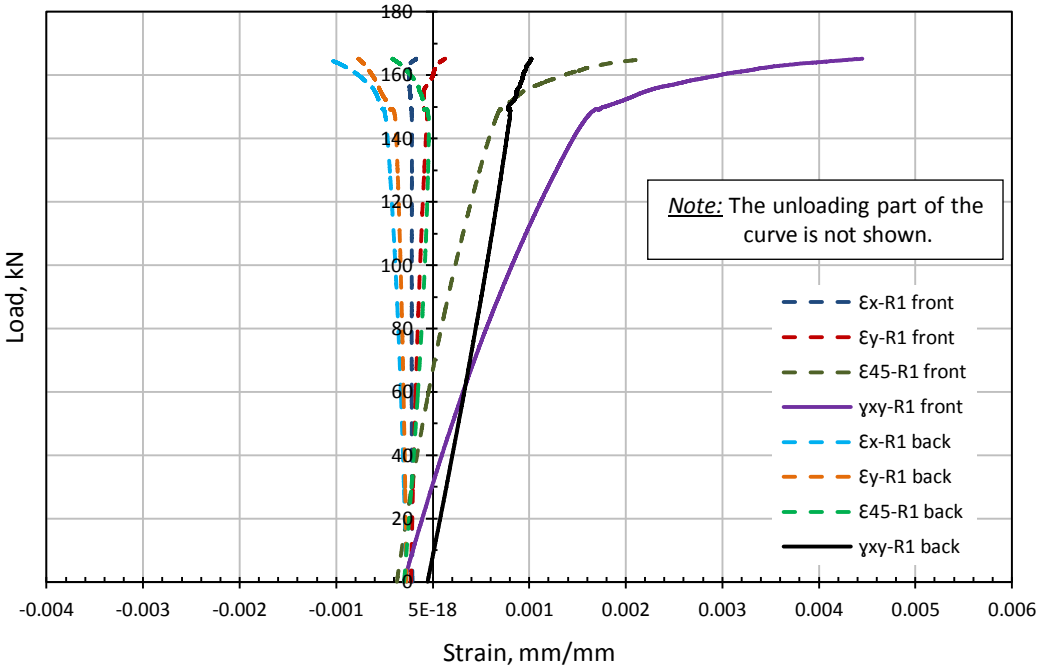

(**c**) SP-6 (CFRP-45° strengthened specimen), Rosette-R_1

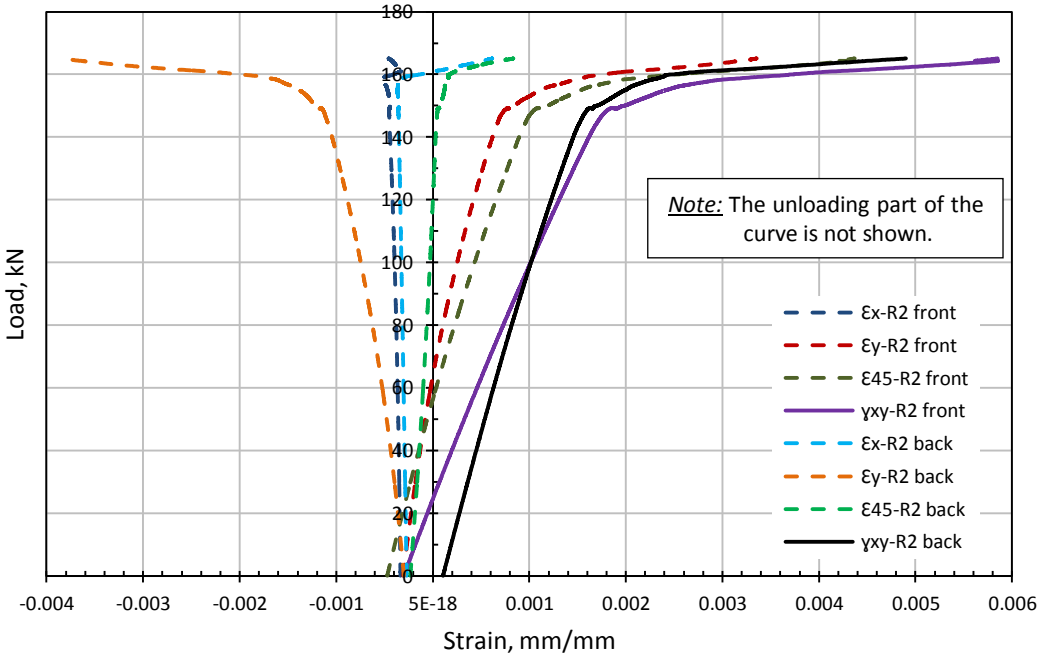

(**d**) SP-6 (CFRP-45° strengthened specimen), Rosette-R_2

Figure (6.22 Cont.): Final residual test rosette strain curves SR-1 through SR-6 for SP-4, SP-5, and SP-6.

Variation of the Maximum and Residual Strain Readings with Increased Number of Loading Cycles

Figure (6.23) shows the variations in the maximum and residual strain readings with increasing the number of the loading cycles from 0 to 2 million cycles of loads for the three specimens tested in this cyclic series of tests (the maximum refers to the measured strain at the maximum loading amplitude after a certain number of loading cycles while the residual refers to the strain measured when the load is released at a certain number of loading cycles).

Figure (6.23a) shows the variation for SP-4 (GFRP strengthened specimen) for only 1 million cycles of loads, afterwards the cyclic test was stopped because the specimen showed very negligible breathing. The first 500,000 cycles were performed with loading range of 35-70% and then based on observation of the strain readings and deformations; the loading range was increased to 40-80% for the second 500,000 cycles of loads. However, from this figure it can be seen that SP-4 showed no significant variations in the strain readings through the 1 million cycles of load; except for the marked dip in the curves because of increasing the loading range, the curves shows almost flat constant strain. This could be attributed to the fact that this specimen showed insignificant breathing due its reversed initial imperfection of -0.38mm. By close examining the residual strain curve for SP-4, an average residual strain of 0.0001mm/mm can be detected after 1 million cycles of loads which is insignificant in comparison to the other two specimens as will be seen next.

Figure (6.23b) shows the variation for SP-5 (CFRP-diagonally strengthened specimen) for 2 million cycles of loads. This specimen showed the most severe variation in the maximum and residual strain readings among the three specimens in this cyclic series of tests. The average residual strain over the 2 million cycles can be shown to be 0.0006 mm/mm (0.0005 after 1 million cycles). The marked dip in the curves at loading cycle number 1,000,000 is due to the fact that the load range was increased from 32-64% to 38-76% of the ultimate capacity. The other dips in the curve were already clarified in section (6.6.2.1) for the out-of-plane displacement variation with the number of cycles.

Figure (6.23c) shows the variation for SP-6 (CFRP-45° strengthened specimen) and for 2 million cycles of loads. This specimen actually proved to be the best in

both strength and behaviour aspects. It can be seen from the figure that the strain patterns are taking a rather typical constant descending order with an average residual strain of 0.0003 mm/mm after 2million cycles of loads (0.0001 after 1 million cycles).

Generally speaking, in the three specimens, the strain had a tendency to descend, which means that the residual strains are usually compression ones even for the strain gauges where tension readings is obtained. It is believed that this phenomenon took place because the cyclic loading range was high and it took the specimen somewhere near the ultimate load where the non-linear behaviour is dominant. This might cause the specimen to cross from the elastic to the elasto-plastic zone where permanent non-reversible strain values accumulate in small amounts continuously with the progression of the cyclic test. This argument is mostly true for the CFRP strengthened specimens SP-5 and SP-6; however, it is true only for some range of strains for SP-4 (GFRP strengthened specimen) which showed very limited breathing as mentioned earlier.

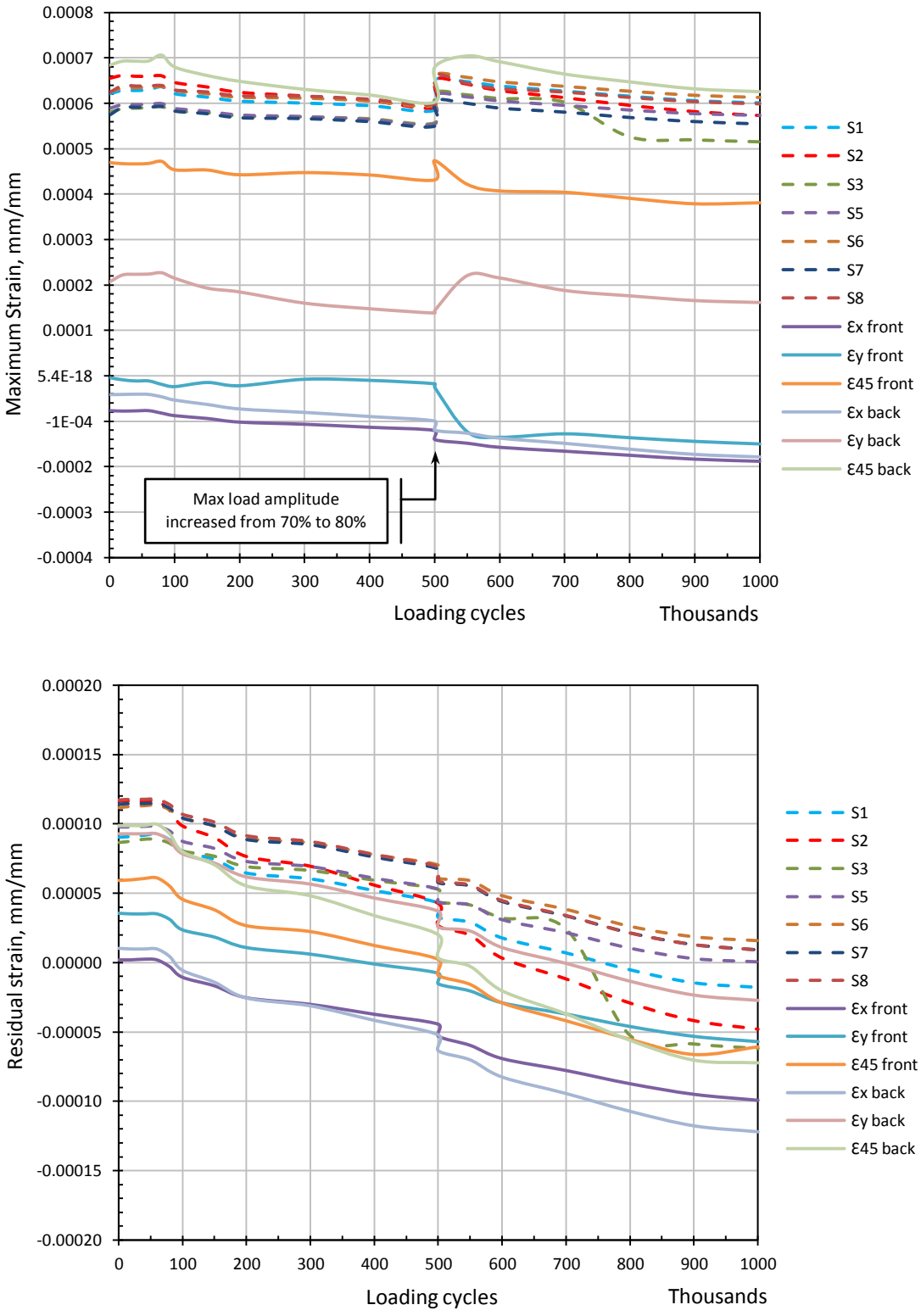

(**a**) SP-4 (GFRP strengthened specimen)

Figure (6.23): Variations in strain readings with increasing the number of loading cycles for SP-4, SP-5, and SP-6.

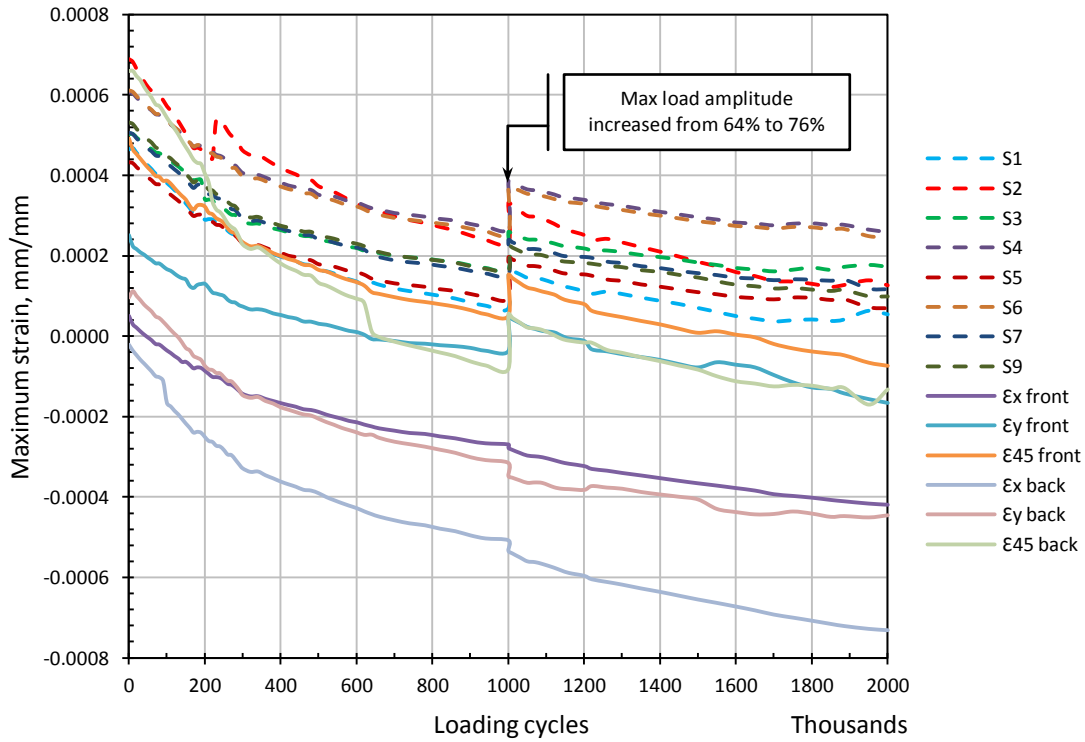

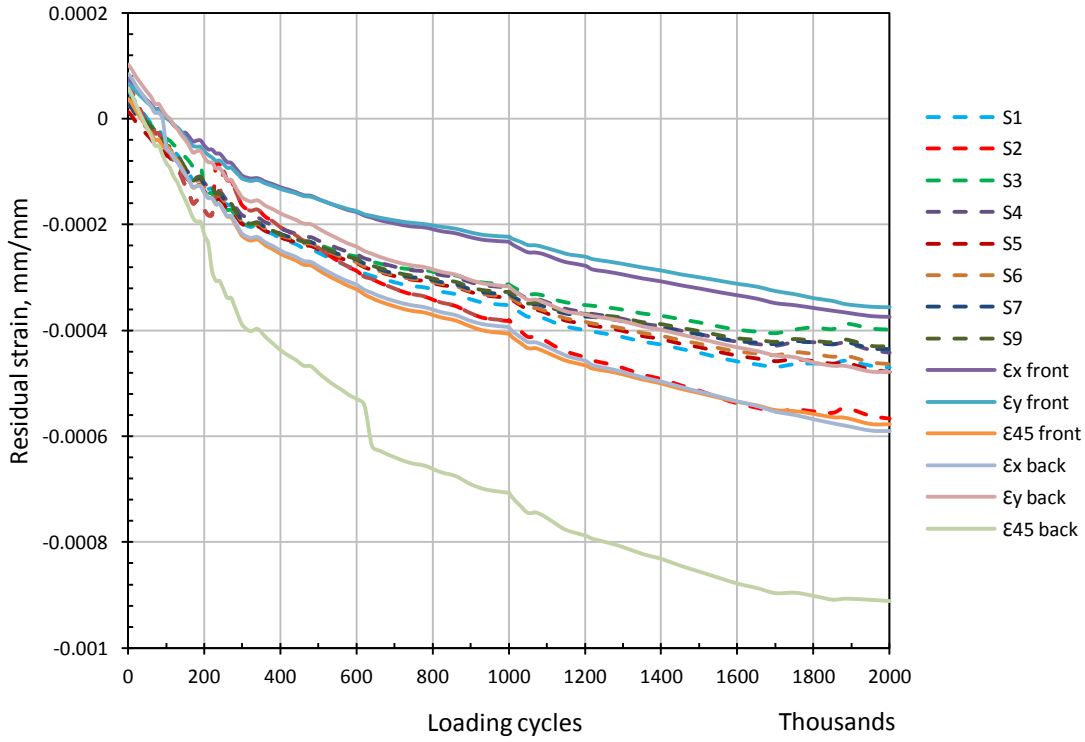

(**b**) SP-5 (CFRP-diagonally strengthened specimen)

Figure (6.23 Cont.): Variations in strain readings with increasing the number of loading cycles for SP-4, SP-5, and SP-6.

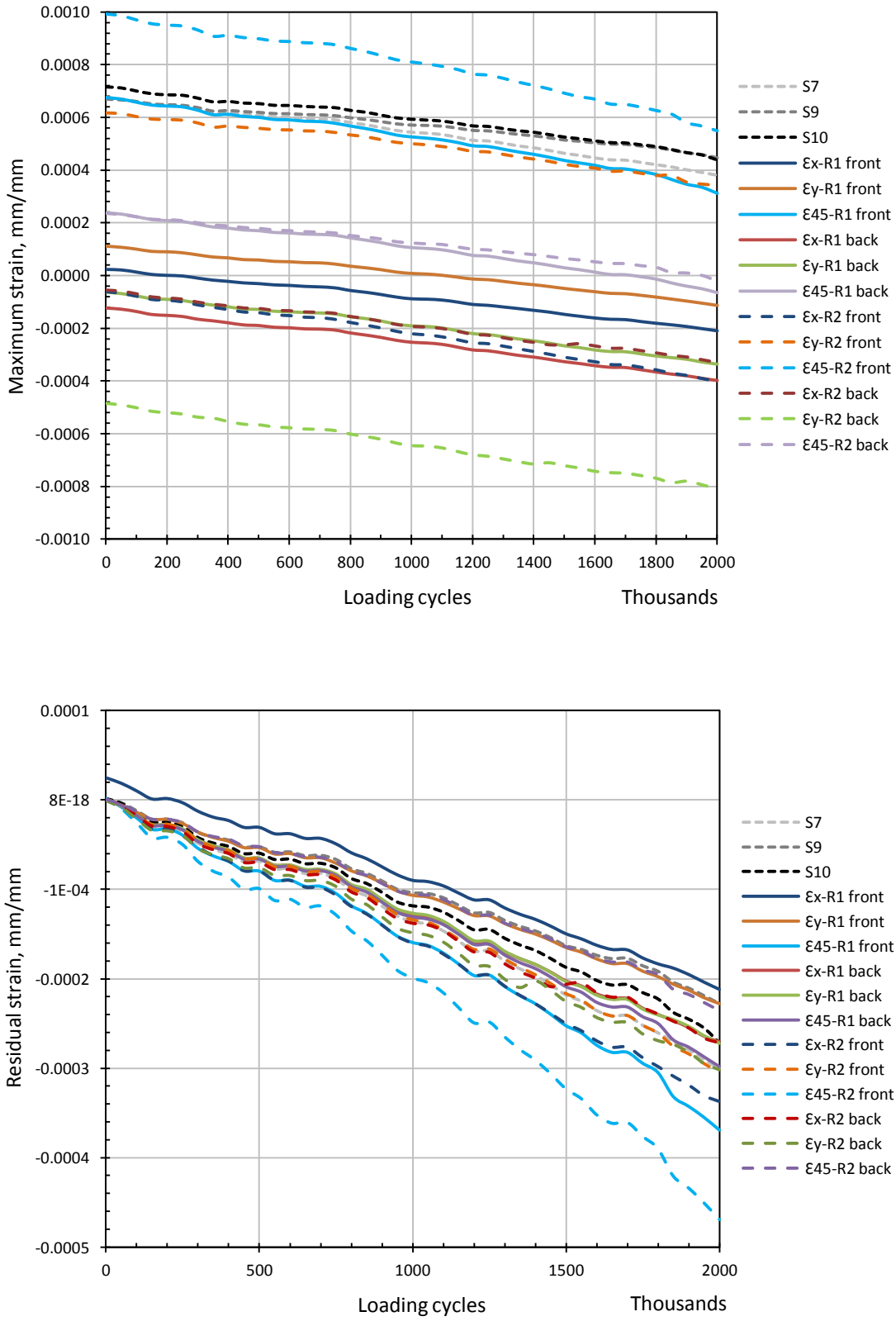

(**c**) SP-6 (CFRP-45° strengthened specimen)

Figure (6.23 Cont.): Variations in strain readings with increasing the number of loading cycles for SP-4, SP-5, and SP-6.

The Difference between Strain Readings of the Steel Plate Tension Strip for Bonded and Unbonded FRP Strips

Figure (6.24) shows the variations in the distribution of the strain readings (S1 through S9) for the tensile steel strip at load increments of 10% of the ultimate load in the final residual test in this cyclic series of tests. Figure (6.24a) shows these variations for SP-4 (GFRP strengthened specimen) and Figure (6.24b) shows it for SP-5 (CFRP- diagonally strengthened specimens). The figure also contains a diagram showing the positions of the strain gauges and what is meant by a strain gauge under bonded and unbonded strip. A strain gauge bonded to the steel plate in a position where an FRP strip is bonded to the opposite face is marked as (1) while a strain gauge bonded to the steel plate in a position where there is no FRP bonded to the other side of the plate is marked as (0). In this order, S1, S3, S5, S7, and S9 are (type-0) strain gauges while S2, S4, S6, and S8 are (type-1) strain gauges.

Generally, both figures show linear strain increment up to 80% of the ultimate capacity of the specimen then the strain suddenly jumps depending on the location of the strain gauge and the deformed shape of the specimen. This linear behaviour is shown by the black arrows in the figure. The major difference in the strain distribution between SP-4 and SP-5 is the high residual compression strain associated with SP-5. However, this was demonstrated in earlier sections.

The main idea behind this graph is to show the difference in the values of strain between bonded and unbonded parts of the tensile steel plate strip. This is difficult to achieve by looking at the curve as it is because of the relatively high strains at the ultimate loading stages. However, if we removed the ultimate loading stage and kept only up to 80% of the ultimate load (the typical loading range) it would be much easier to see that the strain readings under bonded strips is always higher than those under unbonded strips. This is true for Group 2 and 3 as can be seen from the figure (look at the green strips where the arrow ends) and for both specimens. Group 1 was an exception where the strain reading of the bonded strip lay in the second rank both for SP-4 and SP-5.

This phenomenon is believed to be because of the gripping effect of the bonding FRP strip affecting the bonded steel plate strips. The bonding FRP strips tend to push the corresponding (underlying) steel plates strips during its attempt to

resist the diagonal tension and the perpendicular diagonal compression at the same time. A good photo illustrating this phenomenon can be found in Figure (6.14b) for SP-5 after failure. This gripping effect was captured by the right reflection of light and it is not huge as it seems to be.

6.6.3 Comment on the Experimental Results

In section (6.6), the experimental programme of the final series of tests (Phase-3) was reported in two parts, the first one was dedicated for the static subsequent series while the second one was dedicated for the cyclic subsequent series of tests. All aspects of strength and deformational behaviour of the control and strengthened specimens were illustrated. The experimental results show that the strengthening technique succeeded in increasing the shear capacity of the strengthened specimens and improved their deformational behaviour.

In the previous sections, care was taken to illustrate the experimental results and show the effect of different parameters on the behaviour of the static and cyclic specimens. However, in the following sections the improvement in the key elements in the current work; namely, the stiffening effect, ductility, and fatigue life expectancy are going to be quantified and illustrated.

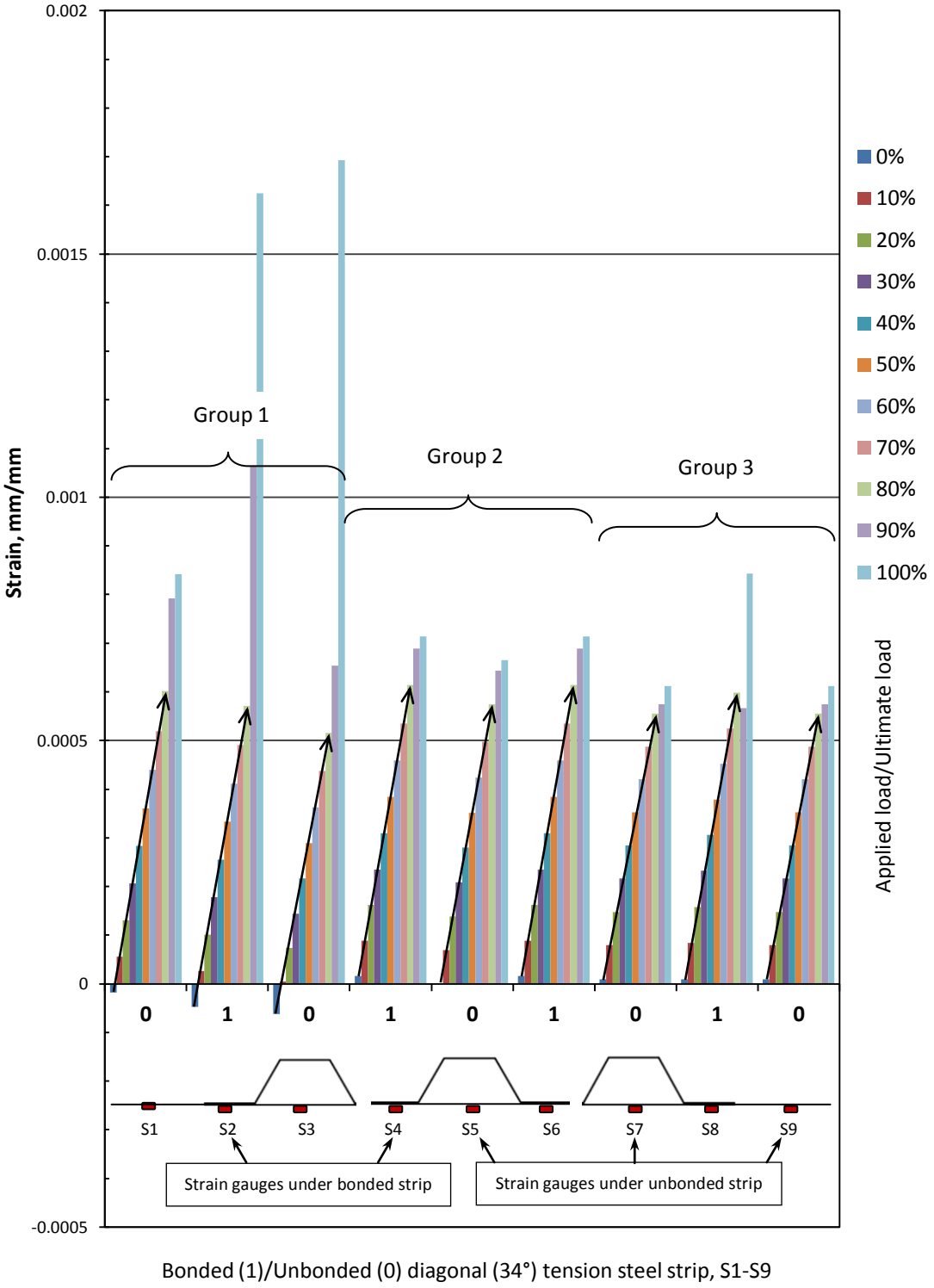

(**a**) SP-4 (GFRP strengthened specimen)

Figure (6.24): Distribution of the tension strip strain gauge readings with respect to the bonded/unbonded regions.

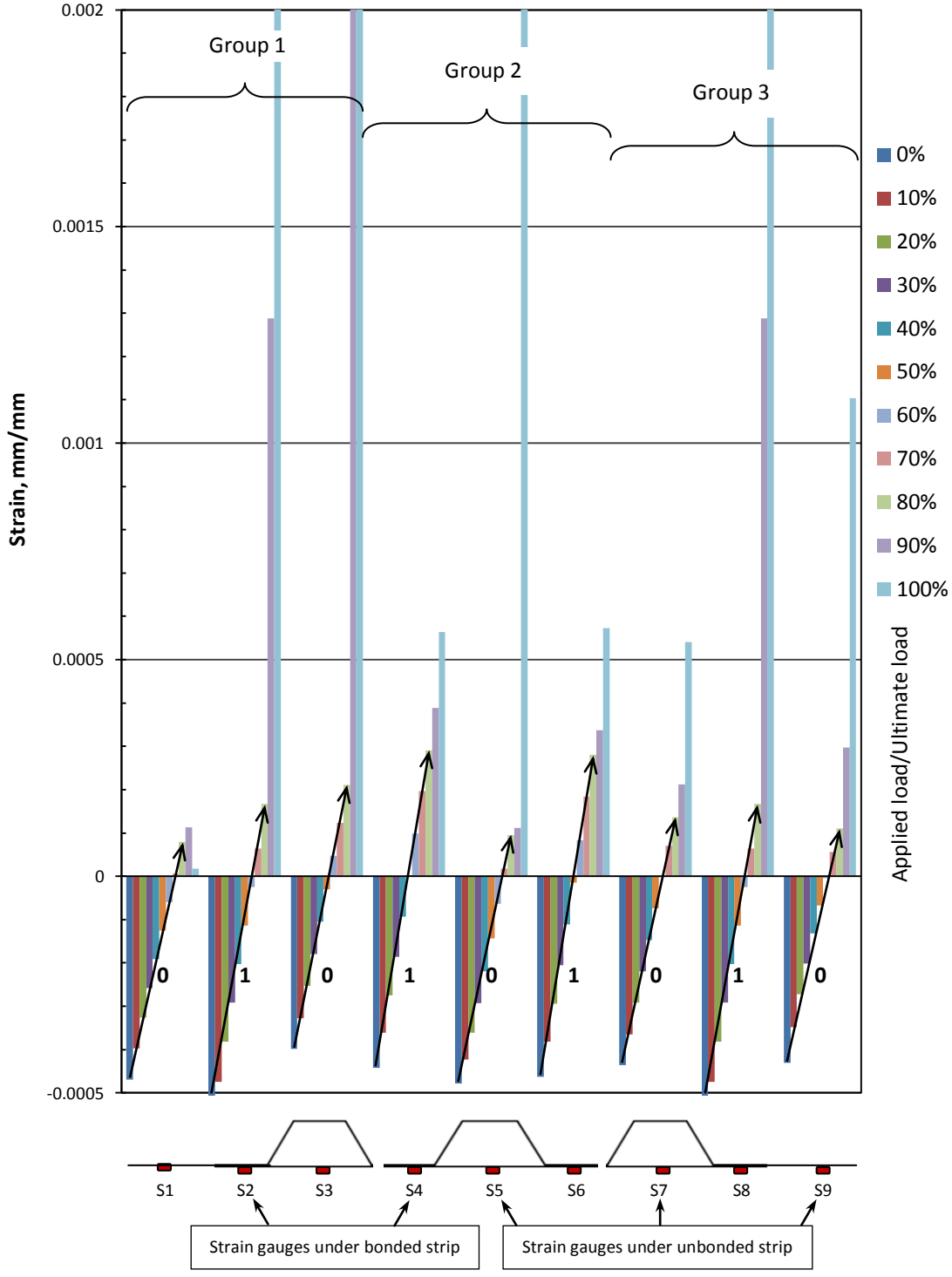

Bonded (1)/Unbonded (0) 45° tension steel strip, S1-S9

(**b**) SP-5 (CFRP-diagonal strengthened specimen)

Figure (6.24 Cont.): Distribution of the tension strip strain gauge readings with respect to the bonded/unbonded regions.

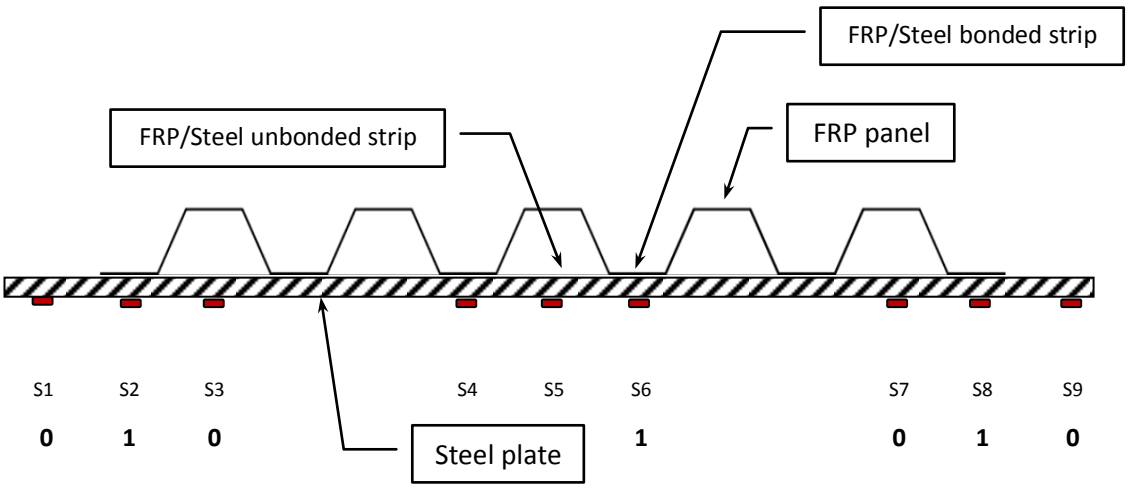

(1) = strain gauge in a bonded strip

(0) = strain gauge in an unbonded strip

(**c**) Bonded/Unbonded strips

Figure (6.24 Cont.): Distribution of the tension strip strain gauge readings with respect to the bonded/unbonded regions.

6.7 NUMERICAL MODELLING OF THE CONTROL SPECIMEN

In this section, the finite element model associated with the control specimen (unstrengthened specimen SP-1) will be presented. This is needed to determine the reduction in the web maximum surface and secondary bending stresses due to the proposed strengthening technique. This consequently will lead to estimate the improvement in the fatigue life performance for the strengthened specimens in comparison to the unstrengthened ones. However, in Chapter 7, the full composite model will be presented and used for a parametric study to support the proposed design method.

Geometrical and material non-linear finite element analysis (GMNA) was used to model the specimens tested in Phase-3 (the final series of tests). S9R5 element type was used to model the web steel plate; refer to section (5.7.1) in Chapter 5 for more details about this element and the Matlab code written to generate the mesh.

The size of the web elements was chosen to be 20×20mm which satisfies the condition of (h_w/20) based on the full convergence study implemented in Chapter 3. All other parts of the specimen (flanges and stiffeners) were modelled using S4R shell element available in standard *Abaqus CAE*. The flanges and stiffeners elements size were approximately 20×20mm and 10×10mm, respectively. This size of elements was chosen based on their corresponding member size and according to a convergence study which showed that changing these element sizes does not cause any significant change in the numerical outcomes.

The initial imperfection was found using the elastic Eigen buckling modes; these were initiated using the buckling analysis available in *Abaqus CAE* and then imposed as an initial imperfection using *Abaqus* script commands in the input file using the experimentally measured initial imperfection values (refer to Table 6.3 and 6.4 for the values of the measured initial imperfections). Figure (6.25) shows the finite element model for the control specimen and the corresponding contour distribution for the out-of-plane displacement.

An elastic-perfectly plastic stress-strain curve was adopted for the steel constitutive model, with a modulus of elasticity (E_s) of 200GPa and yield strength (f_y) of 275MPa and 355MPa for the 2mm web plate and the flanges and stiffeners, respectively.

It is worth mentioning that the finite element model for the control specimen was created before making and testing the specimens and that none of the parameters involved in the numerical model were adjusted to help the finite element model match the experimental results; except of course, for using the experimentally measured initial imperfection.

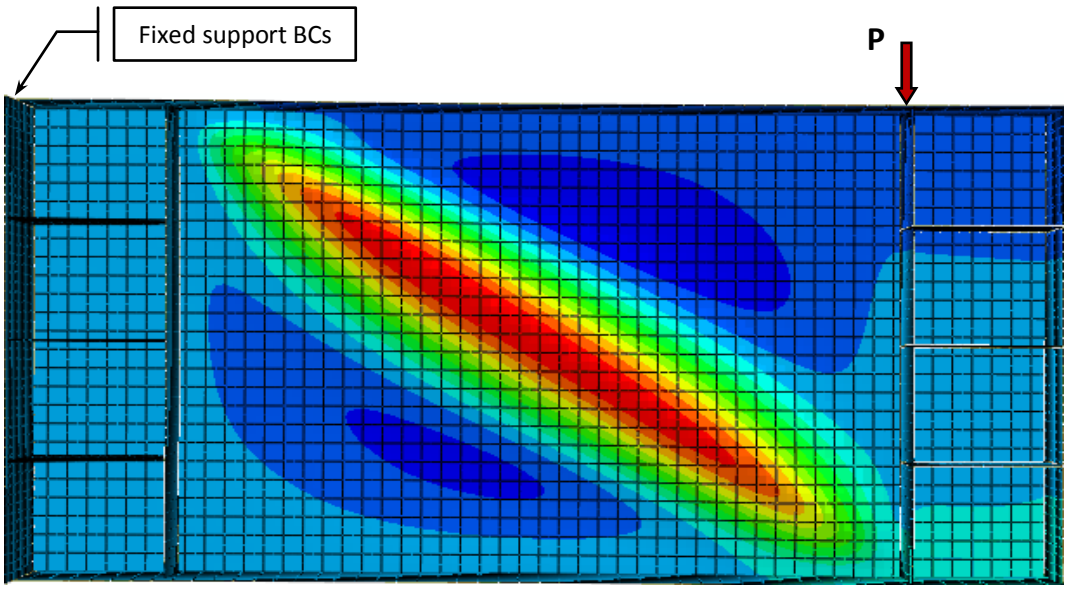

Figure (6.25): Finite element model for the control specimen (SP-1).

6.7.1 Comparison of Deformation

Figure (6.26) compares the experimentally measured deformations of the control specimen (SP-1) in comparison to the ones predicted by the finite element model. In Figure (6.26a) the central out-of-plane displacement is compared while in Figure (6.26b) the in-plane deflection is compared.

The figures show that the finite element model is capable of predicting the in-plane and out-of-plane deformational behaviour of the control specimen both for the loading and unloading stages.

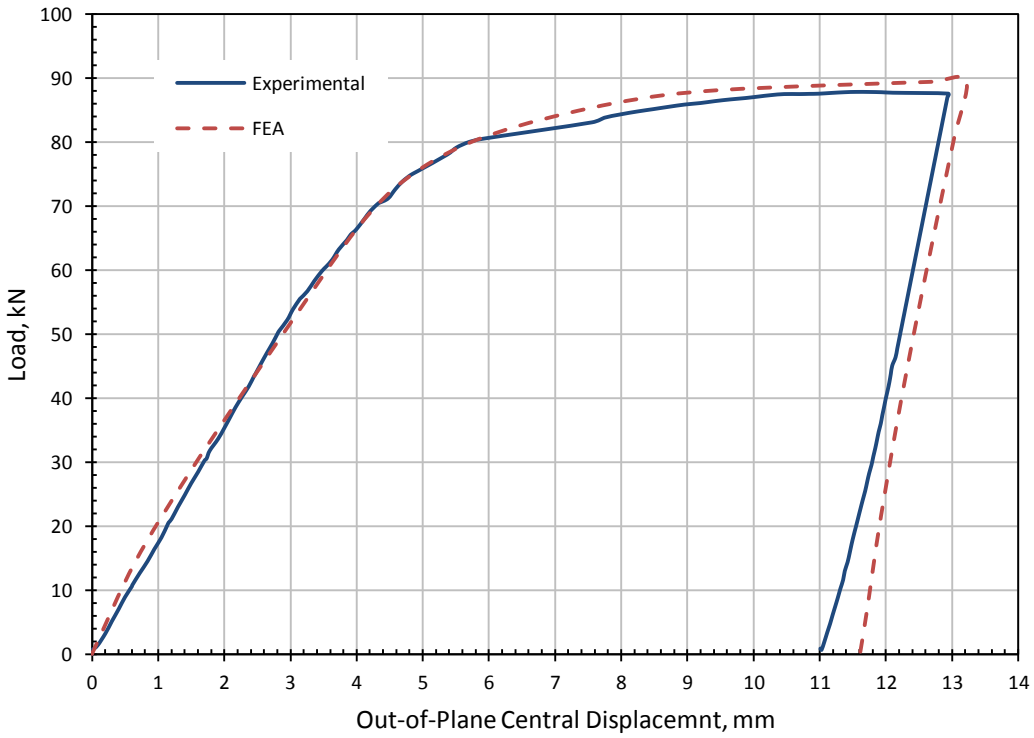

(**a**) Buckling curve of the control specimen (SP-1)

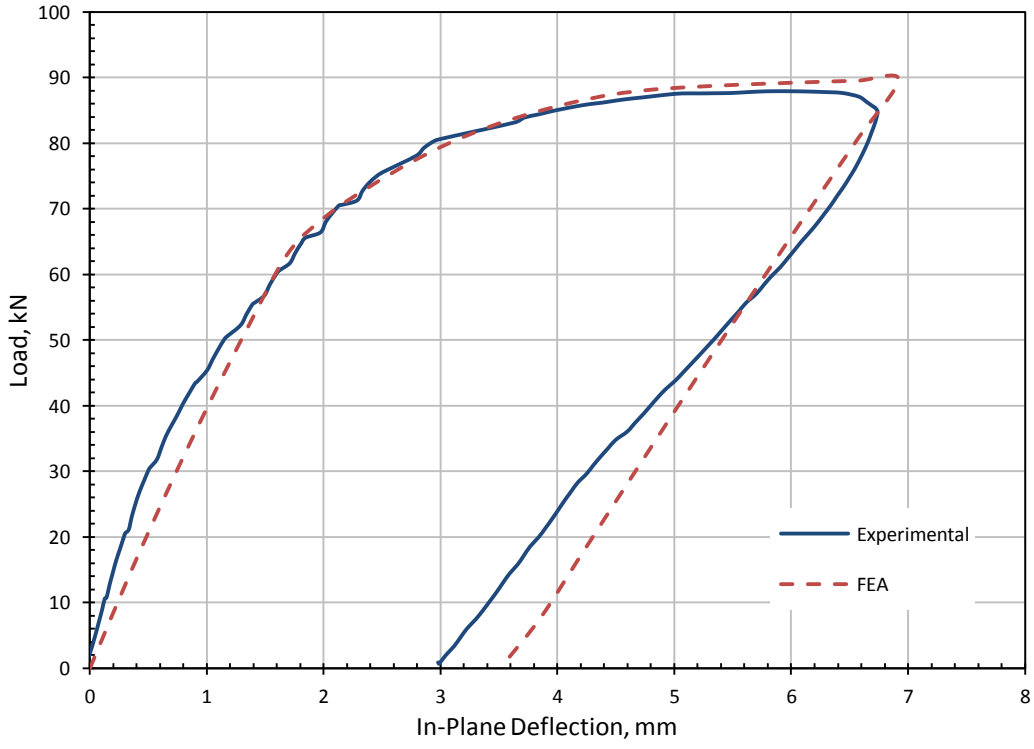

(**b**) Deflection curve of the control specimen (SP-1)

Figure (6.26): Comparison between the experimentally measured deformations and the predictions of the finite element model.

6.7.2 Comparison of Strain

Figure (6.27) shows the experimentally measured strains at the centre of the web of the control specimen (SP-1) in comparison to the ones predicted by the finite element model. There were 2 rosette sets of strain gauges attached to the central point of the web, one for each face of the steel plate (refer to the instrumentation section 6.5). Figure (6.27a through f) respectively compares the horizontal strain component ($\mathcal{E}_x$), the vertical strain component ($\mathcal{E}_y$), and the shear strain (γ_{xy}) (calculated using Equation 5.3 in Chapter 5); both for the top and bottom face of the web steel plate.

From Figure (6.27), the strain can be predicted by the finite element model with almost the same accuracy as it was the case for the deformations in the previous section. One exception to this is $\mathcal{E}_y$ (Figure 6.27c and d), where the finite element model correlated well with the experimental results for all loading stages but it did not reach to the same experimental plastic strain at the end of the test. However, it is important to note that the strain gauge readings are very sensitive for high plastic strain, especially before unloading stage.

6.7.3 Comments on the Control Specimen Finite Element Model

As a general conclusion, the present numerical model can be considered a good model for estimating both the capacity and deformational behaviour for the unstrengthened specimen (control specimen) in this work. This numerical model will be used to estimate the improvement in the fatigue life expectancy, which will be discussed in detail in section (6.9). It is worthwhile emphasizing again that this finite element model was not adjusted to match the experimental results which qualifies it to be upgraded to model the strengthened specimens (composite model) as will be discussed in Chapter 7 where a parametric study is going to be presented to support the proposed design method.

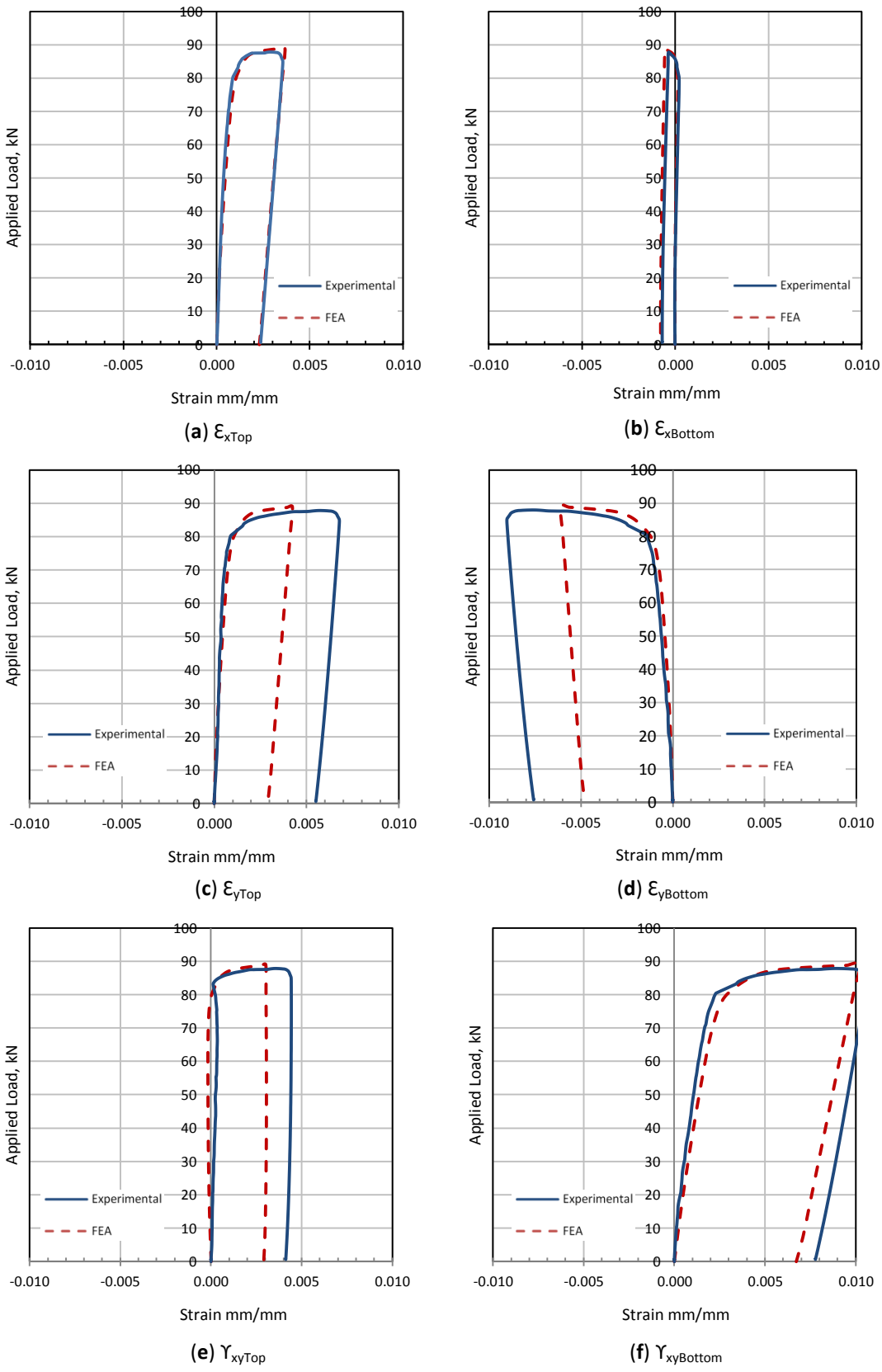

Figure (6.27): Comparison between the experimentally measured strains and the predictions of the finite element model for the control specimen (SP-1).

6.8 ASSESSING THE STIFFENING EFFECT OF THE PROPOSED STRENGTHENING TECHNIQUE

In this section, the same procedure adopted in Chapter 5 for assessing the stiffening effect of the proposed strengthening technique is used (refer to section 5.6.1). This will help in comparing the stiffening effect with respect to different aspect ratios (a_w/h_w). In this chapter (Phase-3, the final series of tests) the specimens had an aspect ratio of 1.5 while in Chapter 5 (Phase-2, this initial series of tests) the aspect ratio was 1.0.

Figure (6.28a) shows the buckling curves for the six specimens tested in Phase-3 (the final series of tests). In this figure, the initial imperfection and the residual out-of-plane displacement (associated with the cyclic tests only) were eliminated for the sake of illustration.

The same increase in stiffness and energy absorption capacity indices used in Chapter 5 (Equations 5.1 and 5.2, respectively) are adopted in this chapter. Only specimens with the typical mode of buckling were investigated, the ones with reversed mode of buckling were excluded (SP-3 and SP-4) because the comparison is not relevant in their cases compared to the control specimen.

Figure (6.28b) shows the dimensionless version of the buckling curves. The load was simply made dimensionless by dividing it by the corresponding shear yielding load using the Von Mises criteria where the yielding shear stress can be taken equal to ($f_y/\sqrt{3}$). For the displacement axis, this was performed by dividing the out-of-plane displacement by a limiting displacement (which is believed to be the limit where the behaviour of the curves turns into non-linear). However, the value of 1.0mm is chosen again in this chapter for the sake of comparison with the outcomes from Chapter 5. It is important to note that the unloading parts of the curves were removed and the loading part was extended to a displacement of 10mm for all considered specimens for the sake of comparison with the control specimen which was truncated at a displacement of 10mm as well.

6.8.1 Determining the Relative Stiffness and Energy Absorption Indices

Figure (6.28c) shows the area over the curve (stiffness) and the area under the curve (energy absorption) for the control specimen (SP-1). Figures (6.28d) and (6.28e)

show an example for calculating the area over the curve (stiffness) and the area under the curve (energy absorption) for an arbitrary specimen (SP-5), respectively. It is worth mentioning that the stiffness area was taken only up to a load equal to the ultimate capacity of the control specimen (87.9kN) for the sake of comparison.

Table 6.5 shows the results for the final series of tests. From this table it can be seen that the stiffness index ranges between a minimum of 3.3 for SP-5 and a maximum of 8.6 for SP-6. It is expected that the strengthening technique will be more effective with specimens having higher aspect ratios (1.5) due to the resulted lower shear buckling coefficients compared to the specimens tested in Chapter 5 which had an aspect ratio of 1.0. However, the relatively high values for the increase in stiffness index could be attributed to the fact that it is coming from specimens with very low initial imperfections. The effect of initial imperfection was previously investigated in Chapter 3 and it was shown that it does affect the shape of the buckling curve significantly. In other words, there is an inherent stiffening effect in specimens with lower initial imperfections and a good comparison would have been gained by comparing the stiffness indices for unstrengthened and strengthened specimens having the same initial imperfection, this will be done in next section (6.8.2).

Table 6.5: Increase in stiffness and energy absorption indices for the final series

Ref.	Specimen	Test method	Stiffness index	Energy absorption index
SP-1	Control Specimen	Static	1.0	1.0
SP-2	GFRP	Static	7.1	1.7
SP-3	CFRP	Static	-	-
SP-4	GFRP	Cyclic	-	-
SP-5	CFRP	Cyclic	3.3	1.9
SP-6	CFRP (45°)	Cyclic	8.6	2.4

The increase in energy absorption index in Table 6.5 ranged between 1.7 and 2.4. This again further proves the superior properties of the proposed strengthening technique and its ability in maintaining the ductile type of failure associated with the

shear collapse of unstrengthened steel plate girders in contrast to the ordinary strengthening techniques known to date. However, the above discussion about the effect of different initial imperfections on the resulting indices is applicable here as well but to much less extent.

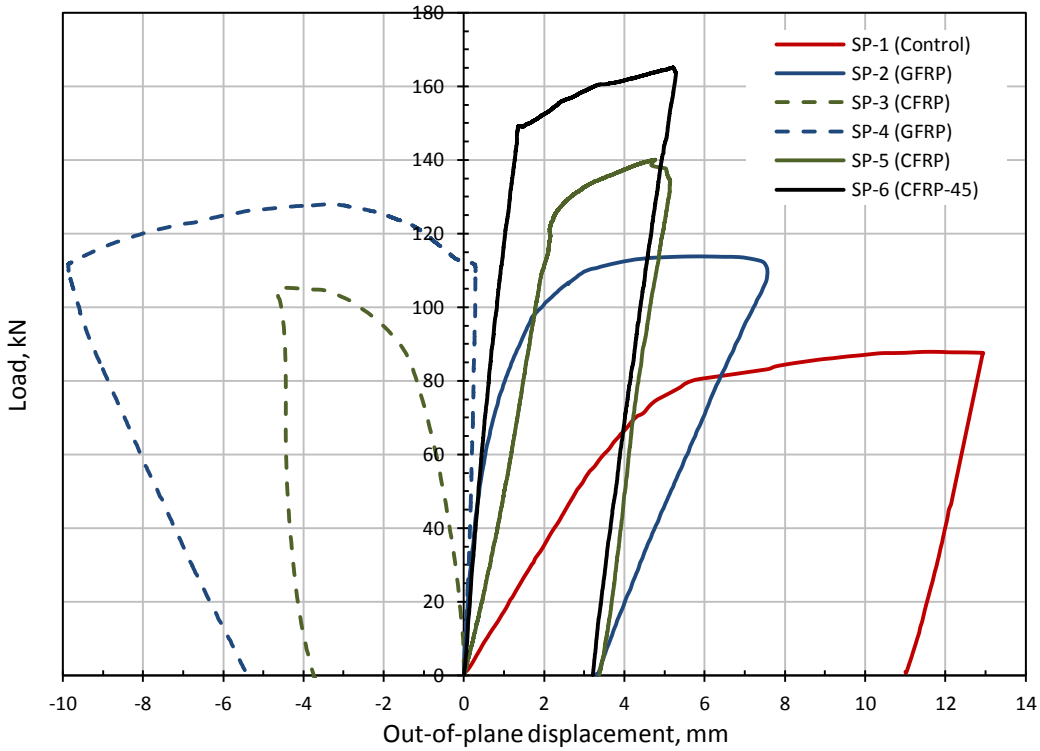

(**a**) Buckling curves for all specimens tested in phase-3

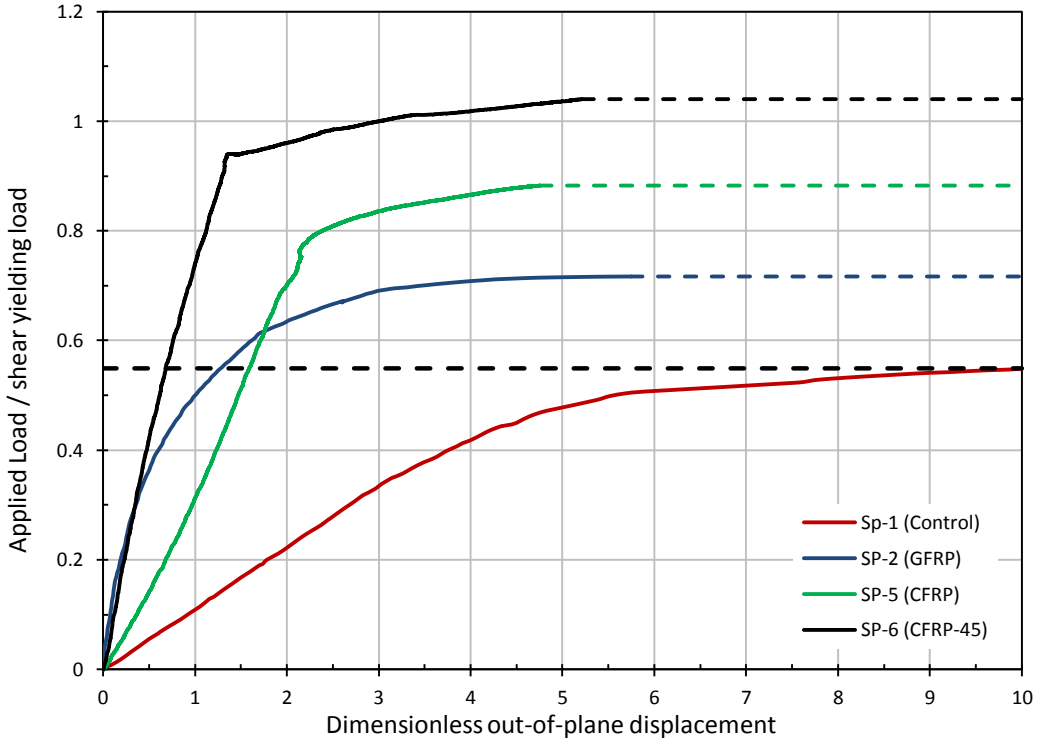

(**b**) Extended dimensionless buckling curves for SP-1, SP-2, SP-5, and SP-6

Figure (6.28): Assessing the stiffening effect of the proposed strengthening technique.

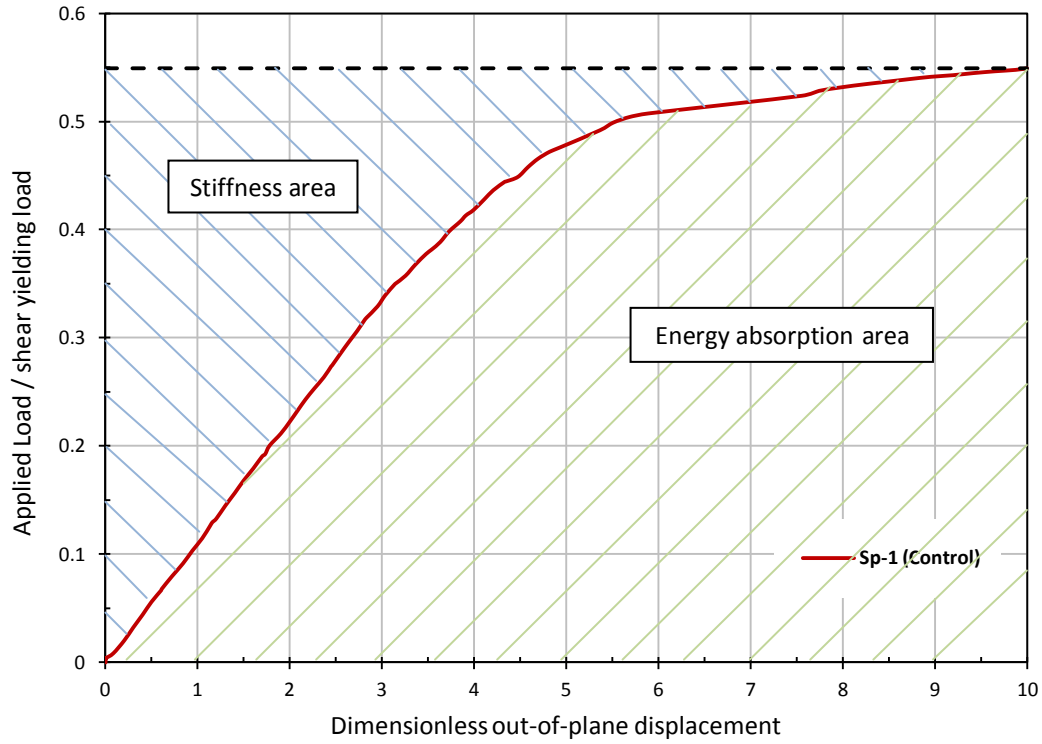

(**c**) Calculating the area under (energy absorption) and over (stiffness) the curve for the control specimen

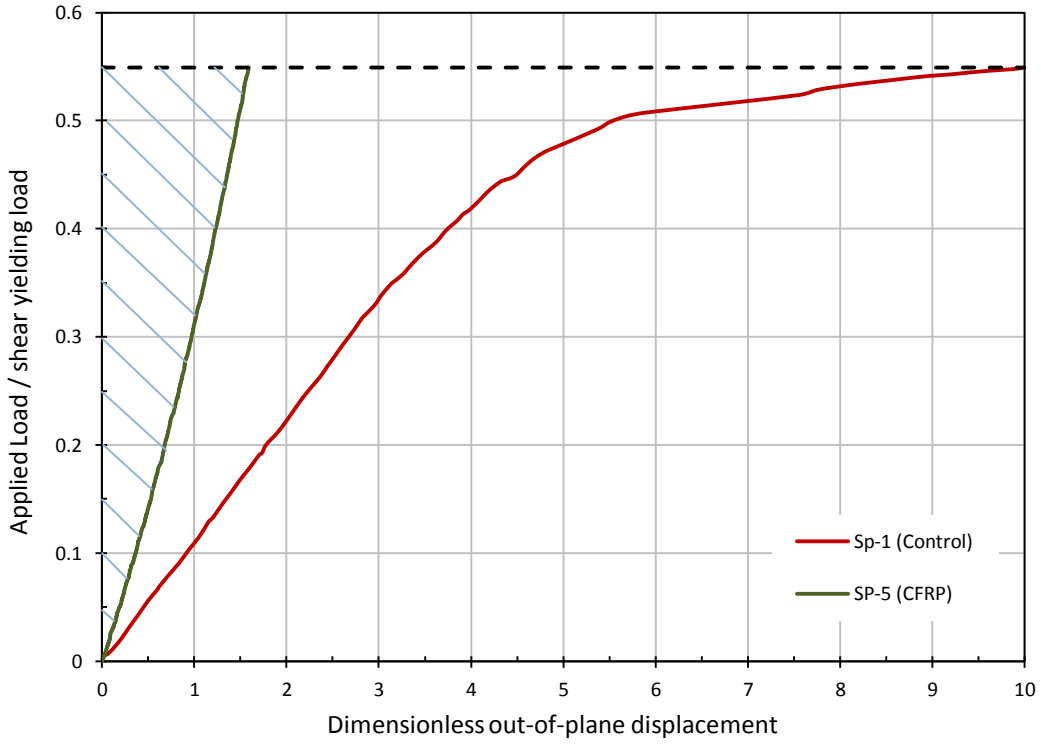

(**d**) An example for calculating the area over the curve (Stiffness) for SP-5

Figure (6.28 Cont.): Assessing the stiffening effect of the proposed strengthening technique.

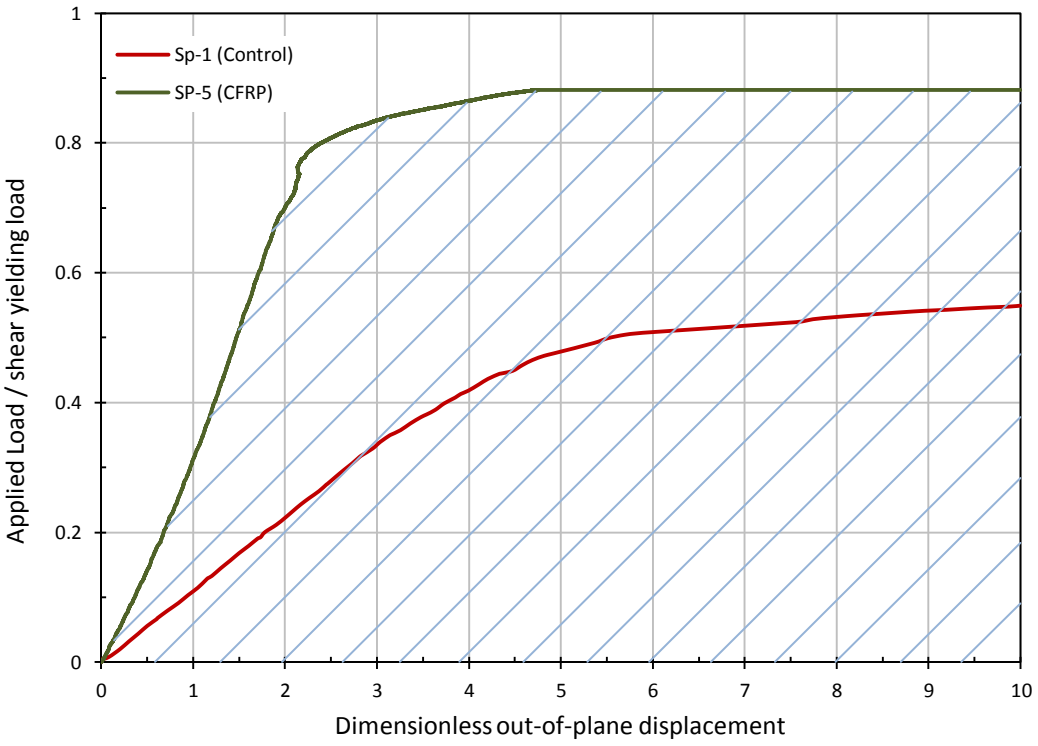

(**e**) An example for calculating the area under the curve (energy absorption) for SP-5

Figure (6.28 Cont.): Assessing the stiffening effect of the proposed strengthening technique.

6.8.2 The Effect of Initial Imperfection

The effect of initial imperfection was discussed in the previous section (6.8.1). In this section, the stiffness and energy absorption indices were recalculated for each specimen with respect to a control specimen having the same initial imperfection analyzed using the numerical model presented in section (6.7).

Table 6.6 shows the new recalculated increase in stiffness index while Table 6.7 shows the new recalculated increase in energy absorption index.

Surprisingly, in spite of the above argument, the values of the new stiffness and energy absorption indices went even higher. However, this can be explained by examining Figure (6.29) which shows the bucking curve for the control specimen with different initial imperfections predicted using the finite element model. From this figure it can be seen that, it is true that the lower initial imperfection increased the initial stiffness at low loading rates, but it also reduced the stiffness of the curve at higher loading stages, leading to this minor unexpected increase in the area over

the curve (stiffness) and consequently reducing the urea under the curve (energy absorption) insignificantly.

From the above discussion, it could be concluded that in spite the fact that the initial imperfection does affect the behaviour of the buckling curve, but it does not affect the stiffness of the strengthened specimens significantly.

Table 6.6: Modified relative stiffness index

Ref.	Specimen	Initial imperfection, mm	Area over the curve	Corresponding Control area over the curve from the FEM	Stiffness index
SP-1	Control Specimen	2.76	1.54	-	1.0
SP-2	GFRP	0.35	0.22	1.72	7.94
SP-3	CFRP	-1.47	-	-	-
SP-4	GFRP	-0.38	-	-	-
SP-5	CFRP	1.14	0.47	1.77	3.74
SP-6	CFRP (45°)	0.03	0.18	1.67	9.36

Table 6.7: Modified relative energy absorption index

Ref.	Specimen	Initial imperfection, mm	Area under the curve	Corresponding control area under the curve from the FEM	Energy absorption index
SP-1	Control Specimen	2.76	3.95	-	1.0
SP-2	GFRP	0.35	6.57	3.82	1.72
SP-3	CFRP	-1.47	-	-	-
SP-4	GFRP	-0.38	-	-	-
SP-5	CFRP	1.14	7.59	3.77	2.02
SP-6	CFRP (45°)	0.03	9.53	3.87	2.46

6.8.3 Comments on the Stiffening Effect of the Proposed Strengthening Technique

As a final conclusion, all the above results can be considered as a very good indication that the proposed strengthening technique succeeded in improving the

stiffness of the tested specimens significantly and it did not only maintained the ductile failure type associated with the unstrengthened steel plate girders, but it did improve it significantly; which is in good agreement with the results from Chapter 5.

It should be noted that this superior behaviour of the strengthened specimens where high stiffness is provided using the proposed strengthening technique in the current work had led to much smaller out-of-plane displacements in the web panel leading to significant reduction in the breathing strain and stresses. Consequently, this will significantly increase the fatigue life estimation for the strengthened specimens as will be seen in the next section (6.9).

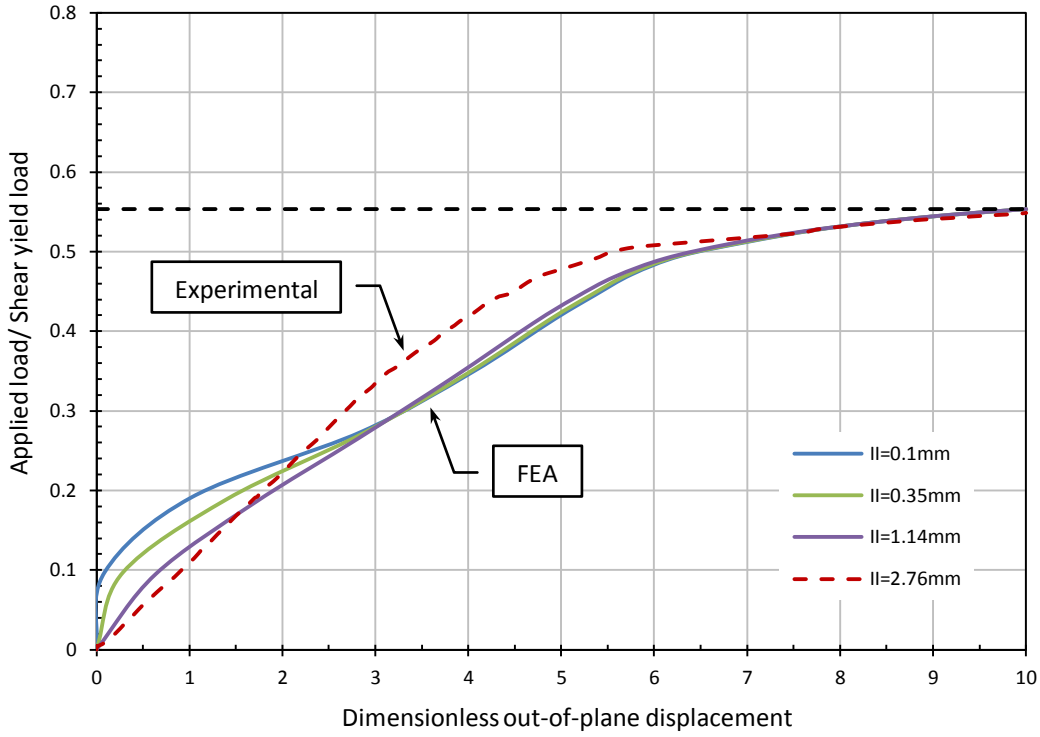

Figure (6.29): Dimensionless buckling curves with different hypothetical initial imperfections analyzed using the FEM.

6.9 FATIGUE LIFE ESTIMATION

There are several methods available to estimate the fatigue life expectancy for different members and mechanical systems depending on their function, material, and the type of applied loads. However, for structural members undergoing high-

cycle fatigue (members that do not encounter high plastic strain within their working stress limits), the stress range method is globally accepted and adopted in most international standards like AASHTO, AISC, and the Eurocode.

For unclassified details, Eurocode 3 recommends that the fatigue assessment be based on the geometric stress range. This is defined as the maximum principal stress range in the vicinity of a weld (Robert et. al., 1995). In the current study the values of the principal surface stress ranges calculated from the experimental strain measurements for the cyclic strengthened specimens (SP-4, SP-5, and CP-6) at the diagonal tension corner near the welding and the ones determined using finite element analysis for the unstrengthened control specimen (section 6.7) will be used in conjunction with the Eurocode fatigue strength curves to estimate the life expectancy of the specimens and study the effect of the proposed strengthening technique in reducing the stress ranges for the same service loads, and consequently to increase their fatigue life limits. Refer to the instrumentation section (6.5) for the location of the rosette strain gauges at the tension corner near the welding. Figure (6.30) shows the Eurocode fatigue strength curves, reproduced form Eurocode 3 (Eurocode, 2005).

The S-N curves under consideration here are the 125-N/mm^2 normal stress range curve and the 80-N/mm^2 shear stress range curve, at 2×10^6 cycles, which are the highest classification curves for welded joints. The normal stress range curve is defined by:

$$\log N_{\sigma r} = 12.601 - 3\log \sigma_r \quad (N_{\sigma r} \leq 5\times10^6) \tag{6.2-a}$$

$$\log N_{\sigma r} = 16.536 - 5\log \sigma_r \quad (N_{\sigma r} > 5\times10^6) \tag{6.2-b}$$

with a cut-off limit of 51 N/mm^2 at 10^8 cycles. The shear stress range is defined by:

$$\log N_{\tau r} = 15.801 - 5\log \tau_r \tag{6.3}$$

with a cut-off limit of 36 N/mm^2 at 10^8 cycles.

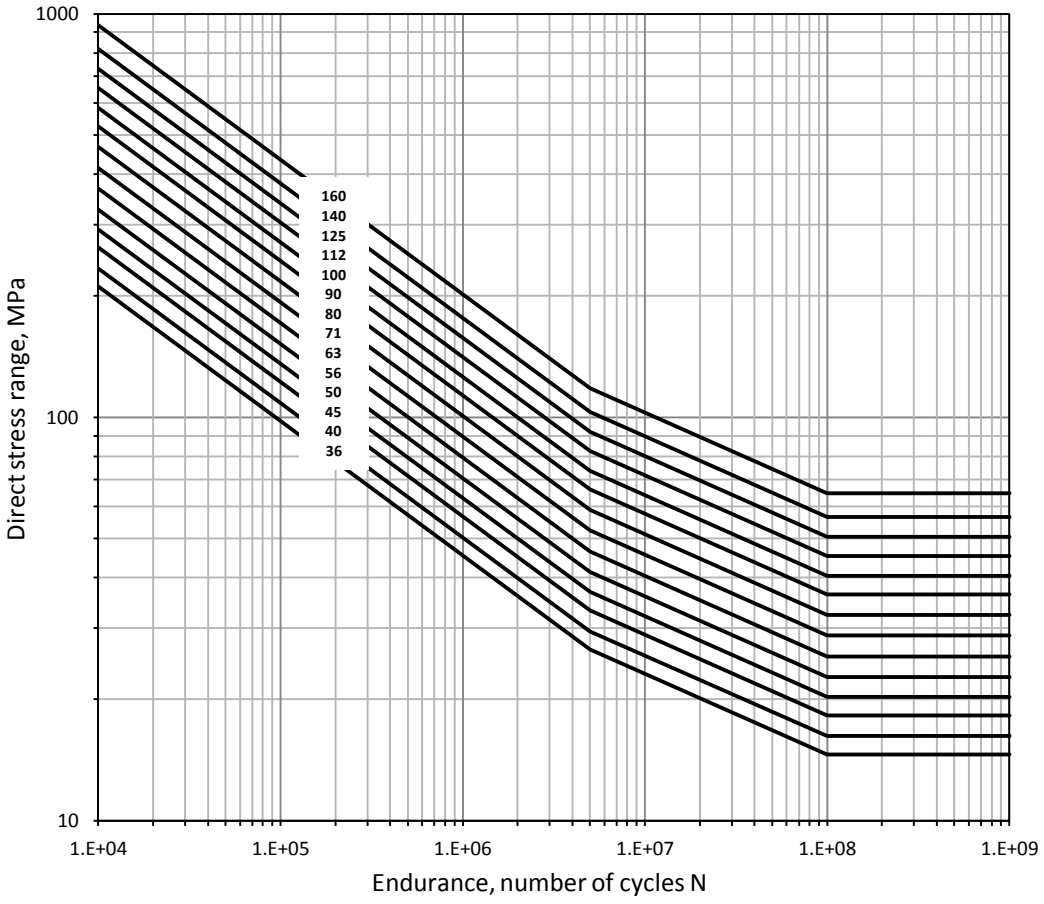

(**a**) Direct stress range

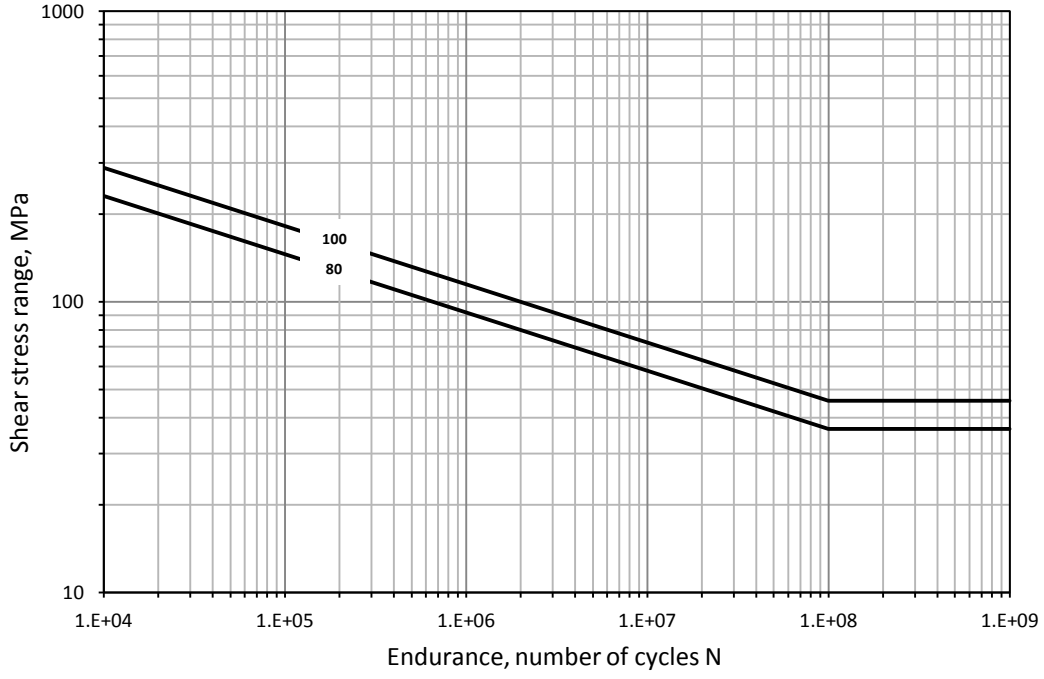

(**b**) Shear stress range

Figure (6.30): Fatigue strength curves According to Eurocode 3.

6.9.1 Control Specimen Tension Corner Strain Distribution

For the fatigue analysis and calculations to be performed, the point where the maximum stress in the vicinity of a weld needs to be located. In a plate girder web panel, this is believed to be in the vicinity of the tension corner at the junction of the web, flange, and stiffener. The stress cannot be measured directly during the test and the strain needs to be measured instead. The strain then is transformed into stress using the generalized Hook's law within the elastic limit.

For practical reasons, sometimes it is very difficult to experimentally determine the full contour strain distribution at the junction of the web plate. This is because of several reasons including the high number of channels required for the data acquisition system, the difficulty associated with attaching the strain gauges to the edge of the web because of the weld, and the high possibility of losing some of the strain gauges during the test. For these reasons, it is sometimes more convenient to determine the strain distribution using finite element analysis, as long as the numerical model is verified against the experimental results.

Figure (6.31) shows the maximum principal strain values determined in the web plate tension corner welded boundaries using the numerical model of the control specimen for two loading stages. Figure (6.31a) shows the strain distribution at a load equal to 80% of the ultimate load while Figure (6.31b) shows the same distribution but at the ultimate applied load (87.9kN). The surface strains (ε_x, ε_y, and γ_{xy}) are determined directly from the numerical outputs both for the tension and compression faces of the web steel plate at the required points, then the membrane and secondary bending strains are calculated using Equation (5.4) and Equation (5.5) previously illustrated in Chapter 5, respectively. The maximum principal strain in each case can be calculated according to the following equations:

$$\varepsilon_{max} = \frac{\varepsilon_x + \varepsilon_y}{2} + \sqrt{\left(\frac{\varepsilon_x - \varepsilon_y}{2}\right)^2 + \left(\gamma_{xy}\right)^2} \tag{6.4}$$

$$\gamma_{max} = \sqrt{\left(\frac{\varepsilon_x - \varepsilon_y}{2}\right)^2 + \left(\gamma_{xy}\right)^2} \tag{6.5}$$

$$\tan 2\varphi = \frac{\gamma_{xy}}{\left(\frac{\varepsilon_x - \varepsilon_y}{2}\right)} \quad (6.6)$$

where

ε_x: is the strain in the horizontal *x*-direction.
ε_y: is the strain in the vertical *y*-direction.
γ_{xy}: is the shear strain in the *xy*-direction.
ε_{max}: is the maximum principal normal strain in the plane.
γ_{max}: is the maximum principal shear strain in the plane.
ϕ: is the angle of maximum principal strain axis.

From Figure (6.31), it can be seen that the surface strain is always higher than the membrane and secondary bending strains which is in agreement with the Eurocode 3 criteria of using the maximum surface stress for the assessment of fatigue. However, the membrane and secondary bending strains already reached close (or even exceeding in some points) the yielding strain (0.0014) at only 80% of the ultimate load and they exceeded this value several times at the ultimate stage. This is a good illustration of how critical the secondary bending strain could be if not taken into consideration, especially when multi-axial fatigue is under considerations.

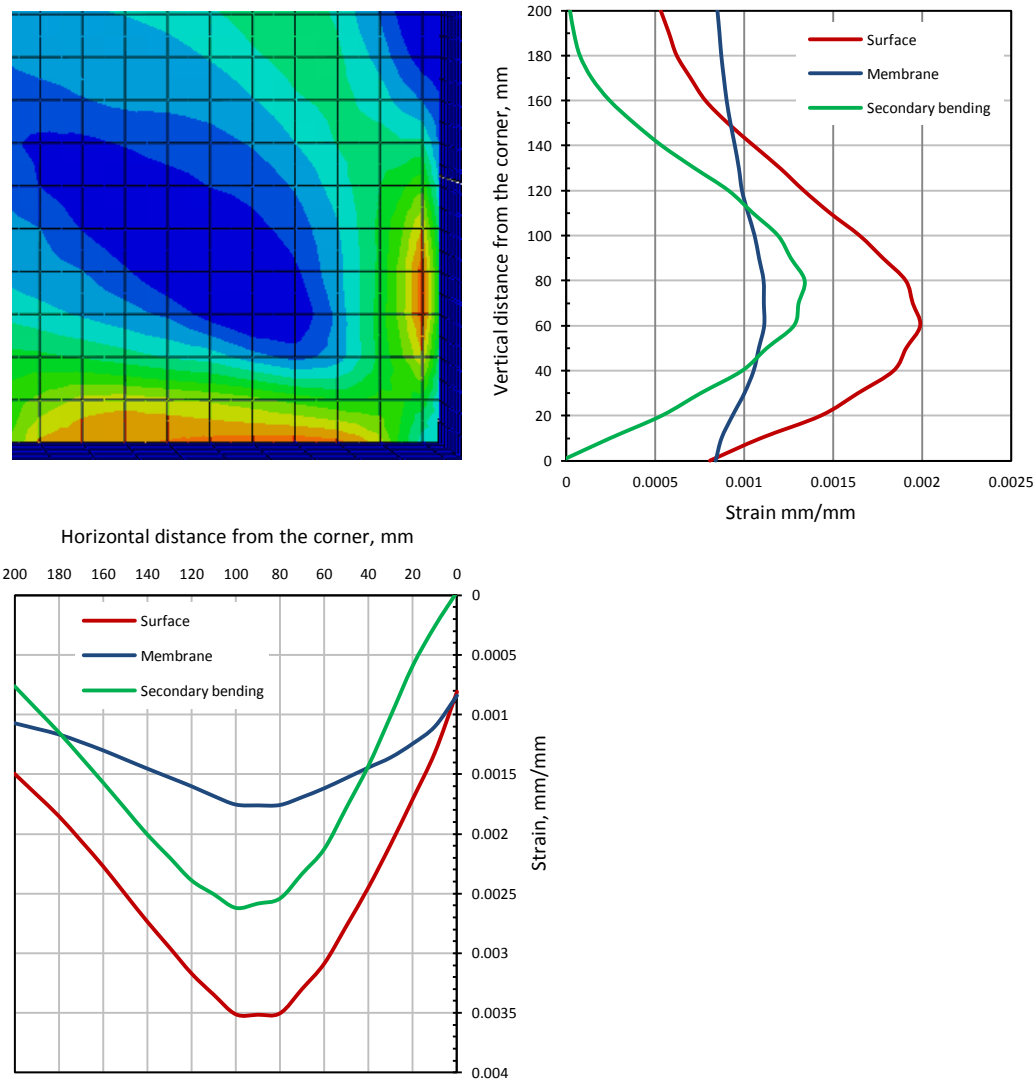

(**a**): Strain distribution at 80% of ultimate load (≈ 70.0kN)

Figure (6.31): Distribution of the maximum principal strain at the tension corner of the control specimen.

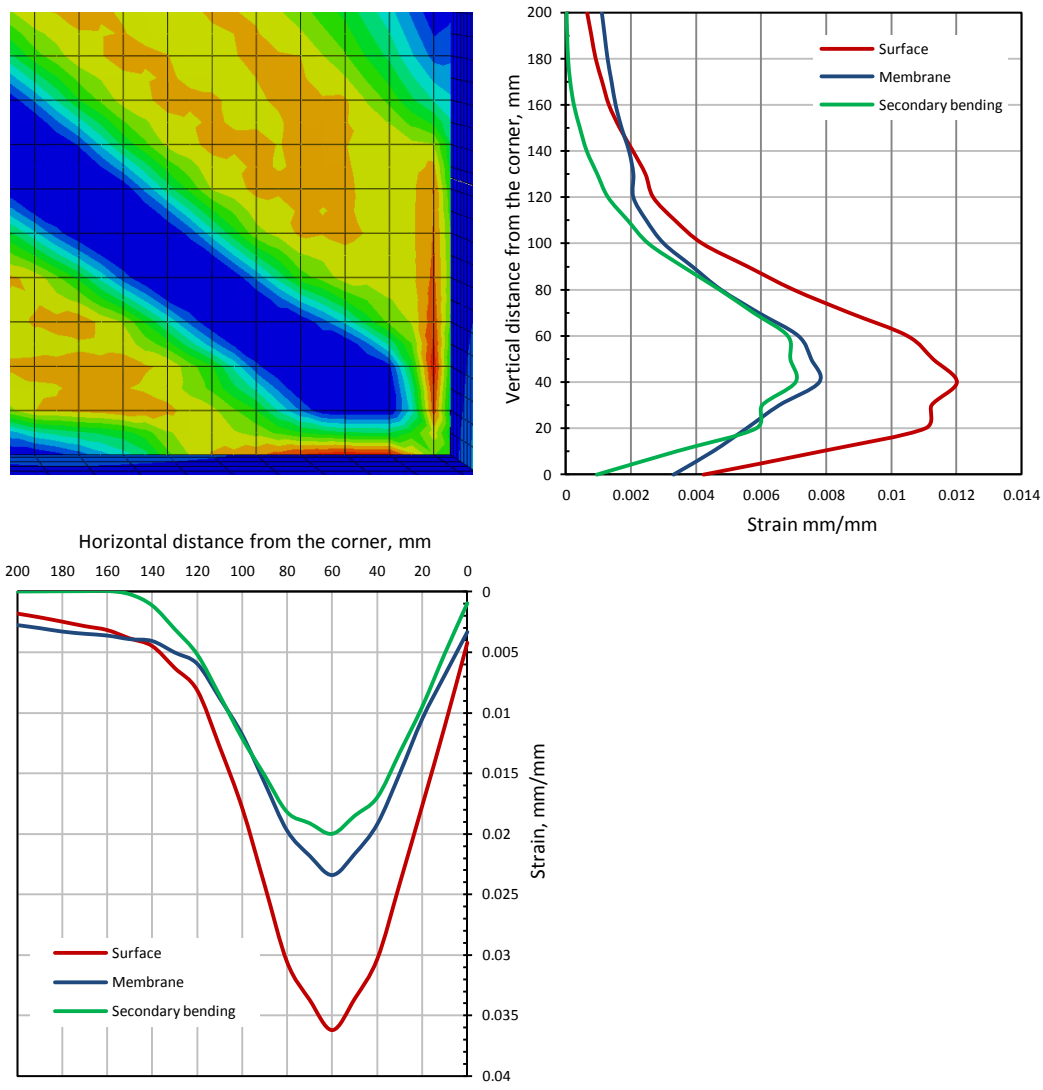

(**b**): Strain distribution at ultimate load (87.9kN)

Figure (6.31 Cont.): Distribution of the maximum principal strain at the tension corner of the control specimen.

6.9.2 Assessment of the Improvement in the Fatigue Life Expectancy Due To the Proposed Strengthening Technique

The fatigue life estimation is calculated according to Eurocode 3, taking the maximum experimentally measured surface stress range at the corner for each of the cyclically tested strengthened specimens (SP-4, SP-5, and SP-6) and comparing it with the corresponding stress range associated with the control specimen for the same applied load range using the finite element model. The results are similar to those determined using AASHTO standards, due to the fact that the effect of the welds and other stress concentrations is reflected in the ordinate of the S-N curves for the various detail categories. The slope of the regression line fit to the test data for the welded details is typically in the range 2.9 to 3.1. Therefore, in Eurocode 3, as well as in the AASHTO and AISC codes, the slopes have been standardized at 3.0 (Dexter and Fisher, 1999).

Figure (6.32) demonstrates how reducing the stress range is reflected by increasing the fatigue life expectancy represented by the number of the loading cycles (*N*) using the Eurocode fatigue curves for normal stress range ($\Delta\sigma_r$) and shear stress range ($\Delta\tau_r$) with a detail category of 125MPa and 80MPa, respectively. In this figure, the experimentally measured stress range for SP-4 (GFRP) is projected on the prescribed detail category taken from Eurocode 3 in comparison to the higher stress range of the control specimen under the same loading amplitude. This reduction in the stress ranges for the same loading amplitude results from strengthening the specimen with the proposed FRP corrugated panel designed and implemented in the current study. From Figure (6.32) it can be seen that the shear stress range criterion gives a fatigue life expectancy several times higher than the corresponding normal stress range criterion. This high discrepancy between the two methods raises a lot of questions about the validity of the shear stress range as a criterion for the assessment of fatigue life expectancy; which is recommended solely by the Eurocode and non of the other standards use this method.

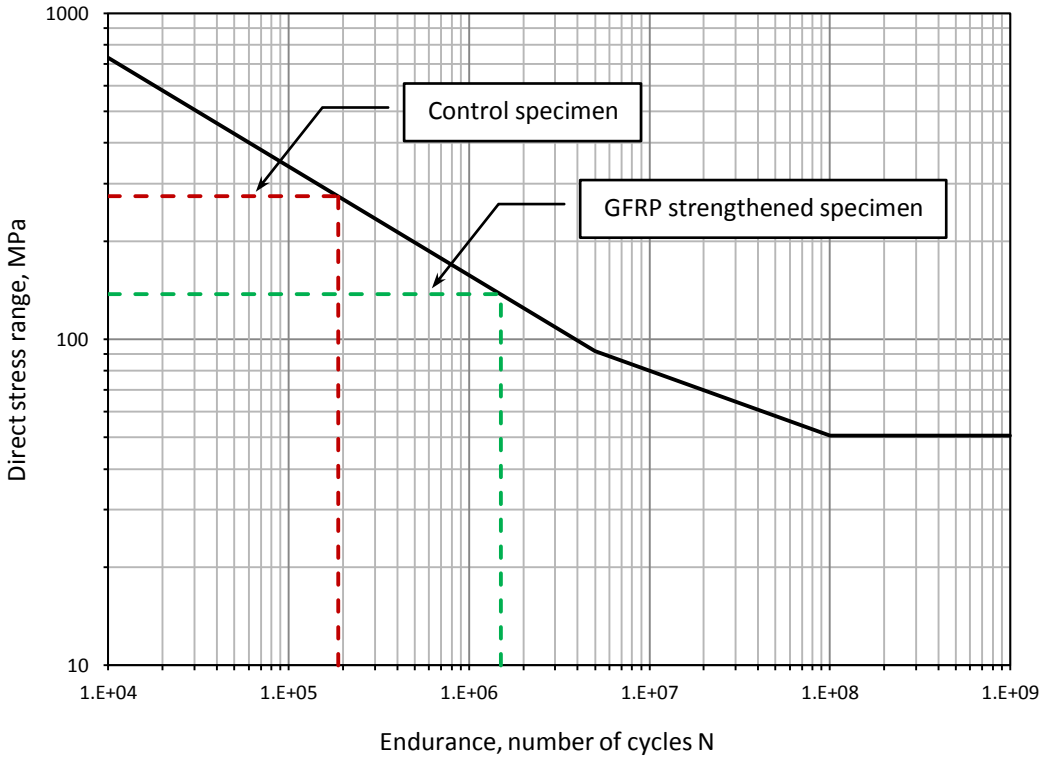

(**a**) Direct stress range – Detail category 125 N/mm2

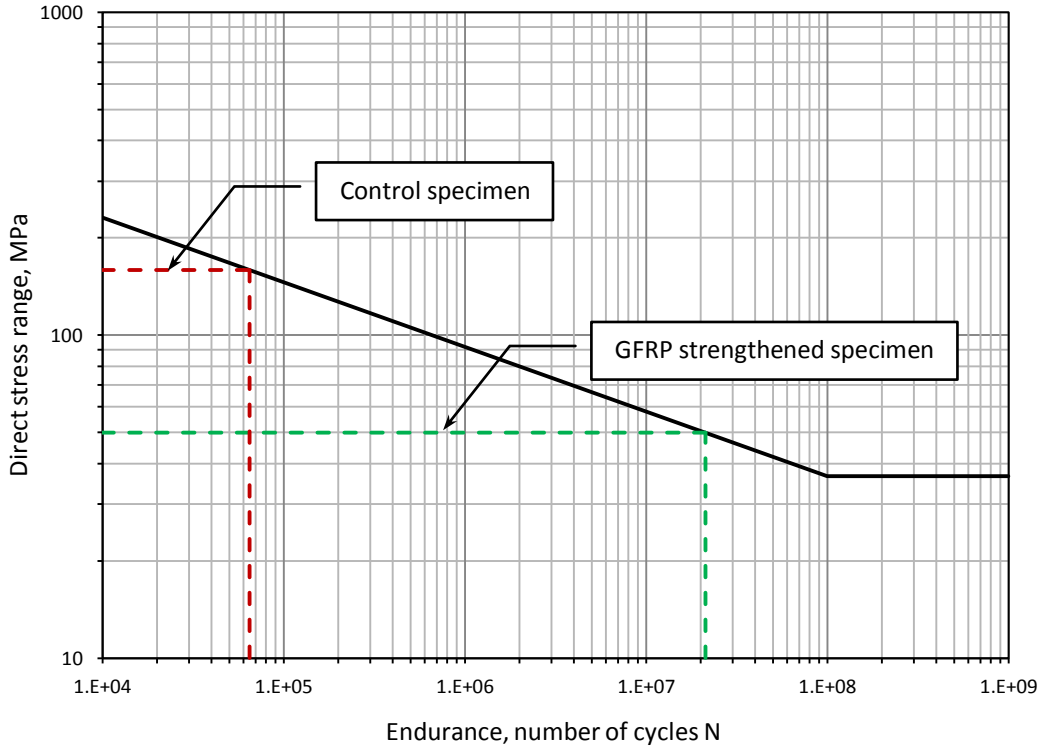

(**b**) Shear stress range - Detail category 80 N/mm2

Figure (6.32): Estimating the increment in fatigue life expectancy due to the reduced surface normal and shear stress ranges using Eurocode 3 fatigue strength curves.

Tables 6.8 through 6.10 show the calculations of the number of cycles required for the fatigue failure according to the Eurocode (Equations 6.2 and 6.3) for the three strengthened specimens tested cyclically in this work. For the strengthened specimens, the strain values at the specific loading range were taken directly from the available test data and then transferred into stresses by multiplying them by the modulus of elasticity and then the maximum principal stress is calculated using Equations (6.4) through (6.6). The same procedure was followed for the control specimen except that the strains at the corner were determined using the finite element model for the same loading range. In Tables 6.8 through 6.10, ΔL is the applied load range, $\Delta\varepsilon$ is the measured normal strain range, $\Delta\sigma_r$ is the calculated normal stress range, $\Delta\gamma$ is the measured shear strain, $\Delta\tau_r$ is the calculated shear stress range, $N_{\sigma r}$ is the number of cycles determined from the normal stress range criterion (Equation 6.2), and $N_{\tau r}$ is the number of cycles determined from the shear stress range criterion (Equation 6.3).

Table 6.8 illustrates these calculations for the GFRP strengthened specimen (SP-4). From this table it can be seen that there are two estimates for the number of cycles, the first one is for the first 500,000 cycles of load applied with a range of 32-64% of the ultimate capacity while the second one is for the second 500,000 cycles of load applied with a range of 40-80%. Taking the average of the two cases, the fatigue life expectancy is increased by a factor of 6.91 and 260.4 times the control specimen for the normal stress range and shear stress range criteria, respectively.

Table 6.8: Fatigue life estimation of SP-4 (GFRP) in comparison to the control specimen with the same loading range

Specimen	ΔL kN	$\Delta\varepsilon$ mm/mm	$\Delta\sigma_r$ MPa	$\Delta\gamma$ mm/mm	$\Delta\tau_r$ MPa	Eurocode fatigue equations	
						$N_{\sigma r}$	$N_{\tau r}$
SP-4	45	0.00072	144.87	0.00065	49.88	1,284,327	21,219,483
Control	45	0.0073	275	0.0063	158.77	187,828	64,958
First range life increase (times the control specimen)						**5.83**	**326.66**
SP-4	51.06	0.00069	137.62	0.00068	52.19	1,498,679	16,918,045
Control	51.06	0.0074	275	0.0064	158.77	187,828	64,958
Second range life increase (times the control specimen)						**7.98**	**260.45**
Average life increase (times the control specimen)						**6.91**	**293.56**

Table 6.9 illustrates the assessment of fatigue life (calculations of the number of cycles to fatigue) for the diagonally strengthened CFRP specimen (SP-5). This table have the same properties described above for Table 6.8 but this time the first 1 million cycle of loads were with a range of 32-64% of the ultimate capacity while the second 1 million cycles were with a range of 38-76%. Taking the average of the two applied ranges for the whole 2 million cycles of load, the fatigue life expectancy is increased by a factor of 6.02 and 142.67 in comparison to the control specimen for the normal stress range and shear stress range criteria, respectively.

Table 6.9: Fatigue life estimation of SP-5 (CFRP-diagonal) in comparison to the control specimen with the same loading range

Specimen	ΔL kN	$\Delta\varepsilon$ mm/mm	$\Delta\sigma_r$ MPa	$\Delta\gamma$ mm/mm	$\Delta\tau_r$ MPa	Eurocode fatigue equations	
						$N_{\sigma r}$	$N_{\tau r}$
SP-5	45	0.0007	139.91	0.0007	53.85	1,426,385	14,476,844
Control	45	0.0073	275	0.0063	158.77	187,828	64,958
First range life increase (times the control specimen)						**7.59**	**222.86**
SP-5	52.89	0.0008	167.15	0.0009	69.44	836,524	4,058,876
Control	52.89	0.0074	275	0.0064	158.77	187,828	64,958
Second range life increase (times the control specimen)						**4.45**	**62.48**
Average life increase (times the control specimen)						**6.02**	**142.67**

Finally Table 6.10 shows the assessment of fatigue life for the 45° strengthened CFRP specimen (SP-6). For this specimen, there was only one loading range of 37.5-75% of the ultimate capacity. However, as can be seen from the table, the fatigue life expectancy is only increased by a factor of 2.51 and 127.86 in comparison to the control specimen for the normal stress range and shear stress range criteria, respectively. This is not because this specimen or the strengthening scheme is not as good as the others. As a matter of fact, this specimen showed the best behaviour throughout the whole 2 million cycles of load and had the maximum residual strength and minimum residual deformations among all three strengthened specimens tested in the cyclic series of tests. Actually this low fatigue life increment compared to the other 2 strengthened specimens is because this specimen had the highest stress range of 189.85MPa, in comparison to 141.25MPa and 153.53MPa for SP-4 and

SP-5, respectively. This caused lower fatigue life expectancy when projected on the Eurocode curves (Figure 6.30). The reason behind this high stress range for SP-6 is because it had the highest load range. This high loading range was chosen because it was expected that this specimen will have the highest ultimate capacity among all other strengthened specimens in this work, and it did. In other words, if we use the same loading range as applied on the other two strengthened specimens we will get the same high fatigue life increment factors. This will be demonstrated in the next section where the same range is going to be used for all the specimens to assess the fatigue life more consistently from a design prospective.

Table 6.10: Fatigue life estimation of SP-6 (CFRP-45°) in comparison to the control specimen with the same loading range

Specimen	ΔL kN	$\Delta\varepsilon$ mm/mm	$\Delta\sigma_r$ MPa	$\Delta\gamma$ mm/mm	$\Delta\tau_r$ MPa	Eurocode fatigue equations	
						$N_{\sigma r}$	$N_{\tau r}$
SP-6	61.83	0.00095	189.85	0.00078	60.2	570831	8,293,723
Control	61.83	0.0075	275	0.0065	158.77	187,828	64,958
Life increase (times the control specimen)						**2.51**	**127.68**

At this point, it is worth remembering that for the strengthened specimens, the strain used in the fatigue calculations was the experimentally measured one while for the control specimen the strain was found using the finite element model. However, the designated location for measuring the strain for the strengthened specimens was decided based on preliminary composite finite element modelling; hence it is believed that this location provided the maximum strain; the final composite model is presented in Chapter 7.

Nevertheless, all these factors can be safely considered the minimum possible increase in the fatigue life expectancy because in all three cases the control specimen calculations were constrained by the yielding stress of 275MPa. It could be easily shown that if a higher plate yield strength were to be used, the resulting stress range for the control specimen would have consequently been higher leading to higher increase in the fatigue life expectancy; this could be seen by looking at the high strain values associated with the control specimen in Tables 6.8 through 6.10, the

control specimen strains exceeded several times the yielding one but nevertheless, the corresponding stress cannot be taken more than the yielding stress of 275MPa.

6.9.3 Design for Fatigue

The comparison shown in section (6.9.2) does not necessarily reveal the actual enhancement in the fatigue life due to the proposed strengthening technique. This is because of several factors like the constraint of the web plate yielding stress and the different applied loading ranges which consequently caused different stress ranges. Looking back at Figure (6.30), the Eurocode fatigue life assessment curves are not linear as they look in the figures. It is a logarithmic equation, meaning that it is non-linear and the degree of its non-linearity depends on the slope of the curve; 3 in our case. This means that actually our equation (Equation 6.2) is a cubic equation and hence any slight change in the stress range could cause a large change in the resulting number of cycles. This is true for the shear stress range criteria (Equation 6.3) as well but to a greater extent because this equation is non-linear to the power of 5. This could be one of the reasons justifying why this high number of cycles is resulting for the shear stress range criterion as can be seen in Tables 6.8 through 6.10.

In this section, a more consistent approach will be used to assess the fatigue life enhancement from a design perspective. This time we will take a range of 20-80% of the ultimate capacity of the control specimen and impose it on the other three strengthened specimens in the cyclic tests. In this case we will be able to calculate the real number of cycles for the same loading range and different strengthening sachems to optimize the best among them. Table 6.11 shows the recalculations and Figure (6.33) demonstrates them.

Now, it is obvious that SP-6 (CFRP-45° strengthened specimen) offers the best enhancement in the fatigue life estimation with a factor of 3.8 times the control one, in comparison to 3.6 and 3.3 for SP-4 (GFRP strengthened) and SP-5 (CFRP-diagonally strengthened) specimens, respectively. In addition to that, from Table 6.11, it can be seen that the numbers are more consistent this time especially with respect to the shear stress range criterion where it is giving more reliable results.

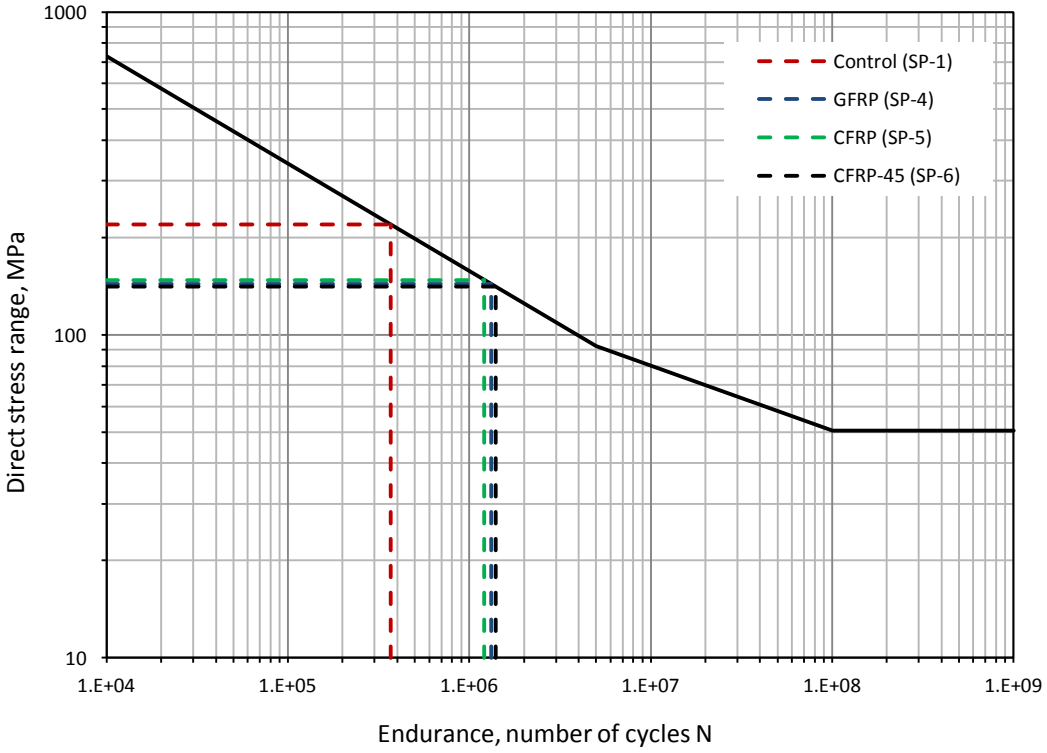

(**a**) Direct stress range – Detail category 125 N/mm2

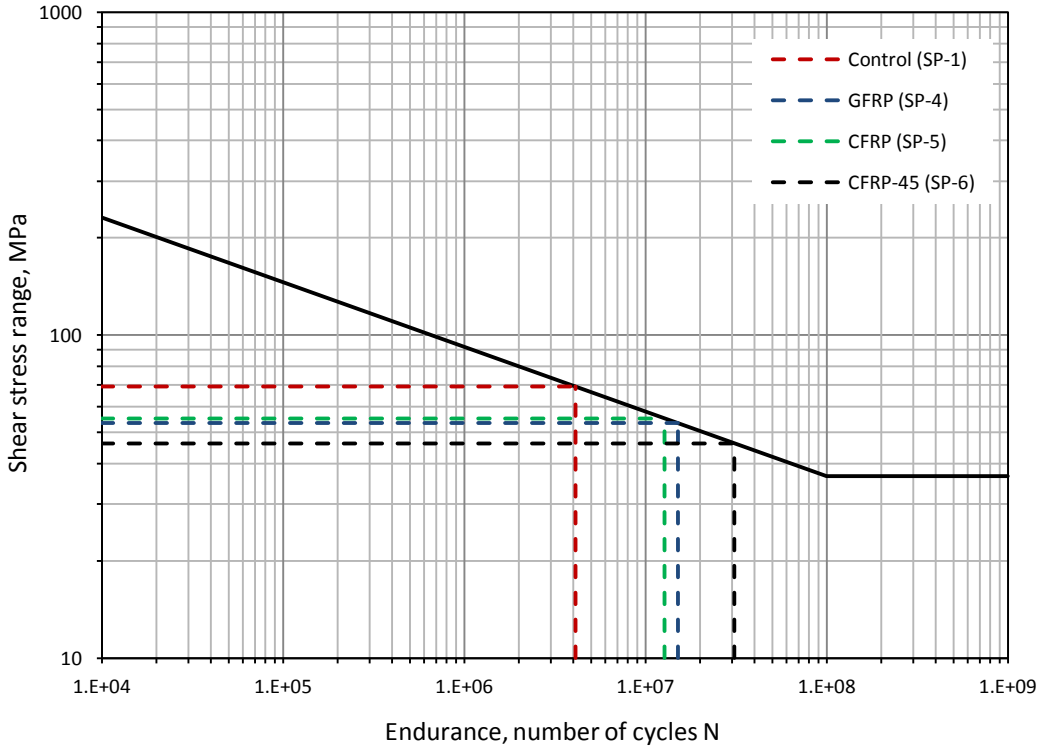

(**b**) Shear stress range - Detail category 80 N/mm2

Figure (6.33): Fatigue life estimation of the strengthened specimens calculated with the same loading range of 20-80% of the capacity of the control specimen.

Table 6.11: Fatigue life estimation of the strengthened specimens calculated with the same loading range of 20-80% of the capacity of the control specimen

Specimen	ΔL kN	$\Delta\varepsilon$ mm/mm	$\Delta\sigma_r$ MPa	$\Delta\gamma$ mm/mm	$\Delta\tau_r$ MPa	Eurocode fatigue equations	
						$N_{\sigma r}$	$N_{\tau r}$
Control	52.7	0.0011	220	0.0009	69.2	366,852	4,120,824
Life increase (times the control specimen)						1.0	1.0
SP-4	52.7	0.00072	143.7	0.0007	53.4	1,316,544	15,122,212
Life increase (times the control specimen)						**3.56**	**3.67**
SP-5	52.7	0.00074	147.9	0.00072	55.3	1,206,855	12,688,721
Life increase (times the control specimen)						**3.29**	**3.08**
SP-6	52.7	0.0007	140.9	0.0006	46.3	1,395,844	30,880,859
Life increase (times the control specimen)						**3.80**	**7.49**

However, this improvement in fatigue life estimation is obviously restricted by the capacity of the control specimen and the applied loading ranges. It would be more convenient if we can see the variations of this improvement with changing the loading range within the maximum capacity of the control specimen. This is shown in Figure (6.34) where the resulting number of cycles is drawn as a function of the loading range taken as 20-40%, 20-60%, 20-80%, and 20-100% of the control specimen ultimate capacity and imposed on the other strengthened specimens.

Figure (6.34a) shows the rate of increase in the number of loading cycles for the direct stress range criterion with reducing the applied loading range. From this figure, it can be seen that the relationship is non-linear and that the rate of increase in the number of loading cycles starts moderately with high loading range (ΔL=70kN) then increases rapidly with reducing the loading range until it reaches to a very high number of loading cycles at a loading amplitude as low as (ΔL=35kN). The same argument can be stated for the relationship between the number of loading cycles and the applied loading range using the shear stress range criterion; however, to a more extreme pattern as can be seen in Figure (6.34b) where the rate of increase in the number of loading cycles changes moderately between a loading range of 70kN and 40kN and then jumps dramatically at a loading range of 35kN.

However, in both cases of Figure (6.34), it can be seen that SP-6 (CFRP-45°) showed the best improvement in the assessment of fatigue life (in terms of the number of loading cycles) using the direct stress range and shear stress range criteria.

Finally, it is clear that fatigue life is improved by using the proposed strengthening technique in stiffening the web plate of steel plate girders which reduced the surface and breathing stresses.

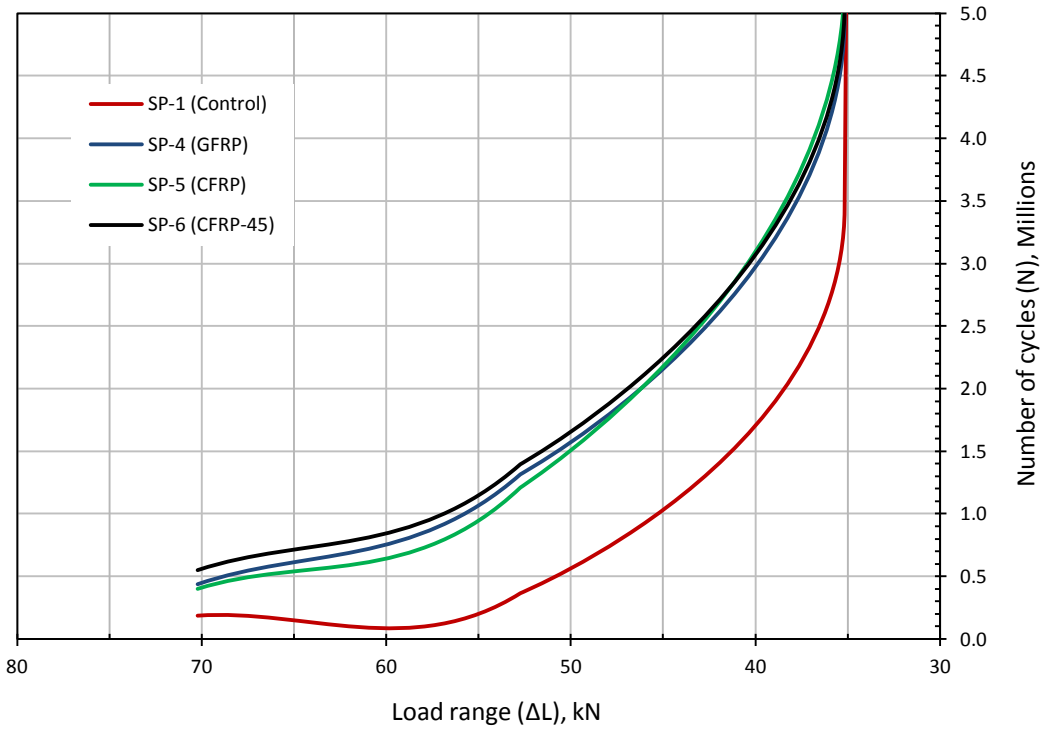

(**a**) Direct stress range criterion

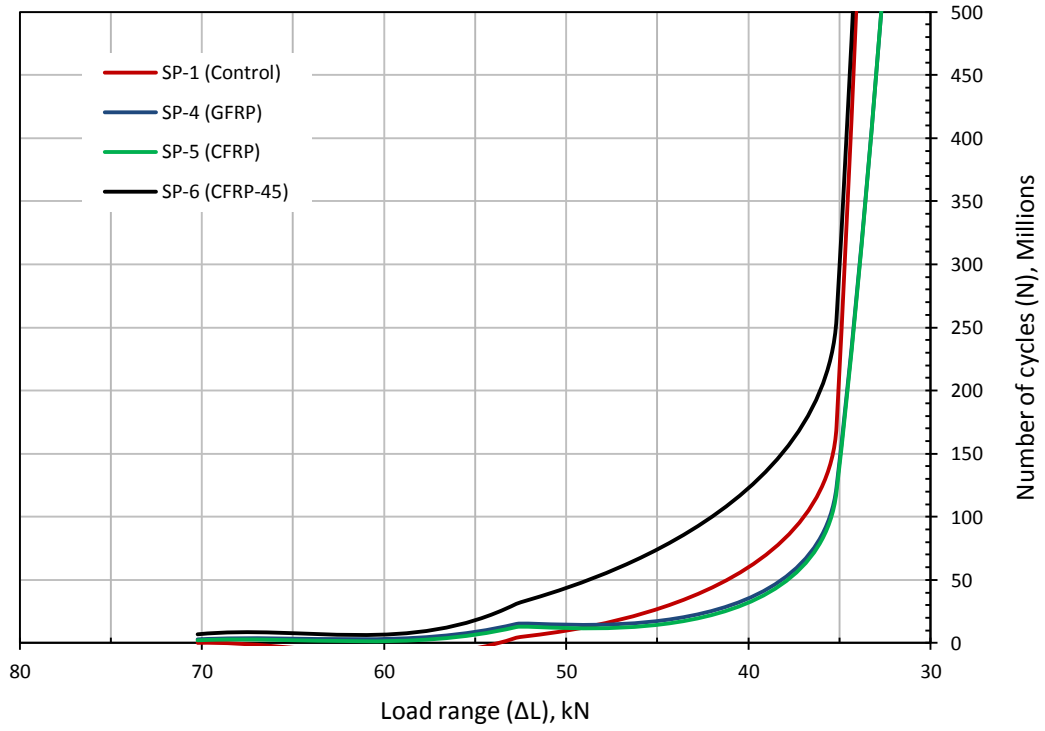

(**b**) Shear stress range criterion

Figure (6.34): Fatigue life estimation of the strengthened specimens calculated with different load ranges.

6.10 SUMMARY AND CONCLUSIONS

A new specimen representing the end panel of a potential steel plate girder was presented in this chapter and tested under cyclic loading with a typical loading range of 40-80% of the ultimate capacity of the specimen. Six specimens were built and 5 of them were strengthened with the optimized FRP panel taking both CFRP and GFRP into considerations.

The final series of tests was divided into two subsequent series of tests. The first one is the static subsequent series which involved testing 3 specimens (one control and two strengthened with GFRP and CFRP panels) to serve as precursor for the other subsequent cyclic series which involved testing another 3 strengthened specimens for 2 millions cycles of load. The specimens in the subsequent cyclic series involved one GFRP and two CFRP strengthened specimens having different strengthening scheme, namely, diagonally and 45° strengthening schemes.

It was shown that a considerable increase in the stiffness of the strengthened specimens is evident in the observed reductions of the maximum out-of-plane displacement. The stiffness of the strengthened specimens is assessed to be increased by a factor ranging between 3 to 9 times the stiffness of the corresponding unstrengthened specimen, depending upon the type of the FRP panel used. The breathing phenomena is also significantly reduced, consequently the surface, membrane and secondary bending stresses are reduced. The 45° strengthening scheme (SP-6) succeeded the best both in reducing the breathing stresses and increasing the ultimate shear capacity of the specimen by 88%.

The web initial imperfection plays an important role in the buckling modes and residual deformations. Therefore, when the initial imperfection is in the favour of the pre-buckling mode of the FRP panel (towards the FRP panel side), the specimen can benefit from both the effects of stiffening (reducing the breathing stresses) and strengthening (increasing the ultimate shear strength) of the plate girder significantly. However, if the initial imperfection was in the reverse direction, then this would not affect the stiffening effect of the FRP panel, but, it will reduce its strengthening effect significantly. In the latter case, it might be a good idea to bond the FRP panel on both faces of the web steel plate if strengthening is required.

Nevertheless, the proposed strengthening technique did not show any debonding or delamination under both static and cyclic loading which makes it a good candidate for strengthening thin-walled structural members, especially, when ductility is a concern. In fact, the proposed strengthening technique succeeded in improving the energy absorption capacity of the strengthened specimens by a factor ranging between 1.5 and 2.5 times the corresponding control specimen which means that the ductile failure type associated with shear buckling of steel plate girder is not only maintained, but it was improved as well. This type of ductile failure is not common in other types of FRP strengthening techniques.

Fatigue analyses indicated that the proposed strengthening technique is able to considerably elongate the life expectancy of the strengthened plate girders by a factor ranging between 2.5 and 7 depending on the applied cyclic load range and the method of assessment.

Finally, a geometrical and material non-linear finite element model is presented for the steel plate girder which showed very good correlation with test results and was capable of predicting both the strength and deformational behaviour of the tested control specimen. This numerical model will be upgraded and further used in Chapter 7 to model the composite strengthened specimens and perform a parametric study to widen the range of variables tested in this chapter and help proposing a new design method.

CHAPTER REFERENCES

EUROPEAN COMMITTEE FOR STANDARDISATION (ENV 2005). Eurocode 3: Design of Steel Structures- Part 1-9: Fatigue. EN 1993-1-9: 1993. Brussels: CEN.

EUROPEAN COMMITTEE FOR STANDARDISATION (ENV 1992). Eurocode 3: Design of steel structures- Part 1.1: General rules and rules for buildings. ENV 1993-1-1, Brussels.

AMERICAN ASSOCIATION OF STATE HIGHWAY TRANSPORTATION OFFICIALS (1994). AASHTO LRFD Bridge Design Specifications, first edition, Washington D.C.

AMERICAN INSTITUTE OF STEEL CONSTRUCTION (1994). Specification for Structural Steel Buildings, ANSI/AISC 360-10, 2010, Chicago, IL.

DEXTER R.J. and FISHER J.W. (1999). “Fatigue and Fracture”, Structural Engineering Handbook, Ed. Chen Wai-Fah, Boca Raton: CRC Press LLC.

ROBERTS T.M., OSMAN M.H., SKALOUD M. and ZORNEROVA M. (1995). “Fatigue crack propagation and residual strength of slender web panels,” International Colloquium on Stability of Steel Structures, Budapest.

This page is intentionally left blank

Chapter Seven

Design Method for FRP-Steel Composite Section

7.1 INTRODUCTION

In the last few chapters, the experimental work was presented. The material programme (Phase-1), the initial series of tests (Phase-2), and the final series of tests (Phase-3) were reported in Chapters 4, 5, and 6, respectively. The experimental programme aimed at designing an easy to install, easy to inspect and cost effective FRP strengthening technique to resist the web out-of-plane deformations and/or strengthening the steel structure to endure higher ultimate shear loads; while maintaining the typical ductile failure of steel plate girders. This goal was fulfilled and the concept of the proposed strengthening technique was validated both under static and cyclic loading. In addition, a numerical model was proposed for the unstrengthened plate girder in Chapter 6, which proved to be helpful in determining the strains at the welded tension corner of the web plate for assessing the fatigue life improvement according to the Eurocode S-N curves.

In this chapter, a modified design method is presented based on the available methods in the literature. However, just like any new proposed method, it needs verification and this cannot be fulfilled with the limited number of specimens available in the current work. For this reason, an FRP-steel composite numerical model is presented at the beginning of this chapter. This composite model is capable of simulating the strengthened plate girder with a good accuracy and it will be validated with the test results from the final series of tests. This model then will be used to perform a parametric study to support the outcomes of the proposed design method.

7.2 NUMERICAL MODEL FOR COMPOSITE STRENGTHENED SECTION

The same model used to simulate the unstrengthened control specimen in Chapter 6 (section 6.7) is used in this chapter except that the corrugated FRP panel is added to simulate the strengthened specimens; Figure (7.1) shows the finite element model where the contour lines show the out-of-plane displacement field.

The FRP panel was modelled using the orthotropic engineering constants constitutive model available in Abaqus CAE. The method for calculating these nine engineering constants is rather long and will be described in the next section (7.2.1) separately. Four node reduced integration shell element (S4R) was used to model the FRP corrugated panel. The size of the element was chosen to be less than 5×5mm to provide several elements in each strip of the FRP panel (especially the bonded strips because this will affect the surface based cohesive behaviour adopted in this model); however, the actual size and shape of the element depends on the location of the element with respect to the FRP panel.

The bond was modelled using surface-based cohesive behaviour. The cohesive interaction properties require the definition of three traction separation parameters, namely, k_{nn}, k_{tt}, and k_{ss}. A lower bound method was used to determine the traction separation parameters required to simulate the same bonding behaviour observed in the experiments. The adopted criterion was to make sure that the finite element model does not show any debonding except at the ultimate loading stage. This means that the correct traction separation parameters are used, a higher value could lead to stiffer behaviour, while a lower value will lead to a premature debonding which can be detected visually in the model when the traction separation stresses exceed the allowable ones. Therefore, the value of 1500 N/mm^3 was chosen on trial and error basis. This value succeeded in reflecting the experimental bond behaviour where no debonding was detected and helped in accelerating the convergence of the numerical model in comparison to the stiffer tie constraints which showed slow convergence and resulted in relatively higher estimations of the ultimate loads in comparison to the adopted cohesive interaction.

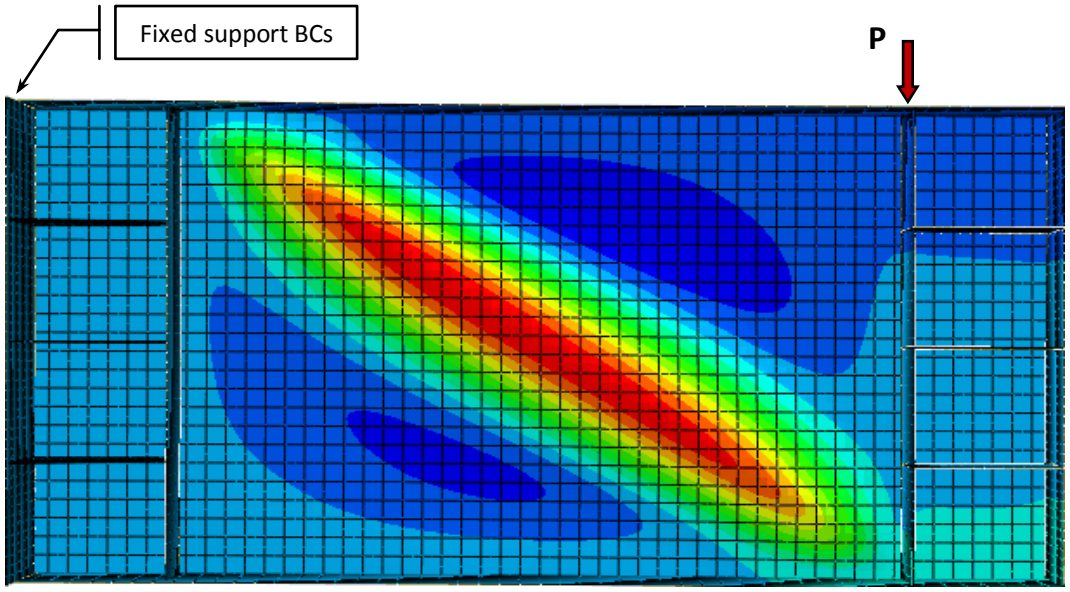

(**a**) Control specimen model (SP-1)

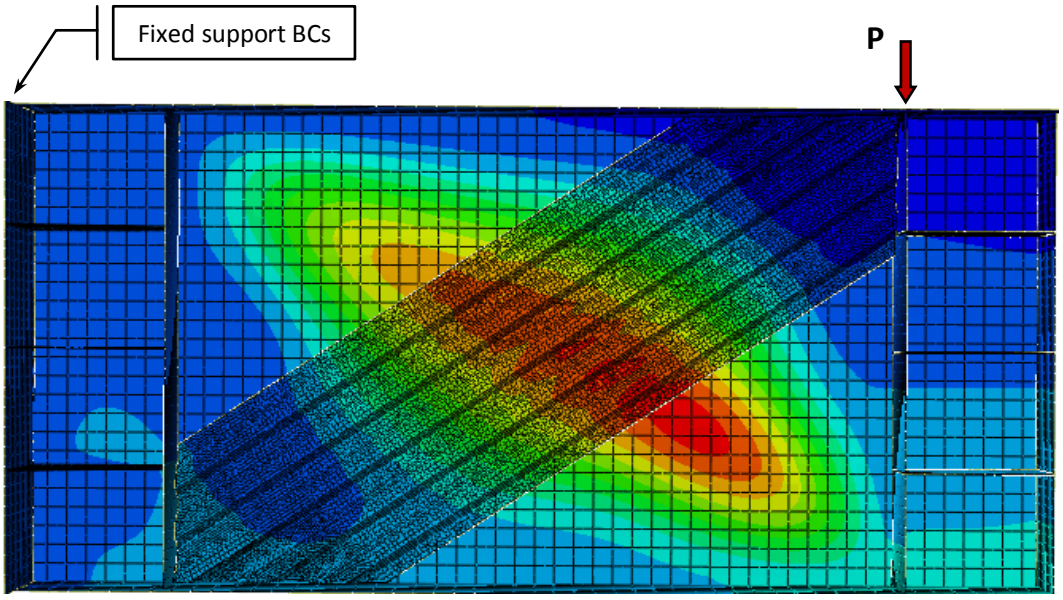

(**b**) Diagonally strengthened model (SP-2 through SP-5)

Figure (7.1): Finite element model for the specimens in Phase-3.

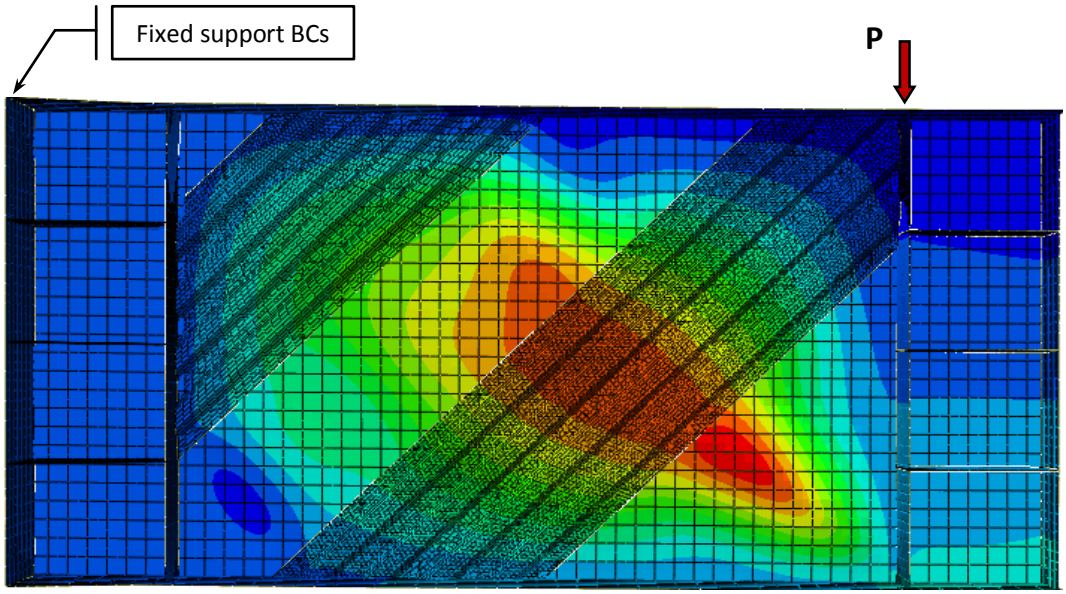

(**c**) 45° strengthened model (SP-6)

Figure (7.1 Cont.): Finite element model for the specimens in Phase-3.

7.2.1 Determining the FRP Orthotropic Global Engineering Constants

For the sake of simplicity from a design prospective, it was decided to model the FRP as a homogenous orthotropic material in the finite element model. In Abaqus, this could be performed using the engineering constants constitutive model which requires the definition of nine material constants. These constants define the modulii of elasticity, the shear modulus, and Poisson's ratios in the three global Cartesian planes as will be seen in the following paragraphs.

Another complication arises when modelling FRP laminates. In this case, we are dealing with different materials (fibres and polymers) with different mechanical properties. The available material properties are usually in the local coordinate system depending mostly on the orientation of the fibre in the matrix. This means that even if we are using the rule of mixture to find the material properties for each lamina, we still need a method to stack them together in one global compliance matrix to inversely calculate the required engineering constants. The global coordinate system mentioned in this section is meant to be for the FRP panel only and it is taken along the axis of corrugation.

The constitutive material properties with respect to the fibre orientations for each lamina can be found as follows:

$$E_1 = E_f V_f + E_m V_m \tag{7.1.a}$$

$$v_{12} = v_f V_f + v_m V_m \tag{7.1.b}$$

$$\frac{G_{12}}{G_m} = \frac{1+\xi\eta V_f}{1-\eta V_f} \tag{7.1.c}$$

$$\eta = \frac{(G_f/G_m)-1}{(G_f/G_m)+\xi} \tag{7.1.d}$$

where:

E_1 : is the tensile composite modulus of elasticity in the direction of the fibre.
E_f , E_m : are the fibre and the matrix modulus of elasticity, respectively.
V_f , V_m : are the fibre and matrix volume fractions, respectively.
v_{12} : is the major Poisson's ratio of the composite.
v_f, v_m : are Poisson's ratios of the fibre and the matrix, respectively.
G_{12} : is the Halphin Tsai in-plane shear modulus of the composite.
G_f, G_m : are the fibre and matrix shear modulus, respectively.
ξ : is the reinforcing factor, and can be assumed conservatively equal to 1.0.

However, the above material properties are not enough to determine the compliance matrix for an orthotropic material. Therefore, the following reasonable approximations are assumed with respect to the two other orthogonal local planes:

$$\left.\begin{array}{l} E_2 = E_m \\ E_3 = E_m \\ G_{13} = G_{12} \\ G_{23} = G_m \\ v_{13} = v_{12} \\ v_{23} = v_m \end{array}\right\} \tag{7.2}$$

Now, knowing the stacking sequence which is [-45/45° -45/45° -45/45°] for the GFRP and [0/90° 0/90° 0/90°] for the CFRP in our case, the local compliance matrix [S'] for each lamina can be calculated as follows:

$$[S'] = \begin{bmatrix} \frac{1}{E_1} & -\frac{v_{12}}{E_1} & -\frac{v_{13}}{E_1} & 0 & 0 & 0 \\ -\frac{v_{12}}{E_1} & \frac{1}{E_2} & -\frac{v_{23}}{E_2} & 0 & 0 & 0 \\ -\frac{v_{13}}{E_1} & -\frac{v_{23}}{E_2} & \frac{1}{E_3} & 0 & 0 & 0 \\ 0 & 0 & 0 & \frac{1}{G_{23}} & 0 & 0 \\ 0 & 0 & 0 & 0 & \frac{1}{G_{13}} & 0 \\ 0 & 0 & 0 & 0 & 0 & \frac{1}{G_{12}} \end{bmatrix} \tag{7.3}$$

However, in order to transfer the compliance matrix from the local coordinates to the global ones, the transformation matrix [T] for each lamina is needed. The original 3-dimensional transformation matrix can be written as follows (Barbero, 2008):

$$[T] = \begin{bmatrix} l_1^2 & m_1^2 & n_1^2 & 2m_1n_1 & 2l_1n_1 & 2l_1m_1 \\ l_2^2 & m_2^2 & n_2^2 & 2m_2n_2 & 2l_2n_2 & 2l_2m_2 \\ l_3^2 & m_3^2 & n_3^2 & 2m_3n_3 & 2l_3n_3 & 2l_3m_3 \\ l_2l_3 & m_2m_3 & n_2n_3 & m_2n_3 + n_2m_3 & l_2n_3 + n_2l_3 & l_2m_3 + m_2l_3 \\ l_1l_3 & m_1m_3 & n_1n_3 & m_1n_3 + n_1m_3 & l_1n_3 + n_1l_3 & l_1m_3 + m_1l_3 \\ l_1l_2 & m_1m_2 & n_1n_2 & m_1n_2 + n_1m_2 & l_1n_2 + n_1l_2 & l_1m_2 + m_1l_2 \end{bmatrix} \tag{7.4}$$

Where *l*, *m*, and *n* are the direction cosines for the angle of rotation with respect to *x*, *y*, and *z*, respectively.

In forming flat laminates, fibre-reinforced laminae are stacked with their x_1x_2-planes parallel but each having its own fibre direction. If the *z*-coordinate of the problem is taken along the laminate thickness, the x_3-coordinate of each lamina will always coincide with the *z*-coordinate of the problem. In such cases, Equation (7.4) can be Easily computed using the coordinate system shown in Figure (7.2). The coordinate of Point *P* in the prime coordinate system can be found from its coordinates in the unprimed system where:

$$x'_1 = x_1 \cos\theta + x_2 \sin\theta \tag{7.5.a}$$

$$x'_2 = -x_1 \sin\theta + x_2 \cos\theta \tag{7.5.b}$$

$$x'_3 = x_3 \tag{7.5.c}$$

or

$$x'_i = a_{ij}\, x_j = l_i x_1 + m_i x_2 + n_i x_3 \tag{7.6.a}$$

or in matrix notation

$$\{x'\} = [a]\{x\} \tag{7.6.b}$$

where a_{ij} are the components of the unit vectors of the primed system e'_i on the unprimed system x_j, by rows as can be seen in Table 7.1.

Table 7.1: Direction cosines for the transformation of the primed and unprimed coordinates in Figure (7.2)

	x_1	x_2	x_3
e'_1	l_1	m_1	n_1
e'_2	l_2	m_2	n_2
e'_3	l_3	m_3	n_3

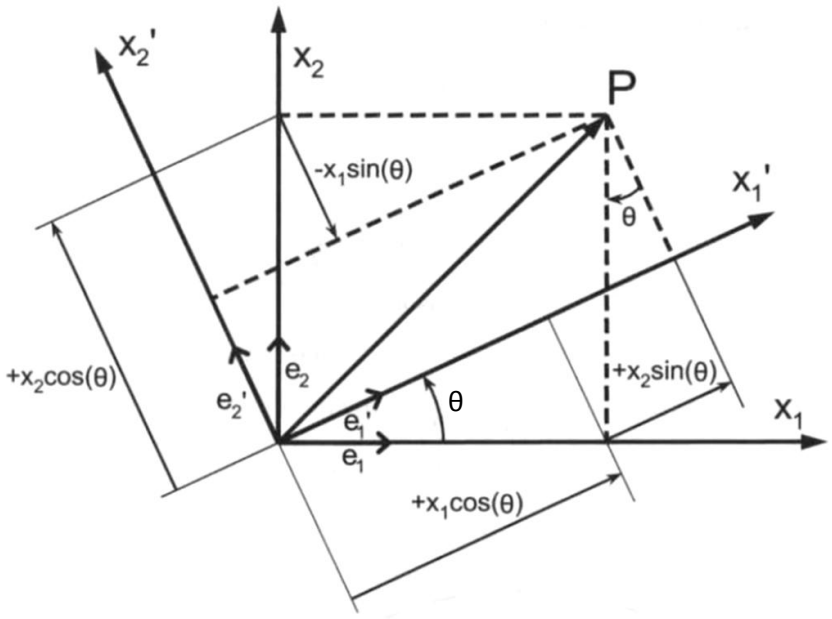

Figure (7.2): Transformation of the coordinate system.

The previous equation transforms vectors from global to local coordinates where primed coordinates denote the material coordinates and unprimed denote the global coordinates. The inverse transformation simply uses the transpose matrix

$$\{x\} = [a]^T\{x'\} \tag{7.7}$$

From Figure (7.2) we know that

$l_1 = \cos\theta \quad m_1 = \sin\theta \quad n_1 = 0$
$l_2 = -\sin\theta \quad m_2 = \cos\theta \quad n_2 = 0$
$l_3 = 0 \quad m_3 = 0 \quad n_3 = 1$ (7.8)

Then, according to Reddy (2004), the transformation matrix becomes:

$$[T] = \begin{bmatrix} \cos^2\theta & \sin^2\theta & 0 & 0 & 0 & \sin 2\theta \\ \sin^2\theta & \cos^2\theta & 0 & 0 & 0 & -\sin 2\theta \\ 0 & 0 & 1 & 0 & 0 & 0 \\ 0 & 0 & 0 & \cos\theta & -\sin\theta & 0 \\ 0 & 0 & 0 & \sin\theta & \cos\theta & 0 \\ -\sin\theta\cos\theta & \sin\theta\cos\theta & 0 & 0 & 0 & \cos^2\theta - \sin^2\theta \end{bmatrix} \quad (7.9)$$

Now it is possible to calculate the Global compliance matrix [S] for each lamina as follows:

$$[S] = [T]^T[S'][T] \quad (7.10)$$

It is important to note that the compliances cannot be added or averaged. The laminate stiffness matrix is obtained by inverting the 6×6 compliance matrix [S] as follows:

$$[C] = [S]^{-1} \quad (7.11)$$

The global stiffness matix of a symmetric laminate with N layers is built by adding the global matrices of the layers multiplied by the thickness ratio t_k/t of each layer, where t is the laminate thickness and t_k denotes the thickness of the k^{th} layer

$$[C] = \sum_{k=1}^{N} \frac{t_k}{t}[C_k] \quad (7.12)$$

Then the global compliance matrix [S] can be found by inversing the global stiffness matrix as follows:

$$[S] = [C]^{-1} \quad (7.13)$$

Finally, since the global compliance matrix represents the orthogonal material properties in the global direction, meaning

$$[S] = \begin{bmatrix} \frac{1}{E_x} & -\frac{v_{yx}}{E_x} & -\frac{v_{zx}}{E_x} & 0 & 0 & 0 \\ -\frac{v_{xy}}{E_x} & \frac{1}{E_y} & -\frac{v_{zy}}{E_y} & 0 & 0 & 0 \\ -\frac{v_{xz}}{E_x} & -\frac{v_{yz}}{E_y} & \frac{1}{E_z} & 0 & 0 & 0 \\ 0 & 0 & 0 & \frac{1}{G_{yz}} & 0 & 0 \\ 0 & 0 & 0 & 0 & \frac{1}{G_{xz}} & 0 \\ 0 & 0 & 0 & 0 & 0 & \frac{1}{G_{xy}} \end{bmatrix} \tag{7.14}$$

Then the laminate constitutive orthogonal material properties can be calculated as follows:

$$\left.\begin{aligned} E_x &= \frac{1}{S_{11}} \\ E_y &= \frac{1}{S_{22}} \\ E_z &= \frac{1}{S_{33}} \\ v_{xy} &= -\frac{S_{21}}{S_{11}} \\ v_{xz} &= -\frac{S_{31}}{S_{11}} \\ v_{yz} &= -\frac{S_{32}}{S_{22}} \\ G_{yz} &= \frac{1}{S_{44}} \\ G_{xz} &= \frac{1}{S_{55}} \\ G_{xy} &= \frac{1}{S_{66}} \end{aligned}\right\} \tag{7.15}$$

where

E_x, E_y, E_z : are the material modulus of elasticity in the x, y, and z directions.
v_{xy} , v_{xz}, v_{yz} : are the material Poisson's ratios in the 3 orthogonal planes.
G_{xy}, G_{xz}, G_{yz} : are the material shear moduli of elasticity in the 3 orthogonal planes.

A Matlab code was written to perform the above calculations and can be found in Appendix (C) where the input values for the local material properties are shown as well. However, Table 7.2 shows the engineering constants calculated both for the GFRP and the CFRP.

Table 7.2: FRP material engineering constants

property	Unit	GFRP	CFRP
E_x	MPa	18434.0	47959.0
E_y	MPa	18434.0	47959.0
E_z	MPa	8002.7	8136.6
v_{xy}	-	0.35	0.048
v_{xz}	-	0.22	0.33
v_{yz}	-	0.22	0.33
G_{xy}	MPa	12058.0	8050.0
G_{xz}	MPa	4722.0	5333.0
G_{yz}	MPa	4722.0	5333.0

It is interesting to note that the moduli of elasticity calculated using the above method is quite close to those measured experimentally both for the 3-layered GFRP and CFRP. The calculated modulus of elasticity for the GFRP is 18434MPa in comparison to the experimentally measured modulus of 18020MPa (average of two tests) while the calculated modulus of elasticity for the CFRP is 47959MPa in comparison to the experimentally measured one of 48120MPa (average of three tests). This is a good proof that the proposed calculation method for the engineering constants is valid and it will be further verified by using them in the composite finite element model.

7.2.2 Validation of the Composite FRP-Steel Numerical Model

The control finite element model was previously verified against the experimental results in Chapter 6 and showed very good correlation in predicting the strength and deformational behaviour of the control specimen (refer back to section 6.7 and Figures 6.26 and 6.27 for further details). However, in this section, the composite model is presented and will be verified against the experimental tests for all the 5 strengthened specimens tested in the final series of tests.

It is important to note that, for the cyclic series, because of the limited residual deformations in the tested specimens and because the cyclic specimens showed similar behaviour and even higher strengths than the static ones; no residual strain or deformation except for the measured web initial imperfection was taken into

considerations in this model. In addition, only one cycle of load were considered in the finite element model for specimens SP-2 and SP-3 tested in the static subsequent series of tests which was tested in 6 cycles of load in order to be able to detect any possible debonding as discussed previously in Chapter 6. However, only the last cycle went to the ultimate load and failed the specimen.

7.2.2.1 Subsequent Static Series

SP-2 (GFRP strengthened specimen)

Figure (7.3) shows the verification curves for the GFRP strengthened specimen (SP-2). Figure (7.3a) compares the web experimental central out-of-plane displacement to the finite element one while Figure (7.3b) compares the in-plane deflection.

From this figure, it can be seen that the model succeeded in modelling the buckling behaviour until very close to the ultimate load where it diverged to go for higher ultimate load estimation. The finite element model predicted the ultimate load of this specimen by 12.6% higher than the experimental ultimate load. However, the behaviour of the model was very similar to the experimental one up to 90% of the ultimate load. Unfortunately, the in-plane deflection did not show the same accuracy as can be seen in Figure (7.3b). This is a general phenomenon in the composite model. However, this is a minor defect considering that the core of study is concentrating on the out-of-plane buckling behaviour and not the in-plane deflection.

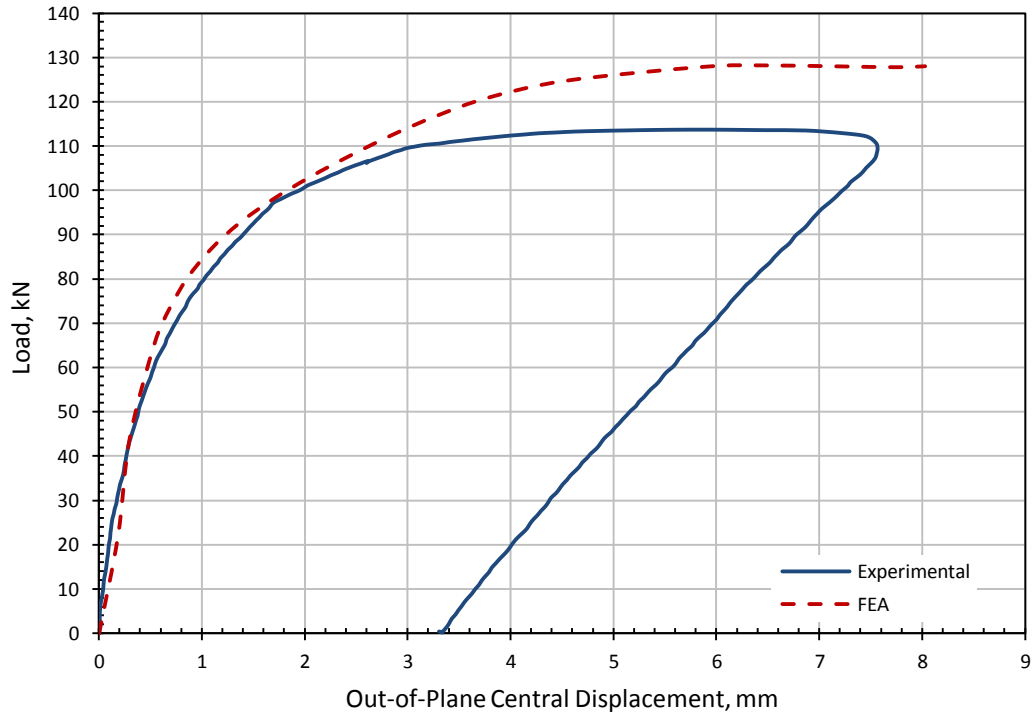

(**a**) Buckling curve

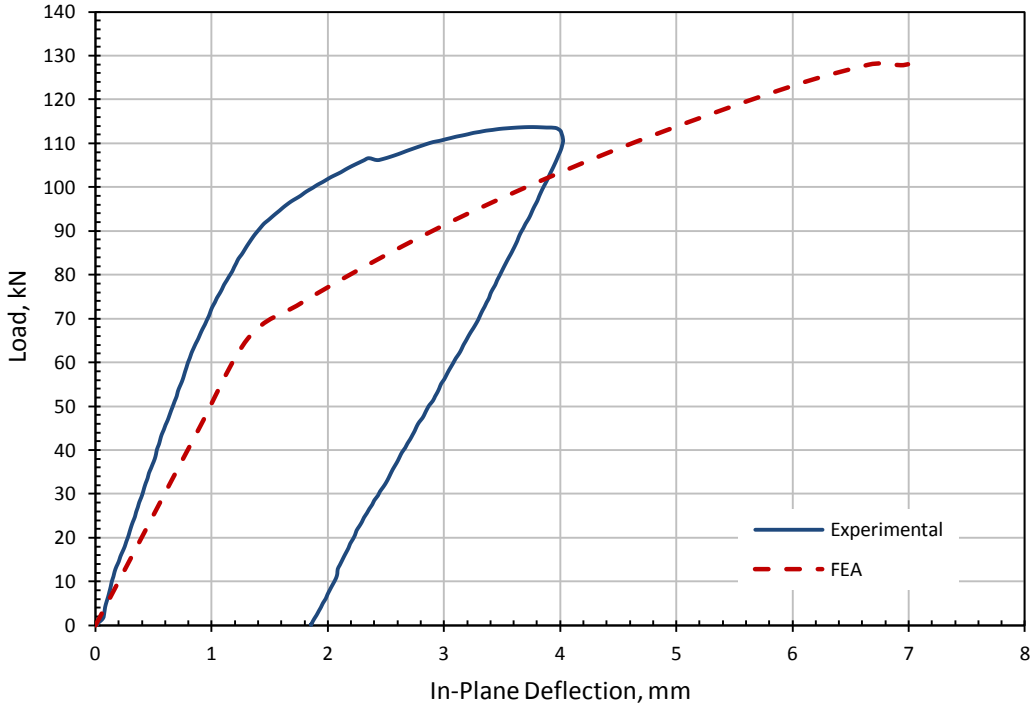

(**b**) Deflection curve

Figure (7.3): Verifications of the FEM against the experimental results for SP-2.

SP-3 (CFRP strengthened specimen)

Figure (7.4) shows the verification curves for the CFRP strengthened specimen (SP-3). Figure (7.4a) compares the web experimental central out-of-plane displacement to the finite element one while Figure (7.4b) compares the in-plane deflection.

From this figure, it can be seen that the finite element buckling curve showed very good correlation with the experimental results up to approximately 90% of the ultimate load and then started diverging to reach an ultimate capacity 27% higher than the experimental one. This could be attributed to the fact that this specimen had a reversed buckling mode for the reasons explained in Chapter 6. This reversed buckling mode caused the experimental load to drop because of the local failure of the CFRP corrugated panel where wrinkles started to take place in the FRP further fibres because it was under compression instead of the expected tension one. This problem was solved by using the 45° strengthening scheme as will be seen in SP-6. The finite element model was not capable of detecting such a deficiency because no failure criterion was provided for the FRP composite. This was left for further work recommended in the future. Nevertheless, this problem could have been avoided by detecting the initial bucking modes and bonding the FRP panel to the face of the web plate in the favour of the pre-designed buckling mode. The numerical model deflection curve showed good correlation with the experimental one up to a load equals 62% of the specimen ultimate capacity and then it diverged showing a bilinear behaviour averaging the remaining two non-linear parts of the curve.

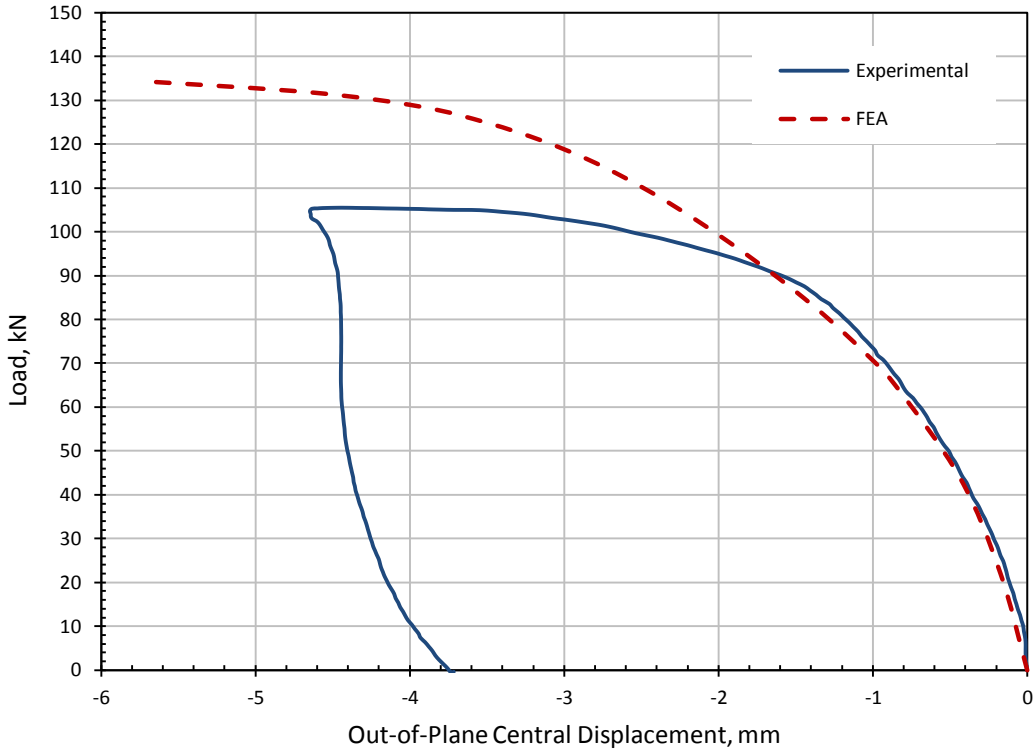

(**a**) Buckling curve

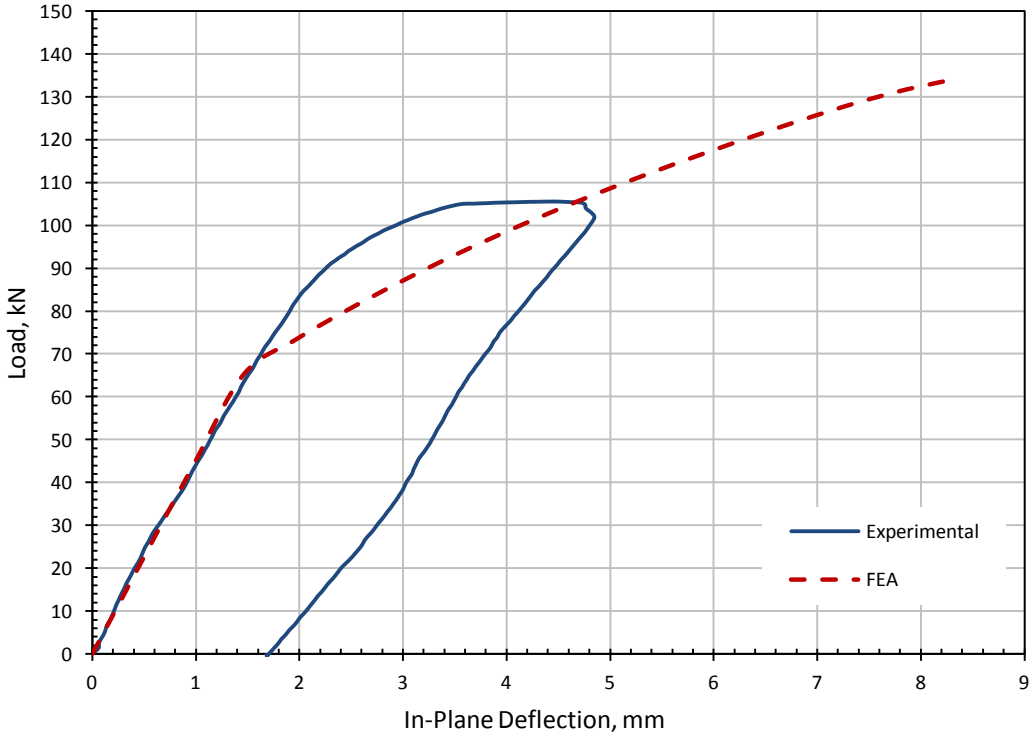

(**b**) Deflection curve

Figure (7.4): Verification of the FEM against the experimental results for SP-3.

7.2.2.2 Subsequent Cyclic Series

SP-4 (GFRP strengthened specimen)

Figure (7.5) shows the verification curves for the GFRP strengthened specimen (SP-4). Figure (7.5a) compares the web experimental central out-of-plane displacement to the finite element one while Figure (7.5b) compares the in-plane deflection.

From this figure, it can be seen that the finite element model faced a difficulty in following the same buckling curve trends of the experimental test. This is because of the small reversed initial imperfection associated with this specimen. As described in details in Chapter 6, this specimen fought to follow the prebuckling mode in spite of the small reversed initial imperfection. This caused this high stiffness at initial loading stage; however, at a load equal to 112.0kN the buckling mode was reversed. The numerical model managed to show the reversed buckling mode but with lesser stiffness at the initial loading stage and reached to a slightly higher load at the ultimate loading stage. The numerical model deflection showed a general pattern similar to that of the experimental test.

SP-5 (CFRP strengthened specimen)

Figure (7.6) shows the verification curves for the CFRP strengthened specimen (SP-5). Figure (7.6a) compares the web experimental central out-of-plane displacement to the finite element one while Figure (7.6b) compares the in-plane deflection.

From this figure, it can be seen that except for the unusual slack in the experimental buckling curve at the initial loading stage, the finite element model succeeded in simulating the out-of-plane displacement efficiently. Even the ultimate load was predicted with high accuracy (approximately 100%). The numerical bucking curve could be approximated to a bilinear trend matching the experimental buckling curve. The deflection predicted by the finite element model had the same pattern as in the case of the buckling. However, the numerical deflection curve started linearly within the first 50% of the ultimate capacity and then changed its slope up to a load close to the ultimate load then a yielding plateau is formed as expected at the ultimate loading stage.

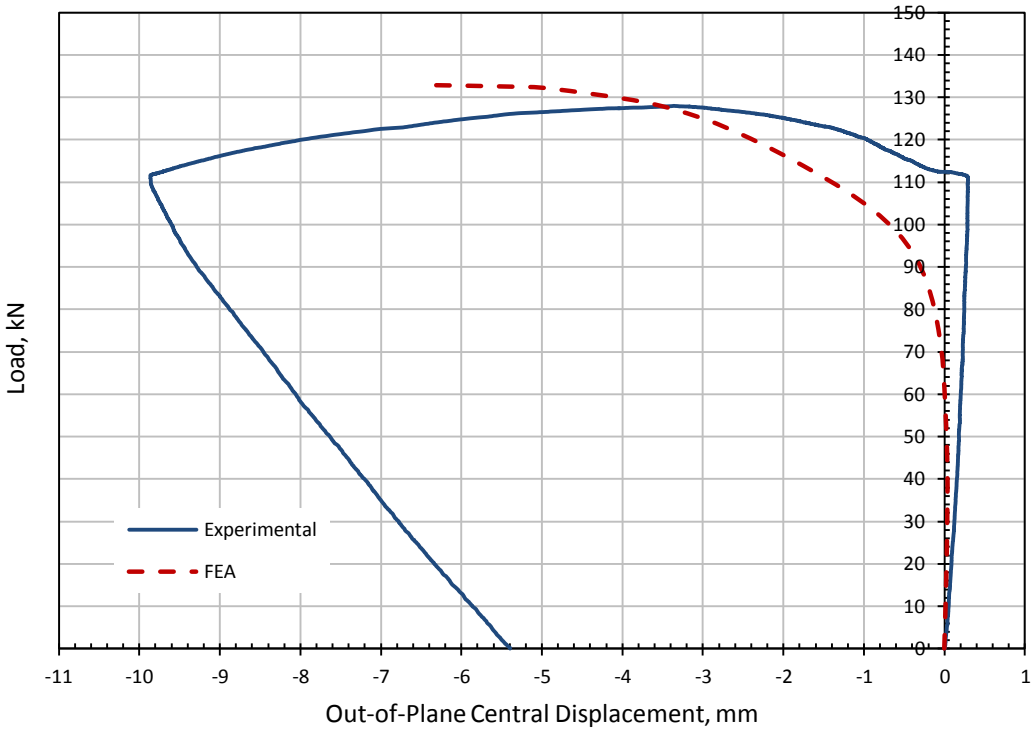

(**a**) Buckling curve

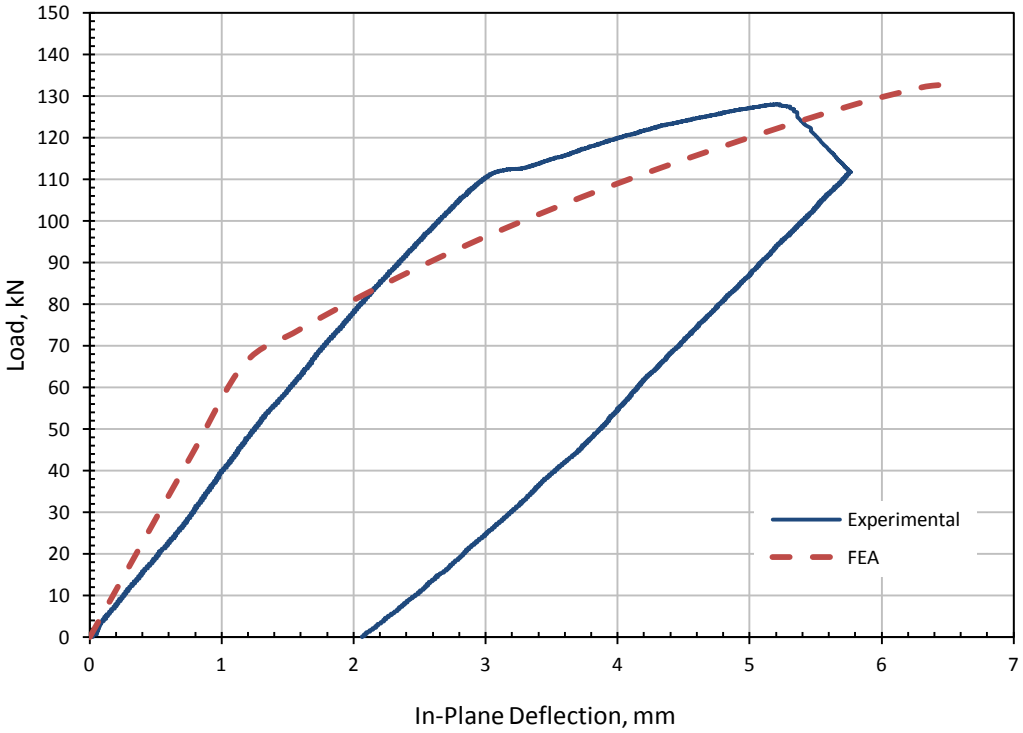

(**b**) Deflection curve

Figure (7.5): Verification of the FEM against the experimental results for SP-4.

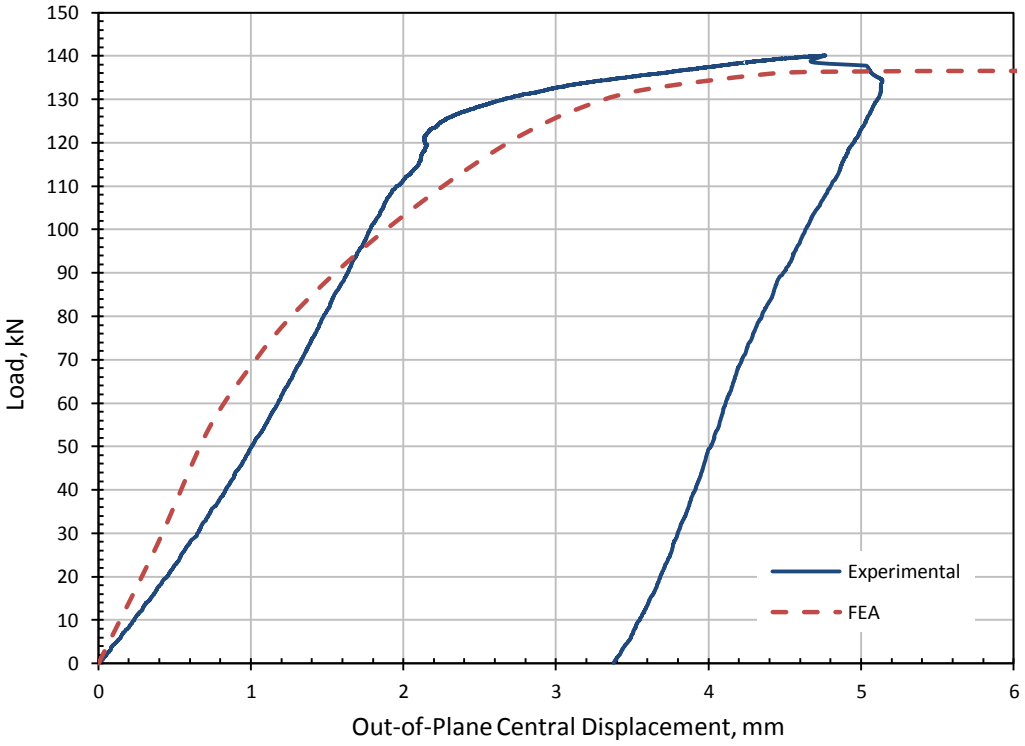

(**a**) Buckling curve

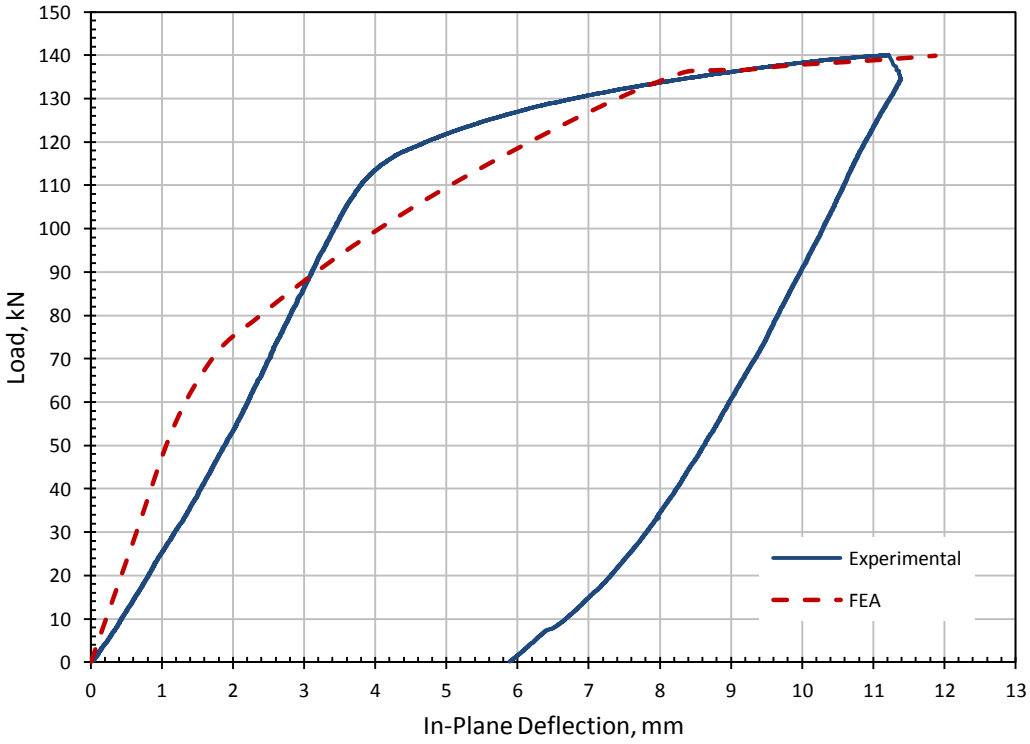

(**b**) Deflection curve

Figure (7.6): Verification of the FEM against the experimental results for SP-5.

SP-6 (CFRP-45° strengthened specimen)

Figure (7.7) shows the verification curves for the CFRP-45° strengthened specimen (SP-6). Figure (7.7a) compares the web experimental central out-of-plane displacement to the finite element one while Figure (7.7b) compares the in-plane deflection.

The figure shows that the numerical model is capable of predicting both the strength and buckling behaviour accurately. The numerical deflection curve showed a good correlation with the experimental one as well; however, with insignificant higher stiffness.

7.2.3 Comments on the Numerical FRP-Steel Composite Model

The model showed generally a good correlation with test results especially for the first 80-90% of the ultimate capacity of the specimens. Specifically, it succeeded in estimating the behaviour of the CFRP strengthened specimens which buckled in the normal expected mode (SP-5 and SP-6) both from strength and deformational aspects and throughout the whole loading stages up to failure.

Looking at Figure (7.7) again increases our confidence and strengthens the reliability of the composite numerical model to simulate the proposed strengthening technique in the current study and consequently we can conclude that the proposed material constitutive model (section 7.2.1) succeeded in calculating the nine engineering constants needed to model the orthogonal FRP material.

For the abovementioned reasons and because the CFRP-45° strengthening scheme succeeded the best in the optimization process, only this strengthening scheme will be considered in the parametric study presented next in section (7.3) which will lead the way for the proposed design method in section (7.4).

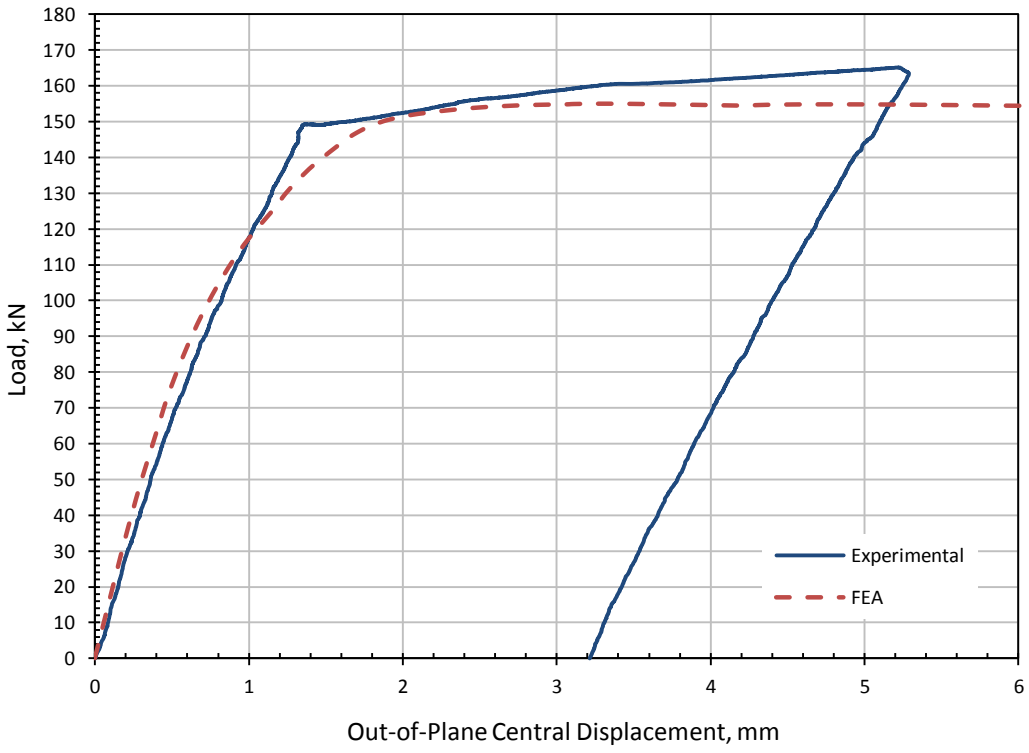

(**a**) Buckling curve

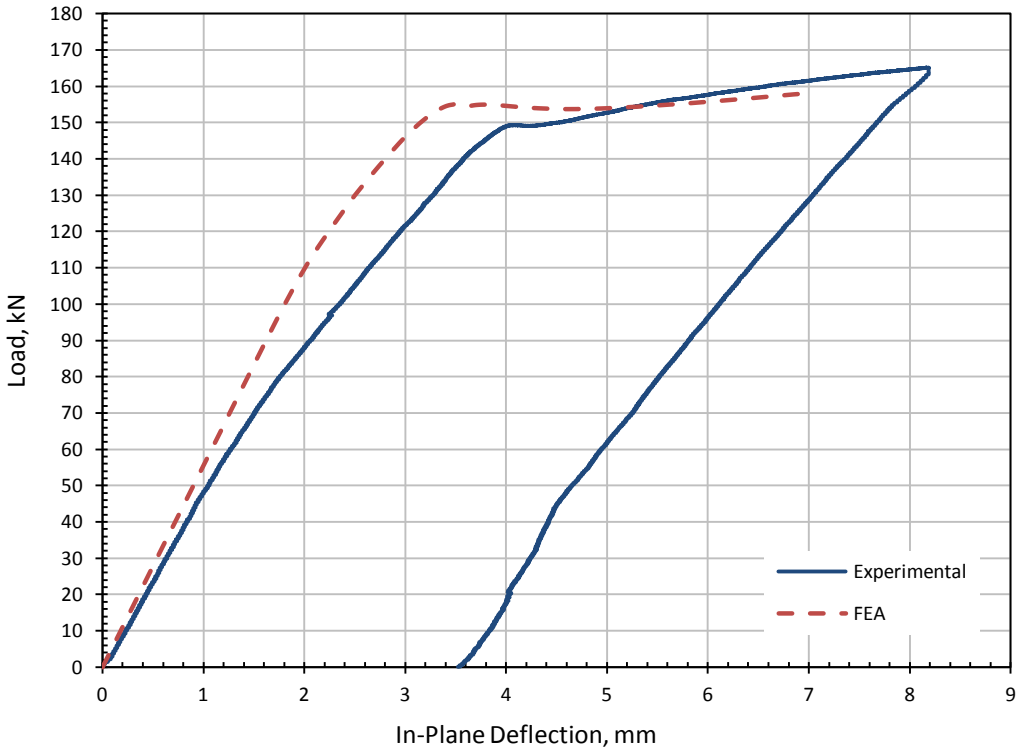

(**b**) Deflection curve

Figure (7.7): Verification of the FEM against the experimental results for SP-6.

7.3 PARAMETRIC STUDY

In the previous section, the composite finite element model was verified against the experimental results. In this section, this numerical model is going to be used for a parametric study that will enrich the range of the examined variables to pave the way for the intended proposed design method.

The numerical model was used to extend the range of examined variables to include the following:

a_w/h_w = 1.0, 1.5, and 2.0 with a_w = 490, 735, and 980mm, respectively.

h_w/t_w = 125, 167, and 250 with t_w = 2, 3, and 4mm, respectively.

This was done because of the limited range of variables tested in the final series of tests (Chapter 6) where the aspect ratio and the slenderness ratio were constant and equal to 1.5 and 245, respectively. In addition to that, it has been decided to only take the optimized strengthening technique into consideration leaving us with only two specimens (out of six), one control specimen and one CFRP-45° strengthened specimen.

To eliminate the scale and boundary conditions effects on the obtained results; all other dimensions and specimen details were kept constant as in the final series of tests discussed in Chapter 6 and the same composite model illustrated in section (7.2) is used. A constant initial imperfection of $h_w/1250$ was used for all the specimens in this parametric study. Generally, this is the smallest initial imperfection that could exist in the web plate from a practical point of view and from experimental observations. This is also the smallest initial imperfection that could alter the buckling behaviour of the web plate from the theoretical flat curve to the more practical initially imperfect one, refer to Chapter 3 where this phenomenon has been discussed in more details. Figure (7.8) shows typical images of the finite element model geometry and mesh where the contour lines show the out-of-plane displacement fields.

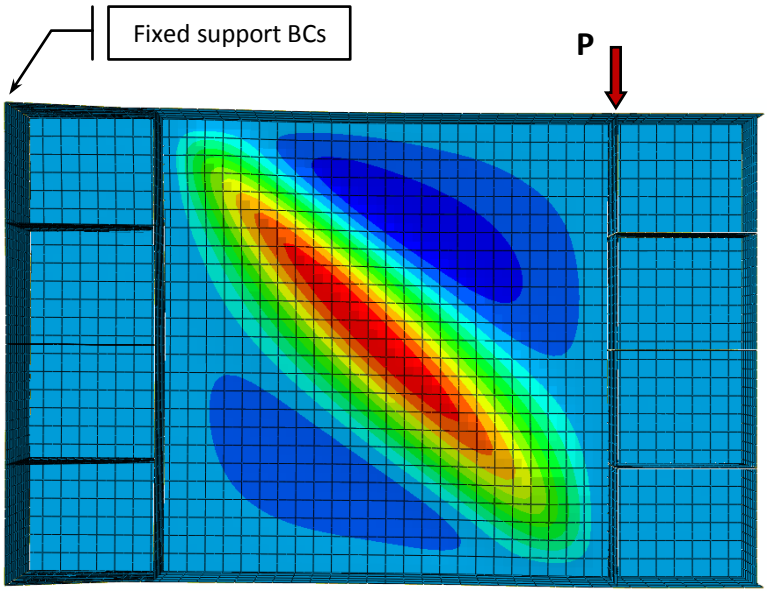

(**a**) Unstrengthened model (a_w/h_w=1.0 and h_w/t_w=167)

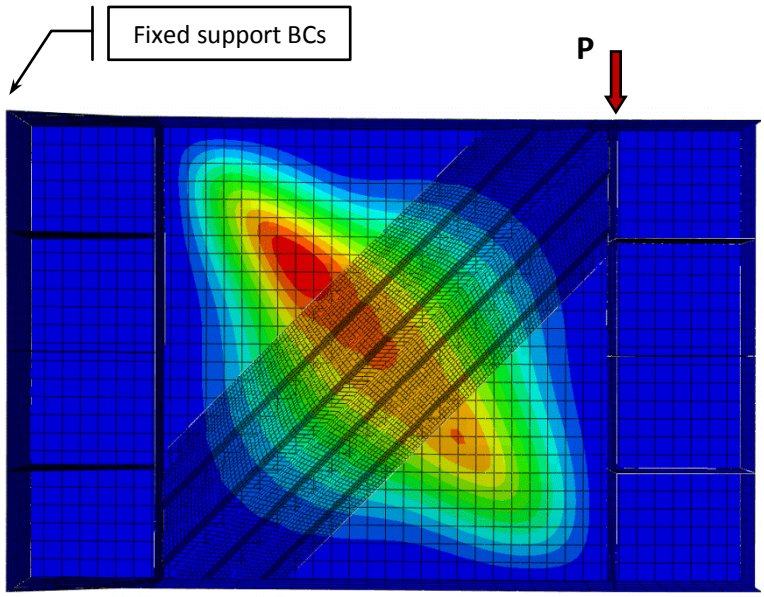

(**b**) FRP strengthened model (a_w/h_w=1.0 and h_w/t_w=167)

Figure (7.8): Finite element models for the specimens tested numerically in the parametric study.

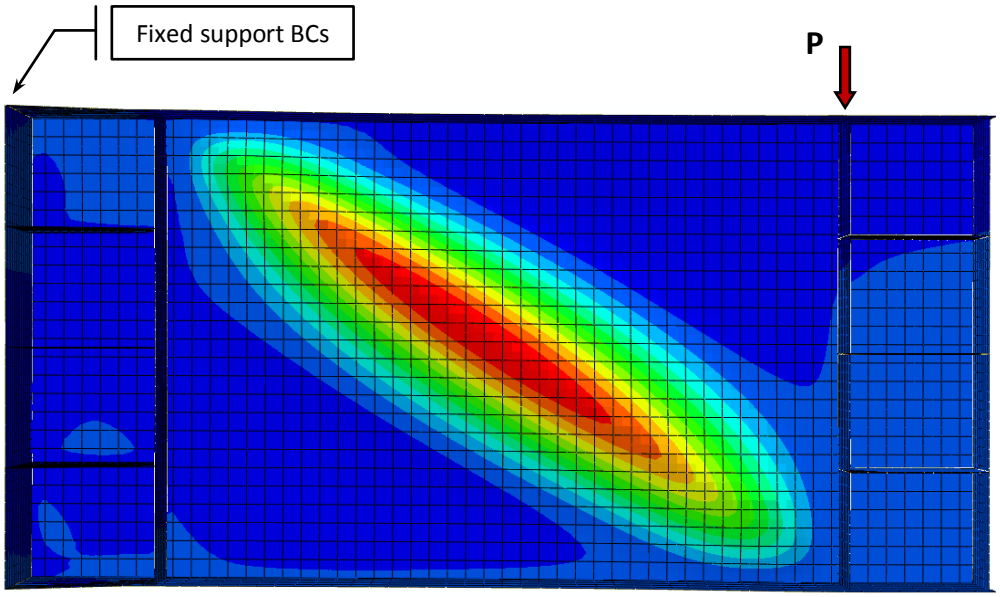

(**c**) Unstrengthened model (a_w/h_w=1.5 and h_w/t_w=167)

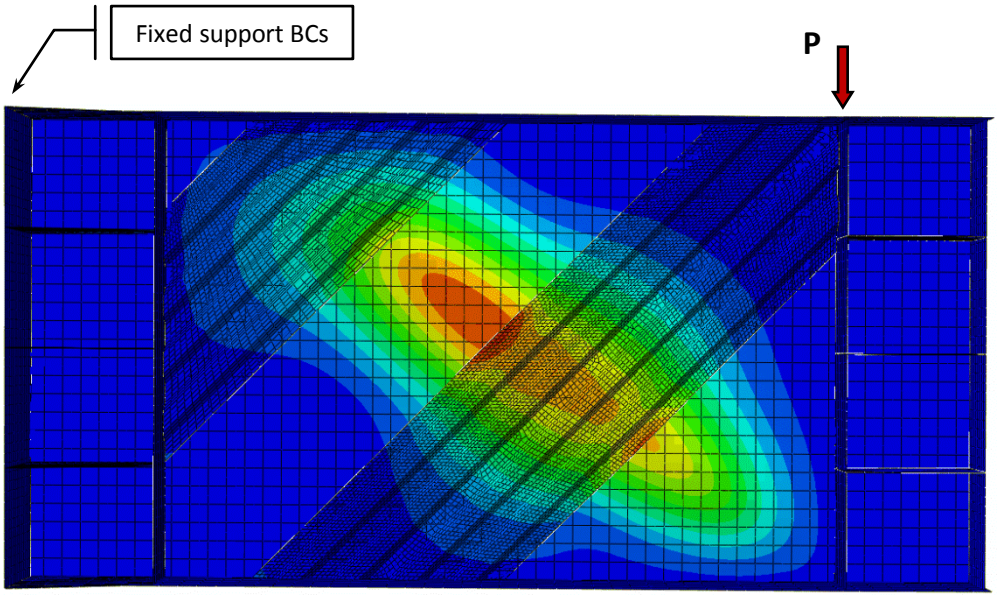

(**d**) FRP strengthened model (a_w/h_w=1.5 and h_w/t_w=167)

Figure (7.8 Cont.): Finite element models for the specimens tested numerically in the parametric study.

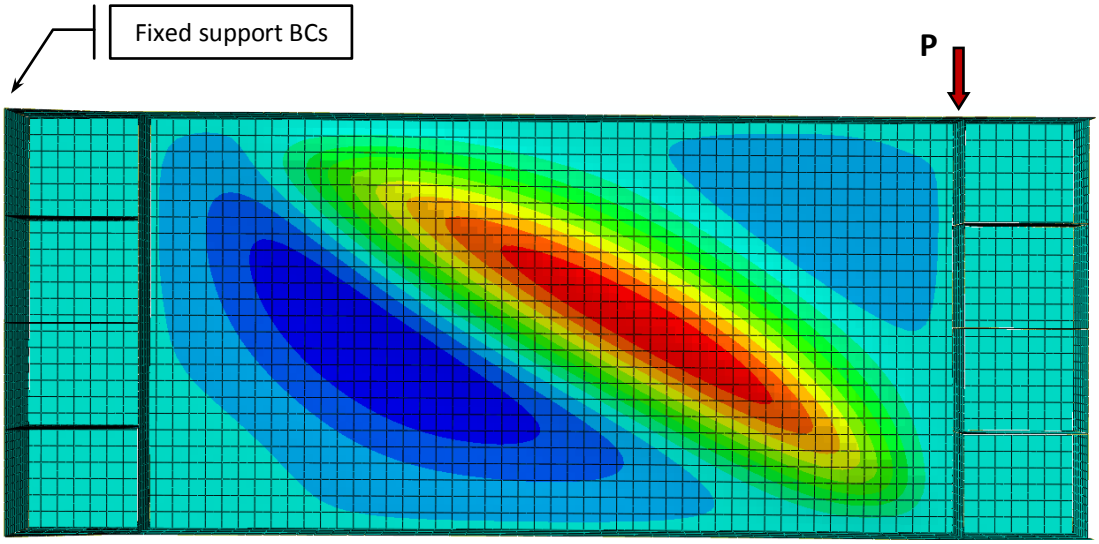

(**e**) Unstrengthened model (a_w/h_w=2.0 and h_w/t_w=167)

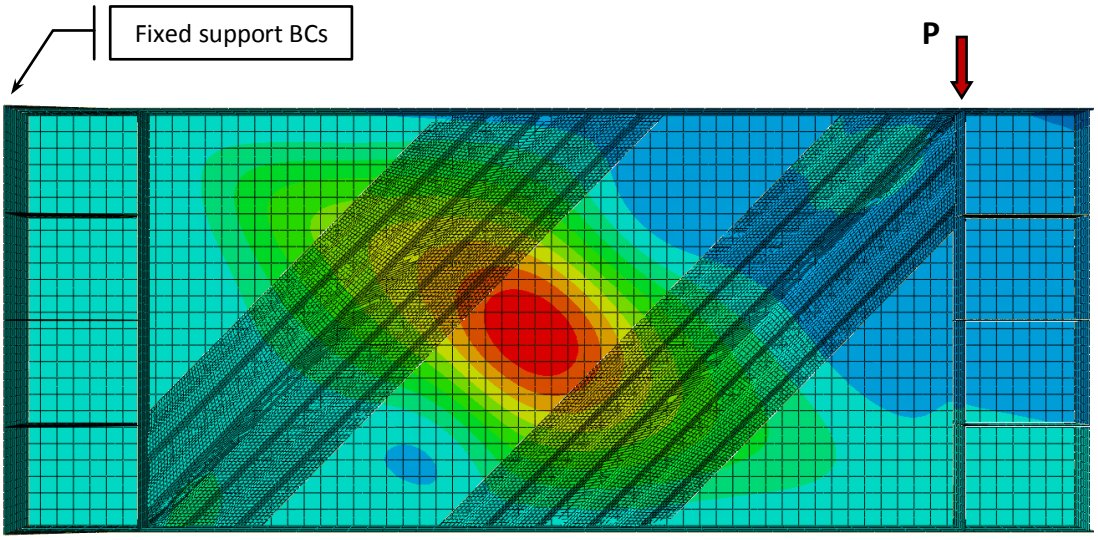

(**f**) FRP strengthened model (a_w/h_w=2.0 and h_w/t_w=167)

Figure (7.8 Cont.): Finite element models for the specimens tested numerically in the parametric study.

Figures (7.9), (7.10), and (7.11) show the resulting curves from the finite element model for the range of variables considered in this parametric study. Both the out-of-plane and in-plane displacements' curves are shown. Figure (7.9) deals with all curves for specimens having an aspect ratio (a_w/h_w) of 1.0, while Figures (7.10) and (7.11) are dedicated to specimens having aspect ratios of 1.5 and 2.0, respectively. In each figure, the strengthened and unstrengthened specimens' behaviour is compared.

A total of 18 specimens were tested numerically, all of them behaved almost in the same pattern. Specimens having aspect ratios of 1.0 and 1.5 buckled typically in an even buckling mode, refer to Figure (7.8a) to see a typical even buckling mode for specimens with low aspect ratios; while specimens with an aspect ratio of 2.0 buckled in an odd buckling mode, refer to Figure (7.8e) to see a typical odd buckling mode. However, generally, beyond the linear initial stage the curves start to change slope until it reaches to a point where it curve dramatically towards the yielding plateau. One exception from this general behaviour is the FRP strengthened specimen with a_w/h_w =2.0 and h_w/t_w =125 where its buckling curve is shown in Figure (7.11a). This specimen had the usual initial stiffness as the corresponding unstrengthened one, but its behaviour was altered with higher loading stages. In this case, the load started to increase with the specimen hesitating to buckle until it reached to a load close to the shear yielding load where the web started to buckle. This behaviour can be justified by the fact that this web is thick and with the additional FRP shear strengthening there was a bending moment interaction due to the length of the specimen in comparison to the others. This could be noted from the extra high deflection needed for the specimen to fail, see Figure (7.11b), and from the high stress readings in the flanges were plastic hinges are expected to develop. Nevertheless, the web buckled eventually and hence the specimen can still be considered in this parametric study.

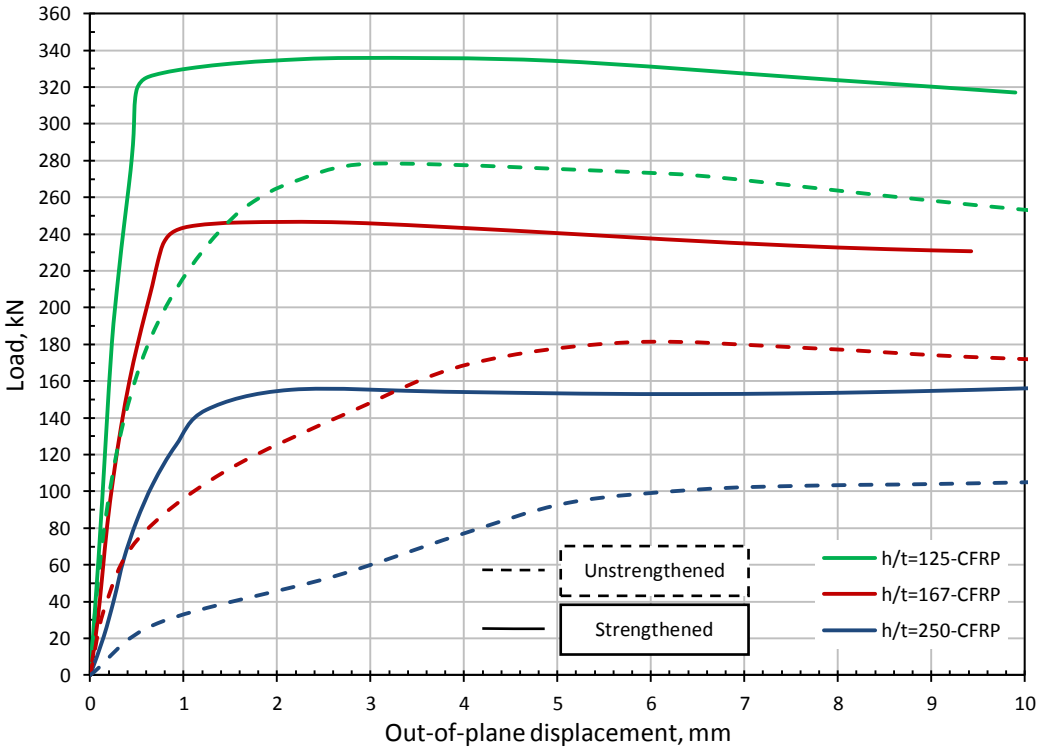

(**a**) Buckling curve

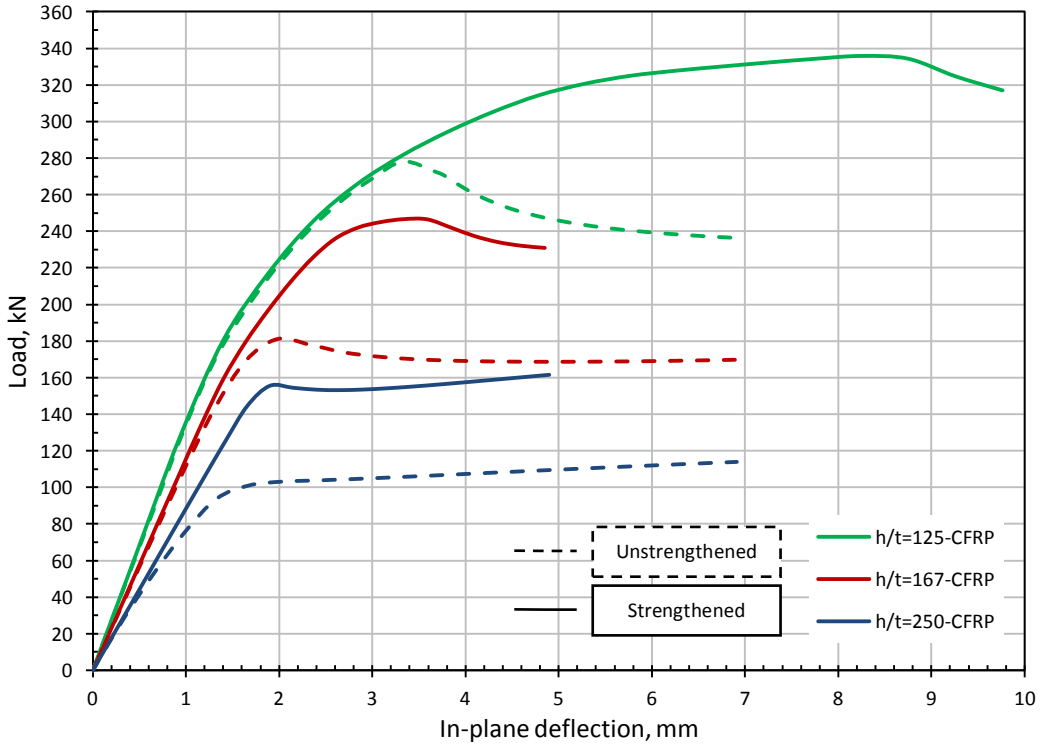

(**b**) Deflection curve

Figure (7.9): Finite element resulting curves for the control (unstrengthened) and FRP strengthened specimens with a_w/h_w =1.0 and for different slenderness ratios.

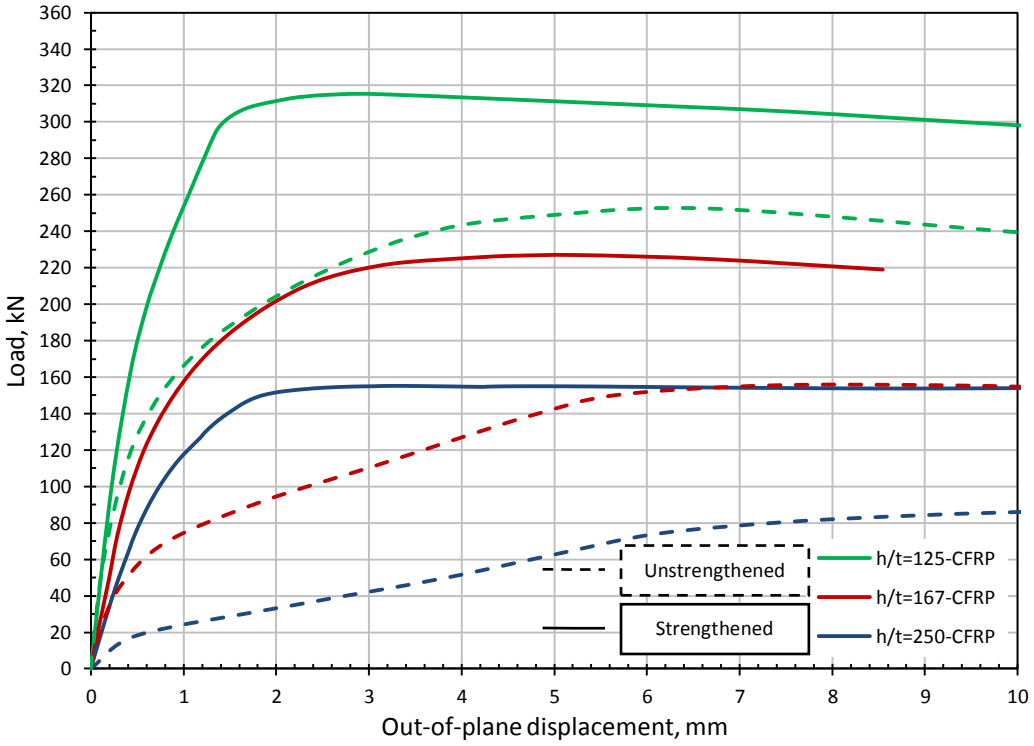

(**a**) Buckling curve

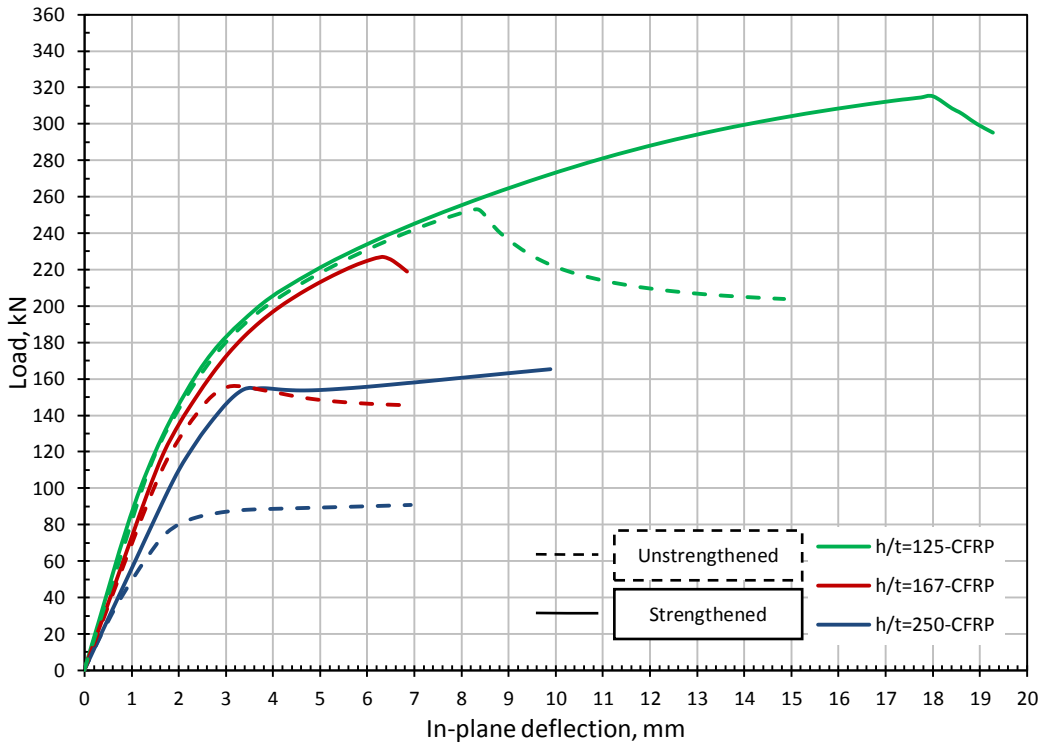

(**b**) Deflection curve

Figure (7.10): Finite element resulting curves for the control (unstrengthened) and FRP strengthened specimens with a_w/h_w =1.5 and for different slenderness ratios.

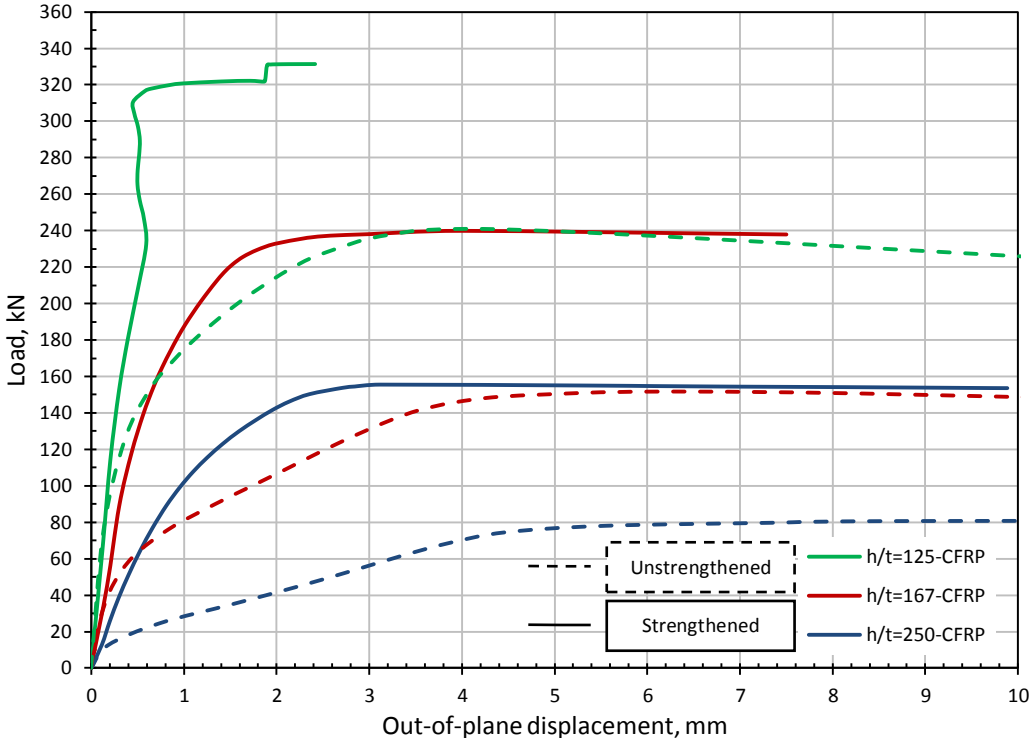

(**a**) Buckling curve

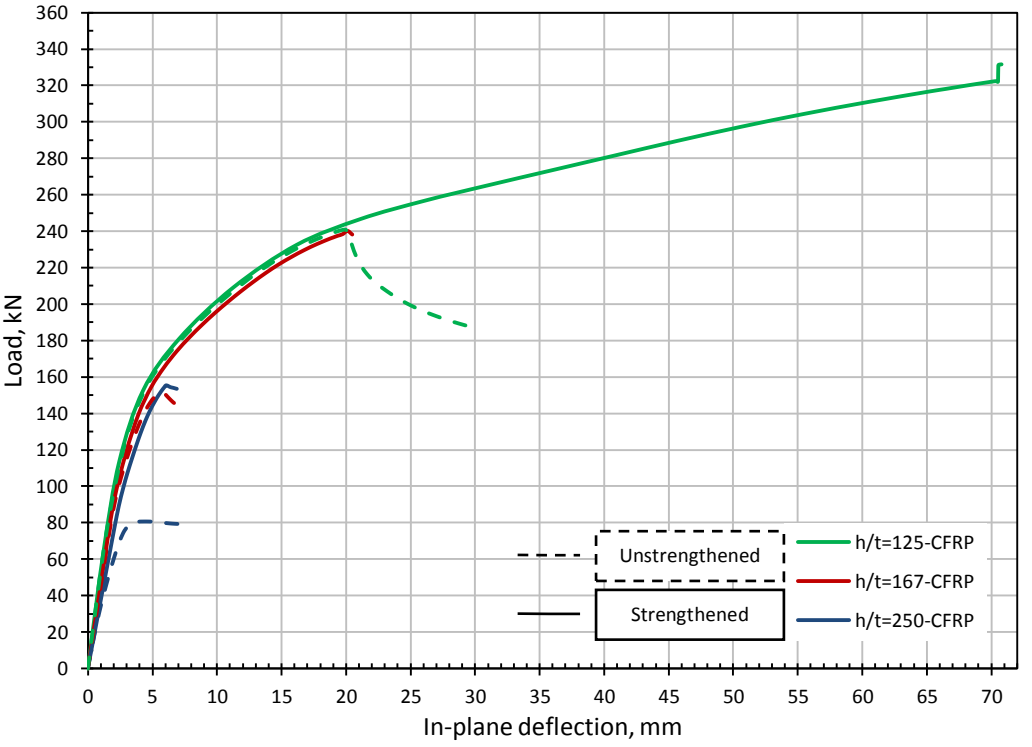

(**b**) Deflection curve

Figure (7.11): Finite element resulting curves for the control (unstrengthened) and FRP strengthened specimens with a_w/h_w =2.0 and for different slenderness ratios.

Another observation from this parametric study is that for specimens with low slenderness ratios (thick web plates), there was some minor debonding between the FRP panel and the steel plate which took place at very high loading stages close or even within the failure plateau. This is a minor effect which could be neglected because it did not affect neither the ultimate load nor the behaviour of the specimen as it took place only in the numerical tests for specimens having low slenderness ratio of 125 and at the ultimate loading stage.

The main conclusion from all these curves and the parametric study is that the FRP strengthening effect was increased with increasing both the aspect and slenderness ratios of the specimen. Table 7.3 compares the ultimate failure load for the 18 numerical tests in this parametric study where P_{CM} is the ultimate load for the control unstrengthened specimens' model and P_{FM} is the ultimate load for the FRP strengthened specimens' model. The distribution of the strengthening ratio $\boldsymbol{P_{FM} / P_{CM}}$ with respect to the aspect and slenderness ratios can be seen in Figure (7.12).

Table 7.3: Numerical ultimate loads for the strengthened and unstrengthened specimens in the parametric study

a_w/h_w	h_w/t_w	P_{CM}, kN	P_{FM}, kN	P_{FM}/P_{CM}
1.0	250	113.95	161.43	1.42
1.0	167	181.26	246.47	1.34
1.0	125	278.25	335.91	1.21
1.5	250	90.67	165.29	1.82
1.5	167	155.58	226.66	1.46
1.5	125	252.89	315.19	1.25
2.0	250	80.66	155.52	1.93
2.0	167	151.65	238.22	1.57
2.0	125	241.04	331.41	1.38

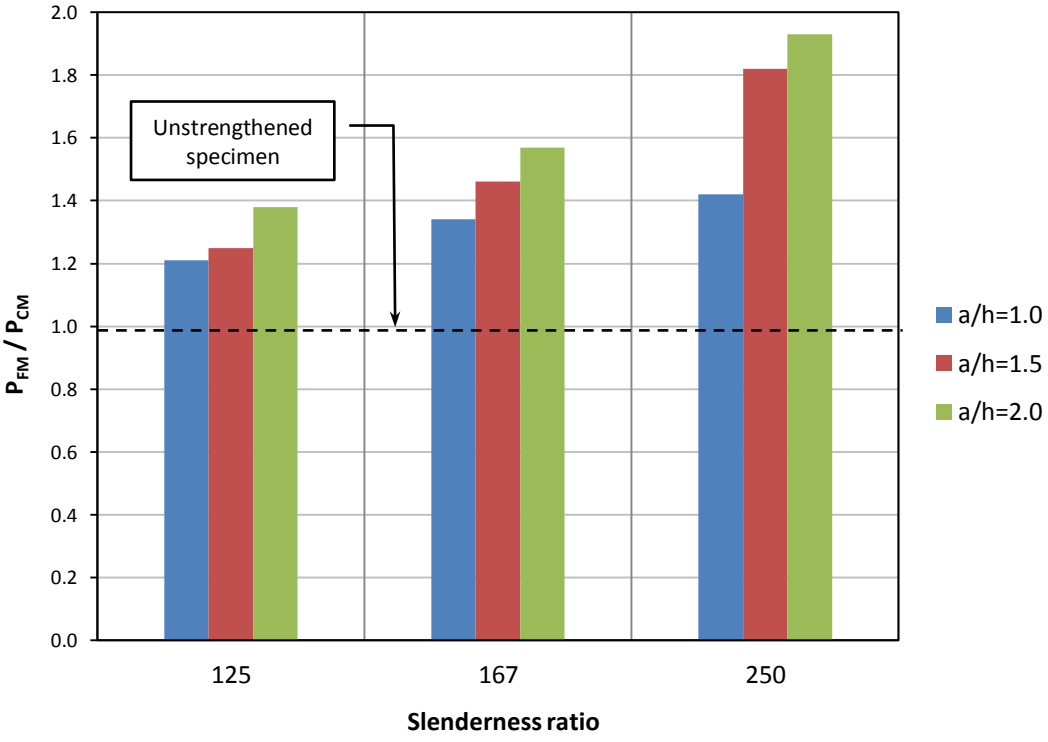

(**a**) Effect of aspect ratio (a_w/h_w)

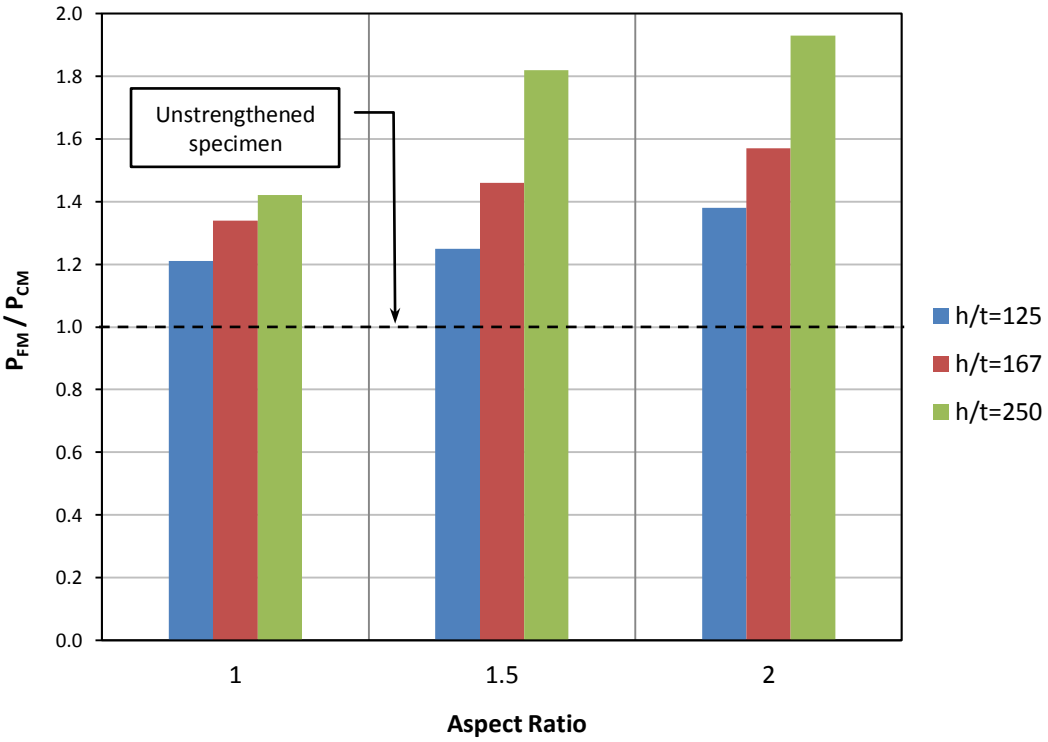

(**b**) Effect of slenderness ratio (h_w/t_w)

Figure (7.12): Variations of the ratio $\boldsymbol{P_{FM} / P_{CM}}$ with the aspect and slenderness ratios.

7.4 PROPOSED DESIGN METHOD

Out of many design equations available in the literature for steel plate girders loaded mainly in shear, four have been chosen as candidates to be checked against the range of data in this work. These four equations will be filtered in this section and the best one among them will be chosen to be modified both for the unstrengthened and FRP strengthened specimens numerically tested in the last parametric study. The equations were previously illustrated in Chapter 2 section (2.2.2.3) where, generally, the ultimate failure load (P_{ult}) is the sum of the buckling load and the post-buckling reserve of strength due to the tension field action. However, these equations will be further discussed in the followings:

Basler's Equation (Basler, 1963)**:**

$$P_{ult} = \tau_{cr} . h_w . t_w + \frac{\sigma_{yw} . h_w . t_w}{2\sqrt{1+\alpha^2}} \left(1 - \frac{\tau_{cr}}{\tau_{yw}}\right) \quad (7.16)$$

$$\tau_{cr} = \frac{k_s \pi^2 E}{12(1-v^2)} \left(\frac{t_w}{h_w}\right)^2 \quad (7.17a)$$

$$k_s = 5.34 + \frac{4.0}{(a_w/h_w)^2} \qquad a_w/h_w \geq 1 \quad (7.17b)$$

where

P_{ult} the ultimate shear load capacity of the plate girder panel,

τ_{cr}: the critical buckling shear stress based on simply supported boundary conditions,

τ_{yw}: the shear yield stress of web material= $\sigma_{yw}/\sqrt{3}$,

σ_{yw}: the tensile yield stress of web material,

h_w: the clear depth of web plate between flanges,

t_w: the thickness of the web plate,

α: the aspect ratio of web panel = a_w/h_w, and

a_w: the clear width of web panel between stiffeners.

Basler-Gaylord Equation (Gaylord and Gaylord, 1972)**:**

As mentioned earlier in Chapter 2, it was pointed first by Gaylord and later by Fujii (1971) that Equation (7.16) does not actually represent the true resistance of Basler model which is correctly given by

$$P_{ult} = \tau_{cr}\, h_w t_w + \frac{\sigma_{yw} h_w t_w}{2\sqrt{1+\alpha+\alpha^2}}\left(1 - \frac{\tau_{cr}}{\tau_{yw}}\right) \quad (7.18)$$

Cardiff Method (Porter et. al, 1975)**:**

The Cardiff method is not just an equation and requires either a Matlab programme or a spreadsheet to utilize it because it is a lower bound theorem and requires the tension field inclination angle (θ) to be changed until the maximum load is achieved. The method is fully described in Appendix (B); however, it can be summarized in the following equations:

$$P_{ult} = \tau_{cr}\, h_w t_w + \sigma_t^y t_w\, sin^2\theta(C_t + C_b) + \sigma_t^y t_w\, h_w\, sin^2\theta(\cot\theta + \cot\theta_d) \quad (7.19a)$$

$$\sigma_t^y = -\frac{3}{2}\tau_{cr} \sin 2\theta_d + \left[{\sigma_{yw}}^2 + {\tau_{cr}}^2\left\{\left(\frac{3}{2}\sin 2\theta_d\right)^2 - 3\right\}\right]^{1/2} \quad (7.19b)$$

$$C_t = \frac{2}{\sin\theta}\left[\frac{M_{pt}}{\sigma_t^y . t_w}\right]^{1/2} \quad (7.19c)$$

$$C_b = \frac{2}{\sin\theta}\left[\frac{M_{pb}}{\sigma_t^y . t_w}\right]^{1/2} \quad (7.19c)$$

where

θ: the angle of inclination of the tension field in the web plate (variable),

θ_d: the angle of inclination of the diagonal of the web plate (constant),

M_{pt}: the plastic moment of the top flange,

M_{pb}: the plastic moment of the bottom flange.

Calladine Method (Calladine, 1973)**:**

Calladine's method is a plastic upper bound method derived on the basis of thin-walled web plates. The method is fully described in Appendix (A); however, the solution depends on the following equations:

$$P_{ult} = \frac{q_l . t_w . h_w . \sigma_{yw}}{2} \quad (7.20a)$$

$$\xi = \left(\frac{x^2 b}{8l}\right)\tan\beta \quad (7.20b)$$

$$q_l = \left(\frac{xb}{l} + 1\right)\tan\beta \quad (7.20c)$$

where

ζ: the dimensionless flange plastic moment with the properties of the web,

q_l: the dimensionless resisting shear force,

l: the inclined length of the developed tension field zone,

x: factor representing the distance of the plastic hinge from the applied load.

7.4.1 Testing the Four Candidate Equations

Table 7.4 shows the calculated ultimate shear load (P_{ult}) according to each one of the four candidate equations and compares it with the finite element model predictions for the unstrengthened specimens. Figure (7.13) shows the variation of the design ratio (P_{ult}/P_{CM}) with the range of variables in this parametric study.

Table 7.4: ultimate loads calculated according to the four candidate equations in comparison to the finite element model predictions

			Basler		**Basler-Gaylord**		**Cardiff**		**Calladine**	
a_w/h_w	h_w/t_w	P_{CM}, kN	P_{ult}, kN	$\frac{P_{ult}}{P_{CM}}$	P_{ult}, kN	$\frac{P_{ult}}{P_{CM}}$	P_{ult}, kN	$\frac{P_{ult}}{P_{CM}}$	P_{ult}, kN	$\frac{P_{ult}}{P_{CM}}$
1.0	250	113.95	105.98	0.93	91.59	0.80	134.10	1.18	118.58	1.04
1.0	167	181.26	179.02	0.99	163.26	0.90	208.88	1.15	159.68	0.88
1.0	125	278.25	276.13	0.99	265.97	0.96	309.65	1.11	194.04	0.7
1.5	250	90.67	85.68	0.94	74.50	0.82	104.49	1.15	92.3	1.02
1.5	167	155.58	149.01	0.96	135.53	0.87	168.03	1.08	122.79	0.79
1.5	125	252.89	236.94	0.94	225.07	0.89	260.26	1.03	153.62	0.61
2.0	250	80.66	71.74	0.89	63.54	0.79	86.09	1.07	70.14	0.87
2.0	167	151.65	129.15	0.85	118.94	0.78	143.78	0.95	95.00	0.63
2.0	125	241.04	212.38	0.88	202.71	0.84	231.32	0.96	115.89	0.48

From both Table 7.4 and Figure (7.13) it can be seen that Calladine method succeeded only in predicting the ultimate load for specimens with low slenderness ratio of (h_w/t_w =250). This is expected because the method is meant for very slender web panels. That is why Calladine method was excluded at this early stage. However, for the other three methods, it can be seen that the data is rather disoriented with no obvious pattern. Nevertheless, Basler's method (Equation 7.16) succeeded the best among them in predicting the ultimate load capacity.

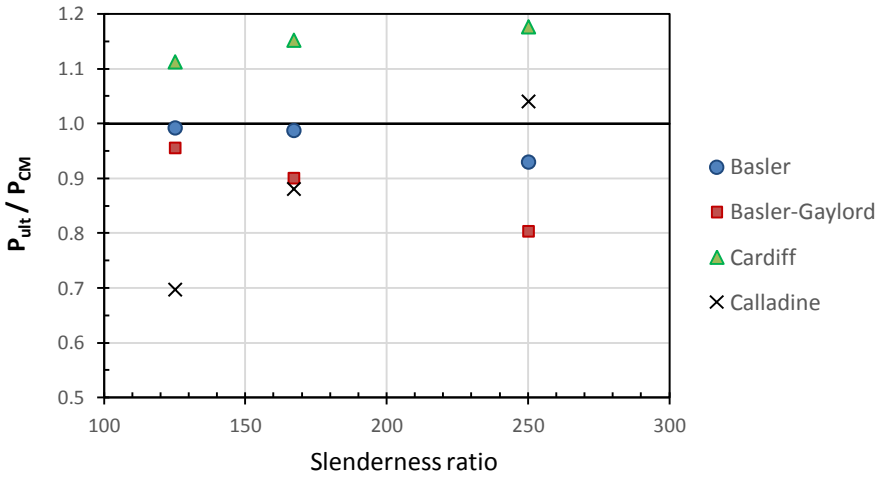

(**a**) a_w/h_w =1.0

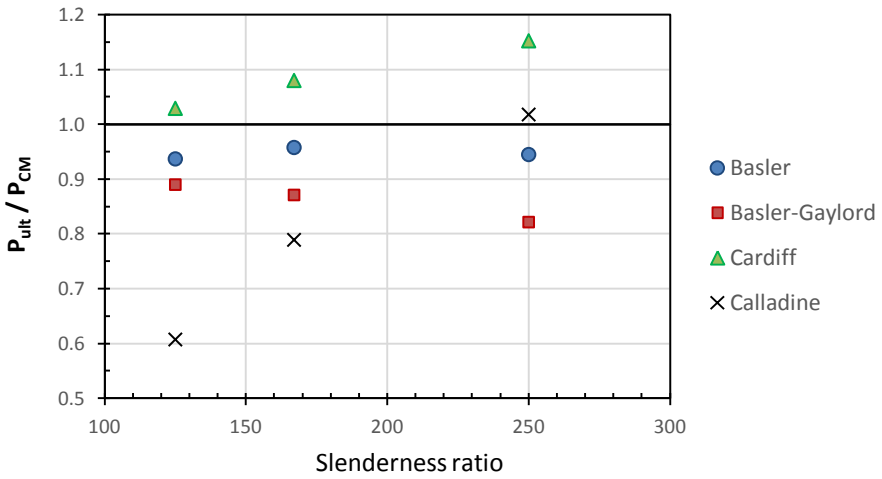

(**b**) a_w/h_w =1.5

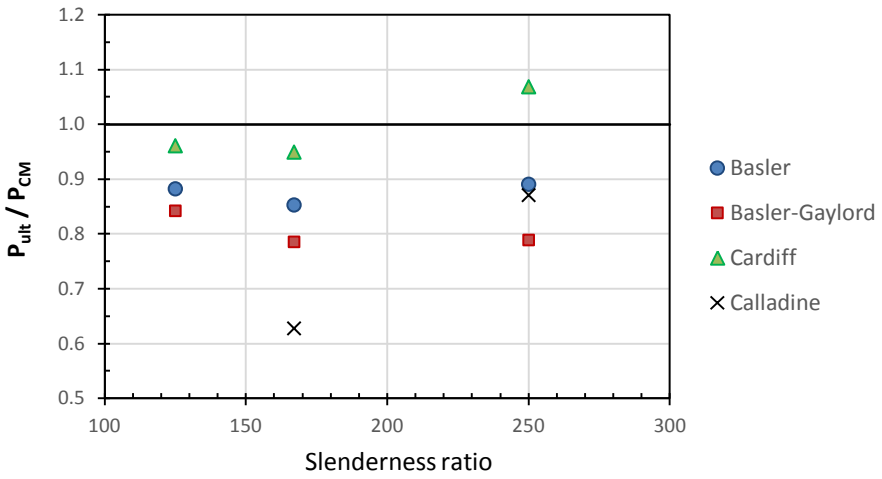

(**c**) a_w/h_w =2.0

Figure (7.13): Variations of the ratio $\boldsymbol{P_{ult} / P_{CM}}$ with the aspect and slenderness ratios.

However, the remaining three methods (Basler, Basler-Gaylord, and Cardiff) are going to be tested again for their compatibility with the new critical buckling shear stress calculated on the basis of the new shear buckling coefficients proposed previously in Chapter 3. This step is going to be performed by deducting the critical buckling shear load part of the equation which is usually calculated using the simply supported boundary conditions as follows:

$$P_{cr} = \frac{k\,\pi^2 E}{12(1-\upsilon^2)}\left(\frac{t_w}{h_w}\right)^2 h_w.t_w \qquad (7.21a)$$

where

$$k = k_s = 5.34 + \frac{4.0}{(a_w/h_w)^2} \qquad a_w/h_w \geq 1 \qquad (7.21b)$$

and then adding the same part after recalculating it with the new proposed shear buckling coefficients as follows:

$$k = k_s + \frac{0.9(k_{sf}-k_s)}{1+e^{-\alpha\left(\frac{t_f}{t_w}-\beta\right)}} \qquad (7.21c)$$

where:

$$\alpha = 2.5 \text{ and } \beta = \frac{a_w}{h_w} + 0.5 \qquad (7.21d)$$

and

$$k_{sf} = 8.98 + \frac{5.61}{(a_w/h_w)^2} - \frac{1.99}{(a_w/h_w)^3} \qquad a_w/h_w \geq 1 \qquad (7.21e)$$

The final results of this step are shown in Table 7.5 and Figure (7.14). From this table and the figure it can be seen that that the data started to shape in a more homogeneous pattern with detectable linear trends. This time (after exchanging the critical buckling shear stress), the updated Basler and Cardiff methods turned out to be rather unconservative and overestimating the ultimate shear strength while the updated Basler-Gaylord (Equation 7.18) is giving the closest predictions to the range of data in the current work.

This is why the updated Basler-Gaylord equation is chosen as the best candidate to be modified in the next sections both for the unstrengthened and FRP strengthened specimens. It is worth mentioning that the calculated value for the ultimate strength of the unstrengthened control specimen (SP-1) using the updated

Basler-Gaylord equation is 84.47kN in comparison to 87.87kN from the experimental test leaving a safety factor of approximately 4%.

Table 7.5: Modified ultimate loads recalculated according the new buckling stress

			S.S. BCs	Prop.	Basler		Basler-Gaylord		Cardiff	
a_w/h_w	h_w/t_w	P_{CM}, kN	P_{cr}, kN	P_{cr}, kN	P_{ult}, kN	$\frac{P_{ult}}{P_{CM}}$	P_{ult}, kN	$\frac{P_{ult}}{P_{CM}}$	P_{ult}, kN	$\frac{P_{ult}}{P_{CM}}$
1.0	250	113.95	27.59	36.23	114.62	1.01	100.23	0.88	142.74	1.25
1.0	167	181.26	93.13	122.21	208.10	1.15	192.34	1.06	237.96	1.31
1.0	125	278.25	220.75	288.22	343.60	1.23	333.44	1.20	377.12	1.36
1.5	250	90.67	21.04	31.01	95.65	1.05	84.47	0.93	114.46	1.26
1.5	167	155.58	71.00	104.44	182.45	1.17	168.97	1.09	201.47	1.29
1.5	125	252.89	168.28	242.04	310.70	1.23	298.83	1.18	334.02	1.32
2.0	250	80.66	18.74	28.79	81.79	1.01	73.59	0.91	96.14	1.19
2.0	167	151.65	63.25	96.39	162.29	1.07	152.08	1.00	176.92	1.17
2.0	125	241.04	14.92	212.42	274.88	1.14	265.21	1.10	293.82	1.22

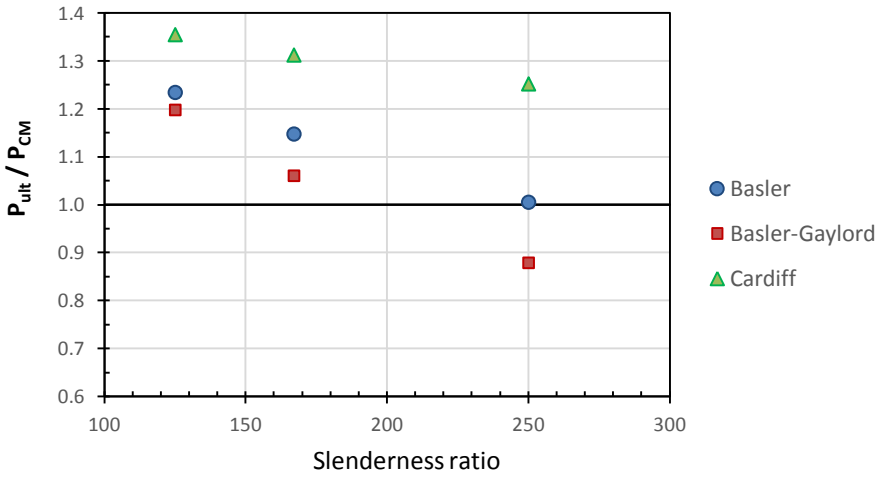

(**a**) a_w/h_w =1.0

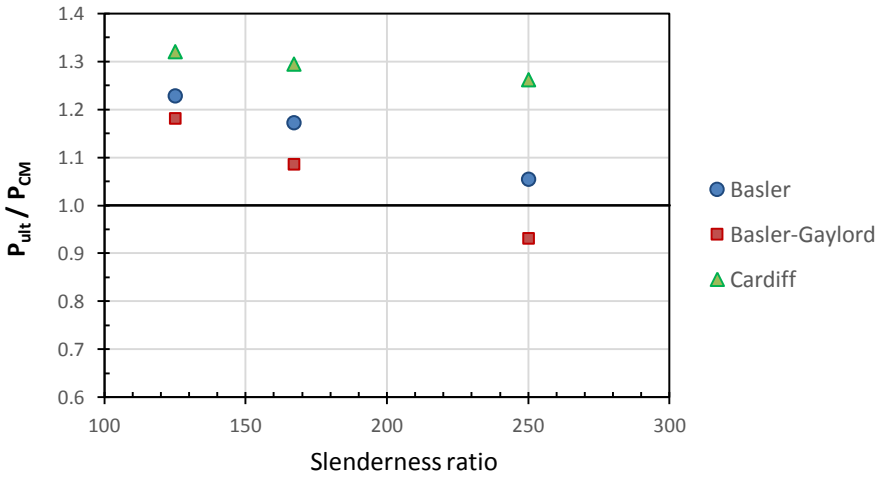

(**b**) a_w/h_w =1.5

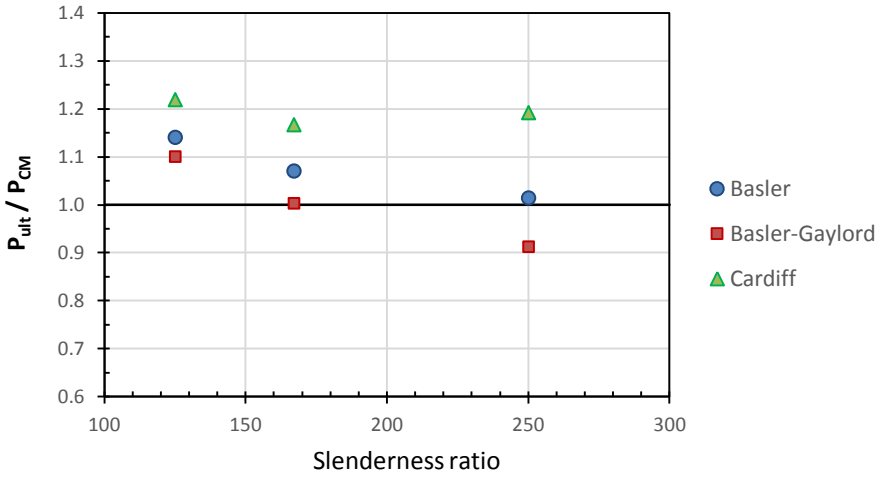

(**c**) a_w/h_w =2.0

Figure (7.14): Variations of the ratio P_{ult} / P_{CM} with the aspect and slenderness ratios for the updated equations.

7.4.2 The Final Proposed Equation

In the previous section, the updated Basler-Gaylord equation succeeded the best in representing the range of data within this work after substituting the new proposed critical buckling shear stress. However, this does not mean that it fits the data in the best way. For this reason, a modification factor was obtained using multivariate regression analysis taking into consideration the effective variables in the behaviour of steel plate girders loaded in shear; mainly, the aspect and slenderness ratios. The modification factor here is called the action factor as it combines the effect of both the aspect and slenderness ratios. The action factor (*AF*) can be written as follows:

$$AF = \left[1 - \left(0.3 - 0.1\frac{a_w}{h_w}\right)\right] \times \left[2.5 - \left(1.5\frac{\frac{h_w}{t_w}}{125}\right)\right] \quad (7.22)$$

Recalculating the ultimate shear load using the modified Basler-Gaylord equation after multiplying it by the action factor (*AF*) yields the results shown in Table 7.6 which is illustrated in Figure (7.15) in comparison to the previous results for the same equation (i.e. before multiplying it by the action factor *AF*). It can be seen that the results now are much more convenient and reliable as they do not overestimate the ultimate shear strength. This superior behaviour can be seen as well from the increased correlation represented by the factor R^2 for the equation estimations before (R^2 =0.993) and after (R^2 =0.997) multiplying it by the action factor.

Table 7.6: Modified Basler equation before and after multiplying it by AF

			Basler-Gaylord		Basler-Gaylord × AF	
a_w/h_w	h_w/t_w	P_{CM}, kN	P_{ult}, kN	$\frac{P_{ult}}{P_{CM}}$	P_{ult}, kN	$\frac{P_{ult}}{P_{CM}}$
1.0	250	113.95	100.23	0.88	110.25	0.97
1.0	167	181.26	192.34	1.06	173.26	0.96
1.0	125	278.25	333.44	1.20	266.75	0.96
1.5	250	90.67	84.47	0.93	90.81	1.00
1.5	167	155.58	168.97	1.09	156.40	1.01
1.5	125	252.89	298.83	1.18	254.01	1.00
2.0	250	80.66	73.59	0.91	77.27	0.96
2.0	167	151.65	152.08	1.00	144.54	0.95
2.0	125	241.04	265.21	1.10	238.69	0.99
		R^2	0.993		0.997	

Hence the final proposed equation for the analysis of unstrengthened steel plate girder can be stated as follows:

$$P_{ult} = \left\{\tau_{cr}\, h_w t_w + \frac{\sigma_{yw} h_w t_w}{2\sqrt{1+\alpha+\alpha^2}}\left(1-\frac{\tau_{cr}}{\tau_{yw}}\right)\right\} \times \left[1-\left(0.3-0.1\frac{a_w}{h_w}\right)\right] \times \left[2.5-\left(1.5\frac{\frac{h_w}{t_w}}{125}\right)\right] \quad (7.23a)$$

where

$$\tau_{cr} = \frac{k\,\pi^2 E}{12(1-v^2)}\left(\frac{t_w}{h_w}\right)^2 \quad (7.23b)$$

$$k = k_s + \frac{0.9(k_{sf}-k_s)}{1+e^{-\alpha\left(\frac{t_f}{t_w}-\beta\right)}} \quad (7.23c)$$

$$\alpha = 2.5 \text{ and } \beta = \frac{a_w}{h_w} + 0.5 \quad (7.23d)$$

$$k_s = 5.34 + \frac{4.0}{(a_w/h_w)^2} \qquad a_w/h_w \geq 1 \quad (7.23e)$$

$$k_{sf} = 8.98 + \frac{5.61}{(a_w/h_w)^2} - \frac{1.99}{(a_w/h_w)^3} \qquad a_w/h_w \geq 1 \quad (7.23f)$$

Some previously mentioned equations have been repeated here to make sure that the right equations are used for calculating the critical buckling shear stress (τ_{cr}).

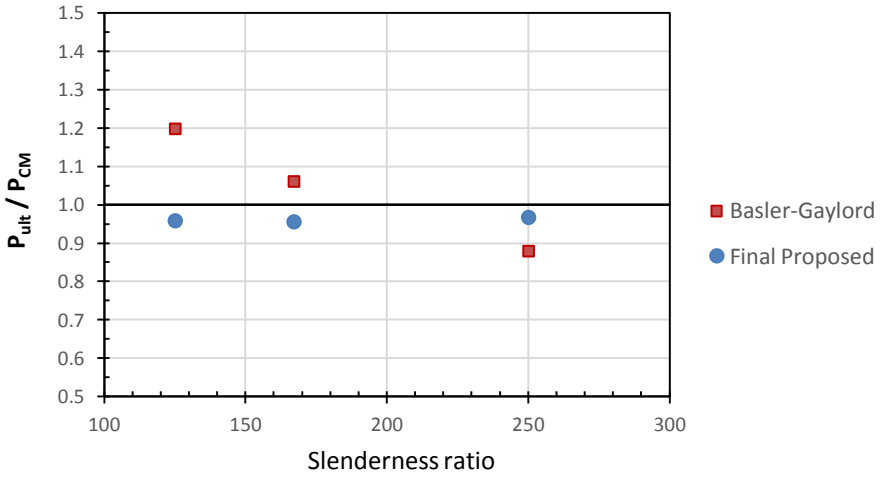

(**a**) a_w/h_w =1.0

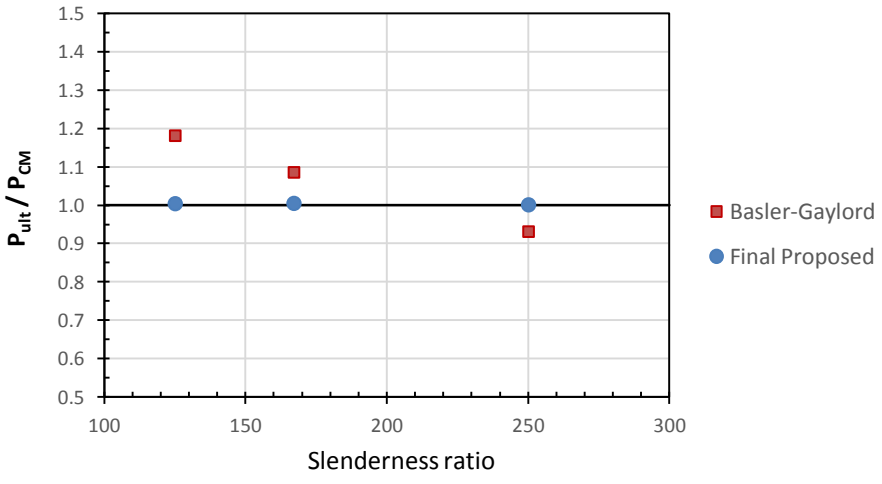

(**b**) a_w/h_w =1.5

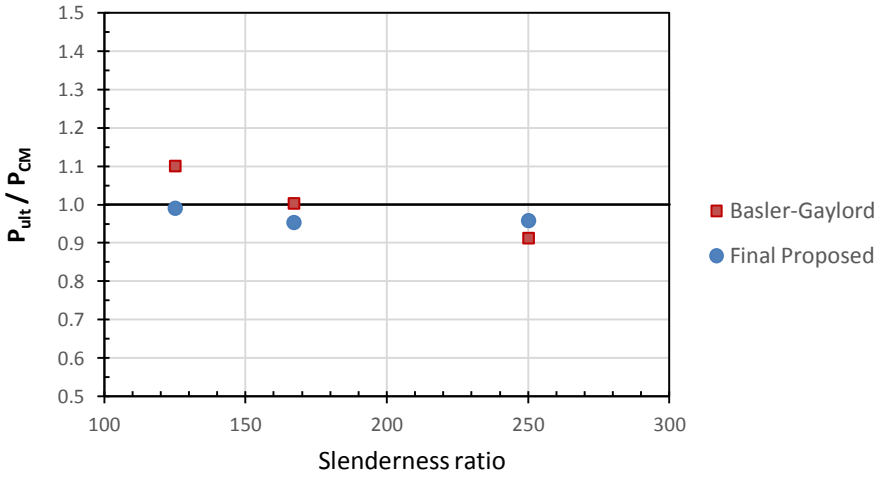

(**c**) a_w/h_w =2.0

Figure (7.15): Variations of the ratio $\boldsymbol{P_{ult} / P_{CM}}$ with the aspect and slenderness ratios for the final proposed equation.

7.4.3 A New Equation for FRP Strengthened Steel Plate Girders

The new proposed Equation (7.23) is meant for unstrengthened steel plate girders and it does not take the effect of the FRP strengthening yet. In this section, the FRP strengthening effect in increasing the ultimate capacity of steel plate girders is going to be included.

There are many ways to include the FRP strengthening effect into the proposed Equation (7.23); however, in the current work it was decided to use the simplest among them. This can be achieved by incorporating a simple empirical fibre factor (F) which is going to be added to Equation (7.23). This fibre factor (F) can be expressed as follows:

$$F = V_{cr}\left(\frac{a_w}{h_w} + 1\right) \tag{7.24a}$$

where V_{cr} in this equation is the shear force resulting from the critical buckling shear stress of a similar simply supported web steel plate having an aspect ratio of 1.0 and a slenderness ratio of 250. Mathematically, V_{cr} can be expressed as follows:

$$V_{cr} = \frac{9.34\,\pi^2 E_s\,{t_w}^2}{3000\,(1-\nu^2)} \tag{7.24b}$$

V_{cr} = 27kN, and is constant with respect to the range of data in this study. Hence the final form of the proposed equation for the strengthened steel plate girders in this work (P_{Fult}) can be expressed as follows:

$$P_{Fult} = \left[\left\{\tau_{cr}\,h_w t_w + \frac{\sigma_{yw} h_w t_w}{2\sqrt{1+\alpha+\alpha^2}}\left(1-\frac{\tau_{cr}}{\tau_{yw}}\right)\right\} \times \left\{1-\left(0.3-0.1\,\frac{a_w}{h_w}\right)\right\} \times \left\{2.5 - \left(1.5\,\frac{\frac{h_w}{t_w}}{125}\right)\right\}\right] + F \tag{7.25}$$

Table 7.7 compares the results of Equation (7.25) with the data obtained from the composite finite element model in this work. The same data is illustrated in Figure (7.16). From the table and the figure, it can be seen that the equation gives a good estimation of the ultimate shear load for the FRP strengthened steel plate girders with respect to the range of data in the current work. The relatively low R^2 value of 0.986 (in comparison to Equation 7.23) can be justified by the fact that the slenderness ratio

was averaged and only the aspect ratio effect was taken into considerations in deriving the fibre factor (F). This was done to keep the equation as simple as possible for practical convenience.

Table 7.7: Comparison of the FEM results with the predictions of Equation (7.25)

a_w/h_w	h_w/t_w	P_{FM}, kN	P_{Fult}, kN	$\frac{P_{Fult}}{P_{FM}}$
1.0	250	161.43	164.25	1.02
1.0	167	246.47	227.26	0.92
1.0	125	335.91	320.75	0.95
1.5	250	165.29	158.31	0.96
1.5	167	226.66	223.90	0.99
1.5	125	315.19	321.51	1.02
2.0	250	155.52	158.27	1.02
2.0	167	238.22	225.54	0.95
2.0	125	331.41	319.69	0.96
		R^2	**0.986**	

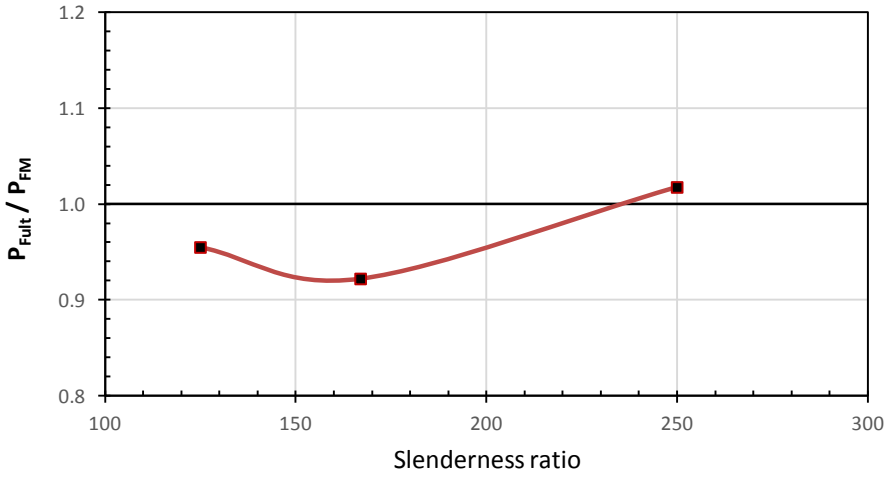

(**a**) a_w/h_w =1.0

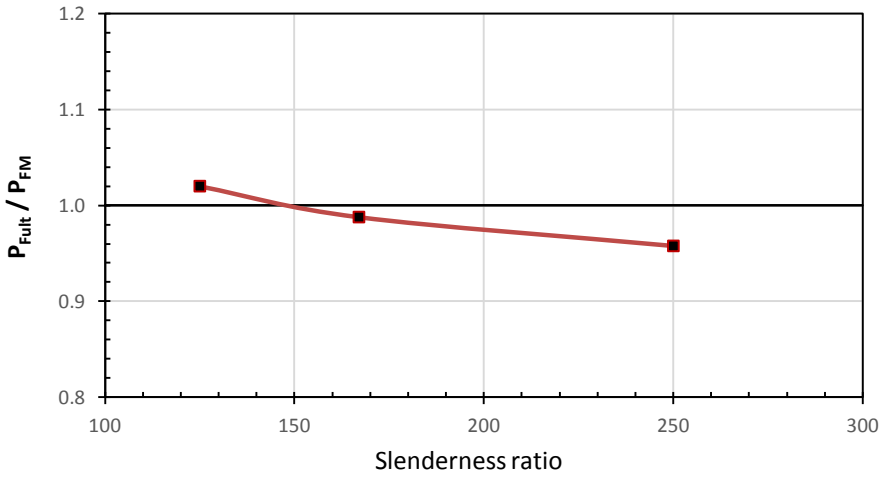

(**b**) a_w/h_w =1.5

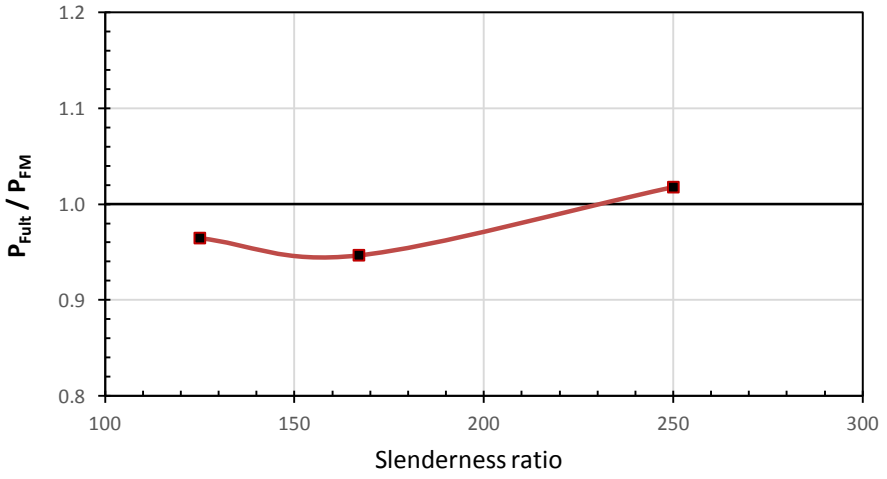

(**c**) a_w/h_w =2.0

Figure (7.16): Variations of the ratio P_{Fult} / P_{FM} with the aspect and slenderness ratios for the final proposed equation after adding the fibre factor F.

7.4.4 Further Additions to the Proposed Design Method

Until now, the proposed design method deals only with the ultimate capacity of the specimen. This is part of this study but it is not the core of it. The core of this study is about reducing the breathing stresses at the tension corner of the steel web plate to increase its life cycle. This was suggested to be done by stiffening the web plate against out-of-flatness deformations represented by the out-of-plane displacement using the optimized proposed strengthening technique.

For this reason, the 18 buckling curves in the finite element method parametric study were reproduced as can be seen in Figure (7.17) to find new patterns that could help in proposing simple design buckling curves to help estimating the reduction in the out-of-plane displacements. In the future, this could lead to a relation between these buckling curves and the maximum surface and secondary bending strains in the web steel plate and consequently estimating the enhancement in the fatigue life of the strengthened steel plate girder.

By examining Figure (7.17), an obvious pattern can be detected. The pattern for the control unstrengthened specimens is trilinear and can be described by two points. The first point P_1 is where the first major change in the slope of the curve occurs (critical buckling stress) and the second point P_2 is where the second major change in the slope of the curve takes place (heading towards the yielding plateau). With respect to the strengthened specimens, the behaviour is bilinear and can be describe using only one point (P) where the slope of the curve is changed dramatically directly heading towards the failure plateau. Each point of course can be defined using two coordinates *x* and *y*. The *x*-coordinate is the out-of-plane displacement in millimetres and the *y*-coordinate is the shear load in kilo Newton's. This is shown in Figure (7.18) and can be described using the following set of equations:

For the control unstrengthened specimens, the coordinates of point P_1 (P_{1x} and P_{1y}), can be found as follows:

$$P_{1x} = \frac{h_w/t_w}{250} \tag{7.26a}$$

$$P_{1y} = P_{cr} = \frac{k_s \pi^2 E}{12(1-v^2)} \left(\frac{t_w}{h_w}\right)^2 h_w . t_w \tag{7.26b}$$

On the other hand P_2 can be located as follows:

$$P_{2x} = \frac{h_w/t_w}{50} + 1 \quad (7.26c)$$

$$P_{2y} = P_{ult}\ (Equation\ 7.23) \quad (7.26d)$$

For the strengthened specimens, the coordinates of the point P can be located as follows:

$$P_x = \frac{h_w/t_w}{125} \quad (7.27a)$$

$$P_y = P_{Fult}\ (Equation\ 7.25) \quad (7.27b)$$

Figure (7.19) shows a typical design buckling curve illustrating Equations (7.26) and (7.27).

It is important to note that these design bucking curves are sensitive to the initial imperfection which was taken constant at h_w/1250 in this parametric study as mentioned earlier and further investigation is required for the effect of initial imperfection on them. However, going back to Figure (3.10) in Chapter 3 would give a very good idea about how the initial imperfection affects the behaviour of the buckling curve. Hence, it could be used as an indicator for adjusting the proposed design curves accordingly but this requires another parametric study with respect to the FRP strengthened plate girders which is not provided in this work.

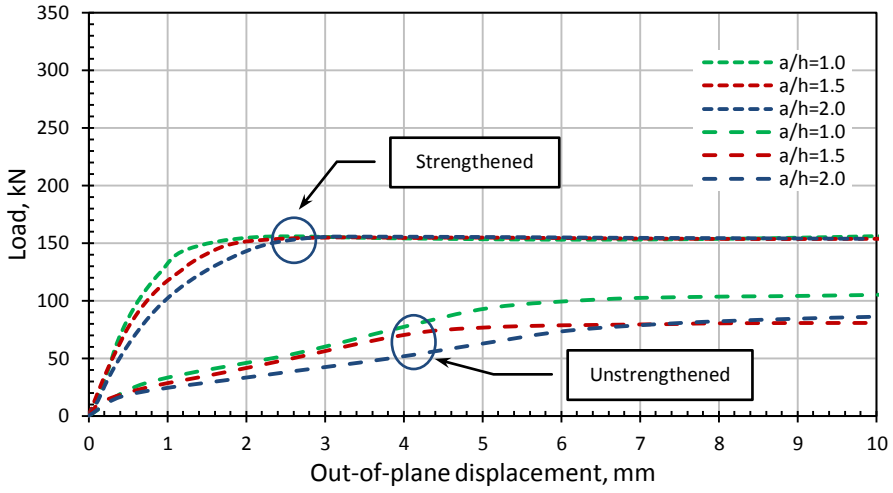

(**a**) h_w/t_w =250

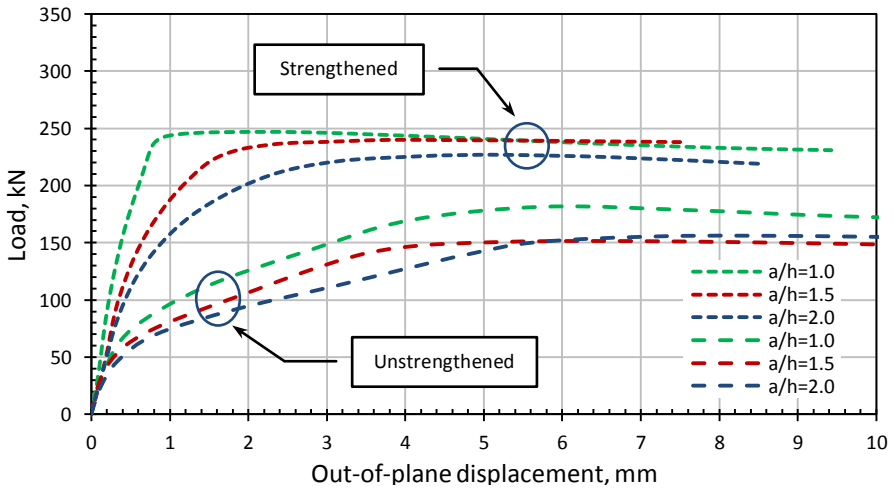

(**b**) h_w/t_w =167

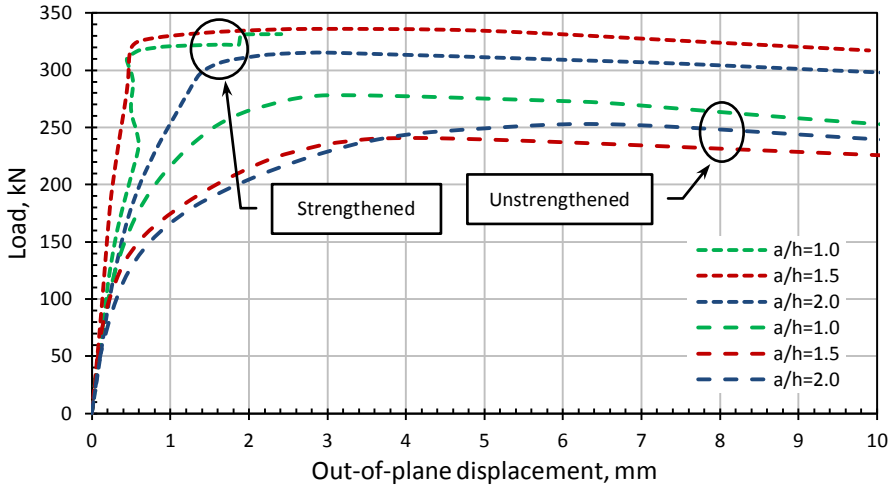

(**c**) h_w/t_w =125

Figure (7.17): Buckling curves reproduced with respect to their slenderness ratio instead of their aspect ratios.

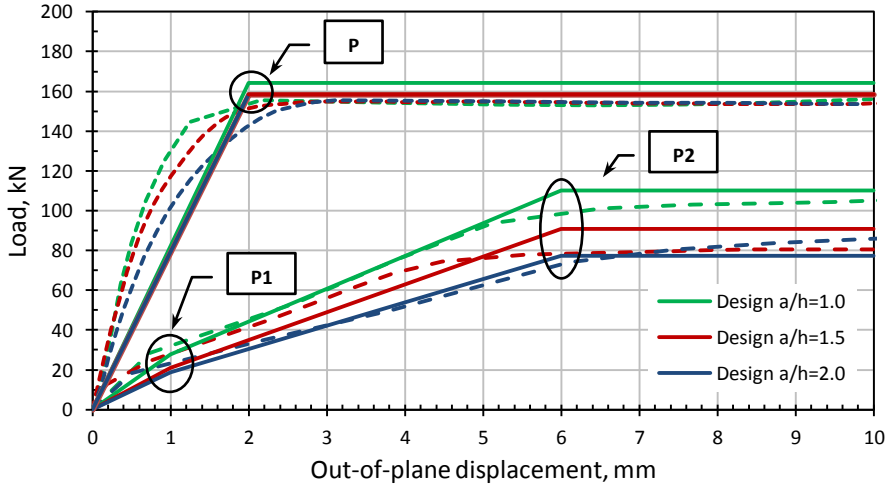

(**a**) h_w/t_w =250

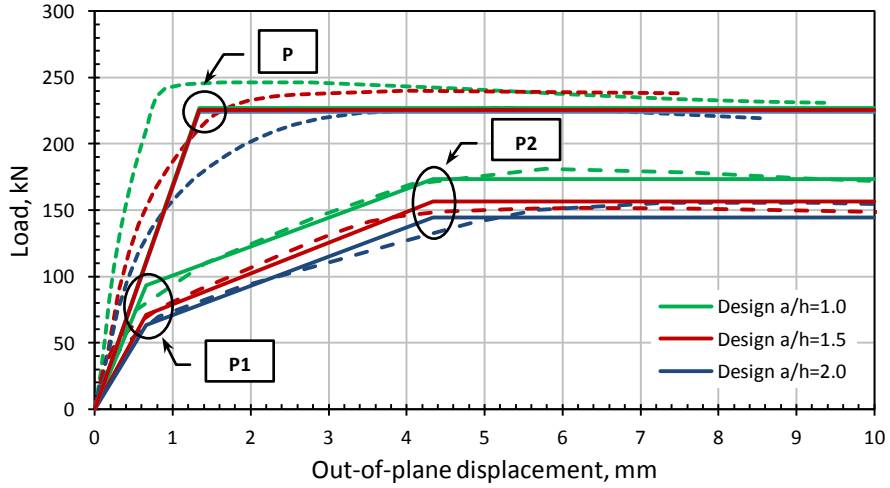

(**b**) h_w/t_w =167

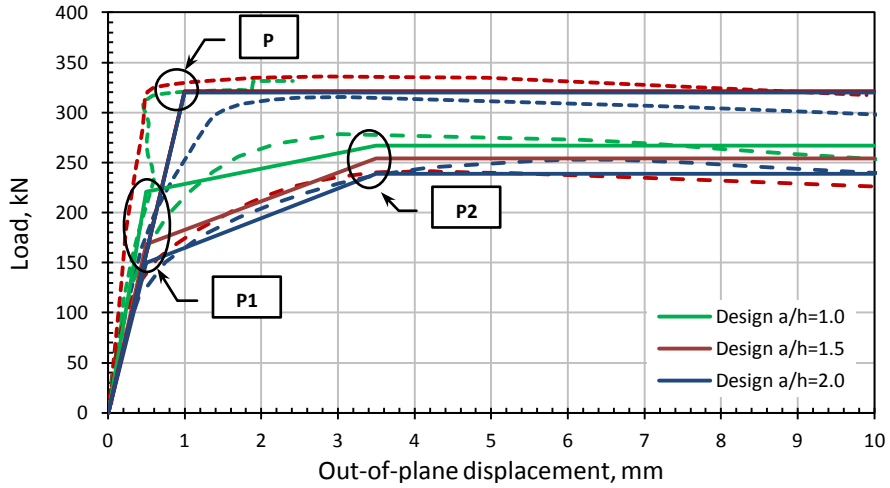

(**c**) h_w/t_w =125

Figure (7.18): Proposed design buckling curves compared to the corresponding finite element predicted ones.

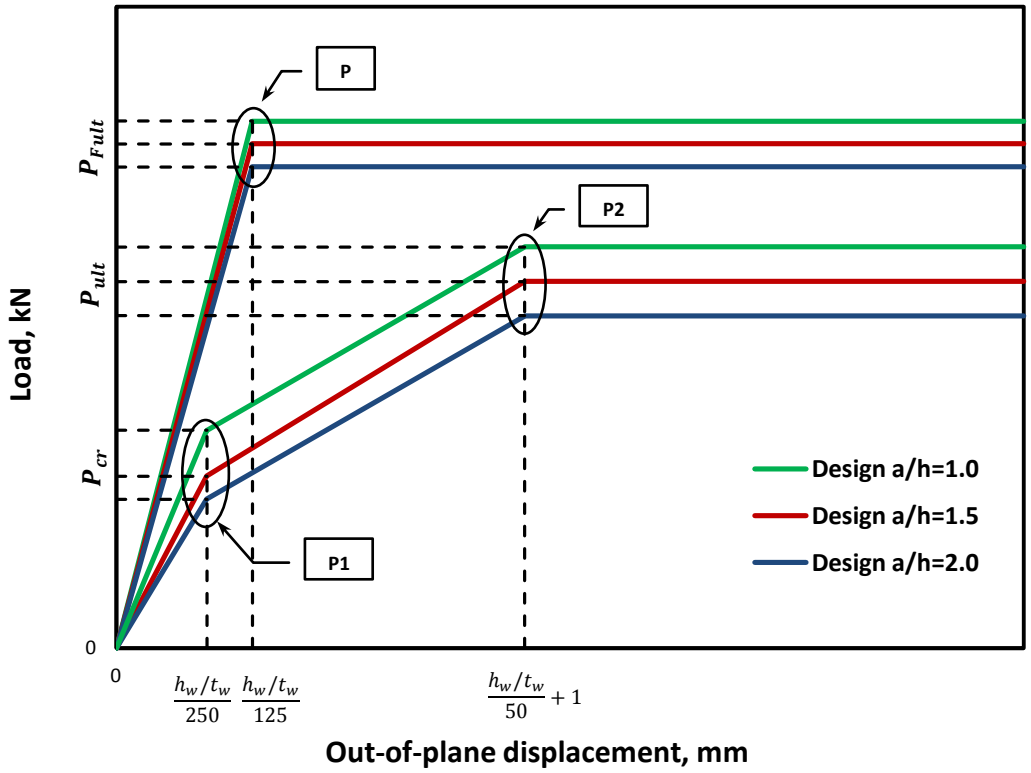

Figure (7.19): Typical proposed design buckling curve for a specific slenderness ratio.

7.4.5 Integrated Proposed Design Method

In the last three sections, a design equation was proposed to estimate the ultimate shear capacity for both unstrengthened (P_{ult}) and FRP strengthened (P_{Fult}) steel plate girders in addition to the proposed design shear buckling curves.

The proposed strengthening technique has proven its efficiency throughout the experimental programme showing neither debonding nor delamination under both static and cyclic loading. In fact, it did not only increase the ultimate capacity and the stiffness of the plate girders significantly, but it also managed to maintain and improve the typical ductile failure type of associated with steel plate girders. All the above mentioned facts are in the favour of using the proposed FRP strengthening technique without any restrictions; however, this is practically impossible for different reasons including, but not limited to the followings:

- This is a novel proposed strengthening technique which has not been used or tested before in any other study.
- The experimental and numerical tests performed in this study are limited to the size and range of variables studied only and cannot be generalized without further investigation.
- Environmental and temperature effects were not taken into considerations in this study which could lead to certain defects in the performance of the proposed strengthening technique.
- The effect of inconsistent epoxy thickness and the possible existence of weak points and air bubbles in the bonding layer are not studied and needs to be taken into considerations.
- No alternative mechanical anchorage was suggested in this work to deal with sudden loss of bond that could happen during extreme events like fire or earthquakes.

For all the above mentioned reasons, it is recommended that only the stiffness increase (the reduced out-of-plane displacement) is taken into consideration in the design process. This will lead to lower surface and secondary bending strains at the web plate welded boundaries, and consequentially increase the fatigue life of the plate girder. This by itself is a very important achievement because aging of structures and bridges is an increasing problem having huge economical consequences all over the world.

In spite the fact that the proposed strengthening technique succeeded in increasing the ultimate shear strength for the FRP strengthened steel plate girders by approximately 90%, it is recommended not to rely on it in the design until further investigation had taken place and more tests are performed. Meanwhile, the ultimate shear capacity should be limited to the ultimate capacity of the unstrengthened steel plate girders as follows:

$$P_{Fult} \leq P_{ult} \tag{7.28}$$

This way the bridge can still survive in case of extreme events caused the FRP to lose all its bonding capacity. Figure (7.20) illustrates this restraining condition.

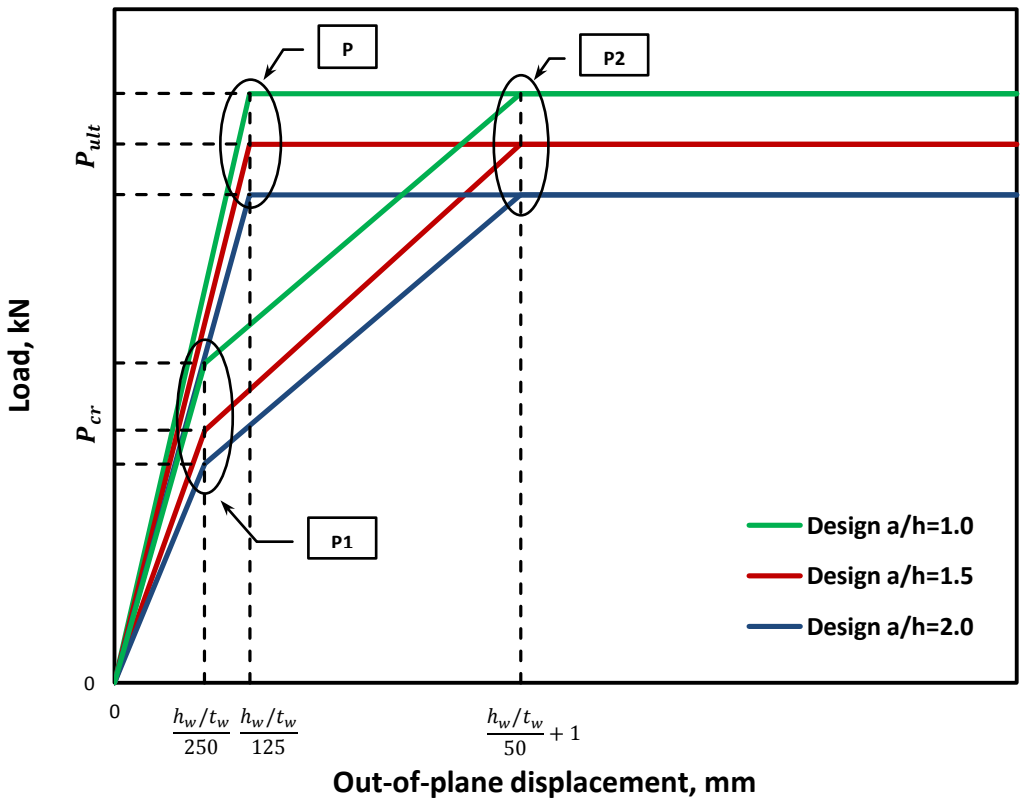

Figure (7.20): Typical proposed design buckling curve for a specific slenderness ratio- Integrated design version.

7.5 SUMMARY AND CONCLUSIONS

This chapter was dedicated for proposing a new design method that could work both for the unstrengthened and FRP strengthened steel plate girders. For this reason, a composite nonlinear FRP-steel finite element model was proposed at the beginning of this chapter which included a method to calculate the nine engineering constants needed for the orthogonal constitutive material model for the FRP composite. This composite model was validated against the experimental results available from Chapter 6 and showed good agreement. Then, the numerical composite model was used to perform a parametric study that helped in extending the range of variables studied in this work. The considered variables were mainly the aspect and slenderness ratios as these are the main parameters that affect the shear strength of a plate girder.

A total of 18 specimens were tested numerically 9 of them were unstrengthened control steel plate girders and the other 9 were FRP strengthened ones. Only the optimized strengthening technique (CFRP-45°) was used in this parametric study. The results of the finite element model were used as benchmarks for the proposed design method.

A design equation was proposed both for the unstrengthened and FRP strengthened steel plate girders which showed good correlation with data in this work. In addition, the behaviour of the buckling curves was examined carefully for the available range of data and simple design shear buckling curves were proposed. This is believed to help in estimating the stiffening effect of the FRP strengthening technique adopted in this study and hence could be linked to the maximum surface and secondary bending strains in the future to estimate the enhancement in the fatigue life of the FRP strengthened steel plate girders.

CHAPTER REFERENCES

BARBERO E.J. (2008). "Finite element analysis of composite materials," CRC Press, USA, 359 pp.

BASLER K. (1963). "Strength of plate girders in shear," Trans. ASCE 128, pp. 683-719.

CALLADINE C.R. (1973). "A plastic theory for collapse of plate girders under combined shearing and bending moment," Journal of the Structural Engineer, Vol. 51, No. 4, pp. 147-154.

FUJII, T., FUKOMOTO, Y., NISHINO, F. and OKUMURA, T. (1971). "Research works on ultimate strength of plate girders and Japanese provisions on plate girder design,". IABSE Colloquium, 21-48.

GAYLORD E.H. and GAYLORD C.N. (1972). "Design of steel structures," McGraw-Hill Book Company, New York, 663 pp.

PORTER D.M., ROCKEY K.C., and EVANS H.R. (1975). "The collapse behaviour of plate girders in shear," Journal of The Structural Engineer, Vol. 53, No. 8, pp. 313-325.

REDDY J.N. (2004). "Mechanics of Laminated Composite Plates - Theory and Analysis," CRC Press, USA, 2nd Edition, 831 pp.

Chapter Eight

Conclusions and Recommendations

8.1 SUMMARY OF WORK

The main idea in the current study is proposing an easy to install, easy to inspect and cost effective FRP strengthening technique to resist the web out-of-plane deformations due to breathing phenomenon and/or strengthening the thin-walled steel structure to endure higher ultimate loads at the same time. This is meant to be achieved without compromising the typical ductile failure associated with steel plate girders as is common with strengthening techniques known to date. Reducing the breathing phenomenon will consequently reduce the surface and secondary bending stresses at the web plate welded boundaries leading to better fatigue performance and prolonged functional life estimation.

This important and ambitious goal was achieved in this study using a new proposed preformed corrugated FRP panel. The proposed strengthening technique depends on bonding this FRP corrugated panel along the compression diagonal of a steel plate girder's web in a 45° alignment scheme. The efficiency of this strengthening technique was proven in this work both under static and cyclic loading regimes.

It was shown that the proposed strengthening technique is capable of stiffening the web plate against breathing (out-of-plane displacement) up to 9 times the unstrengthened ones leading to an increase in fatigue life expectancy between 2.5 to 7 times depending on the applied loading range. In addition, the proposed strengthening technique succeeded in increasing the ultimate shear capacity of the tested steel plate girders by 88%. This was associated with improvement in the ductility of the strengthened specimens up to 2.5 times the unstrengthened ones; this is in contrary to the available strengthening techniques where the usual brittle failure type is a major concern.

The work was presented step by step throughout the pages of the previous seven chapters in this thesis which was divided according to the phases of the experimental and theoretical work done. The first two chapters were introductory

ones where Chapter 1 defined the research problem and Chapter 2 was mainly a comprehensive literature review dealing with different aspects needed in the current study. The conclusions of the remaining chapters will be briefed in the following sections.

8.2 A NEW SHEAR BUCKLING COEFFICIENTS

In Chapter 3, a numerical approach using finite element analysis was adopted to determine the critical buckling shear stress coefficients of steel plate girders with transverse and diagonal stiffeners. The conservative assumption, adopted in most international standards like AISC (1963 and 1994), AASHTO (1973 and 2007), and EN 1993-1-5 (2004), where simply supported boundary conditions are applied at the junction between the web plate, flange, and stiffeners, is revisited and care was made to address the effect of the elastic restraining degree at the junction due to flange and stiffener rigidities. An extensive parametric study to estimate the effect of several important variables on the shear bucking coefficients was performed and a general design equation is proposed (Equation 3.7). This new equation is more efficient in terms of its continuity and correlation to the range of data considered in this work in comparison to the equations previously available in the literature. The effect of transverse stiffener rigidity on the buckling shear stress was studied for the first time in the current work and it has been shown that it does increase the critical buckling shear stress for steel plate girders with an aspect ratio of 1.0 while this increment was insignificant for specimens having aspect ratios of 1.5 and 2.0; refer to Equation (3.7.b).

The effect of web initial imperfection was also studied throughout nonlinear finite element analysis. Three modes of initial imperfection were considered and it was shown that the mode of initial imperfection plays an important role in the behaviour of the buckling curve and the ultimate shear strength at the same time. Generally, lower initial imperfection results in higher ultimate capacity. Specimens with initial imperfection similar to the expected buckling modes always have the lowest buckling stress and specimens with initial imperfection against the expected buckling modes always have the highest buckling stress, while specimens with neutral type of initial imperfection always lie between these two upper and lower

bound limits. However, a simplified linear equation (Equation 3.9) was proposed to reduce the estimated critical buckling stress due to web initial imperfection.

Finally, the shear buckling coefficients for diagonally stiffened plate girders were determined using finite element analysis based on theoretical models solving the shear buckling problem for isosceles triangular plates and a new design equation is proposed (Equation 3.12).

8.3 A NEW FRP STRENGTHENING TECHNIQUE

In Chapter 4 (Phase-1), the geometrical properties of the new proposed FRP corrugated strengthening panel were optimized and its material properties were determined.

Linear buckling finite element analysis was performed to choose the best section among the three proposed ones. The hexagonal FRP corrugated section showed the best performance and managed to reduce the required FRP material by approximately 8 times (volumetrically) and the required bonding epoxy by 7 times.

The material properties for different FRP laminates which have been used in making the proposed corrugated FRP panels were determined using an extensive experimental programme both for the GFRP and CFRP. The resin and the bonding epoxy were chosen using double-lap shear tests and the material mechanical properties for the FRP were measured experimentally using tension tests. These were also compared with the theoretically calculated ones showing a good agreement.

The yield strengths of the used steel plates were determined using tension tests performed on steel dog-bone specimens and the modulus of elasticity was assumed to be the typical 200GPa for the steel throughout this work.

8.4 THE INITIAL STATIC SERIES OF TESTS

In Chapter 5 (Phase-2), the initial series of tests was performed to test the efficiency of the proposed corrugated FRP panel under static shear loading. Thirteen steel plates were strengthened with the proposed preformed corrugated FRP panel and tested using a specially made picture-frame rig. Using this new testing rig led to the conclusion that it is possible to test only the web plate under shear loading instead of having to test the whole plate girder. This actually led to save 95% of the

cost from each test giving us the opportunity to test more specimens and study more variables.

The results of the initial series of tests proved the efficiency of the proposed strengthening technique in increasing the stiffness of the steel plate section up to 3 times and consequently increasing its buckling resistance. In addition to that, the proposed strengthening technique succeeded in preserving the ductile prototype failure associated with intact (unstrengthened) steel plates, which is a very important factor in safety usually neglected by other FRP strengthening techniques. The proposed strengthening technique did not only preserve the ductile failure type but also increased the energy absorption capacity by a factor of 1.5.

No bonding failure could be detected during or after the test even when the steel plate was highly deformed and fully yielded. This is believed to be attributed to the unique design of the FRP corrugated panel where it is strong in the major axis to resist the compression and weak in the minor tension axis to allow the steel plate to deform in tension without having to debond. The variables studied in this series were:

- The effect of FRP material which significantly affected the stiffness and buckling resistance of the strengthened specimens. The CFRP showed more superior behaviour in increasing the stiffness and buckling resistance of the strengthened specimens due to its higher modulus of elasticity than the GFRP.
- The type of section (open versus closed), which showed no significant effect in increasing the stiffness and had no effect on the bonding capacity with respect to the originally proposed open section one.
- The number of the FRP layers used to build the corrugated panel had a significant effect on the behaviour of the strengthened specimens where the 3-layered ones showed higher capacity and much more stable and ductile behaviour especially for the GFRP ones.
- The orientation of the GFRP used, which was taken with respect to the corrugation axis, had a moderate effect on the strength of the strengthened specimens. The 0°-90° succeeded in slightly increasing the ultimate strength

for the 3-layered specimen while it altered the mode of failure to a more brittle one with respect to the 2-layered one.

- The effect of the end cut shape and position of the FRP panel was not very significant in comparing Type-A (i.e. the triangular cut) and Type-B (i.e. the circular cut) where they almost acted the same, but was significant for Type-C (i.e. the long one) even when the mode of failure was altered for the GFRP specimen.

In addition, a geometrical and material non-linear finite element analysis was used to model the test. A simplified picture frame model was utilized in this study to avoid the more numerically expensive original model. The unstrengthened model was able to realistically simulate the behaviour of the specimens throughout all loading stages, while the strengthened model provided convincing results only within working stresses before reaching the failure plateau.

As a final result of this chapter with respect to the optimized FRP section, it was decided to combine the effect of using 3-layered FRP panel with the effect of having Type-C end cut both for GFRP and CFRP materials for further investigation of its efficiency under cyclic loading.

8.5 THE FINAL CYCLIC SERIES OF TESTS

In Chapter 6 (Phase-3), a new specimen representing the end panel of a potential steel plate girder was presented and tested under cyclic loading with typical loading range of 40-80% of the ultimate capacity of the specimen. Six specimens were built and 5 of them were strengthened with the optimized FRP panel taking both CFRP and GFRP into considerations.

The final series of tests was divided into two subsequent series of tests. The first one is the static subsequent series which involved testing 3 specimens (one control and two strengthened with GFRP and CFRP panels) to serve as precursor for the other subsequent cyclic series which involved testing another 3 strengthened specimens for 2 millions cycles of load. The specimens in the subsequent cyclic series involved one GFRP and two CFRP strengthened specimens having different strengthening scheme, namely, diagonal (34°) and 45° strengthening schemes.

It was shown that a considerable increase in the stiffness of the strengthened specimens is evident in the observed reductions of the maximum out-of-plane displacement. The stiffness of the strengthened specimens is assessed to be increased by a factor ranging between 3 to 9 times the stiffness of the corresponding unstrengthened specimen, depending upon the type of the FRP panel used. The breathing phenomenon is also significantly reduced; consequently the surface, membrane and secondary bending stresses are reduced. The maximum surface normal stress at the vicinity of the welded plate boundaries was reduced by 100%, 65%, and 45% for SP-4 (GFRP), SP-5 (CFRP-diagonal), and SP-6 (CFRP-45°); respectively. The maximum surface shear stress was reduced by 204%, 129%, and 164% for SP-4 (GFRP), SP-5 (CFRP-diagonal), and SP-6 (CFRP-45°); respectively.

This reduction in the normal and shear stresses was accompanied by a corresponding reduction in the secondary bending stress which could be as high as the plate yield stress in some cases. The reduction was limited by the low yield strength of 275MPa for the web plate in the current study and it would be even more significant for plates having higher yield strength and in the case strain hardening is taken into consideration. SP-6 (CFRP-45°) behaved the best among all cyclic specimens and showed the best results; however, it did not rank the first in the stress reduction criteria because it experienced the highest loading amplitude. This was demonstrated by another analysis using the same loading range for all three cyclic specimens.

Fatigue analyses indicated that the proposed strengthening technique is able to considerably elongate the life expectancy of the strengthened plate girders by a factor ranging between 2.5 and 7 depending on the applied cyclic loading range. In addition, the proposed strengthening technique did not show any debonding or delamination under both static and cyclic loading which makes it a good candidate for strengthening thin-walled structural members, especially, when ductility is a concern. In fact, the proposed strengthening technique succeeded in improving the energy absorption capacity of the strengthened specimens by a factor ranging between 1.5 and 2.5 times the corresponding control specimen which means that the ductile failure type associated with shear buckling of steel plate girder is not only

maintained, but it was improved as well. This type of ductile failure is not common in other FRP strengthening techniques.

A geometrical and material non-linear finite element model is presented for the steel plate girder which showed very good correlation with test results and was capable of predicting both the strength and deformational behaviour of the tested control specimen with high accuracy.

As a final conclusion, the CFRP-45° strengthening scheme (SP-6) is chosen as the optimized strengthening scheme because it succeeded the best both in reducing the breathing stresses and increasing the ultimate shear capacity of the control specimen by 88%.

8.6 A NEW DESIGN METHOD

In Chapter 7, a new design method that could work both for the unstrengthened and FRP strengthened steel plate girders is proposed. A composite FRP-steel nonlinear finite element model was proposed including a method to calculate the nine engineering constants needed for modelling the orthogonal constitutive material of the FRP composite. This composite model was validated against the experimental results available from Chapter 6 and showed good agreement. Then, the numerical composite model was used to perform a parametric study that helped in extending the range of variables studied in this work. The considered variables were mainly the aspect and the slenderness ratios as these are the main parameters that affect the shear strength of a plate girder.

A total of 18 specimens were tested numerically 9 of them were unstrengthened control steel plate girders and 9 were FRP strengthened ones. Only the optimized strengthening technique (CFRP-45°) was used in this parametric study. The results of the finite element model were used as benchmarks for the proposed design method.

A design equation was proposed for the unstrengthened steel plate girders (Equation 7.23) and the FRP strengthened steel plate girders (Equation 7.25) which showed good correlation with data in this work. In addition, the behaviour of the buckling curves was examined carefully for the range of data in this work and simple design shear buckling curves were proposed. This is believed to help in estimating

the stiffening effect of the FRP strengthening technique adopted in this study and hence, it could be linked to the maximum surface and secondary bending strains in the future to estimate the enhancement in the fatigue life of the FRP strengthened steel plate girders.

8.7 MAIN CONCLUSION AND THESIS STATEMENT

The current study is aimed at proposing a new strengthening technique to stiffen thin-walled steel plate girders against shear buckling and breathing. In order to ensure the viability of this technique, certain criteria must be met. The proposed strengthening technique needs to be cost effective and easy to apply. It should also maintain the typical ductile failure associated with steel plate girders, something which is usually neglected in other common strengthening techniques. Additionally it should be possible to implement the solution on only one face of the plate girder to ensure applicability in cases where reaching the second face is difficult and/or costly. Provided all these conditions can be met the method will provide a relevant and practical solution with many advantages over the limited existing techniques.

All of the goals highlighted above were achieved in the current study by proposing a new engineered preformed corrugated FRP strengthening panel. The FRP panel is bonded along the compression diagonal of the web plate in a 45° alignment scheme. The unique design of this new FRP panel enables effective stiffening of steel plate girder whilst also meeting the additional criteria outlined above. The proposed preformed corrugated FRP panel reduced the required FRP material by approximately 8 times (volumetrically) and the required epoxy bond surface area by 7 times. This leads to a reduction in the cost of the strengthening process whilst causing no reduction to bond strength of the specimen and maintaining the typical ductile failure associated with intact steel plate girders. The preservation of bond strength can be attributed to the design of the corrugated FRP panel where it is strong in the major axis along the compression diagonal and weak along the secondary axis along the tension diagonal to allow the steel plate to extend in tension without debonding.

The panel was designed to be applied to only one face of the web plate forming a prebuckling mode which forces the specimen to buckle towards the outermost

fibres of the FRP panel. This results in the FRP panel being stressed in tension, the stress state for which it performs most efficiently. The only drawback of single side application is that if the web plate has a reversed initial imperfection it could lead to a reversed buckling mode. In this case the outermost FRP fibres would be in compression instead of tension forming local wrinkles causing a premature failure of the FRP panel; however, this could only happen beyond the working stress limit. This problem can be solved by choosing the correct web face to bond the FRP panel by tracking the initial imperfection mode (which is believed to be difficult in field applications). In the latter case where it is difficult to track the initial imperfection, bonding the FRP panel to both sides of the web steel plate will be preferable. However, if this is not possible then the stiffening effect will remain the same and the fatigue performance will be enhanced as suggested. The only drawback would be that the ultimate strength will not be increased as expected, which is something unimportant unless part of the original design.

The FRP panel was optimized with respect to different variables that can affect its performance and its efficiency was tested both under static loading and a cyclic loading regime of 2 million load cycles. As a final statement, using the proposed strengthening technique minimizes the economic and temporal cost of strengthening, increases the life expectancy of the plate girder by up to 7.0 times that of the original design and increases its ultimate capacity whilst maintaining a ductile failure mode.

8.8 RECOMMENDED FUTURE WORK

The recommended future work can be summarized in the followings:

- The size of the specimen and the scale effect needs to be taken into consideration in future studies both for the steel plate girder and the proposed corrugated FRP panel because the proposed stiffening, strengthening and fatigue enhancement factors are limited to the size of the specimen and the range of data investigated in the current study.
- The effect of using a combination of different FRP material such as a mix between CFRP, GFRP and Kevlar in different lamina number and orientations may be studied to optimize the cost/strength ratio for a better economical design.

However, it is believed that using CFRP alone is sufficient to achieve the required stiffening and fatigue enhancement with very minor additional cost.

- The effect of the concrete deck needs to be taken into consideration because it affects the collapse behaviour of composite steel plate girders. However, this action is limited for the cases where strengthening (increasing the ultimate shear strength) is the critical factor and not stiffening against shear buckling for enhancing the fatigue performance.
- Environmental and temperature effects need to be taken into considerations. This can include strengthening steel bridges in hot countries where the ambient temperature could be close or even higher than the glass transient temperature of the bonding epoxy in the summer. This could lead to certain defects in the performance of the proposed strengthening technique.
- The effect of inconsistent epoxy thickness and the possible existence of weak points and air bubbles in the bonding layer need to be taken into considerations.
- Alternative mechanical anchorage may be suggested in future studies to deal with sudden loss of bond that could take place during extreme events like fire or earthquakes.
- The same proposed strengthening technique may be applied to wrought iron because it is widely used in the UK for instance and stainless steel plate girders because the cost of stainless steel is about 4 times the cost of ordinary steel and reducing the thickness of the stainless steel web could lead to ultra saving in the cost of construction, especially with the increase in its applications all over the world.
- Finally, the proposed strengthening technique may be used to stiffen any slender element in steel structures using strut and tie models. The application of this proposed strengthening technique on shear walls and shell structures is also a possible further study.

CHAPTER REFERENCES

AASHTO, LRFD-SI Units (2007). "Standard Specifications for Highway Bridges," 4th Ed., Washington, D.C, USA.

AASHTO, Standard Specifications for Highway Bridges (1973). 11th Ed. American Association of State Highway Officials, Washington, DC.

AISC, LRFD (1994). "Manual of Steel Construction, Load and Resistance Factor Design," 2nd Ed., Vol. I and II, Chicago, Illinois, USA.

AISC, Specification for the design, Fabrication and Erection of Structural Steel for Building (1963). 6th Edn. American Institute of Steel Construction, New York.

CEN, Eurocode 3: Design of Steel Structures , Part 1.5 (2004). "Plated structural elements," Milton Keynes, BSI, ENV 1993-1-5.

This page is intentionally left blank

Appendix -A-

Calladine Method for Analyzing Thin-walled Steel Plate Girders

ALGORITHM OF THE METHOD

Calladine (1973) developed a theoretical procedure to analyse the end panel of a plate girder using plastic theory. The analysis is developed to account for collapse under the action of shearing force and bending moment, simultaneously. The above mentioned procedure may summarize here in step-by-step algorithm as follows:

Step-1: Calculate the value of η as follows:

$$\eta = 1 - \frac{d}{150t} \quad \text{for } \frac{d}{t} < 150 \quad \Rightarrow \quad q = q_h \text{ (assuming buckling)}$$

$$\eta = 0 \quad \text{for } \frac{d}{t} \geq 150 \quad \Rightarrow \quad q = q_l \text{ (assuming no tension field)}$$

where:

d is the depth of the panel,

t is the thickness of the web.

Step-2: Calculate the full plastic moment of the flange, m_p, as follows:

$m_p = ¼ \text{ B} . \text{T}^2 . \sigma_y$ for flange of rectangular section.

where:

B is the width of the flange,

T is the thickness of the flange,

σ_y is the yield stress of the material in simple tension.

Step-3: Calculate the normalised full plastic moment of the flange, ξ, and its square root:

$$\xi = \frac{m_p}{b \cdot t \cdot d \cdot \sigma_y}$$

where:

b is the length of the panel.

Step-4: Use Figure (A.2) to find the dimensionless shear force, q. Note that Q is the shear capacity of the panel,

$$x = c / b$$

where c defines the location of plastic hinge, see Figure (A.1) below.

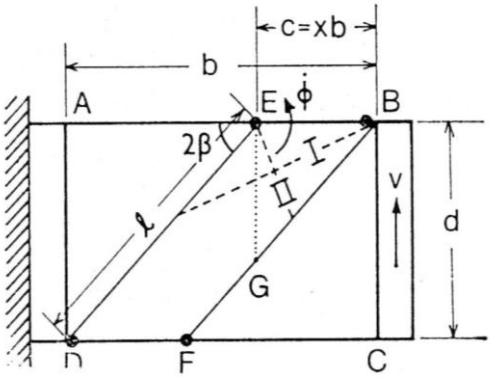

Figure (A-1): Mode of collapse: incipient collapse (Calladine, 1973).

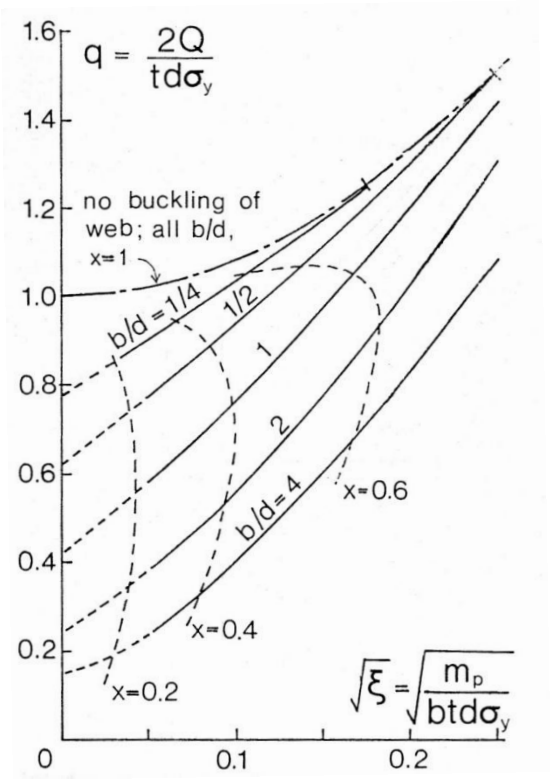

Figure (A-2): Results of basic analysis. The lower curves are on the assumption that a tension field has developed in the plastic zone of the web (Calladine, 1973).

Step-5: Now, the shear capacity of the panel, Q , can be found as follows:

$$Q = \frac{q \cdot t \cdot d \cdot \sigma_y}{2}$$

APPENDIX REFERENCES:

CALLADINE C.R. (1973). " A plastic theory for collapse of plate girders under combined shearing and bending moment," Journal of the Structural Engineer, Vol. 51, No. 4, pp. 147-154.

Appendix -B-

Cardiff Method for Analyzing Plate Girders Loaded Mainly in Shear

B.1 GENERAL

The ultimate strength of a steel plate girder depends on both the critical buckling shear stress and the development of a diagonal tension field in the web during the post-buckling phase. Cardiff Method is a well-known method to solve this problem and it was adopted by several codes of practice. However, this method is applicable in the form presented in (Porter et al., 1975) to internal web panels where the panel under consideration is supported along its transverse boundaries by adjacent web panels. Collapse mechanisms for end bay panels require special attention because of the flexibility of the end posts.

Alternatively, a rigid end post consisting of two double-sided load-bearing transverse stiffeners may be used to anchor the tension field at the end of a plate girder. This treatment is covered by BS 5950-1. The following step-by-step algorithm presents the procedure of Cardiff method for analysing steel plate girders loaded primarily in shear.

B.2 ALGORITHM OF THE METHOD

Step-1: Calculate the inclination of web panel diagonal, θ_d :

$$\theta_{\mathrm{d}} = \tan^{-1}\left(\frac{h_w}{b_w}\right)$$

Step-2: Calculate the elastic critical buckling stress of the web plate, τ_{cr} :

(**a**) Calculate the shear buckling coefficient, k_b:

$$k_b = 5.35 + 4.00 \times \left(\frac{h_w}{b_w}\right)^2 \qquad \text{for} \qquad \frac{b_w}{h_w} > 1.0$$

$$k_b = 5.35 \times \left(\frac{h_w}{b_w}\right)^2 + 4.00 \qquad \text{for} \qquad \frac{b_w}{h_w} < 1.0$$

(**b**) The elastic critical buckling shear stress then can be found:

$$\tau_{cr} = k_b \times \frac{\pi^2 \times E}{12 \times (1-\nu^2)} \times (\frac{t_w}{h_w})^2$$

Step-3: Calculate the tensile membrane stress, $\sigma^y{}_t$, using Von-Mises yield criterion:

$$\sigma^y{}_t = -\frac{3}{2} \cdot \tau_{cr} \cdot \sin 2\theta_d + \left[\sigma_{yw}{}^2 + \tau_{cr}{}^2 \{ (\frac{3}{2} \sin 2\theta_d)^2 - 3 \} \right]^{1/2}$$

where σ_{yw} is the tensile yield stress of the web steel plate.

Step-4: Calculate the values of top and bottom flanges' plastic moments of M_{pt} and M_{pb}:

$$M_{pt} = \sigma_{yft} \cdot b_{ft} \cdot \frac{t_{ft}{}^2}{4}$$

$$M_{pb} = \sigma_{yfb} \cdot b_{fb} \cdot \frac{t_{fb}{}^2}{4}$$

where t_f, b_f, and σ_{yf} are the thickness, the width, and the yields stress of the flanges, respectively; with the subscripts *t* and *b* refers to the top and bottom flanges, respectively.

Step-5: For a given steel plate girder, the only unknown in the equation of V_{ult} is the angle of inclination of the tension field, θ. This value can be found iteratively to maximize V_{ult}.

Now, start with an initial value of θ =10°, the hinge distance, $C_{t\ \&\ b}$ can be found as follows:

$$C_t = \frac{2}{\sin\theta} \left[\frac{M_{pt}}{\sigma_t \cdot t_w} \right]^{1/2}$$

$$C_b = \frac{2}{\sin\theta} \left[\frac{M_{pb}}{\sigma_t \cdot t_w} \right]^{1/2}$$

Step-6: Calculate the ultimate shear strength of the steel girder for the selected θ, V_{ult}:

$$V_{ult} = \tau_{cr} \,.\, t_w \,.\, h_w$$

$$+ \sigma^{y}_{t} \,.\, t_w \,.\, \sin^2\theta\,(C_t + C_b)$$

$$+ \sigma^{y}_{t} \,.\, t_w \,.\, h_w \,.\, \sin^2\theta\,(\cot\theta + \cot\theta_d)$$

Step-7: Increase θ by 5^o and go to Step5 to find the relevant ultimate shear strength of the girder.

Step-8: Plot θ versus V_{ult} to find optimum θ.

APPENDIX REFERENCES

PORTER D.M., ROCKEY K.C., and EVANS H.R. (1975). "The collapse behaviour of plate girders in shear," Journal of The Structural Engineer, Vol. 53, No. 8, pp. 313-325.

BRITISH STANDARDS INSTITUTION, Technical Committee B/521 (BS 5950-1: 2000). "Structural Use of Steelwork in Building, Part 1: Code of Practice for Design – Rolled and Welded Sections," London, UK, 222 pp.

This page is intentionally left blank

Appendix -C-

Matlab Code for Calculating the Global Orthogonal Engineering Constants for the Composite Numerical Model

Matlab Code

```
%This program is to find the material engineering constants in
global
%direction
%*********************************************************************
*
%
clear all;
clc
%
%GFRP
R=[-45 45 -45 45 -45 45]*pi/180;
h=0.476666/1.43;
%First Enter the 9 local Engineering Constants
E1=22088; E2=3800; v12=0.276; v23=0.3; G12=3414; G23=1308;
E3=E2;
v13=v12;
G13=G12;
%%%%%%%%%%%%%%%%%%%%%%%%%%%%%%%%%%%%%%%%%%%%%%%%%%%%%%%%%%%%%%%%%%%%%%%%
%%
%CFRP
%R=[0 90 0 90 0 90]*pi/180;
%h=0.55666667/1.67;
% First Enter the 9 local Engineering Constants
%E1=43878; E2=3800; v12=0.3; v23=0.3; G12=4025; G23=1308;
%E3=E2;
%v13=v12;
%G13=G12;
%%%%%%%%%%%%%%%%%%%%%%%%%%%%%%%%%%%%%%%%%%%%%%%%%%%%%%%%%%%%%%%%%%%%%%%%
%%
%
% Calculating the Compliance matrix components in local coordinates
Sbar(1:6,1:6)=0;
Sbar(1,1)=1/E1;
Sbar(1,2)=-1*v12/E1;
Sbar(1,3)=-1*v13/E1;
Sbar(2,1)=Sbar(1,2);
Sbar(2,2)=1/E2;
Sbar(2,3)=-1*v23/E2;
Sbar(3,1)=Sbar(1,3);
Sbar(3,2)=Sbar(2,3);
Sbar(3,3)=1/E3;
Sbar(4,4)=1/G23;
Sbar(5,5)=1/G13;
Sbar(6,6)=1/G12;
%Sbar
Ctotal(1:6,1:6)=0;
for z=1:length(R)
%Finding T matrix.
l1=cos(R(z));
```

```
m1=sin(R(z));
n1=0;
l2=-1*sin(R(z));
m2=cos(R(z));
n2=0;
l3=0;
m3=0;
n3=1.0;
a=[l1,m1,n1;l2,m2,n2;l3,m3,n3];
T(1:6,1:6)=0;
for i=1:1:3
    for j=1:1:3
        if i==j; alpha=j;else alpha=9-i-j;end
       for p=1:1:3
           for q=1:1:3
               if p==q beta=p; else beta=9-p-q; end
               T(alpha, beta)=0;
               if alpha<=3 & beta<=3;
T(alpha,beta)=a(i,p)*a(i,p);end
               if alpha>3 & beta<=3; T(alpha,beta)=a(i,p)*a(j,p);end
               if alpha<=3 & beta>3;
T(alpha,beta)=a(i,q)*a(i,p)+a(i,p)*a(i,q);end
               if alpha>3 & beta>3;
T(alpha,beta)=a(i,p)*a(j,q)+a(i,q)*a(j,p);end
           end
       end
    end
end
T=double(T);
%Find S=[Ttransopose][Sbar][T]
S=T'*Sbar*T;
C=inv(S);
Ctotal=Ctotal+(C*h);
end
%Ctotal
Sglobal=inv(Ctotal);
Ex=1/Sglobal(1,1)
Ey=1/Sglobal(2,2)
Ez=1/Sglobal(3,3)
Gyz=1/Sglobal(4,4)
Gxz=1/Sglobal(5,5)
Gxy=1/Sglobal(6,6)
vxy=-1*Sglobal(2,1)/Sglobal(1,1)
vxz=-1*Sglobal(3,1)/Sglobal(1,1)
vyz=-1*Sglobal(3,2)/Sglobal(2,2)
```

فحص مصنّع خصيصاً لهذا الغرض باسم "إطار الصورة" والذي تم تصميمه لتسليط الشروط المحيطية والإجهادات التي تماثـــل تلك المسلطة على اللوحة الجذعية في الرافدة الصفائحية. هذه السلسلة الأولية من الفحوصات تحققت من أداء أشكال مختلفة من التقوية تحت تأثير الأحمال الساكنة كمقدمة تحضيرية لسلسلة أخرى من الفحوصات تحت تأثير الأحمال الدورية للتحقق من أدائها الكَلَلِي. تضمنت المتغيرات نوع ألياف التسليح المستخدمة في ألواح البوليمرات المموجة (ألياف كاربون وألياف زجاجية) ومقطع اللوح المموّج (مفتوح أو مغلق) وعدد الطبقات المستخدمة واتجاه الألياف الزجاجية المستخمة في تصنيع اللوح المموج. في السلسلة الثانية من الفحوصات، تم تصنيع ستة نماذج تمثل القسم الطرفي من رافدة صفائحية. تمّ تقوية هذه النماذج بلوح التقوية المموّج المختار من سلسلة الفحوصات السابقة وفحصها تحت تأثير أحمال القص الدورية وبسعة طورية تبلغ 40% - 80% من التحمل السكوني الأقصى.

لقد تم الحصول على زيادة ذات دلالة بيّنة في جساءة النماذج المقوّاة من خلال التقليل الواضح في مقدار الانبعاج خارج مستوي الصفيحة. تم تقدير جساءة النماذج المقوّاة بحوالي 3 إلى 9 أضعاف جساءة النماذج غير المقوّاة اعتماداً على نوع الألياف المستخم والنسبة الباعية للنماذج المفحوصة. كذلك تم تقليل ظاهرة التنفس في الصفيحة الجذعية بشكل ملحوظ مما أدى إلى تقليل الإجهادات السطحية والغشائية وإجهادات الإنحناء الثانوية. نجح نظام التقوية بزاوية 45 درجة بشكل أفضل من باقي أنظمة التقوية المقترحة في تقليل إجهدات ظاهرة التنفس وزيادة قابيلة التحمل لإجهادات القص بنسبة 88%.

أشار تحليل الكلل إلى أن نظام التقوية المقترح قادر على زيادة العمر المتوقع للروافد الصفائحية المقوّاة بمعامل يترواح بين 2.5 و7 أضعاف اعتماداً على السعة الطورية للأحمال الدورية المسلطة. بالإضافة إلى ذلك، فإن تقنيّة التقوية المقترحة لم تُظْهِر أيّ فقدان في خاصيّة الإلتصاق بين طبقات ألواح البوليمرات المسلحة بالألياف أو بينها وبين سطح الصفيحة الحديدية تحت الأحمال الساكنة والدورية على حدٍ سواء، وهذا يجعل منها مرشحاً جيداً لتقوية العنصار الإنشائية الرقيقة أو النحيفة وخاصةً عندما تكون مرونة المنشأ على المحك. في الواقع، فإن تقنيّة التقوية المقترحة نجحت في تحسين مستوى الصلابة أو الطاقة المطلوبة لإتمام عملية التحميل لحين الفشل بمعامل يتراوح بين 1.5 و 2.5 ضعفاً بالمقارنة مع النماذج المقابلة غير المقوّاة وهذا يعني أنه لم يتم المحافضة على طبيعة الفشل المرن النمطية الخاصة بالروافد الصفائحية تحت تأثير أحمال القص فقط وإنما تمّ تحسينها كذلك. هذا النوع من الفشل المرن ليس دارجاً عند استخدام تقانات التقوية الأخرى باستخدام البوليمرات المسلحة بالألياف كما هو الحال في تقنيّة التقوية المقترحة.

أخيراً وليس آخراً، تمّ عرض نموذج رياضي لاخطّي (على صعيد المادة المستخدمة والتشوهات المأخوذة بنظر الاعتبار) سواءاً للحديد أو للمقطع المركّب بعد التقوية. هذا النموذج الرياضي أثبت كفاءةً في التماشي مع نتائج الفحوصات وفي قدرته العالية على استنباط كلاً من المقاومة والانفعالات الخاصة بالنماذج المفحوصة. لقد تمّ استعمال هذا النموذج الرياضي في دارسة المتغيرات التي تؤثر على مقاومة الروافد الصفائحية المقوّاة وغير المقوّاة لدعم طريقة التصميم المقترحة.

الْمُسْتَخْلَصْ

يُواجِهُ المهندِسُون المدنيون في وقتنا الحاضر تحدي تقوية وإصلاح العديد من المنشآت القائمة لضمان وتحسين مستوى سلامتها الإنشائية لأسباب منها تغيير الغرض من استخدام المنشأ وازدياد الأحمال المرورية على الجسور. في العراق على سبيل المثال لا الحصر، فإن الكثير من الجسور السريعة كانت بحاجة لاستيعاب أحمال المركبات المتزايدة خلال عملية نقل المولّدات العملاقة الخاصة بمحطات توليد الطاقة الكهربائية. على كل حال، فإن متطلبات طرق تقوية وإصلاح المنشأ مدفوعة بالحاجة لضمان السلامة والإستدامة للبنى التحتية المتقادمة في العمر على المستوى العالمي والتي يبدوا أنها تتدهور بتسارع أكبر من الإمكانيات المتاحة لإعادة إعمارها وتجديدها. إن الضرر المتزايد بشكل مستمر بسبب التأثيرات البيئية وتآكل الحديد و تدهور الخرسانة تقلل من سلامة المنشآت وتؤدي إلى عرقلة المستخدمين والذي بدوره قد يؤدي إلى عواقب اقتصادية وخيمة.

في الجسور الصفائحية، فإن الروافد الصفائحية عادةً ما تتكون من عتبات على شكل الحرف اللاتيني (I) مصنّعة من مجموعة من الصفائح الحديدية الإنشائية (وليس على شكل مقطع حديدي مصبوب في قالب واحد) غالباً ما تكون ملحومة أو مرتبطة بواسطة براغي، كما هو الحال في الجسور القديمة، لتشكّل الجذع العمودي والشفة الأفقية للعتبة. الوظيفتان الرئيستان لصفيحة الجذع الحديدية في أي رافدة صفائحية هي الإبقاء على مسافة ثابتة بين الشفتان العلوية والسفلية وكذلك لمقاومة إجهادات القص الناتجة عن الأحمال. في معظم الفضائات العملية للجسور المكونة من الروافد الصفائحية فإن إجهادات القص المسلطة تكون قليلة نسبياً عند مقارنتها مع إجهادات الإنحناء في الشفتين والناتجة عن العزوم المسلطة. وكنتيجة لذلك فإن صفيحة الجذع عادةً ما يتم اختيارها أنحف بكثير من صفائح الشفتين. ولهذا السبب فإن اللوحة الجذعية تنبعج تحت تأثير إجهادات قص قليلة نسبياً. بالنسبة للجسور المكونة من روافد صفائحية تحت تأثير أحمال دورية، كما هو الحال مع الأحمال الدورية الناتجة من محاور العجلات على الجسور، هذا يمكن أن يؤدي إلى الظاهرة المعروفة بظاهرة التنفّس، وهي ظاهرة انباعج اللوح الجذعي ذهاباً وإياباً خارج المستوي الأساسي للصفيحة والتي بدورها تؤدي إلى تسليط إجهادات إنحناء ثانوية عالية في منطقة اللحام المتاخم لمحيط الصفيحة الجذعية.

في هذا البحث يتم تطبيق تقنيّة تقوية جديدة باستخدام مقاطع من البوليمرات المسلحة بالألياف والتي تلصق على الصفيحة الحديدية لمقاومة تشوهات الإنبعاج وما ينتج عنها من إجهادات إنحناء ثانوية متأتية عن ظاهرة التنفس آنفة الذكر وأيضاً لإطالة عمر الكلل للروافد الصفائحية. هذه الطريقة الجديدة مختلفة تماماً عن غالبية تطبيقات التقوية بالبوليمرات المسلحة بالألياف والتي تستغل مقاومة الشد العالية لهذه الألياف.

إن الهدف من البرنامج العملي الحالي هو تقوية الروافد الصفائحية المصنّعة من صفائح نحيفة ضد الإنبعاج تحت تأثير حمل القص باستخدام ألواح مموّجة مصنّعة من البوليمرات المسلحة بألياف الكاربون والزجاج وملصوقة خارجياً على طول القطر الإنضغاطي للصفيحة الجذعية. لقد تم تقسم البرنامج العملي إلى ثلاثة مراحل رئيسية، (1) تطوير لوح مموج جديد مصنوع من البوليمرات المسلحة بالألياف، (2 و 3) فحص أدائه من خلال سلسلتين فحص مختبرية متتالية. سلسلة الفحص الأولية تضمنت فحصوصات على ثلاثة عشرة صفيحة حديدة تم تقويتها باستخدام تقنيـــة الألواح المموّجة المقترحة والمصنّعة من البوليمرات المسلحة بالألياف والمعرضة لأحمال قصّية باستخدام هيكل

قَابِلِيَةُ الْتَحَمُّلِ لِلْرَوَافِدِ الْصفَائِحِيَّةِ الْمُقَوَّاةُ بِالْبُولِيمَرَاتِ الْمُسَلَّحَةِ بِالْأَلْيَافِ ضِدَّ إِنْبِعَاجِ الْقَصِّ تَحْتَ الْأَحْمَالِ الْسَاكِنَةِ وَالْدَوْرِيَّةِ

زَيْد مُحَمَّد كَانِي الْعَزَّاوِي

أُطْرُوحَةٌ مُقَدَّمَةٌ لِغَرَضِ نَيْلِ شَهَادَةِ الْدُكْتُورَاه فِي
الْهَنْدَسَةِ الْإِنْشَائِيَّةِ

THE UNIVERSITY
of EDINBURGH

رَجَبْ الْطَيِّبْ 1437هـ

أيار 2016م